VOL.
12
59/60

THE PHYSICS AND CHEMISTRY OF SOLIDS

AN INTERNATIONAL JOURNAL

VOLUME 12 1959/60

Editor-in-Chief HARVEY BROOKS *Cambridge, Mass.*

Associate Editors
H. B. G. CASIMIR *Eindhoven*
G. J. DIENES *Brookhaven*
JACQUES FRIEDEL *Paris*
E. M. LIFSHITZ *Moscow*

Editorial Advisory Board

U.S.A.
E. N. ADAMS, Pittsburgh
D. ALPERT, Illinois
L. APKER, Schenectady
J. BARDEEN, Illinois
D. S. BILLINGTON, Oak Ridge
R. G. BRECKENRIDGE, Cleveland
LEO BREWER, Berkeley, Calif.
E. BURSTEIN, Penn.
J. A. BURTON, New Jersey
N. CABRERA, Virginia
G. C. DANIELSON, Iowa
I. ESTERMANN, Washington, D.C.
J. C. FISHER, Schenectady
F. HERMAN, Princeton
CONYERS HERRING, New Jersey
A. R. VON HIPPEL, Cambridge, Mass
J. H. HOLLOMON, Schenectady
W. V. HOUSTON, Houston
H. B. HUNTINGTON, Troy
H. M. JAMES, Purdue
JOHN G. KIRKWOOD, Yale
C. KITTEL, Berkeley, Calif.
W. KOHN, Pittsburgh
J. A. KRUMHANSL, Cleveland
A. W. LAWSON, Chicago
H. W. LEVERENZ, Princeton
O. T. MARZKE, Pittsburgh
B. T. MATTHIAS, New Jersey
L. R. MAXWELL, Silver Spring
JOSEPH E. MAYER, Chicago
E. W. MONTROLL, Maryland
DAVID PINES, Princeton
GEORGE T. RADO, Washington, D.C.
H. REISS, New Jersey
J. R. REITZ, Cleveland
A. ROSE, Princeton
O. C. SIMPSON, Argonne
R. SMOLUCHOWSKI, Pittsburgh
F. H. SPEDDING, Iowa
D. TURNBULL, Schenectady
J. H. VAN VLECK, Harvard
B. E. WARREN, Cambridge, Mass.
EUGENE P. WIGNER, Princeton
B. H. ZIMM, Schenectady

Canada
R. E. BURGESS, Vancouver
D. K. C. MACDONALD, Ottawa

United Kingdom
A. CHARLESBY, Shrivenham, Berks.
W. J. DUNNING, Bristol
F. C. FRANK, Bristol
H. K. HENISCH, Reading
H. JONES, London
J. W. MITCHELL, Bristol
A. B. PIPPARD, Cambridge
M. H. L. PRYCE, Bristol
R. A. SMITH, Malvern
K. W. H. STEVENS, Nottingham
F. C. TOMPKINS, London

France
E. F. BERTAUT, Grenoble
A. GUINIER, Paris
LOUIS NÉEL, Grenoble
LOUIS WEIL, Grenoble

Germany
M. BORN, Bad Pyrmont
ULRICH DEHLINGER, Stuttgart
R. HILSCH, Göttingen
G. LEIBFRIED, Aachen
E. MOLLWO, Erlangen
H. PICK, Stuttgart
M. VON LAUE, Berlin
H. WELKER, Erlangen

Italy
F. G. FUMI, Pavia

Czechoslovakia
J. TAUC, Praha

Japan
TOSHINOSUKE MUTO, Tokyo

The Netherlands
A. MICHELS, Amsterdam
G. W. RATHENAU, Amsterdam

Sweden
J. O. LINDE, Stockholm
PER-OLOV LÖWDIN, Uppsala

Switzerland
G. BUSCH, Zurich
P. SCHERRER, Zurich

U.S.S.R.
G. S. ZHDANOV, Moscow

PERGAMON PRESS NEW YORK · LONDON · PARIS · LOS ANGELES

NOTES FOR CONTRIBUTORS

I. GENERAL

1. Submission of a paper to the *Journal of the Physics and Chemistry of Solids* will be taken to imply that it represents original research not previously published (except in the form of an abstract or preliminary report), that it is not being considered for publication elsewhere, and that if accepted, it will not be published elsewhere in the same form, in any language, without the consent of the editor-in-chief. It should deal with original research work in the field of the physics and chemistry of solids.

2. Papers should be submitted to the appropriate regional editor (all English-language papers to be sent to the U.S. editor).

3. Papers will be published as quickly as possible after acceptance, and, subject to space being available, should appear in the following issue, if this is due for publication not earlier than three months after the acceptance date. Short communications under the heading of "Letters to the Editor" will receive priority for publication, and will be published in the issue following receipt, if accepted not later than the beginning of the month preceding publication.

4. Fifty free reprints of each paper are supplied. Additional copies can be obtained at a reasonable cost if ordered when proofs are returned. A reprint order form will accompany first proofs.

II. SCRIPT REQUIREMENTS

1. Papers submitted should be concise and written in a readily understandable style. Scripts should be typed and double spaced and submitted in duplicate to facilitate refereeing.

It will be appreciated if authors clearly indicate any special characters used. An abstract, not exceeding 200 words, should be provided in the language of the paper. French and German papers should be submitted with English abstract and titles, but if this is not possible the abstract will be translated by the publishers. To conserve space, authors are requested to mark less important parts of the paper, such as details of experimental technique, methods, mathematical derivations, etc. for printing in small type. The technical description of methods should be given in detail only when such methods are new. Authors will receive proofs for correction when their papers are first set; page proofs will be sent only when the amount of alteration makes it advisable.

2. Illustrations should not be included in the typescript of the paper, and legends should be typed on a separate sheet. Line drawings which require redrawing should include all relevant details and clear instructions for the draughtsman. If figures are already well drawn it may be possible to reproduce them direct from the originals, or from good photo-prints if these can be provided. It is not possible to reproduce from prints with weak lines. Illustrations for reproduction should normally be about twice the final size required. The lettering should be sufficiently large and bold to permit this reduction. Photographs should only be included where they are essential.

3. Tables and figures should be so constructed as to be intelligible without reference to the text. Every table and column should be provided with an explanatory heading. Units of measure must always be clearly indicated. The same data should not be published in both tables and figures. The following standard symbols should be used on line drawings since they are easily available to the printers: ○, ●, +, ×, □, ■, △, ▲, ◇, ◆, ▽, ▼.

4. References are indicated in the text by superior numbers in parentheses, and the full reference should be given in a list at the end of the paper in the following form:

1. HILL R., *J. Iron St. Inst.* **158**, 177 (1948).
2. PEARSON C., *The Extrusion of Metals*, p. 137. Chapman and Hall, London (1944).

Abbreviations of journal titles should follow those given for *Physics Abstracts*. It is particularly requested that authors' initials, and appropriate volume and page numbers, should be given in every case.

Footnotes, as distinct from literature references should be indicated by the following symbols—*, †, ‡, ‡‡, commencing anew on each page; they should *not* be included in the numbered reference system.

5. Due to the international character of the journal no rigid rules concerning notation and spelling will be observed, but each paper should be consistent within itself as to symbols and units.

VOL.
12
59/60

VO
1
1959/

VOL.
12
59/60

CONTENTS

NUMBER 1

J. YAMASHITA and K. INOUE: Hot electron in *n*-type germanium 1

J. BLOEM, C. HAAS and P. PENNING: Properties of oxygen in germanium 22

D. M. GRIMES, R. D. HARRINGTON and A. L. RASMUSSEN: Magnetic properties of polycrystalline material . 28

O. L. ANDERSON: The Debye temperature of vitreous silica 41

P. FLUBACHER, A. J. LEADBETTER, J. A. MORRISON and B. P. STOICHEFF: The low-temperature heat capacity and the Raman and Brillouin spectra of vitreous silica 53

J. W. CARSON, D. F. HOLCOMB and H. RUCHARDT: Microwave studies of color centers in barium oxide . 66

J. P. SUCHET: Règles des prédiction de la semiconductibilité dans les réseaux cristallins minéraux . . 74

P. N. ARGYRES and L. M. ROTH: Theory of electrical conduction in high magnetic fields 89

H. EHRENREICH: Electron mobility of indium arsenide phosphide [$In(As_yP_{1-y})$] 97

Letters to the Editor:

A. C. DAMASK and G. J. DIENES: Neutron-irradiation effects in copper-aluminum alloys 105

M. S. WECHSLER and R. H. KERNOHAN: Reply to letter of DAMASK and DIENES on "Neutron-irradiation effects in coppei-aluminum alloys" 107

NUMBER 2

S. GELLER, R. M. BOZORTH, M. A. GILLEO and C. E. MILLER: Crystal chemical and magnetic studies of garnet systems $M_3^{2+}Fe_2Sn_3O_{12}$— $Y_3Fe_2Fe_3O_{12}$ 111

C. CHILDS and L. SLIFKIN: Annealing of silver chloride crystals containing internal print-out 119

J. W. STEWART: Phase transitions and compressions of solid CH_4, CD_4 and O_2 122

R. M. BARRER and G. C. BRATT: Non-Stoichiometric hydrates—I. Sorption equilibria and kinetics of water loss for ion-exchanged near-faujasites 130

R. M. BARRER and G. C. BRATT: Non-Stoichiometric hydrates—II. Some heats and entropies for water and ammonia in ion-exchanged faujasites 146

R. M. BARRER and G. C. BRATT: Non-Stoichiometric Hydrates—III. The relative importance of cations and of anionic framework in determining the energetics of zeolitic water 154

T. OLSEN: Lattice thermal conductivity in copper alloys 167

A. C. PRIOR: The field-dependence of carrier mobility in silicon and germanium 175

E. O. KANE: Zener tunneling in semiconductors 181

G. W. BRYANT, J. HALLETT and B. J. MASON: The epitaxial growth of ice on single-crystalline substrates . 189

J. S. LANGER and S. H. VOSKO: The shielding of a fixed charge in a high-density electron gas 196

Letters to the Editor:

B. BARANOWSKI and M. SMIALOWSKI: Charging of nickel films with hydrogen evolved electrolytically in the presence of catalytic poisons 206

H. N. HERSH and J. J. MARKHAM: Effects of plastic deformation at 300°K on the X-ray production of color centers in KCl at 5 and 78°K 207

J. C. PHILLIPS: Optical absorption in germanium 208

Book Review 210

NUMBERS 3/4

M. AVINOR and G. MEIJER: Vanadium activated zinc and cadmium sulphide and selenide phosphors . . 211

JEAN PERETTI: Some remarks about frequency spectra of crystal lattices 216

G. SCHAEFER: Das ultrarote Spektrum des *U*-Zentrums 233

G. A. SWARTZ: Low-temperature Hall coefficient and conductivity in heavily doped silicon 245

L. A. GIRIFALCO and V. G. WEIZER: Vacancy relaxation in cubic crystals 260

F. E. WILLIAMS: Theory of the energy levels of donor-acceptor pairs 265

J. J. HOPFIELD and D. G. THOMAS: On some observable properties of longitudinal excitons 276

J. R. DRABBLE and R. D. GROVES: The effect of strain on the Seebeck coefficient of *n*-type germanium . . 285

R. BLINC and I. LEVSTEK: NMR and IR study of $(NH_4)_2SO_4$ and $(NH_4)_2BeF_4$ 295

A. SEEGER und H. KRONMÜLLER: Die Einmündung in die ferromagnetische Sättigung—I. Allgemeine Theorie des Einflusses innerer Spannungen auf das Einmündungsgesetz, mit Anwendungen auf Zwischengitteratome und abgeschreckte Metalle 298

E. MANN und A. SEEGER: Zur halbempirischen Bestimmung der Born–Mayer Konstanten von kubisch-flächenzentrierten Metallen, insbesondere von Kupfer 314

A. SEEGER und E. MANN: Bildungsenergien und Gitterverzerrungen von Zwischengitteratomen und Leerstellen in kubisch-flächenzentrierten Kristallen, insbesondere in Kupfer 326

W. GEIGER und M. KULP: Brillouinstreuung an künstlichen Quarzgläsern 341

S. TUTIHASI: Ultraviolet absorption in thallous halides 344

Letters to the Editor:

J.-P. JAN, S. STEINMANN and P. DINICHERT: The density and lattice parameters of ruby . . . 349

J. ZUCKER: Mobility in high-resistivity germanium at high d.c. electric fields 350

Book Reviews 353

Erratum 354

AUTHOR INDEX TO VOLUME 12

(B) denotes book review

ANDERSON, O. L. 41
ARGYRES, P. N. 89
AVINOR, M. 211
BARANOWSKI, B. 206
BARRER, R. M. 130, 146, 154
BLINC, R. 295
BLOEM, J. 22
BOZORTH, R. M. 111
BRATT, G. C. 130, 146, 154
BRYANT, G. W. 189
CARSON, J. W. 66
CHILDS, C. 119
DAMASK, A. C. 105
DIENES, G. J. 105
DINICHERT, P. 349
DRABBLE, J. R. 285
EHRENREICH, H. 97
FLUBACHER, P. 53
GEIGER, W. 341
GELLER, S. 111
GILLEO, M. A. 111
GIRIFALCO, L. A. 260
GRIMES, D. M. 28
GROVES, R. D. 285
HAAS, C. 22
HALLETT, J. 189
HARRINGTON, R. D. 28
HERSCH, H. N. 207
HILL, T. L. 210 (B)
HOLCOMB, D. F. 66
HOPFIELD, J. J. 276
INOUE, K. 1
JAN, J.-P. 349
KANE, E. O. 181
KERNOHAN, R. H. 107
KRONMÜLLER, H. 298
KULP, M. 341
LANGER, J. S. 196
LEADBETTER, A. J. 53
LEVSTEK, I. 295
MANN, E. 314, 326
MARKHAM, J. J. 207
MASON, B. J. 189
MEIJER, G. 211
MILLER, C. E. 111
MORRISON, J. A. 53
OLSEN, T. 167
PENNING, P. 22
PERETTI, J. 216
PHILLIPS, J. C. 208
PRIOR, A. C. 175
RASMUSSEN, A. L. 28
ROTH, L. M. 89
RUCHARDT, H. 66
SCHAEFFER, F. 233
SEEGER, A. 298, 314, 326
SLIFKIN, L. 119
SMIALOWSKI, M. 206
STEINEMANN, J. 349
STEWART, J. W. 122
STOICHEFF, B. P. 53
SUCHET, J. P. 74
SWARTZ, G. A. 245
THOMAS, D. G. 276
TUTIHASI, S. 344
VOSKO, S. H. 196
WECHSLER, M. S. 107
WEIZER, V. G. 260
WILLIAMS, F. E. 265
YAMASHITA, J. 1
ZUCKER, J. 350

VOL.
12
59/60

VOL.
12
1959/60

J. Phys. Chem. Solids Pergamon Press 1959. Vol. 12. pp. 1–21 Printed in Poland.

HOT ELECTRON IN *n*-TYPE GERMANIUM

JIRO YAMASHITA and KENZO INOUE

Institute for Solid State Physics,
University of Tokyo, Tokyo, Japan

(*Received* 8 *April* 1959)

Abstract—The non-ohmic current in a many-valley semiconductor has been investigated by considering scattering by acoustic and optical modes of vibrations and intervalley scatterings. The intensity of these interactions has been determined from observed data for the temperature-dependence of the ohmic current, and the acousto-electric effect. The theoretical result for the drift velocity is in good quantitative agreement with the observations of GUNN and of RYDER over a wide range of the applied field. The anisotropy in the hot-electron current observed by SASAKI *et al.* is also discussed.

1. INTRODUCTION

IN previous papers,[1,2] which we shall designate I and II, the non-ohmic current in non-polar crystals was investigated. In paper I, a simplified model was used in which the energy surfaces in k-space were assumed to be spherical and the conduction electrons interacted only with the acoustic mode of vibration. By solving the Boltzmann equation for this model to higher orders, we found that the conduction-electron distribution is not Maxwellian, and non-ohmic characteristics follow from the new distribution of electrons in the strong electric field. Although the simplified theory can give a qualitative description of the observed non-ohmic current in germanium and silicon, the quantitative results of the theory are not satisfactory. In particular, quantitative discrepancy is serious in β, which is defined by:

$$\sigma = \sigma_0(1+\beta F^2),$$

when the external field is weak. Here σ is the observed conductivity in n-type germanium, σ_0 is the ohmic conductivity, and F is the intensity of the external field.

In paper II, we considered also the interaction between the conduction electrons and optical modes of vibration. We determined the coupling constant of the interaction, so as to give the correct temperature-dependence of mobility in n-type germanium from 90°K to room temperature. Then, we found that the theoretical values of β at 90°K and room temperature are in good quantitative agreement with experiments, in spite of adopting an unrealistic simplification of the spherical energy surfaces. In the paper II, however, we did not consider the behaviour of the current in the hot-electron region.

The main purpose of the present paper is to compute the hot-electron current for any field intensity and to compare the results with available data on n-type germanium. We shall also remove the restriction of the spherical energy surfaces. Then, we shall find that the current due to the hot electron is anisotropic in some extent.

When we reduced the Boltzmann equation to a solvable form in the previous papers, we neglected some terms without explicit justification. A secondary objective of the paper

is to examine the process of reduction in each step, and to establish the theory on a sounder foundation.

2. BOLTZMANN EQUATION FOR A SIMPLE MODEL

(A) In this section we shall make a systematic investigation of the Boltzmann equation for a simplified model in which the energy surfaces in k-space are assumed to be spherical and scattering is caused only by the interaction with acoustic vibrations. Let us start from the Boltzmann equation:*

$$\left[\frac{\partial f}{\partial t}\right]_{\text{field}} + \left[\frac{\partial f}{\partial t}\right]_{\text{Coll}} = 0.\dagger \tag{1}$$

We assume that the first term is given by:

$$\left[\frac{\partial f}{\partial t}\right]_{\text{field}} = \frac{e}{\hbar} F \cdot \nabla_k f, \tag{2}$$

where f is the distribution function and the derivative is taken to the field direction. In considering the lattice scattering, we assume that the scattering is approximately isotropic. Then, following usual procedures, we obtain the second term in equation (1):

$$\left[\frac{\partial f}{\partial t}\right]_{\text{Coll}} = \frac{VC^2 m}{18\pi^2 M \sqrt{2m}\,\hbar c} \frac{1}{\sqrt{E}} \int_0^{2\pi} \times$$

$$\times d\Phi \int_{g_{\min}}^{g_{\max}} \frac{g^2 dg}{e^{x_g} - 1} \left[\{f(\vec{K}+g)\, e^{x_g} - f(\vec{K})\} + \right.$$

$$\left. + \{f(\vec{K}-g) - f(\vec{K}) e^{x_g}\}\right]. \tag{3}$$

Here V is the crystal volume, C is an energy parameter describing the coupling between conduction electrons and the acoustic vibrations, c is the velocity of sound, M is the mass of the ion, K is a wave number of conduction electrons, E is the energy of conduction electrons, which is assumed to be $E = \hbar^2 K^2/2m$, m is the effective mass of conduction electrons, q is a wave number of acoustical lattice vibrations, ω_q is a circular frequency of the longitudinal mode associated with q, which is assumed to be $\omega_q = cq$, x_q is defined by $x_q = \hbar\omega_q/kT$, k is the Boltzmann constant, and finally T is the absolute temperature.

Now, let us expand the distribution function by a series of spherical harmonics:

$$f = f_0(E) + Kg_1(E)P_1(\Theta) + \\ + K^2 g_2(E) P_2(\Theta) + \ldots, \tag{4}$$

where we measure the angle Θ from the field direction, which is identified as a z-axis. From equations (4) and (3) we have:

$$\left[\frac{\partial f}{\partial t}\right]_{\text{field}} = \frac{eF}{\hbar}\left[g_1 + \frac{2}{3} E \frac{dg_1}{dE} + \frac{\hbar^2}{m}\frac{df_0}{dE} K_z + \right.$$

$$\left. + 2g_2 K_z + \frac{4}{3} E \frac{dg_1}{dE} P_2(\Theta) + \ldots\right]. \tag{5}$$

Inserting equation (4) into (3) and performing some computations, we obtain expression (6) on the following page.

Here we have made some approximations in the derivation of second and third terms, and we have disregarded the terms beyond $P_2(\Theta)$. The validity of these procedures is discussed in Appendix I. Inserting equations (5) and (6) into (1) and arranging terms of the same

* Recently, the basis of the Boltzmann equation has been studied by many investigators, and it is to be hoped that these studies will be extended to the non-ohmic region. At present the validity of equation (1) for a non-ohmic region is assumed. Later we shall find that the theory gives reasonable results, so that the Boltzmann equation may be applicable to the hot-electron problem in non-polar crystals, except when the field intensity is extremely high.

† Here we do not consider the effect of electron-electron collisions. We hope to develop a theory to include this effect.

$$\left[\frac{\partial f}{\partial t}\right]_{\text{Coll}} = \frac{VC^2m}{9\pi M\sqrt{2m}\,\hbar c}\frac{1}{\sqrt{E}}\left[\int_{q_{\min}}^{q_{\max}}\frac{q^2dq}{e^{xq}-1}\{[f_0(E+\hbar\omega_q)\,e^{xq}-f_0(E)]+\right.$$
$$+[f_0(E-\hbar\omega_q)-f_0(E)\,e^{xq}]\}+$$
$$\left.+\frac{8mkT}{\hbar^3c}EK_zg_1(E)+\frac{32m^2kT}{\hbar^5c}E^2g_2(E)P_2(\Theta)\right]. \quad (6)$$

angular dependence, we have a system of equations:

$$\beta_1(E)=\frac{9\pi M\sqrt{2m}\,\hbar^5c^2e}{8VC^2m^3(kT)^2\sqrt{E}}\alpha_0(E). \quad (12)$$

$$\frac{VC^2m}{9\pi M\sqrt{2m}\,\hbar c}\frac{1}{\sqrt{E}}\int_{q_{\min}}^{q_{\max}}\frac{q^2\,dq}{e^{xq}-1}\{[f_0(E+\hbar\omega_q)\,e^{xq}-f_0(E)]+$$
$$+[f_0(E-\hbar\omega_q)-f_0(E)\,e^{xq}]\}=\frac{eF}{\hbar}\left(g_1+\frac{2}{3}E\frac{dg_1}{dE}\right), \quad (7)$$

$$g_1(E)=-\frac{9\pi M\sqrt{2m}\,\hbar^5c^2eF}{8VC^2m^3kT}\frac{1}{\sqrt{E}}\left\{\frac{df_0}{dE}+\frac{m}{\hbar^2}(2g_2)\right\}, \quad (8)$$

and

$$g_2(E)=\frac{3\pi M\sqrt{2m}\,\hbar^5c^2eF}{8VC^2m^3kT}\cdot\frac{1}{\sqrt{E}}\cdot\frac{dg_1}{dE}. \quad (9)$$

Now, we expand each component of the distribution function by a power series of F:

$$\left.\begin{aligned} f_0(E)&=\sum_n\alpha_n(E)\,F^n,\\ g_1(E)&=\sum_n\beta_n(E)\,F^n,\\ g_2(E)&=\sum_n\gamma_n(E)\,F^n. \end{aligned}\right\} \quad (10)$$

We insert equation (10) into equations (7), (8), and (9) and pick up terms of the same power of F. Then, we can determine α_n, β_n, and γ_n by successive approximations. We can immediately find that:

$$\alpha_0(E)=\frac{2}{\sqrt{\pi}(kT)^{3/2}}\exp(-E/kT) \quad (11)$$

satisfies equation (8). We also find that $\beta_0=0$ and β_1 is:

Then, by the usual procedures, we see that the ohmic current comes from this term and ohmic mobility μ_a is given by:

$$\mu_a=\frac{3\pi M\hbar^4c^2e}{VC^2kTm^2\sqrt{2\pi mkT}}. \quad (13)$$

Here the suffix a indicates the acoustic mobility. By successive approximation we also find that

$$\alpha_1=\alpha_3=\alpha_5=\ldots\ldots=0,$$
$$\beta_0=\beta_2=\beta_4=\ldots\ldots=0,$$
$$\gamma_0=\gamma_1=\gamma_3=\gamma_5=\ldots\ldots=0$$

and finally γ_2 is given by:

$$K^2\gamma_2=\frac{\pi}{8}m\left(\frac{1}{kT}+\frac{1}{2E}\right)\mu_\alpha^2\alpha_0(E). \quad (14)$$

Then, we see that the ratio $K^2\gamma_2F^2/\alpha_0$ is approximately given by

$$\frac{\pi}{4}\left(\frac{1}{2}m\bar{v}^2/kT\right),$$

VOL. 12 59/60

where $\bar{v} = \mu_a F$ is the drift velocity of conduction electrons. Since $K\beta_1 F$ is written as

$$\left(\frac{3\sqrt{\pi}}{2}\right)\left(\frac{1}{2}\, m\bar{v}^2/kT\right)^{1/2}\alpha_0(E),$$

we see that series (4) is decreasing with the ratio $(\frac{1}{2}\, m\bar{v}^2/kT)^{1/2}$. This ratio is quite small in a n-type germanium for a moderate field intensity, so that we may safely disregard the third term in series (4). When the field becomes large, we must derive the ratio in another way, and we shall discuss this later.

In order to determine α_n explicitly, we must introduce some approximations. Let us expand the function $f_0(E+\hbar\omega_q)$, $f_0(E-\hbar\omega_q)$ and $\exp(x_q)$ in equation (8) by a power series with respect to $\hbar\omega_q$. This approximation has been made in paper I and the result is:

$$\frac{8eC^2}{3\sqrt{\pi kT}\,\mu_a}\frac{1}{E}\left[E^2 f_0'' + \left(\frac{E^2}{kT}+2E\right)f_0' + \frac{2E}{kT}f_0\right] = \frac{eF}{\hbar}\left(g_1 + \frac{2}{3}E\frac{dg_1}{dE}\right) \tag{15}$$

and

$$g_1(E) = -\frac{3\hbar}{4}\sqrt{\pi kT}\,(\mu_a F)\frac{1}{\sqrt{E}}\frac{df_0}{dE}. \tag{16}$$

Here we have disregarded the higher derivatives of f_0. In Appendix I we show that such terms as f_0''' or f_0^{IV} are quite small compared with the terms retained in the left-hand side of equation (15), unless the field is extremely large. On the other hand, we cannot disregard the term f_0'' in equation (15), because it is a quantity of the same order as the other terms. In equation (16) we have also neglected the contribution from $g_2(E)$. We estimate this contribution in Appendix I. By using equations (15) and (16) we see immediately that $\alpha_2(E)$ must satisfy the following equation:

$$\left[E^2\alpha_2'' + \left(\frac{E^2}{kT}+2E\right)\alpha_2' + \frac{2E}{kT}\alpha_2\right] = (p/F^2)\left(1-\frac{E}{kT}\right)\alpha_0, \tag{17}$$

where p is defined by:

$$p = \frac{3\pi}{16c^2}\,\mu_a^2 F^2. \tag{18}$$

A solution of equation (17) up to the order of F^2 is:

$$\alpha_2 F^2 = p\ln\left(\frac{E}{kT}+p\right)\alpha_0. \tag{19}$$

In a similar way β_3, α_4, and β_5 are determined successively as follows:

$$\beta_3 F^3 = -\frac{3\hbar}{4}\sqrt{\pi kT}\,(\mu_a F)\,p \times \times\left\{\frac{1}{E+pkT} - \frac{1}{kT}\ln\left(\frac{E}{kT}+p\right)\right\}\frac{\alpha_0(E)}{\sqrt{E}}, \tag{20}$$

$$\alpha_4 F^4 = \frac{1}{2}\,p^2\left[\ln\left(\frac{E}{kT}+p\right)\right]^2\alpha_0 \tag{21}$$

and

$$\beta_5 F^5 = -\frac{3\hbar}{4}\sqrt{\pi kT}\,(\mu_a F)\frac{p^2}{\sqrt{E}}\ln\left(\frac{E}{kT}+p\right)\times \times\left\{\frac{1}{E+pkT} - \frac{1}{2kT}\ln\left(\frac{E}{kT}+p\right)\right\}\alpha_0(E). \tag{22}$$

Then, the contributions to the mobility from equations (20) and (22) are

$$\mu' F^2 = -p\,\mu_a \text{ and } \mu'' F^4 = -0\cdot 577\,p^2\mu_a \tag{23}$$

respectively. By performing successive approximations we find that

$$f_0 = \sum_{n=0}\frac{1}{n!}\,p^n[\ln(E/kT+p)]^n\alpha_0(E) = \left(\frac{E}{kT}+p\right)^p\exp(-E/kT). \tag{24}$$

In the paper I we obtained this solution from equation (15) and (16) directly. Eliminating $g_1(E)$ from equation (15), we obtain a differential equation for $f_0(E)$:

$$(E+pkT)f_0''+\left(\frac{E}{kT}+2+pkT/E\right)f_0'+ \\ +\frac{2}{kT}f_0=0. \quad (25)$$

We see that $f_0(E)$ in equation (24) satisfies this equation. By using equation (24) and (9), we find that $g_2(E)$ is quite small as compared with $f_0(E)$, unless the field is extremely large (Appendix I).*

(B) Here we consider the interaction between conduction electrons and the optical modes of vibrations. The fundamental equations have been given in paper II:

$$\frac{A}{\sqrt{E}}\left[E^2f_0''+\left(\frac{E^2}{kT}+2E\right)f_0'+\frac{2E}{kT}f_0\right]+\frac{B}{\hbar\omega\sqrt{E}}\left[\sqrt{E(E+\hbar\omega)}\times\right. \\ \times\left\{f_0(E+\hbar\omega)\exp\left(\frac{\hbar\omega}{kT}\right)-f_0(E)\right\}+\epsilon(E)\sqrt{E(E-\hbar\omega)}\times \\ \left.\times\left\{f_0(E-\hbar\omega)-f_0(E)\exp\left(\frac{\hbar\omega}{kT}\right)\right\}\right] \\ =\frac{eF}{\hbar}\left(g_1+\frac{2}{3}E\frac{dg_1}{dE}\right), \quad (26)$$

and

$$\left\{\frac{A\sqrt{E}}{2mc^2}+\frac{B}{\hbar\omega}\left[\sqrt{E+\hbar\omega}+\epsilon(E)\exp\left(\frac{\hbar\omega}{kT}\right)\sqrt{E-\hbar\omega}\right]\right\}g_1(E)=-\left(\frac{eF\hbar}{m}\right)\frac{df_0}{dE}, \quad (27)$$

where A and B are defined by

$$A=\frac{16VC^2m^3(kT)}{9\pi M\hbar^4\sqrt{2m}}=\frac{8ec^2}{3\sqrt{\pi kT}}\frac{1}{\mu_a}, \quad (28)$$

and

$$B=\frac{VD^2m^3}{\pi M\hbar^4\sqrt{2m}}\left(\frac{\hbar^2\varrho^2}{2m}\right)\left(1/\exp\left(\frac{\hbar\omega}{kT}\right)-1\right), \quad (29)$$

respectively. The meaning of symbols is: $\hbar\omega$ is the characteristic energy of an optical phonon, D is a coupling constant between conduction electrons and the optical mode of vibrations, ϱ is the first non-vanishing reciprocal vector of the lattice, and $\epsilon(E)$ is a step function equal to unity for $E \geqq \hbar\omega$ and equal to zero otherwise. Hereafter we shall denote the non-ohmic mobility by $\mu(F)$, the ohmic mobility by μ, and the ohmic acoustic mobility by μ_a. From experiment we know the ratio (μ/μ_a) at room temperature to be $\sim 0{\cdot}83$.

In order to solve these equations, we believe it is convenient to consider three cases of conductivity separately; (1) in a weak field, (2) in a very strong field, and (3) in a field of intermediate strength. As for case (1), we have already solved the problem in paper II, and we have found that the theoretical results are in reasonable agreement with available experiments.

As to case (2), it is not difficult to solve the system of equations with a sufficient degree of accuracy. If the intensity of the applied field is

* In fact, according to equation (14) $K^2\gamma_2(E)$ becomes infinity when E approaches zero and consequently equation (8) gives a divergent current. However, the expression (10) is not permitted at the origin, while equations (7) – (9) are always valid. If we use a correct solution (24) at the origin, we have a divergent free current (Appendix I).

VOL. 12 59/60

very strong, the temperature of the conduction electrons becomes so high that most of the electrons have an energy greater than $\hbar\omega$. Then, we can expand approximately the functions $f_0(E\pm\hbar\omega)$ with respect to $\hbar\omega$, and disregard $\hbar\omega$ in the square root in comparison with E. After some calculations (see Appendix II), we arrive at the following equation instead of (25):

$$\left(E^2+\frac{pkTE}{\Omega}\right)f_0''+\left(\frac{E_2}{kT}+2E+\left(\frac{pkT}{\Omega}\right)f_0'+\right.$$
$$+\frac{2E}{kT}f_0+\frac{B}{2A}\{\hbar\omega\,(e^s+1)\,(Ef_0''+f_0')+$$
$$\left.+2\,(e^s-1)\,(Ef_0'+f_0)\}=0\,, \qquad (30\text{-}1)$$

where s is defined by: $s=\hbar\omega/kT$. The mobility is also evaluated by the aid of $g_1(E)$:

$$g_1(E)=-\left(\frac{eF\hbar}{m}\right)\frac{2mc^2}{A\Omega}\cdot\frac{1}{\sqrt{E}}\cdot\frac{df_0}{dE}\,, \qquad (30\text{-}2)$$

where Ω is defined by

$$\Omega=1+\frac{B}{A}\frac{2mc^2}{\hbar\omega}\,(1+e^s).$$

We can readily find a solution of equation (30) as:

$$f_0=N\left\{\frac{E}{kT}+\frac{p}{\Omega}+\frac{B}{2A}s\,(e^s+1)\right\}^{p'}\exp\,(-E/kT), \qquad (31)$$

where N is a normalization constant and p' is newly defined as:

$$p'=\frac{p}{\Omega}+\frac{B}{A}\left[\frac{1}{2}s(e^s+1)-(e^s-1)\right]. \qquad (32)$$

Since the field intensity is very strong, we may neglect E in the coefficient of f_0'' and $2E$ in the coefficient of f_0' in comparison with pkT. In this approximation we have a following approximate solution:

$$f_0=N\exp\left\{-[E^2+\frac{2BkT}{A}(e^s-1)\,E]\,/\,2(kT)^2\left[\frac{p}{\Omega}+\frac{B}{2A}s(e^s+1)\right]\right\}. \qquad (33)$$

Then, we obtain the non-ohmic conductivity from equations (33) and (27). The condition of the applicability of this solution is that the energy value where the number density becomes maximum is much larger than $\hbar\omega$. From equation (31) and the condition $(B/A)(\exp(s)-1)\gg\sqrt{p}$, the maximum point appears at:

$$(E/kT)_{\max}=$$
$$p\Big/\frac{2B\Omega}{A}(e^s-1)+s(e^s+1)\Big/4(e^s-1). \qquad (34)$$

According to experimental observations the drift velocity of the hot electrons becomes almost constant when the field is sufficiently large. Here we shall show that the drift velocity derived from equations (33) and (27) has approximately such a character. In n-type germanium the value of $(B/A)(\exp(s)-1)$ is large, so that we may ignore E^2 in equation (33) in comparison with $EkT(B/A)(\exp(s)-1)$, because the number of electrons with very high energy is very small. Then, the distribution function $f_0(E)$ takes a Maxwellian form with the electron temperature

$$T_e/T=\left[\frac{p}{\Omega}+\frac{B}{A}s(e^s+1)\right]\Big/\frac{B}{A}(e^s-1)$$
$$\approx p\Big/\frac{B\Omega}{A}(e^s-1). \qquad (35)$$

Then, we see easily from equations (27) and (30-2) that the ratio of the conductivity of the hot electron to the ohmic conductivity is given by:

$$\frac{\sigma}{\sigma_0}=\frac{\mu_a}{\mu}\frac{1}{\Omega}\left(\frac{T}{T_e}\right)^{1/2}\sim F^{-1}, \qquad (36\text{-}1)$$

and consequently the drift velocity becomes

constant and its saturation value is estimated by the following equation:

$$[\bar{v}(F)]_{Sat} = \left(\frac{\mu_a}{\Omega}\right)\left(\frac{T}{T_c}\right)^{1/2} F = \text{constant}. \tag{36-2}$$

If the field is extremely large, the number of electrons with very high energy is not negligibly small. In that case we expect that the drift velocity increases slowly with increasing field.* If the field strength lies in the intermediate region, (case 3), it is difficult to solve the fundamental equation with sufficient accuracy. There may be two alternative approaches, one from the weak-field approximation and the other from the strong-field approximation. We shall begin with the former.

Let us assume now

$$f_0(E) = \chi(E)\exp(-E/kT). \tag{37}$$

Inserting equations (37) and (27) into (26), we have:

$$\begin{aligned} R[\chi] \equiv & \left(E^2\chi'' - \frac{E^2}{kT}\chi' + 2E\chi'\right) + \left(\frac{B}{A\hbar\omega}\right)[\sqrt{E(E+\hbar\omega)}\,(\chi(E+\hbar\omega) - \chi(E)) + \\ & + e(E)\exp(s)\sqrt{E(E-\hbar\omega)}\,(\chi(E-\hbar\omega) - \chi(E))] + \\ & + p\left(kT\frac{d}{dE} - 1\right)\left\{\frac{E\sqrt{E}(\chi' - \chi/kT)}{\sqrt{E} + \dfrac{B\,2\pi c^2}{A\hbar\omega}[\sqrt{E+\hbar\omega} + e(E)e^s\sqrt{E-\hbar\omega}]}\right\}. \end{aligned} \tag{38}$$

First we expand $\chi(E \pm \hbar\omega)$ by a power series with respect to $\hbar\omega$ and retain terms up to $\chi''(E)$. We denote that equation by:

$$L[\chi_0] = 0, \tag{39}$$

and also denote a solution of equation (39) as $\chi_0(E)$. Then, if $R[\chi_0]$ is almost satisfied by $\chi_0(E)$, we can regard it as an approximate solution of equation (38). However, if $R[\chi_0]$ is not small, we must proceed to the next approximation, where we solve an inhomogeneous differential equation

$$L[\chi_0] = R[\chi_0]. \tag{40}$$

In priciple, we can repeat the process until the residue becomes sufficiently small, but this process is rather laborious in general. However, when the field is not large, $\chi(E)$ is a rather slowly varying function of energy, so that we expect a rapid convergence of this process. In the second approach we first solve equation (30) in the energy region $E \gg \hbar\omega$, for an example $E \geqq 5\hbar\omega$. Then, the distribution function for an energy range between $5\hbar\omega$ and $4\hbar\omega$ is determined with the aid of the equations (26) and (27). By this process we obtain an approximate distribution function for small energy regions.

3. COMPARISON WITH OBSERVATION IN n-TYPE GERMANIUM

Let us discuss the behaviour of the hot electrons in n-type germanium by the theory developed in the previous section. First, we must determine the numerical value of the constants A, B, c, m, p, and $\hbar\omega$. We determine the two interaction parameters A and B so as to fit the observed mobility at 100 and 300°K, as was done in paper II. The calculated ratio (B/A) is shown in Table 1. We determine the effective mass by the relation:

* In a real crystal the electron multiplication due to the impact ionization occurs in the extremely strong field, and the theory developed so far is not applicable to such high-energy electrons.

VOL. 12 59/60

$$1/m = (1/3)(1/m_1 + 2/m_2) \simeq 1/0{\cdot}12m_e ,$$

where $m_1 = 1{\cdot}58m_e$ and $m_2 = 0{\cdot}08m_e$, respectively. We assume that c is $5{\cdot}5\times10^5$ cm/sec, and we take the value of $\Theta = \hbar\omega/k$ as 320°K. We have also determined the field strength which corresponds to $p = 1$ as a function of temperature.* The results are shown in Table 1. First, we mention the result obtained by the weak-field approximation. We have solved the differential equation (39) numerically by the aid of the IBM. computing machine for the cases: $p = 50$ (1100 V/cm), $p = 200$ (2200 V/cm), $p = 400$ (3100 V/cm), and $p = 800$ (4400 V/cm), respectively, at room temperature. We did not correct the solutions by using equation (40), because the process is rather laborious. We find that $R[\chi_0]$ is small for $p = 50$ and 200, so that the solutions may be sufficiently accurate. However, the accuracy is somewhat doubtful in the case of $p = 800$.

Table 1

T (°K)	B/A	$F\,(p=1)$ (V/cm)
77	7·5	20
90	11·5	30
193	44·0	78·5
300	63·0	156

By using these solutions and equation (27), we have computed the ratio $(\sigma(F)/\sigma_0)$. The results are shown in Table 2. The observed values according to GUNN[3] are also shown in this table. We see that the agreement between theory and experiment is fairly good. If on the other hand, we obtain the ratio by the strong-field approximation, it is 0·38 at $p = 800$. Next, we want to estimate the field value which satisfies condition (34) by using the numerical values of the constants mentioned previously.* From equation (34) we

Table 2. *Theoretical and observed values*[3] *of the ratio* σ/σ_0 (*non-ohmic mobility/ohmic mobility*)

p	F (V/cm)	σ/σ_0 (obs.)	σ/σ_0 (calc.)
50	1100	0·73	0·73
200	2200	0·52	0·57
400	3100	0·42	0·45
800	4400	0·31	0·36

Table 3. *Theoretical and observed values of the saturation drift velocity as a function of temperature*

T(°K)	Field intensity (V/cm)			Saturation drift velocity (cm/sec)	
	$E = 10\hbar\omega$	$E = 5\hbar\omega$	$E = 3\hbar\omega$	$\bar{v}$ (calc.)	$\bar{v}$ (obs.)
77	4900	3400	2580	$1{\cdot}1\times10^7$	$0{\cdot}9\times10^7$
193	7100	5000	3700	$9{\cdot}0\times10^6$	$7{\cdot}6\times10^6$
300	8500	6100	4600	$6{\cdot}6\times10^6$	$6{\cdot}2\times10^6$ / $5{\cdot}2\times10^6$

* We assume that the observed mobility at 100°K is an acoustic mobility ($\mu_a = 24000$ cm²/V-sec), and then we estimate the value of μ_a at other temperatures by using a $T^{-1\cdot5}$ law.

* In fact, we encounter a difficulty. We have determined values of the various constants by using the data observed at low temperature, so that we have no reason to expect the applicability of these to phenomena at a high electron temperature.

have evaluated the values of E_{max} which are equal to $10\hbar\omega$, $5\hbar\omega$, and $3\hbar\omega$, respectively. The results are shown in Table 3. By comparison with the observation of GUNN[3] and RYDER[4], we find that the observed drift velocity becomes almost constant in the field region where the condition $E_{max} > 3\hbar\omega$ is satisfied. In Table 3 we also show calculated values of the saturation drift velocity and the corresponding observed values. As can be seen from the table, the agreement is good. However, we do not know the true implication of this agreement, because we have used values of the constants which are not reliable for very hot electrons.

VOL. 12 59/60

4. ELEMENTARY APPROACH

In the previous sections we determined the distribution functions $f_0(E)$, $g_1(E)$, and $g_2(E)$ by solving a system of differential equations. This approach is rather laborious, so that we shall mention here a more elementary approach which is convenient for treating complicated cases. We start from the Boltzmann equation and derive the following relation:

$$\int E\,[\partial f/\partial t]_{\text{coll.}}\,d^3p = -\int E\,[\partial f/\partial t]_{\text{field}}\,d^3p \quad (41)$$

where $[\partial f/\partial t]_{\text{field}}$ is given by equation (5). Inserting equation (5) into (41), we have:

$$\int [\partial f/\partial t]_{\text{coll.}}\,d^3p = \int E\frac{eF}{\hbar}\left(g_1 + \frac{2}{3}E\frac{dg_1}{dE}\right)d^3p, \quad (42)$$

where $g_1(E)$ is given by equation (27). The terms containing $P_i(\cos\Theta)$ $(i \neq 0)$ are dropped out by symmetry. By using equation (27) we reduce the right-hand side of equation (42) to:

$$\text{right-hand side of (42)} = \frac{2(eF)^2c^2}{A} \times$$

$$\times\, 4\pi m\sqrt{2m}\,\frac{2}{3}\int \frac{df_0}{dE}\,I(E,\hbar\omega)\,E\sqrt{E}\,dE,$$

where

$$I(E,\hbar\omega) = \left\{\sqrt{E} + \frac{B}{A}\frac{2mc^2}{\hbar\omega}\left[\sqrt{E+\hbar\omega} + \right.\right.$$

$$\left.\left. + e(E)\,e^s\sqrt{E-\hbar\omega}\right]\right\}^{-1}. \quad (43)$$

On the other hand, by using equation (27) we have an expression of the mobility:

$$\mu(F) = \int v_z K_z g_1(E)\,d^3p =$$

$$\frac{2ec^2}{A}\,4\pi m\sqrt{2m}\,\frac{2}{3}\int \frac{df_0}{dE}\,I(E,\hbar\omega)\,E\sqrt{E}\,dE. \quad (44)$$

From these equations we obtain a relation:

$$e\mu(F)F^2 = \int E\left[\frac{\partial f}{\partial t}\right]_{\text{coll.}} d^3p. \quad (45)$$

We see that this is the energy balance condition, that is, the condition that the energy supplied by the field to conduction electrons is balanced by the energy loss due to collisions with lattice vibrations. By using equation (26), we have an explicit expression of equation (45):

$$e\mu(F)F^2 = -\int E\left\{\frac{A}{\sqrt{E}}\left[E^2 f_0'' + \left(\frac{E^2}{kT} + 2E\right)f_0' + \frac{2E}{kT}f_0\right] + \right.$$

$$+ \frac{B}{\hbar\omega\sqrt{E}}\left[\sqrt{E(E+\hbar\omega)}\,(f_0(E+\hbar\omega)\,e^s - f_0(E)) + e(E)\sqrt{E(E-\hbar\omega)}\,\times\right.$$

$$\left.\left.\times\,(f_0(E-\hbar\omega) - f_0(E)\,e^s)\right]\right\} d^3p. \quad (46)$$

If we insert $f_0(E)$ which satisfies equation (38) into the right-hand side of equation (46) and into (44), both equations give the same value of the mobility. If a function $f_0(E)$ is not a solution of equation (38), then $\mu(F)$ from equation (44) is in general not equal to that from equation (46). However, we can choose some distribution functions which satisfy both equations at the same time. In this approach we assume that the distribution function is represented by a simple analytical function with a parameter. As the simplest example we use here an exponential function

$$f_0(E) = 2\left[\sqrt{\pi}(kT_e)^{3/2}\right]^{-1} \exp(-E/kT_e), \quad (47)$$

where T_e is the electron temperature and is determined so as to satisfy both the equations (44) and (46). In fact, the distribution function (47) does not satisfy equation (38), but we assume here that it is an approximate solution of it. If we once admit this assumption, this approach is quite simple and convenient for treating complicated problems, because we have no need to solve equation (38).

In the following we shall compute the ratio (σ/σ_0) by this elementary method and compare the result with the previous one.

By using equation (47) we have derived relations:

$$\mu(F)/\mu_a = (T/T_e)^{1/2} \int I(x, s_0)\, x \sqrt{x}\, e^{-x} dx \quad (48\text{-}1)$$

and

$$\sigma/\sigma_0 = (\mu(F)/\mu_a)(\mu_a/\mu) = (1/0\cdot 83)(\mu(F)/\mu_a), \quad (48\text{-}2)$$

where x and s are defined by

$$x = E/kT_e \quad \text{and} \quad s_0 = \hbar\omega/kT_e,$$

respectively. Inserting equation (47) into (46) and performing some calculations, we obtain the following equation:

$$p \int I(x, s_0)\, x \sqrt{x}\, e^{-x} dx = \left(\frac{T_e}{T}\right)\left\{2\left(\frac{T_e}{T} - 1\right) + \right.$$

$$\left. + \frac{B}{A}(e^{s-s_0} - 1) \int_0^\infty \sqrt{x(x+s_0)}\, e^{-x}\, dx \right\}, \quad (49)$$

where the integral on the right-hand side is evaluated with the aid of the Bessel function:

$$\int \sqrt{x(x+s_0)}\, e^{-x}\, dx = \frac{1}{2} s_0 \exp\left(\frac{1}{2} s_0\right) K_1\left(\frac{1}{2} s_0\right). \quad (50)$$

When the field is weak, equation (49) is easily reduced and the conductivity is given by:

$$\sigma(F) = \sigma_0 \left\{1 - p\left(\frac{\mu}{\mu_a}\right) \times \right.$$

$$\left. \times \left[2 + \frac{Bs}{A} \int_0^\infty \sqrt{x(x+s)}\, e^{-x}\, dx\right]^{-1}\right\}. \quad (51)$$

By using the values of the constants determined previously, we obtain the numerical value of the non-ohmic correction of the conductivity:

$$\sigma(F) = \sigma_0(1 + \beta F^2). \quad (52)$$

The value of $-\beta$ is $2\cdot 5 \times 10^{-7}$ at room temperature and $1\cdot 0 \times 10^{-5}$ cm^2/V^2 at 90°K. The corresponding values evaluated in paper II are $1\cdot 3 \times 10^{-7}$ and $1\cdot 6 \times 10^{-5}$ cm^2/V^2, and the observed values are $1\cdot 5 \times 10^{-7}$ and $2\cdot 8 \times$ $\times 10^{-5}$ cm^2/V^2, respectively. When the field becomes large, we find easily that equation (49) is reduced to (35), so that the ratio (σ/σ_0) is the same as that computed from the approximate formula (36). In the middle range of the field we must evaluate equations (49) and (44) by numerical calculations. The results are shown in Table 4. Although we have not considered the effects of electron-electron collisions, we suppose that the distribution function (47) may be realized when this interaction is predominant. In the present case we have no experimental evidence to suggest a predominant con-

Table 4. The ratio σ/σ_0 (non-ohmic mobility : ohmic mobility) calculated by the simple method.

p	$(\sigma/\sigma_0 \text{cm})$	p	$(\sigma/\sigma_0 \text{cm})$
50	0·82	500	0·45
100	0·73	600	0·42
200	0·61	700	0·40
300	0·54	800	0·38
400	0·49		

VOL. 12 59/60

tribution from the electron-electron collisions. However, careful investigations from both theoretical and experimental sides are necessary to elucidate the effects of the electron-electron collisions on the hot-electron problem.

5. HOT ELECTRON IN MANY-VALLEY SEMICONDUCTORS

In the previous sections we have found that the theoretical results are in good agreement with those of experiment, although the model used there is still too simple. This simple model assumed a non-degenerate band-edge state with wave vector $K = 0$ and spherical surfaces of constant energy. In the present section we shall remove this restriction and consider the hot electrons in a many-valley semiconductor with ellipsoidal energy surfaces. HERRING has discussed mechanisms of lattice scattering in many-valley semiconductors in detail. He introduced three relaxation times, one for each direction of the principal axis of an ellipsoid. However, he argued that a single relaxation time may be almost sufficient to treat scatterings due to the optical vibrations or the intervalley scatterings. In the present case the temperature of the hot electrons is determined almost entirely by the interaction with the optical mode of vibrations, so that it may be permissible to adopt the single-relaxation-time approximation.

Let us consider any one of eight valleys in n-type germanium whose constant-energy surfaces are ellipsoidal. We chose the direction of its long principal axis as x-axis. Further, we denote the direction cosines of the external field as ξ, η, and ζ, respectively. Then, the energy of a conduction electron is given by

$$E = \frac{\hbar^2 K_x^2}{2m_1} + \frac{\hbar^2}{2m_2}(K_z^2 + K_y^2). \qquad (53)$$

In order to evaluate

$$[\partial f/\partial t]_{\text{field}} = \frac{e}{\hbar}\vec{F}\cdot\nabla f,$$

we expand the distribution function as usual:

$$f = f_0(E) + K_F g(E). \qquad (54)$$

Then, we have:

$$\left[\frac{\partial f}{\partial t}\right]_{\text{field}} = (eF\hbar)\left(\frac{df_0}{dE}\right)\left(\frac{\xi^2}{m_1} + \frac{\eta^2}{m_2} + \frac{\zeta^2}{m_2}\right)K_F + \\ + \frac{eF}{\hbar}\left(g + \frac{2}{3}E\frac{dg}{dE}\right). \qquad (55)$$

On the other hand, $[\partial f/\partial t]_{\text{Coll.}}$ is still given by equation (6), because we assume that the scattering is nearly isotropic, and only one relaxation time is necessary. Therefore, we see that we need only to replace $(1/m)(df_0/dE)\,K_z$ in equations (5), (8), (16) and (27) by:

$$\left(\frac{\xi^2}{m_1} + \frac{\eta^2 + \zeta^2}{m_2}\right)\left(\frac{df_0}{dE}\right)K_F$$

and consequently, p by $p^\star(\xi, \eta, \zeta)$:

$$p^\star(\xi, \eta, \zeta) = m\left(\frac{\xi^2}{m_1} + \frac{\eta^2 + \zeta^2}{m_2}\right)p. \qquad (56)$$

The ohmic mobility of germanium is isotropic as a space average in a cubic symmetric crystal. Thus, the expression of the acoustic mobility μ_a remains valid, if we interpret the mass m as an effective mass defined by:

$$\frac{1}{m} = \frac{1}{3}\left(\frac{1}{m_1} + \frac{2}{m_2}\right). \qquad (57)$$

Now, we shall summarize the programme to solve the hot-electron problem of a many-valley semiconductor. First, we disregard the intervalley scattering and consider each valley as an independent unit. Then, by replacing p in equation (30) or (38) by $p^{\star}(\xi, \eta, \zeta)$, we have a fundamental equation for the distribution function $f_0(E)$ of the valley where the direction cosines of the external field are ξ, η, and ζ, respectively. In this approximation the electron temperature of each valley takes its own value, because the electron temperature depends upon the angle between the field and the principal axes of each valley through the factor $p^{\star}(\xi, \eta, \zeta)$. Therefore, even when the current is averaged spatially over all valleys, anisotropy in the current will remain in some extent. To begin with, we want to know whether the ratio (σ/σ_0) obtained by the simplified model is seriously modified by considering the ellipsoidal structure of the energy surfaces. For convenience, we shall choose a co-ordinate system which refers to the three crystal axes, and we newly define the direction cosines of the external field (ξ', η', ζ') with respect to this system. Then, the direction cosines of the principal axes of eight ellipsoids are shown in Table 5. As an example, we compute the current for three directions of the field: $(\xi', \eta', \zeta') = (1/\sqrt{3})(1, 1, 1)$, $(1/\sqrt{2})(1, 1, 0)$ and $(1, 0, 0)$, respectively. Then, the value of ξ^2 and $(\eta^2 + \zeta^2)$ of each valley is shown in Table 6. With the aid of this table we evaluate $p^{\star}$. We have also estimated the conductivity of each valley as a function of $p^{\star}$ by using interpolation formulae.† By sum-

† Interpolation formulae:
(I) $50 \geqq p : \sigma/\sigma_0 = 1 - 0{\cdot}0054p$; (II) $200 \geqq p \geqq 50 : \sigma/\sigma_0 = -2{\cdot}170/\sqrt{p} + 2{\cdot}721/p^{1/4}$; (III) $400 \geqq p \geqq 200 : \sigma/\sigma_0 = 3{\cdot}097/\sqrt{p} + 1{\cdot}320/p^{1/4}$; (IV) $800 \geqq p \geqq 400 : 2{\cdot}753/\sqrt{p} + 1{\cdot}397/p^{1/4}$; and (V) $p \geqq 800 : 10{\cdot}18/\sqrt{p}$.
These are not very accurate, but they may be sufficient for the present purpose.

Table 5. *Direction cosines of the principal axes of eight ellipsoids*

(1)	$(1/\sqrt{3})(1,1,1)$ $(1/\sqrt{2})(1,\bar{1},0)$ $(1/\sqrt{6})(1,1,\bar{2})$	(2)	$(1/\sqrt{3})(\bar{1},\bar{1},\bar{1})$ $(1/\sqrt{2})(1,\bar{1},0)$ $(1/\sqrt{6})(1,1,\bar{2})$	(3)	$(1/\sqrt{3})(1,1,\bar{1})$ $(1/\sqrt{2})(1,\bar{1},0)$ $(1/\sqrt{6})(1,1,2)$
(4)	$(1/\sqrt{3})(\bar{1},\bar{1},1)$ $(1/\sqrt{2})(1,\bar{1},0)$ $(1/\sqrt{6})(1,1,2)$	(5)	$(1/\sqrt{3})(1,\bar{1},1)$ $(1/\sqrt{2})(1,1.0)$ $(1/\sqrt{6})(1,\bar{1},\bar{2})$	(6)	$(1/\sqrt{3})(\bar{1},1,\bar{1})$ $(1/\sqrt{2})(1,1,0)$ $(1/\sqrt{6})(1,\bar{1},\bar{2})$
(7)	$(1/\sqrt{3})(\bar{1},1,1)$ $(1/\sqrt{2})(1,1,0)$ $(1/\sqrt{6})(1,\bar{1},2)$	(8)	$(1/\sqrt{3})(1,\bar{1},\bar{1})$ $(1/\sqrt{2})(1,1,0)$ $(1/\sqrt{6})(1,\bar{1},2)$		

Table 6

(ξ', η', ζ')	No. of ellipsoid	ξ^2	$\eta^2 + \zeta^2$	$m(\xi^2/m_1 + \eta^2/m_2 + \zeta^2/m_2)$
$(1/\sqrt{3})(1,1,1)$	1 and 2	1	0	0·076
	3–8	1/9	8/9	1·308
$(1/\sqrt{2})(1,1,0)$	1–4	2/3	1/3	0·54
	5–8	0	1	1·46
(1,0,0)	1–8	1/3	2/3	1·00

ming up the contribution from all valleys, we obtain the total current. Then, the total current is a function of the field direction, and its magnitude is given by:†

$$\mathcal{J} = \sigma(\xi \cdot \eta \cdot \zeta) F = \sum_{i=1}^{8} \sigma_i (\xi \cdot \eta \cdot \zeta) F .$$

tervalley scatterings whose effect is to reduce the temperature difference among valleys, and consequently reduce the anisotropy. On the other hand, if the temperatures of the valleys differ, some of the electrons in a high-temperature valley should transfer into the valleys of low temperature, and this effect tends to increase the anisotropy. In order to consider the intervalley scattering in the hot-electron problem, we must solve a system of differential equations about the distribution functions $f_{0i}(E)$ and $g_i(E)$ ($i = 1, - - - -, 8$). We have no intention of solving this complicated problem here but we want to obtain a rough idea of the effect of the intervalley scattering on the anisotropy of the current. For that purpose the method developed in Section 4 is quite convenient.

Table 7 (a)

(ξ', η', ζ')	No. of ellipsoid	Weight	(σ_{i0}/σ_0)		
			$p = 50$	$p = 200$	$p = 400$
$(1/\sqrt{3})$ (1,1,1)	1 and 2	0·076	0·980	0·918	0·836
	3 – 8	1·308	0·689	0·521	0·405
$(1/\sqrt{2})$ (1,1,0)	1 – 4	0·54	0·854	0·635	0·555
	5 – 8	1·46	0·676	0·500	0·390
(1,0,0)	1 – 8	1·00	0·73	0·57	0·45

The results are shown in Table 7. Thus, we find that the many-valley model gives nearly the same values of the ratio (σ/σ_0) as the simple model does. Here we find also that the hot-electron current is slightly anisotropic.

Table 7 (b)

(ξ', η', ζ')	Total current/ohmic current		
	$p=50$	$p=200$	$p=400$
$(1/\sqrt{3})$ (1,1,1)	0·70	0·53	0·41
$(1/\sqrt{2})$ (1,1,0)	0·72	0·55	0·43
(1,0,0)	0·73	0·57	0·45

Hitherto we have assumed that the valleys are mutually independ, entbut this is clearly an oversimplification. In a real case, there are in-

The problem is to generalize equation (49) to include the intervalley scatterings. For that purpose we adopt a simplified model.
(1) We assume that $[\partial f/\partial t]_{\text{coll.}}$ due to the intervalley scattering is given by the same formula as $[\partial f/\partial t]_{\text{coll.}}$ due to the optical scattering. (2) Although the intensity of the intervalley scattering, which corresponds to A or B in other scatterings, depends on the mutual situation of the valleys, we use only one interaction parameter $\langle B \rangle$ in a sense of the average. (3) Further, we assume that the characteristic energy of the intervalley scattering is the same

† In the ohmic case σ_i is given by $\sigma_i = \sigma_{i0} m (\xi_i^2/m_1 + \eta_i^2 + \zeta_i^2/m_2)$ and $\sigma_{i0} = \sigma_0$, so that we have the usual solution. In the case of the hot electron σ_i is different in each valley because of the different temperature in each valley.

as that of the optical scattering, that is, we take $\Theta = \hbar\omega/k$ as 320°K. On these assumptions the factor $[\partial f/\partial t)_{\text{coll.}}$ due to the intervalley scattering is written as:

$$\frac{\langle B\rangle}{\hbar\omega\sqrt{E}}\Big[\sqrt{E(E+\hbar\omega)}\times \times\Big(\sum_{i\neq j} f_{i0}(E+\hbar\omega)\,e^{s} - 7f_{j0}(E)\Big) + + e(E)\sqrt{E(E-\hbar\omega)}\times \times\Big(\sum_{i\neq j} f_{i0}(E-\hbar\omega) - 7e^{s} f_{j0}(E)\Big). \quad (58)$$

Now, in the elementary approach, where the distribution function of each valley is given by equation (47) with different temperature T_{ej} ($j = 1$ to 8), it is quite easy to generalize equation (49) to include equation (58). After some elementary computations, we have the following set of equations:

$$p\int I(x,s_{0j})\,x\sqrt{x}\,e^{-x}\,dx = \left(\frac{T_{ej}}{T}\right)\Big\{4\left(\frac{T_{ej}}{T}-1\right) + \frac{(B+7\langle B\rangle)}{A}\,Q(x,s_{0j}) - - \frac{7\langle B\rangle}{A}\Big[\frac{1}{7}\sum_{i\neq j}\left(\frac{T_{ei}}{T_{ej}}\right)^{1/2}(Q(x,s_{0i}) + Q_1(x,s_{0i})) - - Q(x_1\,s_{0j}) - Q_1(x_1\,s_{0j})\Big]\Big\}, \quad (i,j = 1,\ldots..,8) \quad (59)$$

where $Q(x,s_0)$ and $Q_1(x,s_0)$ are defined as:

$$Q(x,s_0) = (e^{s-s_0}-1)\int_0^{\infty}\sqrt{x(x+s_0)}\,e^{-x}\,dx$$

and

$$Q_1(x,s_0) = \frac{1}{s_0}\int_0^{\infty}[\sqrt{x(x+s_0)} + + e(x)\,e^{s}\sqrt{x(x-s_0)}]\,xe^{-x}\,dx.$$

If the temperatures of all the valleys are equal, the last term in equation (59) disappears, while $\langle B\rangle$ in the second term always represents the effect of the intervalley scattering. The ratio $(B + 7\langle B\rangle)/A$ is to be determined so as to give the observed temperature-dependence of the ohmic mobility. As a simple example, let us investigate the case where the field directions are $(1/\sqrt{3})$, (1, 1, 1) and (1, 0, 0), and $p = 50$ at room temperature. If we disregard the intervalley scattering, we obtain the ratio (σ/σ_0) as shown in part I of Table 8. In order to estimate effects of the intervalley scattering, we must know the ratio $7\langle B\rangle/A$, or the value of $\langle\mathcal{J}\rangle$ defined by $\langle\mathcal{J}\rangle\, s/(e^{s}-1) = (2mc^2/\hbar\omega)\,7\langle B\rangle/A$. We do not know how to choose the value of $\langle\mathcal{J}\rangle$ in the hot-electron problem. However, for the purpose of a rough estimation we take $\langle\mathcal{J}\rangle = 0\cdot02$, (Then, $7\langle B\rangle$ is one-seventh of B). This value of $\langle\mathcal{J}\rangle$ is compatible with a reasonable interpretation of the acousto-electric effect. The results of the analysis by equation (59) are shown in part II of Table 8.

Next, we must consider the electron transfer from hot valleys to cold valleys. Let us denote the number of electrons in the cold valleys by n_j ($j = 1, 2$) and in the hot valleys by n_i ($i =$ 3 to 8), and the transition probability from the valley i to the valley j by $W(i,j)$, and that for the opposite direction by $W(j,i)$. Then there will be a relation between n_i and n_j:

$$n_i\int W_{ij}(E)f_{i0}(E)\sqrt{E}\,dE = n_j\int W_{jj}(E)f_{j0}(E)\sqrt{E}\,dE. \quad (W_{ij}(E) = W_{ji}(E). \quad (60)$$

In equation (58) the transition probability $W(i,j)$ has been assumed to be proportional to K. From equations (60) and (47) we have:

$$n_i/n_j = (T_{ej}/T_{ei})^{1/2} \doteqdot (\mu_i(F)/\mu_j(F)). \quad (60')$$

On the other hand, there is a relation between n_i and n_j when the field direction is $(1/\sqrt{3})(1, 1, 1)$:

$$2n_j + 6n_i = 8n. \quad (61)$$

Table 8. Anisotropy of the current. (I) *Independent-valley model,* (II) *the model where the intervalley interaction is considered, but the number of electrons is assumed to be equal in all the valleys, and* (III) *the model where the intervalley interaction is considered, and the number of electrons of each valley depends upon its electron temperature*

	(ξ', η', ζ')	$1/\sqrt{3}(1,1,1)$		(1,0,0)	Anisotropy ratio: $\frac{\sigma(1,1,1)}{\sigma(1,0,0)}$
	No. of ellipsoid	1 and 2	3–8		
(I)	T_e/T	1·03	1·49		
	σ_{i0}/σ_0	0·982	0·797		0·964
	$\sum \sigma_{i0}/\sigma_0$	0·800		0·830	
(II)	T_e/T	1·23	1·40		
	σ_{i0}/σ_0	0·886	0·824		0·994
	$\sum \sigma_{i0}/\sigma_0$	0·825		0·830	
(III)	n_i/n	1·055	0·981		
	$\sum \sigma_{i0}/\sigma_0$	0·811		0·830	0·976

From equations (60) and (61) and Table 8 we obtain the final result with regard to the anisotropy, which is shown in part III of Table 8. We find that the anisotropy depends sensitively upon the intensity of the intervalley scattering, and its effect on the anisotropy is remarkable, even when this intensity is quite small as compared with that of the optical scattering ($\langle B \rangle - - B/50$). Here, we may mention also that the anisotropy depends upon the field intensity. When the field is weak, the temperature difference among the valleys is small, so that the anisotropy is also small. When the field becomes very strong, the temperature difference among the valleys decreases again as we see qualitatively from equation (59) as s_0 approaches zero. Therefore, we expect that the anisotropy becomes small when the field is very large.*

According to our computation, the anisotropy reaches its maximum when the field is -4000 V/cm at room temperature. The anisotropy is also temperature-dependent, and we easily see that the magnitude of the anisotropy is larger at low temperature, because the effect of the intervalley scattering decreases as the temperature falls. By a similar computation to that mentioned previously, we obtain the degree of the anisotropy at 90°K. The results are shown in Table 9. In fact, we must discuss these results with some caution, for two reasons: (1) the results are derived by the elementary method mentioned previously, and (2) the intensity of the intervalley scattering that has been assumed, is not very convincing However, we suppose that the theory gives roughly the order of magnitude of the anisotropy. Therefore, we think that the anisotropy of the current is really detectable at low temperature. Unfortunately, we are not aware of any

* In the real case, the intensity of the intervalley scattering itself becomes larger for hotter electrons.

VOL. 12 59/60

Table 9. *Anisotropy of the current at* 90°K. (I) *and* (III) *have the same meaning as in Table* 8. (II) *The model where the intensity of the intervalley scattering is extremely weak. Then the temperature of the valleys is nearly equal to that computed by the independent-valley model, but the number of conduction electrons in each valley is approximately determined by the relations* (60) *and* (61). *By this approximation we can estimate the maximum value of the anisotropy*

	p	44·5	277		p	44·5	277
(I)	F	200	500	(III)	$\mu_j(F)/\mu$	0·917	0·765
	σ_{j0}/σ_0	0·973	0·903		$\mu_i(F)/\mu$	0·821	0·591
	σ_{i0}/σ_0	0·815	0·578		n_j	1·083	1·205
	σ/σ_0 (Total)	0·818	0·584		n_i	0·971	0·931
	$\dfrac{\sigma\ (1,1,1)}{\sigma\ (1,0,0)}$	0·97	0·91		σ/σ_0 (Total)	0·80	0·577
					$\dfrac{\sigma(1,1,1)}{\sigma(1,0,0)}$	0·95	0·90
(II)	n_j/n_i	1·193	1·562				
	$\dfrac{\sigma\ (1,1,1)}{\sigma\ (1,0,0)}$	0·93	0·85				

experimental results with which to compare the theory. Such experiments are highly desirable, because they would provide some information about the intensity of the intervalley scattering in the hot-electron regions.

6. THE SASAKI-SHIBUYA EXPERIMENT

If we could carry out very sensitive measurements of the hot-electron current in various crystalline directions, then we would be certain to detect the anisotropy of the current. However, such measurements may be somewhat difficult, because the anisotropy is rather small. SASAKI and SHIBUYA[5] have devised a more sensitive and convenient method for detecting the anisotropy. They are now carrying out a detailed and extensive analysis of their experiments. Therefore, we shall not enter upon a detailed discussion of their results, but shall only mention briefly an interpretation of the experiments based on our own theory developed in the previous sections. First, let us consider a valley where the direction of the applied field is indicated by three parameters (ξ, η, ζ), as in the previous section; then the magnitude of the current is

$$j(\xi, \eta, \zeta) = m\left(\frac{\xi^2}{m_1} + \frac{\eta^2+\zeta^2}{m_2}\right) eF\,\mu\,[p^\star(\xi, \eta, \zeta)] \tag{62}$$

where $p^\star$ is defined by equation (56). Here we determine $\mu[p^\star(\xi.\eta.\zeta)]$ by means of the interpolation formulae derived in the previous section. If we observe the current in the direction $b\,(b_1, b_2, b_3)$, the magnitude of the current is given by:

$$j(\xi, \eta, \zeta \mid b) = m\left\{\frac{(\vec{F}\cdot\vec{b})}{m_2 F} - \right.$$
$$\left. - \xi\, b_1\left(\frac{1}{m_2} - \frac{1}{m_1}\right)\right\} eF\,\mu(p^\star). \tag{63}$$

Thus we see that the direction of the current does not coincide with that of the field in the case of ellipsoidal energy surfaces.

Now, let us extend the consideration to all valleys. Then, the total current is given by:

$$\mathcal{J} = m \sum_i \left(\frac{(\vec{F}_i \cdot \vec{b}^{(i)})}{m_2 F_i} - \right.$$
$$\left. - \xi_i b_1^{(i)} \left(\frac{1}{m_2} - \frac{1}{m_1} \right) \right) eFn_i \mu_i [p_i^\star (\xi_i, \eta_i, \zeta_i)], \tag{64}$$

where n_i is the number of conduction electrons in the valley i, and the direction cosines (ξ_i, η_i, ζ_i) and (b_1^i, b_2^i, b_3^i) are referred to the principal axes of the valley i. If we observe the current in the direction normal to the field, then the current is

$$\mathcal{J}_\perp = - meF \left(\frac{1}{m_2} - \frac{1}{m_1} \right) \sum_i n_i \mu_i (p_i^\star) \xi_i b_1^{(i)}. \tag{65}$$

If the electron temperature is the same throughout all valleys, then all values of μ_i and n_i are equal and the normal component of the current should vanish, because $\sum_i \xi_i b^{(i)}$ is always zero on account of the cubic symmetry of the lattice. However, this is not true in the case of the hot electron, because the factors $n_i \mu_i (p_i^\star)$ are different. This phenomenon is similar to the Hall effect, since it can be represented in the form of a transverse electric field. The effect may be characterized by a Hall angle e, where $\tan e = F_t / F_l = j_t (p^\star) / j_l (p^\star)$. Here suffixes t and l designate the transverse and longitudinal components, respectively. SASAKI and SHIBUYA have measured the Hall angle when the applied field lies in the (1, 1, 0) plane. According to their result the Hall angle reaches its maximum when the angle between the field direction and the (0, 0, 1) axis is about 30°. Hitherto we have used a set of the co-ordinate systems which refers to the principal axes of each valley. For practical purposes, however, it is better to use a co-ordinate system in which the three axes are referred to the crystal axes. Let us denote the field direction by (ξ', η', ζ') and the direction of observation by (α, β, γ); then the field direction of the maximum Hall angle is designated by a set of values $(\xi' = \eta' = 1/2\sqrt{2}, \zeta' = \sqrt{3}/2)$ and a direction normal to this direction in the (1, 1, 0) plane is also given by $(\alpha = \beta = -\sqrt{3/8}, \gamma = 1/2)$. In this applied field the eight valleys are divided into three groups. We show the values of $m(\xi^2/m_1 + \eta^2/m_2 + \zeta^2/m_2)$ for each of three groups in Table 10 together with the values of $\sum_i \xi_i \zeta^{(i)}$.

Table 10

No. of ellipsoid	$m\left(\frac{\xi^2}{m_1} + \frac{\eta^2 + \zeta^2}{m_2}\right)$	$\sum_i \xi_i b_i^{(i)}$
1 and 2	0·318	$(1/12)(\sqrt{3} + 2\sqrt{2})$
3 and 4	1·448	$(1/12)(\sqrt{3} - 2\sqrt{2})$
5 – 8	1·117	$-1/4\sqrt{3}$

First, we shall compute $\mathcal{J}_\perp$ for the cases of $p = 50$ and 400 by the independent-valley model (which means that the temperature of each valley is independent of the state of other valleys and is determined by the effective field $p_i^\star$, and the numbers of conduction electrons are assumed to be equal). The conductivity of each valley is computed by two alternative methods: (1) by using the interpolation formulae and (2) by the elementary approach given by equation (49). The results of the computation are shown

in Table 11. Next, if we assume that the intervalley interaction is extremely weak, then the temperature of the valleys is nearly equal to

Table 11

		Interpolation formulae		Elementary approach	
		$p=50$	$p=400$	$p=50$	$p=400$
σ_{i0}/σ_0	No.1,2	0·914	0·618	0·936	0·697
	No.3,4	0·678	0·399	0·783	0·466
	No.5-8	0·705	0·434	0·816	0·490
σ/σ_0(Total		0·712	0·438	0·813	0·490
tan ε		0·039	0·061	0·033	0·058
$(\tan\varepsilon)_{\max}$		0·10	0·16		0·16

that computed by the independent-valley model, but the number of conduction electrons in each valley is approximately determined by the relations:

$$\left.\begin{aligned} &n_1+n_2+2n_3=4n \\ &n_1/n_3=\mu(p_1^*)/\mu(p_3^*) \\ &n_2/n_3=\mu(p_2^*)/\mu(p_3^*). \end{aligned}\right\} \qquad (66)$$

By this approximation we can estimate the maximum value of tan ε. The results are shown in the last row of Table 11.

Next, we consider effects of the intervalley scattering. The electron temperature of each valley is determined by the method developed in the previous section. By using equation (66), we determine also the number of conduction electrons in each valley. Strictly speaking this process is not rigorous, because we must determine T_{ei} and n_i simultaneously. However, this process is approximately applicable when the number of electrons does not greatly differ among the valleys. The results of the analysis are shown in Table 12. As can be seen from the table, the tangent of the Hall angle is about 0·05 when the field of 3100 V/cm is applied in the direction ($\xi'=\eta'=1/2\sqrt{2}, \zeta'=\sqrt{3}/2$) at room temperature, while the corresponding

Table 12. *Tan* ε *computed by the elementary method*
$F=3100$ V/cm, $T=300°$K.

T_{e1}/T	3·14	σ_{10}/σ_0	0·548	n_1	1·109
T_{e2}/T	4·11	σ_{20}/σ_0	0·464	n_2	0·939
T_{e3}/T	3·82	σ_{30}/σ_0	0·482	n_3	0·975
		σ/σ_0 (total)	0·462	tan ε	0·052

observed value is about 0·07. Thus we find that agreement between theory and experiment is reasonably good, if we take the intensity of the intervalley scattering $\langle\mathcal{J}\rangle$ as 0·02.

7. DISCUSSION

In the course of the theoretical investigations developed in the previous sections, we have inevitably introduced some approximations, so that we must be careful in discussing the results obtained. However, we are almost sure that many of the results have at least a semi-quantitative meaning. In the following we shall pick out some of the results obtained and also some problems untouched.

(1) The reason why the ohmic mobility of n-type germanium deviates from a $T^{-3/2}$ law is ascribed largely to the optical scattering. The effect of the intervalley scattering is quite small as compared with that of the optical scattering.

(2) The formula for the mobility contains a number of parameters, for example, the effective mass or the strength of the interaction between conduction electrons and the lattice vibrations. The values of these parameters are generally determined by using the observed data at low temperatures. At present, we have no reliable knowledge about the limit of applicability of these values when the electron temperature rises. However, according to the re-

sults obtained the relevant range seems to cover some of the hot-electron region.

(3) In this paper we do not consider the effect of electron-electron Coulomb interaction. However, we assume that, if this type of the interaction is very important, it may be correct to assume the distribution function of the type (47). As shown in Section 4, the numerical values of the ratio σ/σ_0 obtained by the elementary treatment are somewhat different from the values obtained by the more elaborate method developed in Section 2, especially in the case of a weak applied field.

(4) The analysis of the anisotropy of the current shows that the intensity of the intervalley scattering is rather small. This conclusion is compatible with the recent interpretation of the observed acousto-electric effect.

(5) Finally, we must note that our theory is based on the Boltzmann equation. We made it a presupposition of our theory and we did not criticise its applicability to the hot-electron problem. This is a rather difficult problem, so that we must postpone this very important point to future investigations. However, the results obtained from the theory are in reasonable agreement with experimental observation, so that we suppose that the Boltzmann equation is approximately applicable to the hot electron in non-polar semiconductors (Appendix III). As to the applicability of the Boltzmann equation to phenomena in a very strong field, for example the electron multiplication process, we are somewhat sceptical.

VOL. 12 59/60

REFERENCES

1. YAMASHITA J. and WATANABE M., *Progr. Theor. Phys. Osaka* **12,** 443 (1954).
2. YAMASHITA J., *Phys. Rev.* **111,** 1529 (1958).
3. GUNN J. B., *J. Electronics* **2,** 87 (1956).
4. RYDER E. J., *Phys. Rev.* **90,** 766 (1953).
5. SASAKI W., SHIBUYA M. and MIZUGUCHI K. *J. Phys. Soc. Japan* **13,** 456 (1958).

APPENDIX I

(1) In deriving equation (6) we have neglected quantities of the order of mc^2/kT against one. From the values of m and c of n-type germanium mentioned previously, we estimate the value of mc^2 as 0·23°K.

(2) In computing the following expression

$$K_x \int_0^{2K} [2\{g_1(E+\hbar\omega_q)e^{x_q} - g_1(E) + g_1(E-\hbar\omega_q) - g_1(E)e^{x_q}\} - \left\{\left(\frac{q^2}{K^2}+\frac{\hbar\omega_q}{E}\right)e^{x_q}g_1(E+\hbar\omega_q) + \left(\frac{q^2}{K^2}-\frac{\hbar\omega_q}{E}\right)g_1(E-\hbar\omega_q)\right\}]\frac{q^2\,dq}{e^{x_q}-1}, \quad \text{(A-1)}$$

we have introduced an approximation:

$$g_1(E+\hbar\omega_q) = g_1(E-\hbar\omega_q) = g_1(E).$$

From equations (16) and (24) we can easily evaluate equation (A-1) and obtain the result:

$$\frac{\hbar c}{kT}\int_0^{2K} q^3\,dq - \frac{4}{K^2}\left(\frac{kT}{\hbar c}\right)\int_0^{2K} q^3\,dq.$$

Therefore, the neglect of the first term means to disregard terms of the order of $(mc^2/kT)\ (E/kT)$ against one.

(3) We expand $f_0\ (E\pm\hbar\omega_q)$ with respect to $\hbar\omega_q$ and retain the terms up to the fourth derivative. Then a simple computation shows that the left-hand side of equation (15) becomes:

$$E^2\left[32\,mc^2\,Ef_0^{\mathrm{IV}} + 8\,mc^2 f_0^{\mathrm{III}} + \left(1+\frac{4\,mc^2}{kT}\right)f_0^{\mathrm{II}} + \frac{2}{E}f_0^{\mathrm{I}} + \frac{1}{kT}\left(1+\frac{4\,mc^2}{3\,kT}\right)f_0^{\mathrm{I}} + \frac{2}{kT\,E}f_0\right]. \quad \text{(A-2)}$$

Thus we see that the terms containing f_0^{IV} and f_0^{III} are quite small, unless these higher derivatives themselves are extremely large.

(4) From equations (24), (8), and (9) we obtain:

$$g_1(E) \equiv g_1^{(1)}(E) + g_1^{(2)}(E) = -\frac{3\hbar}{4}\sqrt{\pi kT}\,(\mu F)(kT)^{3/2}\frac{1}{\sqrt{x}}\frac{df_0}{dx} + \frac{3\hbar}{4}\sqrt{\pi kT}\,(\mu F)(kT)^{3/2}\frac{1}{\sqrt{x}}\left[\frac{3}{8}\frac{\pi m}{kT}(\mu F)^2\frac{1}{x}\times \frac{2x^2+x+3p}{2(x+p)^2}f_0\right], \quad \text{(A-3)}$$

and

$$g_2(E) = \frac{3\hbar^2}{16}\frac{\pi}{(kT)^2}(\mu F)^2\frac{1}{x}\frac{2x^2+x+3p}{2(x+p)^2}f_0, \qquad \text{(A-4)}$$

where $x = E/kT$. The contribution to the current from $g_1^{(2)}(E)$ is:

$$\left|g_1^{(2)}(E)/g_1^{(1)}(E)\right| = \left(\frac{3\pi}{8}\right)\left(\frac{1}{2}m\bar{v}^2/kT\right)\int_0^\infty \frac{2x^2+x+3p}{2(x+p)^2}f_0\,dx \times \times\left[\int_0^\infty \frac{x^2}{x+p}f_0\,dx\right]^{-1}. \qquad \text{(A-5)}$$

If the field is not large, this ratio is quite small owing to the factor $\left(\frac{1}{2}m\bar{v}^2/kT\right)$. On the other hand, if the field is large, the ratio is approximately given by:

$$\frac{3}{2}\left(\frac{3\pi}{8}\right)\left(\frac{1}{2}m\bar{v}^2/kT\right)\int f_0\,dx\Big/\int x^2 f_0\,dx,$$

which is again quite small, unless the field is extremely large.

(5) When the field is large, the distribution function is given by equation (24). Then, the ratio

$$K^2 g_2/f_0 = \frac{3m}{8}(\pi kT)(\mu F)^2\left(f_0'' - \frac{f_0'}{2E_1}\right)\Big/f_0. \qquad \text{(A-6)}$$

is evaluated as: $\sim (2mc^2/kT)$ when $pkT \gg E$ and $\frac{1}{2}mc^2p/kT$ when $pkT \sim E$. The number of conduction electrons whose energy is above pkT is very small, so that we may safely disregard $g_2(E)$ in computing $f_0(E)$.

APPENDIX II

We start from the expression $[\partial f/\partial t]_{\text{coll.}}$ due to the optical scattering. When E is much larger than $\hbar\omega$, it is given by:

$$[\partial f/\partial t]_{\text{coll.}} = \frac{B}{\hbar\omega\sqrt{E}}\left[\left\{f_0(E+\hbar\omega)\exp\left(\frac{\hbar\omega}{kT}\right) - f_0(E)\right\}\frac{\hbar^2}{4m}\int_0^{2K+K\hbar\omega/2E} q\,dq + \left\{f_0(E-\hbar\omega - f_0(E)\exp\left(\frac{\hbar\omega}{kT}\right)\right\}\frac{\hbar^2}{2m}\int_0^{2K-K\hbar\omega/2E} q\,dq\right].$$

If we disregard the second term in $q_{\max} = 2K \pm K\hbar\omega/2E$, then we obtain the same expression as in equation (26), but the second term is important in order to reduce the above equation to a differential equation. After expanding $f_0(E\pm\hbar\omega)$ with respect to $\hbar\omega$ and performing the integration, we obtain the following expression:

$$\frac{1}{2}\frac{B}{\sqrt{E}}\{\hbar\omega(e^s+1)(Ef_0''+f_0') + 2(e^s-1)(Ef_0'+f_0)\}.$$

On the other hand, $g(E)$ is

$$g(E) = -\left(\frac{eF\hbar}{m}\right)\frac{df_0}{dE}\Big/\frac{A\Omega}{2mc^2}.$$

Adding the contribution from the acoustic scattering, we have:

$$E^2 f_0'' + \left(\frac{E^2}{kT}+2E\right)f_0' + \frac{2E}{kT}f_0 + + \frac{1}{2}\frac{B}{A}\{\hbar\omega(e^s+1)(Ef_0''+f_0') + +2(e^s-1)(Ef_0'+f_0)\} = \frac{eF}{\hbar}\left(g + \frac{2}{3}E\frac{dg}{dE}\right).$$

Eliminating $g(E)$ from these equations, we obtain equation (30).

APPENDIX III

In a classical treatment of $[\partial f/\partial t]_{\text{field}}$, we expand $f(v_x+\alpha_x\Delta t)$ with respect to $\alpha_x\Delta t$, and replace the acceleration by a relation: $m\alpha_x = eF_x$. The result is:

$$f(v_x+\alpha_x\Delta t) = f(v_x) + cF_x v_x\frac{df_0}{dE}(\Delta t) + + \frac{(eF)^2}{m}\left(\frac{df_0}{dE}+\frac{2Ed^2f_0}{3\,dE^2}\right)(\Delta t)^2. \qquad \text{(A-7)}$$

By taking a limit $\Delta t \to 0$, we have the usual expression

$$[\partial f/\partial t]_{\text{field}} = eF v_x\frac{df_0}{dE}.$$

In the quantum analogue of these procedures there are some problems.

(1) The mass will be replaced by the effective mass. This problem has been discussed by several investigators, and it has been settled for the ohmic case, but not for the case of the hot electron. However, we suppose that there is no serious difficulty in this point

when the field is sufficiently small as compared with the Zener field.

(2) The time interval Δt should be finite owing to the uncertainty principle. Then, we must compare the second term of equation (A-7) with $(eF/\hbar)(g_1 + \frac{2}{3}Edg_1/dE)$, because both are the quantities of the same order of magnitude. Let us consider the case where the acoustic modes of vibrations are effective for scattering. By using the relation:

$$g_1 = -\frac{3\hbar}{4}\sqrt{\pi kT}\,\mu F\frac{1}{\sqrt{E}}\frac{df_0}{dE}$$

we see easily that the second term in equation (A-7) is equal to $(eF/\hbar)(g_1 + \frac{2}{3}Edg_1/dE)$ when Δt is equal to τ (the relaxation time of electrons due to the acoustic scattering). As a matter of course, Δt should be much smaller than τ, so that the contribution from the second term in (A-7) can be safely disregarded.

VOL.
12
59/60

J. Phys. Chem. Solids Pergamon Press 1959. Vol. 12. pp. 22–27. Printed in Poland.

PROPERTIES OF OXYGEN IN GERMANIUM

J. BLOEM, C. HAAS and P. PENNING

Philips Research Laboratories N. V. Philips'
Gloeilampenfabrieken, Eindhoven, Netherlands

(*Received* 20 *February* 1959; *revised* 10 *April* 1959)

Abstract—Germanium crystals were zone-levelled in an oxygen atmosphere. The oxygen concentration in the crystal, as deduced from infrared absorption at 856 cm^{-1}, is proportional to the oxygen pressure p_{O_2} for $p_{O_2} < 20$ mm Hg; at higher oxygen pressures, the oxygen concentration is constant at 7×10^{17} atoms/cm^3.

On heat treatment at a relatively low temperature (400°C), donors are introduced in the crystal; the donors disappear again if the crystal is heated to a higher temperature (700°C). The number of donors depends strongly on the oxygen concentration. A tentative description of the results is given in terms of the equilibrium between isolated oxygen atoms and donor complexes consisting of four oxygen atoms.

The Hall effect of the oxygen donors indicates the presence of several donor levels.

In germanium crystals levelled under oxygen, two additional absorption bands were found at 1100 and 1260 cm^{-1}.

1. INTRODUCTION

DURING the last three years about twenty papers have been published on the behaviour of oxygen in silicon.* As a result we know that, in a silicon crystal containing oxygen, it is possible to convert the oxygen atoms partly into donors by an appropriate heat treatment. The donors can be made to disappear again by heating the crystal to a higher temperature. The stationary concentration of the donors in the crystal, and their rate of formation and disappearance, are influenced strongly by the temperature and the impurity concentration. The whole situation is very complex, and though much experimental evidence is now available, a satisfactory picture is still lacking.

Much less is known about the properties of oxygen in germanium. KAISER[2] found in some germanium crystals a weak infrared absorption band at 860 cm^{-1} which he ascribed to the presence of about 10^{16} oxygen atoms per cm^3 in the germanium crystal. We decided to study the behaviour of oxygen in germanium in the hope that a comparison of the results with those for silicon might eventually lead to a clarification of the intricate properties of oxygen in germanium and silicon crystals.

2. PREPARATION OF GERMANIUM CRYSTALS CONTAINING OXYGEN

Germanium single crystals containing a considerable amount of oxygen were prepared in two ways:

(*a*) A mixture of nitrogen and oxygen was passed over a germanium crystal rod in a sooted quartz boat in a zone-levelling apparatus.[3]

* References to the effect of oxygen in silicon can be found in recent papers by SMAKULA and KALNAJS and FULLER and DOLEIDEN[1].

A liquid zone was passed through the germanium, which reacted with the oxygen in the gas, as shown by the formation of a germanium oxide deposit on the wall of the tube in which the process took place. Crystals were made under oxygen pressures ranging from 2 to 100 mm Hg. The total pressure of the gas mixture was 1 atm in all cases.

(*b*) A cut was made along a germanium rod and filled with GeO_2 powder. A molten zone was then passed through the crystal in the usual way in a zone-levelling apparatus.

3. INFRARED ABSORPTION AT 860 cm^{-1}

The infrared absorption spectra of crystals prepared in this way were recorded on a Hilger double-beam instrument equipped with a NaCl prism. The spectrum of a crystal prepared under an oxygen pressure of 2 mm Hg and measured at 300 and 77°K is shown in Fig. 1. An

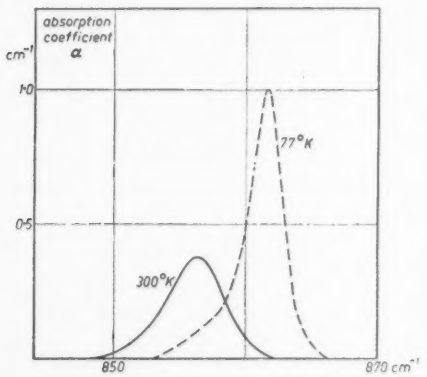

FIG. 1. Infrared absorption of a germanium crystal levelled under 2 mm O_2 pressure; the lattice absorption is subtracted.

absorption band is observed at 856 cm^{-1}; at low temperatures the band shifts to 862 cm^{-1} and becomes sharper. The width of the band at 77°K is only 3 cm^{-1}. KAISER[2] had already found in some germanium crystals a weak absorption band at 860 cm^{-1}, which he ascribed to vibration of oxygen. The fact that this absorption is much stronger in crystals prepared in an oxygen atmosphere confirms KAISER'S conclusion.

The intensity of the absorption is a measure of the oxygen concentration in the crystal. For the relation between the integrated absorption, A, and the number of oxygen atoms/cm^3, N, we take (see Appendix):

$$A = \int \alpha \, d\nu = \frac{2\pi N e^2}{3mc\sqrt{\varepsilon}} \left[\frac{\varepsilon(\varepsilon_0 + 2)}{2\varepsilon + \varepsilon_0}\right]^2. \quad (1)$$

Here ε is the dielectric constant of the crystal, ν the frequency and c the velocity of light, e the effective charge of the vibration involved, and m the effective mass of the vibration, which is given approximately by $1/m = 1/m_O + 1/m_{Ge}$ and $1/m = 1/m_O + 1/m_{Si}$ for germanium and silicon respectively (m_O, m_{Ge}, and m_{Si} represent the atomic masses of oxygen, germanium, and silicon); for ε_0, which is an effective dielectric constant for the oxygen atom, a value of 2·3 (the square of the refractive index of quartz) was taken.

In silicon the infrared absorption has been determined for crystals with an oxygen content known from vacuum-fusion analysis.[4] Using this result and assuming that the oscillator strengths of the vibration of oxygen in germanium and silicon are equal, we can calculate the relation between A and N for germanium from equation (1). In this way we find that an absorption coefficient of 1 cm^{-1} in the maximum of the band (measured at 300°K) corresponds to $1{\cdot}25 \times 10^{17}$ oxygen atoms/cm^3.

Fig. 2 shows, for various crystals, the absorption coefficient in the maximum of the band (300°K) and the calculated oxygen concentration as a function of the partial oxygen pressure in the gas during the zone melting of the crystal. We note that the oxygen concentration is proportional to p_{O_2} for $p_{O_2} < 20$ mm Hg. Beyond this point a deviation from the straight

line begins, and it looks as if the oxygen content saturates at about 7×10^{17} atoms/cm^3. This behaviour is analogous to that recently found in silicon,[5] and can be explained by arguments similar to those WAGNER[6] used to explain the reaction between oxygen and silicon.

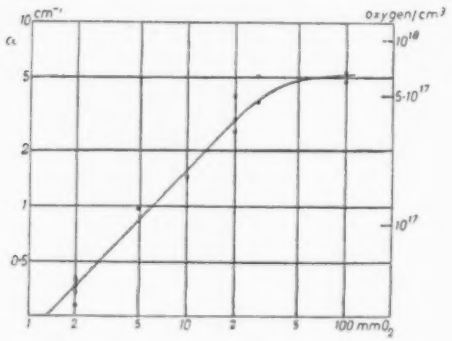

FIG. 2. Absorption coefficient at 856 cm^{-1} (measured at room temperature) and oxygen concentration of germanium crystals as a function of the oxygen pressure during levelling.

Crystals levelled in the presence of liquid GeO_2 contained 7×10^{17} oxygen atoms/cm^3 (method (*b*)).

4. ELECTRICAL PROPERTIES

Donor activity of oxygen in germanium was first observed by ELLIOT.[7] Intrinsic germanium crystals which were grown with oxygen in the way described above also show *n*-type conduction, the specific resistance varying from 0·03 Ω-cm for crystals containing 7×10^{17} oxygen atoms/cm^3 to 40 Ω-cm for crystals with less than 5×10^{16} oxygen atoms/cm^3. It was possible to influence the resistance (all resistances were measured at room temperature) strongly by heat treatment of the crystal. The results of these experiments show a large scattering of the values obtained, so that we are not able to give very quantitative results. However, the following qualitative picture seems fairly well established.

By heating a crystal containing oxygen for a long time, a stationary state can be obtained. The donor concentration in the stationary state at temperature T was determined by heating the crystal for a sufficiently long time at T and measuring the resistivity after quenching the crystal (for example by dropping the crystal in glycol) to room temperature. The results are shown in Fig. 3. We note that at high temperatures the stationary donor concentration is low. At low temperatures the donor concentration is much higher, but it is still considerably smaller than the oxygen concentration as found from infrared absorption spectra. Apparently the donor form of oxygen dissolved in germanium is the more stable configuration at low temperature. At higher temperatures the donors are converted into a neutral form of oxygen which is electrically inactive. These processes are to a large extent reversible: different cyclic heat treatments produce little change in the results. The fact that the maximum donor concentration at low temperatures is considerably smaller than the oxygen concentration indicates that a donor is formed by the association of a number of oxygen atoms.

An attempt was made to describe the experimental results by assuming an equilibrium state between the neutral form N and the donor form D, built up from four oxygen atoms:

$$4N \rightleftarrows D .$$

The equilibrium constant is:

$$K = \frac{N^4}{D} = K_0 e^{-E/RT} . \qquad (3)$$

Curves giving the relation between the donor concentration D and the oxygen concentration N as a function of T, calculated from $K_0 = 6{\cdot}3 \times 10^{67}$ and $E = 2$ eV, (these values give the best agreement with experiment) are shown in Fig. 3. The agreement with the experimental results is far from perfect, but the

VOL. 12 1959/60

major trends are fairly well represented by the calculated curves.

The rate of conversion into the donor form is strongly temperature-dependent. At 700°C a stationary donor concentration is obtained

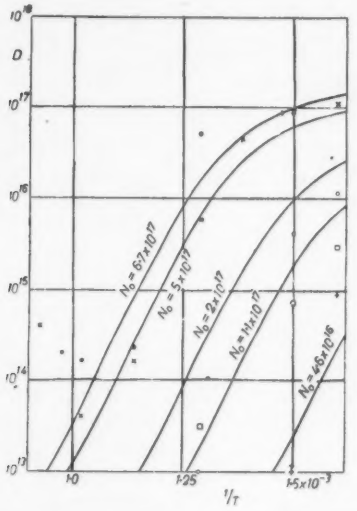

FIG. 3. Stationary donor concentration D after prolonged heating at temperature T (single donors assumed). The curves are calculated from equation (3) with $E=2$ eV, $K_0=6{\cdot}3\times10^{67}$.

● p_{O_2} = 100 mm Hg; × p_{O_2} = 28 mm Hg;
○ p_{O_2} = 10 mm Hg; □ p_{O_2} = 5 mm Hg;
+ p_{O_2} = 2 mm Hg.

after heating the crystal for only a few minutes, while the establishment of the ultimate donor concentration at 350°C may take 10 or more days. Therefore, in order to be able to measure the stationary donor concentration at high temperatures, it is necessary to cool the crystal quickly to room temperature.

The stationary donor concentration at high temperatures does not decrease as rapidly as might be expected from the calculated curves. This effect may be due partly to the fact that the conversion at high temperatures takes place very rapidly and that the cooling to room temperature did not take place fast enough. Also, at high temperatures precipitation of GeO_2, or dissolution of GeO_2 already present in the crystal, may play a part.

The strong dependence of the stationary donor concentration on temperature explains why crystals as grown show a large variation of the specific resistivity; the resistivity at room temperature will depend on the rate of cooling.

The effects just described show a close analogy to the properties of oxygen in silicon. In silicon also there are indications that four oxygen atoms are necessary to form a donor.[8] The fraction of oxygen atoms which may be converted into donors is much larger in germanium than in silicon.

The influence of heat treatment on the infrared absorption is not yet very clear; we have indications that the absorption decreases if the number of donors increases.

5. HALL-EFFECT

The number of electrons in the conduction band as a function of temperature for an oxygen-containing germanium crystal was determined by Hall measurements.* The results are shown in Fig.4. It is not possible to describe the obser-

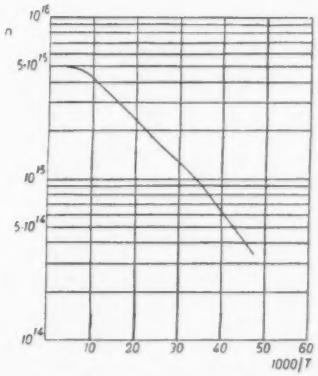

FIG. 4. Number of electrons n from Hall-effect measurements as a function of temperature T.

* The Hall-effect was kindly measured by Mr. J. RIETVELD of this laboratory.

ved curve by a single donor level. A curve of this type is to be expected if there are a number of donor levels at various distances from the conduction band. The case of oxygen in germanium may be analogous to that of oxygen in silicon, where infrared absorption measurements[9] indicate the presence of four different donor levels.

6. OTHER INFRARED ABSORPTION BANDS

In some germanium crystals treated with oxygen, additional absorption bands were found, viz. a rather broad band at 1100 cm^{-1} and a sharp band at 1260 cm^{-1}. The width and frequency of these bands lead us to suppose that they are due to vibrations of a fairly light atom (O, N, C, etc.) incorporated in the crystal. The intensity of these bands was not correlated with the intensity of the band at 860 cm^{-1}. Thus they cannot be ascribed to other vibrations of the oxygen arrangement which causes the main absorption band. It has not so far been possible to relate the two bands with any of the conditions of preparation of the crystal; however, they were never found in crystals which have been grown in an atmosphere free of oxygen.

It is possible that the new absorption bands are due to vibrations of oxygen bonded to another impurity already present in the crystal. The absorption band at 1100 cm^{-1}, the frequency of which just coincides with the frequency of oxygen in silicon, could, for instance, indicate the presence of silicon in the germanium. During the oxygen treatment, the oxygen preferentially oxidizes the silicon dissolved in the germanium, forming Si-O bonds. These presumably will have an infrared absorption band at 1100 cm^{-1}, just as in quartz and in oxygen-containing silicon.

The two bands are usually much weaker than the band at 850 cm^{-1}; the maximum intensity observed was $\alpha = 0{\cdot}3$ cm^{-1} at 1100 cm^{-1} (width of the band ~ 80 cm^{-1}) and $\alpha = 0{\cdot}05$ cm^{-1} at 1260 cm^{-1} (width 20 cm^{-1}). Consequently they will be due to somewhat smaller quantities of impurities. However, the concentrations involved are certainly not small with respect to the concentration of normal donors which are of interest. For example, the band at 1100 cm^{-1} would, if the explanation given above is correct, indicate the presence of $\sim 10^{17}$ Si-O groups/cm^2. The band at 1260 cm^{-1} corresponds to $\sim 10^{16}$ foreign atoms/cm^3.

APPENDIX

To obtain a relationship between the integrated absorption and the number of foreign atoms in the crystals, the effective field acting on the vibrating atoms should be known. A reliable calculation of this field would require a detailed knowledge of the charge distribution and the polarizability around the vibrating atoms. As this detailed information is not available, we may try to derive an approximate result by calculating the effective field for a simple model.

We make a spherical cavity of radius a around the vibrating atom, and assume that the crystal surrouding the cavity may be represented by a homogeneous dielectric constant ε. The atom in the cavity has a polarizability α and an effective charge e. On this charge there acts an effective electric field F equal to the sum of a cavity field and a reaction field. The cavity field $\frac{3\varepsilon}{2\varepsilon+1} E$ (where E is the macroscopic field at a point far from the cavity) would be the field in an empty spherical cavity in a dielectric ε. The field in the cavity induces a dipole in the polarizable atom. This induced dipole polarizes the surrounding dielectric, which in turn produces an extra field, the reaction field. This reaction field is equal to $\frac{3\varepsilon}{2\varepsilon+1} \cdot \frac{f}{1-f} E$, where $f = \frac{\alpha}{a^3} \cdot \frac{2(\varepsilon-1)}{2\varepsilon+1}$ (The calculation of the cavity field and the reaction field is given by BÖTTCHER[10].)

For the integrated absorption we find

$$A = \frac{2\pi N e^2}{3mc\sqrt{\varepsilon}} \left(\frac{F}{E}\right)^2 = \frac{2\pi N e^2}{3mc\sqrt{\varepsilon}} \left[\frac{\varepsilon(\varepsilon_0+2)}{2\varepsilon+\varepsilon_0}\right]^2. \quad \text{(A-1)}$$

Here ε_0 is an effective dielectric constant, defined by $\alpha/a^3 = (\varepsilon_0-1)/(\varepsilon_0+2)$. In equation (A-1) a factor

VOL. 12 959/60

2/3 enters because there are, instead of three degrees of freedom for an isotropic oscillation of the oxygen atom, only the two stretching vibrations which contribute to the absorption in the frequency region which is of interest here.

The value of ε_0, which is a measure of the polarizability of the oxygen atom dissolved in silicon or germanium, is not known. If we assume that the polarizability of oxygen in quartz is equal to the polarizability of dissolved oxygen, we expect that ε_0 will be given approximately by the square of the refractive index of quartz. It is very likely however, that the polarizability of dissolved oxygen is much larger, especially since oxygen has a tendency to become a donor. Therefore, as another extreme case, we can assume that the polarizability of oxygen in the crystal becomes so large that we should take $\varepsilon_0 = \varepsilon$.

KAISER[4] has measured the infrared absorption of silicon with a known content of dissolved oxygen. His results permit us to calculate the effective charge e of the vibration, if ε_0 is known. For ε_0 equal to the square of the refractive index of quartz, we find $e = 1{\cdot}7e_0$ (e_0 is the electronic charge); for $\varepsilon_0 = \varepsilon$, we find $e = 0{\cdot}7e_0$.

These results enable us to calculate the oxygen concentration in germanium from the integrated absorption, assuming that we may use the same values of e and ε_0. We have calculated the oxygen concentrations in germanium from $e = 1{\cdot}7e_0$ and ε_0 equal to the square of the refractive index of quartz. The other extreme case, with $e = 0{\cdot}7e_0$ and $\varepsilon_0 = \varepsilon_{Ge}$ leads to $1{\cdot}6\times$ smaller values of the concentration of oxygen in germanium.

SMAKULA[1] has measured the absorption of oxygen dissolved in silicon, and the absorption of the same amount of oxygen present in the form of small quartz particles dispersed in the silicon crystal. He found that the integrated absorption is approximately the same in both cases. For the absorption of small particles of quartz, dispersed in a medium with dielectric constant ε, an equation of type (A-1) should hold with the appropiate value of e for quartz; ε_0 is in this case equal to the square of the refractive index of quartz. Unfortunately, the value of e for quartz is not known. However, if we combine KAISER'S data with SMAKULA'S we are able to calculate the effective charge for quartz, and we find $e = 1{\cdot}7e_0$. This value is rather high; according to PAULING[11] the Si-O bond is ionic to the extent of ~ 50 per cent, corresponding to an effective charge on the oxygen atom of e_0.

Finally, we compare this result for quartz with the two extreme assumptions for the polarizability of dissolved oxygen:

(a) The polarizability and the effective charge are equal for dissolved oxygen and for oxygen in quartz. The Si-O bond is highly ionic with $e = 1{\cdot}7e_0$.

(b) Oxygen dissolved in silicon has a much larger polarizability than oxygen in quartz. For dissolved oxygen the effective charge is $0{\cdot}7e_0$, and for quartz $1{\cdot}7e_0$.

The observed absorption frequency is practically the same for oxygen dissolved in silicon and for quartz. It does not seem very probable that a large difference in effective charge and polarizability would leave the vibration frequency unaffected. Therefore we have used assumption (*a*), where all properties (vibration frequency, polarizability, and effective charge) of oxygen dissolved in silicon are equal to these properties in quartz.

REFERENCES

1. SMAKULA A. and KALNAJS J., *J. Phys. Chem. Solids* **6,** 46 (1958). FULLER C. S. and DOLEIDEN F. H., *J. Appl. Phys.* **29,** 1264 (1958).
2. KAISER W., KECK P. H. and LANGE C. F., *Phys. Rev.* **101,** 1264 (1956).
3. PFANN W. G., *Zone Melting.* Wiley, New York (1958).
4. KAISER W. and KECK P. H., *J. Appl. Phys.* **28,** 882 (1957).
5. KAISER W. and BRESLIN J., *J. Appl. Phys.* **29,** 1292 (1958).
6. WAGNER C., *J. Appl. Phys.* **29,** 1295 (1958).
7. ELLIOT G., *Nature (Lond.)* **180,** 1350 (1957).
8. KAISER W., *Phys. Rev.* **105,** 1751 (1957).
9. HROSTOWSKI H. J. and KAISER R. H., *Phys. Rev. Letters* **1,** 199 (1958).
10. BÖTTCHER C. J. F., *The Theory of Electric Polarization.* Elsevier, Amsterdam (1952).
11. PAULING L., *The Nature of the Chemical Bond.* Cornell University Press, Ithaca, N.Y. (1955).

J. Phys. Chem. Solids Pergamon Press 1959. Vol. 12. pp. 28–40. Printed in Poland.

MAGNETIC PROPERTIES OF POLYCRYSTALLINE MATERIALS

D. M. GRIMES, R. D. HARRINGTON and A. L. RASMUSSEN

University of Michigan, Ann Arbor, Michigan
National Bureau of Standards, Boulder, Colorado

(*Received* 9 *March* 1959)

Abstract—The variation of the magnetic Q with internal magnetization is discussed, using both the domain rotation and the domain-wall motion model of magnetization change. The variation of the reversible susceptibilities with magnetic moment is reported on four samples, and the results are compared with results from the frequency spectra in the initial and remanent states. The distribution of magnetic moments in the system as a function of the angle between individual and averaged moments is discussed in terms of an infinite series expansion in Legendre polynomials. The coefficients of the first four terms can be measured. Experimental data are given for the first three.

1. INTRODUCTION

THE magnetic susceptibility is defined as the ratio of resultant magnetization to magnetic field intensity. In ferrimagnets it is a function of both field strength and frequency. The reversible susceptibility is that susceptibility effective with a differential magnetic field. The differential field can be superimposed upon a finite biasing field. The reversible susceptibility depends upon the angle between biasing and differential fields, upon the magnetization level in the material, and upon the magnetic history of the specimen.

The susceptibility-producing mechanism is not completely understood. It is often assumed either that domain moments rotate in unison or that the domain walls move to change the net averaged moment of the sample. The reversible susceptibility and resulting differential magnetostriction for each mechanism were discussed and contrasted in an earlier paper, which will be referred to as I.[1]

In that paper, the reversible quantities were discussed in terms of the distribution of magnetic moments. The calculations of predicted behavior of the reversible quantities with magnetic moment were carried out with the assumption that the moments would be distributed in some most probable state determined by a Boltzmann-type distribution of moments about the unit sphere. This argument has the merit that the direction of the moments is strongly influenced by crystallographic orientation, and that the orientation of neighboring grains can be considered independent. This does not mean, however, that the resulting moments must be randomly oriented. A factor of considerable interest, therefore, is a calculation of what the distribution of moments is in a magnetic material.

* Supported in part by the U.S. Air Force Office of Scientific Research and Development Command under Contract No. AF 18(603)-8. Reproduction in whole or in part is permitted for any purpose of the U.S. Government.

VOL. 12 59/60

The detailed calculation of $f(\Theta)$ is possible, at this time, in only the simplest cases. The basic difficulty is that the solution of this problem must involve the solution of essentially the same number of coupled differential equations as there are atomic moments. If the moments are treated in the aggregate, localized potential minima between neighboring grains and neighboring domains must be included, as must the effect of nonmagnetic inclusions. The dominant role played by this type of surface energy has been stressed by GOODENOUGH[2].

The calculation of $f(\Theta)$, then, requires first the development of as realistic as possible a microscopic model of magnetic behavior followed with the distribution of this behavior over the sample. The microscopic models used in I were such that: (A) that the domain moments remained always oriented along the crystallographic directions which minimized the anisotropy energy, and (B) that the static moments remained along "easy" directions, but that the susceptibility arose by the rotation of the domain moments away from those directions in the dynamic case. Neither model is completely correct. Both are highly idealized and, for example, contain neither the "curling" concept discussed by BROWN[3] and by FREI et al.,[4] nor the effect of inhomogeneous fields. A more correct formulation awaits the inclusion of more accurate microscopic models.

There has, however, been ample precedent set for considering magnetic susceptibility as being due either to domain rotation or to domain-wall motion. This lamentable state is continued in the present paper.

It was assumed in I that the frequency of the measuring field was much less than the resonance or relaxation frequency of the magnet. Under these conditions, the magnetization-dependence of the transverse susceptibility on the biasing field is distinctly different for each of the assumed susceptibility sources as long as the anisotropy field remains much larger than the applied field.

The reversible susceptibility, as defined above, is reversible in the thermodynamic sense of zero energy dissipation for only the special case of zero applied frequency. An associated energy loss exists for all nonzero frequencies. This loss is describable as the imaginary part of the complex magnetic susceptibility, ($\chi = \chi' - j\chi''$). The magnetic Q is defined to be the ratio of real to imaginary susceptibility. It is convenient in the following section to discuss the loss in terms of Q. The dependence of Q upon magnetization, field directions, and source of susceptibility is briefly discussed in this paper.

Frequency spectra have commonly been used to investigate the susceptibility sources. This extensively used method depends upon the different dependence of the frequency of susceptibility fall-off on magnetization mechanism to distinguish between sources.[5-8] Some investigators have also measured the spectra of the material magnetized to remanence and have utilized these results to aid spectral interpretation.[6-11] EPSTEIN[12] and BIRKS[13] in particular have utilized spectral information to obtain quantitative determinations of the amount of wall-motional and domain-rotational susceptibility.

2. DISCUSSION

(a) *Distribution function* $f(\Theta)$

The macroscopic material is considered to be composed of randomly oriented crystallites. The crystallites are sufficiently small so that the moment of each crystallite is much less than the aggregate moment of the sample. The crystalline orientation of each grain is taken to be independent of the orientation of its neighbors. For such a model the static moment is always parallel with the static field.

The distribution $f(\Theta)\sin\Theta\,d\Theta$ is defined to be the fraction of the atomic moments in the system oriented at an angle between Θ and $\Theta+d\Theta$ with respect to the applied magnetic field. It is convenient to expand $f(\Theta)$ in an infinite series of Legendre functions such that:

$$F(\Theta)=\sum_{n=0}^{\infty}A_nP_n(\cos\Theta) \tag{1}$$

where A_n is a function of the magnetic field present and the magnetic history of the specimen.

By definition,

$$\langle\cos^n\Theta\rangle=\frac{\int d\Omega\cos^n\Theta f(\Theta)}{\int d\Omega f(\Theta)} \tag{2}$$

where $\langle\cos^n\Theta\rangle$ represents the average value of $\langle\cos^n\Theta\rangle$ over the sample. Substituting equation (1) into equation (2) and integrating over the unit sphere yields:

$$\langle\cos^n\Theta\rangle=\frac{1}{2A_0}\sum_{m=0}^{\infty}A_m\int_{-1}^{1}\gamma^n\,d\gamma\,P_m(\gamma). \tag{3}$$

Upon solving for the coefficients A_m in equation (3), using the orthogonality of the Legendre functions,

$$\frac{A_m}{A_0}=(2m+1)\langle P_m(\cos\Theta)\rangle. \tag{4}$$

Thus the coefficient of the mth term in the infinite series expansion for the distribution function can be determined if $\langle\cos\Theta\rangle$, $\langle\cos^2\Theta\rangle$, ... $\langle\cos^m\Theta\rangle$ are known. So, of course, the first coefficients are:

$$\left.\begin{aligned}A_1/A_0&=3\langle\cos\Theta\rangle\\A_2/A_0&=5/2\,[3\langle\cos^2\Theta\rangle-1]\\A_3/A_0&=7/2\,[5\langle\cos^3\Theta\rangle-3\langle\cos\Theta\rangle]\,.\end{aligned}\right\} \tag{5}$$

Thus the distribution function can be experimentally determined if $\langle\cos^m\Theta\rangle$ can be measured. The A_m coefficients are functions of both magnetic field and magnetic history. The coefficient A_1/A_0 can be determined from the M-H loop. The coefficient A_2/A_0 can be determined from equation (5) and the magnetostriction[14,15] and independently from equations (9) and (10) of I, where it is stated that the susceptibility due to domain rotation is given by:

$$\left.\begin{aligned}\chi_p&=\frac{3}{2}\chi_0(1-\langle\cos^2\Theta\rangle)\\\chi_t&=\frac{3}{4}\chi_0(1+\langle\cos^2\Theta\rangle)\,.\end{aligned}\right\} \tag{6}$$

A_3/A_0 can be determined from a knowledge of A_1/A_0 and the use of equations (16) of I, relating the differential magnetostrictions, namely:

$$\left.\begin{aligned}d_p&=\frac{3}{2}d_0(\langle\cos\Theta\rangle-\langle\cos^3\Theta\rangle)\\d_t&=\frac{3}{4}d_0(\langle\cos\Theta\rangle+\langle\cos^3\Theta\rangle)\end{aligned}\right\} \tag{7}$$

where $d_0=\dfrac{3\lambda_s\chi_0}{M_s}$.

(b) *Magnetic Q (Domain rotation)*

To estimate the magnetization-dependence of the magnetic Q when the susceptibility arises from domain rotation, it is convenient to start with a single-crystal ferromagnet. The domain-rotation effects are assumed to obey the differential equation[16]

$$\frac{\partial M}{\partial t}=\gamma(M\times H)-\frac{\alpha}{M_s}M\times\frac{\partial M}{\partial t}, \tag{8}$$

where M is the magnetic moment, γ is the magnetomechanical ratio, M_s is the spontaneous moment, H is the applied magnetic field, and α is a dimensionless parameter proportional to the power loss. The total sample moment is assumed to be the sum of moments from all crystallites. It is thus necessary to first calculate intergranular effects, then to sum up all moments over the polycrystalline sample.

VOL. 12 59/60

PARK[8] showed that if the magnetic moment of the grains neighboring a given grain averages that of the gross material, then grain size and particle interaction is described by a single constant p, defined by the equation

$$H = h - pM \tag{9}$$

where H is the effective differential field, h is the applied differential field, and M is the gross magnetization. The constant p is a function of the localized packing and remains essentially independent of M; p can be regarded as the demagnetizing factor of the grain partially canceled by the moments of its neighbors.

Upon substituting equation (9) into equation (8) and using the additional assumptions that a large static biasing field is oriented in the Z-direction and sinusoidal time-dependence of an additional applied field, the reversible susceptibility matrix is given by:
(equation (8) of I)

$$\chi = \frac{1}{4}\begin{pmatrix} [1+\langle\cos^2\Theta\rangle](\chi_- + \chi_+), & 2\langle\cos\Theta\rangle(\chi_- - \chi_+), & 0 \\ -2\langle\cos\Theta\rangle(\chi_- - \chi_+), & [1+\langle\cos^2\Theta\rangle](\chi_- + \chi_+), & 0 \\ 0, & 0, & 2[1-\langle\cos^2\Theta\rangle](\chi_- + \chi_+) \end{pmatrix}, \tag{10}$$

where $\langle\ \rangle$ represents the average value in the polycrystal and Θ represents the angle between the spontaneous moment and the applied field. The susceptibilities $\chi_\pm$ are defined by the equation

$$\chi_\pm = \frac{M_x \pm iM_y}{H_x \pm iH_y}, \tag{11}$$

where M_x and H_x are the components of the differential magnetization and field in the x-direction and $i = \sqrt{-1}$. The i operator represents a spatial rotation of $\pi/2$ radians. The resultant algebra from combining equations (8), (9), and (11) for the Q of the elements on the diagonal of equation (10), yields:

$$Q^r = \frac{\omega_0}{a\omega}\,\frac{1-\left(\frac{\omega}{\omega_0}\right)^2(1-a^2)}{1+\left(\frac{\omega}{\omega_0}\right)^2(1+a^2)}, \tag{12}$$

where ω is the applied radian frequency, and $\omega_0 = \gamma H_t$. H_t, in turn, is the sum of the static applied and anisotropy fields, H_{ap} and H_{an}, and the effective internal field pM.

Thus:

$$H_t = H_{ap} + H_{an} + pM. \tag{13}$$

In the low-frequency limit:

$$Q^r = \frac{\omega_0}{a\omega}. \tag{14}$$

Note that Q^r is independent of field direction. The low-frequency initial susceptibility is obtained by combining equations (5) and (10) of I. The result is:

$$\chi_0 = \frac{2\omega_1}{3\omega_0} \tag{15}$$

where $\omega_1 = \gamma M_s$. Combining equations (14) and (15),

$$\chi_0 Q^r = \frac{2\omega_1}{3a\omega}. \tag{16}$$

The product depends upon a and directly measurable quantities, and does not explicitly contain the biasing magnetic field through ω_0.

(c) *Magnetic Q (Wall motion)*

The change in magnetic moment due to 180° wall movement is, in unit volume, given by:

$$\Delta M = \sum_k 2M_s A_k x_k \tag{17}$$

where A_k is the area of the kth wall, and x_k is

the distance through which it is moved by an applied magnetic field H. The wall movement is presumed to be governed by the differential equation:

$$2\mu_0 M_s H = f_k x_k + \beta \frac{dx\hat{k}}{dt} + m \frac{d^2 x\hat{k}}{dt^2} \quad (18)$$

where f_k is the restoring constant for the kth wall, β depends upon the structure-insensitive properties of the material and the parameter a of equation (8), while m depends only upon the structure-insensitive properties of the material. μ_0 is the permeability of free space.

Combining equations (17) and (18), the wall-motional reversible susceptibility under sinusoidal excitation is found to be:

$$\chi_w = 4\mu_0 M_s^2 \sum_k \frac{A_k}{f_k} \left[\frac{\left(1 - \omega^2 \frac{m}{f_k}\right) - j\omega\beta/f_k}{\left(1 - \omega^2 \frac{m}{f_k}\right)^2 + \omega^2 \frac{\beta^2}{f_k^2}} \right]. \quad (19)$$

In the low-frequency limit, the real susceptibility and the Q become:

$$\chi^w = 4\mu_0 M_s^2 \sum_k \frac{A_k}{f_k} \quad (20)$$

$$Q^w = \frac{1}{\omega\beta} \frac{\sum A_k/f_k}{\sum A_k/f_k^2}. \quad (21)$$

Thus for a given material at a fixed low frequency, the Q varies only with β, A_k, and f_k.

The reversible susceptibility is given as a function of magnetization not only by the detailed mechanistic equation (20) above, but also by equations (2) and (18) of I. From these, if $\chi_p^w = \chi_t^w = \chi_0$ for virgin material with $M = 0$ and if χ_p decreases montonically with increasing M, then so must χ_t. Indeed the susceptibilities are related by the equation:

$$\chi_p^w = \left[\frac{\chi_t^w}{1 - \frac{d \ln \chi_t^w}{d \ln M}} \right]. \quad (22)$$

If the average stiffness term f_k increases with magnetization, then so will Q. Since both A_k and f_k vary with field orientation, the parallel and transverse Q's will, in general, differ. This feature is distinctly different from domain rotation.

(d) *Initial and remanent susceptibility*

The initial susceptibility due to domain-wall motion has been approximated by BOZORTH[17] for sinusoidal internal strains arising from magnetostrictive forces present when annealed material is cooled below the Curie temperature. The result is:

$$\chi_0 = \frac{4\mu_0 M_s^2}{3\pi\lambda_s^2 E} \quad (23)$$

where λ_s is the saturation magnetostriction and E is the Young's modulus of the material. Likewise the initial susceptibility due to domain rotation can be approximated as:

$$\chi_0 = \frac{2\mu_0 M_s^2}{3K_1} \quad (24)$$

where μ_0 is the permeability of free space and K_1 is the first-order anisotropy constant. From equations (23) and (24) it is apparent that in pure material the relative importance of the two susceptibility mechanisms depends upon the relative magnitudes of the effective anisotropy and magnetostrictive energy densities in the material.

For material with susceptibility arising by domain rotation, the relationship between the initial susceptibility and the resonant frequency should satisfy the equation:

$$f_0 = \frac{2\gamma M_s}{2\pi \cdot 3\chi_0} \quad (25)$$

where γ is a constant taken to be $2{\cdot}21 \times 10^5$ m/A-sec, f_0 is the resonant frequency, M_s is the spontaneous moment of the material, and χ_0 is the initial susceptibility.

VOL. 12 59/60

BECKER and DÖRING[18] discuss a model of magnetic remanence in which, as the field is decreased from the saturation value to zero, the moments rotate to occupy the same "easy" crystallographic directions occupied in virgin material, except that all components initially antiparallel to the saturation direction become parallel. For this model, the remanent magnetization is 0·5 M_s and the remanent rotational reversible susceptibilities equal the initial rotational susceptibility. This model is valid for hexagonal material with $K_1 > 0$. FOMENKC[9] used it to interpret his permeability spectrum results. If this is also the position of maximum parallel and minimum transverse field susceptibility, then going around the M-H loop the parallel susceptibility peak occurs for M decreasing in magnitude. The remanent and initial susceptibilities will be equal.

The rotational model of gross flux change in cubic crystals would predict moments oriented in the "easy" directions nearest the field directions at remanence. For this case the remanent and rotational susceptibilities taken from the results of I are given in Table 1 for all anisotropy coefficients save $K_1 = 0$. (These are the expected values from reference (1) for $\eta \to \infty$).

Table 1. *Remanent results* M_r/M_s

	Hexagonal $K_1 > 0$	Cubic $K_1 < 0$	Cubic $K_1 > 0$	Hexagonal $K_1 < 0$
M/M_s	0·500	0·866	0·831	0·785
χ_p^r/χ_0^r	1·000	0·366	0·449	0·500
χ_t^r/χ_0^r	1·000	1·318	1·276	1·250

An analysis of the relationships between remanent condition and the reversible susceptibility has been carried out by FREI and SHTRIKMAN[19] on the assumption that the reversible susceptibility is due to domain rotation. Their analysis contains the assumption that the reversible quantities are due to rotation and that the expansion of magnetization in terms of applied field must obey the rotational equations through second order in the ratio of applied to anisotropy fields, as can be seen from their equation (10). Their resulting equation (29) can be put in the form:

$$\frac{M_r}{M_s} = \frac{2M_s \chi_p}{(\chi_p + 2\chi_t)^2}\left[\frac{d(\chi_p + 2\chi_t)}{dM}\right] \qquad (26)$$

for comparison with experimental values.

3. EXPERIMENTAL

(a) *Samples measured*

Four samples were subjected to detailed measurements and are reported here. The compositions of the samples are listed in Table 2. All except the magnesium ferrite sample were fabricated at the University of Michigan.

Table 2. *Composition of ferrites surveyed*

Designation	Composition
F-1-2	$Ni_{0.467}\,Zn_{0.533}\,Fe_2\,O_4$
F-6-2	$Ni_{0.168}\,Zn_{0.533}\,Co_{0.299}\,Fe_2\,O_4$
AA-107-4	$Fe_5\,Y_3\,O_{12}$
I-15-1	$Mg\,Fe_2\,O_4$

The samples with designation starting F-1 and F-6 were prepared by first ball-milling the C.P. oxides weighed to the desired composition in acetone, then decanting, drying, and pressing into a toroidal pill. They were then heated rapidly to 1150°C, heated slowly to 1375°C for ½ hr, slowly cooled to 1200°C, and held for 2 hr. The furnace was then flushed with nitrogen and de-energized. The I-15-1 core was prepared by Dr. D. L. FRESH and is from the same material as that reported on previously by RADO *et al.*[20] as their type-F core. The AA-107-4 core was prepared by firing in air at 1350°C for 4 hr. The mixing

and pressing procedure was the same as for the type-F-1 and F-6 cores.

(b) *Procedures and techniques*

All measurements were taken at ambient temperatures on toroidal samples, since this geometry avoids the complexities of demagnetizing factors. Coaxial line techniques were utilized for the spectral measurements. The complex susceptibility of the F-6 samples was measured from 1·0 to 40 Mc, using the radio-frequency permeameter in conjunction with a Q-meter. For the F-1 samples the real susceptibility from 0·1 to 40 Mc and the imaginary susceptibility from 0·1 to 1·5 Mc were measured with the permeameter. A fixed-length coaxial line and a radio-frequency bridge were used for the remaining higher loss measurements up to 50 Mc. From 50 to 5000 Mc, variable-length coaxial-cavity methods were used for complex susceptibility measurements on both types of samples.

The susceptibility and Q for the variable-field measurements were taken with a Q-meter. For the transverse field measurements, the sample was placed between the pole faces of an electromagnet. The biasing field was along the axis of the toroid. Girdle windings about both outer and inner periphery of the toroid were used to determine the field and magnetization. An extra winding was placed about the toroid to furnish the biasing magnetic field when the parallel field measurements were taken.

(i) *F-6 samples.* Two different samples of F-6 material, code designated F-6-1 and F-6-17, were measured for the frequency spectra. The initial spectrum of F-6-1 is shown in Fig. 1. Both the initial and the remanent parallel spectra of F-6-17 are shown in Fig. 2. All spectra show but a single resonant peak in the real susceptibility. The resonant frequency as determined by the peak in the imaginary susceptibility is seen to be about 130 Mc for F-6-1, with a corresponding low-frequency susceptibility of 47. For F-6-17, the resonant frequency is about 75 Mc, with an initial low-frequency susceptibility of about 82. The remanent loss for F-6-17 also peaked at 80 Mc, with a low-frequency susceptibility of 75. An instability of a few per cent was noted in both samples between different measuring runs.

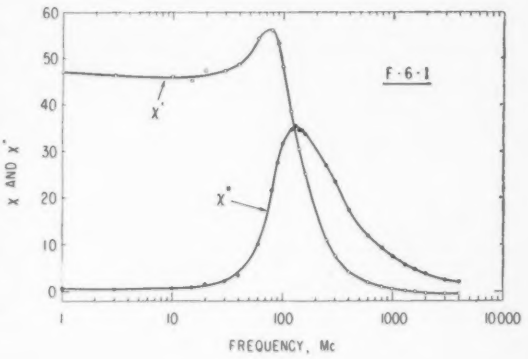

FIG. 1.

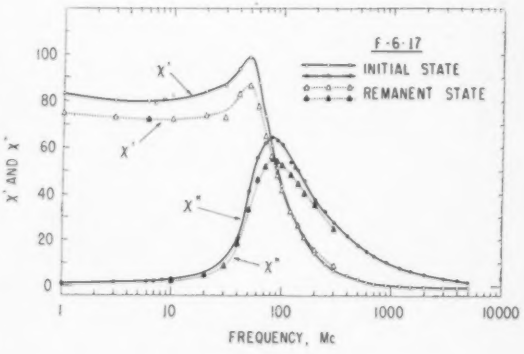

FIG. 2.

Comparing the initial and remanent curves, it is apparent that the positions of the peak in both real and imaginary susceptibilities occur at essentially the same frequency, and that the ratio of remanent to initial susceptibility is about 0·91.

VOL. 12 959/60

The varation of the low-frequency susceptibility with magnetization is depicted in Fig. 3. These data were taken on sample F-6-2. The transverse susceptibility passes through a decided minimum near $M = 0$. Both the measured Q's are essentially constant over a wide range of magnetization, and indeed were never observed to rise to a value equal to twice the initial value.

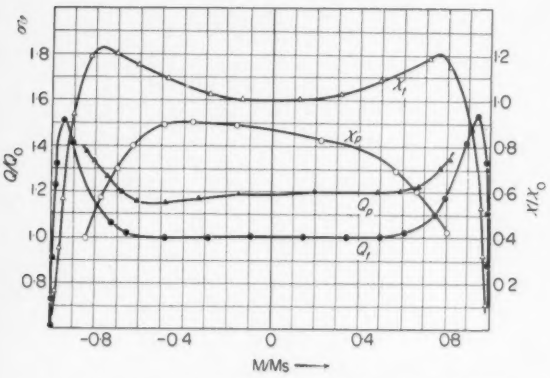

FIG. 3. Parallel and transverse field susceptibilities; Core F-6-2.

(ii) *F*-1 *samples*. The spectra of the sample code designated F-1-5 were tested. Fig. 4

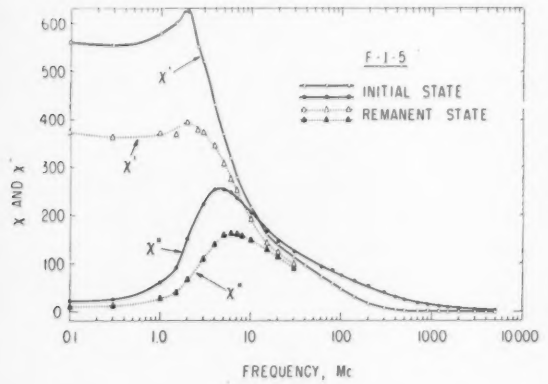

FIG. 4.

shows the complex susceptibility for both initial and parallel remanent states. The initial spectrum of F-1-6 was also measured and found to be similar in all respects to F-1-5. The resonant frequency of F-1-5 was measured at 4·5 Mc as determined by the peak in the imaginary value. The low-frequency susceptibility was measured as 561. The ratio of remanent to initial value of susceptibility was 0·66. The peak in imaginary susceptibility at remanence occurred at about 6 Mc.

The susceptibility was measured as a function of the magnetization on specimen F-1-2 (see Fig. 5). For this core, the transverse susceptibility remained essentially constant over a wide range of magnetization values. The Q's pass through a minimum near $M = 0$. As in the case of F-6-2, the transverse susceptibility remained always larger than the parallel value. The Q's increased rapidly with increasing field to a value more than 10 times the initial value.

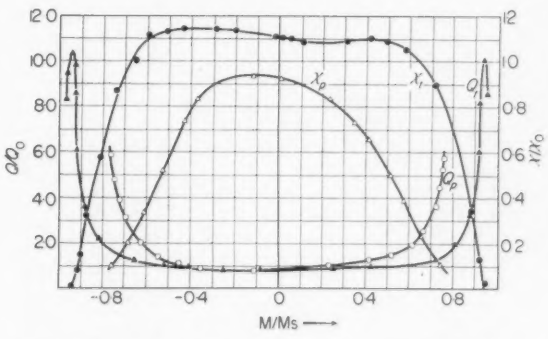

FIG. 5. Parallel and transverse field susceptibilities; Core F-1-2.

(iii) *I*-15-1. The frequency spectrum for this material has been published by RADO *et al.*[20] and corresponds to their "Ferrite F". They conclude that the low-frequency susceptibility is predominately due to the movement of domain walls. The variation of the susceptibilities with magnetization is shown in Fig. 6. For this core, both the susceptibilities pass through a maximum in the vicinity of zero

moment, while the Q's pass through a minimum.

(iV) *AA*-107-4. The frequency spectra for this material have been published by two of

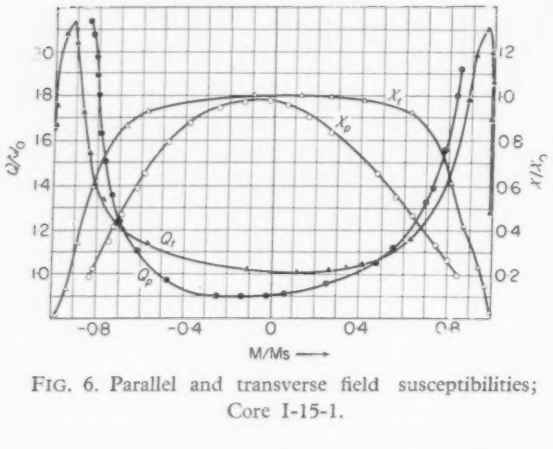

FIG. 6. Parallel and transverse field susceptibilities; Core I-15-1.

us.[21] It was concluded on the basis of spectral information that the susceptibility was predominantly due to domain-wall motion. The variation of the susceptibilities with magnetization is shown in Fig. 7. The transverse susceptibility does not pass through a minimum.

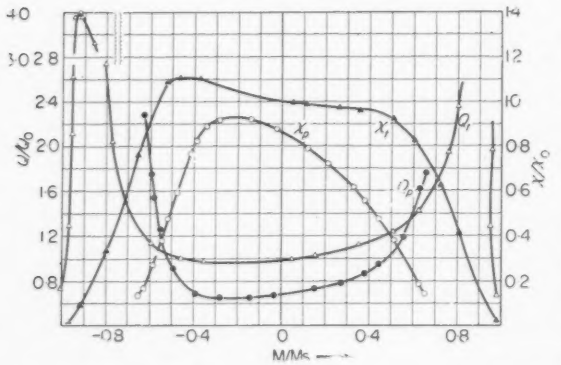

FIG. 7. Parallel and transverse field susceptibilities; Core AA-107-4.

1. INTERPRETATION OF RESULTS

The values of f_0 measured experimentally are listed in Table 3, along with the values calculated from equation (25). The experimental value of f_0 was determined by the frequency of the peak value of imaginary susceptibility.

Table 3. *Resonant frequency* (Mc).

Sample type	Measured	Calculated	$\frac{\chi_p\,(M=0)}{\chi_p\,(H=0)}$
F-6-1	130	179	—
F-6-17	75	102	0·91
F-1-2	45.	15	0·66

The expected variation of the parallel susceptibility with magnetization can be computed from the transverse susceptibility dependence. For the case of wall-motional susceptibility, equation (22) is the proper equation. For the case of rotational susceptibility, equation (10) of I is the proper equation. For equation (10) to be useful, however, the variation of χ_0 with applied field must be known. From equation (15) and the definition of ω_0, it follows that in the absence of a detailed knowledge of the effective anisotropy field, which is always the case for polycrystalline material, χ_0 is known only so long as the biasing field is small compared with the anisotropy field.

The magnetic parameters of the four cores are listed in Table 4.

Plots of χ_p computed from χ_t for each of the four samples measured are shown in Figs. 8-11 and compared with the experimentally measured curves. It is apparent that the rotational curve fits F-6-2 well and that the wall-motional curve fits I-15-1 well. The fit is not good for either of the other specimens, but nevertheless the wall-motional curve fits AA-107 closer than the rotational curve. The conclusion that cores F-6-2 and I-15-1 have susceptibility arising predominantly from rotation and wall motion respectively is substan-

Table 4. Magnetic parameters of four ferrimagnetic cores (320 kc)

Core	Parallel						Transverse			
	χ_0†	Q_0	χ_{p_0}	Q_{p_0}	χ_{pr}	Q_{pr}	χ_{t_0}	Q_{t_0}	χ_{tr}	Q_{tr}
F-6-2	—	—	46·5	72·4	39·6	71·7	52·8	60·8	62·0	61·4
F-1-2*	410	15·2	388	13·2	135	28·1	450	13·5	448	16·7
I-15-1	—	—	54·2	38·1	33·3	53·9	54·2	39·5	43·6	49·8
AA-107-4	36·4	10·9	31·1	7·4	30·0	8·2	36·6	10·4	40·0	9·7

* Values at 500 kc.

† The subscript $_0$ indicates measurements in the virgin state, p indicates parallel and t transverse measurements. p_0 and t_0 represent measurements around the M-H loop at the position $M = 0$ in parallel and transverse fields. pr and tr represent similar measurements at the remanent position.

VOL. 12 59/60

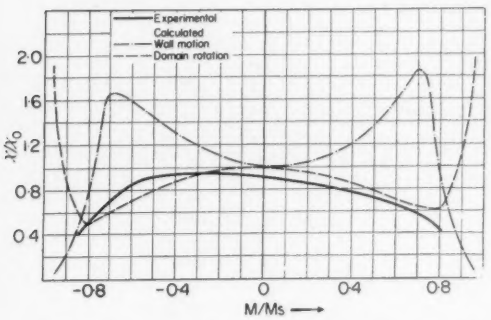

FIG. 8. Parallel reversible susceptibilities; Core F-6-2.

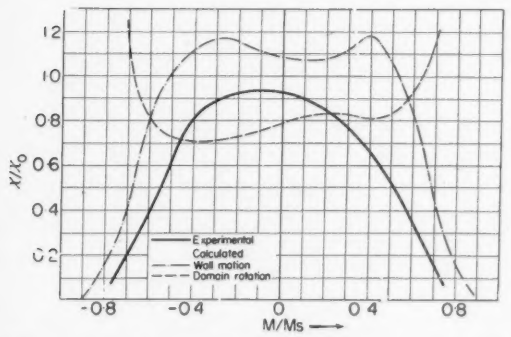

FIG. 9. Parallel reversible susceptibilities; Core F-1-2.

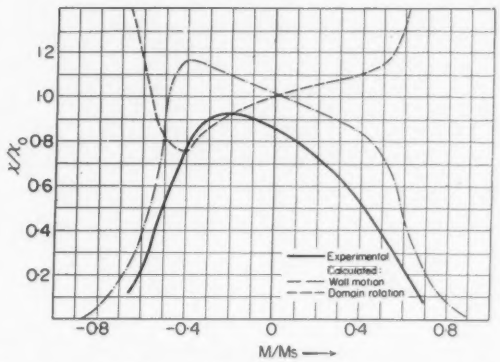

FIG. 10. Parallel reversible susceptibilities; Core AA-107-4.

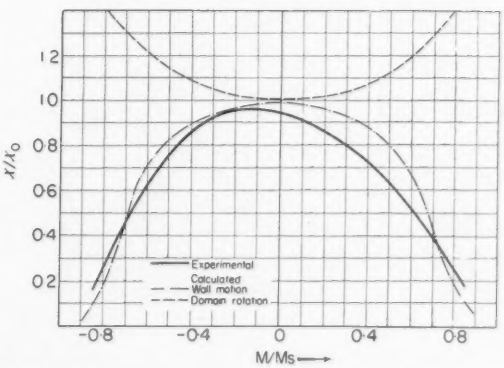

FIG. 11. Parallel reversible susceptibilities; Core I-15-1

tiated by the spectral interpretation of Figs. 1 and 2 and by RADO *et al.*[20]

The curve calculated for χ_p for rotation is valid so long as the anisotropy field remains much larger than the applied biasing field. F-6-2 contains cobalt, and therefore will have a large anisotropy field. Core F-1-2 s a mixed

nickel-zinc ferrite with a corresponding small anisotropy. Thus the lack of agreement with rotational curves is not significant. For the F-1-2 core, there was a slight but real minimum in the χ_t in the vinicity of zero moment. This feature is not consistent with wall motion and the accompanying χ_p behavior. Therefore it is concluded that domain rotation must be present. No such behavior was found in AA-107. In the spectral data, two peaks in the imaginary susceptibility were observed for AA-107, and only one for F-1-2. There must, therefore, be two important mechanisms for the AA-107. These mechanisms are assumed to be rotation and wall motion. For F-1-2, one can say only that domain-rotational effects enter. If wall-motional effects are present, the resonant frequency must occur at the same point as the rotational effect. The essential difference between F-1 and F-6 lies in the value of the anisotropy. Since rotational effects have been shown to exist in the high-anisotropy material, it is expected that they should also exist in the low-anisotropy material.

Material F-6-2 apparently fits the conditions imposed in this paper for the static conditions, namely oriented along easy crystallographic directions, and the susceptibility obeys the rotational equations. This material would not satisfy the conditions of FREI and SHTRIKMAN[19]. On the other hand, F-1-2 does not satisfy the conditions as described in this paper, apparently because of the small anisotropy, but does satisfy the conditions of FREI and SHTRIKMAN. Table 5 compares the values of remanent moment calculated from equation (26) with experimentally measured values. The agreement is not good, and indeed the best agreement is with the material whose susceptibility arises from wall motion.

Table 5

Specimen	Measured M_r/M_s	Calculated M_r/M_s	H_c	M_s $\times 10^{-5}$	M_r $\times 10^{-5}$
AA-107-4	0·389	0·259	160	1·06	0·41
F-6-2	0·660	0·041	127	3·58	2·37
F-1-2	0·610	0·330	100	3·67	2·24
I-15-1	0·730	0·675	175	1·35	0·98

Upon eliminating χ_0 from equation (6), the average value of $\langle\cos^2\Theta\rangle$ is found to be:

$$\langle\cos^2\Theta\rangle = \left(\frac{2\chi_t - \chi_p}{2\chi_t + \chi_p}\right). \tag{27}$$

Solving for $\langle\cos^3\Theta\rangle$ from equations (7),

$$\langle\cos^3\Theta\rangle = \left(\frac{2d_t - d_p}{2d_t + d_p}\right)\langle\cos\Theta\rangle. \tag{28}$$

Note that $\langle\cos^2\Theta\rangle$ should vary from 1/3 in the demagnetized state to unity when the material is saturated. A similar wall-motional equation yields:

$$\frac{2\chi_t - \chi_p}{2\chi_t + \chi_p} = \frac{1 - 2\left(\dfrac{d\ln\chi_t}{d\ln M}\right)}{3 - 2\left(\dfrac{d\ln\chi_t}{d\ln M}\right)}. \tag{29}$$

If the values of χ_t and M are calculated assuming a Boltzmann distribution of moments, then $\chi_t = AM_sL(\eta)/\eta$ and $M = M_sL(\eta)$, where A is a constant for the material, $L(\eta)$ represents the Langevin function of η, and $\eta = AH_t$,

where H_t is the totalized biasing field, including history, anisotropy, and applied field. Substituting these values into equation (29) yields a function which goes from 1/3 for $M = 0$ to unity for saturation.

Plots of $\frac{2\chi_t - \chi_p}{2\chi_t + \chi_p}$ as a function of $\langle \cos \Theta \rangle$ are shown in Figs. 12 and 13. In Fig. 12, the theoretical curve is the value of $\langle \cos^2 \Theta \rangle$ calculated for domain rotation. In Fig. 13, the theoretical

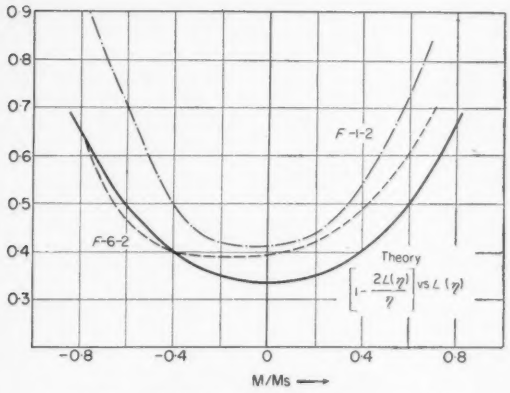

FIG. 12. Variation of $\langle \cos^2 \Theta \rangle$ with $\langle \cos \Theta \rangle$.

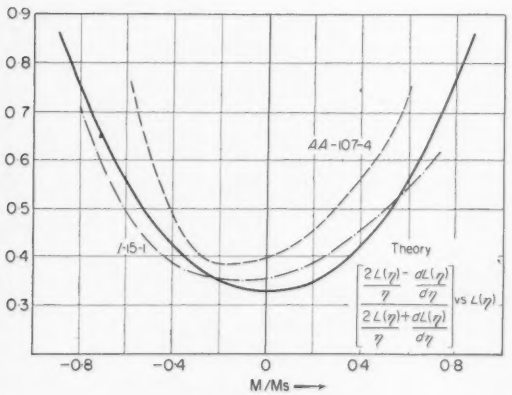

FIG. 13. $\left[\frac{2\chi_t - \chi_p}{2\chi_t + \chi_p}\right]$ versus M/M_s.

curve is based upon domain-wall motion. Both curves are based upon Boltzmann distribution of moments. The rotational curve attributed to domain rotation can be interpreted in terms of variation from the most probable condition. For F-6-2, as the moment is decreased, moments parallel and antiparallel are initially in excess of the most probable condition. However, as M is further decreased towards zero, the parallel-antiparallel components increase to larger than the most probable value. This can be considered the reason for the transverse susceptibility at zero moments being larger than the initial susceptibility, and the corresponding parallel susceptibility at zero moment being smaller than either. Sample F-1-2, if the susceptibility is assumed entirely rotation, maintains at all times a predominant parallel-antiparallel moment configuration. The value of A_2 from equation (5) as a function of magnetic moment can be read directly from Fig. 12 for sample F-6-2.

More detailed determinations and analyses of the distribution functions in other materials must await simultaneous parallel and transverse susceptibility and differential magnetostriction measurements.

5. CONCLUSIONS

The magnetic properties of a ferromagnetic system can be described in terms of a distribution of magnetic moments about the unit sphere. This function cannot be calculated in detail for macroscopic systems. However, assuming idealized models of magnetic behavior such as magnetization by domain-wall motion or magnetization by domain rotation, some reversible properties of ferromagnets can be compared without detailed knowledge of the distribution function. If a detailed distribution function is assumed, then, of course, the magnetic properties can be calculated in detail.

The inverse of this calculation can also be made. The procedure consists of firstly expanding the distribution function in an infinite ser-

ies of Legendre polynomials. Due to the orthogonality properties of these functions, the coefficients of each term in the infinite series can be evaluated if the weighted average value of the proper power of $\langle \cos \Theta \rangle$ over the sample is known; $\langle \cos \Theta \rangle$ itself is, of course, proportional to the magnetic moment of the sample. Under certain conditions $\langle \cos^2 \Theta \rangle$ is proportional to the static magnetostriction. It can also be found from a knowledge of the two reversible susceptibilities, if domain rotation is the source of the susceptibility. Further, under the same susceptibility conditions, the differential magnetostriction can be utilized to find $\langle \cos^3 \Theta \rangle$ and one additional coefficient in the expansion.

The combination of frequency spectra and magnetization dependence of the susceptibilities on the same sample types is utilized to examine the source of the susceptibility. In agreement with other investigators, it is found that the major susceptibility source depends upon the type of ferrite, as well as the method of preparation. The nickel-zinc-cobalt ferrite F-6-2 shows distinctive domain-rotational effects. Sample I-15-1 shows wall-motional effect.

Acknowledgements – The authors wish to acknowledge the invaluable assistance of Mr. R. M. OLSON, Mr. A. H. VOELKER, and Mrs. P. A. MARCHELLO.

REFERENCES

1. GRIMES D. M., *J. Phys. Chem. Solids* **3,** 141 (1957).
2. GOODENOUGH J. B., *Phys. Rev.* **95,** 917 (1954).
3. BROWN W. F., Jr., *Phys. Rev.* **105,** 1479 (1957).
4. FREI E. H., SHTRIKMAN S. and TREVES D., *Phys. Rev.* **106,** 446 (1957).
5. SNOEK J. L., *Physica* **14,** 207 (1948).
6. WIJN H. P. J., GEVERS M. and VAN DER BURGT C. M., *Rev. Mod. Phys.* **25,** 91 (1953).
7. BROWN F. and GRAVEL C. L., *Phys. Rev.* **98,** 442 (1955).
8. PARK D., *Phys. Rev.* **97,** 60 (1955).
9. FOMENKO L. A., *Sov. Phys. JETP* **3,** 19 (1956).
10. HARRISON S. E., KRIESSMAN C. J. and POLLACK S. R., *Phys. Rev.* **110,** 844 (1958).
11. RADO G. T., WRIGHT R. W. and EMERSON W. H., *Phys. Rev.* **80,** 273 (1950).
12. EPSTEIN D. J., Proc. Boston Conf. *Amer. Inst. Elect. Engrs.* **493,** T-91 (1957).
13. BIRKS J. B., *Proc. Inst. Elect. Engrs.* Part B, Suppl. No. 5, 179 (1956).
14. BROWN W. F., Jr., *Phys. Rev.* **53,** 482 (1938).
15. LEE. E. W., *Proc. Phys. Soc.* **72,** 249 (1958).
16. GILBERT T. L., *The Phenomenological Theory of Ferromagnetism.* Armour Research Foundation (1 May, 1956).
17. BOZORTH R. M., *Ferromagnetism* p. 822. Van Nostrand, New York (1951).
18. BECKER R. and DÖRING W., *Ferromagnetismus* Edward Bros., Ann Arbor (1943).
19. FREI E. H. and SHTRIKMAN S., Proc. Boston Conf. *Amer. Inst. Elect. Engrs.* 502, T-91 (1957).
20. RADO G. T., FOLEN V. J. and EMERSON W. H., *Proc. Inst. Elect. Engrs.* Part B, Suppl. No. 5, 198 (1956).
21. HARRINGTON R. D. and RASMUSSEN A. L., *Proc. Inst. Radio Engrs.* **47,** 98 (1959).

J. Phys. Chem. Solids Pergamon Press 1959. Vol. 12. pp. 41–52. Printed in Poland.

THE DEBYE TEMPERATURE OF VITREOUS SILICA

O. L. ANDERSON

Bell Telephone Laboratories, Inc. Murray Hill, New Jersey

(*Received* 10 *March* 1958; *revised* 17 *March* 1959)

Abstract—It is shown that the low-temperature elastic constants of vitreous silica can account for only a small fraction of the low-temperature heat capacity. On the other hand, for quartz the elastic constants account for all the low-temperature heat capacity. The data for cristobalite are not complete, but there is evidence to suggest that the anomaly also exists in this phase of silica. It is shown that the long-wave vibrational properties of vitreous silica, optical and acoustical, are consistent with the analogous properties of ionic solids.

VOL. 12 59/60

1. INTRODUCTION

THE primary purpose of this paper is to show that a low-temperature heat-capacity anomaly exists in vitreous silica, but not in quartz. This anomaly is demonstrated by the fact that the low-temperature elastic constants account for only a fraction of the low-temperature heat capacity. The secondary purpose of this paper is to show that the long-wave vibrational properties, both optical and acoustical, of vitreous silica are normal in the sense that they compare favorably with those of other ionic solids. This is demonstrated by the following facts:

(1) The degree of ionic bonding can be calculated from the dielectric constants and the *Reststrahl*.

(2) The "mean" sound velocity correlates well with the melting temperature.

(3) The change of polarizability with temperature is the same for vitreous silica as for other ionic solids.

According to lattice dynamics, the heat capacity of an insulating solid is composed entirely of acoustic lattice vibrations at very low temperatures.[1]

Experimentally, this is checked by computing the Debye temperature from the elastic constants, $\Theta_{(\text{elastic})}$, and the Debye temperature from calorimetric measurements, Θ_0, and observing that the two values of Θ are equal within experimental error.

There are a number of cases where a discrepancy between the values of Θ has been reported. Improved cyrogenic techniques have subsequently revealed that these reports were erroneous. The crystalline solids MgO and ZnS (cubic) are examples of such erroneous reports. DURAND[2] measured the low-temperature elastic constants of MgO and found $\Theta_{(\text{elastic})}$ to be 949°K. This disagreed with the value of $\Theta_0 = 768$°K reported by GUNTHER[3] on the basis of his heat-capacity measurements (1916). However, BARRON *et al.*[4] recently made very careful thermal measurements down to 10°K and found $\Theta_0 = 946 \pm 4$°K, thus establishing that the agreement which is to be expected from lattice dynamics really exists. BLACKMAN[5] noted that the elastic constants and the specific heat of ZnS lead to very different values of Θ. This discrepancy also was removed by newer specific-heat measurements reported by MARTIN[6]. For these solids, and presumably for other solids where such discre-

pancies have been reported, good agreement between the values of Θ is achieved by careful cyrogenic measurements in the vicinity of 5°K.

It is precisely in this very low-temperature range, where reported anomalies have been discredited, that new cyrogenic experiments have revealed a marked discrepancy between the values of Θ for vitreous silica. Unpublished heat-capacity measurements made by WESTRUM[7] down to 5°K, new heat-capacity data just reported by FLUBACHER *et al.*[8] down to 2·34°K, and sound-velocity measurements by MCSKIMIN[9a] and FINE[9b] down to 5°K are the basis for the computed values of Θ which disagree. Thus, these experiments indicate that at temperatures where no optical vibrations would be expected to be present, there is nevertheless heat-capacity considerably in excess of that due to acoustic lattice vibrations.

2. DEFINITION OF THE DEBYE TEMPERATURE

For elements which have crystallized in lattices with one atom per cell, the two definitions of the Debye temperature are straightforward and unambigous. For example, the definition of the Debye temperature from elastic constants is:

$$\Theta_{(\text{elastic})} = \frac{h}{k}\left(\frac{1}{4\pi}\cdot\frac{n}{v_c}\right)^{1/3} c_m \qquad (1)$$

where h/k is the ratio of Planck's constant to the Boltzmann constant, c_m is the mean sound velocity determined from the density and the elastic constants, n is the number of degrees of freedom per cell* for lattice vibrations, and v_c is the volume per cell. In this simple case, the cell is one atom, so that v_c is specified simply by density and atomic weight; and n is 3, since there are three degrees of freedom per cell, (each cell being only one atom).

When equation (1) is generalized to polyatomic solids, the definition of n and v_c becomes somewhat arbitrary, because of the uncertainty as to the size of the vibrational unit. The value of (n/v_c) will vary depending upon whether the vibrational unit is *assumed* to be an ion, an ion-pair, the molecule defining the solid, or the crystallographic cell.

Because of the confusion in the literature on this point, it is pertinent to demonstrate just how much the value of the Debye temperature depends upon the size of the vibrational unit. Suppose that the solid is composed of a compound having p atoms per molecule which has crystallized in a lattice having α atoms per cell or m molecules per cell. Taking the density as ϱ, the molecular weight as M, and N as Avogadro's number, the following relations hold:

$$v_c = m\frac{M}{N\varrho}, \text{ and } m = \frac{\alpha}{p}$$

For the polyatomic lattice, equation (1) then becomes

$$\Theta_{(\text{elastic})} = \frac{h}{k}\left(\frac{1}{4\pi}\cdot\frac{N\varrho}{M}\right)^{1/3}\left\{\frac{n}{m}\right\}^{1/3} c_m \qquad (2)$$

where the quantities susceptible to various interpretations and assumptions are gathered in the braces. For vitreous silica, the above is $\Theta_{(\text{elastic})} = 5{\cdot}814\times 10^{-4}\ c_m\ \{n/m\}^{1/3}$ and for quartz, $\Theta_{(\text{elastic})} = 6{\cdot}16\times 10^{-4}\, c_m\,\{n/m\}^{1/3}$.

In the literature on lattice dynamics applied to ionic solids, the calculation of $\Theta_{(\text{elastic})}$ is usually made as though the atom were an individual oscillator. This really amounts to representing the solid as a monatomic lattice composed of atoms where the volume per cell is the *average* atomic volume, $Mp/N\varrho$. In terms of our defined quantities, we take $\alpha = 1$ and $n = 3$, and then obtain, from equation (2),

* Not the crystallographic cell.

$$\Theta_{(\text{elastic})} = \frac{h}{k}\{p\}^{1/3}\left(\frac{3}{4\pi}\cdot\frac{N\varrho}{M}\right)^{1/3} c_m . \quad (3)$$

Equation (3) is used widely, but by no means universally. Its chief limitation is that the Θ so defined is a number which characterizes the total vibrational spectrum, and hence the optical and acoustic details cannot be approximated separately; this becomes serious when in fact the optical and acoustic frequencies differ markedly in magnitude at high wave numbers.

Spectroscopists, when dealing with the vibrational spectrum of solids, must distinguish between the acoustic and optical lattice vibrations, so they usually apply equation (2) by assigning three degrees of freedom ($n = 3$) to a vibrational unit larger than one atom, ($a > 1$). In fact, in their paper on silica, LORD and MORROW[10] considered the vibrational unit to be the crystallographic cell. In such a case we have, (setting m equal to q, the number of molecules per crystallographic cell):*

$$\Theta_{(\text{elastic})} = \frac{h}{k}\left\{\frac{1}{q}\right\}^{1/3}\left(\frac{3}{4\pi}\frac{N\varrho}{M}\right)^{1/3} c_m . \quad (4)$$

The difference between the two assumptions can be emphasized by considering CaF_2, where $p = 3$ and $q = 4$. For this case the value of $\Theta_{(\text{elastic})}$ from equation (3) is $12^{1/3}$ times larger than found from equation (4). Equations (3) and (4) are not the only ways of defining $\Theta_{(\text{elastic})}$, since the size of the vibrational unit is susceptible to a variety of interpretations.

The same uncertainty arises in the definition of the Debye temperature from low-temperature heat-capacity measurements. In this case

$$\Theta_{(\text{thermal})} = T(121\cdot 5/C_v)^{1/3}\{n/m\}^{1/3} \quad (5)$$

and

$$\Theta_{(\text{thermal})} \to \Theta_0, \text{ as } T \to 0,$$

where C_v is in calories per gram-molecule.

Since the uncertain quantities occur in exactly the same way in the definitions of $\Theta_{(\text{thermal})}$ and $\Theta_{(\text{elastic})}$, the test on whether the values of Θ are equal is independent of the choice of the vibrational unit, providing the same choice is made in calculating each Θ. This can be shown by defining the ratio.

$$\mathcal{R} = \frac{\Theta_{(\text{thermal})}}{\Theta_{(\text{elastic})}} = \frac{kT}{hc_m}\left(\frac{4\pi}{3}\cdot\frac{121\cdot 5M}{C_v N\varrho}\right)^{1/3} \quad (6)$$

in which the quantities in the braces cancel out.

Equivalently, $\mathcal{R}$ can be defined without explicitly introducing Θ's, by comparing directly the experimental heat capacity with that predicted from the elastic constants:

$$\mathcal{R} = \left(\frac{C_{v\,(\text{elastic})}}{C_{v\,(\text{thermal})}}\right)^{1/3}$$

In the following section we are concerned with the test on the value of $\mathcal{R}$ for vitreous silica and quartz. In Section 4 we will discuss the explicit size of the vibrational unit which is necessary to specify $\{n/m\}$.

3. THE ANOMALY IN VITREOUS SILICA

The chief obstacle in the determination of $\mathcal{R}$ is to find the value of c_m, which is specified by integrating the three sound velocities in all directions, or

$$\frac{3}{c_m^3} = \sum_{j=1}^{3}\int \frac{1}{c_j^3}\cdot\frac{d\Omega}{4\pi} \quad (7)$$

where $d\Omega$ represents the element of solid angle, and the subscript j enumerates the three sound velocities for each direction considered. In isotropic solids, the velocities are independent of direction, so equation (7) reduces to:

$$c_m^3 = c_t^3\,[3/(2 + A^3)] \quad (8)$$

* In this case, it is found that at very high temperatures, where the specific heat approaches the Dulong and Petit limit $3pR$, the acoustic part is only $\frac{3R}{q}$, while the optical part is $\left(\frac{pq-1}{q}\right)3R$. R is the gas constant.

where c_t is the transverse velocity and Δ is the ratio of the transverse and longitudinal velocities. In terms of the Young's modulus and the shear modulus, $\Delta = [(3G - Y)/(4G - Y)]^{1/2}$.

The data for the Young's modulus and the shear modulus for vitreous silica and the resulting value of c_m are listed in Table 1.

Table 1

(Moduli in 10^{11} dynes/cm^2, velocity in 10^5 cm/sec)

Temp. (°K)	Young's modulus, Y*	Shear modulus, G*	Transverse wave velocity, c_t	Mean wave velocity, c_m
5	7·14	3·08	3·74	4·11
7	7·13	3·075	3·74	4·11
10	7·11	3·07	3·73	4·10
15	7·09	3·06	3·73	4·10
20	7·08	3·055	3·73	4·09
180	7·14	3·065	3·73	4·10
273	7·28	3·14	3·78	4·15

* Data from MCSKIMIN and FINE.

The value of c_m changes only about 1 per cent between room temperature and 5°K. The extrapolation to absolute zero indicates that c_m is $4{\cdot}11 \times 10^5$ cm/sec to an accuracy better than 1 per cent, yielding $\Theta_{(\text{elastic})}\{n/m\}^{1/3} = 239$.

The calculation of c_m for quartz is considerably more complicated (see Appendix). The room-temperature values of the elastic constants have been measured by KOGA *et al.*[11], but are not known at low temperatures. The computation is shown in Table 2.

The value of c_m is for the room-temperature values of the elastic constants. The value of c_m at absolute zero will tend to be higher because of higher values of the elastic constants, but lower because of a higher density. However, the value of c_m for vitreous silica changes only 1 per cent between room-temperature and 5°K, so the value $c_m = 4{\cdot}40 \times 10^5$ cm/sec for quartz at absolute zero is probably accurate within a few per cent.

The value for computation of equation (5) for vitreous silica can be obtained from the unpublished specific-heat measurements of WESTRUM[7]. The pertinent values, with the corresponding computation, are shown in Table 3.

Table 3. *Ratio of* $\Theta_{(\text{thermal})}$ *to* $\Theta_{(\text{elastic})}$ *in vitreous silica**

Temp. (°K)	C_v (cal/mole)	$\Theta_{(\text{thermal})} \times \{m/n\}^{1/3}$	$\mathcal{R}$, equation (6)
9·18	0·0459	127	0·531
8·15	0·0293	130·9	0·548
7·01	0·0163	136·9	0·572
5·88	0·0091	139·7	0·585
5·017	0·00509	144·3	0·604
4·031	0·00217	154·2	0·645
2·344	0·00034	166·3	0·696
0	—	(190)	(0·798)

* Specific-heat data after WESTRUM[7] and FLUBACHER *et al.*[8] Possible choices for the ratio m/n are shown in Table 9.

Table 2

(Moduli in 10^{11} dynes/cm^2, velocity in 10^5 cm/sec)

Elastic Constants (room temperature)	c_{11}	c_{33}	c_{44}	c_{66}	c_{12}	c_{13}
	8·683	10·594	5·826	3·987	0·709	1·193
Mean sound velocity*	$c_m = 4{\cdot}40$					
Debye temperature	$\Theta_{(\text{elastic})} \cdot \{m/n\}^{1/3} = 271{\cdot}0$					

* See Appendix for details of the c_m calculation.

Similarly, the corresponding values for quartz are given in Table 4.

*Table 4. Ratio of $\Theta_{(\text{thermal})}$ to $\Theta_{(\text{elastic})}$ in quartz**

Temp. (°K)	C_v (cal/mole)	$\Theta_{(\text{thermal})} \times \{m/n\}^{1/3}$	$\mathcal{R}$, equation (6)
12·58	0·0278	205	0·756
11·68	0·0201	213	0·786
10·70	0·0136	228	0·841
9·90	0·0099	228	0·841
8·80	0·0066	232	0·855
0	—	(268)	(1·00)

* Specific-heat data after WESTRUM[7] whose four lowest measurements are deleted (6–8°) because of large scatter.

The values of $\Theta_{(\text{thermal})} \times \{m/n\}^{1/3}$ at absolute zero are obtained by BARRON and MORRISON'S[12] extrapolation method, which consists of finding the intercept of the ordinate in the plot of C_v/T^3 versus T^2. The extrapolation used for vitreous silica (Table 3) from 2·344°K to zero covers a short range and ought to be reasonably accurate (say, 2 per cent).*

The important conclusion which emerges from Tables 3 and 4 is that the elastic constants cannot account for all of the low-temperature specific heat of vitreous silica, but can account for all the low-temperature specific heat of quartz.

An interpretation of the anomaly in terms of structure requires beforehand an exact knowledge of the size and nature of the vibrational unit, since a small frequency can arise either from a large mass or a small spring constant.

* The actual extrapolation is done in the following paper.[8]

4. THE SIZE OF THE VIBRATIONAL UNIT

The nature and size of the vibrational unit are needed not only to understand the specific-heat anomaly, but also to determine the magnitude of the Debye temperature. In a few limiting cases, the vibrational unit is evident. In ionic crystals where the masses of the two ions are about equal (like KCl), the acoustic and optic branches converge, so that the individual ion can be taken as the vibrational unit with accuracy.[12] In molecular crystals (like benzene), where there is strong binding within the molecule and weak binding between molecules, the chemical molecule itself is the vibrational unit. Many solids, including silica, should be considered to lie between these extremes. The purpose of this section is to demonstrate that, in so far as vibrational properties are concerned, vitroeus silica correlates well with typical polyatomic solids such as KCl, MgO, ZnS, and CaF_2: KCl represents an ideal ionic solid; MgO is another oxide; ZnS has tetrahedral coördination and has about the same degree of ionic bonding as silica; and CaF_2 is triatomic.

The first correlation is that the mean velocity c_m (calculated from the elastic constants and density) is ordered in the same way as the melting points. This is shown in Table 5.

The values of T_s for all the solids (except vitreous silica) were taken from the "*Handbook of Physics and Chemistry*" (Chemical Rubber Publishing Company). The method of finding the values of c_m for the cubic crystals is discussed in the Appendix.

Table 5 shows that the Debye temperature is roughly proportional to the melting temperature for all the ionic solids, which is to be expected by the qualitative features of the Lindeman formula.[13] Further, it is seen that the value for c_m is close for both CaF_2 and vitreous silica, indicating that the same

Table 5. Comparison of mean sound velocity and melting point
(c_m in units of 10^5 cm/sec)

Row	Solid	KCl	(Cubic) ZnS	CaF_2	Vitreous SiO_2	Quartz SiO_2	MgO
1	c_m	2·52	2·92	4·08	4·11	4·37	6·71
2	T_s(°K)	776	1020	1360	~1350*	1470	2500
3	$\Theta_{(\text{elastic})} \cdot \left\{\frac{n}{m}\right\}^{1/3}$	132·2	178·0	242·8	238·8	253·7	390·5
4	(Row 3 ÷ Row 2)	0·172	0·173	0·178	0·176	0·173	0·156

* Estimated by finding center of interval where C_p changes from the Dulong and Petit limit to the value of liquid silica.

rules for the selection of the ratio $\{n/m\}$ in equation (6) ought to apply for both solids. Table 5 shows that it is reasonable to classify silica as a polyatomic solid in so far as acoustic vibrations are concerned.

The second correlation is that the *Reststrahl* of vitreous silica can be calculated by using equations which are strictly applicable to ionic lattices. It is a characteristic of ionic solids that an intense infrared absorption is created by waves of vibrations of oppositely charged ions. For triatomic and diatomic ionic crystals, the absorption is given by

$$\omega_0^2 = 2\beta/\bar{m} \qquad (9)$$

where β is the spring constant and $\bar{m}$ is the reduced mass of the smallest "basic unit" in the crystal,

$$\bar{m} = \frac{1}{N}\left[\sum_{i=1}^{p}(1/M_i)\right]^{-1}.$$

The number of atoms per molecule is p, N is Avogadro's number, and M_i is the atomic weight of the particular atom. For silica, $\bar{m} = (1/28 + 2/16)^{-1} \times (1{\cdot}66 \times 10^{-24}) = 10{\cdot}33 \times 10^{-24}$ per Si-O-Si group (or "basic unit").

As a rough order-of-magnitude calculation, consider the stretching of two adjacent "basic units", where the spring constant is given approximately as the product of group spacing and the elastic stiffness, or $\beta = aC_{11} = (8 \times 10^{11}) \times (3{\cdot}2 \times 10^{-8}) = 2{\cdot}56 \times 10^4$ dynes/cm^2, so that $\omega_0 = 7{\cdot}04$ radians/sec or $\lambda_0 = 26{\cdot}8\mu$. This is satisfactory order-of-magnitude agreement with the infrared absorption found by REITZEL at $21{\cdot}5\mu$.[14] In a molecular crystal, β is low and consequently ω is low. The magnitude of the measured λ_0 tends to confirm the idea that the vibrational unit cannot be much larger than the Si-O-Si "basic unit".

A more precise calculation of λ_0 can be made, provided that the admixture of homopolar bonding (or inversely, the ionicity) in the Si-O bond is known. This calculation is made by means of an equation developed by SZIGETI,[15] in which the spring constant is expressed in terms of the dielectric constants. The ions are assumed to be point charges, but there are correction terms for the deformability and the overlap of the ions. The equation is valid for diatomic and triatomic solids, provided that they are restricted to higher symmetry (cubic or isotropic). A popular version of the SZIGETI equation is

$$\varepsilon_0 = \varepsilon_\infty + \left(\frac{\varepsilon_\infty + 2}{3}\right)^2 \left(\frac{e^\star}{e}\right)^2 \frac{z^2 e^2}{c^2 \pi} \frac{\lambda_0^2}{\bar{m}v} \qquad (10)$$

where ε_0 is the dielectric constant at very long wavelengths; ε_∞ is the dielectric constant at frequencies large compared to $1/\lambda_0$, but small compared to the ultraviolet absorption; λ_0 is the *Reststrahl* wavelength in cm; $e^\star$ is the actual charge of the ion (in contrast to the electronic charge of the ideal ionic solid); c is the velocity of light; and $\bar{v}$ is the volume corresponding to the "basic unit". motion of the electron cloud relative to the nuclei, and $(e^\star/e)$ represents a correction due to the overlap of ions.

Since all quantities in equation (10) are measurable except $e^\star$, the usual procedure is to compute $(e^\star/e)$ and regard the result as the degree of ionic bonding. The reasonableness of the calculated $(e^\star/e)$ value is regarded as the test of the equation. The determination

Table 6. Tabulation of constants involved in $(e^\star/e)$ computation†

Constants	Units	Symbol	Solid				
Basic unit			KCl	ZnS	MgO	CaF_2	Vitreous SiO_2
Density	g/cm³	ϱ	2·032	4·087	3·576	3·110	2·203
Valence, negative ion		z	1	2	2	1	2
Atomic mass, + ion		M_1	39·1	65·38	24·3	40·08	28·06
Atomic mass, − ion		M_2	35·46	32·07	16·0	19·0	16·0
Molecular weight		M	74·56	97·45	40·3	78·08	60·06
Volume/basic unit $(M/N\varrho)$	(Å)³	$\bar{v}$	60·92	39·58	18·72	41·68	45·26
Reduced mass (basic unit)	(10^{-24})	$\bar{m}$	30·88	35·73	16·05	12·75	10·35
Total polarization (low-frequency dielectric constant)		ε_0	4·68	8·3	9·8	8·42	3·78
Ultra violet polarization (high-frequency dielectric constant)		ε_∞	2·13	5·07	2·95	1·99	1·98
Infrared polarization		$\varepsilon_0 - \varepsilon_\infty$	2·55	3·23	6·85	6·44	1·80
Dispersion wavelength	(microns)	λ_0	70·7	33·0	15·3	51·5	21·5
Long-range interaction		$(\varepsilon_\infty+2)/3$	1·385	2·69	1·65	1·33	1·33
Degree ionic bonding		$e^\star/e$	0·78	0·48	0·99	0·75	0·44

† Assuming smallest basic unit for vibrational unit (diatomic, 2 ions; triatomic, 3 ions)

Many of the above expressions have physical significance: ε_0 is the total polaritazion, ε_∞ is the ultraviolet polarization, and $\varepsilon_0 - \varepsilon_\infty$ is the infrared polarization, which has two factors due to electronic interaction. The factor $[(\varepsilon_\infty + 2)/3]^2$ appears because of the

of $(e^\star/e)$ for vitreous silica is detailed in Table 6, along with the other ionic solids of interest.

Most of the values of ε_0, ε_∞, and λ_0 are taken from SZIGETI'S paper.[15] For vitreous silica we use $\varepsilon_0 = 3{\cdot}78$ reported by SOSMAN[16], $\varepsilon_\infty = n^2 = 1{\cdot}96$ found by RODNEY and

SPINDLER,[17] and $\lambda_0 = 21{\cdot}5\mu$ reported by REITZEL[14]†.

An examination of Table 6 reveals two salient points: (1) the polarization properties of vitreous silica are close in value to those of the other solids (for instance, $(\varepsilon_\infty + 2)/3$); and (2) the value of (e^*/e) computed by the SZIGETI formula is as reasonable for vitreous silica as for the other solids. The latter point is detailed further in Table 7.

Table 7. Comparison of degree of ionic bonding by several methods

Method	NaCl	ZnS	MgO	CaF_4	Vitreous SiO_4
Electronegativity of ions†	% 95	% 50	% 91	% 98	% 50
Electron density: X-rays‡	100	—	<100	—	~50
Infrared dispersion: (e^*/e)	74	48	99	75	44

† PAULING[18], BIRMAN[19], ‡ BRILL[20].

It follows from Tables 6 and 7 that it is reasonable to classify vitreous silica as a polyatomic solid in so far as optical vibrations are concerned.

The third correlation is that the variation of the effective molecular polarizability with temperature is the same for vitreous silica and quartz as for well-known ionic solids.

Consider the relation for ionic crystals,

$$f(n) = \frac{4\pi}{3} \cdot \frac{N}{V} \alpha$$

where $f(n)$ is some function of the index of refraction, N is Avogadro's number, V is the molecular volume, and α is the mean molecular polarizability.

The derivative of equation (11) with respect to T is:

$$g(n) \frac{dn}{dT} = \{\alpha' - \beta\} \qquad (12)$$

where β is the coefficient of volume expansion $d\ln V/dT$, α' is the relative change in polarizability $d\ln\alpha/dT$, and $g(n)$ is $f(n)/f'(n)$. Two of the more common approximations of $f(n)$ are shown in the following list, with the corresponding values of $g(n)$:

Approximation	$f(n)$	$g(n)$
Clausius-Mossotti	$(n^2-1)/(n^2+2)$	$6n/(n^2-1)(n^2+2)$
Drude	$(n^2-1)/3$	$2n/(n^2-1)$

The Clausius-Mossotti equation is considered the more representative for the alkali halides, while the Drude equation has been shown[21] to be better for multicomponent glasses.

Since $g(n)$ is always positive, the sign of dn/dT depends upon the difference $(\alpha' - \beta)$.

In Table 8 measured values of n, dn/dT, and β are used to compute values of $d\ln\alpha/dT$ according to the two formulae. The values of n are taken at 1μ (from Table 168 of Landolt-Bornstein) which is outside the dispersion regions.

The values of α' in Table 8 for vitreous silica show that the relation between electronic displacement and temperature is comparable to that of the other solids.† Consequently, it is reasonable to conclude that this

† There are two infrared *Reststrahlen*, equally intense, in silica, at 9·1 and 21·5 μ. Two bands are commonly found in triatomic solids, for instance CaF_2, BaF_2, and SrF_2.

The lowest frequency band is used in the SZIGETI calculation,[15] the value which best satisfies the condition $k \to 0$.

† Although $d\ln\alpha/dT$ is normal for vitroeus silica, the value of dn/dT is positive, but this appears to be merely a reflection of the low expansivity.

Table 8. Computation of $d\ln\alpha/dT \times 10^5$ for several solids by equation (12)

Solid	n	$dn/dT \times 10^5$	$\beta \times 10^5$	α' (Clausius-Mossotti)	α' (Drude)
NaCl	1·53	−3·8	12·04	6·04	2·76
CaF_2	1·43	−1·1	5·7	3·5	2·8
Quartz (⊥)	2·11	−0·66	4·26	3·66	3·5
Quartz (‖)	2·15	−0·76	2·51	2·1	1·6
Vitreous silica	1·40	1·00	0·111	2·3	2·8

VOL. 12 59/60

solid has ionic tightness which is comparable to that of the other polyatomic solids.

In view of the three correlations discussed above, it appears that there are no large groups or clusters in vitreous silica, at least so far as vibrational properties are concerned. Consequently, it is concluded that the same rules for selecting the vibrational unit of polyatomic solids (such as ZnS or CaF_2) should apply to vitreous silica.

This conclusion is consistent with ZACHARIASEN'S[22] view that vitreous silica is a completely cross-linked network with fixed coordination about every ion, but is at variance with several other speculations on the structure of vitreous silica.[23,24]

The exact specifications of the vibrational unit, however, must be assumed. The following table shows how the value of the Debye temperature depends on several models of the vibrational unit.

Case 1 should be used if a single number is desired to approximate both the acoustic and optical vibrations; the value of $\Theta = 495°K.$ is to be used for the Debye temperature. Case 2 is the most likely choice if a number is desired to approximate the acoustic vibrations apart from the optic vibrations; the value $\Theta = 343°K.$ is to be used for the Debye temperature. Case 3 is a possible choice for the acoustic vibrations, but Case 4 should not be used in view of the conclusions stated above.†

Table 9. Debye temperatures for vitreous silica

Case	Vibrational unit	p	n	a	m	$\Theta_{(elastic)}$	Θ_0	S†
1	Single ion (average)	3	3	1	1/3	495°K	395°K	$9R$
2	Si-O-Si (basic unit)	3	3	3	1	343°K	274°K	$3R$
3	SiO_4 tetrahedron	3	3	4	4/3	312°K	249°K	$(9/4)R$
4	Crystallographic cell of cristobalite	3	3	12	4	216°K	172°K	$(3/4R)$

† The limiting value at high temperature of the acoustic specific heat using a single Debye function. R is the gas constant.

In normal solids the heat capacity can be cal-

† See reference 10, however, for the opposite point of view.

culated by using $\Theta_{(\text{elastic})}$ in a Debye function up to a temperature of about $T = \Theta/30$. In this region the excess heat can be calculated by using the formula

$$C_{v(\text{excess})} = C_{v(\text{measured})} - SD\left(\frac{\Theta_{(\text{elastic})}}{T}\right) \quad (13)$$

where $D(\Theta/T)$ is the Debye formula for one degree of freedom, and S and $\Theta_{(\text{elastic})}$ are taken from Table 9. The relative excess heat so computed is shown in Fig. 1, which is independent of the size of the vibrational unit.

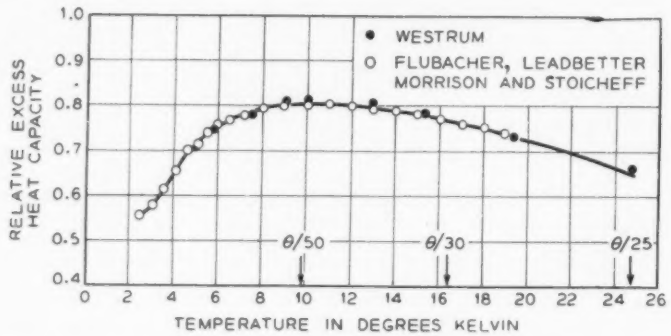

FIG. 1. A plot of the excess specific heat in vitreous silica, equation (13), divided by C_v (measured, using WESTRUM'S and FLUBACHER'S measurements. This plot is independent of the size of the vibrational unit.

5. DISCUSSION

It may be asked: is the excess specific heat characteristic of the glassy state? This anomaly does not exist in quartz, but there is a possibility that excess heat will be found in another crystalline phase of silica, i. e. cristobalite. If so, the answer to the above question is in the negative. According to WESTRUM'S specific-heat measurements, the values of Θ_0 for vitreous silica and cristobalite are close. Therefore, in order for the anomaly to be absent in cristobalite, the elastic constants of cristobalite should be about 30 per cent less in magnitude than those for vitreous silica. This seems unlikely, since the density of cristobalite is about 8 per cent greater than that of vitreous silica. Unfortunately the elastic constants of cristobalite have not been determined, so the issue cannot be resolved at the present time.

If the anomaly persists in cristobalite (and the evidence is in favor of this situation), the question arises: what is the nature of the vibrations which are responsible for the excess heat? Low frequencies can arise from large masses or small spring constants. The results of the previous section indicate that large clusters of atoms (or groups) separated from each other by weak bonds are unlikely in vitreous silica. Therefore, vibrations or oscillations of large masses are probably not the source of the excess heat. Accordingly, we must look for a vibration with a small spring constant. The nature of this spring constant is obscure because the details of the structure of vitreous silica are unknown, and the details of the frequency versus wave-number diagram are unknown.

A vibration with a small spring constant has been postulated for vitreous silica by SMYTH[25]. He proposed a model in which the Si-O-Si bending vibration (O moves perpendicular to the Si-Si projection) was responsible for all the low-temperature specific heat. This model is inconsistent with lattice dynamics, but the

Si-O-Si flexural mode (or something similar) may very well be responsible for the excess heat shown in Fig. 1. This particular mode was established as the cause of the low-temperature acoustic absorption in vitreous silica by ANDERSON and BÖMMEL[26].

Two experiments are needed to help clarify the source of the excess heat: (1) the determination of the elastic constants of cristobalite, and (2) specific-heat measurements in other solids to determine the uniqueness of this anomaly.

Acknowledgements—The writer is grateful to Prof. E. F. WESTRUM, Jr., for access to his unpublished measurements on heat capacity, to helpful comments on lattice dynamics by Dr. MELVIN LAX and Dr. J. PHILLIPS, and to friendly criticism by Dr. H. BARRON.

VOL. 12 59/60

APPENDIX

The value of c_m for quartz was calculated by the method of HOPF and LECHNER[27] on an IBM 704 machine. The program was designed for general use in obtaining c_m for crystals of the trigonal class or higher symmetry.

The elastic constants, the density, the limits of the integration, and the increment of integration are read into the program on data cards. From the initial value of the angles Θ and Φ, the direction cosines and the elements of the sound propagation determinant are computed. The three eigenvalues (or sound velocities) are computed by solving for the roots of the cubic equation obtained by expanding the deteriment. The eigenvalues are stored, the increment of angle is added to Θ and Φ, the new eigenvalues are obtained and stored, and so on, until all the allowed values of Θ and Φ are exhausted. The value of c_m is then computed from the stored eigenvalues by equation (7), using Simpson's rule for the numerical integration. The limits on Θ were 0° and 180°, and on Φ were 0° and 120°.

Using the values of the elastic contants shown in Table 2, the value of c_m was found to be $4{\cdot}40 \times 10^5$ cm/sec for large number of steps in the integration. The dependence of c_m on the number of steps in the integration, n, is shown in Table A-1.

This program was used to compute the values of c_m for the cubic crystals shown in Table 5. The elastic constants used are shown in Table A-2.

The value of c_m found by the IBM program was in excellent agreement with those obtained using DE LAUNAY'S tables.[28]

Table A-1. Mean sound velocity in quartz

n	24	54	96	150	216	864	2400
$\Delta\Phi = \Delta\Theta$	30°	20°	15°	12°	10°	5°	3°
c_m(10^5 cm/sec)	4·438	4·398	4·399	4·399	4·397	4·395	4·395

Table A-2. Tabulation of elastic constants for some cubic crystals

	KCl	ZnS	MgO	CaF_2
Density (g/cm^3)	2·032	4·087	3·576	3·110
c_{11} (10^{10} dyne/cm^2)	49·5	94·3	298·89	167·0
c_{12}	6·0	56·8	85·79	45·7
c_{44}	6·69	43·4	156·79	34·52
c_t (transverse velocity) (10^5 cm/sec)	1·82	3·26	6·62	3·29
c_m (mean velocity)	2·52	2·92	6·71	4·08

REFERENCES

1. BORN M. and HUANG K., *Dynamical Theory of Crystal Lattices* Chap. II. Oxford University Press (1954).
2. DURAND M. A. *Phys. Rev.*, **50,** 449 (1936).
3. GUNTHER P., *Ann. Phys., Lpz.* **51,** 828 (1916).
4. BARRON T. H. K., BERG W. T. and MORRISON J. A., *Proc. Roy. Soc.*, in the press.
5. BLACKMAN M., *Handbuch der Physik* Vol. III, Part I, p. 365. Springer, Berlin (1955).
6. MARTIN D. L., *Phil. Mag.* **46,** 751 (1955).
7. WESTRUM E. F., Jr., Private communication.
8. FLUBACHER P., LEADBETTER A. J., MORRISON J. A., and STOICHEFF B. P., *J. Phys. Chem. Solids* **12,** 53 (1959).

9a. MCSKIMIN H. J., *J. Appl. Phys.* **24,** 988 (1953).

9b. FINE M. E. *et al.*, *J. Appl. Phys.* **25,** 402 (1954).

10. LORD R. C. and MORROW J. C., *J. Chem. Phys.* **26,** 230 (1957).
11. KOGA I. *et al.*, *Phys. Rev.* **109,** 1467 (1958).
12. BARRON T. H. K. and MORRISON J. A., *Canad. J. Phys.* **35,** 799 (1957).
13. GILVARRY J. J., *Phys. Rev.*, **102,** 308 (1956).
14. REITZEL J., *J. Chem. Phys.*, **23,** 2407 (1955).
15. SZIGETI B., *Trans. Faraday Soc.* **45, 155** (1949).
16. SOSMAN R. B., *The Properties of Silica* p. 589. The Chemical Catalog Co., New York (1927).
17. RODNEY W. S., and SPINDLER R. J., *J. Res. Nat. Bur. Stand.*, **53,** 185 (1954).
18. PAULING L., *The Nature of the Chemical Bond* 2nd Ed., p. 73. Cornell University Press, Ithaca, N. Y. (1948).
19. BIRMAN J. L., *Phys. Rev.*, **109,** 810 (1958).
20. BRILL R. W., *Ceram. Age*, **61,** 31 (1953).
21. RITLAND H. N., *J. Amer. Ceram. Soc.*, **38,** 86 (1955)
22. ZACHARIASEN W. H., *J. Amer. Chem. Soc.*, **54,** 3841 (1932).
23. BABCOCK C. L., BARBER S. W., and FAJANS K., *Industr. Engng. Chem.*, **46,** 161 (1954).
24. DANK M. and BARBER S. W., *J. Chem. Phys.*, **23,** 597 (1955).
25. SMYTH H. T., *et al.*, *J. Amer. Ceram. Soc.*, **36,** 327 (1953).
26. ANDERSON O. L. and BÖMMEL H., *J. Amer. Ceram. Soc.*, **38,** 125 (1955).
27. HOPF L. and LECHNER G., *Verhandl. Deut. phys. Ges..*, **16,** 643 (1914).
28. DE LAUNAY J., *J. Chem. Phys.* **21,** 1676 (1954).

J. Phys. Chem. Solids Pergamon Press 1959. Vol. 12. pp. 53–65. Printed in Poland.

THE LOW-TEMPERATURE HEAT CAPACITY AND THE RAMAN AND BRILLOUIN SPECTRA OF VITREOUS SILICA

P. FLUBACHER,* A. J. LEADBETTER,* J. A. MORRISON and B. P. STOICHEFF

Divisions of Pure Chemistry and Pure Physics, National Research Council, Ottawa, Canada

(*Received* 13 *April* 1959)

VOL. 12 59/60

Abstract—The heat capacity of vitreous silica has been measured between 2·3 and 19°K with an estimated accuracy of ±2 per cent at the lowest temperatures and ±0·5 per cent for 10°K $<$ $< T <$ 19°K. The temperature dependence of the heat capacity at the lowest temperatures is very much greater than that observed for simple crystals. Moreover, if Θ_0 is determined in the usual manner by a smooth extrapolation to $T^2 = 0$ of a graph of C/T^3 against T^2, it appears to be less than $\Theta_{(\text{elastic})}$ by about 20 per cent. In order to interpret this unusual behavior, some spectroscopic studies of vitreous silica have been made.

Velocities of transverse and longitudinal waves of frequencies of 3·3 and 5·0 $\times$ 10^{10} sec^{-1} respectively have been determined from measured Brillouin spectra; these agree excellently with velocities determined by acoustic methods at a frequency of 10^7 sec^{-1}. The Raman spectrum has been photographed; its outstanding feature is an intense continuum which extends from 560 cm^{-1} down to 8 cm^{-1}.

These spectroscopic results suggest that the excess heat capacity of vitreous silica is contributed by optical modes of very low frequency. The observed heat capacity can be accounted for quantitatively on this basis.

1. INTRODUCTION

IN the preceding paper,[1] ANDERSON discusses the unexpected behavior of the heat capacity of vitreous silica at low temperatures. ANDERSON'S original deductions were based on heat-capacity results obtained by WESTRUM[2] and sound-velocity measurements made by MCSKIMIN[3]. Because of the striking nature of the results and their probable significance to an understanding of the structure of glasses, it seemed important that they be independently measured. At Dr. ANDERSON'S request, we undertook to measure the heat capacity of vitreous silica again in the region $T <$ 20°K. As we shall see, our results substantiate WESTRUM'S work, but since lower temperatures and rather higher accuracy have been attained, we are able to discuss the heat capacities in greater detail.

The salient point is that the heat capacity of vitreous silica at low temperatures is very much larger than would be expected. This is most readily explained by the occurrence of peaks in its lattice frequency spectrum at very low frequencies. Indeed, KATZ[4] has shown that, in the region $T < \Theta_D/10$, the heat capacity should be very sensitive to such features in a spectrum. While an acceptable interpretation of the experimental results can be made by following KATZ'S general form of analysis, this gives no insight into the origin of the peaks in the frequency spectrum.

* National Research Council Post-doctorate Fellow.

We have therefore also investigated the Raman and Brillouin spectra of vitreous silica.

The Brillouin spectrum provides a method of determining wave velocities at a frequency of $\sim 10^{10}$ sec^{-1}. A comparison of the results with velocities obtained from acoustic measurements at a frequency of $\sim 10^{7}$ sec^{-1} shows directly that dispersion of the lattice waves in vitreous silica is not significant up to a frequency of about 5×10^{10} sec^{-1} at least.

The Raman spectrum yields information of a different nature. The Raman spectrum of vitreous silica has been investigated by several previous workers, but only KRISHNAN[5] has investigated the region below 100 cm^{-1}. He found that the Raman spectrum of vitreous silica differs markedly from that of quartz in that it consists of broad bands and has such a band in the vicinity of 30 cm^{-1}. We have examined the Raman spectrum of two specimens of vitroeus silica and have found the general features described by KRISHNAN. It is also clear, however, that there is a significant number of optical modes of frequency much less than 30 cm^{-1}. These results give direct evidence for low-frequency optical modes whose presence can explain the unusual heat capacity of vitreous silica.

2. THE HEAT CAPACITY

(a) *Experimental*

The sample of vitreous silica used for the heat-capacity measurements was optical-quality Amersil. It was supplied in the form of crushed tubing of 1-mm wall thickness and 4-mm average dimension, which had been annealed at 1100°C after crushing. Prior to filling the calorimeter, the specimen (0·8480 moles) was heated *in vacuo* at 400°C for $\sim$ 40 hr. Dry helium was then admitted and the specimen transferred to a dry box where the calorimeter was filled under an atmosphere of dry nitrogen. The filled calorimeter vessel was evacuated for 18 hr at room temperature and then sealed off with $\sim 2 \times 10^{-6}$ moles of helium inside to act as exchange gas.

The measurements were made with a calorimeter which has been fully described previously.[6] Small modifications in the technique have also been discussed.[7,8] Two separate series of measurements were made, and the two sets of results agreed to within the precision of a single series.

The temperature increments used were $\sim 0{\cdot}5°$ below 7°K and $\sim 1{\cdot}0°$ above 7°K. The heat capacity of the calorimeter vessel comprised 60 per cent of the total heat capacity at 2·5°K and 25 per cent at 20°K.

(b) *Results*

The experimental results are given in Table 1. Their precision may be assessed from the average deviation of the experimental points

Table 1. *Measured heat capacities of vitreous silica*

Units: cal/mole deg.

T(°K)	C_p	T(°K)	C_p
2·344	0·000335	6·488	0·01339
2·465	0·000388	6·769	0·01564
2·790	0·000585	7·129	0·01883
3·018	0·000753	7·293	0·02058
3·278	0·001003	7·976	0·02785
3·522	0·001315	8·982	0·04136
3·784	0·001709	10·039	0·05855
4·031	0·002168	11·015	0·07742
4·267	0·002723	11·991	0·09876
4·565	0·003525	12·993	0·1230
4·719	0·003995	14·006	0·1501
5·017	0·005091	15·048	0·1793
5·225	0·005981	16·062	0·2097
5·504	0·007318	17·051	0·2406
5·724	0·008456	18·015	0·2728
5·989	0·009985	18·980	0·3051
6·226	0·01155		

from a smoothed curve. Above 3°K it is better than 0·2 per cent and below 3°K the maximum scatter of the results is about ± 1 per cent.

The absolute accuracy of the results is limited primarily by the uncertainties in the temperature scale and is estimated to be ± 2 per cent at 2·5°K, increasing to ± 0·5 per cent above 10°K. Good confirmation of these estimates is provided by results obtained for silicon and germanium,[7] for which the same temperature scale was used. For both of these examples, Θ_0 and $\Theta_{(elastic)}$ agreed to within 1 per cent.

VOL. 12 59/60

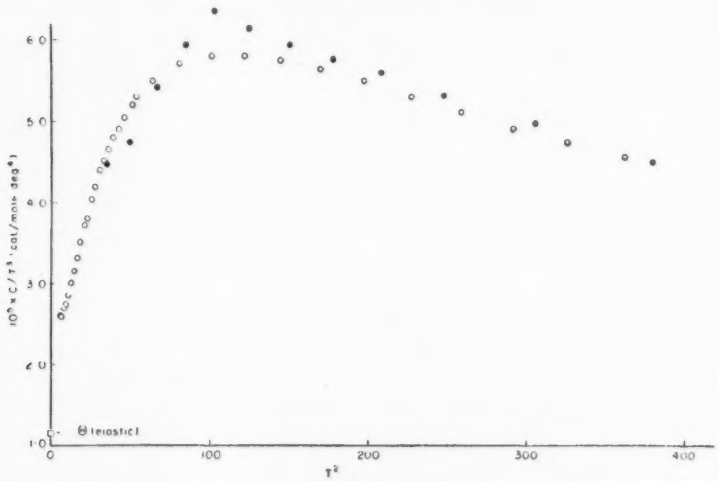

FIG. 1. A graph of C/T^3 versus T^2 for vitreous silica.
○ Present work — annealed at 1100°C.
● WESTRUM[2] — annealed at 1300°C.

The results of the present work, together with those of WESTRUM[2] for vitreous silica annealed at 1300°C, are shown graphically in Fig. 1 as a plot of C/T^3 against T^2. Such a graph is a useful representation of the heat capacity at very low temperatures, because at sufficiently low temperatures the heat capacity of an insulator has the form:

$$C = aT^3 + bT^5 + cT^7 + \ldots\ldots \quad (1)$$

This equation is based on the distribution of acoustic modes of low frequency:

$$G(\nu) = \mathcal{N}(\alpha\nu^2 + \beta\nu^4 + \gamma\nu^6 + \ldots\ldots), \quad (2)$$

where $\mathcal{N}$ is the number of atoms.

Equation (1) has been found to represent the heat capacity of a number of simple insulating crystals up to a temperature of about $\Theta_0/30$.[8,7] The value of the coefficient a, and hence of Θ_0, may readily be obtained from the plot of C/T^3 against T^2 by smooth extrapolation of the results to $T^2 = 0$; provided that the lattice vibrations are harmonic, Θ_0 should agree with $\Theta_{(elastic)}$. As shown by ANDERSON[1] the comparison of Θ_0 and $\Theta_{(elastic)}$ is independent of any assumptions regarding the size of the vibrating unit. The value of $\Theta_{(elastic)}$ for vitreous silica, obtained from the elastic-constant measurements of MCSKIMIN[3], corresponds to a value of C/T^3 of $1{\cdot}155 \times 10^{-5}$ cal/mole deg^4 at 0°K and this is indicated in Fig. 1.

It is at once apparent from Fig. 1 that the heat capacity of vitreous silica at low tempe-

ratures is most unusual. In the first place, the heat capacity increases much more rapidly than would be expected from dispersion of acoustic waves. Secondly, if the graph of C/T^3 against T^2 is extrapolated smoothly to $T^2 = 0$, the value of the intercept is more than twice that calculated from the elastic constants ($\Theta_0 = 395 \pm 5°\mathrm{K}$, cf. $\Theta_{(\mathrm{elastic})} = 495°\mathrm{K}$). This large discrepancy appears to be well outside the limits of experimental error and suggests that the smooth extrapolation is not correct in this case.

3. RAMAN SPECTRUM

(a) *Experimental*

In order to photograph Raman spectra very close to the exciting line, the usual procedure is to excite the spectra with the mercury resonance line at 2537 Å. This line can be reabsorbed by mercury vapour in the path of the scattered light. Thus, any parasitic light (caused by cracks, bubbles, etc., in the specimen) as well as the Rayleigh scattering can be greatly reduced in intensity, thereby reducing to a minimum the blackening of the photographic plate in the region of the exciting line. The use of this technique with vitreous silica is, of course, ideal, since vitreous silica is transparent in this region.

Two specimens of vitreous silica were used in the present investigation. Both were colourless and appeared to be free from cracks, bubbles, and occlusions. Specimen A was a 30-cm length of a 1·3-cm-diameter rod supplied by Amersil and kindly lent to us by McSKIMIN, who had used a section of the same rod for the determination of the sound velocities. On irradiation with λ 2537, specimen A exhibited an intense blue fluorescence extending all the way to the exciting line. An attempt was made to reduce the fluorescence by heating the specimen to 600°C, but this treatment was unsuccessful. Specimen B was a rod 27 cm long and 1 cm diameter of synthetic vitreous silica obtained from Thermal Syndicate, Ltd. It exhibited no fluorescence, and therefore most of the spectroscopic work was carried out with this specimen.

In each experiment a section of the rod 25 cm long was illuminated by a low-pressure mercury discharge lamp placed parallel to the specimen at a distance of 4 cm. The lamp and specimen were surrounded by a light furnace formed by coating a metal enclosure with MgO smoke. The lamp was completely enclosed in a quartz jacket through which distilled water at 40—50°C was circulated. At this wall temperature there is negligible self-reversal of the 2537 Å line, and the observed intensity is a maximum. The lamp contained several drops of mercury and in addition neon gas at a pressure of 5 mm in order to initiate the discharge and to enhance the emission of the 2537 Å line. The operating current was 100 mA at a voltage of 1000 V alternating current.

In order to reduce the stray light, the ends of the rod were painted with Kodak Opaque paint, except for a slit at the front end which served as a window for observing the scattered radiation. Also, the condensing lens used to match the cone of scattered light to the spectrograph aperture was diaphragmed and shielded from unwanted light. Finally, as mentioned above, a 30-cm tube of mercury vapour at room temperature was inserted in the light beam in front of the spectrograph to reduce the intensity of the unshifted line.

With the above conditions of illumination, it was possible to photograph the Raman spectrum in $^1/_2$ — 1 hr with a Hilger medium spectrograph (dispersion 9·4 Å/mm) and in 3—7 hr with a Hilger E1 spectrograph (dispersion 2·9 Å/mm) on Kodak 103aO plates. Several photographs were obtained with spe-

VOL. 12 59/60

cimen B at both low and high dispersion and with a variety of slit widths and exposure times. The spectrum of specimen B was also photographed in the fourth order of a 21-ft grating (dispersion 0·6 Å/mm). An intense photograph was obtained in an exposure time of 23 hr by making use of a cylindrical lens placed in the spectrograph immediately in front of the photographic plate to increase the intensity of the spectral image.[9] Only a few photographs were obtained with specimen A (all at the low dispersion) because of the strong fluorescence exhibited by this specimen. In all of the experiments, the specimens were at about the same temperature as the lamps, namely 45±5°C.

(b) *Observed spectra*

A photograph of the Raman spectrum exhibited by specimen B, showing both the Stokes and anti-Stokes scattering, is reproduced in Fig. 2. A microphotometer trace of this spectrum is shown in Fig. 3 with the frequency shifts of the intensity maxima and the widths of the bands indicated in wavenumber units (cm^{-1}). Microphotometer traces of the spectra exhibited by both specimens at the lower dispersion are shown together, for purposes of comparison, in Fig. 4.

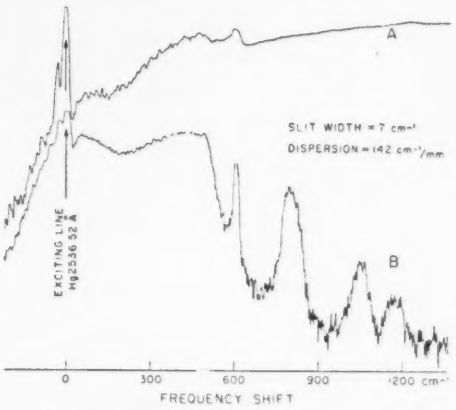

FIG. 4. Microphotometer tracings of the Raman spectra of both specimens, photographed with the Hilger medium spectrograph.

The most prominent feature in all of the spectra is an intense continuum extending from the exciting line out to 560 cm^{-1}. This continuum is characterized by two broad intensity maxima at 48 and 432 cm^{-1}, a sharper peak at 489·5 cm^{-1}, and a sharp intensity cut-

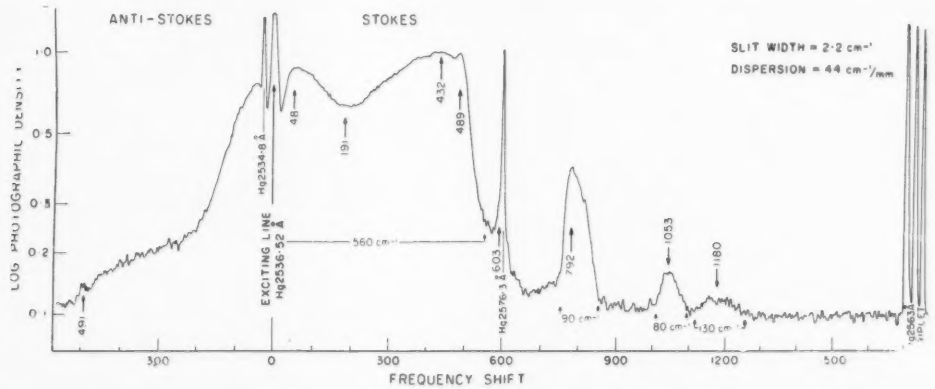

FIG. 3. A microphotometer tracing of the Raman spectrum of specimen B, photographed with the Hilger E1 spectrograph.

off at 560 cm^{-1}. Beyond the continuum, several other very broad features, having widths of $\sim$ 100 cm^{-1}, are observed at frequencies up to 1200 cm^{-1}. The difference in appearance of the spectra due to specimens A and B (Fig. 4) is a result of the masking of the relatively weak Raman spectrum by the intense fluorescence continuum excited in A. However it is evident that the broad feature extending to $\sim$ 560 cm^{-1} is present in the spectrum of specimen A.

The main result of the present investigation is the observation of the spectrum in considerable detail at low frequencies. It is this low-frequency end of the spectrum, lying within $\sim$ 50 cm^{-1} of the exciting line, which is most important for our present purpose of explaining the anomalous heat capacity of vitreous silica. As mentioned earlier, and as is clearly shown in Figs. 2–4, the low-frequency end of the spectrum consists of a very intense continuum. In Fig. 3, this continuum can be followed down to 17 cm^{-1}, where it appears to merge with the exciting line. It can be followed to still lower frequencies, down to about 8 cm^{-1}, in the spectrum photographed with the 21-ft grating. A microphotometer trace of this spectrum below 60 cm^{-1} is shown in Fig. 5. Unfortunately, a clear view of the spectrum below 20 cm^{-1} was not obtained because of the appearance of several weak grating ghosts (labelled g in Fig. 5) in this region. However, an investigation of the intensities of the grating ghosts indicates that their contribution to the spectrum is small and is approximately given by the area between the solid curve and the long-dash curve in Fig. 5. The shape of the remaining part indicates that it contains contributions from the Raman spectrum and from the wing of the Rayleigh line. It is, however, clear from the intensity contour that the Raman continuum extends to at least 8 cm^{-1} and perhaps even to the exciting line. This is indicated in Fig. 5 by the short-dash curves. In the only other investigation of the low-frequency spectrum of vitreous silica, KRISHNAN[5] was able to follow the continuum down to $\sim$ 30 cm^{-1}.

In an attempt to determine the origin of the low-frequency spectrum of vitreous silica, a comparison was made with the Raman spectra of crystalline quartz and of glasses.

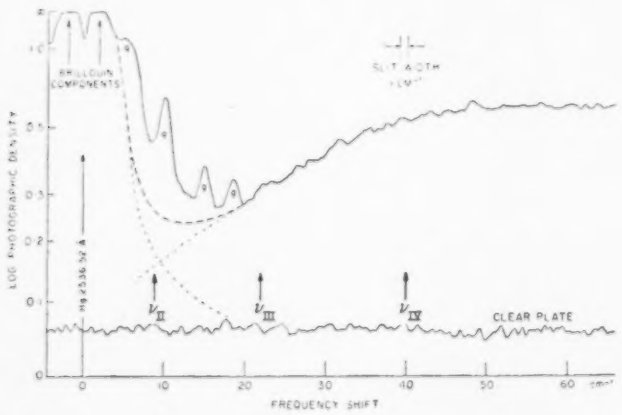

FIG. 5. A microphotometer tracing of the Raman spectrum below 60 cm^{-1} of specimen B, photographed with the 21-ft grating.
— — — Contour of the spectrum after correction for the contributions of the grating ghosts (g).
- - - - - - Estimated contours of the Raman spectrum and the Rayleigh line.
ν_{II}, ν_{III}, ν_{IV} Monochromatic frequencies used in the calculation of the heat capacity.

The published spectrum of crystalline quartz[10] consists of many relatively sharp bands, but none occurs below 128 cm^{-1}. In contrast, the

VOL. 12 59/60

Raman spectra of many glasses are strikingly similar to that of vitreous silica. A large number of different glasses containing Si, Pb, K, B, Al, F, and O have been studied,[11-13] and all except pure boroxide glass, B_2O_3, exhibit a Raman spectrum with an intense continuum out to ~ 550 cm^{-1}. In the investigation of two glasses by RANK and DOUGLAS[13], the continuum was observed at low frequencies, and in one of the spectra a completely depolarized band was found at 30 cm^{-1}. In the other investigations cited, intense fogging of the photographic plate near the Hg 4358 Å exciting line masked the low-frequency region and prevented a detailed study of the spectra below ~ 200 cm^{-1}. Nevertheless one is led to the conclusion that the low-frequency continuum as observed in vitreous silica is probably characteristic of many glasses.

At the present time it is difficult to describe unambiguously the motion giving rise to the low-frequency Raman spectrum. Because of the low frequencies involved (<50 cm^{-1}), the motion cannot be an internal vibration of the atoms within a group (SiO_4, SiO_2, etc.), but may be a translation or libration of such groups. Also, the high intensity of the spectrum clearly shows that it is not a second-order continuum such as is observed in the alkali halides and thought to arise through the anharmonicity of lattice vibrations. Of course, the very presence of a Raman spectrum is proof that the motion involves a change in polarizability from its equilibrium value. A complementary study of the far infrared spectrum could establish whether or not a change in dipole moment is also involved. According to a study of the state of polarization of the Raman spectrum by HARRAND[14] the continuum is strongly polarized at ~ 200-500 cm^{-1}, but depolarized at ~ 100 cm^{-1}. The latter region of the continuum must therefore arise from a degenerate vibration or a hindered oscillation. Unfortunately, HARRAND'S investigation was limited to frequencies above 100 cm^{-1}; its extension to much lower frequencies is highly desirable.

A knowledge of any variations in the spectrum at low temperatures would also be valuable for the detailed understanding of the origin of the low-frequency optical modes of vibration. In this connection the structural relaxation mechanism of ANDERSON and BÖMMEL[15] might be mentioned. It was put forward as an explanation of the strong acoustic and dielectric losses found in vitreous silica at low temperatures and high frequencies, and is based on the random network structure of vitreous silica.[16] The effects are found to be temperature-dependent, and it is suggested that the same mechanism could give rise to an optical relaxation with a frequency of the order of 30 cm^{-1}, at room temperature. If this same mechanism gives rise to the Raman spectrum of vitreous silica and other glasses, marked changes in the spectra would be observed at low temperatures.

In spite of our present difficulty in establishing the origin of the low-frequency spectrum, it should perhaps be pointed out that the observed facts are not inconsistent with the random network structure of vitreous silica and glass. Thus, for example, there would be a sufficient variety of environments and bond lengths and angles, that even the simplest possible motion of only one type of atom would produce a continuum.

4. BRILLOUIN SPECTRUM

(a) *General*

The fine structure observed in Rayleigh scattering from liquids and solids is known as the Brillouin spectrum. It consists of a central (or unshifted) line having the frequency of the

incident light and one, two, or three pairs of shifted lines (known as Doppler or Brillouin components), one member of each pair lying on either side of the central line. These shifted components are due to the scattering of light by the thermal waves existing in the scattering medium. BRILLOUIN[17] has shown that the frequency separation of the shifted components from the central line is given by

$$\Delta\nu = \pm 2\nu_0 \frac{v}{c} n \sin\frac{\varphi}{2}. \qquad (3)$$

Here ν_0 is the frequency of the exciting light, c the velocity of light, n the refractive index at ν_0, φ is the scattering angle, and v is the velocity of the thermal waves with the frequency $\Delta\nu$ in the medium. In a liquid, only longitudinal waves can be propagated, and therefore only one pair of Brillouin lines is observed.[18] In solids, longitudinal as well as two transverse (or shear) waves can be propagated in a specific direction, and therefore three pairs of Brillouin lines are generally observed.[19] Theoretical accounts of Brillouin scattering and related phenomena have been given by BHATIA and KRISHNAN[20] and MUELLER[21]. In isotropic solids such as vitreous silica, only two pairs of lines would be expected, one corresponding to longitudinal waves and the other to transverse waves. KRISHNAN[5] has studied the Brillouin spectrum of vitreous silica, but has observed only the light scattering by longitudinal waves.

The Brillouin spectrum provides a method of determining the velocities of Debye waves having frequencies of the order of 10^{10} sec^{-1}. The frequencies are several orders of magnitude higher than those generally available for the usual ultrasonic measurements. Moreover, advantage is taken of existing Debye waves excited at temperatures $\left(\frac{h\nu}{k}\right)$ of the order of a few degrees K. As shown below, the accuracy of the measurements can be within about 1 per cent.

(b) *Experimental*

According to equation (3), the following experimental conditions have to be satisfied in order to measure $\Delta\nu$ with high accuracy.

(a) High resolution is necessary, since $\Delta\nu$ is of the order of a few cm^{-1}.

(b) An exciting radiation of high frequency (i.e. short wavelength) is necessary because $\Delta\nu : \nu_0$.

(c) The angle φ must be well defined, because its range of variation determines the apparent width of the Brillouin components.

(d) The index of refraction must be known at the wavelength of the exciting line.

In the present experiment the spectrograph was a 35-ft concave grating in an Eagle mounting. It was used in the third order with a dispersion of 0·22 Å/mm (i.e. 3·5 cm^{-1}/mm at λ 2500). The resolving power is approximately 300,000; that is, lines spaced by about 0·13 cm^{-1} at λ 2500 can be resolved.

The Hg 2537 line was again chosen as the exciting radiation, but in order to achieve high resolution, the very narrow line of a single isotope (^{198}Hg) was used. The lamp was identical to that used in the Raman experiment, but with $\sim$ 2 mg of ^{198}Hg replacing the natural mercury. The observed width of the λ 2537 line under these conditions was mainly the instrumental width.

The angle between the incident and emerging radiations was limited to $90 \pm 8°$ by surrounding the specimen with a series of blackened annular diaphragms. These were 4 cm in radius and spaced at intervals of 5 mm. As in the Raman experiments, the lamp and specimen were enclosed in a light furnace.

A preliminary experiment was carried out without the diaphragm system (that is, $\varphi = 90 \pm 45°$), and an intense spectrum showing

VOL.
12
59/60

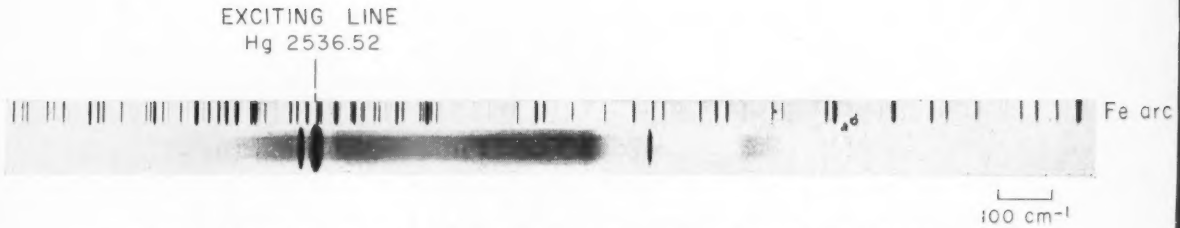

FIG. 2. The Raman spectrum of specimen B, photographed with the Hilger E1 spectrograph.

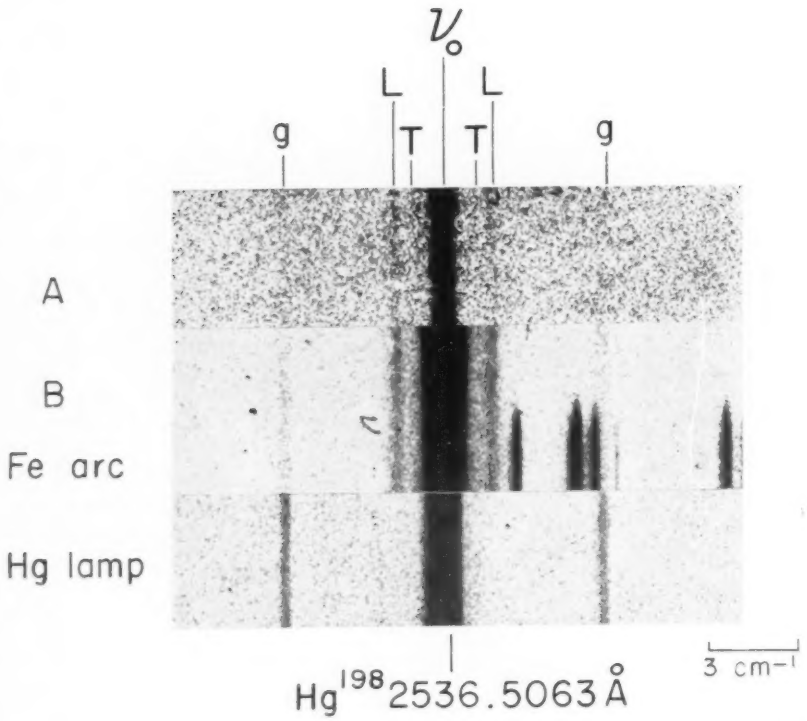

FIG. 6. The Brillouin spectra of both specimens, together with the spectrum of the ^{198}Hg lamp.

very broad wings on either side of the exciting line was obtained in 16 hr. Longer exposures (30-40 hr) were necessary with the diaphragms in place, and a photograph of the spectrum exhibited by each specimen was obtained. The slit width used was 0·09 mm (0·3 cm^{-1}).

(c) *Observed spectrum*

Photographs and microphotometer traces of the Brillouin spectra from specimens A and B are shown in Figs. 6 and 7. Also included is the spectrum of the mercury lamp itself. The spectrum exhibited by A was extremely weak; the incident illumination was shared with the competing process of the excitation of fluorescence; moreover, the spectrum was superimposed on the fluorescence continuum from the overlapping second-order spectrum at λ 3800.

The observed spectra clearly show a sharp line on both the Stokes and anti-Stokes sides of the exciting line. These lines are labelled L in Figs. 6 and 7, and are evidently due to scattering by the longitudinal waves. The expected second pair of lines (due to the transverse or shear waves) is just barely visible at the positions marked *T*. The relative intensity of the scattering due to longitudinal and transverse waves is in agreement with MUELLER'S equation

$$\frac{I_L}{I_T} = \frac{1-2\sigma}{1-\sigma}\left[1+\left(\frac{p_{12}}{p_{44}}\right)^2\right]$$

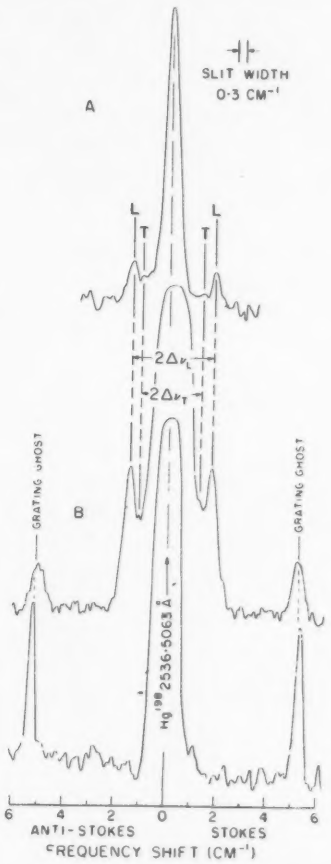

FIG. 7. Microphotometer tracings of the Brillouin spectra of both specimens, showing both the longitudinal (L) and transverse (T) components, and a tracing of the spectrum of the ^{198}Hg lamp.

Table 2. Velocities of acoustic waves in vitreous silica at 45°C

	$\Delta\nu_L$		$\Delta\nu_T$		v_L	v_T
	(cm^{-1})	($10^{10}sec^{-1}$)	(cm^{-1})	($10^{10}sec^{-1}$)	(10^5 cm/sec)	(10^5 cm/sec)
Specimen A	$1{\cdot}67_8 \pm 0{\cdot}02$	$5{\cdot}03_4$	$1{\cdot}04_1 \pm 0{\cdot}07$	$3{\cdot}12_3$	$5{\cdot}99_5 \pm 0{\cdot}08$	$3{\cdot}72 \pm 0{\cdot}3$
					5·98*	3·77*
Specimen B	$1{\cdot}63_6 \pm 0{\cdot}01$	$4{\cdot}90_8$	$1{\cdot}11_1 \pm 0{\cdot}05$	$3{\cdot}33_3$	$5{\cdot}84_5 \pm 0{\cdot}04$	$3{\cdot}97 \pm 0{\cdot}2$

* MCSKIMIN[3]

applicable to our case of $\varphi = 90°$. Here I_L/I_T is the intensity ratio of the longitudinal and transverse components, σ is Poisson's ratio, and p_{12}, p_{44} are photoelastic constants denoting the changes of refractive index caused by stress. The numerical values of the above quantities for vitreous silica are: $\sigma = 0{\cdot}165$, $p_{12} = 2{\cdot}85$, and $p_{44} = 0{\cdot}093$,[22] and they lead to the value $I_L/I_T = 8$.

In spite of the low intensity of the transverse components, it was possible to measure the distance between them with moderate accuracy by means of a photoelectric scanning comparator (similar to that described by TOMPKINS and FRED[23]). Measurements were made at several positions along the spectral lines, and the Stokes and anti-Stokes lines were found to be spaced at equal intervals from the respective longitudinal components, as expected. Both plates were measured four times, along with the juxtaposed iron spectrum used for wavelength calibration. The frequency shifts $\Delta\nu_L$ and $\Delta\nu_T$ in units of cm^{-1} and sec^{-1} are given in Table 2. The small differences in the values for the two specimens may be due to differences in the materials and in the case of the transverse waves also to the added difficulty in measurement.

It must be realized that the shift of the Brillouin components from the unshifted line gives directly the frequencies (in cm^{-1} or sec^{-1}) of the which elastic waves produce the light scattering. The corresponding velocities are then calculated from equation (3). The following values of the constants were used in this calculation: $c = 2{\cdot}99793 \times \times 10^{10}$ cm/sec; $\varphi/2 = 45°$; $\nu_0 = 39412{\cdot}467$ cm^{-1}; $n = 1{\cdot}5057$. The resulting values of v_L and v_T, together with their estimated errors, are given in Table 2. The velocities refer to longitudinal waves having a frequency of $5{\cdot}0 \times 10^{10}$ sec^{-1}, and to transverse waves having a frequency of $3{\cdot}3 \times 10^{10}$ sec^{-1}. They are in excellent agreement with the values at 10^7 sec^{-1} obtained by MCSKIMIN from ultrasonic measurements.

5. DISCUSSION

It is important to establish first whether or not the Raman spectrum and heat capacity which we have measured are generally characteristic of vitreous silica. All the evidence is that they are. Although effects dependent upon thermal history are undoubtedly present, they seem to be too small to have any major significance. Thus, WESTRUM[2] has measured heat capacities of two specimens of vitreous silica annealed at 1100 and 1300°C respectively, and the results differ by only a few per cent. Our results for material from a totally different source are similar (Fig. 1). By contrast, the observed heat capacity is greater than that calculated from the elastic constants by as much as a factor of five. The general apperance of the Raman spectra illustrated in Figs. 2 — 4 is similar to that reported by KUJUMZELIS[11], KRISHNAN[5], HARRAND[14], and others. There is therefore no doubt but that the Raman spectra found here are characteristic of vitreous silica (at 45°C) and are not just a property of our particular specimens.

We turn next to a more detailed discussion of the observations. As was mentioned in Section 1, work of KATZ[4] on the heat capacity of simple solids suggests that excess heat capacity at low temperatures is to be ascribed to peaks occurring in the low-frequency part of the lattice frequency spectrum. Following KATZ'S form of analysis, we find that two peaks containing approximately 1·5 per cent of the modes and having characteristic temperatures of about 10 and 50°K would suffice to give an excess heat capacity of the order observed. It should be borne in mind, however, that KATZ uses the continuum model as a refer-

ence in discussing the heat capacity. We must therefore examine the extent to which this model can be used in describing the properties of the disordered lattice of vitreous silica.

ANDERSON[1] gives cogent reasons to show that the long-wave vibrational properties of vitreous silica are similar to those of simple ionic crystals. For the latter, the departure of the heat capacity from that given by the continuum model is small (< 1 per cent) at temperatures less than $T = \Theta_D/100$.[24] Hence, we should expect the model to be applicable to the acoustic vibrations of vitreous silica in the region $T < 3$ - 5°K, assuming a reasonable choice of vibrating unit (see Table 9 of reference 1). However, even in this region the experimental heat capacity is more than twice that given by the elastic constants. The elastic constants obtained by MCSKIMIN[3] are fully substantiated by the results of the Brillouin scattering experiments (Table 2). Consequently, we must suppose that the required peaks in the lattice frequency spectrum consist of optical modes of unusually low frequency. The presence of such modes is clearly indicated by the observed Raman spectrum.

We cannot rule out the possibility that disorder in the lattice may introduce anomalous features into the acoustic spectrum at higher frequencies; the comparison of the results of Brillouin scattering and ultrasonic experiments shows only that the velocity of the acoustic waves is constant in the frequency range 10^7 to 5×10^{10} sec^{-1}. Nevertheless there seems to be little justification for invoking such features in the region where the wavelengths of the acoustic waves are in excess of 100 Å (i.e. $\nu \sim 5 \times \times 10^{11}$ sec^{-1}). It is also very significant that crystalline quartz has a "normal" heat capacity at low temperatures; its Raman spectrum shows no optical modes at frequencies < 128 cm^{-1}.

Unfortunately, it is not possible to obtain a distribution of the low-frequency optical modes from the observed intensities for the Raman spectrum. A quantitative calculation of the heat capacity was therefore made, assuming for simplicity that the distribution can be represented by a small number of single frequencies. This is not a drastic assumption, because, as KATZ[4] points out, one can hope to determine only the approximate weights and mean positions of peaks from heat capacities alone. The calculation of the heat capacity is illustrated in Fig. 8. The solid curve, which passes through the experimental points within their probable error up to $T = 15$°K, is the sum of individual con-

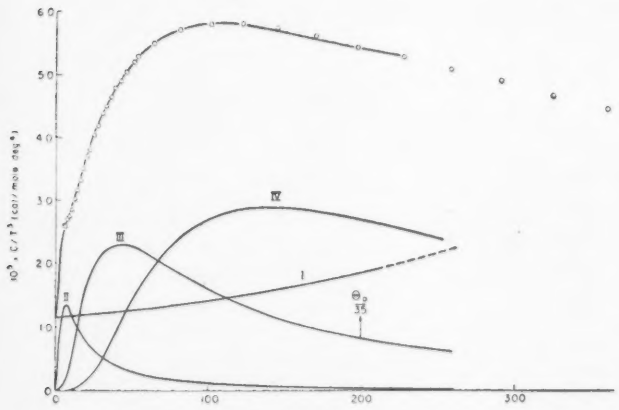

FIG. 8. Graph illustrating the comparison of experimental and calculated heat capacities.
O Experimental results
I-IV Separate contributions to the calculated heat capacity.

tributions illustrated in the lower part of the figure. The calculated heat capacity is given by:

$$C = 1\cdot155\times10^{-5}\,T^3 + 1\cdot5\times10^{-8}\,T^5 + 1\times10^{-10}\,T^7 + 1\cdot36\times10^{-3}\,E\left(\frac{13}{T}\right) + 3\cdot51\times10^{-2}\left(\frac{32}{T}\right) + 2\cdot62\times10^{-1}\,E\left(\frac{58}{T}\right)$$

cal/mole deg., (4)

which has the form of equation (1) with the addition of three Einstein terms. No attempt has been made to fit the results for $T > 15°K$ ($T > \Theta_D/35$), because marked deviations from the form of equation (1) may be expected in this region. Curve I represents the first three terms of equation (4). The coefficient of the term in T^3 corresponds to $\Theta_{(elastic)}$, and the coefficients of the terms in T^5 and T^7 have been estimated from the low-temperature heat capacities of quartz.[2] Curves II, III and IV represent the contributions of monochromatic peaks at 9, 22 and 40 cm^{-1}. The number of modes in these peaks is small, being 0·008, 0·2 and 1·4 per cent respectively of the total number. The positions of the frequencies are indicated by arrows on the microphotometer tracing of the Raman spectrum in Fig. 5.

The important result of the above calculation is that all of the frequencies required to account for the heat capacity are in the region where the presence of optical modes is shown directly by the Raman spectrum. Also, the frequency at 40 cm^{-1} which contains the majority of the extra modes is in the vicinity of the first intensity maximum of the low-frequency continuum. It must not be construed that there are necessarily three peaks in the frequency spectrum. Our calculation uses the minimum number of single frequencies which can represent all of the optical modes in the very low-frequency region. However, it is clear from the general form of the graph of C/T^3 against T^2 that there must be at least two peaks in the spectrum. The position of the lowest peak seems to be reasonably well defined at ~ 9 cm^{-1}, because it is not possible to fit the heat capacity within its experimental uncertainty using a frequency differing from this value by more than 2 or 3 cm^{-1}.

In sum, we see that the unusual heat capacity of vitreous silica can be accounted for by low-frequency optical modes occurring in its lattice frequency spectrum. The origin of the optical modes is still a matter for speculation. The fact that they are seen in the Raman spectrum is by itself not sufficient to assign them unambiguously to particular atomic or molecular motions in the solid. Clearly, further spectroscopic work of a different nature is desirable. The view adopted here that the low-frequency acoustic modes are behaving normally can be tested directly if it proves possible to determine the dispersion relations by neutron spectrometry.

Acknowledgements—We should like to thank Dr. O. L. ANDERSON for stimulating our interest in vitreous silica. We are indebted to him and to Dr. T. H. K. BARRON for helpful comments and suggestions.

REFERENCES

1. ANDERSON O. L., *J. Phys. Chem. Solids* **12,** 41 (1959).
2. WESTRUM E. F., Jr, Unpublished work.
3. MCSKIMIN H. J., *J. Appl. Phys.* **24,** 988 (1953).
4. KATZ E., *J. Chem. Phys.* **19,** 488 (1951).
5. KRISHNAN R. S., *Proc. Indian Acad. Sci.* **A37,** 377 (1953).
6. MORRISON J. A., PATERSON D. and DUGDALE J.S., *Canad. J. Chem.* **33,** 375 (1955).
7. FLUBACHER P., LEADBETTER A. J. and MORRISON J. A., *Phil. Mag.* **4,** 273 (1959).
8. BERG W. T. and MORRISON J. A., *Proc. Roy. Soc.* **A242,** 467 (1957).
9. BOWEN I. S., *Astrophys. J.* **88,** 113 (1938).
10. KRISHNAMURTI D., *Proc. Indian Acad. Sci.* **A47,** 276 (1958).
11. KUJUMZELIS T. G., *Z. Phys.* **97,** 561; **100,** 221 (1935).
12. NORRIS R., *Proc. Indian Acad. Sci.* **A14,** 178 (1941).

13. RANK D. H. and DOUGLAS A. E., *J. Opt. Soc. Amer.* **38,** 966 (1948).
14. HARRAND M., *C. R. Acad. Sci. Paris* **238,** 784 (1954).
15. ANDERSON O. L. and BÖMMEL H. E., *J. Amer. Ceram. Soc.* **38,** 125 (1955).
16. ZACHARIASEN W. H., *J. Amer. Chem. Soc.* **54,** 3841 (1932).
17. BRILLOUIN L., *Ann. Phys. (Paris)* **17,** 88 (1922).
18. VENKATESWARAN C. S., *Proc. Indian Acad. Sci.* **A15,** 322, 362 (1942).
19. KRISHNAN R. S., *Proc. Indian Acad. Sci.* **A41,** 91 (1955).
20. BHATIA A. B. and KRISHNAN K. S., *Proc. Roy. Soc.* **A192,** 181 (1948).
21. MUELLER H., *Proc. Roy. Soc.* **A166,** 425 (1938).
22. VEDAM K., *Phys. Rev.* **78,** 472 (1950).
23. TOMPKINS F. S. and FRED M. J., *J. Opt. Soc. Amer.* **41,** 641 (1951).
24. BARRON T. H. K., BERG W. T. and MORRISON J. A., *Proc. Roy. Soc.* **A242,** 478 (1957); **A250,** 70 (1959).

VOL. 12 59/60

Note Added in Proof. We have recently had the opportunity of photographing the Raman spectrum of specimen B with the 21 ft. grating, under improved conditions. By using a mercury filter at higher temperature and pressure it has been possible to suppress the intensity of grating ghosts close to the exciting line. As a consequence a clear view of the Raman spectrum is obtained down to 10 cm^{-1}, as shown in the accompanying figure, (symbols as in Fig. 5). This new spectrum fully substantiates the analysis given in Fig. 5.

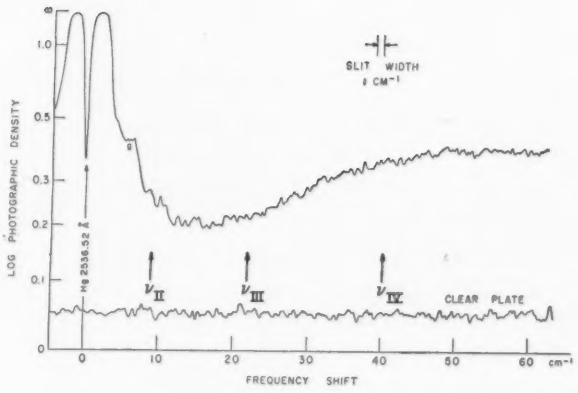

J. Phys. Chem. Solids Pergamon Press 1959. Vol. 12. pp. 66–73. Printed in Poland.

MICROWAVE STUDIES OF COLOR CENTERS IN BARIUM OXIDE*

J. W. CARSON†, D. F. HOLCOMB and H. RÜCHARDT ‡

Cornell University, Ithaca, New York

(*Received* 16 *March* 1959; *revised* 24 *April* 1959)

Abstract—Electron spin-resonance absorption measurements have been made at 9300 Mc/sec on BaO crystals with excess barium. No spin resonance is observed which can be associated with the imperfection responsible for the optical absorption band at 2·0 eV. A resonance is observed in some crystals which can be identified as arising from an *F*-center, i.e., a single electron trapped at an oxygen vacancy in the lattice. This resonance shows a strong central line at $g = 1{\cdot}936 \pm 0{\cdot}006$, and four satellite lines, spaced 68 G apart. This pattern is consistent with the assumption of an *F*-center as the source. Since the *F*-center is observed, but is not correlated with the 2·0-eV optical absorption, it is concluded that the center responsible for the 2·0-eV band is probably an *F*-center, i.e., two electrons trapped at the oxygen vacancy.

Large non-resonant microwave losses are also observed in the colored crystals. The present measurements are unable to distinguish between conduction in colloidal barium particles and electronic conduction in crystalline BaO itself as the source of the large losses.

1. INTRODUCTION

THE present investigation was undertaken in an effort to determine the nature of the imperfection in additively colored barium oxide which is responsible for the 2·0-eV optical absorption band observed by DASH[1]. On the basis of his experiments and those of SPROULL *et al.*[2], DASH concluded that the oxygen vacancy was the seat of the imperfection responsible for the absorption. In the divalent crystal, the energy may be absorbed by a single electron trapped at the oxygen vacancy, an *F*-center, or by a two-electron center, an *F*-center. Previous work on electron spin resonance of *F*-centers in alkali halides[3,4] showed that hyperfine interactions of the color-center electron with surrounding nuclei were the main source of line-broadening. Since only 18 per cent of the barium nuclei and none of the oxygen nuclei in BaO have magnetic moments, the situation appeared quite favorable for the observation of a spin-resonance absorption if the 2·0-eV center in BaO was of the *F*-type. If the imperfection was a two-electron center, there should be no unpaired electron spin and thus no resonance.

2. EXPERIMENTAL DETAILS

The microwave spectrometer used in these measurements was of conventional design. Barretter detection was used in a microwave bridge system very similar to that employed by KAN-

* This work was made possible through a grant from the Alfred P. Sloan Foundation to one of us (D. F. H.) The work was supported in part by the Office of Naval Research.

† Alfred P. Sloan Research Assistant. Now at Hughes Research Laboratories, Culver City, California.

‡ Now at Siemens-Halske Research Laboratory, Munich, Germany.

ZIG[5]. As in KANZIG'S system, a modified Liston-Becker breaker amplifier was used as a phase-sensitive detector for narrow banding. The sample was placed either at the midpoint or at the closed end of a rectangular reflection cavity operating in a TE_{102} mode. The spectrometer was capable of detecting the resonance signal from 5×10^{12} spins at room temperature for a resonance line width of 1G, with about 5 mW of microwave power incident on the sample cavity.

The BaO crystals were prepared in the manner described by SPROULL *et al.*[6]. The coloration process for most of the crystals used involved heating the crystals in barium vapor, as described by DASH[1] and in more detail by SEKULA[7]. Some colored crystals were also prepared by heating the crystals directly in molten barium in an iron crucible. For these runs, the BaO crystals were placed, together with chunks of barium metal, in an iron tube sealed off with dry air inside. This assembly was heated to 1120°C, held for 2 hr and cooled to room temperature over a period of several hours.

Early in the work, it was discovered that single crystals of the colored BaO showed such large microwave losses that it was necessary to use polycrystalline samples. These losses are discussed in somewhat more detail in a later section. Because of the extreme hygroscopicity of BaO, the samples could not be exposed to laboratory air. For some of the measurements, the BaO crystals were placed in the sample cavity in a dry box, and the whole cavity sealed against moist air. For other measurements, the crystals were encapsulated in glass and the glass sample placed inside the cavity. With the polycrystalline samples, 50 mg of heavily colored BaO reduced the cavity Q from its unloaded value of 2900 to about 1500. The measurements, except where indicated, were made at room temperature.

3. THE 2·0-eV CENTER

No electron spin resonance has been observed which can be correlated with the optical absorption band at 2·0 eV. Samples were used with as many as 10^{16} color centres. (The concentration was inferred from measurements of the optical absorption in the sample. SMAKULA'S equation[2] was used, with the assumption that the oscillator strength was unity.) If the center were paramagnetic, at this high concentration its resonance would have been missed only if the line were extremely broad, that is, of the order of 500 G or more, or if the spin-lattice relaxation time were very long. At the lowest power level employed, the rotating r.f. field H_1 was 2×10^{-3} G. For a given value of relaxation time, the most unfavorable case so far as saturation is concerned would obtain if the homogeneous line width were determined by the relaxation time. In this most unfavorable case, it is estimated that the resonance should have been observed unless $T_1 > 10^{-3}$ sec. Such a long relaxation time at room temperature would be surprising for an electron on an atomic center in BaO, since hyperfine and spin-orbit interactions would both be expected to be large. We conclude that if the 2·0-eV band arises from a point defect, the defect is probably not paramagnetic. The most likely candidate is, consequently, the F-center, i.e. two electrons trapped at the oxygen vacancy.

4. F-CENTER RESONANCE

In several of the colored crystals, a resonance was observed which can be identified as arising from an F-center, i.e. a single electron trapped at the oxygen vacancy. The properties of the center will be discussed below. It should be pointed out that the conditions necessary for the formation of the F-center are not known. The resonance was observed in crystals colored

by both techniques mentioned previously. In the crystals prepared in both ways, however, the centers were concentrated in regions near the surfaces. It was found that if the surface regions were ground off in order to prepare a crystal with well-polished surfaces for optical-absorption measurements, the polished crystal no longer exhibited the *F*-center resonance. Total numbers of *F*-centers in those crystals exhibiting the resonance were from $1{\cdot}5 \times 10^{14}$ to 8×10^{14}, these numbers being determined by comparing the intensity of the resonance to that of a standard $CrCl_3$ sample.

In this work, we have concentrated on determining the properties of the center, and no further experiments to determine the conditions necessary for its formation were done.

The resonance characteristics by which we have identified the source as the *F*-center will be described, and in the identification process information about the properties of the center will be collected.

Fig. 1 shows the resonance pattern obtained from the crystals, at approximately optimum signal-to-noise ratio. The experimental trace is the derivative of the absorption lines, with the 8-cycle magnetic-field modulation equal to 4 G. In this particular trace, the magnetic field was not driven (up) far enough to observe the upper companion to the very weak line numbered 2 in Fig. 1. The companion is observed in other runs, however. It will be noted that at this modulation level these outer lines are just observable above the noise. Only by matching up a number of experimental traces over the same field region was the presence of these lines definitely established. One run was made with an 8-cycle field-modulation amplitude of 20 G. which showed these broad outer lines more clearly. The central line is situated at $g = 1{\cdot}936 \pm 0{\cdot}006$.

The properties of the resonance will be discussed in the following categories:

(*a*) Number and relative intensity of components.

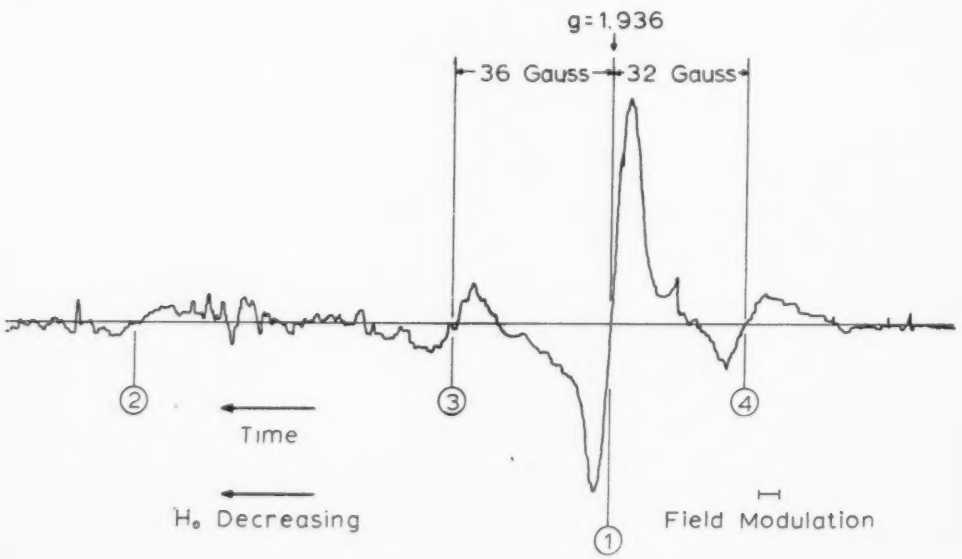

FIG. 1. *F*-center resonance in BaO. The experimental trace is the derivative of the absorption curve.

(*b*) Field splitting of components.

(*c*) Shift of center of gravity of satellites with respect to central line.

(*d*) *g*-value of central line.

(*e*) Line widths.

(a) *Number and intensity of components*

One might expect that the main magnetic interactions of an *F*-center electron in BaO would be those with surrounding nuclear moments via the hyperfine interaction, similar to the situation in MgO.[8] The non-magnetic oxygen nuclei do not enter the problem. The two magnetic barium isotopes, ^{135}Ba and ^{137}Ba, are in abundances of 6·59 and 11·32 per cent respectively. Their nuclear moments are 0·837 and 0·936 nuclear magnetons, both with $I = 3/2$. For the present, we will consider these moments to be approximately equal. Because of these low abundances, 31 per cent of the *F*-centers in the NaCl-type lattice of BaO will have no nearest-neighbor barium nucleus which is magnetic. Forty per cent will have one magnetic neighbor of ^{135}Ba or ^{137}Ba, and 22 per cent will have two magnetic neighbors. Those centers with more than two magnetic neighbors contribute essentially nothing to the resonance intensity. Thus, considering the isotropic hyperfine interaction with only the nearest-neighbor nuclei, we would expect 31 per cent of the intensity of the *F*-center electron spin resonance to appear in a strong central line, 40 per cent in a quartet of equally intense, equally spaced satellites (corresponding to the four possible orientations of one nucleus of spin 3/2) and 22 per cent in a set of seven lines, with intensity ratios 1 : 2 : 3 : 4 : 3 : 2 : 1 and splittings equal to those of the quartet. These three different nuclear environments would give the resonance pattern shown schematically in Fig. 2. Our observed pattern consists of five lines. For the inner trio, the integrated intensity under the absorption curve gives an intensity ratio of 8 : 27 : 10 compared to the predicted ratio 7·3 : 26·5 : 7·3. Since the lines overlap slightly, the tails must be obtained by a subtraction process. As a result, the measured intensities may be as much as 20 per cent in error. If we are indeed observing the *F*-center resonance, one would expect the integrated intensity of the outermost pair of lines to be the same as that of the inner pair. This outermost pair is so weak on account of line-broadening that a meaningful integrated intensity can not be obtained. The line-broadening arises partly from the necessity of using polycrystalline samples, and partly from the 12 per cent difference in the magnetic moments of the two barium isotopes. If we were to write the *F*-center electron wave function in the form of a linear combination of atomic orbitals, we would get an isotropic hyperfine interaction only for the case in which the electron exists in pure *s*-type orbitals on the barium nuclei. In general, the pure *s*-orbitals will not obtain. The result of admixtures of higher states is a dependence of the hyperfine splitting on crystal orientation with respect to H_0. Thus, with our polycrystalline samples, we observe an average splitting over angles of crystal orientation. This orientation effect, combined with the effect of the two barium isotopes, results in a progressively greater broadening of the hyperfine components as we go out from the central line. The observed

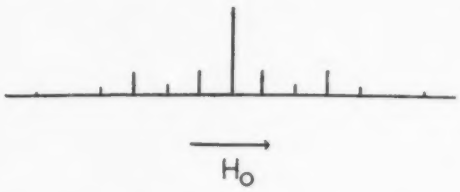

FIG. 2. Predicted pattern of resonance lines from *F*-center electron, in BaO, assuming an isotropic hyperfine interaction and the same line width for all lines.

VOL. 12 59/60

line width of the outermost pair is about 17 G compared to 9 G for the inner pair. The noise level precluded observation of the weaker lines contributed by the *F*-center electrons with two magnetic neighbors, particularly for those lines widely split off from the center. In general, the observed pattern fits the hypothesis of a hyperfine interaction of an electron located symmetrically with respect to six nearest-neighbor barium nuclei.

(b) *Field splitting of components*

The observed spacing of the four approximately equally spaced lines is 68 G.

The effect of the hyperfine isotropic part of the interaction on the energy of the spin transition can be included by adding a term $+ 1/6\ \xi\ A m_I$ to the transition energy, where A is the s-state hyperfine coupling constant for the free atom, and ξ is a measure of the electron probability density at the nucleus for the *F*-center compared to the same quantity for the free atom. The factor 1/6 arises from the fact that in the *F*-center, the electron interacts equally with the six nearest barium neighbors. Using the observed splitting of 68 G, which is a weighted combination of splittings differing by 12 per cent, and a weighted value of A from atomic spectra,[9] one finds that $\xi = 0{\cdot}29$. This is to be compared to a value for ξ of 0·097 for the *F*-center in MgO[8] and 0·6 for the *F*-center in KCl.[3] The value for BaO seems reasonable. Note that for both alkaline earth oxides, ξ is less than for KCl, representing the fact that the single electron is more tightly bound into the divalent vacancy in the alkaline earth oxides

(c) *Shift of center of gravity of satellites with respect to central line*

From Fig. 1, it will be seen that the center of gravity of the inner pair of satellite lines is shifted down in field by 2·2 G with respect to the central line. Such a shift is to be expected if the splitting does indeed arise from the hyperfine interaction. In addition to the first-order splitting discussed in (b) above, the hyperfine interaction Hamiltonian, $\mathbf{AI} \cdot \mathbf{S}$, contributes, in second order, a shift to lower field for all lines. A straightforward calculation, using second-order perturbation theory, yields a contribution.

$$\Delta H = -\frac{\left(\frac{1}{6}\xi A\right)^2}{2g\,\beta H_0}\{m_s[I(I+1)-m_I^2]+ + m_I[S(S+1)-m_s^2]\} \qquad (1)$$

to the field at which the transition should be observed. Using the experimental value of 98 G for the splitting, $1/6\ \xi A$, the second-order shift for the $m_I = \pm 1/2$ lines is calculated to be 2·4 G, in good agreement with the experimental value. (The central line arises from electrons with effectively no hyperfine interaction, and is unshifted). It should be noted that the outer pair of lines with $m_I = \pm 3/2$ should be shifted by a smaller amount. These are so broad and so weak, however, that a good experimental value for their position can not be obtained.

(d) g-*value of the central line*

KAHN and KITTEL[10] have obtained an approximate expression for the g-shift of an *F*-center electron resonance, in which they show that the shift depends linearly on the spin-orbit coupling constant of the electron in the first excited atomic state above the ground state. The optical spectra of singly ionized barium gives the term splitting $6^2P_{1/2} - 6^2P_{3/2}$ as 1691 cm^{-1}.[11] The corresponding splitting for potassium is 58 cm^{-1}. We have not attempted to calculate for BaO the other factors appearing in the KAHN and KITTEL expression, since the result would be a fairly crude approximation, at best. The experimental g-shift in KCl is 0·007.[3] The experimental value in BaO is 0·066. The main point is that the shift

is expected to be relatively large in BaO compared to the alkali halides and MgO because of the large spin-orbit coupling for the barium atomic orbitals, and this is found to be true.

(e) *Line widths*

The peak-to-peak derivative width, δH, of the central line is $4{\cdot}1 \pm 0{\cdot}2$ G. The origin of the broadening is not known. It may well arise from spin-lattice relaxation processes. There is no evidence of saturation of the resonance at $H_1 = 0{\cdot}02$ G, the upper limit of the available microwave power. From this lack of saturation we can estimate an upper limit on T_1, assuming the homogeneous line width to be determined by T_1. The upper limit obtained in this fashion is 3×10^{-6} sec. If the observed broadening does indeed arise from an uncertainty broadening produced by the spin-lattice relaxation, T_1 would be $1{\cdot}4 \times 10^{-8}$ sec. All one can say is that the range of possible values of T_1 is reasonable, considering the rather strong spin-orbit interaction of the *F*-center electron.

The line width of each line of the inner satellite pair is 9 ± 1 G. This extra width compared to the center line presumably arises from the two effects previously mentioned. In the first place, since the two magnetic barium nuclei do differ in magnitude by 12 per cent the hyperfine splitting of the resonance of those electrons with one magnetic nuclear neighbor will vary, depending on the atomic weight of the neighbor. The observed satellites, given the 68 G as a weighted mean splitting, should consist of two lines of intensity weight 37 and 63 per cent with the stronger line 3·5 G farther out. The other broadening effect comes from the admixture of *p*-type wave function into the predominantly *s*-function. There is, of course, also the posibility that T_1 for this set of lines is different from T_1 for the central line, since the hyperfine interaction is much stronger. As a result, one cannot obtain a very precise estimate of the *p*-function admixture. It certainly is rather small, however, since the variation in the splitting of the inner satellite pair with crystallite orientation is at most about 8 G, as indicated by the line widths.

The width of the outermost satellite lines is 17 ± 5 G. One would expect the broadening contribution from the two effects mentioned in the previous paragraph to be three times that for the inner pair. On this basis, one would expect a line width of perhaps 20 G (the intrinsic line width is assumed to be 4 G). Because of the large experimental uncertainty in the line width all one can say is that there is qualitative agreement.

Any optical absorption arising from the *F*-center in BaO may not be observable. If the 2·0-eV optical absorption peak does indeed arise from a transition in a double-electron center at the oxygen vacancy, the transition energy for the more tightly bound single-electron center may well be above the fundamental absorption edge in BaO, which occurs at 3·8 eV.[12]

5. NON-RESONANT LOSSES

It has been noted that the colored BaO crystals exhibit very high microwave losses compared to uncolored BaO crystals. Some quantitative measurements of loss tangents have been made, and the results will be briefly summarized. These measurements were made by observing the shift in the sample-cavity resonant frequency and the change in cavity Q upon insertion of the sample. The cavity-resonance reflection signal, with a 60-cycle modulation of the klystron reflector voltage, was detected and displayed on an oscilloscope. The resonance of a wavemeter cavity was also fed to the vertical plates of the oscilloscope, but with opposite polarity. This scheme, previously employed by SPROULL and LINDER[13], allows rather accurate measurement of the half-power resonance width if the detector output is linear as a function of power input. (The range of linearity of

detector crystals is limited, of course. We operated at power levels within the linear range of the 1N34B crystals used.) The peak amplitude of the wavemeter resonance is adjusted with a series attenuator so that it is just one-half the peak amplitude of the sample-cavity resonance. If the wavemeter is then tuned until the difference in the two resonance signals is zero, as indicated on the oscilloscope, the wavemeter reads the half-power frequency of the sample cavity. The samples used were polycrystalline, contained in a small glass tube which occupied the line of maximum electric field the full width of the cavity at the half-wave position. In calculating the change in cavity Q, the unperturbed Q was taken as that obtaining with an identical empty glass tube in the same position as the sample tube. In practice, it was found that the effect of the dummy glass tube on the cavity Q was almost negligible compared to that produced by the BaO.

The complex dielectric constant of the material is written $\epsilon = \epsilon' + i\epsilon''$. With the polycrystalline samples only the ratio $\epsilon''/\epsilon' = \tan\delta$, the loss tangent, could be measured because of lack of knowledge of the depolarizing factor. From the results of BETHE and SCHWINGER[14], it can be shown that, in the case of small samples in the cavity

$$\frac{\epsilon''}{\epsilon' - 1} = \frac{1/Q - 1/Q_0}{2(f - f_0)/f_0} \qquad (2)$$

where Q and f are the quality factor and resonant frequency of the perturbed cavity and Q_0 and f_0 are the values for the empty cavity. For the case of BaO, the left-hand side of equation (2) is approximately equal to $\tan\delta$, since the low-frequency value of ϵ' is 34.[15]

Attempts were made to produce spherical BaO crystals to give a known depolarizing factor and thus permit an absolute determination of ϵ'. Unfortunately, the very large value of ϵ' makes the measurement of its exact magnitude extremely sensitive to small deviations from spherical shape, and very sensitive to small experimental errors in measuring frequency shifts. Consequently, it was felt that the measurements could not be made reliably.

One could assume that the low-frequency value of ϵ' for pure BaO obtains in the colored crystals at microwave frequencies, and thus calculate the values of ϵ'' from the loss tangent. Unfortunately, there is experimental evidence that such an assumption would be incorrect. Subsequent to our measurements, SEKULA[7] has found that the colored crystals exhibit anomalously large values of ϵ' in the frequency range up to 50 Mc/s, ϵ' in some crystals being as large as 700. Table 1 gives values of $\tan\delta$ at room temperature and liquid-nitrogen temperature for several crystals with different 2·0-eV color-center concentrations.

Table 1. *Values of tan δ for crystals with various* 2·0 eV *color-center concentrations*

Sample	N_F/cc	tan δ	
		300°K	77°K
10	$2{\cdot}2\times10^{17}$	0·008 ± 0·003	0·003
11	$4{\cdot}2\times10^{17}$	0·043 ± 0·003	0·016 ± 0·003
15	$2{\cdot}3\times10^{16}$	< 0·003	
17	$2{\cdot}3\times10^{16}$		
I	$2{\cdot}7\times10^{17}$	0·008 ± 0·001	0·002 ± 0·001
IV	$2{\cdot}8\times10^{17}$	0·037 ± 0·005	0·045 ± 0·005

From the information in Table 1, several observations can be made. The losses are not a simple function of the density of centers responsible for the 2·0-eV band. Moreover, it is clear by comparing crystal IV with the others that more than one mechanism may be involved in the energy absorption, since the sign of the temperature-dependence is reversed in this crystal. Optical absorption measurements on crystal IV by SEKULA show a distorted 2·0-eV absorption band.

The observed temperature-dependence in the well-behaved crystals could be explained by

either of two mechanisms. The losses might arise from the present of colloidal barium particles small in comparison with the r.f. skin depth, in which case the observed more-or-less linear dependence on T would be the temperature-dependence of the metallic resistivity. Alternatively, the losses might arise from a reasonable bulk conductivity in the crystals arising from thermally excited conduction electrons. If the second alternative is the correct one, it is known from the low values of the d.c. conductivity measured by DOLLOFF[16] in colored crystals that there would need to be grain-boundary barriers in the crystals to prevent d.c. charge transfer. It should be noted that the large values of ϵ' measured by SEKULA in the colored crystals lead one to favor the second alternative. Polarization across the barriers could lead to large measured values of ϵ'. Colloidal metal particles would also increase the measured values of ϵ', but it is difficult to account for the magnitude of the increase in this way with any reasonable estimate of the concentration of metallic barium present.

Acknowledgements—The authors would like to acknowledge the considerable assistance and advice of Prof. R. L. SPROULL and other members of his group working on barium oxide. In particular, we received great assistance from Dr. S. T. SEKULA, who prepared most of the colored crystals, and initiated us into techniques for handling BaO. R. O. GARRETT and T. R. SLIKER assisted in many of the measurements. The resident author (D.F.H.) would like to thank Dr. R. H. SILSBEE for many profitable discussions.

REFERENCES

1. DASH W. C., *Phys. Rev.* **92.** 68 (1953).
2. SPROULL R. L. BEVER R. S. and LIBOWITZ G. *Phys. Rev.* **92,** 77 (1953).
3. KIP A. F., KITTEL C., LEVY R. A. and PORTIS A. M., *Phys. Rev.* **91,** 1066 (1953).
4. LORD N. W., *Phys. Rev.* **105,** 756 (1957).
5. KANZIG W., Private communication.
6. SPROULL R. L., DASH W. C., TYLER W. W. and MOORE A. R., *Rev. Sci. Instrum.* **22,** 410 (1951).
7. SEKULA S. T., Thesis, Cornell University (1958).
8. WERTZ J. E., AUZINS P., WEEKS R. A. and SILSBEE R. H., *Phys. Rev.* **107,** 1535 (1958).
9. LANDOLT-BORNSTEIN, *Zahlenwerte und Funktionen* Band I, Teil 5. Springer-Verlag, Berlin (1952).
10. KAHN A. and KITTEL C., *Phys. Rev.* **89,** 315 (1953).
11. LANDOLT-BORNSTEIN, *Zahlenwerte und Funktionen* Band I, Teil 1. Springer-Verlag, Berlin (1952).
12. TYLER W. W. and SPROULL R. L., *Phys. Rev.* **83,** 548 (1951).
13. SPROULL R. L. and LINDER E. G., *Proc. Inst. Radio Engrs.* **34,** 305 (1946).
14. BETHE H. A. and SCHWINGER J., OSRD Contract OEMsr-429 report dated March 1943.
15. BEVER R. S. and SPROULL R. L., *Phys. Rev.* **83,** 801 (1951).
16. DOLLOFF R. T., *J. Appl. Phys.* **27,** 1418 (1956).

VOL. 12 59/60

J. Phys. Chem. Solids Pergamon Press 1959. Vol. 12. pp. 74–88. Printed in Poland.

REGLES DE PREDICTION DE LA SEMICONDUCTIBILITE DANS LES RESEAUX CRISTALLINS MINERAUX

J. P. SUCHET

Service de Recherche Fondamentale, Manufactures de Saint-Gobain, Paris

(*Received* 28 *January* 1959; *revised* 27 *March* 1959)

Abstract—Study of the exact significance of the "8-*N*" rule, well known to chemists and metallurgists, shows that the rule proposed by MOOSER and PEARSON for compound semiconductors must be supplemented by two analogous rules for 3- and 2-co-ordinated nets. Purely covalent formulae are preferable to ionic ones for visualizing such electronic rules, and bonding schemes using them are capable of including defect lattices by treating the vacant sites as atoms of zero valency. A new concept of a "compensated lattice" is introduced, based upon our knowledge of interactions between substitutional and interstitial impurities in germanium and silicon, and is applied to the study of compounds such as Li_3Bi which do not satisfy the bonding schemes mentioned above. The Bi_2-Te_3-type structure is discussed in detail, and a classification of all known inorganic semiconductors in a few fundamental lattice types is proposed.

Sommaire — L'étude de la signification exacte de la règle de "8-*N*", bien connue des chimistes et des métallurgistes, montre que la règle proposée par MOOSER et PEARSON pour les composés semiconducteurs doit être complétée par deux règles analogues pour les réseaux tri- et dicoordonnés. Les formules covalentes pures sont préférables aux formules ioniques pour mettre en évidence de telles règles électroniques, et les schémas de filiation les utilisant sont susceptibles d'inclure les réseaux lacunaires si l'on considère les sites vacants comme des atomes de valence nulle. Un concept nouveau de "réseau compensé" est introduit à partir de notre connaissance des interactions entre impuretés de substitution et impuretés interstitielles dans le germanium et le silicium, et appliqué à l'étude des composés tels que Li_3 Bi qui ne satisfont pas les schémas de filiation mentionnés ci-dessus. La structure de type Bi_2 Te_3 est discutée en détail et une classification de tous les semiconducteurs minéraux connus en quelques types fondamentaux de réseau est proposée.

1. LA RÈGLE DE MOOSER ET PEARSON ET SES ORIGINES

MOOSER et PEARSON[1] ont exposé il y a trois ans un point de vue assez original sur les liaisons interatomiques dans les solides semiconducteurs. Observant que la différence d'électronégativité entre atomes constituant les binaires est généralement inférieure à l'unité, ce qui correspond, d'après PAULING[2] à un caractère ionique de 25 pour cent au plus, ils ont conclu que la semiconductibilité était essentiellement liée à l'existence d'un réseau continu de liaisons covalentes (ou homopolaires), et suggéré que l'occupation de tous les niveaux électroniques *s* et *p*, qui est de règle dans le cas des éléments, pouvait n'être réalisée que pour un atome sur deux dans le cas des composés.

Ils étaient ainsi conduits à affirmer que l'un des éléments constituants devait être à droite de la frontière de ZINTL pour pouvoir com-

pléter son octet de valence, et que la concentration n_e des électrons de valence par molécule satisfaisait la relation simple, dite "règle de MOOSER et PEARSON":

$$\frac{n_e}{n_a} + b = 8$$

où n_a était le nombre d'atomes des groupes IV à VII (à l'exception des métaux de transition), et b le nombre de liaisons que forme éventuellement l'un de ces derniers atomes avec d'autres similaires. Une frontière était ainsi tracée entre semiconducteurs et métaux.

Il y a lieu de rappeler que les idées exposées par KREBS et SCHOTTKY[3] à Innsbrück en 1953, puis par KREBS[4] à Amsterdam en 1954 et enfin dans deux articles de KREBS[5,6], sur l'influence des liaisons homopolaires sur la structure des sels minéraux avaient ouvert la voie au point de vue ci-dessus.

La règle de MOOSER et PEARSON a été exposée par ses auteurs avec plus de détails et en se référant à un nombre croissant de composés à Rugby en 1956[7], puis dans une série de publications ultérieures [8–11] ainsi qu'à Brooklyn en 1957 par FISCHER et PEARSON[12].

Si l'on considère la classification des éléments due à MENDELEEV avec les périodes longues, on y distingue souvent les ensembles M (métaux électropositifs des colonnes ou groupes I_A et II_A), T (métaux de transition des groupes III_A à $VIII_A$) et B (groupes II_B à VII_B), le groupe I_B pouvant être rattaché à T ou B. Les travaux de ZINTL[13,14] montrent qu'il existe une frontière à l'intérieur de l'ensemble B, telle que les combinaisons MB, TB ou BB' donnent des phases multiples avec les groupes I_B à III_B (ainsi qu'entre alcalins et éléments lourds de IV_B) et des composés d'indices simples avec les groupes IV_B à VII_B. Certaines de ces phases multiples obéissent à des règles de concentration électronique par atome, et l'on connaît notamment celles de HUME-ROTHERY[15,16] pour les alliages TB et I_B-B. Elles s'accordent avec les résultats de ZINTL pour conférer un caractère spécial aux éléments du sous-ensemble B_Z (groupes IV_B à VII_B) à droite d'une frontière dite de ZINTL approximativement située entre les groupes III_B et IV_B. Nous désignerons par la suite ces éléments sous le nom d'"éléments de ZINTL".

On sait par ailleurs que ces éléments suivent la règle de "8-N" de BRADLEY et HUME-ROTHERY, suivant laquelle chaque atome possède 8-N voisins immédiats, N étant le numéro du groupe auquel appartient l'élément. Cette règle exprime simplement le fait que ces atomes tendent à remplir leurs niveaux électroniques supérieurs par le jeu de liaisons covalentes (homopolaires) et acquièrent ainsi autant d'électrons supplémentaires qu'ils forment de liens. La quantité 8-N représente donc la coordinence covalente et l'on est tenté d'écrire également cette règle:

$$a + b = 8 \qquad (1.1)$$

avec $a = N$, nombre d'électrons de valence (s et p) de l'atome, et $b = 8 - N$, nombre de liens qu'il forme avec ses voisins.

Si nous admettons maintenant avec MOOSER et PEARSON que la semiconductivité liée à l'existence d'un réseau continu de liaisons covalentes peut subsister même quand ce réseau n'est plus formé d'atomes identiques, nous voyons que les composés semiconducteurs feront partie des composés d'indice simple cités plus haut, et qu'une règle de concentration électronique par atome analogue aux règles de HUME-ROTHERY va pouvoir être déduite de la relation (1.1) ci-dessus en remplaçant a par le rapport du nombre n_e d'électrons de valence pouvant participer aux liaisons covalentes au nombre n_a d'atomes des éléments de ZINTL entrant dans le composé. Cette règle n'est autre que celle de MOOSER et PEARSON où le composé semiconducteur est considéré comme un élément

VOL. 12 59/60

simplement "gonflé" par un apport électronique extérieur. (MOSS[17] a d'ailleurs suggéré que les éléments de ZINTL devaient pouvoir exister sous une forme semiconductrice). La lettre b continue, dans ces conditions. à désigner le nombre de liens que forme chaque atome de ZINTL avec d'autres atomes de ZINTL.

2. EXTENSION DE LA RÈGLE DE MOOSER ET PEARSON

La présence d'un certain nombre d'exceptions à cette règle—et en particulier du groupe de PbS—nous a amenés à reconsidérer l'interprétation de la règle 8-N. Cette règle donne la coordinence covalente, et par suite le type de réseau cristallin à l'intérieur duquel les atomes se groupent en molécule géante. Ce type de réseau est intimement lié au type d'orbitale utilisé par les liaisons covalentes. MOOSER et PEARSON (référence 8, p 633) estiment que les liaisons dans les semiconducteurs comprennent habituellement quelque forme d'hybridation sp et qu'il n'est plus possible de maintenir une distinction entre orbitales s et p. Cette opinion n'est sans doute pas toujours valable, car les études faites par KREBS[3,18] sur le réseau type sel gemme du groupe de PbS montrent bien que l'on a surtout affaire en ce cas à des fonctions propres p, et que les hybridations de fonctions s et p n'apparaissent que progressivement lorsque les atomes lourds sont remplacés par des atomes plus légers. Même lorsqu'on est passé au réseau rhomboédrique de l'arsenic, par exemple, la fraction de fonction s peut encore être négligée, le caractère directionnel le plus marqué n'apparaissant que pour les fonctions hybrides sp^3 du type diamant. Par ailleurs, il ne faut pas négliger l'éventualité d'une liaison s^2 entre certains atomes lourds.

Nous pouvons donc considérer en première approximation que la règle 8-N s'applique aux quatre cas suivants:

Coordinence 4, groupe IV_B, type diamant, liaison tétraédrique, orbitales sp^3.

Coordinence 3, groupe V_B, type arsenic, liaison trirectangle, orbitales p^3.

Coordinence 2, groupe VI_B, type sélénium, liaison rectangle, orbitales p^2.

Coordinence 1, groupe VII_B, type iode, orbitale p.

(étant entendu que ces coordinences peuvent être doublées par des mécanismes de résonance) Il est à craindre dans ces conditions que la forme donnée à la relation (1.1) dont découle la règle de MOOSER et PEARSON ne soit applicable en toute rigueur que pour la coordinence 4, puisque nous y avons implicitement supposé que tous les électrons s et p jouaient un rôle identique dans les liaisons. Nous suggérons donc de ne considérer que les électrons qui participent effectivement aux liaisons, en laissant de côté les paires inertes, ce qui nous donne les règles 8-N, 6 — (N-2), 4 — (N-4), et 2 — (N-6) où la coordinence, pour un nombre total d'électrons donné, est naturellement indépendante de la règle utilisée. Nous en tirons non dlus une, mais 4 règles du type de MOOSER et PEARSON, dont la dernière n'offre pas d'intérêt puisqu'il ne peut pas exister de composé isoélectronique de l'iode:

$$\frac{n_e}{n_a} + b = 8 \qquad (2.1)$$

$$\text{»} \quad = 6 \qquad (2.2)$$

$$\text{»} \quad = 4 \qquad (2.3)$$

$$\text{»} \quad = 2 \qquad (2.4)$$

Nous maintenons pour n_e la définition donnée à la section précédente, sensiblement différente de celle donnée par MOOSER et PEARSON: nombre d'électrons de valence pouvant participer aux liaisons covalentes compatibles avec le type de réseau (il se peut d'ailleurs que l'on soit amené dans certains cas à recenser des électrons susceptibles d'être excités à un niveau supérieur).

VOL. 12 59/60

Quelle est la signification exacte que nous devons attacher à cet ensemble de règles? Il semble bien que ce soient simplement les règles d'existence d'un réseau de liaisons à caractère covalent prédominant. Dans ces conditions, parler d'un type de liaison particulier aux semiconducteurs risque peut-être d'entraîner des confusions puisque la semiconductibilité peut également apparaître suivant d'autres mécanismes que par impuretés de substitution dans des cristaux à caractère prédominant ionique (non-stoéchiométrie) ou même moléculaire (doubles liaisons conjuguées).

Remarquons par ailleurs le lien étroit qui existe entre l'emplacement de la frontière de ZINTL et la coordinence covalente de base considérée. La valeur minima de N pour les éléments de ZINTL était 4, car—selon la remarque de MOOSER et PEARSON[1]—un atome ne peut gagnér par le processus de mise en commun un nombre d'électrons supérieur à sa valence et doit avoir 4 électrons au moins au départ pour compléter son octet. Ceci n'est valable en toute rigueur que pour la coordinence 4 où, les électrons s et p intervenant tous dans la liaison, les valences des éléments possèdent les valeurs traditionnelles. Dans le cas de la coordinence 3, en effet, les chimistes savent bien que la valence apparente des éléments lourds des groupes III_B à VII_B est diminuée de deux unités du fait de la stabilité de la paire d'électrons s. De la sorte, la valeur minimale de N sera 3, moitié du sixtet p^6 et valence apparente du bismuth, et nous sommes conduits à tracer la frontière à la gauche de cet élément en rejetant le plomb hors des éléments de ZINTL. Le tracé de la frontière sera incertain pour germanium et étain puisque ces atomes peuvent présenter aussi bien la coordinence 3 que la coordinence 4.

Enfin, il convient de ne pas oublier la restriction de MOOSER et PEARSON selon laquelle la différence d'électronégativité entre les atomes composant les binaires est généralement inférieure à l'unite. Ceci nous amène à chasser en principe de nos préoccupations les composés où interviennent les éléments très électronégatifs tels que N-O-F-Cl-Br.

L'ensemble des remarques faites dans cette section est résumé sur la Fig. 1, qui donne la

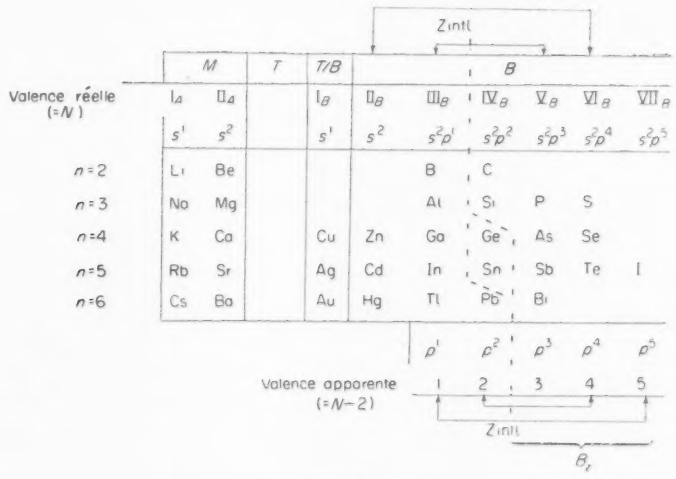
Zintl
M
T
T/B
B
Valence réelle (=N)
I_A II_A I_B II_B III_B IV_B V_B VI_B VII_B
s^1 s^2 s^1 s^2 s^2p^1 s^2p^2 s^2p^3 s^2p^4 s^2p^5
n=2 Li Be B C
n=3 Na Mg Al Si P S
n=4 K Ca Cu Zn Ga Ge As Se
n=5 Rb Sr Ag Cd In Sn Sb Te I
n=6 Cs Ba Au Hg Tl Pb Bi
p^1 p^2 p^3 p^4 p^5
Valence apparente (=N−2)
1 2 3 4 5
Zintl
B_t

FIG. 1.

valence réelle des éléments légers et la valence apparente des éléments lourds (ou plus exactement les valeurs de N et de N-2), la position de la frontière de ZINTL, et montre l'analogie existant entre les composés III-V et II-VI, dérivant par substitution isoélectronique des éléments IV, et les composés IV-VI (PbS) et III-VII (TlI), dérivant par substitution isoélectronique des éléments V. Les composés des éléments de transition sont systématiquement laissés de côté.

3. STRUCTURES ET RÈGLES DE FILIATION

Les remarques développées précédemment expliquent que nous désirions placer au premier plan les considérations de structure et nous voyons l'intérêt qu'il y a à aborder celles-ci en les classant par coordinence et type de réseau, suivant le mode d'exposition récemment adopté par WELLS[19]. D'après le postulat de MOOSER et PEARSON, tout réseau semiconducteur comporte l'alternance régulière d'un atome de ZINTL, et d'un atome à caractère plus métallique. Si ces deux atomes constituent un binaire isoélectronique d'un élément de ZINTL, le réseau aura la coordinence de ce dernier élément (donc 4, 3 ou 2) S'il n'en est rien, il y aura lieu de distinguer la coordinence de l'atome de ZINTL (4 ou 3) et celle du maillon métallique qui est nécessairement inférieure pour que l'alternance soit respectée, mais 4 avec maillon 3 conduirait à un réseau trop complexe de sorte que la coordinence du maillon ne peut être que 2. En tenant compte du phénomène de résonance décrit par PAULING, susceptible de doubler la ou les coordinences apparentes, nous pouvons donc prévoir l'existence des dix réseaux suivants:

(a) Coordinence uniforme de 4 sans résonance: un seul type de réseau connu, blende et structure dérivées des binaires III-V, II-VI et I-VII.

(b) Coordinences 4 et 2 sans résonance: pas de réseau réel connu.

(c) Coordinence uniforme de 4 avec résonance (soit 8 apparente): pas de réseau réel connu, compte tenu de la limite approximative des 25 pour cent de caractère ionique.

(d) Coordinences 4 et 2 avec résonance (soit 8/4 apparente): un seul type de réseau connu, fluorite et structures dérivées des binaires II-IV.

(e) Coordinence uniforme de 3 sans résonance: pas de réseau réel connu pour des composés à quelques exception près (SnS) qui peuvent facilement être décrites parmi les composés à coordinence 6. Nous reviendrons sur ce cas à la section 5.

(f) Coordinences 3 et 2 sans résonance: réseau des II-V présentant une liaison entre atomes V, seuls exemples connus CdSb et ZnSb.[1,7,36-40] On peut également rattacher aux II-V la proustite Ag_3AsS_3.[54,78]

(g) Coordinence uniforme de 3 avec résonance (soit 6 apparente): réseau du sel gemme et structures voisines dérivées des binaires IV-VI et III-VII.

(h) Coordinences 3 et 2 avec résonance (soit 6/4 apparente): pas de réseau réel connu.

(i) Coordinence uniforme de 2 sans résonance: pas de chaînes linéaires connues pour les composés (voir section 5, une exception possible).

(k) Coordinence uniforme de 2 avec résonance (soit 4 apparente): pas de réseau réel connu.

Nous sommes donc ramenés pratiquement à trois types de réseau seulement: blende (4) avec 3 binaires, fluorite (8/4) et sel gemme (6) avec deux binaires.

Le rapprochement de tous les composés connus à l'intérieur d'un même type de réseau permet d'établir des filiations par susbtitution isoélectronique telles que, par exemple, entre les composés suivants, cités par WELLS dans le réseau de la blende: ZnS-$CuFeS_2$-Cu_2FeSnS_4.

Pour que de telles filiations aient une valeur générale, il y a intérêt à substituer aux symboles des atomes le chiffre romain correspondant au nombre N de leur groupe, et à isoler par des parenthèses les atomes résultant de la substitution à l'atome de caractère métallique du binaire:

$$II_4\,VI_4\text{-}(I_2\,III_2)\,VI_4\text{-}(I_2\,II\;IV)\,VI_4$$

La règle de MOOSER et PEARSON ne s'appliquerait plus en effet au dernier composé si l'atome IV était considéré comme un atome de ZINTL, car il n'occupe pas un site cristallographique équivalent à ceux des atomes VI. Nous voyons par là le danger d'appliquer les régles électroniques à un composé mal connu, et la nécessité de connaître son réseau et sa filiation.

Au lieu d'appliquer une règle électronique du type de MOOSER et PEARSON en additionnant des nombres d'électrons, on peut songer à écrire simplement la formule du composé de manière à mettre en évidence le nombre des électrons de valence de chaque atome, c'est-à-dire en notant ceux-ci sous une forme ionisée. GOODMAN[20] a ainsi proposé de leur assigner une formule entièrement ionique rendant compte du remplissage des différents niveaux électroniques. Il semble toutefois peu indiqué d'affecter les symboles chimiques d'indices utilisés couramment — et notamment par MOTT et GURNEY[21] — pour décrire l'état des atomes dans les cristaux ioniques puisque nous nous intéressons surtout ici aux cristaux où les liaisons sont essentiellement du type covalent.* Une telle notation risque d'amener une confusion dangereuse entre, d'une part, le nombre d'électrons susceptibles d'être cédés ou acceptés pour arriver à une configuration plus stable (généralement l'octet), c'est-à-dire l'électrovalence d'un atome (par exemple 2 pour le barium et l'oxygène dans $Ba^{2+}\,O^{2-}$), et d'autre part le modification de structure électronique que subit un atome lorsqu'il s'intègre dans un réseau où la coordinence covalente diffère du nombre d'eléctrons de valence qu'il possède. Ainsi SHOCKLEY[22] note As^+ l'atome d'arsenic intégré dans le réseau du germanium où la coordinence atomique est 4 et où un élément du groupe V_B est supposé perdre son électron surnuméraire, et note de même Ga^- l'atome de gallium qui est supposé avoir fixé un quatrième électron. Pour exprimer que le binaire GaSb cristallisant dans la structure de la blende remplit les conditions électroniques nécessaires à l'établissement d'un réseau de liaisons covalentes, il semble donc plus logique d'écrire $Ga^-\,Sb^+$ que $Ga^{3+}\,Sb^{3-}$, mais le résultat est atteint dans les deux cas, car le "plan de symétrie" des deux notations (groupe IV_B) se trouve être le même. C'est pour la même raison que la règle de MOOSER et PEARSON, bien qu'énoncée pour des cristaux covalents, se trouve également valable pour les halogénures alcalins et les oxydes alcalino-terreux, par exemple.

Puisque des formules telles que $Zn^{2+}\,S^{2-}$ sont de toute manière partiellement fausses, et que toute notation simple est nécessairement conventionnelle, avec pour seul but un dénombre-

* Il est bon de préciser ce qu'il faut entendre par là puisque la liaison de valence n'a été définie en toute rigueur que pour des atomes identiques. MOOSER et PEARSON se sont référés à une faible différence d'électronégativité entre les constituants d'un binaire. Nous préférons en donner une définition plus pratique: liaisons existant dans les cristaux ou l'apparition des porteurs libres résulte généralement de la présence d'impuretés de substitution, suivant un mécanisme analogue au dopage du germanium. Au contraire, des liaisons essentiellement de type ionique supposeront que l'apparition de porteurs libres soit généralement liée à l'existence d'une non-stoechiométrie locale, suivant un mécanisme analogue à la création d'un centre coloré. Cette distinction, forcément arbitraire, sera reprise dans le Tableau 6.

VOL. 12 59/60

ment aisé des électrons de valence, nous suggérons l'adoption des formules parfaitement covalentes telles que celles utilisées par SHOCKLEY, c'est-à-dire:

$$I^{3-}\ II^{2-}\ III^{-}\ V^{+}\ VI^{2+}\ VII^{3+}$$

Il va de soi que ces formules ne sont applicables qu'aux réseaux de coordinence de base 4 (blende et structures dérivées) et les remarques faites à la section 2 nous montrent que l'on aura pour la coordinence de base 3 (sel gemme) les symboles:

$$III^{2-}\ IV^{-}\ VI^{+}\ VII^{2+}$$

auxquels on peut ajouter I^{2-} et II^{-} si l'on suppose que les électrons *s* sont susceptibles d'être excités dans des états *p*.

Dans le cas des chaînes linéaires (coordinence 2), on peut suggérer $III^{-}\ V^{-}\ VII^{+}$. Enfin, nous aurons pour les maillons à caractère métallique:

$$I^{-}\ III^{+}\ IV^{2+}\ V^{3+}\ VI^{4+}$$

Dans ces conditions, l'exemple de filiation considéré plus haut par substitution isoélectronique dans la structure de la blende sera noté:

$$II_4^{2-}\ VI_4^{2+} - (I_2^{3-}\ III_2^{-})\ VI_4^{2+} - (I_2^{3-}\ II^{2-}\ IV)\ VI_4^{2+}$$

ce qui met bien en évidence, à l'intérieur de la parenthèse, la conservation du nombre total d'électrons participant aux liaisons.

4. RÉSEAUX LACUNAIRES ET RÉSEAUX COMPENSÉS

Les raisons particulières que nous avions de préférer les notations de SHOCKLEY généralisées à celles de MOTT et GURNEY vont apparaître plus clairement dans cette section.

Considérons par exemple sur le Tableau 1, qui rassemble les structures à coordinence 4 rattachées à la blende, les composés dérivant des binaires $II^{2-}\ VI^{2+}$: il n'y a pas de difficulté à établir la filiation de (CuCdIn) Te_3 ou de la série (Cu_2Sn) Se_3, mais le composé $In_2^{-}\ Te_3^{2+}$ par exemple y est réfractaire parce que les charges ne sont pas équilibrées et parce que le nombre d'atomes est impair. L'analyse aux rayons X montre qu'il s'agit d'un réseau lacunaire de la blende. Le cas de tels réseaux s'est déjà présenté dans les composés intermétalliques à phases multiples, soumis aux règles de HUME-ROTHERY, et RAYNOR[23] a montré par exemple que les alliages nickel-aluminium contenant un excès d'aluminium ne présentent pas une substitution de ce métal dans les sites du nickel, mais au contraire des sites vacants dans le sous-réseau du nickel de manière à laisser constant le nombre d'électrons par maille (d'où le nom de "composés électroniques" donné à ce type d'alliage). Nous inspirant de ce résultat, nous suggérons de considérer le site vacant comme un atome de valence zéro et de le faire figurer dans le schéma de filiation où il se trouvera donc affecté de l'indice supérieur 4^{-}. Nous sommes alors conduits à noter ce composé sous la forme $(\square^{4-}\ In^{2-})\ Te_3^{2+}$ et l'on remarque qu'une telle formule est plus explicite qu'une formule ionique $In_2^{3+}\ Te_3^{2-}$ où l'attention n'est pas attirée sur l'anomalie de structure par un déséquilibre des charges.

Nous allons maintenant aborder la notion de réseau compensé,* qui se trouve introduite naturellement par l'étude des interactions entre impuretés dans les réseaux covalents purs tels que ceux du germanium et du silicium. On sait que ces réseaux sont beaucoup moins compacts que les réseaux metalliques, de sorte qu'il est plus facile à des atomes étrangers d'y diffuser dans les sites interstitiels. Pour prendre un exemple classique, le lithium diffuse dans le germanium à température relativement peu élevée, et l'on considère généralement qu'il se trouve à l'état d'ion Li^{+}. La description de l'état des atomes de lithium, ou au contraire de celui

* *Note ajoutée sur épreuves* — Le concept de réseau compensé et son application au cas de Bi_2Te_3 ont été mentionnés par l'auteur au cours des discussions sur les matériaux semiconducteurs à la "Convention on Transistors" organisée par l'I. E. E. à Londres en Mai 1959.

Tableau 1.

RIC	0 I II III IV V VI VII	Structure	Atomes admis dans la structure	Référence des premiers travaux
I_2^+	III^- V^+ / I^{3-} V^+	*B*3 blende		
		*B*32 "TlNa" lacun. ou bl. compensée	Cs-Sb	28 – 19
	III_2^- V_2^+ / II^{2-} IV V_2^+	*E*1 chalcopyrite	ZnCd-SiGeSn-PAs	41 – 10 – 42 – 20
	II_3^{2-} VI_3^{2+}	*B*3 blende		43 – 44 (HgTe)
	I^{3-} II^{2-} III^- VI_3^{2+}	*B*3 blende	Cu-Cd-In-Te	20
	I_2^{3-} IV VI_3^{2+}	*B*3 blende	Cu-SiSn-SeTe	20
	$\square^{4-}$ III_2^- VI_3^{2+}	*B*3 bl. lacunaire	GaIn-Se-Te	45 – 46 – 47 – 48 – – 10
	II_4^{2-} VI_4^{2+}			
	I_2^{3-} III_2^- VI_4^{2+}	*E*1 chalcopyrite	AgCu-AlGaInTl--SSeTe	49 – 50 – 51
	$\square^{4-}$ II^{2-} III_2^- VI_4^{2+}	*B*3 ou *E*3 bl. ou chalco. lacunaire	ZnCdHg-AlGaIn--SSeTe	52 – 53
	I_2^{3-} II^{2-} IV VI_4^{2+}	$H2_6$ stannite	Cu-FeNi-GeSn--SSe	50 – 20
	I_3^{3-} V^+ VI_4^{2+}	$H2_5$ famatinite	Cu-AsSb-SSe	54 – 20
	I_4^{3-} VII_4^{3+}	*B*3 blende	CuAg-I	
	$\square^{4-}$ I_2^{3-} II^{2-} VII_4^{3+}	*B*3 ou *E*3 bl. ou chalco. lacunaire	CuAg-Hg-I	55 – 56 – 10
	$\square_2^{4-}$ II_2^{2-} VII_4^{3+}	*C*13	Hg-I	10

d'autres atomes étrangers occupant les sites normaux du réseau, fera donc nécessairement appel à un système de notation dualistique où un certain nombre d'entités — atomes ionisés ou non — se trouvent réparties en un certain nombre de sites cristallographiques, de manière que des atomes occupant des sites non-équivalents ne puissent être confondus. Dans un tel système développé par REES[24], nous aurons:

$$(Li_x^+ e_x^-/\triangle)\,Ge \text{ ou } Ge_{1-x}(Ga_x^- p_x^+/\square)$$

Li^+ étant noté suivant MOTT et GURNEY. et Ga^- suivant SHOCKLEY.

Il est intéressant de remarquer que, bien que le lithium et le gallium aient tous deux un carac-

VOL. 12 59/60

tère électropositif marqué, ils se trouvent ainsi en position de s'attirer l'un l'autre. REISS, *et. al.*[25] ont prouvé l'existence de ces interactions, ainsi que celles de véritables réactions chimiques telles que:

$$Ge_{1-x}(Ga_x^- p_x^+/\square) + \\ + y\,Li \rightarrow Ge_{1-x}(Li_y^+/\triangle)(Ga_x^- p_{x-y}^+/\square)$$

probablement responsables du camouflage de nombreuses impuretés dans le germanium et le silicium lorsqu'on s'efforce de les déceler par mesure de la résistivité électrique.[26] Si l'on convient de ne considérer que des réseaux à liaisons essentiellement covalentes où les *ions* étrangers occuperont toujours les sites interstitiels, il est possible de simplifier la notation de REES, à condition de préciser sans ambiguité, par exemple en les mettant entre crochets, les atomes formant le réseau covalent soumis aux règles électroniques du type MOOSER et PEARSON, et le cas précédemment envisagé pourra être écrit:

$$[Ge_{1-x}\,Ga_x^-]\,Li_y^+\,p_{x-y}^+$$

C'est d'ailleurs la notation préconisée par KETELAAR[27] pour les composés "onium" tels que $[NH_4]^+\,Cl^-$ ou $[BF_4]^-\,H^+$.

Nous proposons de considérer des réseaux tels que $Ge_{1-x}\,Ga_x\,Li_x$ comme des réseaux compensés comprenant un réseau partiel covalent tel que $(Ge_{1-x}\,Ga_x)^{x-}$ et un réseau interstitiel compensateur (RIC) tel que Li^{x+}. Cette conception correspond à une structure réelle dans le cas du réseau covalent pur envisagé cidessus, et il semble donc logique de l'étendre aux composés dans notre système de notations, puisque nous y considérons artificiellement un réseau covalent pur dans le simple but de dénombrer plus aisément les électrons de valence. Il est bien entendu toutefois qu'aucune conclusion ne saurait en être tirée — notamment par exemple pour les binaires II-VI et I-VII — quant à la réalité des charges affectées aux deux réseaux et le signe du dipôle lié au réseau partiel covalent. D'ailleurs la suggestion de translocations électroniques dans certains réseaux n'est pas entièrement nouvelle, et nous référerons notamment à KREBS[6] et MOOSER et PEARSON[8], qui ont suggéré pour Li_3Bi la notation $Li_I^+\,Li_{II}^-\,Li_{II}^-\,Bi^+$, et à JACK et WACHTEL,[28] qui ont suggéré pour Cs_3Sb une ionisation suivant $Cs_2^+\,Cs^{3-}Sb^+$. Nous proposons d'écrire ces deux composés $[Li_2Bi]^-\,Li^+$ et $[CsSb]^{2-}\,Cs_2^+$ où les réseaux partiels covalents $[Li_2Bi]^-$ et $[CsSb]^{2-}$ vérifient bien la relation (2.1) en tenant compte des électrons supplémentaires désignés par la charge globale affectée à ces réseaux. En outre, en dépit des réserves que nous avons faite sur l'application de cette conception aux structures réelles, on peut noter que la distance $Li_{oct.}$ Bi est de $a/2$ contre $\sqrt{3}\,a/4$ seulement pour $Li_{tétr.}$ Bi, en accord avec un caractère ionique plus marqué.

Nous devons signaler que l'on a généralement le choix, pour un composé ne satisfaisant pas aux règles de filiation, entre un réseau lacunaire et un réseau compensé, et que seule l'étude de la structure, de l'équivalence des différents sites cristallographiques et des distances interatomiques permet de décider. Ainsi $[Li_2Bi]^-\,Li^+$ sera préféré à $Li_6^-\,Bi_2^+\,\square^{4+}$ mais par contre, dans la même structure de base, $(\square^{2-}Zn_3)\,P_2^+$ sera préféré à $[Zn_6\,P_3]^{3+}\,P^{3-}$. Un premier recensement des réseaux compensés a surtout permis d'en déceler dans les structures connexes de la blende et de la fluorite où les sites interstitiels peuvent être occupés par des cations peu volumineux (alcalins). Notons enfin qu'un réseau compensé ne vérifie pas nécessairement les relations électroniques du type de MOOSER et PEARSON.

Les Tableaux 2 et 3 rassemblent les structures respectivement rattachées à la fluorite et au sel gemme. Nous y avons indiqué, comme dans le Tableau 1, quelques références sur les premiers travaux publiés sur chaque type de composé.

Tableau 2.

RIC	0 I II III IV V VI VII	Structure	Atomes admis dans la structure	Référence des premiers travaux
I^+	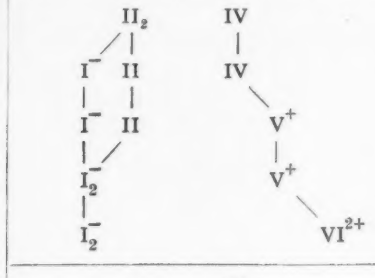	*C*1 fluorite		57–58–59–60
		*DO*3 "BiF_3" ou fl. compensée	Li-Mg-Sn	61
		*C*1*b* fluorite	LiNaKAg-MgZn--AsSbBi	8–62
I^+		*DO*3 "BiF_3" ou fl. compensée	LiCu-SbBi	63–8
		*C*1 fluorite ou struct. voisines	LiNaKAg-SeTe	64–43–63–8–65
	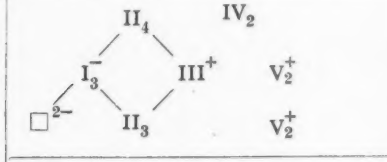	*E*9*d* fluorite	Li-AlGa-N	66–67–68
		*D*5$_3$–*D*5$_9$ fluorite lacunaire	BeMgZnCd-NPAs	69–70–71–72––73–74
	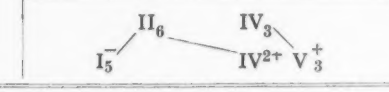	*C*1 fluorite	Li-SiGe-NPAs	75

Tableau 3.

RIC	(I II) III IV V / 0 1 2 3 — VI / 4 — VII / 5	Structure	Atomes admis dans la structure	Références des premiers travaux
	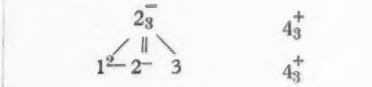	*A*7 ou *B*1 arsenic ou sel gemme	GeSnPb-SSeTe	76–18 etc.
		seligmannite	Cu-Pb-As-S	77
	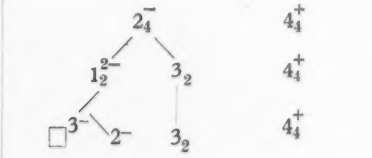	*B*1 ou *F*5$_6$ sel gemme) ou wolfsbergite (chalcostibite)	NaKCuAgTl--AsSbBi-S	79–80–18–54––77
		*F*5$_6$ wolf. lacunaire	Pb-AsSb-S	10
	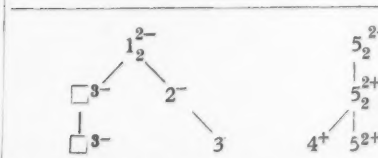	"TlI"	Tl-I	19
		*C*6 "NiAs" lacun.	CdPb-I	18–19
		~*C*6	Bi-Te-BrI	18

5. PSEUDO-ÉLÉMENTS ET RÉSEAUX MOLÉCULAIRES

Nous désignerons par le terme de "pseudo-éléments" les composés ou réseaux partiels covalents qui ne satisfont pas les règles de filiation à partir des binaires mais peuvent être considérés comme dérivant des éléments semiconducteurs. Le réseau partiel $[Ge_{1-x}\ Ga_x]^{x-}$ envisagé à la section précédente répond à cette définition, ainsi que les solutions solides Ge-Si ou le composé SiC, tous dérivant des éléments IV_B. On ne connaît pas de réseau partiel $[GeGa]^-$ ou $[GeAs]^+$ probablement parce que la structure de la blende ne s'y prête pas, mais on pourrait en imaginer, de même que des réseaux $[BiSe]^+$ dérivant des éléments V_B. Nous allons voir que cette dernière hypothèse présente un certain intérêt pour quelques composés jusqu'ici réfractaires à toute règle de prédiction.

KREBS[18] a suggéré l'existence de liaisons covalentes dans la structure C33 de la tetradymite Bi_2Te_2S, dans laquelle se rangent également Bi_2Te_3, Bi_2Se_3, Sb_2Te_3 et $Bi_2(S, Se)_3$ (forme guanajuatite). Il pensait, raisonnant par analogie avec la structure du sel gemme de PbS, que des liaisons p^3 avec résonance existaient entre les atomes des rangées obliques par rapport aux plans parallèles des cinq couches Te-Bi-S-Bi-Te successives dans chaque feuillet qui avaient été identifiées par HARKER[29] pour Bi_2Te_2S, puis par LANGE[30] pour Bi_2Te_3. L'intérêt de cette structure s'est trouvé accru par les études faites sur ce dernier composé en tant que semiconducteur à effet Peltier intense pour la réfrigération thermoélectrique par GOLDSMID et DOUGLAS[83], VLASOVA et STIL'BANS[84], VASENIN[85], KONOROV[86], LAGRENAUDIE[87], etc. Le schéma des liaisons envisagées par KREBS et reprises par LAGRENAUDIE était assez sommaire, et, MOOSER et PEARSON ayant toût d'abord considéré ce composé comme un alliage métallique, DRABBLE et GOODMAN[31] cherchent à en rendre compte plus exactement en attribuant les liaisons Bi-S (ou Bi-Te central) aux orbitales hybrides d^2sp^3, en accord avec leurs longueurs de liaison un peu plus élevées, et suggèrent une liaison Te-Te interfeuillets du type van der Waals à densité électronique nulle pour rendre compte du clivage basal. MOOSER et PEARSON enfin[11] envisagent des orbitales hybrides p^3d^3 et suggèrent une translocation électronique $Bi^+ S^-$.

A la suite des vues exposées dans les sections précédentes, il est naturel de se demander si KREBS a eu raison de chercher initialement une analogie entre la structure de Bi_2Te_2S et celle de PbS, et si l'on ne pourrait pas la rapprocher au contraire de celle de l'arsenic idéal avec ses doubles couches à liaisons p_3 sans résonance.

On peut en effet faire dériver de l'arsenic, comme nous l'avons vu plus haut, le réseau partiel covalent $[BiTe]^+$, susceptible de constituer une double couche Bi-Te, et il est intéressant de rappeler que SEMILETOV[32] a justement identifié une phase Bi-Te par diffraction électronique sur des couches minces obtenues par condensation des vapeurs. Un tel réseau partiel n'est évidemment stable qu'en présence d'un réseau interstitiel compensateur (RIC) qui pourrait parfaitement être constitué par les atomes de soufre du feuillet central (voir Fig. 2) Nous sommes ainsi conduits à noter la tétradymite $[BiTe]_2^+ S^{2-}$, et l'on vérifie facilement que le réseau partiel satisfait la relation (2.2) avec $n_e = 3 + 4 - 1$, $n_a = 2$ et $b = 3$. Ici encore, comme dans le cas de Li_3Bi, nous pensons qu'il est possible d'accorder un certain caractère réel — au moins en tant qu'approximation — à cette notation, même lorsqu'on passe de la tétradymite au composé Bi_2Te_3. On tire en effet de l'étude de LANGE que la distance Bi-Te^{2-} est de 3,22 Å contre 3,12* pour la distance Bi-Te^+,

* *Note ajoutée sur épreuves* — distances 3,24 conte 3,04 Å d'après AJRAPETIANTZ S. V. & EFIMOVA B. A. *Zh. Tekh. Fiz.* URSS **28**, 1768 (1958) qui ont envisagé l'existence dions Te^{2-}.

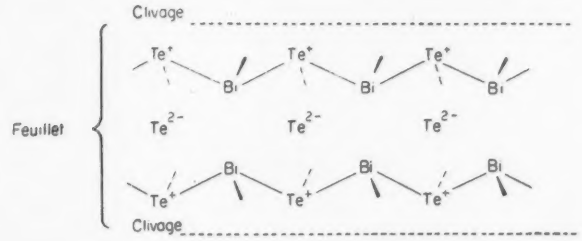

écart en accord au moins qualitatif avec la dimension élevée (2,2 Å) de l'ion Te^{2-} et le caractère ionique de la liaison.

Il semble que cette conception puisse être étendue à tous les composé de même structure que la tétradymite cités plus haut, ainsi qu'à la composition Bi_2Te_2Se identifiée indirectement par AUSTIN et SHEARD[33]. Leur filiation est schématisée par le Tableau 4, mais le cas qu'ils présentent reste un cas assez isolé, à moins que les composés InSe et TlSe ne puissent être considérés comme un cas analogue de pseudo-éléments dérivés du groupe VI (Tableau 5). MOOSER et PEARSON proposent en effet une translocation électronique mais avec une liaison par hybrides sp^3.

Pour terminer, signalons qu'il y a malgré tout des exceptions aux règles électroniques et

Tableau 4.

R I C	(I II) III IV V VI VII 1 2 3 4 5	Structure	Atomes admis dans la structure	Référence des premiers travaux
4^{2-}	3_4 — 3_2 4_2^+	*A*7 arsenic	PAsSb	
		*C*33 arsenic compensé	Bi-SeTe	30–81–82–43–83–84–85–86–87–18–31–11–33

Tableau 5.

R I C	(I II) III IV V VI VII 1 2 3	Structure	Atomes admis dans la structure	Référence des premiers travaux
1^+	2_3 / 1^- — 2_2	*A*8 châine linéaire	SeTe	
		*B*37 idem (?)	In-Tl-Se	88–89–63–7–8–46

aux règles de filiation. Ainsi la structure $D5_8$ de la stibine (ou antimonite) Sb_2S_3 dans laquelle cristallisent également Bi_2S_3, Sb_2S_3, et $Bi_2(S, Se)_3$ (forme paraguanajuatite) constitue une transition entre les coordinences 3 et 2 et ne peut dans ces conditions satisfaire aucune relation de caractère général. On peut l'écrire, d'après KREBS[18] et MOOSER et PEARSON[11] $(Sb_4\ S_2^+\ S_2\ S_2^-)_n$ avec un tiers seulement des atomes de soufre jouant sous la forme S^+ un rôle analogue à l'antimoine. Il en est de même de la plupart des composés de DÖNGES[34,35] qui peuvent être notés $(V_2\ VI_2\ VII_2)_n$ (à l'exception de deux d'entre eux qu'on trouvera au Tableau 3). Tous ces cristaux sont à considérer comme des réseaux moléculaires. La présence d'éléments VII ou VI^- semble une condition nécessaire de leur existence.

6. CONCLUSION

Nous nous sommes efforcés, en nous appuyant largement sur les travaux antérieurs, notamment ceux de KREBS et de MOOSER et PEARSON, de compléter et d'étendre la domaine d'application de la règle électronique de ces derniers ainsi que de développer les filiations à partir des binaires dont quelques exemples avaient été donnés par GOODMAN. Si la prédiction de la semiconductibilité dans un réseau cristallin ne peut malheureusement pas encore être faite avec certitude, du moins la cohérence de l'ensemble de ses règles et des notations des composés sont-ils sensiblement améliorés et nous espérons que cet exposé facilitera la découverte de nouveaux semiconducteurs.

Nous pensons notamment qu'il doit exister un plus grand nombre de réseaux compensés

Tableau 6.

Réseau	Mécanisme de la conductibilité	Structures connues avec nombre de coordination	Exemples
(1) *Composés dont les atomes possèdent des niveaux* d *et* f *vides ou complétement remplis :*			
ionique	non-stoéchiométrie	structures diverses	halogénures alcalins, oxydes alcalino-terreux, etc.
compensé	principalement impuretés de substitution	blende compensée (4+8) fluorite compensée (4/8+4) arsenic compensé (3+1,5)	Cs_3Sb Li_3Bi Bi_2Te_3
atomique ou covalent	impuretés de substitution	blende (4) et fluorite (4/8) arsenic (3) et sel gemme (6)	InSb, ZnS, Mg_2Si SnS, PbS, TlI
moléculaire (minéral)	résonance (?)	structures diverses notamment stibine	AsI_3, SnI_4 Sb_2S_3
moléculaire (organique)	doubles liaisons conjuguées		naphtalène, anthracène
macromoléculaires	(?)		
(2) *Composés dont certains atomes possèdent des niveaux* d *ou* f *partiellement remplis :*			
ionique	induction de valence	diverses, notamment spinelle, perowskite,...	oxydes semiconducteurs
atomique ou covalent	impuretés de substitution	nickeline (6) Skutterudite (4/6)	NiAs, MnTe, $CoAs_3$, $CoSb_3$

es que leur étude peut être intéressante en raiton des différents mécanismes de semiconductibilité qui y sont théoriquement possibles (substitutions dans le réseau partiel covalent ou le RIC, ou nonstoéchiométrie relative des deux réseaux). Par ailleurs leur conception peut constituer une approximation intéressante pour l'application de la théorie des bandes à certains composés, tels que Bi_2Te_3. .

Le Tableau 6 place la présente étude dans son contexte, parmi les différents types de réseaux semiconducteurs connus. Les composés des métaux de transition, qui y sont mentionnés, seront traités d'une manière plus détaillée dans une publication ultérieure.

VOL. 12 9/60

BIBLIOGRAPHIE

Bibliographie sur les règles de prédiction :

1. MOOSER E. et PEARSON W. B., *Phys. Rev.* **101,** 1608 (1956).
2. PAULING L., *The Nature of Chemical Bond.* Cornell University Press, Ithaca, N. Y. (1948).
3. KREBS H. et SCHOTTKY W., *Halbleiterprobleme* I, p. 25. Vieweg, Braunschweig (1954).
4. KREBS H., *Physica* **20,** 1125 (1954).
5. KREBS H., *Z. anorg. Chem.* **278,** 82 (1955).
6. KREBS H., *Acta Cryst.* **9,** 95 (1955).
7. MOOSER E. et PEARSON W. B., Rep. Meeting Semiconductors, Phys. Soc., Rugby (April 1956).
8. MOOSER E., et PEARSON W. B., *J. Electronics* **1,** 629 (1956).
9. MOOSER E. et PEARSON W. B., *Canad. J. Phys.* **34,** 1369 (1956).
10. MOOSER E. et PEARSON W. B., *J. Chem. Phys.* **26,** 893 (1957).
11. MOOSER E. et PEARSON W. B., *J. Phys. Chem. Solids* **7,** 65 (1958).
12. FISHER G. et PEARSON W. B., *Symposium on Role of Solid State Phenomena, Brooklyn,* (April 1957).
13. ZINTL E., GOUBEAU J. et DULLENKOPF W. *Z. Phys. Chem.* **A154,** 1 (1931).
14. ZINTL E. et KAISER H., *Z. anorg. Chem.* **211,** 113 (1933).
15. HUME-ROTHERY W., *The Structure of Metals and Alloys.* Institute of Metals, London (1936).
16. HUME-ROTHERY W., *Electrons, Atoms, Metals and Alloys.* Illiffe, London (1948).
17. MOSS T. S., *Photoconductivity Conference (Atlantic City,* 1954). (Ed. R. G. DRECKENRIDGE *et al.*) p. 427. John Wiley, New York (1956).
18. KREBS H., *Z. Electrochem.* **61,** 925 (1957).
19. WELLS A. F., *Solid State Physics* (Ed. SEITZ and D. TURNBULL) Vol. 7, p. 45. Academic Press, New York (1958).
20. GOODMAN C. H. L., *J. Phys. Chem. Solids* **6,** 305 (1958).
21. MOTT N. F. et GURNEY R. W., *Electronic Processes in Ionic Crystals,* Clarendon Press, Oxford (1946).
22. SHOCKLEY W., *Electrons and Holes in Semiconductors* (Van Nostrand, New York (1950).
23. RAYNOR G. V., *Progress in Metal Physics.* Ed. B. CHALMERS) Vol. I, p. 1. Butterworts, London (1949).
24. REES A. L. G., *Chemistry of the Defect Solid State.* Methuen, London (1954).
25. REISS H., FULLER C. S. et MORIN F. J., *Bell Syst. Tech. J.* **35,** 535 (1956).
26. SUCHET J. P., *Congr. Intern. Phys. Etat Sol., Bruxelles* (Juin 1958).
27. KETELAAR J. A. A., *Chemical Constitution.* Elsevier, Amsterdam (1958).
28. JACK K. H. et WACHTEL M. M., *Proc. Roy. Soc.* **A239,** 46 (1957).
29. HARKER D., *Z. Krist.* **89,** 175 (1934).
30. LANGE P. W., *Naturwissenschaften* **27,** 133 (1939).
31. DRABBLE J. R. et GOODMAN C. H. L., *J. Phys. Chem. Solids* **5,** 142 (1958).
32. SEMILETOV S. A., *Trudy Inst. Krist. Akad. Nauk S.S.S.R.* **10,** 76 (1954).
33. AUSTIN I. G. et SHEARD A., *J. Electronics* **3,** 236 (1957).
34. DÖNGES E., *Z. anorg. Chem.* **263,** 112 (1950).
35. DÖNGES E., *Z. anorg. Chem.* **265,** 56 (1951).

Bibliographie sur les composés semiconducteurs :

36. SMITH A. W., *Phys. Rev.* **32,** 178 (1911).
37. MOCHAN I. V., *Zh. Tekh. Fiz.* **18,** 1485 (1948).
38. ZHUSE V. P., MOCHAN I. V. et RYVKIN S. M., *Zh. Tekh. Fiz.* **18,** 1494 (1948).
39. DEVYATKOVA E. D., MASLAKOVETS Y. N. et STIL'BANS L. S., *Zh. Tekh. Fiz.* **22,** 129 (1952).
40. JUSTI E. et LAUTZ G., *Z. Naturforsch.* **7a,** 191, 602 (1952); *Abhandl. Braunschw. Wiss. Ges.* **4,** 107 (1952); **5,** 36 (1953).
41. WELKER H., cité par MOOSER et PEARSON (Ref. 10).

42. GOODMAN C. H. L., *Nature*, Lond. **179,** 828 (1957).
43. BRAITHWAITE J. G. N., cité par SMITH R. A., *Semiconducting Materials*. Butterworths, London (1951).
44. BLUM A. I., MOKROVSKII N. P. et REGEL A. R., *Izv. Akad. Nauk SSSR, Ser. Fiz.* **16,** 139 (1952).
45. HAHN H. et KLINGLER W., *Z. anorg. Chem.* **259,** 135; **260,** 97 (1949).
46. APPEL J. et LANTZ G., *Physica* **20,** 1110 (1954).
47. HARKEKE G. et LAUTZ G., *Z. Naturf.* **11a,** 1015 (1956).
48. BRICE J. C., NEWMAN P. C. et WRICHT H. C., *Brit. J. Appl. Phys.* **9,** 110 (1958).
49. HAHN H., FRANK G., KLINGLER W., MEYER A. D. et STÖRGER G., *Z. anorg. Chem.* **271,** 153 (1953).
50. GOODMAN C. H. L. et DOUGLAS R. W., *Physica* **20,** 1107 (1954).
51. AUSTIN I. G., GOODMAN C. H. L. et PENGELLY A. E. S., *J. Electrochem. Soc.* **103,** 609 (1956).
52. HAHN H., FRANK G., KLINGLER W., STÖRGER A. D. et STÖRGER G., *Z. anorg. Chem.* **279,** 241 (1955).
53. BUSCH G., MOOSER E. et PEARSON W. B., *Helv. Phys. Acta* **29,** 192 (1956).
54. WERNICK J. H. et BENSON K. E., *J. Phys. Chem. Solids* **3,** 157 (1957).
55. KETELAAR J. A. A., *Z. Krist.* **87,** 435 (1934).
56. HAHN H., FRANK G. et KLINGLER W., *Z. anorg. Chem.* **279,** 271 (1955).
57. BOLTAKS B. I., *Dokl. Akad. Nauk SSSR* **64,** 487, 653 (1949).
58. ROBERTSON W. D. et UHLIG H. H., *Trans. Amer. Inst. Min. (Metall.) Engrs.* **180,** 345 (1949).
59. BAUER G. et TIESLER J., *Z. anorg. Chem.* **262,** 309 (1950).
60. BOLTAKS B. I., *Zh. Tekh. Fiz.* **20,** 180 (1950).
61. LAVES F., cité par MOOSER et PEARSON (ref. 10).
62. JUNOD P., MOOSER E. et SCHADE H., *Helv. Phys. Acta* **29,** 193 (1956).
63. MOOSER E. et PEARSON W. B., *Phys. Rev.* **101,** 492 (1956).
64. RAHLFS P., *Z. phys. Chem.* B**31,** 157 (1936).
65. BUSCH G. et JUNOD P., *Helv. Phys. Acta* **30,** 470 (1957).
66. JUZA R. et HUND F., *Z. anorg. Chem.* **257,** 13 (1948).
67. NOWOTNY H. et GLATZL B., *Mh. Chem.* **82,** 720 (1951).
68. JUZA R., WEBER H. H. et MEYER-SIMON *Z. anorg. Chem.* **273,** 48 (1953).
69. HEIKE W., *Z. anorg. Chem.* **118,** 255 (1921).
70. BOLTAKS B. I. et ZHUSE V. P., *Zh. Tekh. Fiz.* **18,** 1459 (1948).
71. MOSS T. S., *Proc. Phys. Soc.* **B63,** 167 (1950).
72. BRUNS H. et LAUTZ G., *Ericsson Tech.* **2,** 227 (1955).
73. JUZA R. et BÄR K., *Z. anorg. Chem.* **283,** 230 (1956).
74. LAGRENAUDIE J., *J. Phys. Radium* **17,** 359 (1956).
75. JUZA R. et SCHULZ W., *Z. anorg. Chem.* **275,** 65 (1954).
76. MOSS T. S., *Proc. Phys. Soc.* **B62,** 741 (1949).
77. WERNICK J. H., GELLER S. et BENSON K. E., *J. Phys. Chem. Solids* **4,** 154 (1958).
78. HARKER D., *J. Chem. Phys.* **4,** 381 (1936).
79. BOON J. W., *Rec. Trav. Chim. Pays Bas* **63,** 32 (1944).
80. KOLOMIETS B. T. et GORIUNOVA N. A., *Zh. Tekh. Fiz.* **25,** 984 (1955).
81. DAVIDENKO V. A., *Zh. Tekh. Fiz.* **4,** 170 (1941).
82. GIBSON A. F. et MOSS T. S., *Proc. Phys. Soc.* **A63,** 176 (1950).
83. GOLDSMID H. J. et DOUGLAS R. W., *Brit. J. Appl. Phys.* **3,** 386 (1954).
84. VLASOVA R. M. et STIL'BANS L. S., *Zh. Tekh. Fiz.* **25,** 569 (1955).
85. VASENIN F. I., *Zh. Tekh. Fiz.* **25,** 397 (1956).
86. KONOROV P. P., *Zh. Tekh. Fiz.* **26,** 1400 (1956).
87. LAGRENAUDIE J., *J. Phys. Radium* **18,** 39A (1957).
88. KLEMM W. et VOGEL H., *Z. anorg. Chem.* **219,** 45 (1934).
89. KETELAAR J. A. A., *Z. Kristallogr.* **101,** 396 (1939).

J. Phys. Chem. Solids Pergamon Press 1959. Vol. 12. pp. 89–96. Printed in Poland.

THEORY OF ELECTRICAL CONDUCTION IN HIGH MAGNETIC FIELDS*

P. N. ARGYRES and L. M. ROTH

Lincoln Laboratory, Massachusetts Institute of Technology,
Lexington, Massachusetts

(*Received* 29 *April* 1959)

VOL. 12 59/60

Abstract—It is pointed out that previous quantum-mechanical theories of transport in high magnetic fields are deficient in that they neglect the effect of the electric field on scattering. It is demonstrated here that in the case of large Hall angles, i.e. $\omega_0\tau \gg 1$, the transverse current can be obtained by a direct expansion in powers of the scattering potential. Both elastic and inelastic collisions are considered. It is found that the transverse current can be described in terms of the drift of the centers of cyclotron orbits of the electrons in the magnetic field. This justifies the original semi-classical method of calculation of TITEICA. It is pointed out, however, that such a procedure is correct only for a non-oscillating electric field. No applications are made.

1. INTRODUCTION

THE phenomenon of electrical conduction in magnetic fields so large that the quantization of the electron orbits becomes important has recently received considerable attention from both the experimental and theoretical points of view. The primary theoretical interest stems, perhaps, from the fact that it provides a very simple situation for which the usual Boltzmann transport equation is not applicable and a quantum-mechanical theory of transport is necessary. We shall be concerned here exclusively with the theory of this phenomenon. In particular we shall study the more interesting case of an electric field transverse to the magnetic field.

The first calculation on this topic was done by TITEICA[1]. He calculated the transverse current by tacitly assuming that it is produced only by the drift of the centers of the cyclotron orbits of the electrons in the magnetic field due to the electric field and the scattering by the imperfections in the crystal. This neglects the possibility that the cyclotron motion itself may make a contribution to the current. Essentially the same method of calculation was followed by a number of different workers[2] in various applications to metals and semiconductors. The question of the validity of the method of calculation of the transverse current was, however, left untouched.

Recently LIFSHITZ[3] and one of us[4] have attempted to develop a transport theory for this phenomenon on the basis of quantum-mechanical principles. In the Landau representation, i.e. in the stationary states of an electron in a magnetic field, it is realized that one needs, for the calculation of the transverse current, the off-diagonal matrix elements of the density oper-

*The work reported in this paper was performed by Lincoln Laboratory, a center for research operated by Massachusetts Institute of Technology with the joint support of the U. S. Army, Navy and Air Force.

ator, which is the quantum-mechanical generalization of the classical distribution function. This is so because the Landau states do not have any average velocity perpendicular to the magnetic field, as they represent stationary circular motions. For the calculation of the transverse current it is, however, necessary to know the probability of finding an electron in states that have average transverse velocity, i.e. states described by linear combinations of Landau states. Therefore, the off-diagonal elements of the density matrix are required. It was then suggested[3] that these matrix elements obey a transport equation analogous to the classical Boltzmann equation. The collisions were there assumed to be described by an operator, which was taken for convenience to be a scalar relaxation frequency. The rate of change of the density operator due to collisions was, for the steady state, balanced by that due to the electric field, and thus a steady-state density matrix was found, which determined the induced current. In reference 4 the quantum-mechanical transport equation was established by use of time-dependent perturbation theory, and an explicit expression was given for the scattering operator in the Landau representation for elastic and inelastic collisions. These two theories gave, in general, expressions for the transverse current different from that assumed by TITEICA[1].

It is now clear, however, that these latter calculations[3,4] are deficient in the following respect. The terms that arise from the interference of the electric field and the scattering have not been taken into account. In other words, in reference 4, the terms of order (electric field) $\times$ (scattering potential)^2 in the time development of the density matrix were neglected. These terms are of higher order in the classical Boltzmann equation. In our case, however, where we are dealing with the off-diagonal elements of the density matrix, they make a contribution of the same order as the other terms, as can easily be seen from the proposed transport equations. In other words, the collisions take place in the presence of the electric field, and this makes the "relaxation distribution" different from that characteristic of thermodynamic equilibrium in zero electric field. Thus, the effects of both the magnetic and the electric fields on the scattering are important for the correct understanding of charge transport in high magnetic fields.

The influence of the electric field on the scattering can be taken into account within the framework of the calculation of reference 4. We shall not, however, pursue this point of view here. Instead, we shall investigate the problem by a different and more direct approach. Our starting point is the observation that in the absence of any scattering an electric field E, transverse to the magnetic field H, induces a finite current, perpendicular to both E and H, in contradistinction to the case of zero magnetic field. The quantization of the electron orbits does not affect this result, as we shall show below. We are thus led to seek the induced current in powers of the scattering potential V. Clearly such procedure is valid for large magnetic fields, i.e. when the electron completes many cyclotron orbits before it collides, or $\omega_0\tau \gg 1$, where $\omega_0 =$ cyclotron frequency and $\tau =$ relaxation time. Under these conditions the current is almost perpendicular to both the electric and magnetic fields, except for a small component in the direction of the electric field. This is an important situation experimentally, as only then can cyclotron resonance absorption and some quantum-mechanical effects be observed.

Working again in the Landau representation, we carry out such a procedure in the following two sections for elastic and inelastic scattering, respectively. Taking account of the effect of the electric field on the scattering, we find that the

VOL. 12 59/60

original method of calculation of the transverse current used by TITEICA is correct. Thus our work constitutes a detailed justification of TITEICA'S assumption that the transverse current is brought about by the net drift of the cyclotron orbits of the electrons, the detailed motion around these centers not contributing anything to the net current. At the same time, however, it points out that such a procedure is correct only for an electric field of zero frequency. Although not explicitly studied here, it is clear from this work that an oscillating electric field induces a current not entirely describable by the motion of the centers of the cyclotron orbits alone.

After most of this work was done, we became aware of the work of KUBO *et al.*[5] and ADAMS and HOLSTEIN[6], where the same topic was discussed. KUBO developed the analysis of this phenomenon on the basis of his theory of irreversible processes.[7] Our results agree with his. ADAMS and HOLSTEIN considered the problem in terms of the eigenstates of the electron in both the magnetic and electric fields. Their final results are correct only to the first order in the electric field, as ours are, and both methods give identical results for elastic scattering. They did not consider inelastic collisions. We feel, however, that our starting point has certain advantages. In particular, it can be applied very easily to driving forces other than the static electric field, whereas their method depends on the possibility of finding eigenstates in the presence of the driving force.

2. THE CURRENT DENSITY FOR ELASTIC COLLISIONS

The Hamiltonian of an electron (charge e, mass m) in a magnetic field H in the z-direction is taken to be

$$H_0 = (1/2m)\,[p_x^2 + (p_y + m\omega_0 x)^2 + p_z^2], \quad (2.1)$$

where $\omega_0 = |e|H/mc$ is the cyclotron-resonance angular frequency. Its eigenstates may be characterized by the oscillator quantum number n (0, 1, 2, ...) and the two-dimensional wave vector $\mathbf{k}\,(k_y, k_z)$ as follows:

$$\psi_{n\mathbf{k}}(r) = \Phi_n(x - X)\, e^{ik_y y}\, e^{ik_z z}\, (L_y L_z)^{-1/2}, \quad (2.2)$$

where Φ_n are the harmonic oscillator wave functions, and $X = -\hbar k_y/m\omega_0$ is the center of the cyclotron orbit corresponding to this particular state. Its eigenvalues are

$$\epsilon_{n\mathbf{k}} = \left(n + \frac{1}{2}\right)\hbar\omega_0 + \hbar^2 k_z^2/2m. \quad (2.3)$$

We want to make a transport theory of charge on the basis of these states. In other words we shall treat the action of the electric field and the scattering by the imperfections in the crystal as small perturbations over the exact motion of the electrons in the magnetic field.

In this Landau representation the transverse components of the velocity operator have off-diagonal matrix elements in the quantum number n. Namely

$$(n'\mathbf{k}' \mid v_x + iv_y \mid n\mathbf{k}) = 2i\,(\hbar\omega_0/2m)^{1/2}\,(n+1)^{1/2}\,\delta_{n',n+1}\,\delta_{k',k}. \quad (2.4)$$

The current density is given in general by the trace of the velocity operator and the steady-state density operator ϱ, or, on account of the nature of the matrix elements of the transverse velocity, equation (2.4),

$$\langle \mathcal{J}_x + i\mathcal{J}_y \rangle = (e/\Omega)\,\mathrm{Tr}\,\{\varrho(v_x + iv_y)\} = 2ei\,(\hbar\omega_0/2m)^{1/2}\,(2/\Omega)\sum_{n\mathbf{k}} (n+1)^{1/2}\,\varrho_{n\mathbf{k},\,(n+1)\mathbf{k}}, \quad (2.5)$$

with the following normalization

$$(1/\Omega)\,\mathrm{Tr}\,\{\varrho\} = N = \text{electron concentration}. \quad (2.6)$$

The determination of the steady-state density matrix $\varrho_{n,\,n+1}$ is thus the main problem. For an assembly of dynamically independent elect-

rons, the density operator $\varrho(t)$ is given by the one-electron Liouville equation

$$i\hbar\, d\varrho/dt = [H_0 + V + F, \varrho], \qquad (2.7)$$

where F denotes the interaction with the transverse electric field E, taken in the x-direction, i.e.

$$F = -eEx, \qquad (2.8)$$

and V is the scattering potential, schematized as a set of impurities randomly distributed in space.

Before we turn the electric field on (at $t = 0$), the ensemble is taken to be in thermal equilibrium, i.e.

$$\varrho(O) = f(H_0 + V), \qquad (2.9)$$

where $f(x) = K \exp(-x/kT)$ is the Boltzmann distribution function. We are interested in finding the steady-state value of $\varrho(t)$ to the first order in the electric field. As KOHN and LUTTINGER[8] have proved, we achieve this most simply by studying the Laplace transform

$$P(s) = s \int_0^\infty e^{-st}\, \varrho(t)\, dt \qquad (2.10)$$

for $s \to 0^+$. To the first order in E,

$$P(s) = f(H_0 + V) + p(s) \qquad (2.11)$$

$$[H_0, p(s)] - i\hbar s\, p(s) = C + [p(s), V], \qquad (2.12)$$

where

$$C = [f(H_0 + V), F]. \qquad (2.13)$$

As mentioned in the introduction, in the absence of scattering there is a finite current in the y-direction. This can easily be seen from equation (2.12). We are, therefore, prompted to seek a solution of equation (2.12) in powers of V. It is clear that such an expansion will be valid only for large Hall angles, or, equivalently, for $\omega_0 \tau \gg 1$, where τ denotes the order of magnitude of the relaxation time. Expanding in powers of V we therefore have

$$p(s) = p^{(0)}(s) + p^{(1)}(s) + p^{(2)}(s) + \ldots, \qquad (2.14)$$

where, from equation (2.12), we see

$$p^{(l)}_{\mu\nu}(s) = \frac{C^{(l)}_{\mu\nu} + [p^{l-1}(s), V]_{\mu\nu}}{\epsilon_{\mu\nu} - i\hbar s}. \qquad (2.15)$$

Here we have expanded $f(H_0 + V) = f^{(0)} + f^{(1)} + f^{(2)}$ in powers of V and denoted the commutator $[f^{(l)}, F]$ by $C^{(l)}$. Also $\epsilon_{\mu\nu} = \epsilon_\mu - \epsilon_\nu$ and μ (or ν) stands for a set of quantum numbers nk_yk_z. It is clear from the usual expansion[8] of $\exp(a+b)$ in powers of b that

$$C^{(0)}_{\mu\nu} = [f(H_0), F]_{\mu\nu} = [f(\epsilon_\mu) - f(\epsilon_\nu)]\, F_{\mu\nu} \equiv f_{\mu\nu} F_{\mu\nu} \qquad (2.16)$$

$$C^{(1)}_{\mu\nu} = [f^{(1)}, F]_{\mu\nu} = \sum_\lambda \left(\frac{f_{\mu\lambda}}{\epsilon_{\mu\lambda}} V_{\mu\lambda} F_{\lambda\mu} - F_{\mu\lambda} V_{\lambda\nu} \frac{f_{\lambda\nu}}{\epsilon_{\lambda\nu}} \right) \qquad (2.17)$$

In equation (2.17) we understand that $f_{\mu\nu}/\epsilon_{\mu\nu} \to df(\epsilon_\mu)/d\epsilon_\mu \equiv f'(\epsilon_\mu)$ if $\epsilon_\mu = \epsilon_\nu$.

In finding the limit $\underset{s \to 0^+}{L}\, p^{(i)}(s)$, we make use of the well-known relation

$$\underset{s \to 0^+}{L} \frac{1}{x - is} = P\left(\frac{1}{x}\right) + i\pi\delta(x). \qquad (2.18)$$

In the following we shall neglect the $P(1/x)$ term, as it gives rise only to shifts of the energy levels due to the imperfections, which affect by a small amount the reversible current in the y-direction.

We thus find from equations (2.15) to (2.18) for the matrix elements of interest (dropping for convenience the common wave numbers $\mathbf{k}$)

$$\varrho^{(0)}_{n,n+1} = \underset{s \to 0^+}{L}\, p^{(0)}_{n,n+1}(s) = \frac{f(\epsilon_{n+1}) - f(\epsilon_n)}{\hbar\omega_0} F_{n,n+1} \qquad (2.19)$$

$$\varrho^{(2)}_{n,n+1} = \underset{s \to 0^+}{L}\, p^{(2)}_{n,n+1}(s) = \frac{A_{n,n+1} + B_{n,n+1}}{\hbar\omega_0}, \qquad (2.20)$$

where:

$$A_{nn'} = -i\pi \sum_{\mu\nu}{}' \left[\delta(\epsilon_{n\mu}) \left(\frac{f_{n\nu}}{\epsilon_{n\nu}} F_{n\nu} V_{\nu\mu} V_{\mu n'} - \right.\right.$$

$$\left. - \frac{f_{\nu\mu}}{\epsilon_{\nu\mu}} V_{n\nu} F_{\nu\mu} V_{\mu n'} \right) + \delta(\epsilon_{\nu n'}) \left(\frac{f_{\mu' n}}{\epsilon_{\mu n'}} V_{n\nu} V_{\nu\mu} F_{\mu n'} - \right.$$

$$\left.\left. - \frac{f_{\nu\mu}}{\epsilon_{\nu\mu}} V_{n\nu} F_{\nu\mu} V_{\mu n'} \right) \right], \qquad (2.21)$$

$$B_{nn'} = -i\pi \sum_{\mu\nu} \Big[\delta(\varepsilon_{n\mu}) \Big(\frac{f_{n\nu}}{\varepsilon_{n\nu}} V_{n\nu} F_{\nu\mu} V_{\mu n'} - \frac{f_{\nu\mu}}{\varepsilon_{\nu\mu}} F_{n\nu} V_{\nu\mu} V_{\mu n'} \Big) + \delta(\varepsilon_{\nu n'}) \Big(\frac{f_{\mu n'}}{\varepsilon_{\mu n'}} V_{n\nu} F_{\nu\mu} V_{\mu n'} - \frac{f_{\nu\mu}}{\varepsilon_{\nu\mu}} V_{n\nu} V_{\nu\mu} F_{\mu n'} \Big) \Big] . \quad (2.22)$$

$\sum'$ indicates summation over the off-diagonal elements of F only. The diagonal elements of F contribute nothing to $A_{nn'}$, because $p^{(0)}_{\mu\mu}(s) = C^{(0)}_{\mu\mu}/(-i\hbar s) = (f_\mu - f_\mu) F_{\mu\mu}/(-i\hbar s) = 0$. We note that, on account of the δ-functions, the terms from the off-diagonal elements of F in $A_{nn'} + B_{nn'}$ cancel each other and we are left only with the terms arising from the diagonal elements of F in $B_{nn'}$, i.e.

$$\varrho^{(2)}_{n,n+1} = \frac{i\pi}{\hbar\omega_0} \sum_{\mu} V_{n\mu} V_{\mu,n+1} f'(\varepsilon_\mu) [\delta(\varepsilon_{n\mu}) (F_{nn} - F_{\mu\mu}) + \delta(\varepsilon_{\mu,n+1}) (F_{n+1,n+1} - F_{\mu\mu})] . \quad (2.23)$$

It is clear that this simplification occurs only for a non-oscillating electric field. In the opposite case, the contributions from the off-diagonal matrix elements of F do not cancel. In other words, an oscillating electric field correlates somewhat the motion of the electrons around their cyclotron centers, thus inducing an additional net current. As we shall see below $\varrho^{(2)}_{n,n+1}$ is purely imaginary and therefore contributes only to $\langle \mathcal{J}_x \rangle$. On the other hand, $\varrho^{(0)}_{n,n+1}$ of equation (2.19) is real and contributes only to $\langle \mathcal{J}_y \rangle$.

Now, since the matrix elements of F are

$$F_{\mu\mu} = (-eE) X_\mu = (-eE)(-\hbar k_y/m\omega_0) \quad (2.24)$$

$$F_{n,n+1} = (-eE)(\hbar/2m\omega_0)^{1/2} (n+1)^{1/2} , \quad (2.25)$$

we have for the transverse current density

$$\langle \mathcal{J}_y \rangle = (-e^2E/m\omega_0)(2/\Omega) \sum_{n\mathbf{k}} (n+1) [f(\varepsilon_{n+1}) - f(\varepsilon_n)] = -eNcE/H \quad (2.26)$$

$$\langle \mathcal{J}_x \rangle = (-e^2E)(2/\Omega) \sum_{n\mathbf{k}} \delta(\varepsilon_{\nu\mu}) f'(\varepsilon_\nu) (X_\nu - X_\mu) \times (\pi/\hbar)(\hbar/m\omega_0)^{1/2} [\sqrt{2(\mu+1)}\, V_{\mu\nu} V_{\nu,\mu+1} + \sqrt{2(\mu)}\, V_{\mu-1,\nu} V_{\nu\mu}] . \quad (2.27)$$

Here (μ) denotes the quantum number n of the set μ: (nk_yk_z) and $\mu \pm 1$ stands for $(n \pm 1, k_y k_z)$.

It is clear that equation (2.26) gives the unperturbed current in the y-direction. The collisions do not affect it in the second order, and it is identical to its classical value. The quantization of the levels has no effect upon it. We are neglecting, as we mentioned above, the small changes due to the shifting of the energy levels on account of the interaction with the impurities.

The component of the current in the direction of the electric field, equation (2.27), is due entirely to collisions. The physical meaning of the various terms is not obvious in this form. This equation can, however, be transformed into a more physically meaningful expression with the help of the properties of the hermite polynomials. We show this in the Appendix. We find for sufficiently symmetric scattering intereaction

$$\langle \mathcal{J}_x \rangle = (-e^2E)(1/\Omega) \sum_{\mu\nu} f'(\varepsilon_\nu) (X_\nu - X_\mu)^2 W_{\mu\nu} \quad (2.28)$$

where $W_{\mu\nu} = (2\pi/\hbar) |V_{\mu\nu}|^2 \delta(\varepsilon_\mu - \varepsilon_\nu)$ is the transition probability rate from state μ to ν. This describes the irreversible current in terms of the net drift of the centers of the cyclotron orbits along the electric field. This is essentially the same as the expression used by TITEIKA[1] who proposed this on intuitive grounds.

We have established above equation (2.28) for classical statistics. For quantum statistics, it is only necessary to use in equation (2.28) the Fermi-Dirac function f^F instead of f, as was proved by KOHN and LUTTINGER[8] for elastic scattering. We can then write, making use

of the properties of f^F and the δ-function in $W_{\mu\nu}$

$$\langle \mathcal{J}_x \rangle = \frac{e^2 E}{kT} \left(\frac{1}{\Omega}\right) \sum_{\mu\nu} f^F(\epsilon_\nu)\,[1 - f^F(\epsilon_\mu)] \times \times (X_\nu - X_\mu)^2\, W_{\mu\nu}\,. \qquad (2.29)$$

The y-component of the current, equation (2.26), remains the same.

3. SCATTERING BY LATTICE VIBRATIONS

We consider here the case of inelastic collisions. In particular we sketch briefly the main steps of the calculation for electron-phonon interaction. It is suggested from the physical interpretation of the last formula (2.29) that in this case only the transition probabilities $W_{\mu\nu}$ will be different, appropriate to the inelastic electron-phonon scattering. We prove this below.

We denote the Hamiltonian of the lattice vibrations by H_L and its eigenstates and eigenenergies by $|N>$ and E_N, respectively. The deviation of the density matrix from thermal equilibrium R, is given by

$$i\hbar dR/dt = [\tilde{H}_0 + H_L + \tilde{V}, R] + [F, f(\tilde{H}_0 + + H_L + \tilde{V})],\ R(0) = 0\,, \qquad (3.1)$$

where

$$\tilde{H}_0 = \sum_i H_0(i) = \sum_\mu \epsilon_\mu\, a_\mu^+ a_\mu\,;\ \tilde{H}_0 |n> = E_n |n> \qquad (3.2)$$

$$F = \sum_i F(i) = \sum_{\mu\nu} F_{\mu\nu}\, a_\mu^+ a_\nu\,. \qquad (3.3)$$

$$\tilde{V} = \sum_i V(i) = \sum_{\mu\nu} V_{\mu\nu}\, a_\mu^+ a_\nu\,. \qquad (3.4)$$

a_μ^+ and a_ν are the creation and destruction operators for the electrons in the Landau states. Clearly $V_{\mu\nu}$ is an operator in phonon space.

The current operator for the whole system is

$$\tilde{\mathcal{J}} = \sum_i \mathcal{J}(i) = \sum_{\mu\nu} \mathcal{J}_{\mu\nu}\, a_\mu^+ a_\nu\,. \qquad (3.5)$$

For the average current density we have

$$\langle \tilde{\mathcal{J}} \rangle = \mathrm{Tr}\,\{\tilde{\mathcal{J}} R\} = \sum_{\mu\nu} \mathcal{J}_{\mu\nu}\, \varrho_{\nu\mu}\,, \qquad (3.6)$$

where

$$\varrho_{\nu\mu} = \mathrm{Tr}\,\{a_\mu^+ a_\nu R\} = \sum_{nn'} \sum_N < Nn|R|Nn' > < n'|a_\mu^+ a_\nu|n>\,. \qquad (3.7)$$

The steady-state value of R, up to second order in V, is obtained as before from equation (3.1). Since $\tilde{F}$ has, in the occupation number representation $|n>$, diagonal and off-diagonal matrix elements connected only with the diagonal and off-diagonal matrix elements of F, respectively, we have

$$< Nn|R^{(0)}|Nn' > = f(E_N)\, \frac{f(E_n) - f(E_{n'})}{E_n - E_{n'}}\, \tilde{F}_{nn'}, \qquad (3.8)$$

$$< Nn|R^{(2)}|Nn' > = = \frac{i\pi}{kT}\, \frac{f(E_N)}{E_n - E_{n'}} \sum_{N'',\, n''} [\delta(E_{n''N'} - - E_{n'N})\, f(E_{n'})\, \tilde{V}_{nN,\, n''N'}\, \tilde{V}_{n''N',\, n'N} \times \tilde{F}_{(n'n'} - \tilde{F}_{n''n'')} - \delta(E_{nN} - E_{n''N'})\, f(E_n) \times \times \tilde{V}_{nN,\, n''N'}\, \tilde{V}_{n''N',\, n'N}\, (\tilde{F}_{n''n''} - \tilde{F}_{nn})]. \qquad (3.9)$$

The $R^{(0)}$ gives rise to the unperturbed current density which is, of course, equal to its classical value, equation (2.26), namely $\langle \mathcal{J}_y^{(0)} \rangle = - NecE/H$, $\langle \mathcal{J}_x^{(0)} \rangle = 0$, as can be seen directly. In the framework of this calculation it can be obtained from equation (3.7), (3.8) and (3.3). It is easily seen from the usual properties of the operators a_μ^+, and a_ν that

$$\varrho_{\nu\mu}^{(0)} = \mathrm{Tr}\,\{a_\mu^+ a_\nu R^{(0)}\} = \frac{f^F(\epsilon_\nu) - f^F(\epsilon_\mu)}{\epsilon_\nu - \epsilon_\mu}\, F_{\nu\mu}\,, \qquad (3.10)$$

where $f^F(\epsilon)$ denotes the Fermi-Dirac function

$$f^F(\epsilon_\nu) = \mathrm{Tr}\{f(\tilde{H}_0)\, a_\nu^+ a_\nu\} = \{1+\exp[(\epsilon_\nu - E_F)/kT]\}^{-1}. \quad (3.11)$$

Therefore, according to equations (3.6) and (2.25),

$$\langle \mathcal{J}_y^{(0)} \rangle = (-\epsilon^2 E/m\omega_0) \sum_{nk} (n+1)[f^F(\epsilon_{n+1}) - f^F(\epsilon_n)] = -NecE/H. \quad (3.12)$$

The calculation of $\varrho_{\nu\mu}^{(2)}$ is more complicated. By use of the representation of $\tilde{F}$ and $\tilde{V}$ in terms of the operators a_μ^+, a_ν, their well-known properties, the relation (3.11) and the corresponding ones for products of the occupation number operators, i.e.

$$\mathrm{Tr}\{f(H_0)\, N_\mu N_\nu\} = f^F(\epsilon_\mu) f^F(\epsilon)\,(\nu \neq \mu),$$

we find from equation (3.9)

$$\varrho_{\nu\mu}^{(2)} = \frac{i\pi}{kT}\frac{1}{\epsilon_\nu - \epsilon_\mu} \sum_{NN'} f(E_N) \sum_\lambda V_{\nu N, \lambda N'} V_{\lambda N', \mu N} \times \times (1-f_\lambda^F)[f_\nu^F (F_{\nu\nu} - F_{\lambda\lambda})\, \delta(\epsilon_\nu + E_N - \epsilon_\lambda - E_{N'}) + f_\mu^F (F_{\mu\mu} - F_{\lambda\lambda}) \times \times \delta(\epsilon_\mu + E_N - \epsilon_\lambda - E_{N'})]. \quad (3.13)$$

With the help of equations (3.6), (3.13) and (2.24), we get for the current density

$$\langle \mathcal{J}_x \rangle = \frac{\epsilon^2 E}{kT}\frac{2}{\Omega} \sum_{NN'} f(E_N) \sum_{\mu\nu} (X_\nu - X_\mu) f^F(\epsilon_\mu) \times \times [1-f^F(\epsilon_\nu)]\, \delta(\epsilon_\mu + E_N - \epsilon_\nu - E_{N'}) \times \times (\pi/\hbar)(\hbar/m\omega_0)^{1/2} [\sqrt{2(\mu+1)} \times \times V_{\mu N_\nu, \nu N'} V_{\nu N', \mu+1 N} + + \sqrt{2(\mu)}\, V_{\mu-1 N, \nu N'} V_{\nu N', \mu N}]. \quad (3.14)$$

By a procedure analogous to that in the Appendix, the previous expression can be rewritten in a more meaningful form, as follows

$$\langle \mathcal{J}_x \rangle = \frac{e^2 E}{kT}\frac{1}{\Omega} \sum_{\mu\nu} f^F(\epsilon_\mu) \times \times (X_\mu - X_\nu)^2 W_{\mu\nu} [1-f^F(\epsilon_\nu)], \quad (3.15)$$

where $W_{\mu\nu}$ is the rate of transition probability form state μ to ν, i.e.

$$W_{\mu\nu} = (2\pi/\hbar) \sum_{NN'} f(E_N) \times \times |V_{\mu N, \nu N'}|^2\, \delta(\epsilon_\mu + E_N - \epsilon_\nu - E_{N'}). \quad (3.16)$$

This proves the assertion made in the beginning of this section.

We shall not make any detailed applications of this theory here. The interested reader is referred to the extensive work of ADAMS and HOLSTEIN[6] mentioned in the introduction. The details of the oscillatory effects are not rigorously treated in any of these theories, however.

APPENDIX

For our model of scattering

$$V(\mathbf{r}) = \sum_i v(\mathbf{r} - \mathbf{r}_i) = (1/\Omega) \sum_{\mathbf{q}} W(\mathbf{q})\, e^{i\mathbf{q}\cdot\mathbf{r}} \sum_i e^{-i\mathbf{q}\cdot\mathbf{r}_i}, \quad (A\text{-}1)$$

where $W(\mathbf{q})$ is the Fourier transform of $v(\mathbf{r})$. For a random distribution of scattering centers we have for the ensemble average

$$V_{\mu\nu} V_{\nu\lambda} = (N_I/\Omega) \sum_{q_x} W(q_x, \mathbf{k}_\mu - \mathbf{k}_\nu) \times \times W(-q_x, -\mathbf{k}_\mu + \mathbf{k}_\nu) \mathcal{J}_{\mu\nu}(q_x)\, \mathcal{J}_{\nu\lambda}(-q_x)\, \delta_{\mathbf{k}_\mu \mathbf{k}_\nu}, \quad (A\text{-}2)$$

where

$$\mathcal{J}_{\mu\nu}(q_x) = \int_{-\infty}^{+\infty} \Phi_\mu(x - X_\mu)\, e^{iq_x x}\, \Phi_\nu(x - X_\nu)\, dx, \quad (A\text{-}3)$$

and Ni impurity concentration. Clearly we have

$$\mathcal{J}_{\mu\nu}(q_x) = \mathcal{J}_{\nu\mu}(q_x) = \mathcal{J}_{\mu\nu}^*(-q_x) \quad (A\text{-}4)$$

From the well-known relations, (where $\alpha = (m\omega_0/\hbar)^{1/2}$)

$$\alpha^{-1}\sqrt{(2n+1)}\, \Phi_n(x) = \left(x - \frac{1}{\alpha^2}\cdot\frac{d}{dx}\right) \Phi_n(x) \quad (A\text{-}5)$$

$$\alpha^{-1}\sqrt{2n}\, \Phi_{n-1}(x) = \left(x + \frac{1}{\alpha^2}\cdot\frac{d}{dx}\right) \Phi_n(x), \quad (A\text{-}6)$$

and equations (A-2) and (A-4), we have for $W^2(-g_x) = W^2(g_x)$

$$\alpha^{-1}\left[\sqrt{2(\mu+1)}\,V_{\mu\nu}V_{\nu,\mu+1}+\sqrt{2\mu}\,V_{\mu-1,\nu}V_{\nu\mu}\right]$$
$$= (N_I/\Omega)\sum_{q_x} W^2(q_x,\mathbf{k}_\mu-\mathbf{k}_\nu)\,\mathcal{J}_{\mu\nu}(q_x)\int 2(x-X_\mu)\times$$
$$\times\,\Phi_\mu(x-X_\mu)\,e^{-iq_x x}\Phi_\nu(x-X_\nu)\,dx$$
$$= (N_I/\Omega)\sum_{q_x} W^2(q_x,\mathbf{k}_\mu-\mathbf{k}_\nu)\,\mathcal{J}_{\mu\nu}(q_x)\times$$
$$\times\,[\mathcal{J}_{\nu\mu}(-q_x)(X_\nu-X_\mu)+K_{\mu\nu}]\,, \qquad \text{(A-7)}$$

where

$$K_{\mu\nu} = \int [2x-(X_\mu+X_\nu)]\,\Phi_\mu(x-X_\mu)\,e^{-iq_x x}\;\times$$
$$\times\,\Phi_\nu(x-X_\nu)\,dx = K_{\nu\mu}\,. \qquad \text{(A-8)}$$

The first term in (A-7) is antisymmetric in the indices μ and ν, whereas the second is symmetric. In the expression (2.27) for the current density, the other factors are antisymmetric in μ and ν and, therefore, the second term of (A-7) contributes nothing, while the first can be written as $(X_\nu - X_\mu)\,V_{\mu\nu}V_{\nu\mu}$. We thus have.

$$\langle \mathcal{J}_x\rangle = (-e^2E)\,(2/\Omega)\sum_{\mu\nu} f'(\varepsilon_\nu)\,(X_\nu - X_\mu)^2$$
$$(\pi/\hbar)|V_{\mu\nu}|^2\,\delta(\varepsilon_{\mu\nu})\,. \qquad \text{(A-9)}$$

REFERENCES

1. TITEICA V. S., *Ann. Phys. Leipzig* **22,** 129 (1935).
2. DAVYDOV B. and POMERANCHUK I., *J. Phys. (USSR)* **2,** 147 (1940).
   ZILBERMAN G. E., *Zh. Eksper. Teor. Fiz.* **29,** 762 (1955); translation: *Soviet Phys. JETP* **2,** 650 (1956).
   APPEL J., *Z. Naturforsch.* **11a,** 892 (1956).
3. LIFSHITZ E. M., *J. Phys. Chem. Solids* **4,** 11 (1958).
4. ARGYRES P. N., *Phys. Rev.* **109,** 1115 (1958); *J. Phys. Chem. Solids* **8,** 124 (1959).
5. KUBO R., HASEGAWA H. and HASHITSUME N., *J. Phys. Soc. Japan* **14,** 56 (1959).
6. ADAMS E. N. and HOLSTEIN T. Unpublished work.
7. KUBO R., *J. Phys. Soc. Japan* **12,** 570 (1957).
8. KOHN W. and LUTTINGER J. M., *Phys. Rev.* **108,** 590 (1957).

J. Phys. Chem. Solids Pergamon Press 1959. Vol. 12. pp. 97–104. Printed in Poland.

ELECTRON MOBILITY OF INDIUM ARSENIDE PHOSPHIDE $[In(As_yP_{1-y})]$

H. EHRENREICH

General Electric Research Laboratory, Schenectady, New York

(*Received* 1 *May* 1959; *revised* 1 *June* 1959)

VOL. 12
959/60

Abstract—The electron mobility of InP, InAs and of the alloys $In(As_yP_{1-y})$ is calculated using existing evidence for the band structure of these materials and shown to be determined primarily by a combination of polar optical mode and charged impurity scattering between about 200 and 500°K. The mobility of $In(As_y P_{1-y})$ as a function of y at room temperature calculated on the basis of these scattering mechanisms agrees within about 30 per cent with the experimental data of WEISS. These calculations are performed without use of adjustable parameters. The experimental information necessary to determine the conduction band structure and the quantities entering the mobility of InP and InAs is available. The band structure and the electron effective mass of the alloys can be established reasonably well from existing experimental evidence. A linear interpolation procedure is used to deduce the remaining quantities entering the mobility. The validity of this procedure can be checked experimentally. The disagreement between theory and experiment in the alloy arises in part from a 25 per cent discrepancy for InAs. When the calculated and experimental mobilities are matched for InAs and InP by adjusting the effective ionic charge, the shapes of the calculated and experimental curves are found to agree fairly well for the entire range of y. This indicates that alloy scattering, arising specifically from the disorder of the lattice, does not play a dominant role in determining the electrical properties of the alloy.

1. INTRODUCTION

IN previous work[1] it was shown that of all the lattice scattering mechanisms, the polar electron-phonon interaction is by far the most important mechanism scattering electrons in InSb. Because the degree of polarity increases as the constituents of a 3-5 compound are replaced by lighter elements, one suspects that polar scattering should also predominate in determining the electron mobility of compounds like InAs and InP which are believed to have the same conduction band structure as InSb. Even further, one may ask to what extent the electron mobility of indium arsenide phosphide alloys is determined by polar scattering in order to ascertain the importance of alloy scattering arising from the disorder of the crystal. This question is currently of some importance in connection with considerations relating to thermoelectric power generation. Experimental information on the electrical and thermal properties of these alloys has recently been obtained by the groups at Siemens[2] and Westinghouse.[3] The latter work emphasized the temperature range above 300°K in order to explore the utility of these alloys as high temperature thermoelements. In the present paper we shall be concerned primarily with the electrical properties of In (As_yP_{1-y}) at room temperature. We shall therefore use the experimental results of WEISS[2] in

comparing with theory. These results agree with reasonable extrapolations of the data of BOWERS *et al.*[3]

In Section 2 of this paper we shall review the evidence establishing the band structure of InP, InAs and its alloys. Section 3 will be devoted to a calculation of the mobility as a function of temperature for InP and InAs. We shall show that a combination of polar and ionized impurity scattering appears to account for the magnitude and fairly well for the temperature dependence of the mobility of InP, In $(As_{0\cdot8}P_{0\cdot2})$ and InAs between about 200 and 500°K.† The experimental information required to deduce the effective ionic charge and effective mass of InP and InAs is now available so that these calculations can be performed without use of any adjustable parameters. In the case of the alloys a linear interpolation procedure is used to determine the effective mass and the quantities entering the effective ionic charge e^*. Such a procedure can be justified for the determination of the effective mass and its validity checked experimentally for the effective ionic charge. In Section 4 the results of the mobility calculation for In (As_yP_{1-y}) as a function of y are discussed. It is shown that the calculations based on combined polar and impurity scattering agree, within about 30 per cent, with the experimental results of WEISS.[2] An estimate of the influence of alloy scattering indicates that this mechanism does not play a dominant role in determining the electrical properties of the alloys.

2. BAND STRUCTURE

The results of infrared cyclotron resonance experiments[5] and analysis of data elucidating the valence bands[6] of InAs all point to a band structure of this compound which is analogous to that proposed for InSb.[7] The work on InAs -InP alloys[2] indicates that the band gap in these alloys appears to vary linearly with concentration between the two limiting compounds InAs and InP. In addition, recent optical data[8] on InP show that the fundamental absorption above about 10 cm^{-1} has a slope comparable to that of InSb. Thus it appears likely that InP too is characterized by direct transitions. Further, measurements of the magneto-resistance[9] show that for small electron concentrations ($<10^{16}$ cm^{-3}) the effective mass is isotropic. These pieces of evidence suggest that InP has a band structure analogous to that of InSb and InAs. While the conduction band mass of InAs ($m_n=0\cdot03$) is fairly well established experimentally, that of InP is still uncertain. Indeed there is some evidence[8,9] that the effective mass increases rather rapidly as one proceeds up into the conduction band from the edge. However, the mass at the edge may be estimated using the experimental results for another substance — like Ge, InSb or GaAs— whose band structure is probably the same as that of InP. Further, KANE'S theory may be applied with the fact that the matrix element P (connecting the conduction and the light mass and split-off valence bands) appears to be approximately constant. The conduction band mass $m_n^{(1)}$, band gap $E_G^{(1)}$, and spin-orbit splitting $\Delta^{(1)}$ of one crystal is then related to the corresponding quantities $m_n^{(2)}$, $E_G^{(2)}$, and $\Delta^{(2)}$ of the other crystal by the equation

$$m_n^{(1)}/m_n^{(2)} = (E_G^{(1)}/E_G^{(2)})\left[1+\frac{1}{2}E_G^{(2)}/(E_G^{(2)}+\right.$$
$$\left.+\Delta^{(2)})\right]/\left[1+\frac{1}{2}E_G^{(1)}/(E_G^{(1)}+\Delta^{(1)})\right]. \quad (1)$$

Using the data for GaAs[10] one finds $m_n=0\cdot07$ for InP. This is perhaps the most

† It has been previously shown[4] that polar scattering also appears to be the dominant mechanism determining the electron mobility of GaAs.

VOL. 12 959/60

reliable extrapolation because the band gaps of InP and GaAs are most similar. On the other hand extrapolation from InSb and Ge yields masses $m_n=0{\cdot}06$ and $m_n=0{\cdot}05$ respectively. This small variation in the deduced mass indicates that P is roughly independent of band gap for a group of materials of similar band structure whose $k=0$ gaps vary betweeen 0·23 and 1·55 V. Extrapolation from the $m_n=0{\cdot}07$ value of InP by using eq. (1) yields $m_n=0{\cdot}02$ for InAs. This value is very close to other deduced values for the mass at the bottom of the conduction band.[6]

Because of the already noted linear variation of the band gap of $_{\frac{1}{4}}^{\frac{3}{4}}\mathrm{In}(\mathrm{As}_y\mathrm{P}_{1-y})$ with y we may conclude that the band edges in these alloys lie at $k=0$ for all concentrations y. Since it is likely that the valence bands of these alloys will have same structure as that already experimentally established for Ge,[11] InAs[12] and GaAs[13] and, since P is approximately the same for InAs and InP and does not appear to vary strongly with band gap, it is reasonable to assume that P is constant for the range of compositions used here. Thus, we may use eq. (1) to establish that, except for small corrections due to spin-orbit effects, the effective mass also varies linearly with y.

3. MOBILITY OF InP AND InAs

An expression for the electron mobility due to polar scattering, which includes screening effects, is given in an earlier paper.[14] This expression assumes the adequacy of Boltzmann statistics, an assumption that we shall also make in the present simple calculations. The parameters entering the mobility are all known experimentally. PICUS *et al.*[15] have obtained the reststrahlen frequency ω_t and the static and dynamic dielectric constants ϵ_0 and ϵ_∞ from infrared reflectivity measurements on InAs and InP. NEWMAN[8] has performed a similar study on InP. As has been stressed repeatedly in previous work[1] the square of the effective ionic charge entering the mobility† is not very accurately determined by these measurements since it is proportional to $\epsilon_0-\epsilon_\infty$ which in weakly polar semiconductors is considerably smaller than either ϵ_0 or ϵ_∞. Thus, although the agreement between the reflectivity measurements of PICUS *et al.* and Newman is fairly good, the deduced effective ionic charges differ significantly. One obtains $e^\star = 0{\cdot}23e$ in the former case and $0{\cdot}29e$ in the latter.

In the crystals we shall consider, impurity scattering still plays a significant role. We shall calculate this contribution from the BROOKS-HERRING formula[16] and combine mobilities according to the simple relationship††

$$\mu^{-1} = \mu_{\text{polar}}^{-1} + \mu_{\text{impurity}}^{-1}. \qquad (2)$$

In Fig. 1 we show the calculated mobility of InP as a function of temperature, and for comparison the experimental data of REID and WILLARDSON.[17] The effective ionic charge was determined from the data of NEWMAN[8], and the mass was taken to be $0{\cdot}07m$. Two impurity concentrations are considered: $n_I = 4\times 10^{15}$ cm^{-3} and 6×10^{16} cm^{-3}.

† This effective ionic charge is not to be confused with that defined by Szigeti which is tabulated in Reference 15. The difference between these charges is discussed in Reference 1.

†† Previous experience with the calculation of mobilities for correctly combined polar and electron-hole (or impurity) scattering using a complete variational procedure indicates that the preceding simple relationship is quite accurate when impurity scattering is somewhat less important than polar scattering, as it is in the present case. Further, in the present paper we shall not make the fine distriction between Hall and drift mobilities which will differ here by less than 20 per cent.

The former value assumes that the number of impurities equals the number of free carriers as determined from the Hall coefficient, and the latter that an appreciable amount of compensation is present as suggested by the estimates made by REID and WILLARDSON. It is seen that between 200 and 400°K the results corresponding to the lower impurity concentration agree rather well with the experimental data. The behavior at lower temperatures indicates that some degree of compensation is evidently present in the measured sample but that it may not be as great as that contemplated by REID and WILLARDSON. The calculated mobility at 300°K which we shall use in the discussion of the alloys is seen to be rather insensitive to the impurity concentration. The increasing deviation of the experimental and calculated curves at temperatures above 400°K is not understood but may possibly be associated with the yet unexplained increase in effective mass (already mentioned) which occurs when regions of the band somewhat removed from the band edge become appreciably populated. It should be noted that the agreement between theory and experiment would have been rather poorer if we had used the data of PICUS *et al.*[15] to calculate the effectve ionic charge. This indicates the extreme sensitivity of e^* to the values of the static and dynamic dielectric constants deduced from the reflectivity measurements.

The corresponding results for InAs are also shown in Fig. 1. The experimental curve is that obtained by ANTELL *et al.*[18] The discontinuity at 300°K arises because a different sample was used to obtain the mobility over the lower temperature range. At higher temperatures the experimental results shown agree well with those of FOLBERTH *et al.*[19] The calculated mobility was obtained by using PICUS' results which lead to an effective ionic

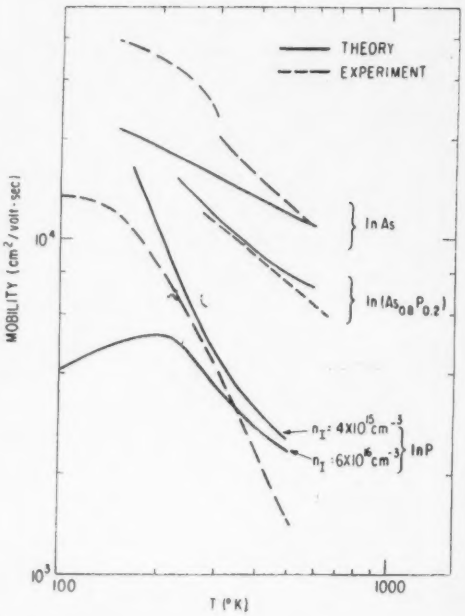

FIG. 1. Electron mobility of InAs, $In(As_{0.8}P_{0.2})$ and InP vs. temperature. Theory for combined polar and impurity scattering. Impurity concentrations are given on Table 1. Experimental data taken from references 18, 2 and 17 respectively.

charge $e^*=0.22\,e$ and the effective mass $m^*=0.03$ deduced from optical data by SPITZER and FAN[20]. The contribution due to impurity scattering was calculated assuming an impurity concentration $n_I=5\times10^{16}$ cm^{-3} equal to the carrier concentration obtained from the Hall coefficient in the extrinsic range. The theoretical mobility is seen to be *smaller* than the experimental mobility, indicating that the two scattering mechanisms considered here are sufficient to account for the magnitude of the mobility. It may be that the deduced effective ionic charge is somewhat large. The temperature dependence of the mobility is not well accounted for by the present calculations. This is due, at least in part, to the fact that effects of degeneracy, which should become important in the region above room

temperature, have been neglected. Since our main purpose in the present work is the calculation of the mobility of the alloys made from the two materials at room temperature, where effects of degeneracy are not important, we shall not attempt to present a more accurate treatment here.

The assertion that the neglect of degeneracy effects may account for the discrepancy of the temperature dependence is given some support by the rather good agreement between theory and experiment[2] of the mobility vs. temperature of $In(As_{0\cdot8}\ P_{0\cdot2})$ also shown in Fig. 1. As indicated on Table 1, the band gap and effective mass of this material are both about 40 per cent larger than in InAs whereas the extrinsic carrier concentration, $n = 2\cdot1\times10^{16}$, is comparable. Degeneracy effects would therefore be expected to set in at a higher temperature than in InAs. The details of the calculation are discussed immediately below.

VOL. 12 59/60

ledge of the parameters listed in Table 1. As already pointed out in Section 2 the effective mass of the alloy can be expected to vary linearly with y. In order to determine the longitudinal optical frequency ω_l and the dielectric constants ϵ_0 and ϵ_∞ we shall make the *ad hoc* assumption that these parameters also vary linearly with y. Since it is a simple enough matter to check this assumption experimentally simply by repeating the experiments and analysis of PICUS *et al.*[15] and NEWMAN[8] for these alloys, it appears to be more satisfactory to settle this point experimentally rather than by theoretical argument. The quantities in question however do not vary very much over the entire range of y and from this point of view a linear interpolation does not appear unreasonable. In order to compute e^* we need to know also the reduced atomic mass M in terms of the atomic masses M_{In}, M_{As}, M_P of indium, arsenic and phosphorus and the volume per unit cell v_a. We calculate the former

Table 1. Parameters for $In(As_y P_{1-y})$ *used in calculations and results (Fig. 2)*

y	E_G (0°K) (eV)	m_n	ω_l (10^{12}sec^{-1})	ε_o	ε_∞	e^*	n_I (10^{18}cm^{-3})	μ_{polar} (10^4cm^2/V-sec)	$\mu_{impurity}$ (10^4cm^2/V-sec)
0 (InP)	1·43	0·07	6·5	15	10·6	0·29	0·40	0·47	21
0·6	0·86	0·05	5·2	14·6	11·1	0·27	1·2	0·91	13
0·8	0·66	0·04	4·8	14·4	11·3	0·24	2·1	1·3	9·7
I (InAs)	0·47	0·03	4·4	14·3	11·5	0·22	4·0	2·1	7·0

Band gap E_G, effective mass m_n, longitudinal optical frequency ω_l, static and dynamic dielectric constants ε_o and ε_∞, mobility effective ionic charge e^*, impurity concentration n_I of the alloy specimen, considered in the present calculations, and calculated polar and impurity mobility μ_{polar} and $\mu_{impurity}$. The resultant mobility is shown in Fig. 2.

4. MOBILITY OF In (As_yP_{1-y})

We turn now to a discussion of the mobility of $In(As_y P_{1-y})$ as a function of concentration y at room temperature. An absolute calculation of the mobility presupposes know-

from the relationship $M^{-1} = M_{In}^{-1} + M_y^{-1}$, where $M_y = y\ M_{As} + (1\text{-}y)\ M_P$, and the latter by assuming that the interatomic spacing varies linearly with y. Again, the determination of these quantities involves the

assumption of linear interpolation. The values of e^* given in Table 1 result when the listed data are substituted into equation (23) of Reference 1. We may then calculate the mobility as a function of the concentration y using equation (2).To evaluate the contribution due to impurity scattering we use the actual impurity concentrations n_I listed in Table 1 which were found in the samples measured by WEISS[2]. It is evident from Table 1 that detailed experimental information has been presented for only four values of y, although WEISS does give a result for the mobility of the alloy characterized by $y=$ 0·4 which has been used in plotting the experimental curve shown in Fig. 2. The theoretical curve in Fig. 2 is smooth in spite of the fact that the impurity concentrations n_I fluctuate from sample to sample. This is because impurity scattering is rather less important than polar scattering at room temperature, as is seen from the entries in Table 1.

In discussing the agreement between theory and experiment the point of view taken in these calculation should be kept in mind. We have regarded the alloy $In(As_yP_{1-y})$ as a polar semiconductor whose properties can be characterized by linear interpolation of the quantities entering the mobility between the limiting compounds InAs and InP. This point of view has some justification in the case of the effective mass, but represents an assumption for the other quantities, which can be checked experimentally. It should be emphasized that no explicit account has been taken of alloy scattering arising from the fact that the lattice containing As and P atoms is disordered. In addition, aside from the assumptions just discussed, there are no adjustable parameters in the theory.

This viewpoint leads to results, shown in Fig. 2, whose agreement with experiment indicates that its essential aspects are qualitatively correct. The relatively large slope at the InAs end, and the relatively small slope at the InP end of the curve, are seen to arise in part from the $m^{*-3/2}$ dependence of the mobility. Since m^* varies linearly between

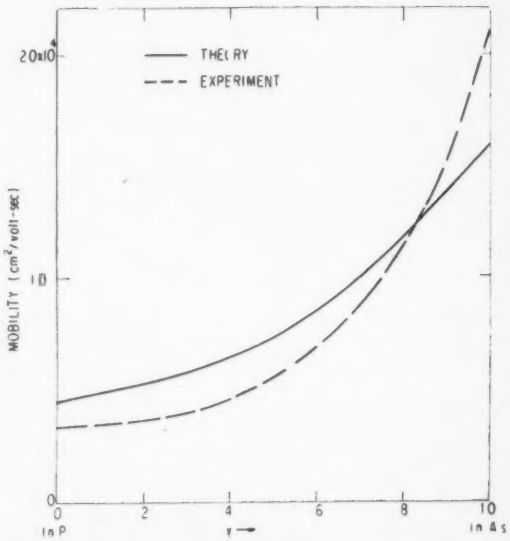

FIG. 2. Electron mobility of $In(As_yP_{1-y})$ vs. y. Theory for combined polar and impurity scattering. Input data and partial results are given in Table 1. Experimental data are taken from reference 2.

the two compounds and the effective mass is considerably smaller for InAs the fractional change in $m^{*-3/2}$ is largest for $y \approx 1$ and smallest for $y \approx 0$.

The possible contribution of alloy scattering cannot really be estimated from Fig. 2 because part of the discrepancy between theory and experiment arises from the disagreement that occurs in the calculation for pure InAs and InP.† In order to estimate this contribution, we adjust e^* so that agreement

† It should be noted, however, that the agreement lies within the uncertainty of the effective ionic charge.

VOL. 12 59/60

is obtained for these two compounds and then perform a linear interpolation along the lines mentioned previously. Specifically, we first subtract the influence of impurity scattering from the *experimental* curve using equation (2) and then compare the result with the theory for polar scattering alone. We assume ω_l and ϵ_∞ are correctly determined, and calculate ϵ_0 from the values of e^* required to produce agreement between theory and experiment for InP and InAs. The value $\epsilon_0 = 17{\cdot}6$ is found in the case of InP, and 13·2 in the case of InAs. Curve (1) of Fig. 3 shows the results obtained when ϵ_0, ϵ_∞, ω_l, etc., are linearly interpolated to obtain their values for $0 < y < 1$.

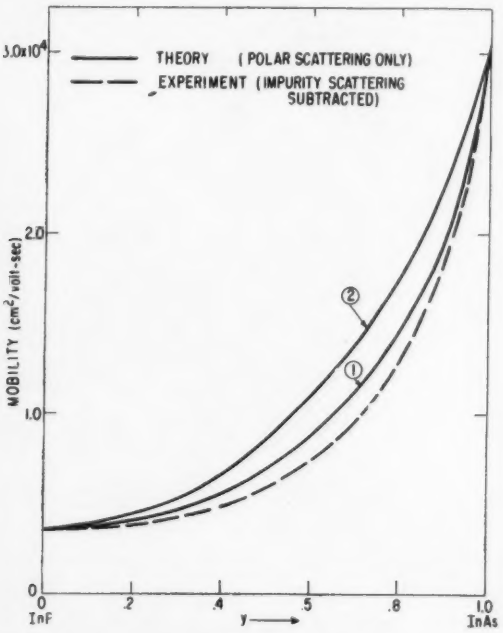

FIG. 3. Electron mobility of $In(As_yP_{1-y})$ vs. y. Theory for polar scattering alone; experiment with the contribution of charged impurity scattering removed. Curve (1): theory assuming linear interpolation of ϵ_0, ϵ_∞, ω_l, M and v_a; curve (2): theory assuming linear interpolation of e^*. Both curves matched with experiment at $y = 0$ and 1.

Another reasonable assumption concerning the variation of e^* that could have been made is that e^* itself varies linearly, rather than the quantities entering it. This leads to curve (2) of Fig. 3. The resulting poorer agreement with the experimental curve can be understood by inspection of the behavior of ϵ_0 and ϵ_∞ shown in Table 1. It is seen that ϵ_0 decreases and ϵ_∞ increases as y becomes larger. Thus, if ϵ_0 and ϵ_∞ are assumed to vary linearly with y, the fractional change of $e^{*2} \sim (\epsilon_0 - \epsilon_\infty)$ is greatest in the region $y \approx 1$ and smallest in the region $y \approx 0$. This accentuates the behavior of the mobility, already discussed, arising from the variation of the effective mass with y. This effect is absent when e^* is assumed to vary linearly with y.

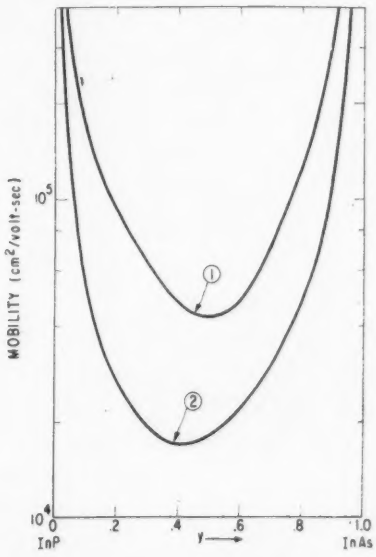

FIG. 4. Estimated electron mobility due to alloy scattering in $In(As_yP_{1-y})$ vs. y. Curves 1 and 2 correspond to the cases considered in Fig. 3.

The results shown in Fig. 3 permit a *crude* estimate of the mobility due to alloy scattering. With the help of the relationship

$$\mu^{-1}_{\text{polar}}(\text{exp.}) = \mu^{-1}_{\text{polar}}(\text{theory}) + \mu^{-1}_{\text{alloy}} \quad (3)$$

we obtain the values of μ_{alloy} shown in Fig. 4. Curves (1) and (2) correspond to those shown in Fig. 3. The approximate symmetry of the curves around $y=0{\cdot}5$, where alloy scattering is expected to be largest, lends some credibility to these estimates. The assumptions leading to curve (1) are seen to result in only a 10 per cent maximum contribution of alloy scattering to the resultant mobility, whereas the assumptions leading to curve (2) produce a 40 per cent contribution. We may therefore conclude that alloy scattering does not dominate in these alloys at room temperature. A better estimate of this contribution might be obtained from data at lower temperatures. Some difficulty, however, could be encountered when charged impurity scattering plays a significant role, since the present theory does not account well for the low temperature behavior of the mobility in pure InAs and InP.

Acknowledgment—The author would like to thank DORIS OLECHNA for performing very capably the numerical calculations connected with this work.

REFERENCES

1. EHRENREICH H., *J. Phys. Chem. Solids* **2,** 131 (1957); **9,** 129 (1959).
2. WEISS H., *Z. Naturf.* **11a,** 430 (1956).
3. BOWERS, BAUERLE and CORMISH, *Bull. Amer. Phys. Soc.* (Ser. II) **4,** 134 (1953).
4. GRAY P. V. and EHRENREICH H., *Bull. Amer. Phys. Soc.* (Ser. II) **3,** 255 (1958).
5. LAX B., *Rev. Mod. Phys.* **30,** 122 (1958).
6. MATOSSI F. and STERN F., *Phys. Rev.* **111,** 472 (1958).
7. KANE E. O., *J. Phys. Chem. Solids* **1,** 249 (1957).
8. NEWMAN R., *Phys. Rev.* **111,** 1518 (1958).
9. GLICKSMAN M., *J. Phys. Chem. Solids* **8,** 511 (1959).
10. SPITZER W. G. and WHELAN J. M., *Phys. Rev.* (to be published).
11. BRIGGS H. B. and FLETCHER R. C., *Phys. Rev.* **91,** 1342 (1953).
12. STERN F. and TALLEY R. M., *Phys. Rev.* **108,** 158 (1957).
13. BRAUNSTEIN R., *J. Phys. Chem. Solids* **8,** 280 (1959).
14. EHRENREICH H., *J. Phys. Chem. Solids* **8,** 130 (1959).
15. PICUS G., BURSTEIN E., HENVIS B. W. and HASS M. *J. Phys. Chem. Solids* **8,** 282 (1959).
16. BROOKS H., *Advances in Electronics,* Vol. 7, p. 156. Academic Press, New York (1956).
17. REID F. J. and WILLARDSON R. K., *J. Electron. and Control* **5,** 54 (1958).
18. ANTELL, CHASMAR, CHAMPNESS and COHEN, *Rugby Semiconductor Conference Report,* Phys. Soc. London, p. 99, (1956).
19. FOLBERTH, MADELUNG and WEISS, *Z. Naturf.* **9a,** 954 (1954).
20. SPITZER W. G. and FAN, H. Y., *Phys. Rev.* **106,** 882 (1957).

Neutron-irradiation effects in copper-alluminum alloys

(*Received* 1 *February* 1959; *revised* 21 *April* 1959)

IN a recent paper,[1] WECHSLER and KERNOHAN presented and interpreted a study of the decrease in resistivity in Cu-Al alloys produced by neutron irradiation. We have published a series of experiments[2-5] on the α-Cu-Zn system. The experiments of the two groups on two different materials are surprisingly similar whenever carried out under comparable conditions. We have interpreted our experiments in terms of radiation-enhanced diffusion leading to increased short-range order in Cu-Zn, such an interpretation being also in agreement with the available thermodynamic data for this system. The enhanced diffusion rate originates in the extra steady-state concentration of mobile defects established during reactor and electron irradiation. WECHSLER and KERNOHAN suggest that their results, and by inference our own, can be interpreted in terms of radiation-induced annealing of excess vacancies which were inadvertently introduced during preparation of the sample.

We wish to comment on the salient disagreements in interpretation.

1. We cannot accept the suggestion that decreases in resistivity in α-brass may be caused by the annealing of inadvertently introduced vacancies for the following reasons:

(a) DAMASK[3] has shown in a series of detailed studies that decreases in resistivity may be produced by appropriate *thermal* treatment as well as by irradiation (the initial state of a sample was that obtained by quenching a suitably annealed specimen from 320°C). *Thermal* rate studies showed that the activation energy associated with the *thermal* treatment is that of self-diffusion whether the temperature is raised or lowered. If quenched-in vacancies were involved, the relevant energy associated with a decreased temperature would be that for the motion of vacancies (i. e. about half of that observed).

(b) FEDER *et al.*[9] showed that the lattice parameter of α-brass *decreases* both upon suitable heat treatment and upon irradiation, in excellent correlation with the decrease in resistivity. They found the kinetics of these changes to be in good agreement with the resistivity studies and interpreted their results in terms of changes in short-range-order parameter. If any of the decreases in resistivity were to be associated with a decrease in the concentration of vacancies, then the corresponding change in lattice parameter would be expected to go in just the opposite direction. Since the lattice is collapsed around a vacancy in a metal, the lattice parameter would increase when the vacancies anneal.

2. We cannot accept the suggestion that our reactor-irradiation results can possibly be interpreted in terms of the radiation annealing of a non-equilibrium concentration of quenched-in vacancies in α-brass. A special site for vacancy annihilation, such as a damage cluster, seems to be essential for the mechanism proposed by WECHSLER and KERNOHAN. According to their interpretation, interstitials and vacancies annihilate each other, and the material is the same as before irradiation (and the subsequent anneal permitting annihilation), except that some of the vacancies collapse in the interior of the damage cluster. The *decrease* in resistivity is strictly a result of this collapse. It was shown some time ago[4] that electron-irradiation results in decreased resistivity for several alloys in a manner analogous to the neutron case.

VOL. 12 59/60

Electron irradiation, however, will not result in the type of damage cluster needed for vacancy collapse. Without vacancy collapse the WECHSLER and KERNOHAN mechanism does not operate. Electrons produce, however, more close vacancy-interstitial pairs, which can recombine without long-range diffusion, than neutrons and hence are expected to be less efficient in enhancing diffusion.

3. In our opinion the energies of formation and migration, as determined experimentally so far for Cu-Al alloys, indicate that no measurable concentration of vacancies can be quenched-in from around 200°C. We take the overall activation energy for diffusion as 1·81 eV and that for migration as 1·08 eV from the work of LI and NOWICK[10] (the latter is in good agreement with the value of 1·01 eV determined by WECHSLER and KERNOHAN and hence the energy of vacancy formation as 0·73 eV. With this energy of formation and assuming a pre-exponential factor of one, we obtain an equilibrium vacancy concentration of $1{\cdot}73\times10^{-6}$ atomic per cent at 200°C, a value which should be accurate to a factor of ~5. If the 0·2-$\mu\Omega$-cm change in resistivity observed by WECHSLER and KERNOHAN is to be explained by the annealing of quenched-in vacancies, then the electrical resistivity increase per atomic per cent of vacancies would have to be about 10^5 $\mu\Omega$-cm rather than the generally accepted value of 1-2 $\mu\Omega$-cm. Alternatively, if the 1-2 $\mu\Omega$-cm value is accepted, they would have had to quench from about 1000°C to obtain a sufficient concentration of vacancies, and the results can hardly be explained as an unavoidable quench from 200–300°C.

4. We wish to take this opportunity to clarify our position on the correlation of stress relaxation, self-diffusion, and resistivity measurements. For α-brass the argument is as follows. If there is no short-range order (or segregation) in an alloy, then there is no Zener-type internal-friction peak. Since the activation energies for self-diffusion, for the relaxation time in stress relaxation, and for the relaxation time of resistivity are almost identical, we conclude that a solid-state reaction, i.e. rearrangement of the atoms, is the controlling mechanism for all these rate processes.

From the above arguments (as well as others given before[3,5]), we conclude that the changes in resistivity observed in our experiments in α-brass are associated with changes in short-range order and not with quenched-in vacancies, and that we have measured true radiation-enhanced diffusion by our techniques. If the mechanism proposed by WECHSLER and KERNOHAN were valid, an appreciable temperature-dependence should be observed during the early stages of irradiation, since the activation energy is high when the cluster concentration is low. Our experiments showed, however, that the diffusion coefficient under irradiation is temperature-independent over a wide range of temperatures. This temperature-independence, in our interpretation, is a simple consequence of the steady rate of production of defects by irradiation coupled with the migration of these defects to fixed sinks.

A. C. DAMASK
G. J. DIENES
Brookhaven National Laboratory,
Upton, New York

VO
1
1959/

REFERENCES

1. WECHSLER M. S. and KERNOHAN, R. H., *J. Phys. Chem. Solids* **7,** 307 (1958).
2. ROSENBLATT D. B., SMOLUCHOWSKI R. and DIENES, G. J., *J. Appl. Phys.* **26,** 1044 (1955).
3. DAMASK A. C., *J. Appl. Phys.* **27,** 610 (1956).
4. DAMASK A. C., *J. Phys. Chem. Solids* **4,** 177 (1958).
5. DIENES G. J. and DAMASK A. C., 1958 *Geneva Conference on Peaceful Uses of Atomic Energy Paper No.* 612; *J. Appl. Phys.* **29,** 1713 (1958).

6. BIRCHENALL C. E., *Trans. Amer. Inst. Min. (Metall.) Engrs.* **171,** 166 (1947).
7. GUTTMAN L., *Trans. Amer. Inst. Min. (Metall.) Engrs.* **175,** 178 (1948).
8. MASAMOTO H., SAITO H. and SUGIHARA M., *Sci. Rep. Res. Inst. Tohoku Univ.* **A4,** 481 (1952).
9. FEDER R., NOWICK A. S., and ROSENBLATT D. B., *J. Appl. Phys.* **29,** 984 (1958).
10. LI C. Y. and NOWICK A. S., *Phys. Rev.* **103,** 294 (1956).

Reply to the letter of Damask and Dienes on "Neutron-irradiation effect in copper-aluminium alloys"

(*Received* 9 *March* 1959; *revised* 30 *April* 1959)

IN the paper[1] discussed by DAMASK[2], and DIENES experiments are described in which decreases in the electrical resistivity of α-Cu-Al alloys were produced as a result of reactor irradiation. Also, several mechanisms are considered as possible explanations of our observations. Included among the interpretations discussed is the possibility suggested by investigators at Brookhaven National Laboratory[3-6] as a result of similar experiments on α-Cu-Zn alloys, namely that the irradiation introduces vacancies which enhance diffusion, thereby causing short-range ordering with an attendant decrease in resistivity. However, since the concept of radiation-ordering has been widely discussed,* relatively little space is devoted to this idea in our paper. Furthermore, for reasons outlined below, it seems to us that the evidence presently available does not favor the radiation-ordering hypothesis so strongly as to preclude the advisability of examining other possibilities. Thus, we have discussed alternate explanations. One of these alternate explanations depends upon the idea that it is difficult, if not impossible, to cool the alloy sufficiently slowly to avoid retaining a non-equilibrium concentration of vacancies and that the irradiation has the effect of enhancing the annealing of these vacancies. Because this approach had not previously been considered and because it is amenable to some quantitative analysis, we were led to describe it in somewhat greater detail.

We may discuss the reasons for our hesitation to accept completely the radiation-ordering hypothesis by considering the two principal arguments advanced in its favor.

(1) The resistivity *decreases* upon neutron irradiation. As was pointed out in our paper,[1] it is by no means established that an increase in short-range order is necessarily accompanied by a decrease in resistivity. In fact, measurements[7,8] of the resistivity of Cu_3-Au at temperatures above the critical temperature have led to the conclusion that an increase in short-range results in an increase in resistivity. Also, a theoretical analysis[9] predicts a slight increase in resistivity for α-brass upon short-range ordering.

(2) The decay times associated with the decrease of resistivity of quenched α-brass were found to be consistent with the relaxation times observed in the stress-relaxation experiments of CHILDS and LE CLAIRE[10]. In the preceding letter,[2] the point was made that this observation indicates that the relevant energy with which the quench-annealing occurs is the self-diffusion energy, Q and not the motion energy of vacancies, ϵ_M, which should be about $0{\cdot}5Q$. In this regard the behavior of Cu-Al alloys differs from that of Cu-Zn alloys, since, as is described in a recent paper,[11] resistivity measurements of the annealing of quenched Cu-Al alloys give an activation energy that increases from 0·7 to 1·2 eV during the annealing. This energy is about one-half of the self-diffusion energy of $Q = 1{\cdot}8$ eV obtained from stress relaxation experiments[10,12] on annealed

* Cf. the review papers cited in Ref. (1).

samples of Cu-Al alloys. Furthermore, stress-relaxation measurements[12] on quenched Cu-Al alloys yield the lower relaxation times characteristic of additional vacancy concentrations and a corresponding activation energy for vacancy motion of $\epsilon_M = 1{\cdot}08$ eV. In our experiments[1] on the kinetics of the radiation-induced decrease in resitivity, the effective motion energy was measured during the course of the annealing and was found to approach asymptotically the value 1·0 eV, in good agreement with LI and NOWICK's value of 1·08 eV for vacancy motion. This comparison between stress-relaxation effects and resistivity changes upon quenching and irradiation suggests that some consideration should be given to the possibility that the resistivity changes are associated with changes in vacancy concentrations.

The point raised by DIENES and DAMASK (item 3) concerning the theoretical energy of formation of vacancies of 0·73 eV obtained by taking the difference of the diffusion and motion energies raises valid doubts concerning whether the equilibrium concentration of vacancies at 200°C is sufficiently large to cause an excess resistivity of 0·2 $\mu\Omega$-cm. However, resistivity measurements[11] made at temperature and upon quenching show that an excess resistivity contribution is indeed made at 200°C and higher, and the energy of formation corresponding to this excess resistivity is about 0·2 eV. If this value is used for the formation energy of vacancies and if the presently accepted values for the pre-exponential factor (of the order of unity) and the resistivity increase due to vacancies (1-2 $\mu\Omega$-cm per atomic per cent vacancies) are selected, then one finds that vacancies quenched-in from 200°C could reasonably contribute a resistivity of 0·2 $\mu\Omega$-cm. It has been pointed out[11] that low energies of formation have been reported for other alloys. Still, if the energy of formation of vacancies were as low as 0·2 eV, the question arises as to why the sum of the formation and motion energies, $0{\cdot}2 + 1{\cdot}0 = 1{\cdot}2$ eV, falls short of the 1·8 eV required for diffusion. It may be that a fraction of the equilibrium number of vacancies remains bound to solute atoms and is not able to take part in the diffusion process, although it does contribute to the resistivity. This would have the effect of increasing the diffusion energy by an amount corresponding to the binding energy of a vacancy-solute atom pair. However, the necessary binding energy appears rather large.

As concerns the last paragraph in the preceding letter, the dependence of the rate of decrease of resistivity upon the temperature of irradiation also indicates a difference in the behavior of Cu-Al and Cu-Zn alloys. Our in-pile measurements of the resistivity of Cu-Al alloys show a considerable variation in the decay rate when the irradiation temperature is varied over a sufficiently wide range. For example, the times for 50 per cent decrease in resistivity for the 15 atomic per cent Al alloy are 1·3 and 20 hr for irradiation temperatures of 100 and 45°C, respectively.

The point regarding the recent measurements[13] of lattice parameter of α-brass upon irradiation is well taken. Measurements of changes in lattice parameter and density upon irradiation of α-Cu-Al are in progress at ORNL.

It should be said that it is not our contention that no short-range order is present in either Cu-Zn or Cu-Al alloys. A truly random solid solution is expected to occur rarely, because of the difficulty in achieving a zero value for the mixing energy, $W_{AA} + W_{BB} - 2W_{AB}$. Furthermore, if the irradiation causes the annealing of a non-equilibrium number of vacancies, it is not unlikely that a change in the short-range order will take place in the course of the atomic rearrangement brought about by this vacancy motion. The essential question seems to be whether the decrease in restivity upon irradiation is primarily due to a reduction of the num-

ber of vacancies present or to changes in short-range order. Our experiments on Cu-Al alloys indicate that it is not easy at present to answer this question. It seems to us that a reasonable view to adopt is that, although some information is available, the origin of the radiation-induced decreases in resistivity has not been clearly established. Further careful investigation is necessary before a reliable interpretation can be made.

M. S. WECHSLER

R. H. KERNOHAN

Solid State Division, Oak Ridge National Laboratory, Oak Ridge, Tennessee

VOL. 12 59/60

REFERENCES

1. WECHSLER M. S. and KERNOHAN R. H., *J. Phys. Chem. Solids* **7**, 307 (1958).
2. DAMASK A. C. and DIENES G. J., **12**, 105 (1959)
3. ROSENBLATT D. B., SMOLUCHOWSKI R., and DIENES G. J., *J. Appl. Phys.* **26**, 1044 (1955).
4. DAMASK A. C., *J. Appl. Phys.* **27**, 610 (1956).
5. DAMASK A. C., *J. Phys. Chem. Solids* **4**, 177 (1958).
6. DIENES G. J. and DAMASK A. C., *J. Appl. Phys.* **29**, 1713 (1958).
7. BURNS F. P. and QUIMBY S. L., *Phys. Rev.* **97**, 1567 (1955).
8. DAMASK A. C., *J. Phys. Chem. Solids* **1**, 23 (1956).
9. GIBSON J. B., *J. Phys. Chem. Solids* **1**, 27 (1956).
10. CHILDS B. G. and LE CLAIRE A. D., *Acta Met.* **2**, 718 (1954).
11. WECHSLER M. S. and KERNOHAN R. H., *Acta Met.* **7**, 599 (1959).
12. LI C. Y. and NOWICK A. S., *Phys. Rev.* **103**, 294 (1956).
13. FEDER, R., NOWICK A. S., and ROSENBLATT D. B. *J. Appl. Phys.* **29**, 984 (1958).

VC
1
1959/

Printed in Poland to the order of Państwowe Wydawnictwo Naukowe, Warszawa
by Zakłady Graficzne im. M. Kasprzaka, Poznań

J. Phys. Chem. Solids Pergamon Press 1959. Vol. 12. pp. 111–118. Printed in Great Britain.

CRYSTAL CHEMICAL AND MAGNETIC STUDIES OF GARNET SYSTEMS $M_3^{2+}Fe_2Sn_3O_{12}$—$Y_3Fe_2Fe_3O_{12}$

S. GELLER, R. M. BOZORTH, M. A. GILLEO and C. E. MILLER

Bell Telephone Laboratories, Inc., Murray Hill, New Jersey

(*Received* 2 *June* 1959)

VOL. 12 59/60

Abstract—A complete solid-solution range exists in the system $Ca_3Fe_2Sn_3O_{12}$(CIS)—$Y_3Fe_2Fe_3O_{12}$ (YIG). Because of its large size, the Sn^{4+} ion prefers the octahedral positions; thus for dilute solutions of CIS in YIG the saturation magnetization at 0°K increases. A maximum of 7·3 μ_B per formula unit is reached at about 20 mol. per cent CIS solid solution. However, the plot of $n_B(\infty, 0)$ vs. composition deviates markedly from that which depends only on a simple interaction model. At 33 mol. per cent CIS, $n_B = 5{\cdot}2\ \mu_B$, and at 50 mol. per cent, $n_B = 1{\cdot}2\ \mu_B$, even though the Sn^{4+} ions are very nearly all in the octahedral sites. At 67 mol. per cent CIS, 90 per cent of the octahedral sites are filled with Sn^{4+} ions, as determined by X-ray diffraction, and $n_B \approx 0{\cdot}25\ \mu_B$. The magnetic behavior of this system may be explained on the basis of the reduction of the number of octahedral–tetrahedral magnetic-ion interactions with increasing concentration of CIS and, at the higher concentrations, the establishment of two magnetic sublattices among the tetrahedral ions.

No other end-members $M_3^{2+}Fe_2Sn_3O_{12}$ were obtained, but with M = Sr the extent of solubility in YIG is ~ 33 mol. per cent, and when M = Ba, < 5 mol. per cent. Some inconclusive experiments also indicated some solution when M = Cd, Zn, Mn, Ni and Mg.

1. INTRODUCTION

THE garnet structure belongs to space-group O_h^{10}—*Ia*3*d* with metal ions in 16*a*, 24*c* and 24*d* and oxygen ions in 96*h*. If the distribution of the metal ions is known, it is convenient to write the chemical formula of one unit as $\{A_3\}[B_2](C_3)O_{12}$,[1] where { } represents a *c* or dodecahedral site, [ ] an *a* or octahedral site and ( ) a *d* or tetrahedral site. The dodecahedral and octahedral sites are accessible to both magnetic and nonmagnetic ions of a large variety; the tetrahedral sites are accessible to a large variety of nonmagnetic ions also, but only *one* magnetic ion, namely Fe^{3+}. Except for Co^{2+}, the octahedral and tetrahedral sites in the garnets prefer to be filled with ions having spherical electronic configurations;[2,3] the dodecahedral sites are nonselective as to electronic configuration, but are usually preferred by ions of large size.

In work reported earlier,[2] substitution of other trivalent ions for Fe^{3+} in $\{Y_3\}[Fe_2](Fe_3)O_{12}$ was investigated. The results of this work indicated that among *nonmagnetic* ions the larger ones preferred the octahedral sites, the smaller ones the tetrahedral sites. Despite the fact that the Cr^{3+} ion is smaller than Fe^{3+},[4] it prefers the octahedral site, presumably because only in the octahedral crystal field is the ground state of Cr^{3+} spherical.

Attempts to make new silicate garnets with magnetic ions in both the dodecahedral and octahedral positions by direct-synthesis techniques did not prove fruitful.[5] However, a number of new silicate garnets, as well as all those which occur in nature, have been synthesized at high pressures by COES[6].

Garnets containing the Ge^{4+} ion, presumably analogous to silicate garnets, were first synthesized by TAUBER *et al.*[7], but it has been established in at least two cases[7,8] that all of the Ge^{4+} ions do not occupy tetrahedral sites. In fact, even in the silicates, it is probable that sometimes Si^{4+} ions go into octahedral sites.[8] The *amounts* of ions in particular sites will depend largely on their electronic structures and their relative sizes. For example, although the solid solution

$$\tfrac{2}{3}(Y_3Fe_2Fe_3O_{12})\text{–}\tfrac{1}{3}(Ca_3Fe_2Ge_3O_{12})$$

has the ionic distribution given by

$$\{Y_2Ca\}[Fe_{1.85}Ge_{0.15}](Fe_{2.15}Ge_{0.85})O_{12},^{[8]}$$

the garnet $\{Gd_3\}[Mn_2](GaGe_2)O_{12}$ has the distribution indicated by the brackets, i.e. the Ga^{3+} and Ge^{4+} ions fill the tetrahedral sites.[1]

The discovery of the garnet $Ca_3Fe_2Sn_3O_{12}$ and of solid solutions with $Y_3Fe_2Fe_3O_{12}$ was first reported by GELLER and MILLER some time ago,[9] but the magnetic and crystallographic studies on this and related systems have only recently been completed and these form the subject matter of the present paper.

At the outset, one wonders whether the tetravalent nonmagnetic atoms will behave like the trivalent ones, i.e. whether the size is important in determining the site preference. The question also arises as to the effect on the magnetic properties of the amount of the substitution of Sn^{4+} for Fe^{3+}. It would be particularly interesting if the Sn^{4+} ion showed a great preference for the octahedral positions, as would be expected on the basis of its size. It will be remembered that there appeared to be limitations on the extent to which studies could go of substituting large trivalent ions, Sc^{3+} or In^{3+}, for Fe^{3+} ions in the octahedral sites.[2] It has turned out that the Sn^{4+} ion has permitted us an extension of our magnetic studies on the garnets.

2. EXPERIMENTAL

(a) *Preparation of compounds*

In the preparation of $Ca_3Fe_2Sn_3O_{12}$ and solid solutions of this garnet in $Y_3Fe_2Fe_3O_{12}$ and specimens in related systems to be described in this paper, the required amounts of oxides were thoroughly mixed and ground together in an agate mortar. Pellets were made by compacting the thoroughly mixed reaction mixtures. These were fired at 1400°C in air for 2 hr. Usually specimens were reground and refired two to four times until pure garnet phases were obtained, as shown by X-ray powder photographs with sharp lines. The end-member $Ca_3Fe_2Sn_3O_{12}$ was not obtained without the presence of small amounts of $CaSnO_3$ (perovskite-like structure) and α-Fe_2O_3.

(b) *Diffraction data*

X-ray powder photographs were taken of all specimens with Straumanis-type Norelco cameras of 114·59 mm. diameter; CrK radiation was used. Diffraction patterns were also recorded for samples of nominal formulae $CaY_2Fe_4SnO_{12}$ and $Ca_2YSn_2Fe_3O_{12}$ with a Norelco diffractometer, using filtered CuK_α radiation. The integrated intensities obtained were used for determining the ionic distributions in these specimens.

(c) *Magnetic measurements*

The measurements on the solid solution

$$\{Ca_{0.25}Y_{2.75}\}[Fe_{1.75}Sn_{0.25}](Fe_3)O_{12}$$

shown in Fig. 1 were made by the method described briefly in Reference (2). All other magnetic

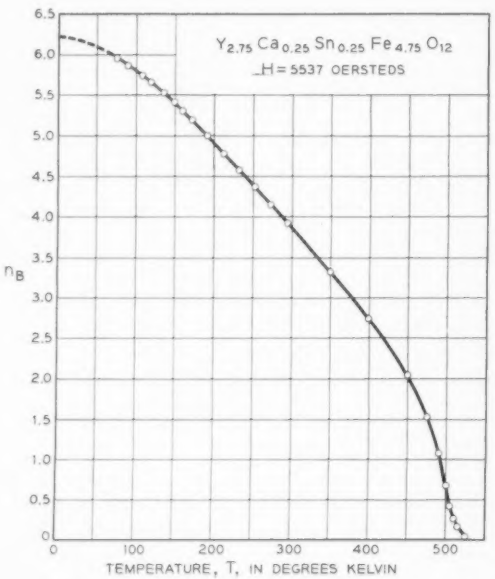

FIG. 1. Magnetization of $\frac{1}{12}$CIS–$\frac{11}{12}$YIG.

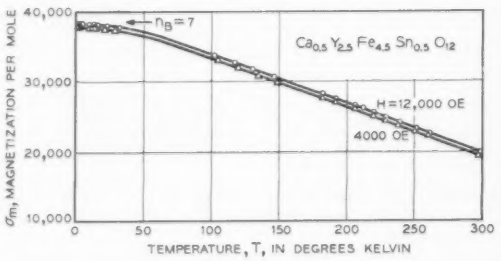

FIG. 2. Magnetization of $\frac{1}{8}$CIS–$\frac{7}{8}$YIG.

measurements (see e.g. Figs. 2 and 3) were made as described in Reference (8) in fields to 12,500 Oe and at temperatures of 1·3–300°K (Figs. 2 and 3).

Saturation magnetization was determined in the garnets of Figs. 2 and 3 by extrapolation to $T = 0$ and to $H = \infty$, using the $1/H^2$ relation from $H = 8000$ to 12,000 or 12,500 Oe. For still higher tin contents the proper method of extrapolation was not entirely clear; in the case of $Ca_2YSn_2Fe_3O_{12}$ the extrapolation was made to $H = 0$.

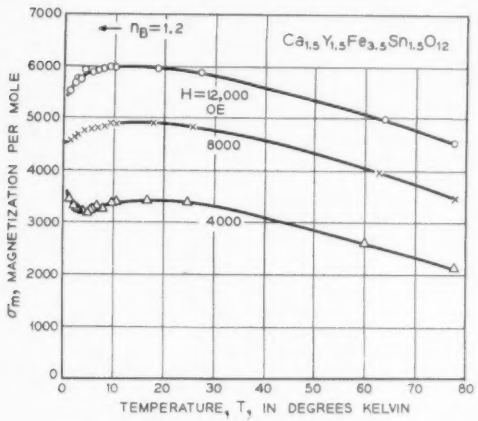

FIG. 3. Magnetization of $\frac{1}{2}$CIS–$\frac{1}{2}$YIG.

3. CRYSTALLOGRAPHIC DATA

The systems studied crystallographically were

$$M_3^{2+}Fe_2Sn_3O_{12}–Y_3Fe_2Fe_3O_{12},$$

where M = Ca, Sr, Ba, Cd, Zn, Mn, Ni or Mg. Only in the case of calcium does a complete solid-solution range exist. The lattice constants for the specimens prepared in the system M = Ca are listed in Table 1 and plotted in Fig. 4. The limit of

Table 1. *Lattice constants of the* $Ca_3Fe_2Sn_3O_{12}$–$Y_3Fe_2Fe_3O_{12}$ system

Mol.-% $Ca_3Fe_2Sn_3O_{12}$	Lattice constant (Å)
0	12·376
8·3	12·407
16·7	12·44
33·3	12·502
41·7	12·530
50·0	12·558
66·7	12·620
100	12·728*

* This is the largest garnet cell reported to date.

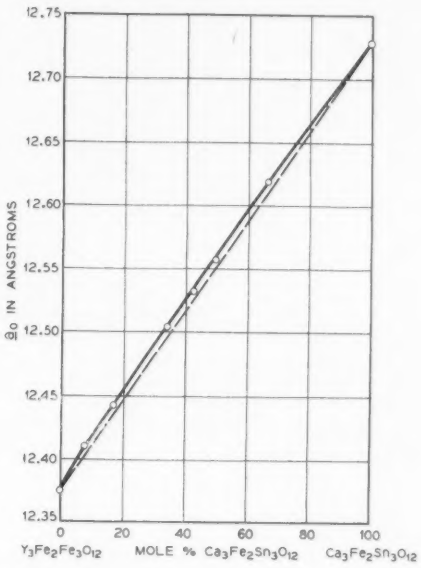

FIG. 4. Lattice constant vs. composition of $Ca_3Fe_2Sn_3O_{12}$–$Y_3Fe_2Fe_3O_{12}$ system.

solid solubility in the system for which M = Sr (Table 2 and Fig. 5) appears to be close to 33 mol. per cent, because a 67 mol. per cent "$Sr_3Fe_2Sn_3O_{12}$"

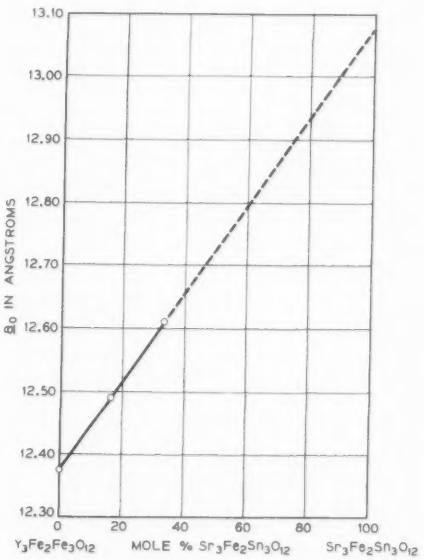

FIG. 5. Lattice constant vs. composition of "$Sr_3Fe_2Sn_3O_{12}$"–$Y_3Fe_2Fe_3O_{12}$ system.

Table 2. Lattice constants of the "$Sr_3Fe_2Sn_3O_{12}$"–$Y_3Fe_2Fe_3O_{12}$ *system*

Mol.-% "$Sr_3Fe_2Sn_3O_{12}$"	Lattice constant (Å)
16·7	12·49
33·3	12·61

sample yielded the perovskite $SrSnO_3$ and a garnet phase of lattice constant approximately that of the 33·3 mol. per cent "$Sr_3Fe_2Sn_3O_{12}$" specimen. The limit of solubility of "$Ba_3Fe_2Sn_3O_{12}$" in YIG is < 5 mol. per cent under the conditions of the experiment. A specimen made with the starting reactants equivalent to this solid solution yielded a garnet phase with lattice constant $12{\cdot}390 \pm 0{\cdot}004$ Å. However, the powder photograph indicated the presence of at least one foreign phase. In the cases of the five other divalent ions, 8·3 and 25 mol. per cent solid solutions were tried. In all cases there was indication of some solution, but none of the specimens produced gave a single garnet-phase powder-diffraction photograph.

In the cases of Sr^{2+} and Ba^{2+} it is probable that the end-members

$$\{M_3^{2+}\}[Sn_xFe_{2-x}](Fe_ySn_{3-y})O_{12}$$

do not exist because of the large sizes of these two ions. In the other cases the interrelationships of the ionic sizes are unfavorable. Possibly the problem is a chemical one, that is, the compounds do not exist under the particular conditions of these experiments; perhaps these could be made at high pressures, as in the case of $\{Mn_3\}[Fe_2](Si_3)O_{12}$.[5,6]

The composition vs lattice constant relation for the $Ca_3Fe_2Sn_3O_{12}$–$Y_3Fe_2Fe_3O_{12}$ system (Fig. 4) is not linear. Similarly one should not expect this relation to be linear for the "$Sr_3Fe_2Sn_3O_{12}$"–$Y_3Fe_2Fe_3O_{12}$ system, although the deviation from linearity should not be very great. Thus if the garnet $Sr_3Fe_2Sn_3O_{12}$ did exist, its lattice constant would be $\sim 13{\cdot}07$ Å (Fig. 5).

4. ION DISTRIBUTION FROM X-RAY DIFFRACTION ANALYSIS

From the X-ray powder photographs taken of the various specimens in this system, it was apparent that the Sn^{4+} ions must prefer the octahedral sites. The best sample on which to test this hypothesis quantitatively appeared to be that containing 67 mol. per cent $Ca_3Fe_2Sn_3O_{12}$. (The end-member $Ca_3Fe_2Sn_3O_{12}$ was not obtained as a completely isolated phase; some $CaSnO_3$ and probably some Fe_2O_3 were present.) This sample and the others with higher $Y_3Fe_2Fe_3O_{12}$ content were all pure, and gave sharp powder photographs. If all of the Sn^{4+} ions went into the octahedral sites, the formula of this solid solution would be

$$\{Ca_2Y\}[Sn_2](Fe_3)O_{12}.$$

Actually it appears that the octahedral sites are probably filled only to the extent of about 90 per cent by Sn^{4+} ions and about 10 per cent by Fe^{3+} ions, so that the formula is more likely to be closer to

$$\{Ca_2Y\}[Sn_{1{\cdot}8}Fe_{0{\cdot}2}](Fe_{2{\cdot}8}Sn_{0{\cdot}2})O_{12}.$$

The distribution of ions was estimated as follows; powder X-ray diffraction patterns of the sample were recorded with a Norelco diffractometer, using CuK_α radiation. Integrated intensities were measured. The temperature factors of the atoms and the distribution of ions were determined by trial and error. In the calculation of intensities,* the following atomic scattering factors were used: for Fe^{3+}, Y^{3+} and Sn^{4+} the values of THOMAS and UMEDA[10], for Ca^{2+} those of JAMES and BRINDLEY[11] and for O^{2-} those of BERGHUIS *et al.*[12] for O arbitrarily modified so that $f_{O^{2-}} = 10{\cdot}00$ at $(\sin\theta)/\lambda = 0$ and $f_{O^{2-}} = f_O$ for all values of $(\sin\theta)/\lambda > 0{\cdot}20$. Corrections were made for dispersion[13] of the CuK_α radiation by the metal ions. (Only the real part of the correction was applied.)

The atomic coördinates of the oxygen atoms were estimated on the basis of other structural knowledge. In the

$$\{Y_3\}[Fe_2](Fe_3)O_{12}$$

crystal the octahedral Fe–O distance[14] is 2·00 Å. In

$$\{Y_3\}[Al_2](Al_3)O_{12}{}^{[15]}$$

and in

$$\{Ca_3\}[Al_2](Si_3)O_{12},{}^{[16]}$$

the octahedral Al–O distance is 1·95 Å. The CN(6)

* $I_{hkl} = p|F_{hkl}|^2L \cdot P \times 10^{-6}$, where p = multiplicity factor, F = structure amplitude, $L \cdot P$ = Lorentz-polarization factors.

radii obtained from the perovskite-like compounds[17] give 1·97 and 1·90 Å respectively for the Fe–O and Al–O octahedral distances. Thus the average difference between the values obtained from these radii and the known distances in the garnets is ~ 0·04 Å.

The volume per formula unit of the perovskite-like $CaSnO_3$[18] is very close to that of $YScO_3$.[19] Furthermore, Ca^{2+} and Y^{3+} have very nearly the same size in the garnets.[16] Therefore it may be assumed that the Sc^{3+} and Sn^{4+} ions have very nearly the same effective CN(6) sizes in both the perovskite-like compounds and in the garnets. The Sc–O octahedral distance obtained from the CN(6) radii derived by GELLER[17] is 2·03 Å. Thus one may assume that the octahedral Sn–O distance in the tin garnets is 2·07 Å, taking into consideration the 0·04 Å difference mentioned earlier. This value is also in accord with the values 2·052 and 2·056 Å obtained[20] for the Sn–O distances in SnO_2 with the rutile-type structure.

Further consideration of the results of the structure refinements of

$$\{Y_3\}[Fe_2](Fe_3)O_{12}$$

and

$$\{Ca_3\}[Al_2](Si_3)O_{12},$$

together with the ideas formulated above, led to the following estimates for the oxygen parameters: $x = -0{\cdot}026$, $y = 0{\cdot}057$, $z = 0{\cdot}152$. In calculations of intensities,* ion distribution was varied from 100 to 80 per cent Sn^{4+} in octahedral sites.† Also, temperature factors were changed to bring about a better fit of calculated with observed data. Oxygen coördinates were not varied because of the lack of sensitivity of the observed intensities (see Ref. 14) to changes in these coördinates. The final temperature factors used are: $B_{Ca} = 1{\cdot}0$, $B_Y = 0{\cdot}5$, $B_{Fe} = 0{\cdot}8$, $B_{Sn} = 0{\cdot}0$ and $B_O = 1{\cdot}8$ Å^2. The calculated

* We wish to thank Dr. R. G. TREUTING for aiding us in the use of his IBM 704 programs for these computations. We wish also to thank Miss D. Leagus for her aid with some of the calculations.

† A calculation based on 50 per cent Sn^{4+} ion in octahedral sites was also made. This calculation left no doubt that the occupancy by Sn^{4+} of the octahedral sites was much higher than 50 per cent.

Table 3. Calculated and observed intensities for $\{Ca_2Y\}[Sn_{1.8}Fe_{0.2}](Fe_{2.8}Sn_{0.2})O_{12}$ *(CuK_α radiation)*

$h^2+k^2+l^2$	$d_{calc.}$	$I_{obs.}$	$I_{calc.}$	$h^2+k^2+l^2$	$d_{calc.}$	$I_{obs.}$	$I_{calc.}$
8	4·462	89	87	116	1·172	30	29
16	3·155	176	177	120	1·152	56	55
20	2·822	190	196	128	1·115	34	30
22	2·691	17	17	136	1·082	5	5
24	2·576	248	285	144	1·052	29	27
26	2·475	11	9	148	1·037	6	7
30	2·304	8	6	152	1·024	65	63
32	2·231	7	6	160	0·9977	4	4
38	2·047	11	5	168	0·9737	4	7
40	1·995	36	35	180	0·9406	19	20
48	1·822	7	5	184	0·9304	40	36
52	1·750	71	77	192	0·9108	16	16
56	1·686	235	232	200	0·8924	15	15
64	1·578	46	51	208	0·8750	21	20
72	1·487	16	14	212	0·8668	17	20
80	1·411	55	54	216	0·8587	88	89
84	1·377	35	34	224	0·8432	7	8
88	1·345	44	46	232	0·8285	0*	5
96	1·288	7	8	244	0·8079	30	28
104	1·237	10	11	248	0·8014	134	134

Note: All lines not listed were either space-group absences or were not observed with corresponding calculated values all less than 1.

* This line could be lost in the background.

and observed intensities are listed in Table 3. The agreement is seen to be quite satisfactory for 90 per cent Sn^{4+} ion in octahedral sites.

Following the magnetic measurements on the various specimens, it appeared necessary (see later discussion) to analyze at least one other specimen in the same way as we did the specimen

$$\{Ca_2Y\}[Sn_{1.8}Fe_{0.2}](Fe_{2.8}Sn_{0.2})O_{12}.$$

The specimen chosen had the formula

$$\{Ca_2Y\}[Sn_{1.8}Fe_{0.2}](Fe_{2.8}Sn_{0.2})O_{12}.$$

This specimen gave a saturation magnetization of 0°K of 5·2 μ_B, indicating that perhaps the Sn^{4+} ions might be more nearly equally distributed over the octahedral and tetrahedral sites. Having found that most of the Sn^{4+} ions in

$$\{Ca_2Y\}[Sn_{1.8}Fe_{0.2}](Fe_{2.8}Sn_{0.2})O_{12},$$

were in octahedral sites, it seemed unlikely that the specimens containing less Sn^{4+} would have more Sn^{4+} ion in tetrahedral sites.

As before, the diffraction pattern of

$$CaY_2SnFe_4O_{12}$$

was taken on the Norelco diffractometer, using CuK_α radiation. Atomic scattering and temperature factors were the same as those used before. Dispersion corrections were also made (real part only). Oxygen coördinates were taken halfway between those of YIG and those used to calculate intensities for

$$\{Ca_2Y\}[Sn_{1.8}Fe_{0.2}](Fe_{2.8}Sn_{0.2})O_{12},$$

namely (—0·026, 0·057, 0·151). Because it was felt that the distribution should be very nearly as indicated by $\{CaY_2\}[SnFe](Fe_3)O_{12}$, the calculations were based on this model. It is seen (Table 4) that the agreement between calculated and observed intensities confirms the predicted ion distribution.

Intensities have also been measured and calculated for $Ca_3Fe_2Sn_3O_{12}$. It is highly probable that 90 per cent or more of the octahedral sites are filled with Sn^{4+} ions in this compound also.

As expected, it has been found that when $Ca_3Fe_2Sn_3O_{12}$ melts, it decomposes into the perovskite-like $CaSnO_3$ and α-Fe_2O_3.

5. DISCUSSION

The results of this work, together with those in other reports,[3,8] indicate that the tetravalent Group IV ions of Si, Ge and Sn behave in much

Table 4. *Calculated and observed intensities for* $\{CaY_2\}[SnFe](Fe_3)O_{12}$ (CuK_α *radiation*)

$h^2+k^2+l^2$	$d_{calc.}$	$I_{obs.}$	$I_{calc.}$	$h^2+k^2+l^2$	$d_{calc.}$	$I_{obs.}$	$I_{calc.}$
6	5·104	6	8	84	1·364	43	41
8	4·420	23	22	88	1·333	36	32
16	3·126	130	135	116	1·161	39	36
20	2·796	214	240	120	1·141	40	39
22	2·665	13	8	128	1·105	27	26
24	2·552	191	205	144	1·042	20	19
26	2·452	13	9	148	1·028	9	9
30	2·283	16	14	152	1·014	38	44
38	2·028	18	15	176	0·9424	4	4
40	1·977	12	11	180	0·9318	28	25
48	1·805	19	16	184	0·9217	28	25
52	1·734	86	84	192	0·9023	18	14
54	1·701	5	3	200	0·8840	n.o.	4
56	1·671	170	175	208	0·8669	14	14
64	1·563	42	46	212	0·8586	32	25
72	1·473	3	3	216	0·8507	64	64
80	1·398	43	40	244	0·8004	48	38
				248	0·7939	97	101

Note: All lines not listed were either space-group absences or were not observed with corresponding calculated values all less than 2.

the same way in their *site preference* in the garnet structures as the trivalent nonmagnetic ions.[2] That is, in their substitution in the octahedral and tetrahedral sites they satisfy first of all the criterion of spherical electronic configuration, and secondly the larger the ion the greater is its preference for the site which allows it more space, namely the octahedral site.

The saturation magnetizations at 0°K of the various specimens are listed in Table 5 and plotted in Fig. 6. Also plotted are the expected values

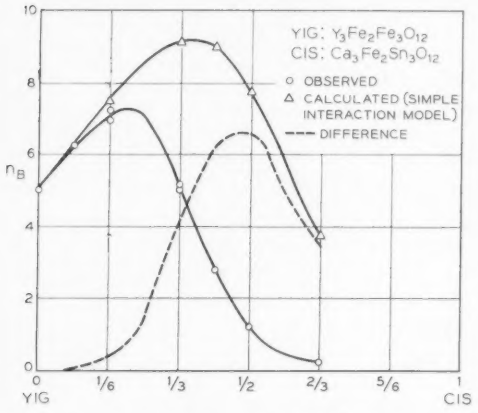

FIG. 6. n_B vs. composition for CIS–YIG system. For discussion of "difference" line, see text.

Table 5. *Saturation magnetizations at* 0°K *and some Curie temperatures of the* $x Ca_3Fe_2Sn_3O_{12}$–$(1-x)Y_3Fe_2Fe_3O_{12}$ *specimens*

x	n_B(Bohr magnetons)	T_C(°K)
0	5·0	545
$\frac{1}{12}$	6·25	498
$\frac{1}{6}$	7·1	≈ 400
$\frac{1}{3}$	5·2	260
$\frac{5}{12}$	2·9	220
$\frac{1}{2}$	1·2	
$\frac{2}{3}$	0·25	

based on the following assumptions: (1) the *a–d* interactions remain the strongest ones regardless of substitution; (2) for all specimens containing more than three Fe^{3+} ions per formula unit, the Sn^{4+} ions are assumed to be entirely in the octahedral sites; (3) the formula for calculating the expected saturation magnetization at 0°K is that given in reference (2) and discussed below. Were all the Sn^{4+} ions in octahedral sites in the specimen $\{Ca_2Y\}Sn_2Fe_3O_{12}$, its saturation magnetization at 0°K would be identically zero, provided that no unbalanced ordering occurred within the tetrahedral sites.

Fig. 6 indicates a marked deviation of the magnetic behavior of the system

$$xCa_3Fe_2Sn_3O_{12}\text{–}(1-x)Y_3Fe_2Fe_3O_{12}$$

from the simple model. This deviation begins at $\frac{1}{12} < x < \frac{1}{6}$, increasing to a maximum of about 6·6 μ_B at $x \simeq \frac{1}{2}$. In this simple model it is considered that the resultant saturation magnetization is determined only by the number of interacting ions. In the paper by GILLEO and GELLER[2], the formula for the saturation magnetization at 0°K is derived by considering that magnetic ions linked only to nonmagnetic ions on the nonequivalent sites do not contribute to the resultant magnetic moment. If this *approach* is correct, the model is obviously only an approximation which, as seen in Fig. 6, is not good beyond about $x = \frac{1}{6}$.

GILLEO[21] has recently extended the above considerations and has found that a model based on the assumption that only those magnetic ions which have interactions with *two* or more magnetic ions on the nonequivalent sites are considered to contribute to the resultant magnetic moment. He has quantitatively accounted for the position of the principal maximum in the n_B vs. composition curve of the CIS–YIG system. The actual predicted values of the saturation magnetizations at 0°K are very close to the observed ones, and the calculated Curie temperatures of several of the compositions are closer to the observed values than would be given by the formula in the GILLEO–GELLER paper.[2]

The model of interaction deduced by GILLEO gives a good approximation to the moment one would expect, if very low-temperature effects are ignored. The character of the magnetization curves for the higher tin contents (Fig. 3 and Fig. 1 of Reference 8) is indicative of possible transitions at very low temperatures (perhaps below 10°K) of the type discussed by YAFET and KITTEL[22]. It appears that when the octahedral sites become filled, or almost filled, with nonmagnetic ions, the system becomes antiferromagnetic or weakly

ferrimagnetic* with possibly two antiparallel magnetic sublattices existing among the magnetic ions in the tetrahedral sites. This behavior is similar to that of the $MnFe_2O$–$ZnFe_2O$ system.[23]

A neutron-diffraction study of this system would prove valuable in determining the exact nature of the magnetic interactions.

We have also observed that in the system

$$Ca_3Fe_2Sn_3O_{12}–Y_3Fe_2Fe_3O_{12},$$

different heat treatments of the specimens do not appear to affect significantly the distribution of the ions; this is unlike the spinel systems.

REFERENCES

1. GILLEO M. A. and GELLER S., *Conference on Magnetism and Magnetic Materials, Phila., Pa.*, Paper No. 131 (1958); also *J. Phys. Chem. Solids* **10,** 187 (1959).
2. GILLEO M. A. and GELLER S., *Phys. Rev.* **110,** 73 (1958).
3. GELLER S. and MILLER C. E., *Acta Cryst., Camb.* (in press).
4. GELLER S., *Acta Cryst., Camb.* **10,** 248 (1957).
5. GELLER S. and MILLER C. E., *Amer. Min.* **44,** 665 (1959).
6. COES L., *J. Amer. Ceram. Soc.* **38,** 298 (1955).
7. TAUBER A., BANKS E., and KEDESDY H., *J. Appl. Phys.* **29,** 385 (1958).
8. BOZORTH R. M. and GELLER S., *J. Phys. Chem. Solids* **11,** 263 (1959).
9. GELLER S. and MILLER C. E., *American Crystallographic Assn. Meeting, Milwaukee, Wis.*, Paper No. A10 (1958).
10. THOMAS L. H. and UMEDA K., *J. Chem. Phys.* **26,** 293 (1957).
11. JAMES R. W. and BRINDLEY G. W., *Z. Krist.* **78,** 470 (1931).
12. BERGHUIS J., HAANAPPEL I. M., POTTERS M., LOEPSTRA B. O., MACGILLAVRY C. H., and VEENENDAAL A. L., *Acta Cryst., Camb.* **8,** 478 (1955).
13. DAUBEN C. H. and TEMPLETON D. H., *Acta Cryst., Camb.* **8,** 841 (1955).
14. GELLER S. and GILLEO M. A., *J. Phys. Chem. Solids* **3,** 30 (1957).
15. PRINCE E., *Acta Cryst., Camb.* **10,** 787 (1957).
16. ABRAHAMS S. C. and GELLER S., *Acta Cryst., Camb.* **11,** 437 (1958).
17. GELLER S., *Acta Cryst., Camb.* **10,** 248 (1957).
18. MEGAW H., *Proc. Phys. Soc.* **58,** 133 (1946).
19. GELLER S., *Acta Cryst., Camb.* **10,** 243 (1957).
20. BAUR W. H., *Acta Cryst., Camb.* **9,** 515 (1956).
21. GILLEO M. A., to be published.
22. YAFET Y. and KITTEL C., *Phys. Rev.* **87,** 290 (1952).
23. GORTER E. W., *Philips Res. Rep.* **9,** 321 (1954) (see also references in this paper).
24. GELLER S., BOZORTH R. M., MILLER C. E. and DAVIS D. D., *J. Phys. Chem. Solids* (in press).

* It is noteworthy that the garnet $\{YCa_2\}[Zr_2](Fe_3)O_{12}$ gives a very similar result, namely its saturation magnetization at 0°K is 0·18 μ_B per formula unit. The system $x\{YCa_2\}[Zr_2](Fe_3)O_{12}–(1-x)Y_3Fe_2Fe_3O_{12}$ has been investigated[24] and details will be published soon.

VOL.
12
59/60

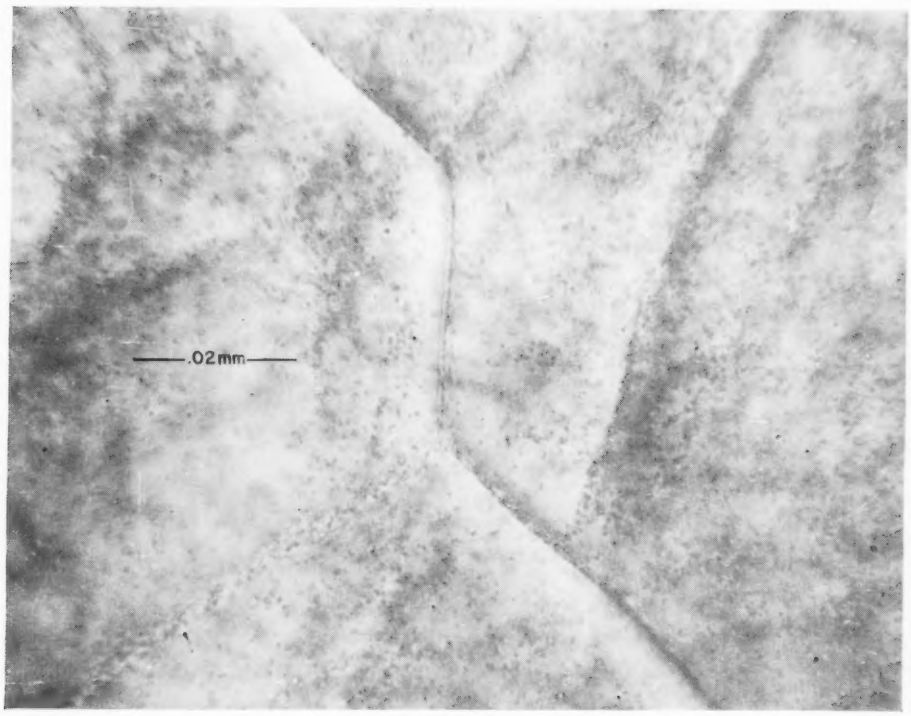

FIG. 1. Substructure formed after acquiring print-out and annealing by taking crystal to 425°C and then cooling to room temperature at an initial rate of 20°C/hr.

[See CHILDS and SLIFKIN, pp. 119–121.]

[*facing p.* 118

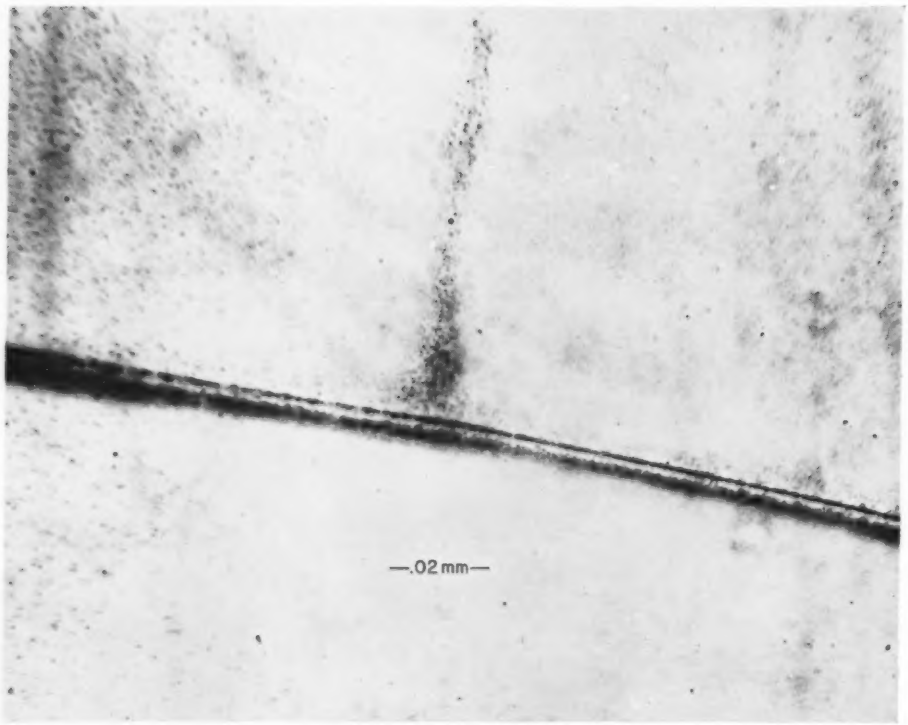

FIG. 2. Substructure formed after acquiring print-out and annealing by taking crystal to 425°C and then cooling to room temperature at an initial rate of 20°C/hr. All substructure, like that of Figs. 1 and 2, had a "three-branch network" where it "joined" with other substructure, as similarly reported by MITCHELL[6].

VOL.
12
59/60

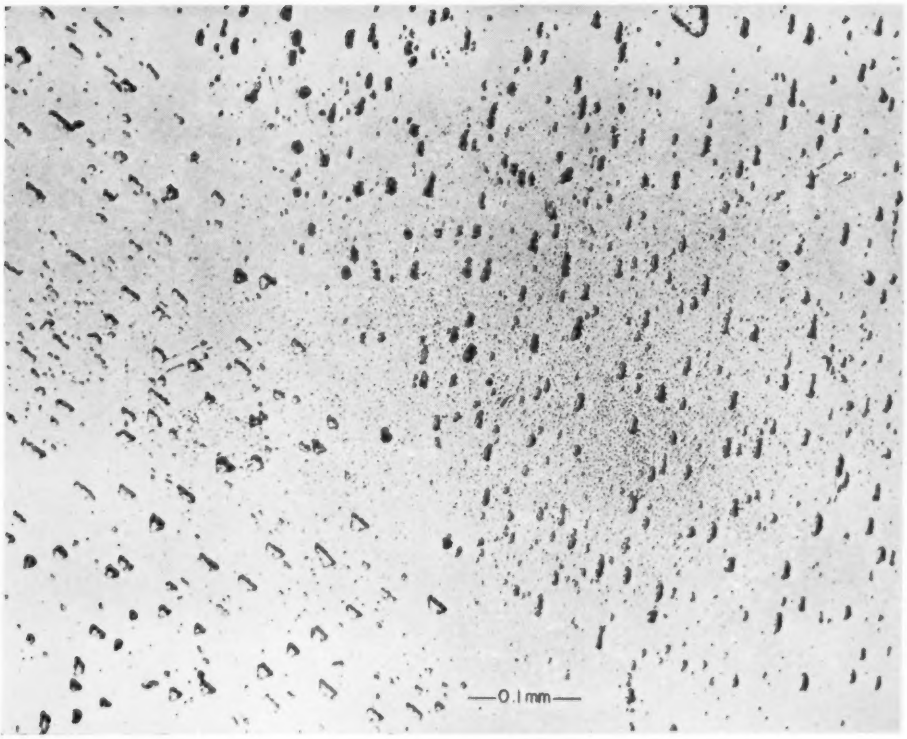

FIG. 3. Large-angle grain boundary on surface of a crystal. The thermal etch-pits were obtained after the crystal had extensive internal print-out and an anneal at 425°C for 10 hr.

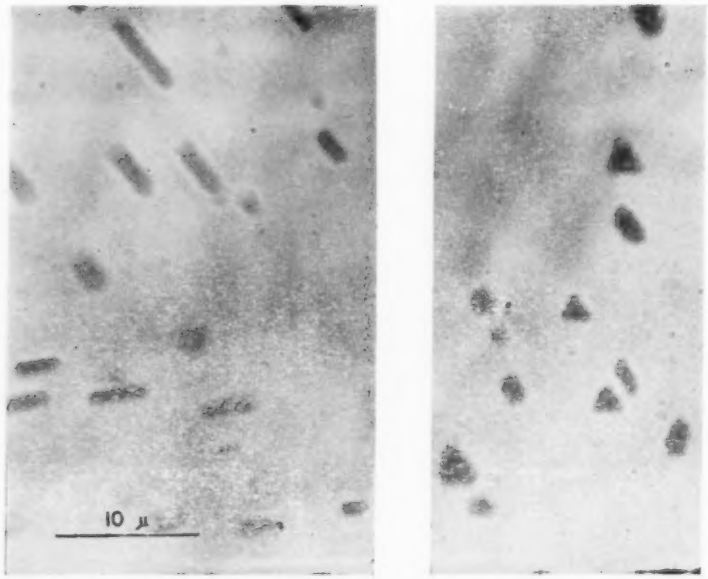

FIG. 4. Internal precipitates after annealing to 425°C and then cooling to room temperature at an initial rate of 20°C/hr, following the formation of internal print-out.

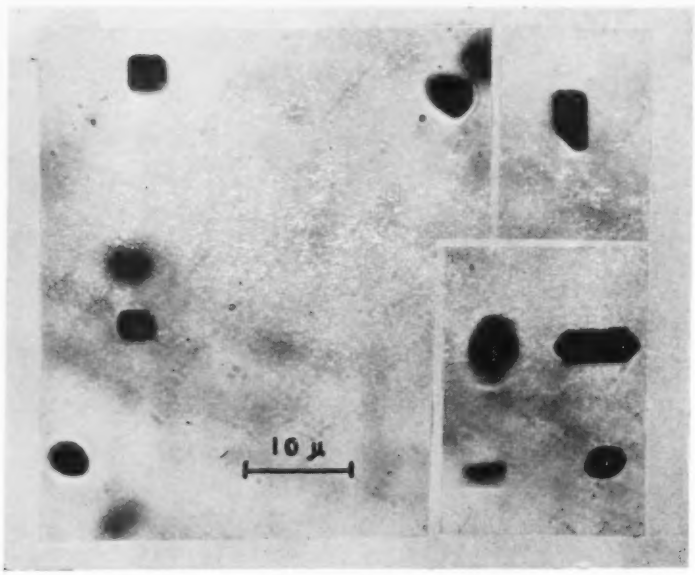

FIG. 5. Internal precipitates after annealing to 425°C and then cooling to room temperature at an initial rate of 20°C/hr, following the formation of internal print-out. Similar silver formations have been observed by AMELINCKX[7] in sodium chloride.

VOL.
12
59/60

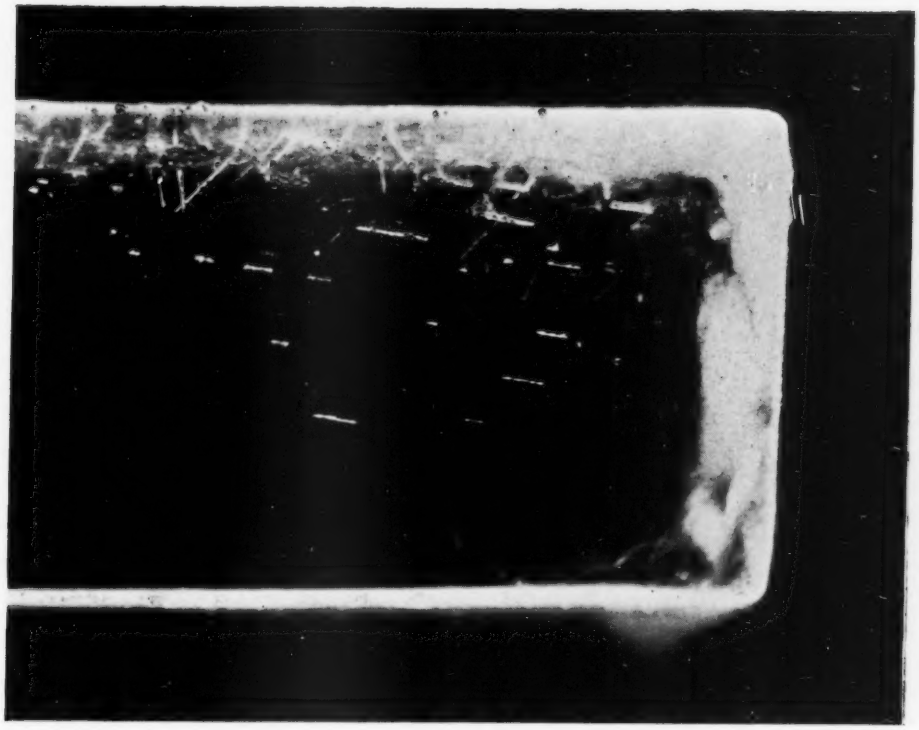

FIG. 6. Typical dark-field illumination of elongated precipitates after annealing in MgO for 40 hr at 425°C. The illumination distorts the diameter of several of the line-precipitates. The precipitates formed throughout volume containing print-out. Shown crystal thickness was approximately 3 mm.

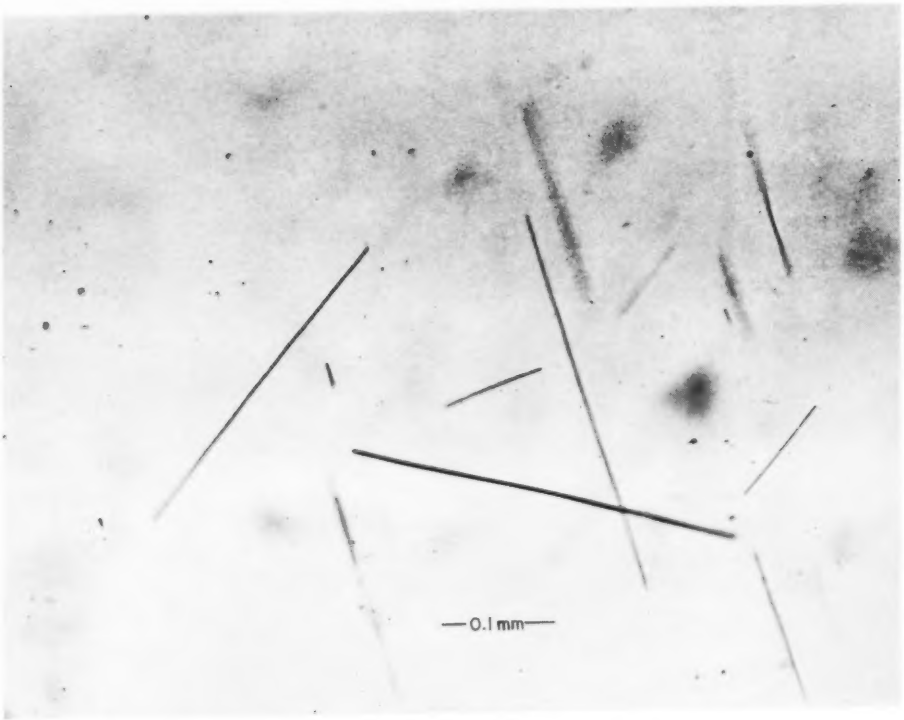

FIG. 7. Line precipitates with larger magnification.

VOL.
12
59/60

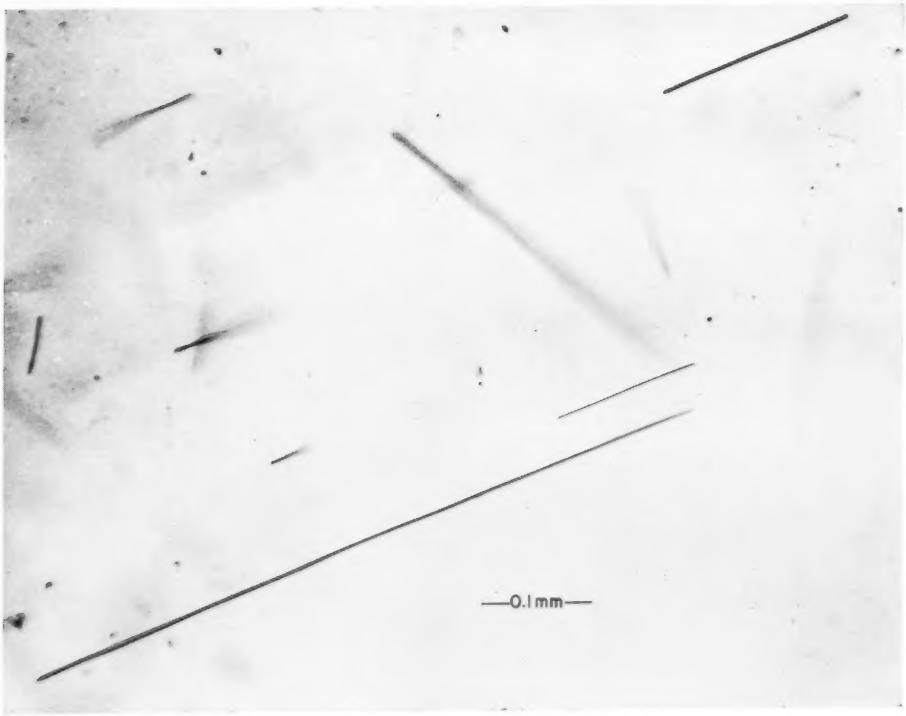

FIG. 8. One of the longer line precipitates observed.

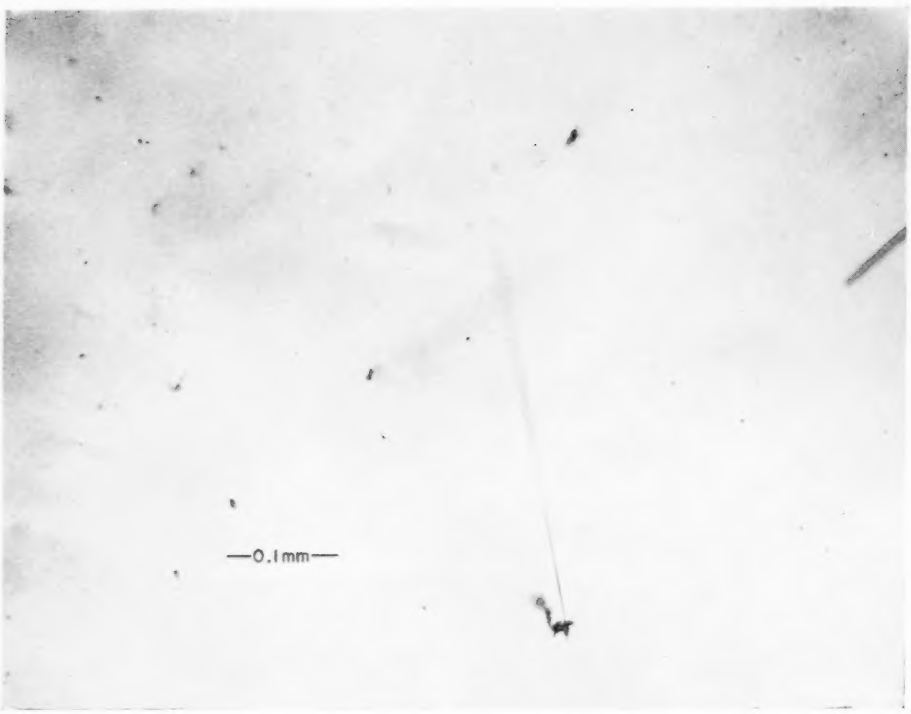

FIG. 9. "Foilage" formed at elongated precipitates when crystals containing the lines are reëxposed. The microscope was focused on the precipitate-end to which electrons would be swept by the decaying polarization field; consequently, the rod appears as a "comet".

J. Phys. Chem. Solids Pergamon Press 1959. Vol. 12. pp. 119–121. Printed in Great Britain.

ANNEALING OF SILVER CHLORIDE CRYSTALS CONTAINING INTERNAL PRINT-OUT*

C. CHILDS† and L. SLIFKIN

University of North Carolina, Chapel Hill, N.C.

(*Received* 23 *June* 1959)

Abstract—The HAYNES–SHOCKLEY technique was used to obtain internal print-out in single silver chloride crystals. Print-out was produced in all crystals from various boules after observing that, in some discs from the boules, the surface deformation from manufacturer disc-shaping had a depth of 2·54 mm. After internal print-out was produced, the crystals were given a short MgO anneal at 425°C, which decorated substructure and produced small internal precipitates with definite geometric configurations. Annealing at 425°C for 40–50 hr produced uniform cylindrical precipitates with diameters of approximately 2 μ and lengths $< 0{\cdot}7$ mm. An investigation of these elongated precipitates showed that they were in the six [110] crystallographic directions. The growth process of these precipitates are shown and discussed.

VOL. 12 59/60

1. INTRODUCTION

HAYNES and SHOCKLEY[1] utilized synchronous pulses of electric field and ultraviolet light to drive electrons deep into silver chloride crystals, resulting in the formation of specks of metallic silver at trapping sites distributed throughout the crystal. Modifications by WEBB[2], HAMILTON *et al.*[3], and SÜPTITZ[4] have further extended the potentialities of this technique. The present paper is concerned with the effects of subsequent annealing on the distribution of the colloidal silver. In particular, under appropriate conditions long, perfectly straight whisker-like formations may be produced in the interior. Observations of the distribution of silver in small and large grain boundaries near the surface are also reported.

2. EXPERIMENTAL

The specimens were in the form of single-crystal slabs milled from Harshaw material. During preparation they were exposed only to light from a yellow "safe-lite". In the subsequent grinding and polishing on metallographic papers, at least 1·75 mm were removed from the surfaces to be exposed to eliminate the material which had been distorted by the machining. Later work showed that some surfaces required 2·54 mm removal before internal print-out was obtained. The crystals were then etched in 3 per cent KCN and washed, resulting in specimens ~ 1 cm^2 in area and 2–5 mm thick. Prior to the ultraviolet exposure, they were annealed for 40–50 hr in air on a powdered MgO surface at ~ 425°C and cooled at a rate of 20°/hr. Another light etch in 3 per cent KCN served to render the surface clear again.

The crystals were exposed to flashes of ultraviolet light provided by a GE BH–6 mercury lamp powered by the repetitive discharges of a Sprague H–850 pulse-forming network. The discharges were initiated by the firing of a 4C35 hydrogen thyratron, which in turn was triggered 1000 times per second. By applying the network potential across the crystal through insulating layers in a manner similar to that employed by HAYNES and SHOCKLEY, voltage pulses of 2 kV were synchronized with the light flashes. These pulses, produced as a result of the short-circuiting of the network, were due to the ionic polarization at the crystal surfaces and served to drive the photoelectrons into and through the crystal. Each flash created approximately 10^9 photoelectrons/cm^2 of crystal

* Supported in part by the Office of Ordnance and Research, Department of the Army.

† Present address: National Aeronautics and Space Administration, Washington, D.C.

surface. The decay time of the flash was 10 μsec, and the subsequent build-up time of the network to one-quarter of its original maximum potential was approximately 200 μsec, thus allowing adequate time for the photoelectrons to complete their trajectories before the polarization field was neutralized. After exposures of the order of 12 hr, a column of colloidal silver could be seen extending throughout the thickness of the crystal. It is the redistribution of this silver upon further annealing with which this paper is concerned.

3. SURFACE OBSERVATIONS

Immediately after exposure, one observes a surface mosaic pattern of print-out consisting of regions of silver of varying intensity, demarcated by lighter lines which are presumably small-angle boundaries. Heating to 225°C produced no visible change, but a brief anneal to 425°C resulted in a clearing up of the dark regions on the surface. The sub-boundaries had now become delineated by an intense collection of silver. This substructure was visible only within about 0·1 or 0·2 mm of the surface. Examples of such decorated boundaries are shown in Figs. 1 and 2. Interestingly, the boundary often appears as a *pair* of planes instead of a single surface. It has been suggested by ESHELBY *et al.*[5] that in alkali halides the charges on dislocations would cause a dislocation wall to really consist of two parallel walls. It may well be that the double patterns seen here are due to a similar effect in silver chloride. It was also observed, as already reported by MITCHELL[6], that large-angle boundaries were not decorated. Fig. 3 is a photograph of the surface of a specimen consisting of two grains. The thermal etch-pits clearly show the presence of a large-angle boundary, but no silver is in evidence.

Prolonged annealing at 425°C results in the complete disappearance of the silver in the surface regions. Presumably, the silver diffuses out of the crystal along the small-angle boundaries at which it had been collected. The fact that no silver is observed on large-angle boundaries, even after a brief anneal at 425°C, may be due to a faster diffusion rate along the large-angle boundaries.

4. INTERNAL OBSERVATIONS

After exposure for 12 hr, the crystals had a cloudy appearance due to the colloidal silver dispersed in the interior. No distinct patterns were observable in the interior, perhaps because of the large amount of scattered light. A brief anneal at 225°C imparted a pink coloration which disappeared within 5 days upon standing in the dark at room temperature, but otherwise there were no apparent effects resulting from the anneal.

Heating to 425°C and immediately cooling at 20°/hr produced some aggregation of the silver into microscopically visible triangular and cylindrical formations with dimensions of the order of a few microns. Examples of these are shown in Figs. 4 and 5. The axes of the rods were parallel to the sides of the triangles. In cases where these patterns were sharply developed, as in Fig. 5, one observed formations identical to those described by AMELINCKX[7] in sodium chloride. These formations were never observed within 0·2 mm of the surface of the crystal.

Prolonged annealing at 425°C ($\sim$ 40–50 hr) produced an unusual effect. After etching, the crystals were perfectly clear, indicating complete disappearance or aggregation of the colloidal silver. Closer examination, however, revealed the presence of very long, whisker-like rods in the interior. Fig. 6 is a dark-field photograph showing these rods (but with diameters exaggerated by the scattered light). These rods were perfectly straight, of constant cross-section and, within the resolving power of the microscope, absolutely smooth. Their appearance under higher magnification is illustrated in Figs. 7 and 8. The density and lengths of these rods varied with the extent of exposure and the initial distribution of print-out silver. Typically, the widths were 2 or 3 μ and the lengths of the order of tenths of a millimeter. The longest rod, shown in Fig. 8, had a length $>$ 0·6 mm. A measurement of the direction cosines of 90 rods in one crystal demonstrated that they were oriented in six directions with angles between them characteristic of the crystallographic [110] axes. In only one case out of hundreds of observations was there found a rod which was fused with another. No rods of any sort were found within 0·2 mm of the surface after the prolonged high-temperature treatment.

One question which arises is whether these whisker-like precipitates have the mechanical strength exhibited by the more conventional whiskers. It was found that, upon etching away the

matrix with hypo, the exposed rods simply crumbled, the only surface change being that the etch-pits at the protruding rods were about three times larger than other etch-pits. It would be surprising if such regular growths were not single crystals, or at least cohesive. Further efforts to extract whole whiskers from the silver chloride matrix are in progress.

In some cases, specimens were re-exposed after producing the rods. It was observed that foliage-like growths appeared at one end of each of those rods which were not approximately normal to the applied field (Fig. 9). This "foliage" always formed at the end toward which the field would drive photoelectrons, thus demonstrating that the rods conduct electrons. After short exposures, this foliage could be seen to have a [110] dendritic structure. It is interesting that whereas the "whiskers" are stable against a 450°C anneal, such an anneal "disolves" the foliage. Elongated precipitates in crystals have been observed before, as in copper-doped aluminum by RUFF and KUSHNER[8], but the present phenomenon is unusual in that the precipitates appear to be straight and regular.

VOL. 12 59/60

5. GROWTH MECHANISM

A possible mechanism for the growth of these whiskers is suggested by the observations of prismatic dislocation "smoke rings" around inclusions in AgC1 by JONES and MITCHELL[9], BARTLETT and MITCHELL[10] and PARASNIS and MITCHELL[11]. These rings move out along the [110] slip directions, each leaving behind a vacant disc one atom distance thick. It thus appears that, in the early agglomeration of the silver, some particles become large enough to "blow out" such rings. At high temperatures, AgC1 is very soft and the stress required to generate and move such rings may well be quite small. One then imagines that the finer particles ionize, evaporate and condense at the ends of the larger rods, generating new dislocation rings as more space is needed. Since no large protrusions are observed at the crystal surfaces, the dislocation rings presumably interact with other dislocations before reaching the surface.

REFERENCES

1. HAYNES J. H. and SHOCKLEY W., *Phys. Rev.* **82,** 935 (1951).
2. WEBB J. H., *J. Appl. Phys.* **26,** 1309 (1955).
3. HAMILTON J. F., HAMM F. A., and BRADY L. E., *J. Appl. Phys.* **27,** 874 (1956).
4. SÜPTITZ P., *Z. Phys.* **153,** 174 (1958).
5. ESHELBY J. D., NEWEY C. W. A. PRATT P. L. and LIDIARD A. B., *Phil. Mag.* **3,** 75 (1958).
6. MITCHELL J. W., *Dislocations and Mechanical Properties of Crystals* (Ed. FISHER J. C. *et al.*), Lake Placid Conference (1956).
7. AMELINCKX S., *Dislocations and Mechanical Properties of Crystals* (Ed. FISHER J. C. *et al.*), Lake Placid Conference (1956).
8. RUFF A. W., Jr. and KUSHNER L. M., *Proceedings of the 2nd International Symposium on X-Ray Microscopy and X-Ray Microanalysis*, Stockholm (1959) (to be published).
9. JONES D. A. and MITCHELL J. W., *Phil. Mag.* **3,** 1 (1958).
10. BARTLETT J. T. and MITCHELL J. W., *Phil. Mag.* **3,** 334 (1958).
11. PARASNIS A. S. and MITCHELL J. W., *Phil. Mag.* **4,** 171 (1959).

J. Phys. Chem. Solids Pergamon Press 1959. Vol. 12. pp. 122–129. Printed in Great Britain.

PHASE TRANSITIONS AND COMPRESSIONS OF SOLID CH_4, CD_4 AND O_2*

J. W. STEWART

University of Virginia, Charlottesville, Virginia

(*Received* 1 *June* 1959)

Abstract—The piston-displacement technique previously described has been applied to a study of phase transitions and isothermal compressibilities of solid CH_4, CD_4 and O_2 over the pressure range 0–19,000 kg/cm^2 and the temperature range 4–120°K. Phase transitions appear as discontinuities in V (first order) or in $(dV/dP)_T$ (second order).

Solid CH_4 and CD_4 both show three phases and one triple point. The transitions appear to be of the second order, with rather large "regions of indifference". There are isotopic differences between the two methanes. At atmospheric pressure CH_4 shows only one of the transitions, at 20·5°K, while CD_4 has both, at 22·1° and 27·2°K. There is at present disagreement between our results for CH_4 and those obtained by STEVENSON.

In the case of solid oxygen, the two well-known transitions have been traced to high pressure. The lower transition is evidently of the second order. The upper first-order transition has a large volume discontinuity. Some difficulty was experienced from ignition of the steel pressure chambers by the solid oxygen under high pressure.

Pressure–volume relations for the three substances have been obtained at various temperatures.

1. INTRODUCTION

THE specific-heat anomaly in solid CH_4 at 20·5°K at atmospheric pressure was first observed by CLUSIUS[1] in 1929. Since the specific-heat maximum appeared to be finite, it was assumed that this transition was second order. Later work by SCHALLAMACH[2], employing X-ray diffraction, showed that there was no change in the f.c.c. structure of solid methane at 20°K. The transition was assumed to involve a change in the rotational states of the CH_4 molecules. However, proton-resonance measurements by THOMAS *et al.*[3] showed that a state of free rotation of the molecules was not realized at 20·5°K, but only at much higher temperature.

KRUIS *et al.*[4] investigated the specific heat of solid CD_4 at low temperatures and observed two anomalies, at 22·2 and 27·1°K. These also appeared to be second order. Studies[5] of mixtures of CH_4 and CD_4 showed that the upper transition in CD_4 is analogous to the single transition in CH_4, and that the lower transition in CD_4 has no equivalent in CH_4 at atmospheric pressure. The lowest-temperature phase in CD_4 is now known to be weakly doubly refracting, so that its structure cannot be strictly f.c.c. The lower transition must therefore be first order, with a very small latent heat of transition.

By means of specific-heat measurements at atmospheric pressure, GIAUQUE and JOHNSTON[6] observed two transitions in solid oxygen. Both were believed to be first order, with measured heats of transition 22·4 cal/mole at 23·7°K and 177·6 cal/mole at 43·8°K. However, X-ray studies by VEGARD[7] indicate no change in crystal structure at the lower transition, and subsequent thermal measurements by BOROVIK–ROMANOV *et al.*[8] also lead to the identification of the lower transition as being of the second order.

The only previous high-pressure work with solid CH_4 appears to be that of TRAPEZNIKOVA and MILJUTIN[9]. They measured the specific heat at pressures up to 2000 atm, and found a second transition in CH_4 at elevated pressures, evidently corresponding to the lower transition in CD_4.

* Supported by the Department of Army, Office of Ordnance Research.

VOL. 12 59/60

There appeared to be a triple point in CH_4 near 33°K and 2600 atm. The recent work of STEVENSON[10] will be discussed below. The present results for CH_4 represent an extension of results previously presented[11] in a preliminary fashion. There has apparently been no previous high-pressure work with solid CD_4. STEVENSON[12] has also obtained high-pressure data for solid O_2.

2. EXPERIMENTAL TECHNIQUE

Throughout the present investigation, the piston-displacement technique previously described in detail[13] has been used. Volume vs. pressure data have been obtained over the pressure range 0–19,000 kg/cm² and the temperature ranges 4–120°K for CH_4, 4°–90°K for CD_4 and 30°–65°K for O_2. Pressure is applied by the piston directly to the sample. Plasticity of the solidified gas is relied upon for transmission of the applied uniaxial compressive stress as an approximate hydrostatic pressure. A variable-temperature cryostat of the type designed by SWENSON[14] has been employed. Liquid helium was the coolant for temperatures between 4° and 77°K, and liquid nitrogen was used for temperatures above 77°K. The temperature of the sample was determined by means of an indium resistance thermometer of the type suggested by WHITE and WOODS[15]. This thermometer will be described in detail elsewhere.[16]

Four sizes of sample-holder were used: $\frac{5}{8}$ in. diameter (stainless steel, Type 304) for pressures of 0–3000 kg/cm² (later replaced by a $\frac{1}{2}$-in. stainless-steel cylinder, pressure range 0–5000 kg/cm²); $\frac{5}{16}$ in. diameter (AISI 4615 steel, heat-treated), 0–12,000 kg/cm²; $\frac{1}{4}$ in. diameter (AISI 4615 steel, heat-treated), 0–19,000 kg/cm². As before,[13] the high-pressure pistons were constructed from heat-treated Ketos tool steel. The larger-diameter cylinders give greater sensitivity at relatively low pressures than is afforded by the $\frac{1}{4}$-in. cylinders. All the cylinders used were $\frac{3}{4}$–1 in. in depth.

First-order transitions in the sample produce volume discontinuities in the V vs. P data, while with a second-order transition the volume is continuous but there is a break in the slope $(dV/dP)_T$. Friction in the sample-holders tends to "round the corners" of either type, and, unless the volume discontinuity is quite large, it is impossible to determine the order of a transition from the V vs. P data alone. The friction was reduced by lining the pressure cylinder with 0·005-in. indium foil.

After initial compaction of the sample by one or two applications and releases of pressure, the pressure was decreased from its maximum value to zero in regular steps, and then was likewise increased again to the maximum value. This is the method originated by BRIDGMAN[17] for compressibility measurements on solids. At each point, the position of the piston was observed after all drift had stopped. A micrometer slide and telescope were used to follow the motion of a scratch on the upper (room-temperature) end of the stainless-steel compression member. After completion of one or two such "hysteresis loops", the sample was expelled by warming up the system and applying pressure. The background stretch of the press was then obtained by means of a pressure hysteresis loop with the piston in contact with the bottom of the empty sample-holder. For reasons of economy of liquid helium, these "blank" runs were always carried out at 77°K. The elastic constants of the stainless-steel tension and compression members change very little with temperature in the range of these measurements. The sample length at zero pressure was determined from the blank run, as previously described.[13]

The temperature of the sample was controlled by adjustment of a needle valve in the helium-discharge line from the cryostat. Liquid helium was forced through a vacuum-jacketed transfer tube into the heat-exchanger of the cryostat by pressurizing a 25-l. storage Dewar with gaseous helium. The flow rate of the evaporated helium could be monitored with a wet test meter. The temperature, as recorded by the indium resistance thermometer mounted on the bottom of the press in good thermal contact with the sample-holder, was held constant within 0·5°K for periods up to 3 hr.

Data at temperatures above the melting points of the substances were obtained by initially applying pressure at a lower temperature and then allowing the sample to warm up at constant pressure. A hysteresis loop at pressures above the melting pressure was then run.

3. RESULTS AND DISCUSSION

(a) *Methanes*

Phillips Petroleum Company research-grade CH_4 (99·5 per cent or higher purity) was used. The CD_4 was obtained from Tracerlab, Inc., and was stated to be at least 95 per cent CD_4. No additional purification was carried out in either case.

The behavior under pressure of the solid CD_4 and CH_4 was rather peculiar. The transitions were always much more conspicuous on the decreasing-pressure side of the hysteresis loop than on the increasing-pressure side. The break in slope on the decreasing side was accompanied by unusually large drift of the piston, which continued for 15 or 20 min after a change of pressure had been made. The drift first appeared several decrements of pressure above the apparent transition point, and increased in magnitude and duration at each point until the transition was complete. As the pressure was further reduced, there was no drift of the piston until very low pressures were reached. On account of friction, all the solidified gas samples studied so far have shown some drift of the piston at the extreme low-pressure end of the decreasing-pressure leg of the hysteresis loop.

On the increasing-pressure side of the V vs. P loop, it was difficult to distinguish breaks in slope

from frictional irregularities in the piston motion. There was little or no drift as the transition was approached from the low-pressure side. The size of feasible pressure increments could not be reduced below a minimum value. The piston motion became jerky if the increments were made too small, with a tendency for alternate points to lie on a smooth curve. These effects are believed to be caused by frictional "hanging up" of the piston on the wall of the cylinder, arising from the finite shear strength of the solidified samples.

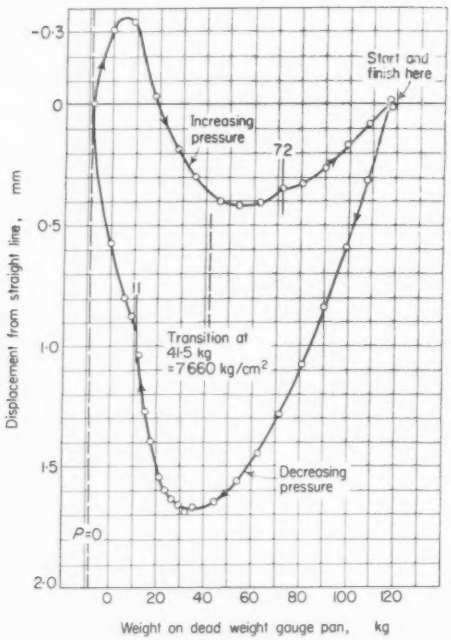

FIG. 1. "Hysteresis" loop for locating phase transitions in solid CH_4. A straight line was drawn connecting the maximum and zero pressure points on a plot of piston position vs. weight on dead-weight gauge pan. The ordinate on the graph shown here is the difference between the piston position corresponding to the actual point and that corresponding to the linear relation. The abscissae are essentially pressure; 1 kg on the dead-weight gauge pan is equivalent to 154 kg/cm² sample pressure for the ¼-in. sample-holders. The run shown is for solid CH_4 at 57°K.

The transitions appear more clearly if the data are plotted against pressure as differences between the observed piston position and a straight line drawn between the maximum and zero pressure points. This increases the scale of the irregularities in piston motion over those appearing in a direct V vs. P plot. A typical plot of this kind is shown in Fig. 1. The transition pressure is taken as the arithmetic mean of the pressures of the breaks in the decreasing- and increasing-pressure curves.

The phase diagram for solid CH_4 is shown in Fig. 2, and that for CD_4 in Fig. 3. In the case of CH_4, the present results disagree in part with those of TRAPEZNIKOVA and MILJUTIN[9] and of STEVENSON[10]. Agreement is perfect with TRAPEZNIKOVA and MILJUTIN for the I—II transition, but the present II–III curve lies at a substantially higher pressure than those of either TRAPEZNIKOVA and MILJUTIN or STEVENSON. The reason for this discrepancy is not known. It is felt that our observed points for the II—III transition are more accurate than those at higher pressure.

In the present work, no evidence was found of the fourth phase (δ), stable at high pressure and low temperature, reported by STEVENSON[10]. A careful search was made for this, but no irregularities in the piston motion consistent enough to be associated with a phase transition were observed. There is evidence that solid CH_4 becomes increasingly brittle in this region of the PT plane. When the pressure was changed, the piston moved in jerks accompanied by crunching sounds. Except for the lack of consistency between data at neighboring temperatures, it would be possible to mistake this behavior for a phase transition. Where the sample is brittle, the applied uniaxial compressive stress is not transmitted throughout as hydrostatic pressure, and the stress system in the sample is complicated. The compressibility and phase-transition data then have doubtful validity.

Previous extrusion experiments in this laboratory have shown that solid CH_4 is quite plastic near atmospheric pressure at 77°K. A pressure of 800 kg/cm² applied to a solid sample in a ¼-in. cylinder extruded the sample smoothly through a coaxial ⅛-in. hole in the bottom of the cylinder. However, as the temperature is lowered, solid methane becomes increasingly brittle.

At higher temperatures, the present disagreement with STEVENSON on the location of the I—III transition curve appears to arise from the fact that he was there working near the top of his available pressure range, where the transition data are quite inaccurate.

VOL. 12 59/60

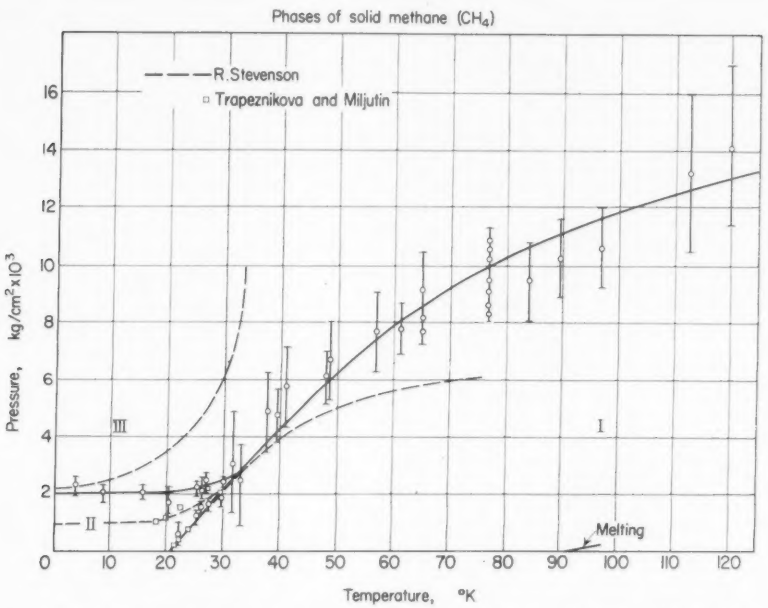

FIG. 2. Phase diagram for solid CH_4. The results of earlier investigators are shown.

All three sets of data lead to very nearly the same I—II—III triple-point parameters, namely 33°K and 2700 kg/cm². In Fig. 2 the I—II and I—III transitions are shown as a continuous straight line through the triple point. From a consideration of thermodynamic potentials, it can be shown that at a triple point the transition line dividing the regions of stability of the *i*th phase and the *j*th phase must, when projected through the triple point, enter the region of stability of the *k*th phase. This theorem applies to transitions of all orders. Thus the I—III line cannot bend away from the temperature axis at the triple point (Fig. 2).

Presumably because of greater impurity content, the CD_4 transitions appeared less distinctly than those for CH_4. BRIDGMAN[18] has pointed out that the corners of transitions when plotted on a V vs. P diagram are rounded by the presence of impurity. In contrast to the situation in CH_4, both transitions in CD_4 occur at atmospheric pressure. Otherwise the two phase diagrams are qualitatively similar. At a given temperature, the transition pressure for CD_4 is lower than the corresponding pressure for CH_4. The triple-point parameters for CD_4 are 40°K and 3000 kg/cm². These are less accurately known than is the case for CH_4. There is no evidence in the present data for a fourth phase in CD_4 analogous to STEVENSON's δ in CH_4.

The experimental uncertainties in the transition pressures are of the order of the smallest pressure increment that could be applied without irregular piston motion. The transitions observed in the larger holders have a smaller absolute error than those observed in the smaller, higher-pressure, holders. The relative uncertainties are nearly the same. The large spread in transition pressures observed at 77°K is not understood. Some of the earlier values[11] are now believed to be too high and have been assigned smaller weight in the location of the transition curves.

The spread between the transition points observed with increasing and decreasing pressure is considerably greater than the friction. With a closely fitting piston and indium liner, the half-width of the friction hysteresis loop was of the order of 5 per cent of the maximum pressure. The width of the "region of indifference" was at least as large as the friction, but showed no obvious dependence upon temperature, pressure, sample length or sample-holder diameter. In general, the

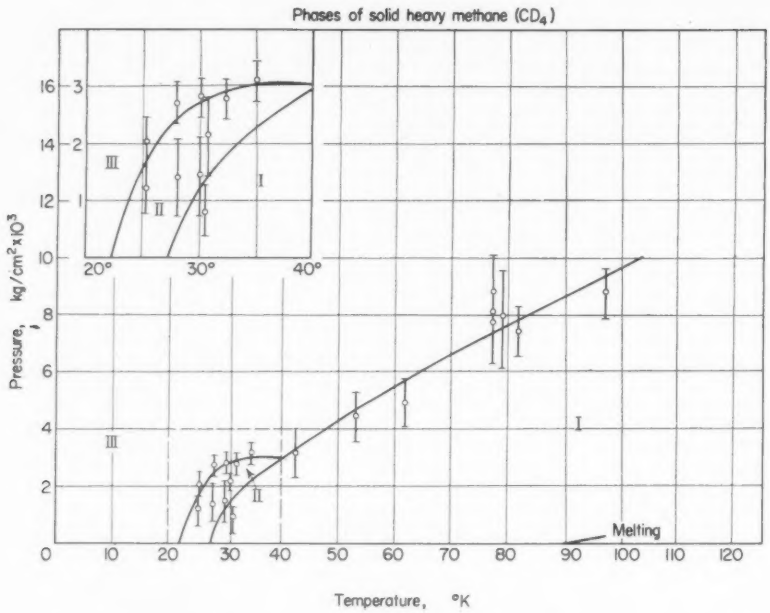

FIG. 3. Phase diagram for solid CD_4. The inset shows the lower portion of the diagram at twice the scale of the main plot.

friction tends to be less with a small length-to-diameter ratio for the sample. On the other hand, the magnitude of the piston displacement then becomes inconveniently small, so that one does not gain in accuracy by reducing the sample length below a certain value. The samples used in this investigation had length-to-diameter ratios of between 1·0 and 2·0.

A total of 36 runs was made with CH_4 and 18 with CD_4. One to four separate runs were made with each sample, the most common number being two.

The pressure–volume relations for CH_4 and CD_4 at 77°K are shown in Table 1. The method of calculation is the same as that described previously.[13] The observed difference between $\Delta V/V_0$ for CH_4 and for CD_4 is less than the estimated 5 per cent precision of measurement. One might expect CD_4 to be slightly less compressible than CH_4, particularly at low pressure, because of the smaller zero-point energy of CD_4. Owing to the width of the regions of indifference, the difference in compressibility at the transitions cannot be determined accurately. One must extrapolate the experimental curves from each side of the transition so that they meet without a discontinuity in volume. In all cases it is observed that the compressibility of the high-pressure phase is greater than that of the low-pressure phase at the transition point.

The molar volume data for solid CH_4 given in Table 1 are based upon a value of $0{\cdot}507\pm0{\cdot}004$ g/cm³ for the density at 77°K, obtained in this laboratory by LAROCK[19]. Since no accurate measurement of the density of solid CD_4 seems to have been made, no molar volumes are given.

In the previous determinations of PV isotherms for solidified gases,[13,20] the Murnaghan theory of finite strain was found to be quite useful for empirical fitting of the experimental data. However, because of the phase transitions, no attempt has been made to apply this theory to the present compressibility data. At a given temperature, different values of the two adjustable constants would be needed for each phase. It was not felt that this representation would be particularly useful.

Table 1. *Compression data for solids* CH_4, CD_4 *and* O_2

Pressure (kg/cm²)	CH_4 77°K $\rho = 0.507$ g/cm³		CD_4 77°K	32°K	O_2 51°K $\rho = 1.36$ g/cm³	
	Mol. vol. (cm³)	$-\Delta V/V_0$	$-\Delta V/V_0$	$-\Delta V/V_0$	Mol. vol. (cm³)	$-\Delta V/V_0$
0	31·6	0	0	0	23·5	0
1000	29·9	0·054	0·049	0·032	—	—
1100	—	—	—	—	22·2	0·054*
1100	—	—	—	—	21·2	0·096*
2000	28·8	0·090	0·083	0·058	20·6	0·122
2500	—	—	—	0·067*	—	—
4000	27·1	0·141	0·133	0·097	19·6	0·167
6000	25·9	0·179	0·169	0·128	18·8	0·198
7400	—	—	0·187*	—	—	—
7900	—	—	—	—	18·4	0·219*
8000	25·0	0·208	0·196	0·151	—	—
10,000	24·3	0·230*	0·221	0·170	17·8	0·241
12,000	23·7	0·251	0·242	0·187	17·4	0·258
14,000	23·1	0·268	0·260	—	17·1	0·272
16,000	22·7	0·281	0·274	—	16·8	0·283
19,000	22·2	0·299	0·292	—	16·5	0·298

* Phase transition.

VOL. 12 59/60

(b) *Oxygen*

Linde Company oxygen (U.S.P.) was used without additional purification. Judging by the sharpness of the transitions, the purity must have been quite high. Both transitions were evident on both the decreasing- and increasing-pressure legs of the hysteresis loop. Fig. 4 shows the phase diagram for solid oxygen. The present results agree closely with those of STEVENSON[12].

A previous extrusion experiment similar to that described above for CH_4 showed that solid oxygen is brittle at 4°K. However, it appears to transmit hydrostatic pressure satisfactorily at temperatures above 30°K.

The lower-temperature transition (β–γ, Fig. 4) is assumed to be of the second order. The discontinuity in piston motion for this transition was very small, and because of friction it is not possible to distinguish between a small volume change and a jump in $(dV/dP)_T$. The compressibility of phase γ is greater than that of phase β at the transition pressures observed (7900 kg/cm² at 51°K, 2500 kg/cm² at 32°K). The differences between the compressibilities appear to be smaller than is the case with the second-order transitions of the solid methanes.

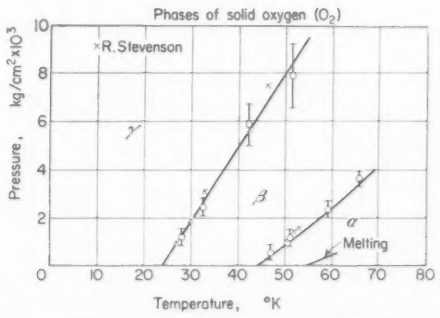

FIG. 4. Phase diagram for solid O_2.

The α–β transition shows a large volume change, and is certainly first-order. X-ray data[7] show that, in the α phase, pairs of O_2 molecules are arranged with their centers in a f.c.c. array. In the β phase the structure is either trigonal or rhombohedral. The γ phase was found to have the same structure as the β phase.

The volume changes observed for the α–β transition were $1{\cdot}09\pm0{\cdot}05$ cm^3/mole at 47° and $0{\cdot}98\pm\pm0{\cdot}05$ cm^3/mole at 51°K. Less accurate values, which appear to be smaller, were obtained at 59° and 66°K. The latter two were not converted to cm^3/mole, because the pressure hysteresis loop could not be carried to zero pressure at temperatures above the melting point of oxygen. A linear extrapolation of the results at 47° and 51°K leads to $\Delta V = 1{\cdot}18\pm0{\cdot}06$ cm^3/mole at 43·8°K, the temperature of the transition at atmospheric pressure.

Using GIAUQUE's[6] value for the latent heat of the transition ($177{\cdot}6\pm0{\cdot}5$ cal/mole) and the slope, dP/dT, of the α–β transition line (determined from Fig. 4) in Clapeyron's equation, we calculate $\Delta V = 1{\cdot}16\pm0{\cdot}14$ cm^3/mole. The agreement is excellent.

The density of solid oxygen at 51°K was calculated from an extrapolation to the melting point of values of the density of the liquid as a function of temperature given by VAN ITTERBECK[21] and from the volume change at fusion (54·3°) determined from Clapeyron's equation. GIAUQUE's[6] value of the latent heat of fusion (106 cal/mole) and LISMAN's[22] determination of dP/dT based upon melting-curve measurements to 170 kg/cm^2 were used. The value adopted for the density at 51°K was $1{\cdot}36\pm0{\cdot}01$ g/cm^3. From this the molar volumes in Table 1 were determined.

In some of the oxygen runs trouble was experienced from chemical reaction at high pressure of the solid oxygen samples with the steel pressure cylinder. Once such a reaction started, it proceeded explosively, and pressure was quickly lost as the sample vaporized and leaked past the piston. This happened on three separate occasions, as follows: (1) 41°K, 12,000 kg/cm^2, on initial increase of pressure; (2) 51°K, 16,000 kg/cm^2, as pressure was being increased for the third time on that particular sample (after a successful run had been completed); (3) 70°K, 19,000 kg/cm^2, sample warming up at constant pressure. In each case, as the oxygen escaped, a channel was melted in the piston and cylinder. This combustion could usually be prevented by the indium liner. On the first occasion no liner was used; on the latter two occasions it presumably was torn. One might suppose that it would be impossible to initiate this spontaneous reaction at reproducible temperatures and pressures, since it presumably requires sufficient activation energy to be supplied by the compression at one spot on the wall of the pressure chamber. This would vary with friction.

4. CONCLUSION

The exact nature of the phase transitions of methane is not yet understood theoretically. They are believed to involve changes in rotational states of the molecules in the solid crystal, although there must also be a slight change in the crystal structure in the lower-temperature transition of solid CD_4 to account for the anisotropy of phase III. The same might well be true for the II—III transition of CH_4. No studies of the refractive properties of phase III of CH_4 have been made. JAMES and KEENAN[23] have carried out a classical statistical-mechanical calculation for CD_4 at atmospheric pressure, based upon octopole–octopole interaction between the molecules. This accounts reasonably well for the observed two transition temperatures. This theory is not yet applicable to CH_4, for which quantum effects are more important. Neither does it apply to CD_4 under pressure, because lattice compressibility is neglected. It is the author's understanding that further calculations to take account of these effects are in progress at the present time.

Further experimental studies of the solid methanes under pressure would be highly desirable. In particular, specific-heat measurements, nuclear magnetic-resonance measurements and perhaps neutron-diffraction measurements should be carried out at as high a pressure as possible. In order to improve materially upon the present accuracy of the piston-displacement technique, it will be necessary to embed the solid methane in a medium which transmits hydrostatic pressure. Solid hydrogen could be used at the lower temperatures. Gaseous helium would be suitable over the entire range if only relatively low pressures were desired.

Acknowledgements—The author wishes to express his appreciation to Major R. I. LAROCK and Major R. F. PATTERSON for their invaluable assistance in designing some of the equipment and especially in the taking of the data. He would also like to acknowledge the contribution of Mr. P. SOMMER, who constructed much of the apparatus.

VOL. 12 59/60

REFERENCES

1. CLUSIUS K., *Z. phys. Chem.* B**3,** 41 (1929).
   CLUSIUS K. and PERLICK A., *Z. phys. Chem.* B**24,** 313 (1934).
2. SCHALLAMACH A., *Proc. Roy. Soc.* A**171,** 569 (1939).
3. THOMAS J., ALPERT N. and TORREY H., *J. Chem. Phys.* **18,** 1511 (1950).
4. KRUIS A., POPP L. and CLUSIUS K., *Z. Elektrochem.* **43,** 664 (1937).
   CLUSIUS K. and POPP L., *Z. phys. Chem.* B**46,** 63 (1940).
5. BARTHOLOME E., DRIKOS G. and EUCKEN A., *Z. phys. Chem.* B**39,** 371 (1938).
6. GIAUQUE W. F. and JOHNSTON H. L., *J. Amer. Chem. Soc.* **51,** 2300 (1929).
7. VEGARD L., *Nature, Lond.* **136,** 720 (1935).
8. BOROVIK–ROMANOV A. S., ORLOVA M. P. and STRELKOV P. G., *Doklady Akad. Nauk S.S.R.* **99,** 699 (1954).
9. TRAPEZNIKOVA O. and MILJUTIN G., *Nature, Lond.* **144,** 632 (1939).
10. STEVENSON R., *J. Chem. Phys.* **27,** 656 (1957).
11. STEWART J. W., *Proceedings of the Fifth International Conference on Low-Temperature Physics and Chemistry*, p. 522. University of Wisconsin Press, Madison (1958).
12. STEVENSON R., *J. Chem. Phys.* **27,** 673 (1957).
13. STEWART J. W., *J. Phys. Chem. Solids* **1,** 146 (1956).
14. SWENSON C. A. and STAHL R., *Rev. Sci. Instrum.* **25,** 608 (1954).
15. WHITE G. K. and WOODS S. B., *Rev. Sci. Instrum.* **28,** 638 (1957).
16. STEWART J. W., *Rev. Sci. Instrum.* To be published.
17. BRIDGMAN P. W., *Proc. Amer. Acad. Arts Sci.* **74,** 425 (1942).
18. BRIDGMAN P. W., *The Physics of High Pressure*, p. 191. G. Bell and Sons, London (1949).
19. LAROCK R. I., Thesis, University of Virginia (1958). For details of the method, see Reference 20.
20. STEWART J. W. and LAROCK R. I., *J. Chem. Phys.* **28,** 425 (1958).
21. VAN ITTERBECK A., *Progress in Low-Temperature Physics* (Ed. GORTER C. J.) Vol. 1, p. 366. International Publishers, New York (1955).
22. LISMAN J. and KEESOM W., *Physica s'Grav.* **2,** 901 (1935).
23. JAMES H. and KEENAN T., *J. Chem. Phys.* **31,** 12 (1959).

J. Phys. Chem. Solids Pergamon Press 1959. Vol. 12. pp. 130–145. Printed in Great Britain.

NON-STOICHIOMETRIC HYDRATES—I

SORPTION EQUILIBRIA AND KINETICS OF WATER LOSS FOR ION-EXCHANGED NEAR-FAUJASITES

R. M. BARRER and G. C. BRATT*

Physical Chemistry Laboratories, Chemistry Department, Imperial College, London, S.W.7

(*Received* 18 *June* 1959)

Abstract—Properties of water have been studied in Li-, Na-, K-, Rb-, Cs-, Ca-, Sr-, Ba-, Ni-, Co- and Cu-rich forms of a synthetic zeolite of the faujasite group. Thermogravimetry, differential thermal analysis and measurement of equilibrium vapour pressures were the principal methods of study. Several of the ion-exchanged forms were altered by water vapour at higher temperatures; others were more resistant. The volume occupied by intracrystalline water molecules depends on the cations present: in one group fall the alkali-metal ions; in a second, the alkaline-earth-metal ions; in a third, the ions of the transition metals cobalt, nickel and copper. Isotherms where reversible sorption occurred cannot be described by any simple isotherm model, but in certain instances empirical equations such as

$$\ln K_2 = \ln \frac{p(1-\theta)}{\theta} - B_2\theta$$

and especially

$$\ln K_3 = \ln \frac{p(1-\theta)}{\theta} - B_3\theta^2$$

gave a successful description of the isotherms over a considerable range of values in θ. K and B are here constant coefficients. An analysis of the thermogravimetric curves in terms of diffusion is given, and the limitations encountered in interpreting this and similar investigations are indicated.

1. INTRODUCTION

WATER is associated with other crystal-building units in a great variety of structures, and the properties of intracrystalline water have attracted much attention. Crystallohydrates may be stoichiometric or non-stoichiometric in composition; in the non-stoichiometric group of hydrates the water may be present as guest molecules in a host lattice (the zeolites), or it may form the host lattice within which guest molecules are encaged (gas hydrates).[1] A statistical thermodynamic theory of gas hydrates[2,3] has met with considerable success. However, its extension to zeolitic hydrates presents difficulty, because the treatment rests upon the cell theory of LENNARD–JONES and DEVONSHIRE[4,5] in which one molecule only is present per cage or cell. Multiple occupation of cages presents mathematical difficulties which become extreme in the case of zeolites, where there may be clusters of water molecules in each cavity. These clusters may, for example, reach 12–14 molecules in chabazite, about 27 molecules in Linde Sieve A and nearly 32 molecules in near-faujasites such as Linde Sieve X.[6] Indeed, in the last structure these water clusters are clearly joined into a continuous distribution of intracrystalline fluid. However, a thermodynamic study of such systems remains possible and will be considered in the present work (Parts I, II and III).

Non-equilibrium properties of water are of equal interest in these systems, and will to some extent be investigated in this work. Thermogravimetry and differential thermal analysis are

* Present Address: c/o Electrolytic Zinc Co. Ltd., Risdon, Tasmania.

considered in particular, and in a cognate research the self-diffusion and "chemical" diffusion of intracrystalline water have been investigated.[7] The cations in faujasite, which are located in the same channels as the water molecules, may be systematically exchanged, so as to vary the cation radius and valence, while the anionic framework remains virtually unaltered. Accordingly an opportunity is provided for determining the effect of the cations in these porous heteroionic crystals upon both equilibrium and non-equilibrium properties of the water.

2. EXPERIMENTAL

(a) *Materials*

The crystalline zeolite studied was Linde Sieve X, a synthetic species of the faujasite group,* supplied by Linde Air Products Ltd. When fully hydrated, its oxide composition was $Na_2O.Al_2O_3.2{\cdot}67SiO_2.6H_2O$. The essential features of the structure have been established,[8–10] and it has been shown that a series of very wide cavities are arranged like the atoms in diamond and are joined by wide windows to give an arrangement of channels organized as are the bonds in diamond. Each cavity has a free diameter of 12–13 Å, and opens into four other identical cavities by way of common windows, tetrahedrally distributed, of 8–9 Å free diameter, and consisting of rings of twelve $(Al,Si)O_4$ tetrahedra. The cations and water molecules are distributed throughout this system of cavities and channels. In addition the structure contains smaller cubo-octahedral cages of free diameter $\sim 6{\cdot}6$ Å in which a limited number of water molecules may occur, and which may contain some cations. Finally, hexagonal prism units are present, which however have little free volume and need not be considered as a location for water molecules.

The sorbates used were water, ammonia and methanol. Freshly distilled water was freed from dissolved gases by repeated pumping at 0°C, followed by evacuation at liquid-air temperatures. The water was then fractionally distilled, with cooling and pumping between each stage. "AnalaR" methanol was further purified by a method described by WEISSBURGER[11], and ammonia was prepared and purified as described by FARKAS and MELVILLE[12].

Starting from the Na-faujasite, cation exchange was effected by methods described elsewhere[13] to give crystals rich in K, Rb, Cs, Ca, Sr, Ba, Cu, Co and Ni. Cationic compositions were determined by standard analytical procedures, and these compositions and a few details about the preparations are given in Table 1.

(b) *Apparatus and methods*

Control over products and evidence of possible side reactions during ion exchange and in handling the crystals was provided by X-ray powder photography, using a Hilger HRX X-ray unit, with 39-kV filtered CuK_α radiation.

Two principal sorption systems were operated, using the silica spring balance of MCBAIN and BAKR[14], to determine gravimetrically sorption isotherms for the sorbates in any of the ion-exchanged forms of faujasite listed in Table 1. A low-temperature apparatus was employed in the range 30–80°C in which the balance case and manometer were immersed in a single thermostat through which hot water was circulated continuously. The mercury **U**-tube manometer, attached to the balance case by one limb and to the vacuum line through the other, was of 1-cm-diameter tubing; the pressure differences between the limbs, as well as the lengths of the silica spring, were read by a cathetometer. Sorbate vapours of methanol or water were supplied at any desired vapour pressure or in doses of any size from reservoirs in subsidiary thermostats. All tubing used to lead between sorbate reservoirs and the balance case was heated electrically to prevent condensation.

The affinity between polar sorbates and the zeolite crystals was such that often an insufficient range of sorption could be measured in the low-temperature system. Accordingly a high-temperature apparatus was also made. The balance case was heated electrically by means of a furnace so made that diametrically opposite vertical strips were transparent. Accordingly the spring lengths could be read at temperatures up to 450°C. Temperatures within the balance case were read by means of a platinum resistance thermometer in a **U**-tube placed within the spirals of the silica spring.

* Although these crystals show differences from natural faujasite,[15] it will be convenient to refer to them in Parts I, II and III as "faujasites", for reasons of brevity. They are based upon the same type of aluminosilicate framework as faujasite.

VOL. 12 59/60

Table 1. *Preparation of ion-exchanged forms of zeolite*

Cationic form	Starting material	Weight (g)	Solution used and concentration (wt.-%)	Method	Volume of solution (l.)	Time of percolation	Percentage exchange
Li	Na-zeolite	5	20% LiCl	Percolation	2·5	3–4 days	100% Li
K	Na-zeolite	5	20% KCl	Percolation	2·5	3–4 days	100% K
Rb	Ca-zeolite	3	15% RbCl	Batch	0·15	1 day	
			15% RbCl	Batch	0·15	6 days	
			70% RbCl	Batch	0·06	3 hr	
			80% RbCl	Percolation (all in succession)	0·15	1 day	44% Rb
Cs	Ca-zeolite	2·5	1% CsCl	Percolation	0·5	1 hr	
			5% CsCl	Percolation	0·1	12 hr	
			50% CsCl	Percolation	0·02	12 hr	
			180% CsCl	Percolation (all in succession)	0·015	1½ hr	58% Cs
Ca	Na-zeolite	5	20% $CaCl_2$	Percolation	2·5	3–4 days	98% Ca
Sr	Na-zeolite	5	20% $SrCl_2$	Percolation	2·5	3–4 days	95% Sr
Ba	Na-zeolite	5	20% $BaCl_2$	Percolation	2·5	3–4 days	85% Ba
Co	Na-zeolite	5	2% $CoCl_2$	Percolation	20	1 day	79% Co
Cu	Na-zeolite	5	5% $CuSO_4$	Percolation	4·0	25 hr	88% Cu
Ni	Na-zeolite	5	20% $NiCl_2$	Percolation	2·5	15 hr	79% Ni

The thermometer could be connected either to a Callendar–Griffiths bridge or to a temperature regulator.

Before the balance case and sorbent in either apparatus were raised above room temperature, the apparatus and zeolite (0·7–0·8 g) were very carefully outgassed and pumped down to 10^{-5} mm Hg for about 12 hr. This removed ~ 30 per cent of the zeolitic water. Outgassing was then commenced at temperatures raised progressively to 350°C over a period of 8–10 hr. The temperature was finally held at 350°C for a further twelve hours' evacuation. In the low-temperature sorption unit, the furnace was then removed and the thermostat filled with water. Two methods of measuring the sorption were employed. In the first a series of doses was successively admitted at constant temperature and a series of isotherms separately determined. In the second procedure the temperature was varied up and down the complete temperature range for each dose admitted.

In pressure measurements with the catheto-meter, the positions of both base and crown of the mercury menisci were found, and the capillary depression calculated from the data of VICKERS and GOULD[16]. For the limb in contact with water vapour, the surface tension of mercury in contact with liquid water was assumed.[17] Correction was also made for variation of the density of mercury with temperature. In the high-temperature system temperature differences between the balance case and the barometer as high as 300°C were sometimes involved. At pressures of 0·01 cm Hg a thermomolecular pressure correction of 2·5 per cent may be required (BENNETT and TOMPKINS[18]). Measurements at high temperatures in this pressure range were accordingly avoided.

Differential thermal analysis was used, in

conjunction with thermogravimetry, to investigate water loss and thermal effects associated with water loss, and lattice perturbation, recrystallization or breakdown. The differential thermal-analysis apparatus has been described briefly by BARRER and LANGLEY[19]. The thermogravimetric apparatus was based on a sensitive balance, the sample being suspended in a bucket from one arm of this balance. The rate of heating of the sample was governed by the same programme controller as that which determined the rate of heating (10°C/min) during differential thermal analysis.

Some observations were made of dielectric loss in a powder composed of the zeolite crystals, using a *Q*-meter. A capacitor was made from two concentric "Nicosel" cylinders, the annular space of 1 mm being maintained by "Kovar" glass sealed to their lower ends. The sample of zeolite hydrate was packed into the annular space, and the whole cell was then suspended in a glass tube by its connecting leads. Tube and cell were thermostatted and could be outgassed, isolated from the remainder of the apparatus or filled with known amounts of water at measured pressures.

3. EXPERIMENTAL RESULTS

(a) *Water content and cation volume and type*

The water contents of the various crystals of Table 1 were determined thermogravimetrically after equilibration over saturated $Ca(NO_3)_2$ solution. The unit cells of the various cationic forms of

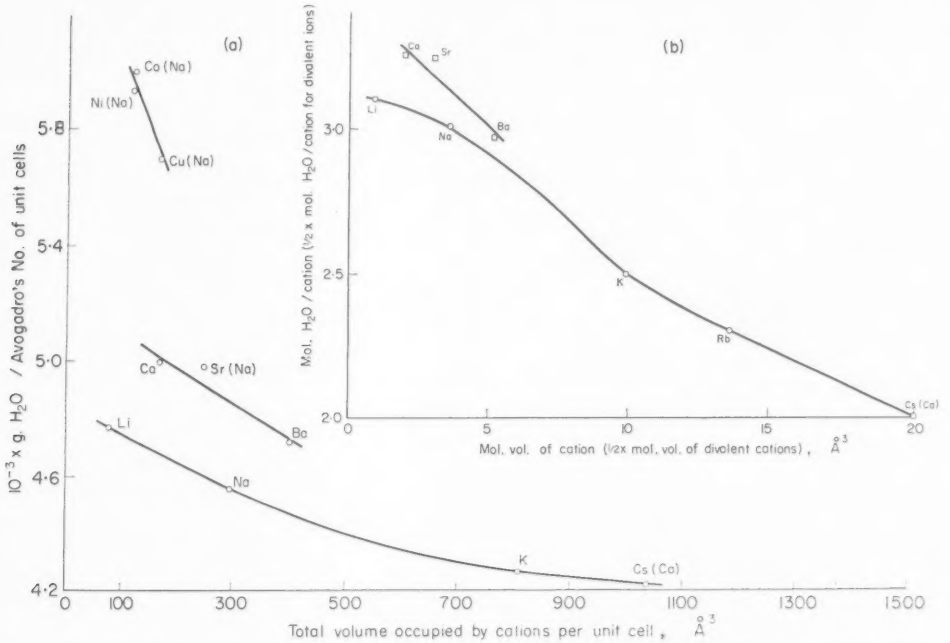

FIG. 1a. The relation between water content and cation volume and type for ion-exchanged faujasites. (b) An analogous plot for ion-exchanged chabazites.[20]

The zeolite vary little in dimensions.[15] Accordingly since the aluminosilicate frameworks are virtually unaltered as shown by X-rays, the extent of the intracrystalline free volume will depend *inter alia* upon the volume occupied by the cations. The water contents, when plotted against the total cation volume, lie on three separate curves (Fig. 1a), one for Li, Na, K and Cs, a second for Ca, Sr and Ba and a third for the transition-metal ions Co, Ni and Cu. Similar correlations have been observed between water content and cation volume for chabazite[20] (Fig. 1b). The curves of Fig. 1a extrapolate at zero volume of cations to $4{\cdot}9 \times 10^3$,

$5{\cdot}2\times10^3$ and $\sim 6{\cdot}6\times10^3$ g/*g* unit cell.* Taking the edge of all unit cells as 24·75 Å, we obtain 0·53, 0·57 and 0·72 g of water per cm³ of crystal. These weights of water must occupy nearly the same intracrystalline volumes, since, as noted, ion exchange leaves the aluminosilicate framework virtually unaltered.

It thus appears that a water molecule cannot occupy the same volume in the cases of the three curves of Fig. 1. If the molecular volume is equal to that in liquid water for either the alkali-metal or the alkaline-earth-metal ion forms of the zeolite, the water must have a considerably smaller molecular volume in the Co, Ni and Cu forms. Much of the water in these latter forms is therefore different and is probably co-ordinately linked to the metal cations. Support for this view is given by the pink, green and blue colours of hydrated Co-, Ni- and Cu-faujasites. Moreover, anhydrous Co-faujasite is blue. At a water content of ~ 4 molecules per cation, there is a slow change to pink. Such colour changes may be associated with changes in co-ordination number, and thus of arrangement of co-ordinating atoms around the cobalt ion.

(b) *Dielectric loss*

Dielectric-loss measurements were made at frequencies below 30 Mc/s, using outgassed Na-faujasite and this zeolite with varying water content. The outgassed crystals at 22°C showed a fairly constant value of tan δ (apparent) = 0·03. The introduction of water produced a rather flat peak in this curve of tan δ vs. frequency. With increasing water content the peak moved to a higher frequency. Thus, for 0·22 g of water per g of anhydrous crystals, the peak at 25°C was at 250 kc/s, while at 52°C it was at 1 Mc/s. If this shift is interpreted in terms of an activation energy for dipole rotation, this energy is $\sim 9{\cdot}9$ kcal/mole, intermediate between that for ice and that for liquid water.[21]

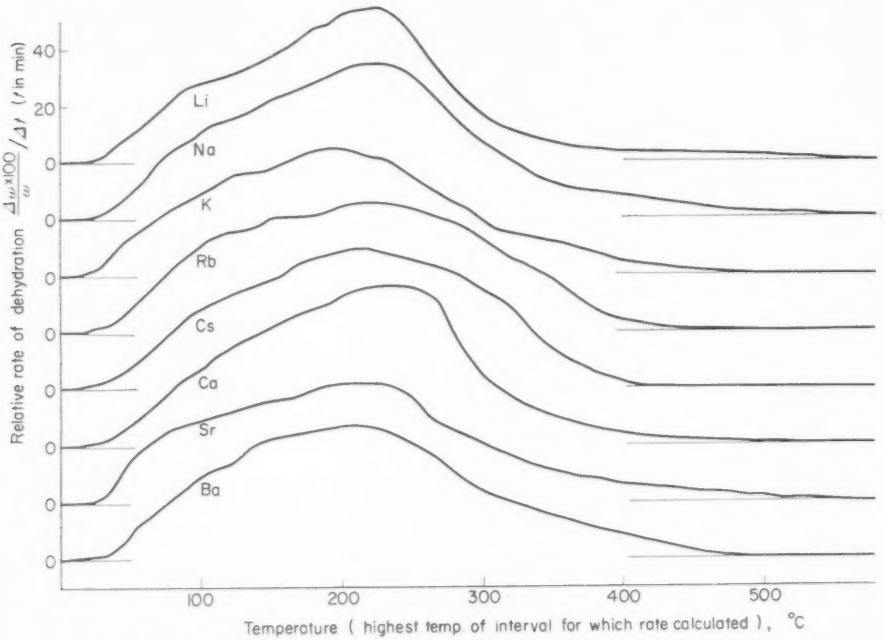

FIG. 2. Differential thermogravimetric curves for different ion-exchanged faujasites.

(c) *Thermogravimetry*

Thermogravimetric curves of weight loss against

* The *g* unit cell denotes one Avogadro number of unit cells. It is the most convenient unit for comparison of sorptions by different ion-exchanged forms of the zeolite.

temperature and time were determined for the heating rate of 10°C/min. Differential thermogravimetric curves were then obtained by finding decrements in weight (Δw) in each minute (Δt). Curves of $\Delta w/\Delta t$ vs. temperature are shown in Fig. 2 for several ion-exchanged forms of the zeolite. Among the homoionic forms the maximum rate of loss occurs at about the same temperature for Li- and Na-faujasites and at a lower temperature for K-faujasite. In Ca-, Sr- and Ba-faujasite the temperature of the maximum rate of water loss decreases as cation size increases. The differential base-line drift which sometimes occurred. Water loss for alkali-metal and alkaline-earth-metal forms takes place endothermally over all water contents. From Cu-, Ni- and Co-faujasites, on the other hand, processes associated with this water loss are at first endothermal and finally exothermal. This situation may arise from lattice perturbations involving ion movements and side reactions (*q.v.*). Thermograms and differential thermogravimetric curves for Li-, Na-, K-, RbCa-, Ca-, Sr- and Ba-faujasites show a correspondence of prominent features.

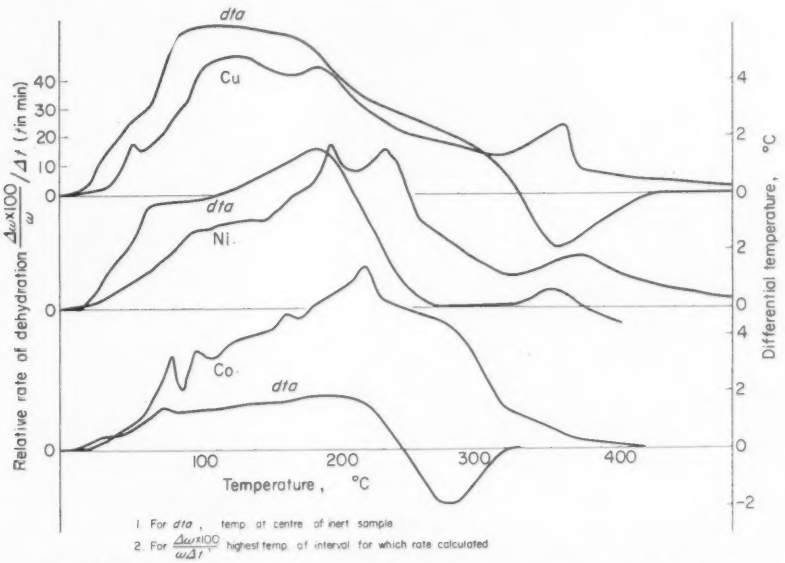

FIG. 3. Comparison of differential thermogravimetric curves and differential thermal analyses of Cu-, Ni- and Co-faujasites.

thermogravimetric curves for Cu-, Ni- and Co-faujasites (Fig. 3) are less smooth than are those of Fig. 2. There is a tendency over one or more temperature intervals for water to be released in bursts, superposed upon the normal course of the curves.

(d) *Differential thermal analysis*

Thermograms of Li-, Na-, K-, RbCa-, CsCa-, Ca-, Sr- and Ba-faujasites are shown in Fig. 4. Fig. 3 compares these curves for Cu-, Ni- and Co-faujasites with the differential thermogravimetric curves for the same species. All thermograms in Figs. 3 and 4 have been corrected as far as possible for the

(e) *Irreversible sorption processes*

Completion of the measurements necessary for the evaluation of families of isotherms required at least six weeks for each ion-exchange faujasite. During this time the crystals were in contact with water vapour at temperatures up to 80°C or, in the high-temperature apparatus, much above 80°C under pneumatolytic conditions. Water vapour at higher temperatures can sinter and weather many gels, oxides and minerals. Under these conditions several cationic forms of the zeolite exhibited irreversible behaviour. Thus at temperatures below 90°C, Sr- and Co-faujasite showed hysteresis on sorption–desorption cycles which persisted to low

pressures, and isotherms could not be reproduced after outgassing (Fig. 5a). X-ray powder photographs of both forms showed that after a series of experiments considerable decomposition had occurred.

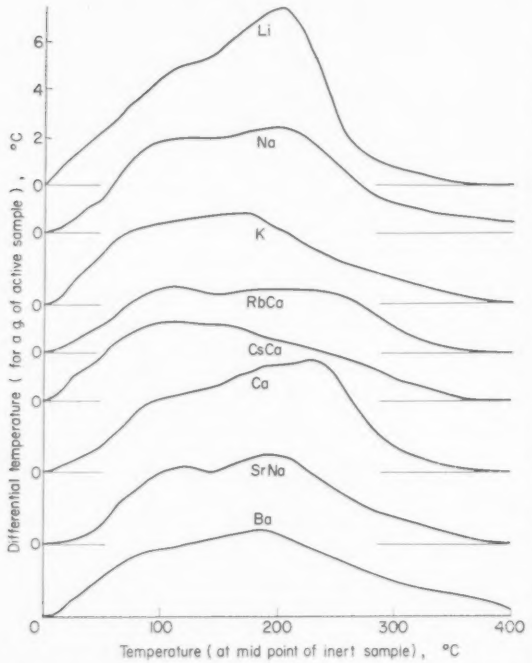

FIG. 4. Differential thermal analyses of alkali-metal and alkaline-earth-metal ion-exchanged forms of faujasite.

Irreversibility was observed at high temperatures, up to 450°C, in the case of Ca-faujasite. The Na-form gave reversible values for sorption and desorption temperature cycles, provided that for temperatures between 120° and 300°C the amount sorbed was kept small (Fig. 5b), but after outgassing at high temperatures the initial results could not be reproduced. X-ray examination showed no observable decomposition, but the high initial isosteric heat (Part II[22]) was much reduced.

A different kind of irreversibility was observed with methanol sorbed in Na-faujasite. There was no observable breakdown of the crystals, but some decomposition of methanol to give gases incondensable in liquid air ($\sim$ 1·4 per cent after several heating and cooling cycles). The equilibrium point in the reaction

$$CH_3OH \rightleftharpoons CO+2H_2$$

at 25°C corresponds to 2·2 per cent[23] decomposition of methanol.

(f) *Reversible sorption*

Reproducible sorption isotherms were obtained for the following systems and temperatures:

H_2O-Li-faujasite	T = 30°, 40°, 50°, 60° and 70°C
H_2O-Na-faujasite	T = 30°, 60°, 70°, 80°, 120°, 150°, 180°, 210° and 270°C
H_2O-K-faujasite	T = 40°, 50°, 60° and 70°C
H_2O-CsCa-faujasite	T = 40°, 50°, 60° and 70°C
H_2O-Ca-faujasite	T = 30°, 40°, 50°, 60° and 70°C
NH_3-Na-faujasite	T = 30°, 40°, 50°, 60°, 70° and 80°C.

Fig. 5b shows isotherms for water in Na-faujasite, and in Fig. 5c a comparison is made of isotherms at 70°C for a sequence of ion-exchanged crystals. Among the homoionic forms where reversible sorption was measured, the sorptions at a chosen higher relative pressure fall in the order Ca > Li > Na > K. The isotherm which should be obtained for fully exchanged Cs-faujasite can also be estimated from those for Ca- and CsCa-faujasites, and is shown in Fig. 5c.

Fig. 6, which shows families of isotherms for ammonia in Na-faujasite and for water in K-faujasite, illustrates several properties of zeolitic solid solutions. Since water and ammonia have comparable molecular weights, it is evident that the effective molecular volume of ammonia is much larger than that of water. In filling the intracrystalline volume the idea of sorption sites in the Langmuir sense is inappropriate, and the behaviour resembles instead that expected in packing molecules into a limited volume. This behaviour is further illustrated by the way in which apparent saturation values decrease with rising temperature (Fig. 6). Amplitudes of molecular vibration, and molecular co-volumes, of a dense fluid would be expected to increase with temperature in this way. The behaviour now recorded has also been observed and analysed for hydrocarbon sorbates in faujasites.[24]

4. THE FREE-ENERGY FUNCTION

The Polanyi sorption potential, ϵ, is approximated by

$$\epsilon = RT \ln(p_0/p) \qquad (1)$$

VOL. 12 59/60

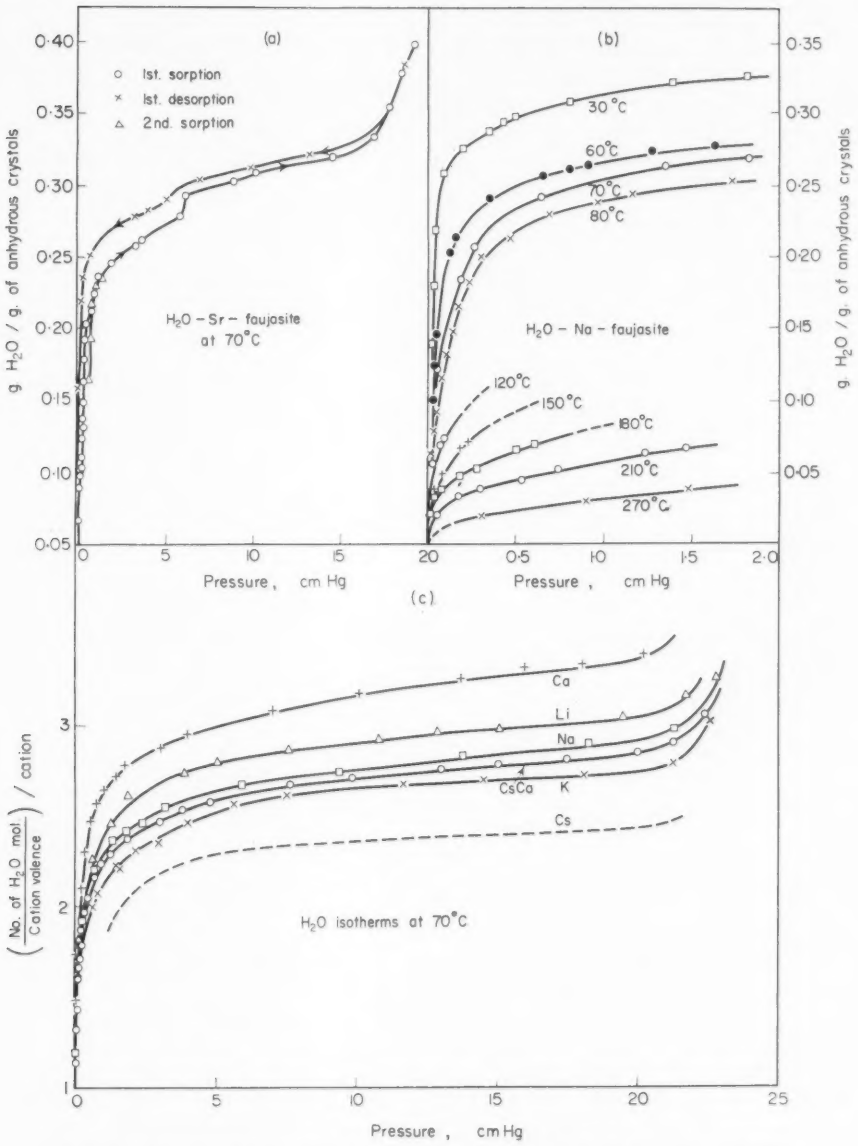

FIG. 5. (a) Irreversible sorption observed in the water-Sr-faujasite system at 70°C. (b) Reversible sorption obtained for water in Na-faujasite. (c) Reversible isotherms obtained at 70°C for water in various cation-exchanged forms of faujasite. The dotted curve shows the estimated position of the iso-therm for a pure Cs-faujasite.

where p/p_0 denotes the relative pressure. When ϵ is plotted against $\phi = x/\delta_T$ (where x denotes the amount sorbed in g, and δ_T is the density of liquid sorbate at temperature T), a characteristic curve should result, according to the Polanyi theory,[25] and should be the same for all temperatures. However, the data for the typical case of water in Li-faujasite show that the "characteristic curve" is dimensions

$$\text{Log}\, x = C - D[\log p_0/p]^2 \qquad (2)$$

where x is the amount sorbed, C and D are constants at constant temperature and p_0 denotes the vapour pressure of liquid sorbate. When this relation was applied to the H_2O-Li-faujasite isotherms at 50 and 70° C, there was only a limited

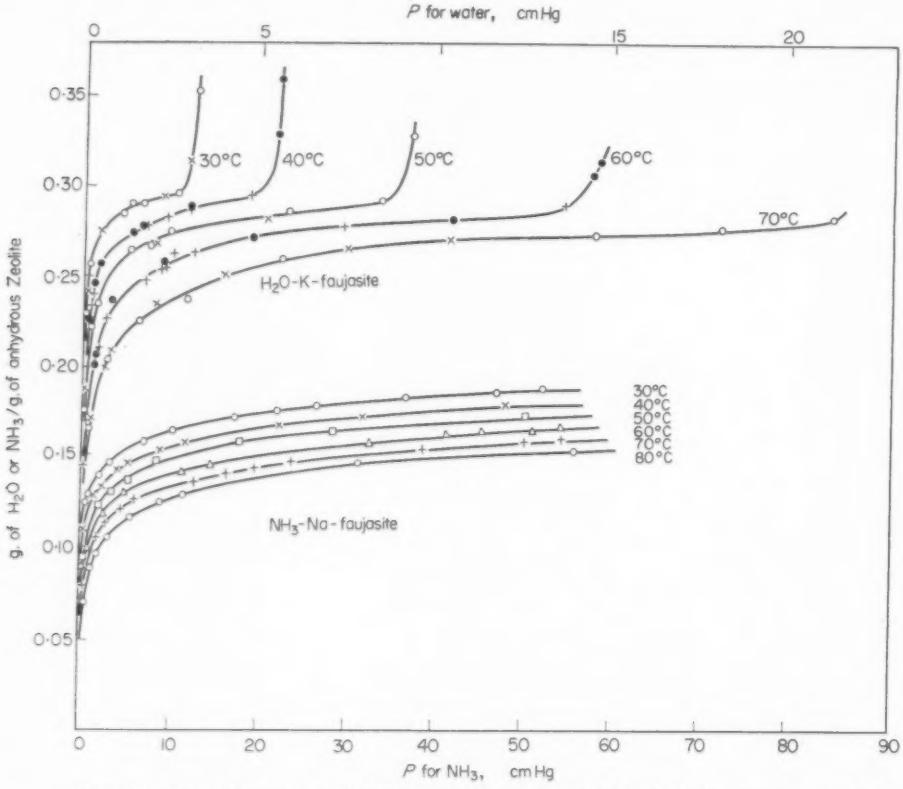

FIG. 6. Isotherms for water in K-faujasite and for ammonia in Na-faujasite. In the case of the isotherms for water ○ and ● refer to adsorption points, and + and × to desorption points.

different at 50 and at 70°C. BARRER and BROOK[26] observed in the case of chabazite that the more polar the sorbate the poorer the agreement with POLANYI's theory. At least for polar sorbates in porous heteroionic crystals, this theory is not adequate.

DUBININ[27], in a development of potential theory, has suggested that for porous materials in which the pore diameters approach molecular region over which the curves were linear. The ratio of slopes was not the ratio of the squares of the experimental temperatures, as required by DUBININ's theory, and over an extended range in amounts sorbed the curves were sigmoid in form.

A third approach to the free-energy function may be made in terms of the Langmuir isotherm, $K_1 = p(1-\theta)/\theta$, where K_1 is the Langmuir quotient. If, at 70°C, $\log p(1-\theta)/\theta$ was plotted against

θ, this quotient was not constant, but for larger values of θ ($0{\cdot}7 < \theta < 0{\cdot}9$) a linear part of the curve was obtained, so that in this range

$$K_2 = \frac{p(1-\theta)}{\theta} \exp(-B_2\theta). \qquad (3)$$

Rather longer linear sections were also observed when $\log p(1-\theta)/\theta$ was plotted against θ^2, corresponding to

$$K_3 = \frac{p(1-\theta)}{\theta} \exp(-B_3\theta^2). \qquad (4)$$

The constants B_2 and B_3 are summarized in Table 2. If B_2 is interpreted according to the model of

Table 2

H_2O in *M*-faujasite	B_2	B_3	$2w/z$ ($z = 4$) (cal/mole)	$2w/z$ ($z = 6$) (cal/mole)
M = Ca	6·7	4·2	1070	710
Li	6·3	3·4	1310	870
Na	7·7	4·7	790	530
K	4·6	3·6	1020	680
CsCa	6 0	3·6	1150	770

localized sorption with interaction,[28] the interaction energies, given for co-ordination numbers $z = 4$ and 6 in columns 4 and 5 of Table 2, correspond to repulsions between the water molecules. This situation could arise if at higher values of θ the water dipoles were similarly oriented owing to their association with anionic oxygens of the framework and with cations. However, in Part II it will be shown that this explanation cannot be generally correct, and that the results are explained in terms of loss of entropy due to partial "freezing" of water molecules in the structure for denser intracrystalline fluid.

For the K- and Cs-rich faujasites the empirical relationship in equation (4) gives a good representation of the isotherm over a considerable range in θ, as indicated in Table 3. The agreement for Li and Ca forms is, however, less satisfactory.

5. CHANGES IN THERMODYNAMIC PROPERTIES OF THE ZEOLITIC FRAMEWORK DUE TO ZEOLITIC WATER

When a guest molecule is intercalated in a host lattice, there is a decrease in chemical potential of the host lattice and changes occur in its partial molal entropy and heat content. Thus the "filled" structure is more stable than the same structure when free of zeolitic water. It is this feature which enables zeolites to form readily under alkaline hydrothermal conditions,[29] so that the behaviour is of considerable interest.

We will refer changes in chemical potential and differential entropy or enthalpy of the zeolite to a structural unit which is $\frac{1}{192}$ part of the unit cell content. This unit contains two oxygen atoms and is $(Na_{0{\cdot}43}Al_{0{\cdot}43}Si_{0{\cdot}57})O_2$, and in the neutral framework derived by replacing all Al atoms by Si atoms it would be SiO_2. In one mixed mole of sorbate A plus structural units let the mole fractions be N_A and N_S for the sorbate and sorbent respectively. In the gas phase N_A^g is always unity. From the Gibbs–Duhem equation at constant temperature, and for one mixed mole of sorbate plus lattice forming units,

$$N_A\, d\mu_A + (1-N_A)\, d\mu_s = V\, dP \qquad (5)$$

where V is the volume of the mixed mole, P denotes pressure and μ_A and μ_s are respectively the chemical potentials of sorbed water (or other sorbate) and of lattice units. For the gas phase $d\mu_A^g = V_g\, dP$, where μ_A^g is the chemical potential of the gaseous sorbate of molecular volume V_g. At equilibrium $d\mu_A^g = d\mu_A$ and suitable rearrangement of equation (5) then gives

$$d\mu_s = \frac{V\, dP - N_A\, d\mu_A^g}{(1-N_A)} \qquad (6)$$

However, $d\mu_A^g = RT\, d \ln p_A$, where p_A is the equilibrium pressure of the sorbate and $P = p_A$. Thus from equation (6) we obtain

$$\Delta\mu_s = \mu_s - \mu_s^{\text{ref}} = \int_{p_A^{\text{ref}}}^{p_A} \frac{V\, dp_A}{(1-N_A)} - RT \int_{p_A^{\text{ref}}}^{p_A} \frac{N_A}{(1-N_A)}\, d \ln p_A. \qquad (7)$$

Integration is between a chosen reference state for

which the equilibrium pressure of sorbate vapour is p_A^{ref}, and any other state having equilibrium pressure p_A. It would be convenient to chose $p_A^{ref} = 0$, where $N_A = 0$. If V_M is the molecular volume of a lattice-forming unit of molecular weight M and x is the weight sorbed when the sorbate has a molecular weight m, equation (7) becomes*

$$\Delta\mu_s = V_M(p_A - p_A^{ref}) + \frac{MRT}{m}\int_{p_A^{ref}}^{p_A} \frac{x}{p_A}\cdot dp_A \qquad (8)$$

Owing to the energetic character of sorption and consequent rectangular form of the isotherms, it was not possible to measure these down to $N_A = 0$.

Table 3. Equilibrium "constants", K_3, for equation (4)

θ	K_3		
	Na-faujasite	K-faujasite	CsCa-faujasite
0·294	0·056	$0·030_8$	$0·029_9$
0·353	0·054	$0·028_7$	$0·028_7$
0·412	0·050	$0·035_6$	$0·027_5$
0·471	0·042	$0·036_3$	$0·027_7$
0·529	0·029	$0·039_0$	$0·027_6$
0·588	0·022	$0·038_2$	$0·027_1$
0·647	0·025	$0·038_2$	$0·027_0$
0·706	0·024	$0·040_6$	$0·026_4$
0·765	0·024	$0·042_7$	$0·027_0$
0·823	0·025	$0·039_8$	$0·029_0$
0·882	0·025	$0·033_6$	$0·028_3$

Accordingly, for water in Na-, Ca- and CsCa-faujasite the lowest convenient mole fraction $N_A = 0·34$ was chosen. For ammonia in Na-faujasite the calculations were made for $N_A = 0·34$

* In this zeolitic solid solution the volume V is virtually independent of the amount of intracrystalline sorbate. Thus, the partial molal volume of the sorbate is zero, and that of the lattice units of the crystal is a constant, equal to V_M. Accordingly, for n_s moles of lattice units, $V = V_M \cdot n_s$ and for one mixed mole of lattice units and sorbate, $V = V_M \cdot N_s$. Thus $V_M = V/(1-N_A)$.

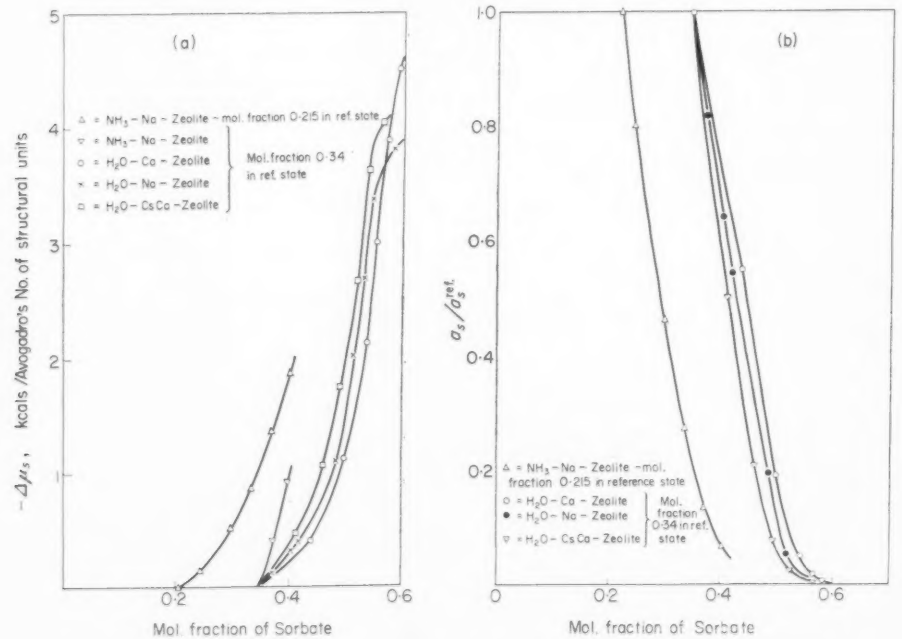
(a)
△ = NH3 – Na – Zeolite – mol. fraction 0·215 in ref. state
▽ = NH3 – Na – Zeolite
○ = H2O – Ca – Zeolite
× = H2O – Na – Zeolite
□ = H2O – CsCa – Zeolite
Mol. fraction 0·34 in ref. state
– Δμs, kcals /Avogadro's No. of structural units
Mol. fraction of Sorbate
(b)
△ = NH3 – Na – Zeolite – mol. fraction 0·215 in reference state
○ = H2O – Ca – Zeolite
● = H2O – Na – Zeolite
▽ = H2O – CsCa – Zeolite
Mol. fraction 0·34 in ref. state
as/as ref.
Mol. fraction of Sorbate

FIG. 7. (a) Lowering of chemical potential of the faujasite host crystals as a result of additions of water and of ammonia as guest molecules. (b) Changes in activity of the host lattice due to water and ammonia.

and $0{\cdot}21_5$. The change in chemical potential of lattice-forming units is shown in Fig. 7a. For water in the three cationic forms of the zeolite, there is considerable similarity between the curves, and both for water and for ammonia the changes in chemical potential are large. If we write $\mu_s - \mu_s^{ref} = RT \ln(a_s/a_s^{ref})$ where a_s and a_s^{ref} are the activities of lattice units corresponding respectively to μ_s and μ_s^{ref} then the variation of a_s/a_s^{ref} with

6. THERMOGRAVIMETRIC DESORPTION KINETICS

In the Appendix, a treatment is given of the diffusion-controlled desorption kinetics of zeolitic water under thermogravimetric conditions. Provided that D, the diffusion coefficient, does not depend on the amount of zeolitic water present in the crystals, if $-\log[d \ln w_r/dt]$ is plotted against $1/T$, a straight line would be expected, after an

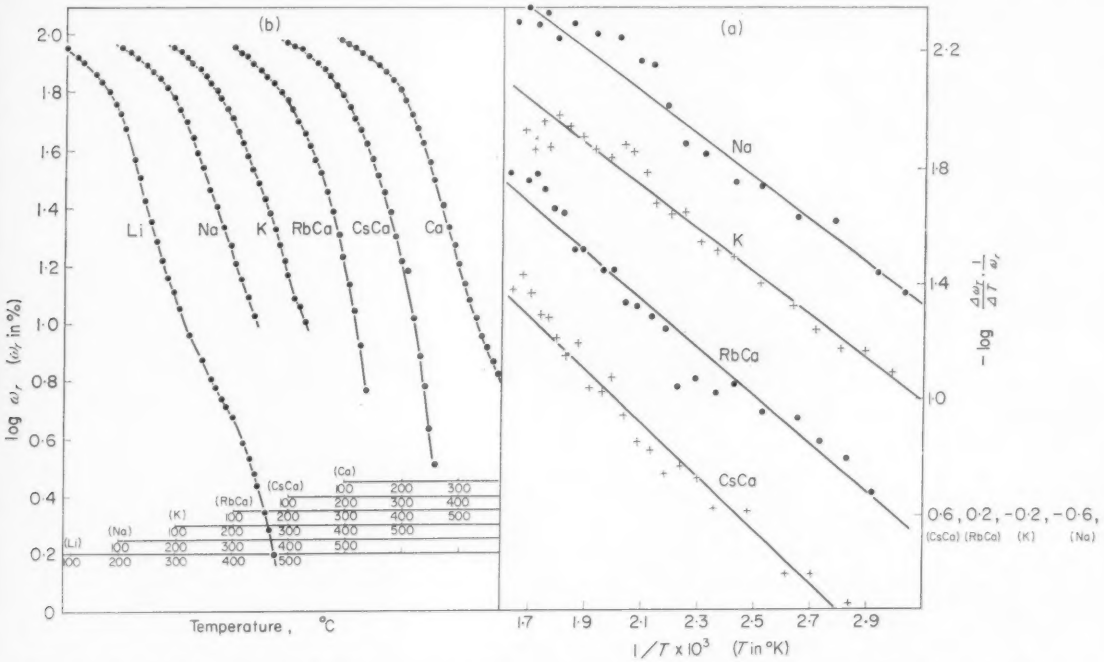

FIG. 8a. Plots of $-\log(\Delta w_r/\Delta T \cdot 1/w_r)$ against $1/T$ for water loss from various cation-exchanged forms of faujasite. w_r is the proportion of water remaining, expressed as a percentage, and Δw_r and ΔT are decrements in w_r and corresponding increments in temperature T. (b) Kinetics of water loss showing plots of log w_r against temperature for ion-exchanged faujasites.

N_A is indicated in Fig. 7b. In whichever way the results are considered, it is clear that uptake of water or ammonia greatly stabilizes the lattice. Thus the zeolitic component is demonstrably a major factor in the synthesis and paragenesis of porous crystals such as zeolites. These structures will not be expected to form in the absence of the stabilizing filler, and the catalysis by water of the formation of the crystals is placed upon a thermodynamic basis.

initial period, the slope of which is $-E/2{\cdot}303R$, where E denotes the activation energy for diffusion and w_r the weight of water remaining at time t. Fig. 8a shows typical plots of the above kind for several ion-exchanged faujasites, but with $\Delta w_r/\Delta T \cdot 1/w_r$ replacing $d \ln w_r/dt$.

The release of water from the crystal powder tends to some extent to occur in irregular bursts, as shown by the differential thermogravimetric curves of Figs. 2 and 3. These fluctuations are

reflected in the curves of Fig. 8a, which are derived from experimental values of $\Delta w_r/\Delta T$ and w_r rather than from smoothed curves. There is a considerable temperature coefficient in

$$\log\left(-\frac{\Delta w_r}{\Delta T}\cdot\frac{1}{w_r}\right) = \log\left(-\frac{\Delta w_r}{\alpha\Delta t}\cdot\frac{1}{w_r}\right).$$

In the foregoing relationship the increase in temperature, ΔT, for a constant rate of heating is proportional to that in time, Δt (see Appendix), and α denotes the constant of proportionality. Then, from the mean slopes of the four curves of Fig. 8a, one obtains the apparent energies of activation, E, given below:

	Range in percentage dehydration covered	E(Kcal/mole)
Na-faujasite	2·2–88·5	3·5
K-faujasite	5·2–89·4	3·5
RbCa-faujasite	4·0–90·4	4·0
CsCa-faujasite	4·2–93·2	4·5

These values of E are comparable with energies of activation for diffusion in, or fluidity of, liquid water or aqueous electrolytes. However, this analogy is of uncertain significance, since firstly the density of the intracrystalline aqueous fluid varies continuously as water is lost from the crystal, and secondly for a reason to be discussed below.

In Fig. 8b are given plots of ln w_r against temperature T (where, as in Appendix 1, $T = T_0+\alpha t$). These curves show that in H_2O-Li-faujasite and in H_2O-Ca-faujasite in particular two stages of water loss occur, and that there is a strongly retained smaller fraction of intracrystalline water and a much larger fraction which is readily released. In these two systems at least the diffusion coefficients depend on the amount of zeolitic water as well as upon the temperature. This behaviour is not apparent for the Rb- and Cs-rich faujasites. The analysis of Appendix 1 permits an estimate of diffusion coefficients, since $-\Delta w_r/\Delta t \cdot 1/w_r$ tends to $D\pi^2/l^2$ for larger times. Values of this quantity may be derived either from the slopes of the curves of Fig. 8b or from the ordinates of the experimental points of Fig. 8a. From Fig. 8a, taking $\pi^2/l^2 = 4{\cdot}8$, where $l/2$ is the depth of the bed of powder, values of D were derived, which led to the smoothed curves of Fig. 9. Numerical values of D must be regarded as approximate only, but the trends with temperature and degree of zeolitic water loss are more accurately defined.

The significance of mean diffusion coefficients for an unconsolidated bed of zeolite powder is of considerable interest. There can be movement of water inside crystallites, its loss at the surface of each crystallite and its flow in the interparticle spaces. The movement within the particles will be governed by an intracrystalline diffusion coefficient $D_i = D_{i0}\exp(-E_i/RT)$; the loss through the surface will be proportional, *inter alia*, to exp $(\Delta H/RT)$, where ΔH is the heat of *sorption*; while flow in the gas phase can be regarded as a rapid, nearly temperature-independent process. Thus the observed diffusion coefficients are complex, although they will tend to be governed by the slowest processes, which will be intracrystalline diffusion or surface evaporation. The observed temperature coefficients (l.c.) are considerably smaller than would be required by the term $\exp(\Delta H/RT)$. On the other hand, the concentration-dependence of D tends to reduce these coefficients, since rising temperature in the thermogravimetric apparatus

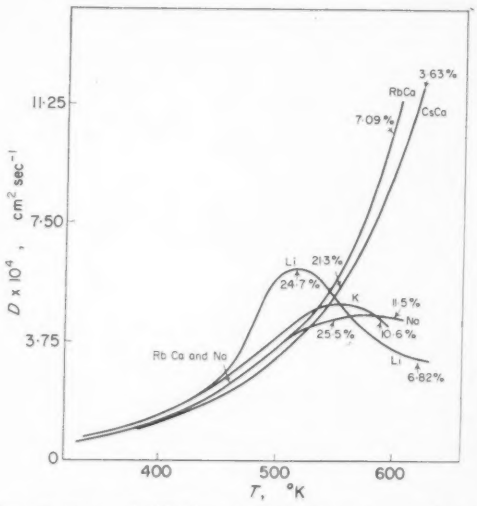

FIG. 9. Plots of diffusion coefficients vs. temperature in porous beds of various ion-exchanged faujasites. Maxima observed for Li-, K- and Na-faujasites suggest that different fractions of intracrystalline water have different mobilities. The percentages marked on the curves are the percentages of the total water still remaining at the temperatures indicated by the arrows.

results in falling water content and therefore smaller D, an effect which is usually, but not always, offset by the rise in temperature. Thus it is not possible to say whether D is governed by rates of intracrystalline diffusion or by "evaporation barriers" at the crystallite surfaces.

APPENDIX

FREEMAN and CARROLL[30] have considered the quantitative interpretation of thermogravimetric curves for reactions of the type

$$A_{\text{solid}} \rightarrow B_{\text{solid}} + C_{\text{gas}},$$

in which the rate of disappearance of A is governed by the equation

$$-\frac{d[A]}{dt} = k[A]^n,$$

n being the order of reaction. This treatment, however, cannot apply to a diffusion-controlled loss of a volatile zeolitic constituent. This problem will therefore be treated.

We consider an unconsolidated mass of crystallites in a container of uniform cross-section such that escape of zeolitic water occurs only from the upper surface of the bed of powder. Diffusion is then in the x-dimension only, and if the depth of the bed is $l/2$ the problem is that of water loss by diffusion through the boundary at $x = 0$ and of no flow through that at $x = l/2$ (or radially). Thus the problem can be treated in the same way as for linear diffusion in a slab of length l with water loss at the faces $x = 0$ and $x = l$, since then $dc/dx = 0$ at $x = l/2$.

This diffusion equation and boundary conditions are:

(i) $$\frac{\partial c}{\partial t} = \frac{\partial}{\partial x}\left(D\frac{\partial c}{\partial x}\right),$$

where D is the diffusion coefficient for water in the porous mass at position x and at time t and c is the concentration of water;

(ii) temperature T is assumed independent of x in the specimen;

(iii) T increases linearly with time throughout the specimen so that

(a) $T - T_0 = \alpha t$, where T_0 is the temperature at $t = 0$;

(b) $dT = \alpha dt$;

(iv) $D = D_0 \exp(-E/RT) = D_0 \exp(-E/\alpha t + T_0)$ (from condition (iii));

(v) D may also be a function of concentration C; however, we will assume D independent of C and therefore, because of (ii), independent of x;

(vi) $C = C_0$ for $0 \leqslant x \leqslant l$ at $t = 0$;

(vii) $C = \phi(t)$ at $x = 0$ and $x = l$ for $t > 0$. $\phi(t)$ must also be a function which tends to zero for large enough t, since the bed eventually loses all its water. The function $\phi(t)$ need not however be specified further.

According to conditions (iv) and (v), we may rewrite (i) as:

(viii) $$\frac{\partial c}{\partial t} = D(t)\frac{\partial^2 c}{\partial x^2}.$$

We may now let

$$\tau = \int_0^t D(t)\,dt, \text{ and so } d\tau = D(t)\,dt.$$

Thus, equation (viii) becomes, in terms of the new variable, τ,

(ix) $$\frac{\partial c}{\partial \tau} = \frac{\partial^2 c}{\partial x^2},$$

while we may also re-write boundary condition (vii) to read

(x) $C = \phi(t) = \Phi(\tau)$ at $x = 0$ and $x = l$ for $t > 0$.

These transformations allow the solution to be obtained by a procedure already known:[31]

$$C = \frac{4C_0}{\pi} \sum_{m=0,1,2,\ldots} \frac{1}{(2m+1)} \cdot \frac{\sin(2m+1)\pi x}{l} \cdot \exp\left[-\frac{(2m+1)^2\pi^2\tau}{l^2}\right] + \frac{4\pi}{l^2} \sum_{m=0,1,2,\ldots} (2m+1)\times$$

$$\times \frac{\sin(2m+1)\pi x}{l} \exp\left[-\frac{(2m+1)^2\pi^2\tau}{l^2}\right] \times \int_0^\tau \exp\left[\frac{(2m+1)^2\pi^2\Lambda}{l^2}\right]\Phi(\Lambda)\cdot d\Lambda,$$

where

$$\Lambda = \int_0^\tau D(\Lambda)\,d\Lambda.$$

From this relationship the flux, J, in the $-x$ direction through unit area of the surface at $x = 0$ is evaluated:

$$J = D\left(\frac{\partial c}{\partial x}\right)_{x=0} = \frac{4C_0D}{l} \sum_{m=0,1,2,\ldots} \exp\left[-\frac{(2m+1)^2\pi^2\tau}{l^2}\right] +$$

$$+ \frac{4\pi^2D}{l^3} \sum_{m=0,1,2,\ldots} (2m+1)^2 \cdot \exp\left[-\frac{(2m+1)^2\pi^2\tau}{l^2}\right] \int_0^\tau \exp\left[\frac{(2m+1)^2\pi^2\Lambda}{l^2}\right] \Phi(\Lambda)\, d\Lambda.$$

Similarly, Q, the amount of water remaining in the bed at time t is

$$Q = \frac{1}{2}\int_0^l C \cdot dx = \int_0^{l/2} C \cdot dx = \frac{4C_0l}{\pi^2} \sum_{m=0,1,2,\ldots} \frac{1}{(2m+1)^2} \cdot \exp\left[-\frac{(2m+1)^2\pi^2\tau}{l^2}\right] +$$

$$+ \frac{4}{l} \sum_{m=0,1,2,\ldots} \exp\left[-\frac{(2m+1)^2\pi^2\tau}{l^2}\right] \int_0^\tau \exp\left[\frac{(2m+1)^2\pi^2\Lambda}{l^2}\right] \cdot \Phi(\Lambda) \cdot d\Lambda.$$

For longer times, only the term where $m = 0$ need be retained in either expression, and so the ratio

$$\frac{J}{Q} \to \frac{D\pi^2}{l^2}$$

and should serve to determine D, the effective diffusion coefficient in the porous mass. At two successive times in the same experiment, when the temperatures are T_1 and T_2,

$$\ln\frac{J_1}{Q_1} - \ln\frac{J_2}{Q_2} = \ln D_1 - \ln D_2 = \frac{E}{R}\left[\frac{1}{T_2} - \frac{1}{T_1}\right]$$

so that the effective energy of activation, E, can be derived.

In this treatment the assumption (ii), that the temperature is constant throughout the mass, cannot be accurate. It could, however, be a better approximation if the rate of heating was reduced and if inert fine metal wire were interwoven through the mass of powder to serve as a conductor of heat. A second assumption which is not likely to be generally correct is that D is independent of the concentration of the diffusing zeolitic constituent. However, if the method is found satisfactory in other respects, it will still yield mean values of D over a concentration range. It should be noted that J is proportional to $-dw_\tau/dt$ and Q to w_τ, where w_τ denotes the weight of water remaining at time t. Thus $J/Q = -d\ln w_\tau/dt$.

Acknowledgements—The work described in this paper and in Parts II and III forms part of a programme of research on the properties of water, originally sponsored at Imperial College by the D.S.I.R. and the Rockefeller Foundation. One of us (G.C.B.) is glad to acknowledge the award of a research scholarship which made his participation possible. The authors are indebted to Dr. I. KERR of this department for helpful discussion, and to P. J. REUCROFT, B.Sc., for calculations of changes in chemical potential of the zeolite lattice.

REFERENCES

1. BARRER R. M., *Experientia, Supplementum VII*, p. 113 (1957).
2. VAN DER WAALS J. H., *Trans. Faraday Soc.* **52,** 184 (1956).
   PLATTEEUW J. C. and VAN DER WAALS J. H., *J. Mol. Phys.* **1,** 91 (1958).
3. BARRER R. M. and STUART W. I., *Proc. Roy. Soc.* A**242,** 172 (1957).
4. LENNARD-JONES J. E. and DEVONSHIRE A. F., *Proc. Roy. Soc.* A**163,** 53 (1957); A**165,** 1 (1938).
5. PRIGOGINE I. and GARIKIAN G., *J. Chim. Phys.* **45,** 273 (1948).
6. BARRER R. M., *The Structure and Properties of Porous Materials* (Colston Papers) Vol. 10, p. 6. Butterworths Scientific Publications, London (1958).
7. BARRER R. M. and FENDER B. E. F. In preparation.
8. LINDE AIR PRODUCTS LTD., private communication from Dr. BRECK.
9. BARRER R. M., BULTITUDE F. W. and SUTHERLAND J. W., *Trans. Faraday Soc.* **53,** 1111 (1957).
10. NOWACKI W., *Experientia* **12,** 418 (1956).
11. WEISSBERGER A., *Techniques of Organic Chemistry*, Vol. 7, p. 333. Interscience Publishers, New York (1955).
12. FARKAS A. and MELVILLE H. W., *Experimental Methods in Gas Reactions*, p. 162. Macmillan, London (1939).

13. E.g. BARRER R. M. and MEIER W. M., *Trans. Faraday Soc.* **54,** 1074 (1958).
14. MCBAIN J. W. and BAKR A. M., *J. Amer. Chem. Soc.* **48,** 690 (1926).
15. C.f. BARRER R. M., BUSER W. and GRUTTER W. F., *Helv. Chim. Acta* **39,** 518 (1956).
16. GOULD F. A. and VICKERS T., *J. Sci. Instrum.* **29,** 85 (1952).
17. *Handbook of Chemistry and Physics*, 1958–59, p. 2142. Chemical Rubber Publishing Co., Cleveland (1958).
18. BENNETT M. J. and TOMPKINS F. C., *Trans. Faraday Soc.* **53,** 184 (1957).
19. BARRER R. M. and LANGLEY D. A., *J. Chem. Soc.* 3804 (1958).
20. BARRER R. M. and LANGLEY D. A., *J. Chem. Soc.* 3817 (1958).
21. DAVIES M. M., *Quart. Rev. Chem. Soc. Lond.* **8,** 250 (1954).
22. BARRER R. M. and BRATT G. C., *J. Phys. Chem. Solids* **12,** 146 (1959).
23. *Selected Values of Chemical Thermodynamic Properties*, U.S. National Bureau of Standards, Washington, D.C. (1952).
24. BARRER R. M. and SUTHERLAND J. W., *Proc. Roy. Soc.* A**237,** 439 (1956).
25. C.f. BRUNAUER S., *The Physical Adsorption of Gases and Vapours*, Chap. 5. Oxford University Press (1944).
26. BARRER R. M. and BROOK D. W., *Trans. Faraday Soc.* **49,** 940 (1953).
27. DUBININ M. M., *Symposium on Industrial Carbon and Graphite, London*, 1957, Session III, p. 1.
28. E.g. FOWLER R. H. and GUGGENHEIM, E. A., *Statistical Thermodynamics* p. 441. Cambridge University Press (1939).
29. E.g. BARRER R. M., *Trans. Brit. Ceram. Soc.* **56,** 155 (1957).
30. FREEMAN E. S. and CARROLL B., *J. Phys. Chem.* **62,** 394 (1958).
31. CARSLAW H. S. and JAEGER J. C., *Conduction of Heat in Solids*, p. 85. Oxford University Press (1947).

VOL. 12 59/60

J. Phys. Chem. Solids Pergamon Press 1959. Vol. 12. pp. 146–153 Printed in Great Britain.

NON-STOICHIOMETRIC HYDRATES—II

SOME HEATS AND ENTROPIES FOR WATER AND AMMONIA IN ION-EXCHANGED FAUJASITES

R. M. BARRER and G. C. BRATT

Physical Chemistry Laboratories, Chemistry Department, Imperial College, London, S.W.7

(*Received* 18 *June*)

Abstract—The differential heat and entropy of zeolitic water have been evaluated in Li-, Na-, K-, Cs- and Ca-rich forms of faujasite, over a range in amount sorbed, and the same heat and entropy have been determined for zeolitic ammonia in Na-faujasite. The main features of these quantities have been discussed, and the heats interpreted in terms of dispersion forces and interactions of molecules with electrostatic fields and field gradients within the crystals. Heterogeneity may initially be present to an extent which is a function both of the molecule being sorbed (argon, nitrogen or water), and of the intracrystalline cation present. It is ascribed to a relatively small number of ionic centres associated with high local electrostatic fields and field gradients.

1. INTRODUCTION

THE free-energy function discussed for zeolitic water in Part I[1] shows that no simple description of the isotherm contours can be given in terms, for example, of a statistical-thermodynamic model. The complexity of these crystal–water systems is evident, but some light may be thrown upon them by further developing the thermodynamic approach. In the present paper therefore the enthalpy and entropy changes associated with uptake of zeolitic water will be considered. One may then hope to explain salient features of the variation of these quantities with increasing water content, and finally to interpret some of them quantitatively. The classification of non-stoichiometric hydrates can be made in terms of structure[2] on the one hand, and of thermodynamic properties on the other.[3] Some structural features of non-stoichiometric hydrates are now understood,[3–8] but a thermodynamic description is almost entirely lacking.*

2. ENERGETICS OF SORPTION

Two heats may be considered, associated respectively with water loss during differential thermal analysis and with the change of sorption equilibrium with temperature. By calibrating the differential thermal-analysis apparatus, using reactions with known heat changes, molar integral heats, q_{dta}, associated with water loss have been determined for a series of ion-exchanged chabazites.[10] Owing to intrinsic difficulties in using a differential thermal analyser quantitatively,† such heats are more accurate in a comparative than in an absolute sense and are best considered only for a series of closely related structures. Values of q_{dta} have accordingly been derived from the thermograms for a series of ion-exchanged faujasites, using the calibration method of BARRER and LANGLEY[10].

Isosteric heats of sorption, q_{st}, were derived from curves of log p against $1/T$, where p denotes the equilibrium pressures for a constant amount sorbed. A family of such curves is shown for water in Li-faujasite in Fig. 1. Within the limits of accuracy of measurement, these curves appear linear and the slope of each is

$$\frac{\partial \ln p}{\partial \frac{1}{T}} = -\frac{q_{\mathrm{s}}}{R}.$$

* Considerable progress has been made in the statistical-thermodynamic description of clathrate solid solutions in water.[9]

† For a discussion see MACKENZIE[11].

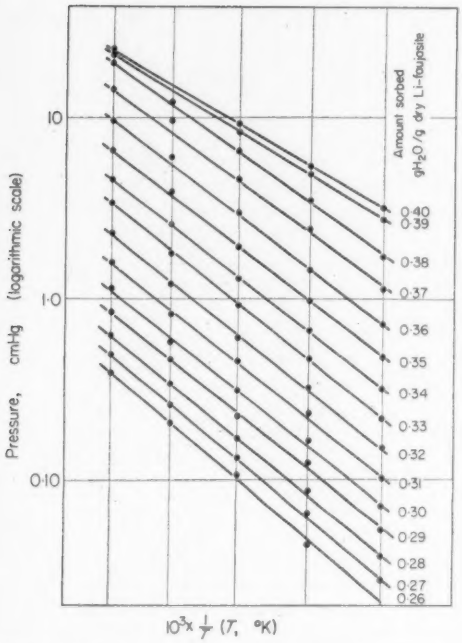

FIG. 1. Plots of log p vs. $1/T$ for various amounts of water sorbed in Li-faujasite.

Using these heats, integral heats, q_{int}, can be obtained from the relation

$$q_{int} = \frac{1}{n_s} \int_0^{n_s} q_{st}\, dn_s,$$

where n_s denotes the number of moles of water sorbed. However, isotherm data down to $n_s = 0$ were not normally obtained, owing to the difficulty in measuring equilibrium pressures for smaller sorptions. An exception was the H_2O-Na-faujasite system (Part I).

Integral heats associated with water loss and integral heats derived from isosteric heats from the relation

$$q_{int} = \frac{1}{n_2 - n_1} \int_{n_1}^{n_2} q_{st}\, dn_s$$

are given in Table 1, columns 2 and 5; n_1 and n_2, in moles of water per cation, are given in column 3. In columns 6 and 8 of Table 1 values of q_{dta} are quoted[10] respectively for a natural chabazite having an alumina : silica ratio of 1 : 5·05, and for a synthetic phase of chabazite-type in which this

Table 1. *Some integral heats associated with water loss during d.t.a.* (q_{dta}) *and with sorption equilibria* (q_{st})

Cationic form of zeolite	q_{dta} for homoionic forms (Kcal/mole)	$q_{int} = \frac{1}{(n_1 - n_2)} \int_{n_1}^{n_2} q_{st}\, dn_s$			q_{dta}[10] for homoionic natural chabazites (Kcal/mole)	q_{dta}(faujasite) $-q_{dta}$(natural chabazite) (Kcal/mole)	q_{dta}[10] for synthetic chabazite G3 (Kcal/mole)
		Limits of integration (as moles H_2O per cation)		q_{int} (Kcal/mole)			
		n_1	n_2				
Li	22·1	0·41	3	16·9	12·7	9·4	19·4
Na	16·1	0	3	14·0	14·3	1·8	16·6
K	21·4	1	2·9$_8$	16·1	14·9	6·5	16·0
Rb	23·1	—	—	—	13·3	9·8	—
Cs	26·1	1	2·6$_4$	15·1	15·0	11·1	—
Ca	13·9	2	6·8$_6$	13·7†	20·3	−6·4	22·0
		3	7·0	15·7‡			
Sr	11·8*	—	—	—	15·7	−3·9	—
Ba	15·9	—	—	—	24·2	−8·3	—
Cu	25·7*	—	—	—	—	—	—
Co	5·8*	—	—	—	—	—	—
Ni	22·3*	—	—	—	—	—	—

* Irreversible lattice changes occurred.
† Calculated from 60 to 70°C isotherms.
‡ Calculated from 30 to 60°C isotherms.

ratio is 1 : 2·65,[12] so that the phase is almost identical in composition with the synthetic faujasite of this work (Part I). Lattice structures and cation arrangements are, however, quite different.[5,6] The differences in q_{dta} for faujasites and the corresponding chabazites are of opposite sign for alkali-metal ionic forms on the one hand and alkaline-earth-metal ionic forms on the other (column 7).

In general it is seen that q_{dta} exceeds q_{int}. However, because high values of q_{st} are likely as $n_s \to 0$ (cf. Fig. 3),

$$q_{int} = \frac{1}{(n_2 - n_1)} \int_{n_1}^{n_2} q_{st}\, dn_s$$

should be less than

$$q_{int} = \frac{1}{n_2} \int_{0}^{n_2} q_{st}\, dn_s,$$

which may account for part of the difference apparent in Table 1. Part may also rest on uncertainties in differential thermal analysis as a quantitative procedure. In the water-Na-faujasite system, q_{int} was found over the full range of water contents $n_s = 0$ to $n_s = 3$ moles per cation. In this case $(q_{dta} - q_{int}) = 2{\cdot}1$ kcal/mol. In the same system, by comparing thermogram and thermogravimetric curves for identical heating rates, one may find

$$\frac{d(q_{dta})}{dn_s} = \bar{q}_{dta}.$$

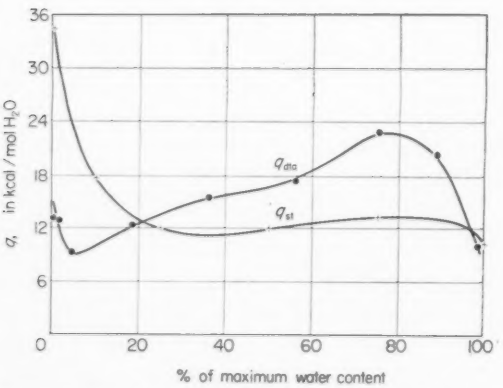

FIG. 2. Comparison of isosteric heat of sorption of water in Na-faujasite with differential heat associated with water loss as obtained from the thermogram.

The differential heats so derived are compared with q_{st} in Fig. 2. $\bar{q}_{dta}$ does not correspond to equilibrium conditions because, during the kinetic stage of desorption the water is not uniformly distributed in the crystals.

In Fig. 3 the isosteric heats of sorption for several cationic forms of faujasite are plotted as functions of θ.* Although q_{st} was found as $n_s \to 0$ only in the

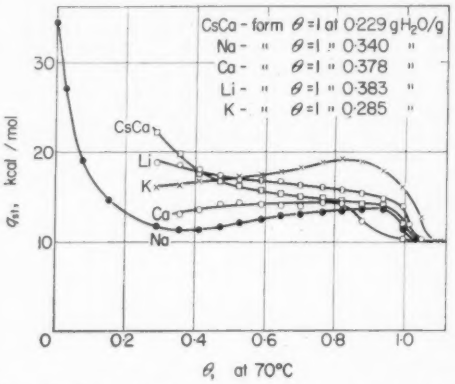

FIG. 3. Isosteric heats of sorption of water in ion-exchanged faujasites.

case of Na-faujasite, it is probable that all cationic forms would show a similar initial decrease for small values of n_s. This is followed sometimes, but not always, by a gradual rise for larger values of the amount sorbed, and then finally, as saturation of the crystals is approached and passed ($\theta \geqslant 1$), there is a rapid fall in heat towards the latent heat of vaporization of water. The gradual rise indicates exothermal water–water interactions in the intracrystalline fluid, and is apparent in the Na- and K-faujasites. Where this interaction "hump" is not found the self-potential developed by the water may be outweighed by falling values of other potential-energy terms between water and the lattice.

In Table 2 a comparison is made between some isosteric heats for ammonia and water in Na-faujasite. The heats for ammonia decrease monotonically as θ increases, and they are smaller than some heats earlier obtained for a natural Ca-richchabazite[10] (Table 2, column 4). It is

* By θ we mean the fraction of saturation of the intracrystalline volume of the crystals.

Table 2. Comparison of isosteric heats for NH_3 *and* H_2O *in* Na-*faujasite* (*Kcal/mole*)

θ	Na-faujasite		Chabazite[13]	Nett heats (Na-faujasite)	
	NH_3	H_2O	NH_3	NH_3	H_2O
$0{\cdot}26_1$	14·2	12·2	23·1	9·3	2·0
$0{\cdot}30_4$	13·8	11·7	22·1	8·9	1·5
$0{\cdot}34_8$	13·4	11·4	21·5	8·5	1·2
$0{\cdot}39_1$	12·9	11·3	21·0	8·0	1·1
$0{\cdot}43_5$	12·5	11·4		7·6	1·2
$0{\cdot}47_8$	12·1	11·7		7·2	1·5
$0{\cdot}52_2$	11·7	12·1		6·8	1·9
$0{\cdot}56_5$	11·2	12·3		6·3	2·1
$0{\cdot}60_9$	10·8	12·5		5·9	2·3
$0{\cdot}65_2$	10·3	12·7		5·4	2·4
$0{\cdot}69_6$	9·5	12·9		5·0	2·7
$0{\cdot}73_9$	9·5	13·0		4·6	2·8

VOL. 12 59/60

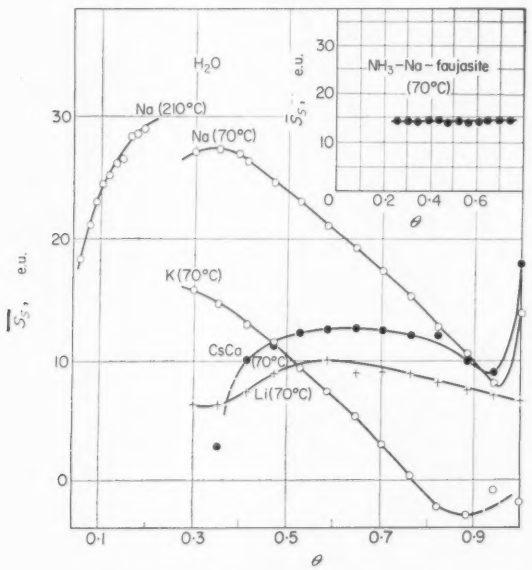

FIG. 4. Differential entropies of zeolitic water and ammonia in ion-exchanged faujasites.

interesting that the nett heats (i.e. the isosteric heat minus the heat of vaporization of sorbate) are considerably larger for ammonia than they are for water (columns 5 and 6).

3. ENTROPY OF ZEOLITIC WATER AND AMMONIA

From isosteric heats of sorption the partial molal entropies, $\bar{S}_s$, of zeolitic water or ammonia may be derived:

$$\bar{S}_s = \tilde{S}_g - \frac{q_{st}}{T}, \qquad (1)$$

where $\tilde{S}_g$ denotes the molal entropy of gaseous sorbate at the equilibrium pressure, which may be determined as described elsewhere.[14] Fig. 4 then

shows the values of $\bar{S}_s$ as a function of amount sorbed for various ionic forms of faujasite. The differential entropy, $\bar{S}_s$, may be expressed as the sum of differential configurational and thermal entropies:

$$\bar{S}_s = \bar{S}_c + \bar{S}_{\mathrm{Th}}. \qquad (2)$$

The entropy curves of Fig. 4 behave, qualitatively, in an inverse manner to the heat curves of Fig. 3, a maximum in the one being reflected by a minimum in the other, and conversely. This behaviour can be understood in the following terms. As the initially high heat of sorption diminishes, the corresponding thermal entropy, $\bar{S}_{\mathrm{Th}}$, of zeolitic water or ammonia increases. This outweighs any change in configurational entropy, $\bar{S}_c$, and so there is a rise in $\bar{S}_s$. For larger amounts sorbed, where q_{st} changes less rapidly with θ, the diminishing configurational entropy becomes more important and so $\bar{S}_s$ decreases. Finally, however, sorption as multilayers, or capillary condensation, upon external surfaces begins to supersede intracrystalline sorption ($\theta \to 1$ and $\theta > 1$), and an increase in $\bar{S}_c$ and probably also in $\bar{S}_{\mathrm{Th}}$ begins (Fig. 4).

Isosteric heats for K- and Na-faujasites have begun to increase for values of $\theta > 0{\cdot}4$ (Fig. 3), and accompanying this is a steady decrease in $\bar{S}_s$ (Fig. 4). In these two systems at least it must be the decrease in $\bar{S}_s$ which determines the positive slope in the curves of $\log(1-\theta)/\theta$ vs. θ (Part I), rather than a nett repulsion between water molecules, because the slope of the curves of q_{st} vs. θ (Fig. 3) indicates an exothermal water–water interaction in the relevant range of θ.

In the systems NH_3-Na-faujasite at 70°C for $0{\cdot}26 < \theta < 0{\cdot}74$, and H_2O-Li-faujasite for $0{\cdot}29 < \theta < 1{\cdot}0$, $\bar{S}_s$ does not vary greatly. Here there must be an approximate balance between a decrease in configurational and an increase in thermal entropy as θ rises. This behaviour was noted previously at 173°K for nitrogen in Li- and Na-faujasites in the range $0 < \theta < 0{\cdot}5$ and for argon in Ca-faujasite in the range $0 < \theta < 0{\cdot}3$, for which a similar explanation was offered.[15] The general character of all these curves of $\bar{S}_s$ against θ can be qualitatively understood, but in the cases cited and for zeolitic ammonia and water no idealized model is compatible with the entropy functions or isotherms, and accordingly at the present stage no detailed analysis of the entropy function will be made.

4. ANALYSIS OF ENERGETICS OF ZEOLITIC WATER IN Na-FAUJASITE

The isosteric heat, q_{st}, is given by

$$q_{\mathrm{st}} = \bar{E}_g - \bar{E}_s + RT = \bar{\phi} - \bar{\phi}_0 + RT - \bar{F}(T) \qquad (3)$$

where $\bar{E}_g$ is the molar energy of gaseous sorbate, $\bar{E}_s$ is the molar differential energy of zeolitic water, $\bar{\phi}$ is the molar differential sorption potential and $\bar{\phi}_0$ is the differential zero-point energy. $\bar{F}(T)$, a function of temperature, occurs because as temperature rises the sorbed molecule acquires vibrational energy in excess of the zero-point energy, while the gas molecule also gains in translational energy. Thus for monatomic classical oscillators $\bar{F}(T) = \frac{3}{2}RT$, since a vibrational mode involves two "square terms" and a translation only one.

$\bar{\phi}$ is the sum of differential dispersion ($\bar{\phi}_D$), repulsion ($\bar{\phi}_R$), polarization ($\bar{\phi}_P$), field-dipole ($\bar{\phi}_{F,\mu}$), field gradient-quadrupole ($\bar{\phi}_Q$) and molecule–molecule self-potentials (ϕ_{SP}):

$$\bar{\phi} = \bar{\phi}_D + \bar{\phi}_R + \bar{\phi}_P + \bar{\phi}_{F\ \mu} + \bar{\phi}_Q + \bar{\phi}_{SP} \qquad (4)$$

Also q_{st}^0, the isosteric heat at 0°K, is related to q_{st} at temperature T by the expression

$$q_{\mathrm{st}} = q_{\mathrm{st}}^0 - \int_0^T \Delta C_p \, dT \qquad (5)$$

where $-\Delta C_p = (\bar{C}_g - \bar{C}_s)$ and $\bar{C}_g$ and $\bar{C}_s$ denote molar and molar differential heat capacities of the sorbate in the gas phase and in the crystal, respectively. In terms of the integral sorption potential, ϕ, and zero-point energy, ϕ_0, and of the function $\bar{F}(T)$

$$q_{\mathrm{st}} = (\phi - \phi_0) - \left(\frac{\partial(\phi-\phi_0)}{\partial n_s}\right)_{P,T,n_{\mathrm{sorbent}}} + RT - \bar{F}(T). \qquad (6)$$

At 0°K

$$q_{\mathrm{st}} = (\bar{\phi} - \bar{\phi}_0) = (\phi - \phi_0) - n_s\left(\frac{\partial(\phi-\phi_0)}{\partial n_s}\right)_{P,T,n_{\mathrm{sorbent}}} \qquad (7)$$

Table 3. Physical constants for some molecular species

Molecule	Radius (Å)	Diamagnetic susceptibility, $\chi \times 10^{30}$ (c.g.s. units)	Polarisability, $\alpha \times 10^{24}$ (cm^3)	Dipole moment, $\mu \times 10^{18}$ (Debyes)	Quadrupole moment, $\times 10^{26}$ (e.s.u.)
A	1·92	31·0	1·62	0	0
N_2	1·50, 2·05	18·3	1·73	0	$\Theta = 1{\cdot}3$*
H_2O	1·38	21·5	1·48	1·84	$(\Theta_a + \Theta_b) = 3{\cdot}9$†, 1·2†, 0·43‡
NH_3	1·70	31·0	2·28	1·47	$\Theta = 1{\cdot}3$**, 0·66*, 0·14‡)

* From micro-wave spectra.[16a]
† From difference in hydration energy of F^- and K^+.[16b and e]
‡ From theoretical calculation.[16d]
** From difference in energy of ammoniation of F^- and K^+.[16b]

and then $(\bar{\phi}-\bar{\phi}_0) = (\phi-\phi_0)$ either when $n_s = 0$ or

when $$\left(\frac{\partial(\phi-\phi_0)}{\partial n_s}\right)_{P\ T,\, n_{\text{sorbent}}} = 0.$$

The energetics of sorption in various cationic forms of faujasite have been discussed for argon and nitrogen.[15] This analysis provides a starting point for consideration of zeolitic water or ammonia in Na-faujasite. Relevant physical constants are summarized in Table 3. Argon has no dipole or quadrupole moment; nitrogen has no dipole but a considerable quadrupole moment; while water and ammonia have large permanent dipoles, and also possess quadrupole moments.[16] The largest values of the quadrupole moments for water and ammonia in Table 3 may be upper limits only, and very much smaller values have been calculated.[16] Despite this uncertainty, a comparison of the energetics for each of these molecules in Na-faujasite can lead to an estimate of the important terms contributing to the differential sorption energy and can throw light upon the causes of energetic heterogeneity.

In Na-, K- and Ba-faujasites the polarization energy for argon was very small and no energetic heterogeneity was observed.[15] The energy of sorption is accounted for dispersion and repulsion energies which for the sodium form gave a resultant of $\sim 2{\cdot}5$ kcal/mole independent of θ for $0 < \theta < 0{\cdot}3$, this being the range covered by the experiments. For $0 < \theta < 0{\cdot}3$ argon–argon interactions are not important. Because of this result for argon it seemed reasonable to assume that $\bar{\phi}_D$ and $\bar{\phi}_R$ would be initially independent of θ for nitrogen[1] and also for water and ammonia. Indeed energetic homogeneity for sorption in Na-faujasite has been established for a number of species which have no appreciable dipoles (e.g. CH_4,[6] CF_4, C_2F_6 and SF_6[17]) and whose behaviour is governed largely by zero-point, dispersion and repulsion energies. However, energetic heterogeneity was observed for nitrogen in Li- and Na-faujasite, and was attributed to field gradient–quadrupole interaction,[15] in which a few ions only, being specially located, play a dominant role. For water and ammonia the largest quadrupole moments quoted in Table 3 are comparable with those of nitrogen. However, for water interacting with a cation, when the orientation of the molecule is governed by the dominant cation–dipole interaction, the cation–quadrupole energy is endothermic.[16b] For the purpose of the present calculation this quadrupole energy will be considered to balance the exothermic polarization energy. Accordingly the large energetic heterogeneity shown for small θ in the water-Na-faujasite system (Fig. 3) can be attributed mainly to a field–dipole interaction which is especially strong for a few ions only. These ions are thus distinguishable from most of the ions present and may represent centres of disorder or defects in the structure.

Table 4. Component energy terms for argon, nitrogen and water in Na-faujasite (Kcal/mole)

Energy term	Gases, and Range in θ		
	A ($0 < \theta < 0{\cdot}3$)	N_2 ($0 < \theta < 0{\cdot}5$)	H_2O ($0 < \theta < 0{\cdot}3$)
$\bar{\phi}_D+\bar{\phi}_R$	2·5	$\leqslant$4 (at 173°K)	3
$\bar{\phi}_P$	small	small	small
$\bar{\phi}_{F,\mu}$	0	0	$\bar{\phi}_{F,\mu}+\bar{\phi}_Q$ ~34 at $\theta = 0$
$\bar{\phi}_Q$	0	2·5 at $\theta = 0$; small at $\theta = 0{\cdot}5$	~ 9 at $\theta = 0{\cdot}3$
$\bar{\phi}_{SP}$	small	small	small

From the data of BARRER and STUART[15] and those of the present paper, it is possible to estimate the component energy terms for argon, nitrogen and water in Na-faujasite. Without taking zero-point energy corrections into account, these are given in Table 4. The value of $\bar{\phi}_D+\bar{\phi}_R$ is estimated by allowing for the difference in the dispersion constant for argon and water. It is further assumed that, as with argon, $\bar{\phi}_D+\bar{\phi}_R$ does not vary appreciably with amount sorbed.

Neglecting the opposing quadrupole and polarization terms as mentioned above,

$$(q_{st})_{\theta=0} - (q_{st})_{\theta=0{\cdot}3} = (\bar{\phi}_{F,\mu})_{\theta=0} - (\bar{\phi}_{F,\mu})_{\theta=0{\cdot}3} = 25 \text{ Kcal/mole.}$$

Since $\Delta\bar{\phi}_{F,\mu} = \Delta(\mu F)$, and if it is assumed that the change in $\bar{\phi}_{F,\mu}$ is due only to a change in field strength, then the change in effective field strength may be calculated. Thus $\Delta F = 0{\cdot}94\times10^6$ e.s.u. ($2{\cdot}82\times10^8$ V/cm). This value is comparable with the field due to a sodium ion at a distance given by $r_{Na^+}+r_{water}$ ($0{\cdot}89\times10^6$ e.s.u.). The decrease in field strength suggests initial occupation by water of sites near a few exposed ions which can behave virtually as though isolated.

It may be concluded that major factors in the initial energetic heterogeneity of faujasite are (i) high electrostatic fields probably associated with a small number of ionic centres, and (ii) high field gradients probably also associated with the same exposed ionic centres. Electrostatic fields give field-dipole energy terms (water and ammonia) and to a very much smaller extent polarization-energy terms (argon in Ca-faujasite[15]). Field gradients result in energy terms by interaction with quadrupoles (water or ammonia in Na-faujasite or nitrogen in Na- or Li-faujasites[15]). In the case of argon and nitrogen, initial heats are highest when the cation present is small or divalent. In these circumstances both the field and the field-gradient associated with any partly unscreened cations will be expected to have their largest values, and one may infer the existence of certain specially sited cations in the crystal lattice, which are more exposed than are the majority of the ions.

REFERENCES

1. BARRER R. M. and BRATT G. C., *J. Phys. Chem. Solids* **12,** 130 (1959).
2. BERNAL J. D., *J. Chim. Phys.* 1950, **50,** CNRS, No. 53.
3. BARRER R. M., *Experientia, Supplementum VII,* 113 (1957).
4. REED T. B. and BRECK D. W., *J. Amer. Chem. Soc.* **78,** 5972 (1956).
   BARRER R. M. and MEIER W. M., *Trans. Faraday Soc.* **58,** 1074 (1958).
5. BERGERHOFF G., KOYAMA H. and NOWACKI W., *Experientia* **12,** 418 (1956).
   BARRER R. M., BULTITUDE F. W. and SUTHERLAND J. W., *Trans. Faraday Soc.* **53,** 1111 (1957).
6. DENT L. S. and SMITH J. V., *Nature, Lond.* **181,** 1794 (1958).
7. TAYLOR W. H., *Proc. Roy. Soc.* A**145,** 80 (1934).
8. VON STACKELBERG M. and MULLER H. R., *Naturwissenshaften* **38,** 456 (1951).
   MULLER H. R. and VON STACKELBERG M., *ibid.* **39,** 20 (1952).

9. PLATTEEUW J. C. and VAN DER WAALS J. H., *J. Mol. Phys.* **1,** 91 (1958).
BARRER R. M. and STUART W. I., *Proc. Roy. Soc.* A**242,** 172 (1957).
10. BARRER R. M. and LANGLEY D. A., *J. Chem. Soc.* 3817 (1958).
11. MACKENZIE R. C., *Differential Thermal Analysis*, Chap. 3. Mineralogical Society, London (1957).
12. BARRER R. M. and BAYNHAM J. W., *J. Chem. Soc.* 2882 (1956).
13. BARRER R. M., *Proc. Roy. Soc.* A**167,** 392 (1938).
14. GARDEN L. A. and KINGTON G. L., *Proc. Roy. Soc.* A**234,** 24 (1956).
BARRER R. M., *Quelques Problemes de Chimie Minerale*, p. 21. Institut International de Chimie Solvay, Brussels (1956).
15. BARRER R. M. and STUART W. I., *Proc. Roy. Soc.* A**249,** 464, 484 (1959).
16. (a) HIRSCHFELDER J. O., CURTISS C. F. and BIRD R. B., *Molecular Theory of Gases and Liquids*, p. 1029. Wiley and Co. New York (1954).
(b) BUCKINGHAM A. D., *Disc. Faraday Soc.* No. 24, 151 (1957).
(c) ROWLINSON J. S., *Trans. Faraday Soc.* **47,** 102 (1951).
(d) DUNCAN A. B. and POPLE J. A., *Trans. Faraday Soc.* **49,** 217 (1953).
(e) See also EVERETT D. H., *Disc. Faraday Soc.* No. 24, 229 (1957).
RANDLES J. E. B., *ibid.*, p. 230.
17. BARRER R. M. and REUCROFT P. J. In preparation.

VOL. 12 59/60

J. Phys. Chem. Solids Pergamon Press 1959. Vol. 12. pp. 154–166. Printed in Great Britain.

NON-STOICHIOMETRIC HYDRATES—III

THE RELATIVE IMPORTANCE OF CATIONS AND OF ANIONIC FRAMEWORK IN DETERMINING THE ENERGETICS OF ZEOLITIC WATER

R. M. BARRER and G. C. BRATT

Physical Chemistry Laboratories, Chemistry Department, Imperial College, London, S.W.7

(*Received* 18 *June* 1959)

Abstract—In the range of amount sorbed outside the range where energetic heterogeneity is important, it was found that no clear correlation exists between heat of sorption of zeolitic water and the cation present in a series of ion-exchanged faujasites. Polarization energy, whether due to charge screening or saturation of induced polarization or both, contributes little to the energy of sorption of argon, and probably to that of nitrogen, water or ammonia. Although field-dipole energy for water or ammonia is considerably reduced below the value expected for interaction with isolated ions, it continues to play an important role. In porous, oxygen-rich heteroionic crystals it is the anionic oxygens which for larger amounts sorbed appear to determine the energy of sorption of water, argon or nitrogen, with cations and self-potential exercising moderating influences.

1. INTRODUCTION

In Part II[1] the initial energetic heterogeneity of porous, heterionic faujasite-type crystals was shown to be associated with a relatively small number of cations which are evidently located differently within the structure from the average cation. However, for larger amounts sorbed energetic heterogeneity is less important.[1,2] It is then of interest to assess for strongly polar molecules, such as water or ammonia, the relative importance of cations (bearing a high charge) and of the more numerous framework atoms of oxygen (polar, but bearing only a small net charge) in determining the magnitude of the heat of sorption. For a non-polar species such as argon, it has already been demonstrated that the anionic framework determines this energy.[2] It is proposed in the present paper to approach the problem for polar molecules by finding whether correlations exist between the heats of sorption of zeolitic water in the ion-exchanged faujasites and the electrostatic energies which could arise between water dipoles, the several intracrystalline cations and the anionic environment.

2. NORMAL CHARGE DISTRIBUTIONS

There are 82 monovalent cations in each unit cell of $\sim 24{\cdot}7$ Å edge, in the sample of near-faujasite used.[3] In an aluminosilicate framework with $Al_2O_3 : SiO_2 = 1 : 2$ the anionic charge should be uniformly distributed over all oxygens, since Al–O–Si bonds only are then present. This average anionic charge per framework oxygen atom is $0{\cdot}25e$. In the faujasite studied in this paper the average charge per oxygen atom is $0{\cdot}214e$, although this charge may not be distributed quite uniformly, since some disorder among Al and Si atoms is possible. The uniformity of distribution may be further decreased when divalent ions are present. In the most siliceous zeolites, mordenite or ptilolite, with $Al_2O_3 : SiO_2 = 1 : 10$, the average charge per oxygen atom has fallen to $0{\cdot}083e$, and will almost certainly not be uniformly distributed. In faujasite the normal cation positions are not known, although for smaller ions (Li^+, Na^+, Ca^{++} and Sr^{++}) they may be located near the centres of the six-membered rings as in Linde Sieve A,[4] while larger ions (K^+, Rb^+, Cs^+ and Ba^{++}) would for steric reasons be displaced to one side of these rings.

Measurement of self-diffusion kinetics of Na^+ in hydrated Na-faujasite has demonstrated a high cation mobility,[5] so that energy barriers for ion movements from one part of the hydrated crystal

to another are small. In the dehydrated structure the problem of ion migration may be approached by calculating electrostatic energy differences for ions as they move across the plane of a 12-membered silicate ring; or as they approach axially an *n*-membered ring. Polarization is not considered, and each oxygen is assumed to have a net charge of 0·214*e*. It was then calculated that:

(i) as an ion moves along a diameter of an isolated plane 12-membered ring of 8 Å free diameter, the difference in energy for an ion at its equilibrium position and at the centre of the ring is 27 kcal/g-ion for Na^+ and 50 Kcal/g-ion for Ca^{++};

(ii) when a sodium ion approaches a 4-, 6-, 8- or 12-membered ring along the axis normal to the plane of the ring and passing through the ring centre, the minimum electrostatic energies are:

n	*Energy (Kcal/g-ion)*
4	142
6	154
8	155
12	157

The faujasite framework is composed of 4-, 6- and 12-membered rings,[3] while those of Linde Sieve A[4] and of chabazite[6] are composed of 4-, 6- and 8-membered rings. The calculations suggest that translations of certain ions between 6- and 8-membered rings may not involve large energy changes, but that, taking (i) and (ii) together, there would be a preference for the ion to adhere to the inner edge of the 12-membered ring.

The exact charge distributions in water and ammonia are still subjects of discussion.[7–10] However, these charge distributions are such as to give large permanent dipole moments and also quadrupole moments (Table 3, Part II). Suppose we have a distribution of charges e_i at points r_i relative to a point whose position from 0 is r. Then the potential V at r due to this charge system can be expressed as:[10]

$$V = \frac{q}{r} - \frac{\mu \cos\theta}{r^2} - \\ - \frac{1}{2r^3}\{\Theta_a(3\cos^2\theta_x - 1) + \Theta_b(3\cos^2\theta_y - 1)\} \quad (1)$$

where $\Theta_a = \Theta_{zz} - \Theta_{xx}$, $\Theta_b = \Theta_{zz} - \Theta_{yy}$, and Θ_{xx}, Θ_{yy} and Θ_{zz} are the principal quadrupole moments of the charge distribution. θ_x, θ_y and θ_z are the angles specifying the directions of the principal axes relative to the position vector of the point r. If the charge distribution is axially symmetric, as for ammonia,

$$\Theta_a = \Theta_b = \Theta = \sum_i e_i(z_i^2 - x_i^2)$$

$$= \tfrac{1}{2}\sum_i e_i(3z_i^2 - r_i^2) \quad (2)$$

(where x_i, y_i and z_i are the co-ordinates of charge e_i), so that*

$$V = \frac{q}{r} - \frac{\mu\cos\theta}{r^2} + \frac{\Theta}{2r^3}(3\cos^2\theta - 1) - \ldots \quad (3)$$

For a spherical ion of charge Ze the interaction energy with an uncharged molecule whose dipole axis lies along the z-direction is

$$\phi = -ZeV \quad (4)$$

where V is given by equation (1) for the water molecule and equation (3) for the ammonia molecule, in each case without the term q/r, since the water and ammonia molecules have no net charge. In the most favourable configuration, where $\theta_z = 0$ for interaction with a positive ion or π for an anion, equation (1) gives

$$\phi = \phi_{F,\mu} + \phi_Q = -\frac{|Z|e\mu}{r^2} + \frac{Ze(\Theta_a + \Theta_b)}{2r^3} - \ldots \quad (5)$$

Unfortunately there is poor agreement between the values of quadrupole moments obtained by different workers either for water or for ammonia, and no available method is free from criticism.[8,12] Theoretical estimates[8] give $(\Theta_a + \Theta_b) = 0{\cdot}43 \times \times 10^{-26}$ e.s.u. for water and $\Theta = 0{\cdot}14 \times 10^{-26}$ e.s.u. for ammonia. Estimates from the different heats of hydration and ammoniation of F^- and K^+ give $(\Theta_a + \Theta_b) = 3{\cdot}9 \times 10^{-26}$ e.s.u. for water and $\Theta = 1{\cdot}3 \times 10^{-26}$ for ammonia.[10] It has however been suggested that the quadrupole moment thus derived for water is considerably too high, because of an over-estimate of the difference in hydration heat

* According to an alternative definition, the linear quadrupole moment is taken as

$$Q = \Sigma\, e_i(3z_i^2 - r_i^2), \text{ so that } \Theta = \tfrac{1}{2}Q.$$

Table 1. Energies of interaction, $-\phi$, for water and ammonia with isolated ions at contact ($r_{ion}+r_{H_2O \text{ or } NH_3}$), in Kcal/mole. An ideal dipole is assumed*

Ion	Radius, r (Å)	Polarizability $\alpha \times 10^{24}$ (cm^3)	Diamagnetic susceptibility χ, $\times 10^{30}$	$-\phi$									
				Ion-Dipole		Ion-Quadrupole		Polarization		Dispersion +Repulsion		Total	
				(1)	(2)	(1)	(2)	(1)	(2)	(1)	(2)	(1)	(2)
Li^+	0·60	0·029	1·05	32·7	17·7	−16·9	−7·2	16·1	11·6	0·3	0·1	32·2	22·2
Na^+	0 95	0·19	7·0	23·7	13·7	−10·4	−4·8	8·8	6·7	0·7	0·4	22·8	16·0
K^+	1·33	0·84	27·7	17·5	10·5	− 6·7	−3·2	4·5	4·0	1·2	0·7	16·5	12·0
Rb^+	1·48	1·41	58·0	15·7	9·6	− 5·7	−2·8	3·7	3·5	1·5	1·0	15·2	11·3
Cs^+	1·69	2·44	91·0	13·6	8·5	− 4·7	−2·2	2·8	2·6	1·8	1·1	13·5	10·0
Ca^{++}	0·99	0·47	22·1	45·7	26·5	−20 0	−9·0	31·3	25·3	1·5	0 9	58·3	43·7
Sr^{++}	1·13	0·86	46·4	40·6	24·1	−16·7	−7·8	25·3	20·8	2·1	1·2	51·3	38·3
Ba^{++}	1·35	1·56	76 0	34·4	20·8	−13·0	−6·2	18·9	15·6	2·2	1·4	42·5	31·6
O^{--}	1·40	3·9	20·9	33·3	20·2	+12·4	+6 0	18·1	14·9	1·8	2·3	65·6	43·4
$O^{0.214e}$	1·40	3·9	20·9	3·3	2·2	+ 1·3	+0 6	2·3	0·8	1·8	2·3	8·9	5·9

* For the necessary physical constants of H_2O and NH_3 see Part II, Table 3.[1]

(1) Values refer to ion–water interactions.

(2) Values refer to ion–ammonia interactions.

between F^- and K^+. A further calculation on this basis then gave $(\Theta_a+\Theta_b) = 1{\cdot}2\times10^{-26}$ e.s.u.[12] A value of Θ of $0{\cdot}66\times10^{-26}$ has been assigned to ammonia from pressure broadening of rotational lines.[7] ROWLINSON[9] has also estimated quadrupole moments of water from the second virial coefficient.

We will take $(\Theta_a\times\Theta_b) = 3{\cdot}9\times10^{-26}$ e.s.u. for water and $\Theta = 1{\cdot}3\times10^{-26}$ e.s.u. for ammonia, in order to estimate what may be upper limits to the magnitudes of quadrupole energies. In Table 1 some interaction energies for isolated water–ion pairs are given, on the following bases. To allow for the effect of temperature on orientation the mean interaction energy should be calculated from equation (vii) of the Appendix, but because of the complexity of this relationship and the fact that it does not give the contributions of the separate terms, an approximation method has been used. The separate maximum exothermal values of $\phi_{F,\mu}$ and $(\phi_{\text{ind}}+\phi_{\text{P}})$ (equations (i), (ii) and (iv) of the Appendix) were found not to differ appreciably from their mean values (equations (viii) and (x) of the Appendix), and since the main concern is to show the relative values of the interaction energy for the various ion–water pairs, the use of equations (i)–(iv) for an orientation determined by the ion-dipole term (i.e. $\theta = 0$) is justifiable. This orientation causes ϕ_Q to assume its maximum endothermal value for interaction with the cations. The resultant of dispersion and repulsion energies is based on the approximation that the repulsion energy is half the dispersion energy, and the dispersion constant is calculated from the Kirkwood–Muller relationship[11] and the repulsion constant is derived from this assuming that equilibrium separation is

$$r_0 = r_{\text{ion}}+r_{\text{water}}.$$

A linear dipole of length 0·6 Å and charges $\pm0{\cdot}61e$ gives the observed moment $1{\cdot}84D$ for water and approximates to that required by the geometry of this molecule. As compared with a point dipole

$$\frac{\phi_{F,\mu} \text{ for dipole of length } l}{\phi_{F,\mu} \text{ for point dipole}} = 1+\beta+\beta^2+\ \ldots$$

where $\beta = l^2/4r^2$. Even in the case of the Li^+ ion and water, taking $r = 2{\cdot}0$ Å, the correction is only about 2 per cent, so that corrections to field-dipole energy of this kind need not usually be made.

For the monovalent ions, on the basis of values for Θ suggested by BUCKINGHAM[10], quadrupole energy for cations and water nearly offsets the sum of polarization, dispersion and repulsion energies. On the other hand if one uses values of Θ calculated by DUNCAN and POPLE[8], these quadrupole energies are reduced nine-fold, and are relatively insignificant. A distinction between oxygen anions, or the anionic oxygen of the lattice framework, and the cations arises because of the change in sign of the quadrupole energy, associated with orientation of water by ion-dipole forces which for water and ammonia enhances the solvation energy of anions relative to cations.[10]

Whether quadrupole energies are included in the total interaction energies or not, comparison of the results in Table 1 with heats in Table 1 of Part II[1] shows that calculations based on isolated cation–water interactions do not represent either the magnitudes or sequence of the heats of sorption of water in different cationic modifications of faujasite or of chabazite.[13] Reasons for this are considered in the following sections. Comparison of the total interaction energies for water and ammonia with the sodium ion suggest that for the sorption of these materials in Na-faujasite at small coverages where a few largely unscreened Na-ions may be concerned (Part II), the heat of sorption of water should exceed that for ammonia by as much as 6·8 Kcal/mole. However, the experimental values (Table 2, part II) show that the heat of sorption of water in Na-faujasite is already 2·0 kcal less than that for ammonia at the lowest coverage available for comparison ($\theta = 0{\cdot}26$). Evidently, as suggested in Part II, at this value of θ no effectively unscreened ions remain.

3. CHARGE SCREENING AND POLARIZATION ENERGY

Calculations of polarization energy, whether based on equation (ii) or (x) of the Appendix, draw attention to the large value of this energy. On the other hand the energetics of sorption of argon and of nitrogen in ion-exchanged faujasites[2] have emphasized the smallness of the contribution actually made by polarization energy to the heat of sorption. It may be assumed that this tends to be

true of sorbates in general, and a basis for such behaviour must be sought.

LENNARD–JONES and DENT[14] demonstrated that the polarization energy for argon approaching a heteropolar surface of alternate K^+ and Cl^- ions in potassium chloride was very small. There was very complete screening of the effects of positive ions by negative ions and vice versa. Charge distributions in faujasite are however very different, the anionic charge being spread in smaller units on a larger number of atoms than the cationic charge (Section 2). Polarization energies may therefore be considered for the water molecule approaching a 6-ring of tetrahedra in or near the plane of which are cations of various dimensions. Such a ring has a free diameter determined by six anionic oxygens each carrying a charge of $0{\cdot}214e$. We will take the free diameter to be 2·2 Å and the distance between the centres of opposite oxygen atoms as 5·0 Å. Li^+, Na^+, Ca^{++} and possibly Sr^{++} ions are each small enough to be placed in the centre of the ring; K^+, Rb^+, Cs^+ and Ba^{++} are displaced for steric reasons to one side or the other of this ring (Fig. 1a). Water

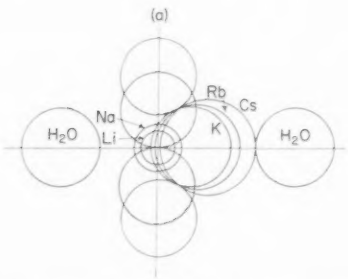

FIG. 1a. Interaction of water-dipoles with a ring of six anionic oxygens (from six $(Al,Si)O_4$ tetrahedra) plus an associated cation. A water molecule is shown on both sides of the ring. The cations Li and Na are in the plane of the ring; the larger ions K, Rb and Cs are shown displaced by appropriate amounts to one side of the ring.

molecules may approach the ring from the same or the opposite side to that to which the larger cations are displaced.

In Table 2 are given the ratios $(\phi_{net}/\phi_+)_P$ for the various possible cases which can arise. In this ratio $(\phi_+)_P$ denotes the polarization energy according to the equation:

$$(\phi^+)_P = -\tfrac{1}{2}\alpha F_+^2 \qquad (2)$$

where F_+ is the field due to the cation alone at the centre of the water molecule. These calculations show very large screening effects in some circumstances, which are always more important for

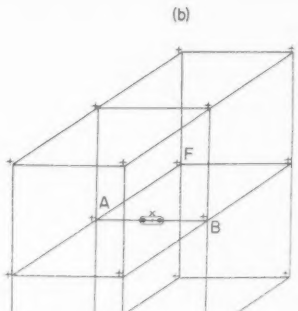

FIG. 1b. A system of 18 univalent cations with a dipole centred on point X and directed along the line AB.

polarization than for field-point dipole interactions (columns 3 and 4). Calculations were also made for the dipole of length 0·6 Å displaced along the line AB in the symmetrical group of cations of Fig. 1b. The polarization energy was zero when the centre of the dipole was at the centre of symmetry of the charge system, but as the dipole was displaced towards the cation A the energy, from equation (2), increased rapidly towards the value of the polarization energy in the presence of an isolated cation A.

Polarization energy is thus very sensitive to the symmetry of charge distribution, but is insufficiently reduced in some positions for the models considered to account, for example, for the minor role played by polarization in the argon-Na-faujasite system. There is however another possibility which may reduce polarization energies still further. In deriving equation (2) the induced dipole moment is regarded as proportional to the inducing field:

$$\mu = \alpha F. \qquad (3)$$

This relation is valid only for weak fields; strong fields may introduce terms in higher powers of F[15] (in F^3, F^5 etc.). There may then be an

Table 2. Ratios $(\phi_{net}/\phi_+)_P$ *and* $(\phi_{net}/\phi_+)_{ion\text{-}dipole}$ *for water interacting with 6-ring + cation systems (Fig. 1a)*

Distance from H_2O centre to ring centre (Å)	Corresponds to contact at $(r_{ion}+r_{H_2O})$	$(\phi_{net}/\phi_+)_P$	$(\phi_{net}/\phi_+)_{ion\text{-}dipole}$
(a) *Monovalent cation at ring centre*			
2·0	Li^+ at ring centre	0·48	0·69
2·35	Na^+ at ring centre	0·35	0·59
2·73	—	0·24	0·49
2·88	—	$0·20_2$	0·45
3·00	—	$0·17_5$	0·42
(b) *Divalent cation at ring centre*			
2·39	Ca^{++} at ring centre	0·64	0·78
2·53	Sr^{++} at ring centre	0·59	0·77
2·73	—	0·55	0·74
2·88	—	0·52	0·73
3·00	—	0·50	0·71
(c) *Molecule and cation on same side of ring*			
3·82	K^+	0·38	0·62
4·31	Rb^+	0·40	0·63
4·90	Cs^+	0·42	0·65
3·90	Ba^{++}	0·65	0·81
(d) *Molecule and cation on opposite side of ring*			
1·64	K^+	0·17	0·41
1·45	Rb^+	0·14	0·37
1·28	Cs^+	0·081	0·29
1·60	Ba^{++}	0·49	0·70
(e) *No cation associated with ring*			
2·0	—	0·076	0·28
2·35	—	0·133	0·40
2·73	—	$0·20_6$	0·46
2·88	—	0·24	0·49
3·09	—	0·28	0·53

approach to saturation of polarization for stronger fields. This behaviour can be represented by

$$\mu = \frac{2\mu_\infty}{\pi}\tan^{-1}\frac{F}{a} \qquad (4)$$

where a is a constant equal to $2\mu_\infty/\pi\alpha$. As F/a becomes large, μ, according to equation (4), tends to μ_∞, while for small F, equation (3) is recovered. Also, as required, μ changes sign with F. The polarization energy is then

$$\phi_P = \frac{4\mu^2_\infty}{\pi^2\alpha}\ln\left[1+\left(\frac{F}{a}\right)^2\right]^{\frac{1}{2}} - \frac{2\mu_\infty F}{\pi}\cdot\tan^{-1}\frac{F}{a} \qquad (5)$$

Induction energies for a water molecule near or in contact with monovalent ions such as those of the alkali metals for various values of μ_∞ are shown in Fig. 2a, and are much less than this energy calculated from equation (2) for reasonable choices of μ_∞. A combination of charge screening, symmetry

of charge distribution and saturation of polarization may thus explain the small values of the polarization energy encountered in intracrystalline sorption, in some heteroionic porous crystals.

4. FIELD-DIPOLE ENERGY

According to the analysis of Part II, field-dipole energy for water is considerable at $\theta = 0{\cdot}3$ but is nevertheless well below the calculated energies of Table 1. Perhaps more important still, experimental heats do not follow the order of these calculated ion-dipole energies which would require the following sequence in heats for the ion-exchanged forms:

$$Ca > Sr > Ba > Li > Na > K > Rb > Cs.$$

A comparison of the total energies of Table 1 and integral heats for finite additions of water is shown in Table 3. Charge screening can play an important part, as shown in Table 3, column 3,* but such screening for the ring-cation systems of Fig. 1a reduces field-dipole energy proportionately no more for divalent than for monovalent ions, and thus cannot explain the sequence of heats.

Four additional factors must be considered:

(i) Where a divalent ion is associated with a silicate ring, as in Fig. 1a, the local excess of positive change could be reduced by attraction of negative charge from rings which are not associated with divalent ions. Each two Na^+ ions, for example, are replaced by one Ca^{++} ion, so that the number of empty rings should be increased accordingly. Thus the increased screening produced for Ca^{++}, if the net anionic charge per anionic

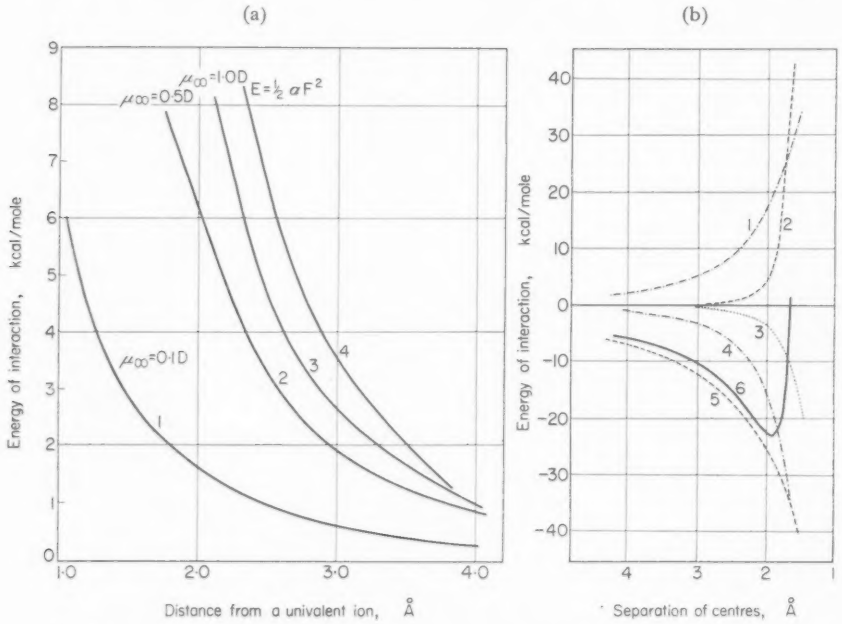

FIG. 2. (a) Calculations of polarization energy as a function of distance between ion and molecule centres. Using equation (5) and several values of μ_∞, curves 1, 2 and 3 are obtained. (b) Field-dipole (curve 5), quadrupole (curve 1), polarization (curve 4), dispersion (curve 3) and repulsion (curve 2) energies for an isolated Na^+ ion and a linear water-dipole, as functions of the distance between ion and dipole centres. Curve 6 gives the resultant interaction energy.

* Energies were calculated for the conditions of Sections *a*, *b* and *c* of Table 2, as appropriate. Contact at $(r_{ion}+r_{H_2O})$ was assumed.

Table 3. Total interaction energies, $-\phi$, between water and isolated cations compared with some integral heats (Kcal/mole)

Ion	$-\phi$*	Value of $-\phi_{F,\mu}$ for ring-cation systems (Fig. 1a)	$\int_{n_s=1}^{n_s=2} q_{st}\, dn_s$	$\int_{n_s=0}^{n_s=1} q_{st}\, dn_s$
Li^+	32·2	22·2	17·3	—
Na^+	22·8	13·6	12·4	16·7
K^+	16·5	10·5	16·8	—
Cs^+	13·5	8·8	17·5	—
Ca^{++}	58·3	35·2	13·4	—

* From Table 1.

VOL. 12 59/60

oxygen in the 6-ring rose to 0·428*e*, would reduce $-\phi_{F,\mu}$ at contact from 35·2 to 26·6 Kcal/mole.

(ii) Oriented dipoles associated with intracrystalline charge systems may repel one another, and the dipole–dipole repulsion energies then reduce the heats of sorption. This behaviour was investigated for isolated Na^+, Cs^+ and Ca^{++} ions attracting clusters of water molecules, the cation–water distance being in all cases $(r_{ion}+r_{H_2O})$. Oriented water tripoles in linear, plane triangular, planar square, tetrahedral and octahedral coordination, were considered. Although the repulsion energy was considerable in some instances, the effects were never large enough to modify the sequence of energies of Table 1, if these energies were governed by the cations present. This result agrees with earlier analogous calculations for tetrahedral and octahedral distributions.[10]

(iii) The contact distance $(r_{ion}+r_{H_2O})$ derived from crystallographic radii will often not be the true equilibrium distance in the zeolite. For an isolated Na^+-ion interacting with a water molecule, Fig. 2b shows field-dipole, quadrupole, polarization, dispersion and repulsion energies as functions of the distance between ion and molecule centres. For this calculation the water was treated as a linear dipole with the negative charge at the centre of the oxygen atom and having also a point quadrupole at this point. The dispersion constant was obtained from the Kirkwood–Muller relationship,[11] and to calculate the repulsion constant it was assumed that $r_0 = r_{ion}+r_{water}$. Polarization was calculated from the equations (ii) and (iv). The minimum energy appears at a smaller separation than corresponds to $(r_{ion}+r_{H_2O}) = 2{\cdot}35$ Å.

(iv) The energy of interaction at the equilibrium separation of two particles is very sensitive to the value and the variation (with separation) of the repulsion energy. In all the present calculations the method adopted is that outlined under (iii). This method depends upon the validity of the application of the LENNARD–JONES potential to polar molecules and the correct choice of the value of r_0. There are no satisfactory alternatives to this method, which is itself crude so that the equilibrium energies can be considered as only approximate.

The cations must form a more or less regular array within the aluminosilicate framework, and so the field-dipole energy may be briefly considered in the limited simple cubic arrangement of 18 cations shown in Fig. 1b. The distance *AB* was taken as 6 Å and 4·8 Å, both spacings being compatible with the faujasite lattice. These two values are obtained by considering a single cubic arrangement of cations within, on the one hand, the total volume of the unit cell and, on the other, the total free volume of this cell. The dipole axis is constrained to move along *AB* and its centre is initially at the centre of symmetry, *X*, of the array. It is then displaced along the line *AB*, and the field-dipole linear energies, $\phi_{F,\mu}$, calculated (Table 4). In the symmetrical position with its centre at *X*, $-\phi_{F,\mu}$ is zero, but this energy increases rapidly as the dipole moves along *AB*, although remaining considerably less than for an isolated cation

Table 4. Field-dipole energies for a water dipole (0·6 Å in length) in the cation lattice of Fig. 1b

Distance of dipole centre from X, (Å)	$-\phi_1$ (isolated cation +water)	$-\phi_2$ (cation group of Fig. 1b and water)	ϕ_2/ϕ_1	$-\phi_3$ (water and cation group of Fig. 1b with vacancy at F)	$-\phi_4$ (water and cation group of Fig. 1b with vacancy at A)
(a) *Cation–cation distance* = 6 Å					
0	14·3	0	0	0·9	14·3
0·3	18·1	6·4	0·35	7·7	18·1
0·6	22·6	12·5	0·55	13·8	22·5
0·9	29·2	18·1	0·62	19·4	26·6
1·2	40·5	28·3	0·70	29·7	35·6
(b) *Cation–cation distance* = 4·8 Å					
0	22·5	0	0	—	—
0 3	29·2	12·1	0·42	—	—
0·6	40·4	25·6	0·63	—	—

(c) *Maximum displacements along* AB *at ion–water contact and corresponding values of* $-\phi_{F,\mu}$

Ions on sites	Maximum displacement from X (Å)		$-\phi_{F,\mu}$ at maximum displacement	
	AB = 4·8 Å	AB = 6·0 Å	AB = 4·8 Å	AB = 6 0 Å
Li^+	0·4	1·02	16 0	22·2
Na^+	0 07	0 67	2·8	13·0
K^+	—	0·29	—	6·0
Rb^+	—	0·14	—	3·2
Ca^{++}	0 03	0·63	1·2	24·8
Sr^{++}	—	0·49	—	19·2
Ba^{++}	—	0·29	—	11·2

interacting with the dipole (Table 4a and 4b, columns 2, 3 and 4).

Cation vacancies at such lattice sites as F produce little effect upon $-\phi_{F,\mu}$, as shown in Table 4a, column 5; but on the other hand a vacancy at A, immediately adjacent to the dipole results in profound changes in $-\phi_{F,\mu}$ as the dipole moves towards B (column 6). This result is of interest because often there are insufficient cations in the zeolite to fill all cation sites allowed by the lattice symmetry, and because such vacancies may be a cause of the energetic heterogeneity noted in the water-Na-faujasite (Part II) and the argon-Ca-faujasite[2] systems. Finally, in Table 4c the values of field-dipole energy at contact of ion and dipole are given, when the lattice sites of Fig. 1b are occupied by the cations listed in column 1. Again these energies are not in accordance with the observed sequence of integral heats given in Table 3.

The results of Section 3 and of this section lead rather decisively to the conclusions that the role of cations in determining the energetics of intracrystalline sorption of water is not dominant, and that no parallel with the sequence of observed heats of sorption of water in a series of ion-exchanged faujasites can be based upon water–cation interactions alone. Instead we must consider features of these water–zeolite systems which are common to all of them, that is the anionic framework and the water molecules themselves, with the cations exerting only a moderating influence, except in the region of energetic heterogeneity which is normally restricted to small values of θ.

5. FRAMEWORK-DIPOLE ENERGY

In the unit cell of faujasite of the composition used in this work, there are 82 monovalent or 41 divalent cations. The unit cell also contains 384 framework oxygen atoms, each with an average

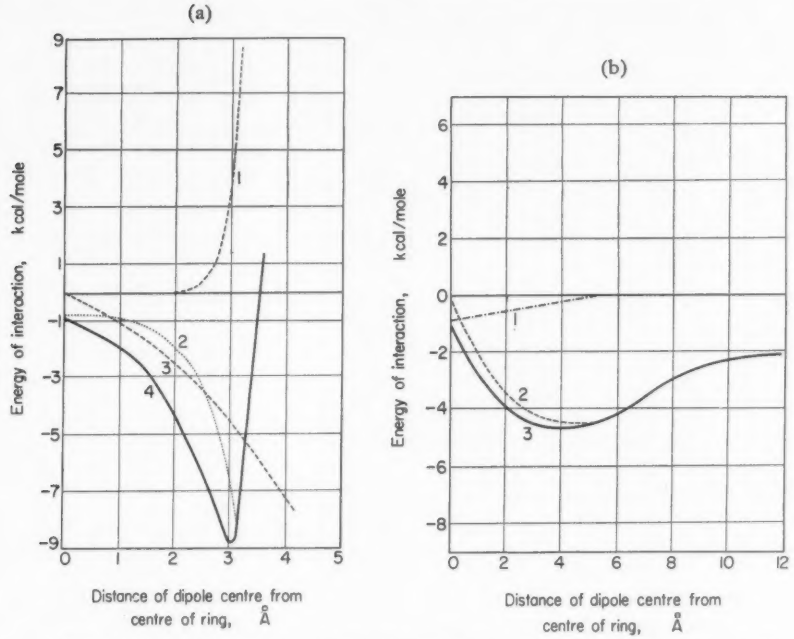

FIG. 3. (a) Field-dipole (curve 3), dispersion (curve 2) and repulsion (curve 1) energies for radial movement of a linear water-dipole across a 12-membered ring. Curve 4 gives the resultant interaction energy. (b) The same energies for axial approach of a water-dipole to a 12-membered ring. Curves 1 and 2 are respectively dispersion and field-dipole interactions, and curve 3 gives the resultant interaction.

charge of 0·214*e*, and when the crystal is saturated with water there are in addition 256 polar oxygen atoms provided by the corresponding water molecules. The 192 Al+Si atoms are so screened within tetrahedra of oxygen atoms that they are unlikely to play any significant role in determining sorption energies. It may be the smaller number of divalent cations which results in the integral heat of Table 3, column 4, being lower for the Ca-form than it is for most of the cationic forms containing monovalent ions. It is, however, almost certainly the large numbers of anionic oxygen atoms that determine the general similarity in magnitudes of these heats for the various cationic forms[16] (Part II, Fig. 2).

The faujasite structure may be regarded as built by stacking cubo-octahedral cages in tetrahedral co-ordination.[3] These cages, of free diameter 6·6 Å, may enclose some water molecules, but most of the water is present in very large cages of 12–13Å free diameter, which are spaces left by the arrangement of the cubo-octahedra. Each of these large cages is joined by common 12-membered rings of 8–9Å free diameter to four other identical cages. With this structure in mind calculations were made of interactions between anionic structural units and the water dipole (Table 5).

Thus, as the anionic charge changes from a continuous distribution to a discontinuous one (cases 1 or 2 to case 3 of Table 5) the field-dipole energy changes from zero to a large value. A perfectly uniform distribution of anionic charge does not arise; there are gaps in this distribution over the surface of each large cage due, for example, to the 12-membered ring openings. Moreover, the distribution is in discrete units of average magnitude 0·214*e*, each unit being associated with an oxygen atom. Thus a behaviour intermediate between cases 1 and 3 will be encountered. The total interaction energy between a water-dipole and an

Table 5. *Interaction energies of water-dipole with anionic structural units (Kcal/mole)*

	Structural unit	Interaction energy with water-dipole
1	Spherical cage. Electric charge continuously and uniformly distributed over the surface of sphere. Free diameter 12 Å. Oxygen atoms at a density of $2{\cdot}47\times10^{22}$/cm^3 uniformly distributed through space surrounding the cage.	No field-dipole energy. Maximum dispersion and repulsion energy $\sim -3{\cdot}8$. Polarization energy small.
2	Cylindrical channel lined by uniformly spread and continuous charge distribution.	No field-dipole energy.
3	Five equally spaced $O^=$ ions, with polar co-ordinates $(0, 0, R), \left(\frac{2\pi}{5}, \frac{2\pi}{5}, R\right), \left(\frac{4\pi}{5}, \frac{4\pi}{5}, R\right), \left(\frac{6\pi}{5}, \frac{6\pi}{5}, R\right), \left(\frac{8\pi}{5}, \frac{8\pi}{5}, R\right)$, $R = 7{\cdot}4$ Å, on surface of sphere of free diameter $\sim$ 12 Å.	Maximum resultant of field-dipole, dispersion and repulsion energies $= -36{\cdot}5$, when dipole moves along a radius passing through an $O^=$ ion.
4	Radial movement across the plane of a 12-membered ring of oxygen atoms, each oxygen having a charge of 0·214e, and the free diameter being 8 Å.	Maximum resultant of field-dipole, dispersion and repulsion energies $= -8{\cdot}8$ (Fig. 3a).
5	Approach to same 12-membered ring along an axis normal to the plane of the ring and passing through the ring centre.	Maximum resultant of field-dipole, dispersion and repulsion energy $= -4{\cdot}7$ (Fig. 3b).

isolated $O^{-0{\cdot}214e}$ polar atom is −8·9 Kcal/mole (Table 1).

A distribution of net anionic charge in units of 0·214e leads to maximum interaction energies of reasonable dimensions for radial (−8·8 Kcal/mole) and axial (−4·7 Kcal/mole) movements of the water-dipole relative to a 12-membered ring (Table 5 and Figs. 3a, 3b). From Fig. 3b one sees that the dipole shows its maximum interaction for an axial approach to the ring when its centre is about 4 Å from the ring centre.

6. DISCUSSION

The dipole–ring interactions of Sections 3, 4 and 5 represent only part of the total interactions between water-dipoles and the crystal lattice. Moreover, as the cavities fill with water molecules, new interactions arise between water molecules. Without reference to specific geometrical relations between water molecules and lattice units, we may consider the numbers of atoms per cm^3 in the empty lattices of several zeolites, in the full lattices and in liquid water respectively (Table 6). The

Table 6. *Numbers of atoms*[14] *per cm*^{3} *of crystal or liquid*, $\times 10^{22}$

Crystal or liquid	Hydration state	Al+Si	O	H	Monovalent cations
Faujasite	Empty	$1{\cdot}2_5$	2·5	—	0 54
($Al_2O_3 : SiO_2 = 1 : 2$ 67)	Full	$1{\cdot}2_5$	4·1	3·3	0 54
Chabazite	Empty	1·5	3·0	—	0·50
($Al_2O_3 : SiO_2 = 1 : 4{\cdot}0$)	Full	1·5	4·5	3·0	0 50
Linde Sieve A	Empty	1·3	2·6	—	0 65
($Al_2O_3 : SiO_2 = 1 : 2{\cdot}0$)	Full	1·3	4·1	3·0	0·65
Liquid water	—	—	3·3	6·6	—

(Al+Si) play little part (l.c.), and the sorptive behaviour might then be expected to correlate with the number of oxygen atoms in the porous oxygen-rich crystals where special structural features, such as the dimensions of the cavities, and the cations exercise only a moderating influence. On this basis the heat of sorption of water should be comparable in all three crystals. The values of the integral heats, q_{dta}, are 16·1(14·0), 14·3 and 18·5[13] Kcal/mole for the Na-forms of faujasite, chabazite and Linde Sieve A, respectively. The figure in brackets is the integral heat, q_{int}, obtained from the isosteric heat. It should also be noted that a figure somewhat less than 18·5 Kcal/mole has been obtained calorimetrically for Linde Sieve A.[17]

VOL. 12 59/60

These heats are higher than the latent heat of vaporization of liquid water (9·7 kcal/mole at 100°C), in part for a reason discussed previously,[13] namely that if clusters of water molecules were removed endothermically from water, the liquid surrounding the cavities created would collapse exothermally into the cavities. On the other hand, when equal-sized clusters are removed from zeolitic cavities, fully emptying them, no such collapse of the surrounding anionic framework occurs. When due allowance is made for this difference, the heats involved are indeed comparable for vaporization of water from liquid water and from the zeolites. In zeolites practically every oxygen atom in the framework is accessible to contact with water molecules.

Heats of vaporization of water from concentrated solutions of $CaCl_2$, NaOH, KOH and LiCl and from pure water are not very different even for 20 M solutions.[18] Thus the argument of the previous paragraph regarding heats of vaporization of water from zeolites and from liquid water applies also to these heats from zeolites and from some electrolyte solutions. A hydrated zeolite as porous as faujasite, chabazite or Linde Sieve A does indeed resemble a solid, strong electrolyte solution. In the zeolite, cations and water molecules are mobile but not the constituents of the anionic framework. In water-filled Na-faujasite there are 18·2 g-ions of Na^+ per 1000g of water. Such concentrations are reached in solutions of very soluble electrolytes.

APPENDIX

Interaction energies of importance in this paper include:

(i) ion and dipole:

$$\phi_{F,\mu} = -F\mu\cos\theta = -\frac{Ze\mu}{r^2}\cdot\cos\theta$$

(ii) ion-induced dipole:

$$\phi_P = \tfrac{1}{2}\alpha F^2 = -\frac{1}{2}\frac{\alpha(Ze)^2}{r^4}$$

(iii) ion-linear quadrupole:

$$\phi_Q = \frac{\Theta Ze}{2r^3}(3\cos^2\theta-1) = \frac{QZe}{4r^3}(3\cos^2\theta-1)$$

(iv) dipole-induced dipole:

$$\phi_{\text{ind}} = -\frac{\mu^2\alpha}{2r^6}(3\cos^2\theta+1).$$

In these expressions θ denotes the inclination of the dipole or quadrupole axis to the line of length r joining charge and dipole or quadrupole centres. F is the field intensity at the centre of dipole or induced dipole due to the charge, Ze; α is the polarizability of the molecule in which a dipole is induced; μ is the permanent dipole moment; and Θ and Q denote quadrupole moments according to two definitions (l.c.).

It is of interest to evaluate without approximation the KEESOM[19] average interaction energy for certain of these terms and sums of these terms. Where both quadrupole and dipole axes and centres coincide, only one angle θ is involved. Then for a fixed separation of interacting centres the KEESOM average is:

$$\langle v\rangle = \frac{\int \phi\exp\left(-\frac{\phi}{kT}\cdot d\omega\right)}{\int \exp\left(-\frac{\phi}{kT}\cdot d\omega\right)}$$

where $d\omega = \sin\theta d\theta$. In the general case where

(vi) $$\phi = \phi_P+\phi_Q+\phi_{F,\mu}+\phi_{\text{ind}},$$

the integral gives[20]

(vii) $$\langle\phi\rangle = A-B+D-\frac{C^2}{12(B+D)}+\tfrac{1}{2}kT-\sqrt{\left(\frac{kT}{3\pi(B+D)}\right)}\times$$

$$\times\frac{\left[\left(\frac{C}{2}+3B+3D\right)\exp-\frac{C}{kT}-\left(\frac{C}{2}-3B-3D\right)\exp\frac{C}{kT}\right]\exp-\frac{1}{kT}\left(\frac{C^2}{12(B+D)}+3B+3D\right)}{\operatorname{erf}\left\{\frac{\frac{C}{2}+3B+3D}{\sqrt{[3kT(B+D)]}}\right\}-\operatorname{erf}\left\{\frac{\frac{C}{2}-3B-3D}{\sqrt{[3kT(B+D)]}}\right\}}$$

where

$$A=-\frac{1}{2}\frac{\alpha(Ze)^2}{r^4};\ B=\frac{QZe}{4r^3};\ C=-\frac{Ze\mu}{r^2};$$

and

$$D=-\frac{\mu^2\alpha}{2r^6}.$$

This expression takes full account of various interaction terms between the four contributions to the potential given by equation (vi).

From equation (v) we may also obtain the KEESOM average potentials, without approximation, for other simpler cases. Thus,

(viii) $$\langle\phi\rangle_{F,\mu}=C\coth C+kT$$

(ix)

$$\langle\phi\rangle_Q=-B-\frac{\sqrt{\left(\frac{3BkT}{\pi}\right)}\exp\left(-\frac{3B}{kT}\right)}{\operatorname{erf}\sqrt{\left(\frac{3B}{kT}\right)}}+\tfrac{1}{2}kT$$

(x)

$$\langle\phi\rangle_P+\langle\phi\rangle_{\text{ind}}=A+D-\frac{\sqrt{\left(\frac{3DkT}{\pi}\right)}\exp-\frac{3D}{kT}}{\operatorname{erf}\sqrt{\left(\frac{3D}{kT}\right)}}+\tfrac{1}{2}kT$$

where the coefficients A, B, C and D are as previously defined.

It is seen from equations (vii), (viii), (ix) and (x) that the corresponding mean energies, $\langle\phi\rangle$, have temperature coefficients. That for equation (viii) is

(xi) $$\frac{1}{k}\cdot\frac{d\langle\phi\rangle_{F,\mu}}{dT}=1-\left(\frac{C}{kT}\right)^2\operatorname{cosech}^2\frac{C}{kT}$$

while the temperature coefficients for the similar equations (ix) and (x) take the form

(xii) $$\frac{1}{k}\cdot\frac{d\langle\phi\rangle}{dT}=\frac{1}{2}-\frac{2x+1}{2}\sqrt{\left(\frac{x}{\pi}\right)}\times\frac{\exp-x}{\operatorname{erf}\sqrt{(x)}}-\frac{x}{\pi}\frac{\exp(-2x)}{\operatorname{erf}^2\sqrt{(x)}}$$

where $x=3B/kT$ for equation (ix) and $3D/kT$ for equation (x). These temperature coefficients were calculated and were shown to be small. In systems having a quadrupole interaction with a field gradient, a more important temperature coefficient may arise with the onset of rotation of the quadrupole, since its moment then decreases substantially.[2]

REFERENCES

1. BARRER R. M. and BRATT G. C., *J. Phys. Chem. Solids* **12,** 146 (1959).
2. BARRER R. M. and STUART W. I., *Proc. Roy. Soc.* A**249,** 464, 484 (1959).
3. BARRER R. M., BULTITUDE F. W. and SUTHERLAND J. W., *Trans. Faraday Soc.* **53,** 1111 (1957).
4. REED T. B. and BRECK D. W., *J. Amer. Chem. Soc.* **78,** 5972 (1956).
   BARRER R. M. and MEIER W. M., *Trans. Faraday Soc.* **54,** 1074 (1958).
5. BARRER R. M., BUSER W. and GRUTTER W. F., *Helv. Chim. Acta* **39,** 518 (1956).
6. DENT L. S. and SMITH J. V., *Nature, Lond.* **181,** 1794 (1958).
7. HIRSCHFELDER J. O., CURTISS C. F. and BIRD R. B., *Molecular Theory of Liquids and Gases*, p. 1029, Wiley and Son, New York (1954).
8. DUNCAN A. B. and POPLE J. A., *Trans. Faraday Soc.* **49,** 217 (1953).
9. ROWLINSON J. S., *Trans. Faraday Soc.* **47,** 120 (1951).
10. BUCKINGHAM A. D., *Disc. Faraday Soc.* No. 24, 151 (1957).
11. MULLER A., *Proc. Roy. Soc.* A**154,** 1624 (1936).
12. EVERETT D. A., *Disc. Faraday Soc.* No. 24, 229 (1957).
    RANDLES J. E. B., *ibid.* No. 24, 230 (1957).
13. BARRER R. M. and LANGLEY D. A., *J. Chem. Soc.* 3817 (1958).
14. LENNARD-JONES J. E. and DENT B. M., *Trans. Faraday Soc.* **24,** 93 (1928).
15. VAN VLECK J. H., *The Theory of Electric and Magnetic Susceptibilities*, p. 85. Oxford University Press (1932).
16. Cf. BARRER R. M., *Nature, Lond.* **181,** 176 (1958).
17. FROHNSDORFF G. and KINGTON G. L. Private communication.
18. BRATT G. C., Ph.D. Thesis, London University, Fig. 1b.
19. KEESOM W. H., *Phys. Z.* **22,** 129 (1921).
20. KERR I. S. Private communication.

J. Phys. Chem. Solids Pergamon Press 1959. Vol. 12. pp. 167–174. Printed in Great Britain.

LATTICE THERMAL CONDUCTIVITY IN COPPER ALLOYS*

T. OLSEN†

Department of Physics, Brown University, Providence 12, R.I.

(*Received* 1 *June* 1959)

VOL. 12 59/60

Abstract—The thermal conductivity has been measured of a series of copper–zinc alloys in the range 4·2–1·1°K, and the lattice part of the conductivity was determined. The value obtained for K_{ge} is $1{\cdot}1 \times 10^{-3}\ T^2$ W/cm-deg, which is compared with the lattice thermal conductivity that can be deduced from ultrasonic measurements in pure copper. From this it is estimated that the shear thermal modes carry about 25 times as much heat as the longitudinal one. As expected theoretically, the shear wave interaction with electrons is found to be much smaller for thermal phonons than with ultrasonic waves. The residual electrical resistance was also measured in the same copper–zinc alloys.

1. INTRODUCTION

HEAT is carried in metals by both the electrons and the lattice vibrations. Since the electronic conductivity is much greater than the lattice conductivity, the latter cannot be measured in pure metals except in superconductors far below the transition temperature. However, in alloys the electronic mean free path is much reduced compared to that in pure metals and the two components become comparable.

The theoretical description of the lattice thermal conductivity in metals has never been fully satisfactory. One of the main difficulties has been in understanding the contribution of shear waves relative to that of longitudinal waves. In the usual quantum treatment, pure shear waves do not scatter electrons to the approximations used, because there is no interaction when there is no volume change. On the other hand, several measurements,[1–4] as well as those made in the present investigation of the lattice thermal conductivity, show values too large to be accounted for by longitudinal phonons alone. Several authors[5,6] have suggested that shear waves play an important part as carriers, but have been unable to predict the relative sizes of the different contributions. However, MORSE[7] has recently shown that it is possible to estimate this from ultrasonic-attenuation measurements in pure metals.

The total thermal conductivity can be written

$$K = K_e + K_g, \tag{1}$$

where K_e is the electronic and K_g the lattice part. At liquid-helium temperatures we have $K_e \propto T$ and $K_g = K_{ge}$, where K_{ge} is the conductivity as limited by electron scattering.[5,8,9] Following MORSE, K_{ge} can be related to the ultrasonic attenuation α because the phonon mean free path is given in terms of this attenuation as $l_p = (2\alpha)^{-1}$. He assumes the following general frequency-dependence of the attenuation

$$2\alpha = A\omega^r, \tag{2}$$

where A is a constant except in the superconducting state, and r an integer. It should be noted that his treatment holds regardless of the phonon type. In the case where phonons are limited by electrons, and as long as the electron mean free path l_e is larger than the phonon wavelength λ, then the phonon mean free path is inversely proportional to

* Partially supported by a contract with the U.S. Air Force through the Office of Scientific Research of the Air Research and Development Command, and with the Office of Naval Research.

† On leave from the University of Oslo, Norway.

the frequency, or $2\alpha = A\omega$. In this case the term K_{ge} can be written:

$$\frac{K_{ge}}{T^2} = B = B_l + 2B_t$$

$$= \frac{1{\cdot}20k^3}{\pi^2\hbar^2}\{(u_l^2 A_l)^{-1} + 2(u_t^2 A_t)^{-1}\}, \qquad (3)$$

where the subscript l and t refer to longitudinal and transverse phonons respectively, and u with the appropriate subscript is the sound velocity. Thus K_{ge} can be estimated from ultrasonic measurements, provided that it is valid to extrapolate results in the frequency region of these measurements (10–100 Mc/s) to the thermal phonons with frequencies several thousand times larger. MORSE argues the validity of this from the magnitude of the dimensionless parameters $(\omega\tau)$, (ql_e) and (δ/λ), where τ is the electron relaxation time, $q = (2\pi/\lambda)$, and δ the classical skin depth. The very fact that one cannot hope to observe K_g unless K_e is small (say < 1 W/cm-deg), means that l_e must be many times smaller than it is in pure metals where the direct phonon–electron interaction is measured ultrasonically. This compensates for the wide difference in frequencies between ultrasonic and thermal phonons, so that the parameters ql_e and $\omega\tau$ are of about the same size in both cases. However, the parameter δ/λ, which is of importance with shear waves, does not scale. Approximately speaking, $\delta/\lambda > 1$ for thermal waves but $\delta/\lambda < 1$ for ultrasonic waves. On the basis of the theory developed by PIPPARD[10], MORSE shows that the ultrasonic shear wave interaction should be considerably larger than that for thermal waves. Thus the K_{ge} predicted by equation (3) using ultrasonic measurements should be smaller than the measured K_{ge}, the difference being attributable to differences in the shear wave interactions for the two kinds of measurements.

There is also the possibility that the electron mean free path could be short enough so that $ql_e < 1$ for a substantial number of phonons. For these phonons the attenuation has more nearly a square-law frequency-dependence, i.e. $2\alpha = A'\omega^2$. The effect of this will be to give a term in K_{ge} which varies proportionally to T. Thus

$$K_{ge} \sim BT^2\left(1 + \frac{\hbar u}{kl_e}\cdot\frac{1}{T}\right). \qquad (4)$$

The additional term in K_{ge} has the temperature-dependence of K_e; i.e. $K_e = (L_0 T)/\rho_0$, where L_0 is the Lorentz ratio and ρ_0 the residual resistance. If such a term were present, one would tend to overestimate the electronic contribution and to find a contradiction of the Wiedemann–Franz law.[11] For in such a case the total conductivity would be approximately of the form

$$K = (L_0/\rho_0 + D)T + BT^2. \qquad (5)$$

Furthermore, the constant D would tend to *increase* with ρ_0 in contrast to the first term in the bracket. The possibility of such a contribution to the conductivity has also been pointed out by PIPPARD[12].

From recent ultrasonic measurements in copper, it is possible to estimate the interactions A_l and A_t. Since one can assume with some reliability that A_l is the same for both ultrasonic and thermal phonons (since ql and $\omega\tau$ are comparable), it is of interest to measure the lattice conductivity in copper in order to compare the values of A_t in the two cases. The present investigation attempts to measure the lattice conductivity by the use of copper–zinc alloys. As will be shown later, substantial agreement with the treatment outlined above has been found.

2. SPECIMENS

The specimens were cylindrical rods about 10 cm long and of various cross-sections. With one exception, all the samples were obtained directly from the mill. Z2O, however, was made from a piece of metal previously subjected to a considerable amount of cold work. The samples were chemically analyzed and, after machining to the

Table 1. *Content of copper and of elements other than zinc as determined by chemical analysis*

Sample	Content (wt.-per cent)				Annealing conditions	
	Cu	Fe	Ni	Pb	Time (hr)	Temp. (°C)
Z4	95·40	—	—	0·01	21	540
Z10	89·02	0·01	0·10	2·02	17	500
Z20	86·56	0·01	—	—	17	500
Z15	84·53	0·02	—	0·02	21	540
Z30	69·95	0·02	—	0·01	21	540

VOL. 12 59/60

desired shape, annealed in an ordinary atmosphere. Table 1 shows the content of copper and impurities, together with annealing times and temperatures for the different samples.

3. APPARATUS

The thermal conductivity was measured in a conventional way. The sample was mounted in a cylindrical can with a heating coil wrapped around its lowest end. The top part of the sample protruded through the lid into the liquid-helium bath (Fig. 1). A steady flow of heat was established and

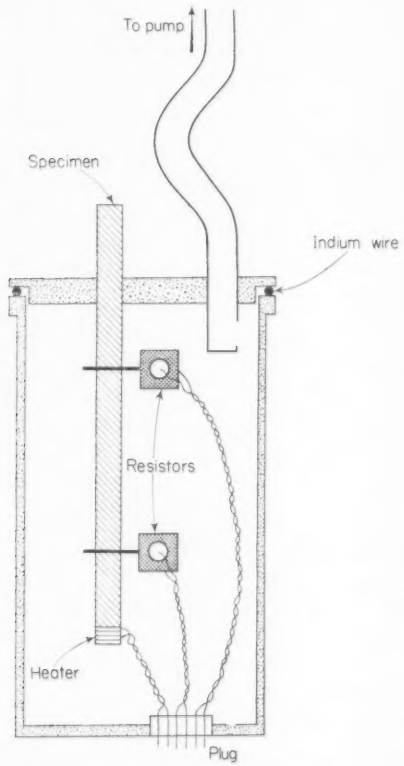

FIG. 1. Experimental chamber (schematic).

the temperature measured at two points along the sample. The thermometers used were two 130-Ω Speer carbon resistors mounted on a thin copper ring around the sample. The wires from the resistors, as well as to the heater, were thin-gauge Manganin wire. To assure good thermal grounding, these leads were taken into the helium bath through a Winchester plug in the bottom of the can. The lid and the lower part of the can were joined together with a simple **O**-ring joint, using a gasket made of indium wire with overlapping ends. The vacuum in the can was kept better than 10^{-5} mm Hg.

The resistance thermometers were calibrated against the vapor pressure of the liquid helium while they were mounted in place. The temperature-dependence of the resistors could be described by the expression.[13]

$$\log_{10}R+B^2(\log_{10}R)^{-1} = A/T+2B,$$

where A and B are constants. Since reading the temperature from large-scale calibration curves was found sufficiently accurate and more convenient, this was done instead of using the empirical formula.

The thermal conductivity was determined from the relation $K = Qd/A\Delta T$, where Q is the heat power, A the cross-section of the sample, d the distance and ΔT the temperature difference between the two thermometers. The uncertainty in ΔT was the principal factor in determining the accuracy with which K could be measured. It is estimated that ΔT was known to about ± 4 per cent for a ΔT value of about 0·1°. The overall uncertainty in K should be about ± 5 per cent.

4. RESULTS AND CONCLUSIONS

The thermal conductivity was measured for the samples listed in Table 1 over the temperature region 4·2–1·1°K. The results are plotted in Figs. 2 and 3. To find the constant B in the expression for the lattice thermal conductivity, the results have been plotted as K/T vs. T. This should give straight lines having slope B if K has the form given in equation (5). Figs. 4 and 5 show such plots. The values of B obtained are plotted against percentage of copper in Fig. 6.

The value found for B with the sample Z2O is considerably smaller than the other values. The explanation for the discrepancy lies probably in the history of the sample. It was the only sample that had been subjected to considerable cold work and a higher dislocation density could be expected. The phonon thermal resistance caused by dislocations has the same temperature-dependence as that from electrons and will make K_{ge} smaller,[3] which is in the direction indicated.

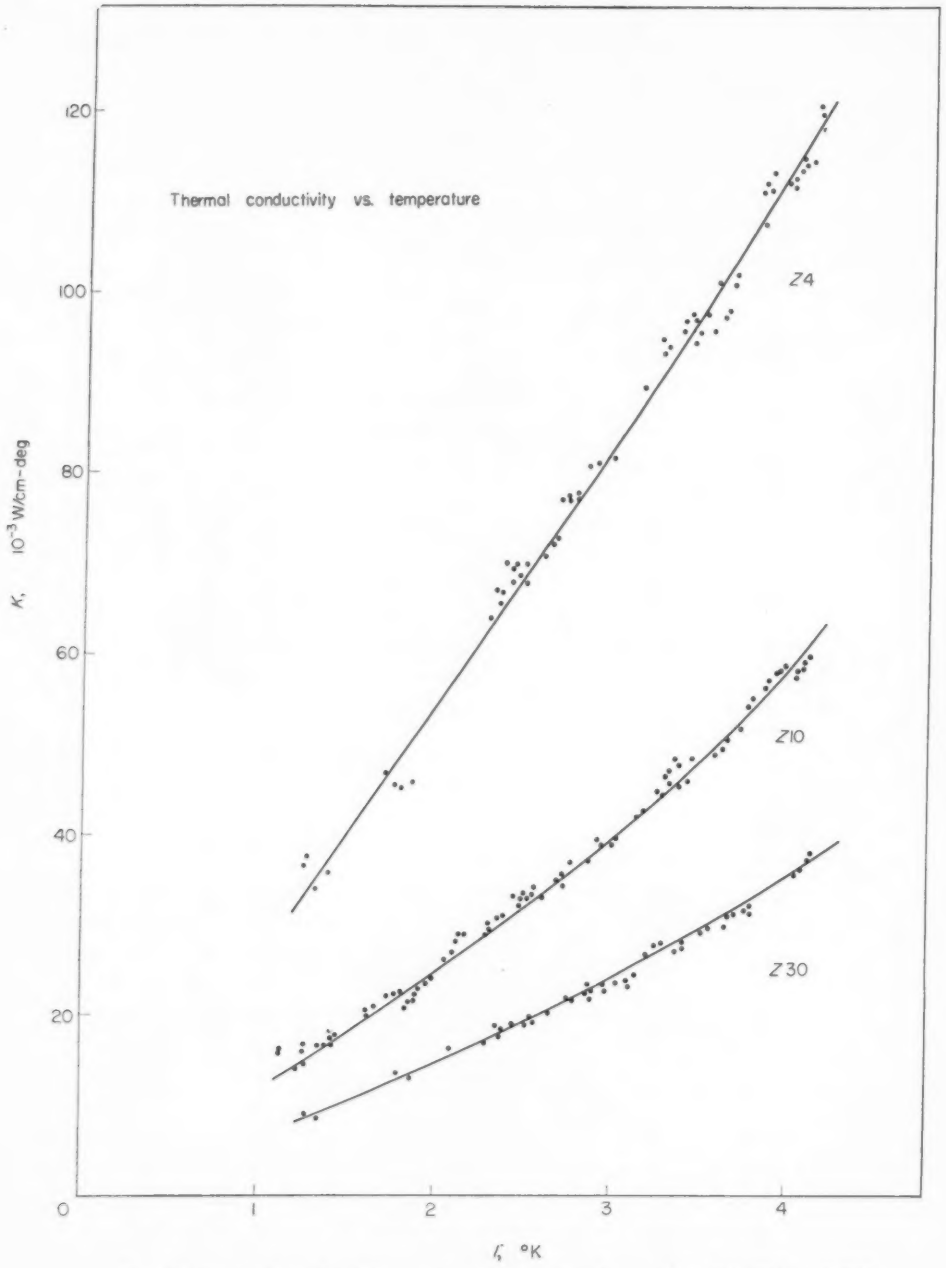

FIG. 2. Thermal conductivity vs. temperature for the samples Z4, Z10 and Z30.

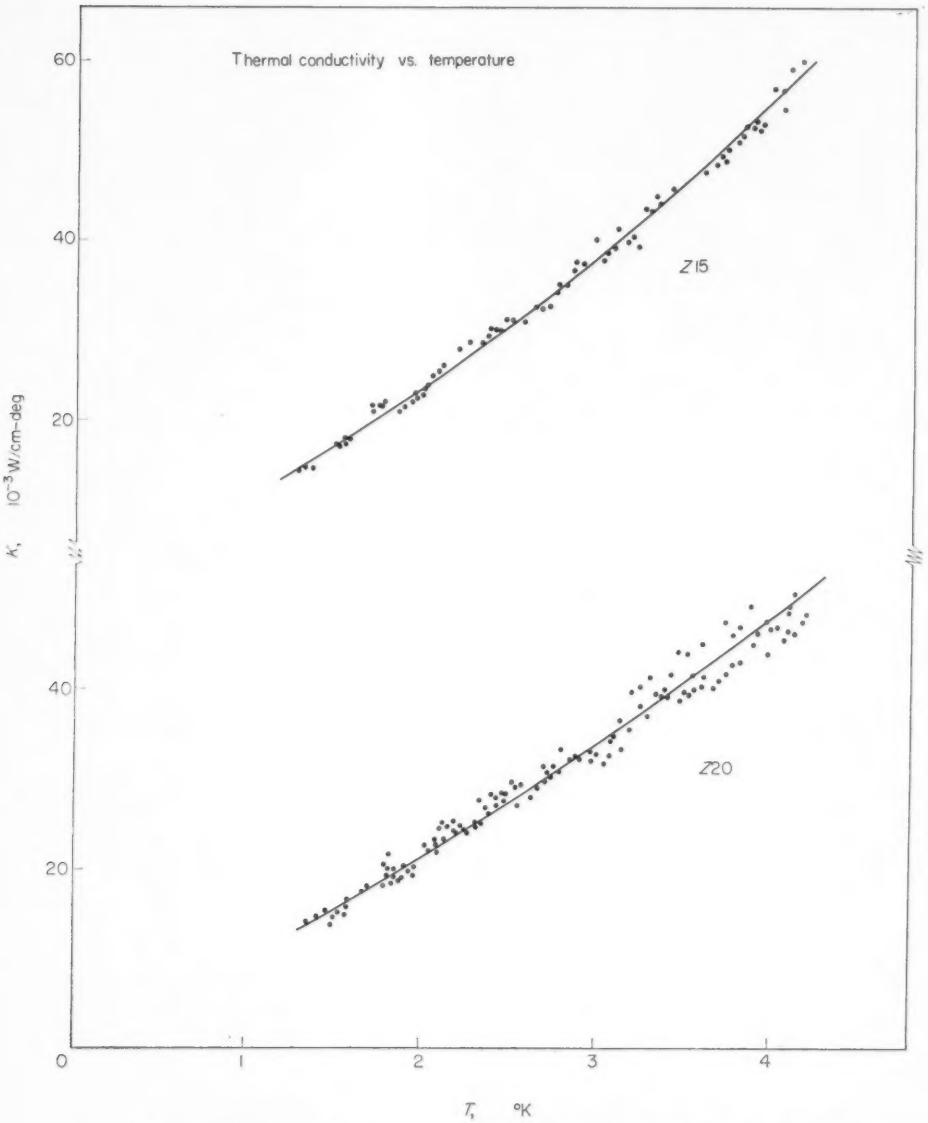

FIG. 3. Thermal conductivity vs. temperature for the samples Z15 and Z20.

If Z20 is left out of consideration, the other samples give $B = 1{\cdot}1 \times 10^{-3}$ W/cm-deg.[3] This is less than the value given by WHITE and WOODS[4] for their copper +0·056 per cent iron sample and larger than most of the values of KEMP *et al.*[3] for annealed copper–zinc alloys. However, in the last-named results, the intercept which is derived from the residual electrical resistance seems to have been given too much weight. This question will be raised again shortly.

Any value for B of the size obtained here cannot be explained without attributing some of the heat transported to shear waves. This is also pointed out by KLEMENS[6] in his interpretation of the

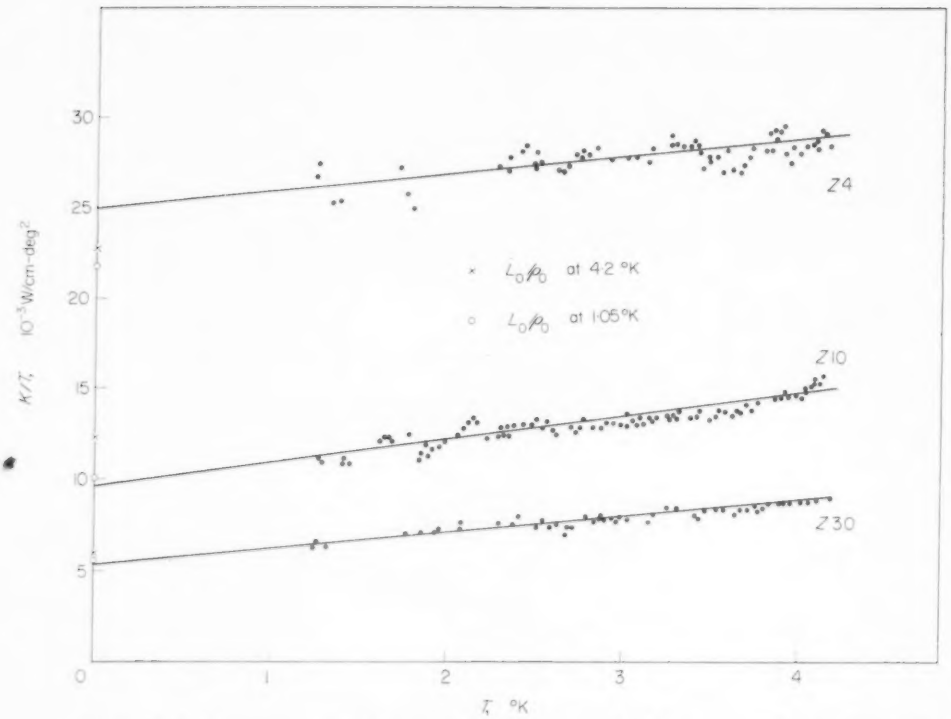

FIG. 4. K/T vs. temperature for the samples Z4, Z10 and Z30. L_0/ρ_0 measured at 4·2 and 1·05°K.

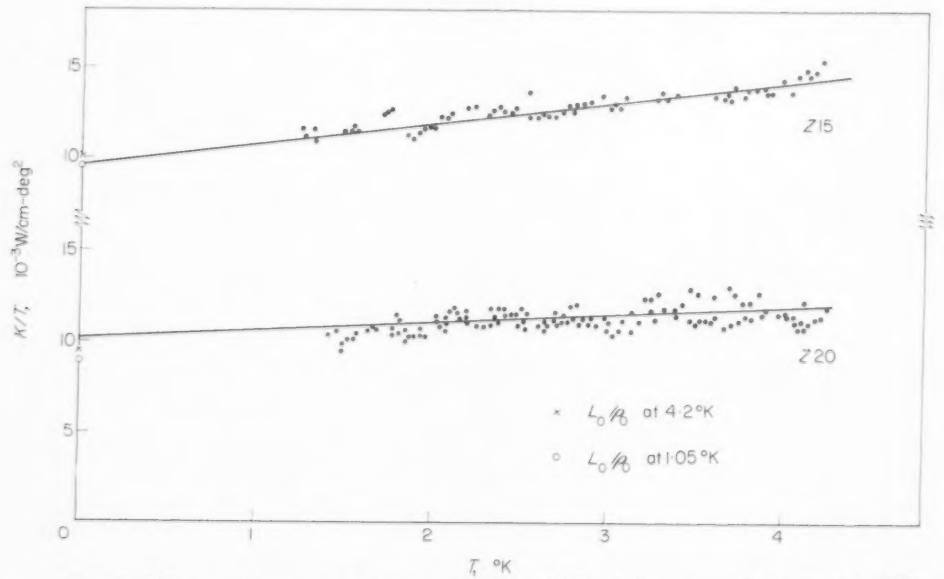

FIG. 5. K/T vs. temperature for the samples Z15 and Z20. L_0/ρ_0 measured at 4·2 and 1·05°K.

data of ESTERMANN and ZIMMERMAN[1]. Using the model that all modes interact equally with the electrons, he estimated K_{ge} to be $1{\cdot}4\times10^{-3}\,T^2$ W/cm-deg.

From the ultrasonic measurements by MORSE *et al.*[14] it would appear that most of the heat is carried by the shear modes rather than the longitudinal one. Using their results, MORSE[7] gets

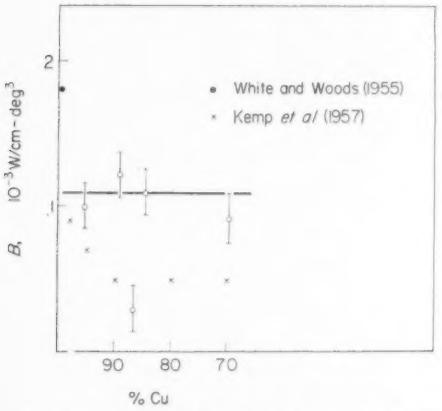

FIG. 6. B as measured from the slopes of the K/T vs. T curves, plotted against percentage of copper.

$A_l = 3{\cdot}54\times10^{-9}$ sec/cm and therefore $B_l = 0{\cdot}4\times10^{-4}$ W/cm-deg^3. The difference between this and the observed value of B gives a shear lattice thermal conductivity about 25 times larger than the longitudinal part. This corresponds to a value of $A_t = 0{\cdot}63\times10^{-9}$ sec/cm for thermal shear phonons, or about 7·5 times smaller than the value observed ultrasonically. This is in the direction one would expect, for the ultrasonic interaction should involve a large free-electron interaction of the type calculated by PIPPARD[10]. This interaction should be largely absent for thermal phonons because $\delta/\lambda \gg 1$. Presumably the remaining interaction which is observed for thermal phonons, is a measure of the "real" metal coupling between shear waves and electrons. If this is true, then the ratio of the interaction constant* for shear waves to the longitudinal interaction constant is $C_t/C_l = (B_l/B_t)^{\frac{1}{2}} = 0{\cdot}27$.

* "Interaction constant" is being used here in the manner employed by KLEMENS[6] and others. The interaction constant C is related to the attenuation as $2\alpha = (m^*C)^2\omega/(2\pi\rho u^2\hbar^3)$, where ρ is the density.

The electrical resistance was measured in all the samples at the temperatures 4·2 and 1·05°K. The values measured are shown in Table 2. They indicate a resistance minimum in all specimens, the most pronounced minimum being in Z10. Since the explanation for a resistance minimum at the present time is uncertain, there is some doubt as to what value to take for the residual resistance of the samples. Using the relation $LT/\rho_0 = K_e$, where L is the Lorentz ratio, both the values obtained for $(K/T)_0$ were plotted in Figs. 4 and 5. For the Z10 sample, where the difference was greatest, the value of ρ_0 measured at 1·05° gave the best fit to the K/T vs. T line. This is the opposite of what WHITE and WOOD[4] concluded for their copper +0·056 per cent iron sample. All $(K/T)_0$ values taken at 1·05° fitted the lines in the K/T vs. T plots within the experimental error. In other words, any contribution to K_{ge} proportional to T is too small to be of any significance in these alloys. Knowing ρ_0, this can be verified from equations (4) and (5), giving $D \sim B(\hbar u/kl_e)$. Since $\rho_0 = mu_F/Ne^2l_e$, where N is the number of electrons, m their mass and u_F the Fermi velocity, we can estimate D to be of the order of $0{\cdot}2\times10^{-3}$ W/cm-deg^2, a value too small to be observed here. There remains, therefore, a need for systematic measurements to be made of the lattice thermal conductivity in copper by using other copper alloys with higher residual resistance to find this interesting term.

Table 2. Residual electrical resistance measured at 4·2 and 1·05°K

Sample	ρ_0 (10^{-6} Ω-cm)		$(K/T)_0 = L_0/\rho_0$ (10^{-3}W/cm-deg^2)	
	4·2°K	1·05°K	4·2°K	1·05°K
Z4	1·08	1·13	22·7	21·6
Z10	1·98	2·43	12·4	10·1
Z20	2·58	2·73	9·5	9·0
Z15	2·36	2·55	10·2	9·6
Z30	4·10	4·22	6·0	5·8

Acknowledgements—The author would like to express his thanks to Professor R. W. MORSE for suggesting this

problem and his helpful discussions throughout the work. The author is also indebted to Dr. H. V. BOHM, Mr. J. D. GAVENDA and Miss GUDRUN ADENSTEDT for help with various parts of this investigation. This work was done while the author held a fellowship from the Royal Norwegian Council for Scientific and Industrial Research.

REFERENCES

1. ESTERMANN I. and ZIMMERMAN J. E., *J. Appl. Phys.* **23** 578 (1952).
2. KEMP W. R. G., KLEMENS P. G. and TAINSH R. J,. *Aust. J. Phys.* **10** 454 (1957).
3. KEMP W. R. G., KLEMENS P. G., TAINSH R. J. and WHITE G. K., *Acta Met.* **5,** 303 (1957).
4. WHITE G. K. and WOODS S. B., *Canad. J. Phys.* **33,** 58 (1955).
5. MAKINSON R. E. B., *Proc. Camb. Phil. Soc.* **34,** 474 (1958).
6. KLEMENS P. G., *Aust. J. Phys.* **7,** 57 (1954).
7. MORSE R. W., to be published; see also *Bull. Amer. Phys. Soc.* **3,** 203 (1958).
8. SONDHEIMER E. H., *Proc. Roy. Soc.* A**203,** 74 (1950).
9. WILSON A. H., *Theory of Metals*, Cambridge University Press (1953).
10. PIPPARD A. B., *Phil. Mag.* **46,** 1104 (1955).
11. SLADEK W. J., *Phys. Rev.* **91,** 1280 (1953).
12. PIPPARD A. B., *J. Phys. Chem. Solids* **3,** 175 (1957).
13. NICOL J. and SOLLER T., *Bull. Amer. Phys. Soc.* **2,** 63 (1957).
14. MORSE R. W., BOHM H. V. and GAVENDA J. D., *Phys. Rev.* **109,** 1394 (1958).

J. Phys. Chem. Solids Pergamon Press 1959. Vol. 12. pp. 175–180. Printed in Great Britain.

THE FIELD-DEPENDENCE OF CARRIER MOBILITY IN SILICON AND GERMANIUM

A. C. PRIOR

Royal Radar Establishment, Malvern, England

(*Received* 3 *June* 1959)

Abstract—The variation of mobility with electric field has been measured for *n*- and *p*-type silicon and germanium with fields up to 10^5 V/cm. For *p*-type silicon the variation is found to depend on hole concentration. For the other materials any variation with concentration must be smaller, and these experiments are inconclusive as to its existence.

VOL.
12
59/60

1. INTRODUCTION

THE variation of carrier drift velocity with electric field has been measured by RYDER[1] for the four materials *n*- and *p*-type germanium and *n*- and *p*-type silicon with fields of the order of 10^4 V/cm, and by GUNN[2] on *n*-type germanium with fields up to 7×10^4 V/cm. In the course of some high-field measurements by the author on high-resistivity *p*-type gold-doped silicon, it appeared that the current/voltage characteristic was more nearly ohmic than was indicated by RYDER's data or by the present author's earlier measurements on lower-resistivity material. A systematic series of measurements using samples of *p*-type silicon having various resistivities was therefore undertaken to investigate the effect of resistivity on high-field mobility. A significant variation was in fact found, but corresponding measurements on *n*-type silicon and on both *n*- and *p*-type germanium showed only minor variations of doubtful experimental significance. In the course of this work the observations for *n*- and *p*-type silicon and for *p*-type germanium were extended to higher fields than have previously been reported, and the results are summarized below. All the measurements were made at room temperature. The germanium and the *n*-type silicon crystals were grown by pulling in a gas, and the *p*-type silicon by pulling *in vacuo*.

2. EXPERIMENTAL METHOD

The experimental technique, in which the voltage/current characteristic of bar-type specimens is measured with short pulses, was similar to that described by GUNN[2]. He used germanium of 2-Ω-cm resistivity in which the displacement current was negligible in comparison with the conduction current; most of the present measurements were, however, made on material of considerably higher resistivity, and this necessitated the use of pulses of 6×10^{-9} sec duration—three times longer than those used by GUNN. Even then, with the higher resistivities, the oscillations resulting from the displacement current and the lead inductances were not completely damped within the duration of the pulse, and this substantially reduced the accuracy of the measurements. This difficulty placed the upper limit to the resistivity that could be measured at ~ 500 Ω-cm.

The range of field strengths was covered by using three or four bars of each material with lengths varying from 0·05 to 1·5 cm. The cross-sections were adjusted to give an effective resistance at the field being used of ~ 500 Ω. On the germanium specimens, contacts, ohmic at low fields, were made to the whole end faces by soldering. Contacts to the silicon specimens were made by chemical nickel plating[3] followed by soldering; these contacts were not ohmic, but high-field measurements on *p*-type specimens with such contacts were not significantly different from those obtained with aluminium-alloyed contacts. Presumably the contact barrier is either insignificant or is broken down at the high fields, while the pulse

length is normally short enough for injection effects not to be serious. With the shorter specimens, particularly those under 1 mm in length, a rise in current with time was sometimes observed and attributed to injection. With the specimens of lower resistivity, valid measurements could still be made by extrapolating the current back to the germanium, does it seem likely that an avalanche occurred within the body of the specimen. Where a sharp rise in current was observed, this increased much more gradually both with voltage and with time than the characteristic effect observed on the same apparatus with low-resistivity *n*-type germanium; the values of the field at which much more

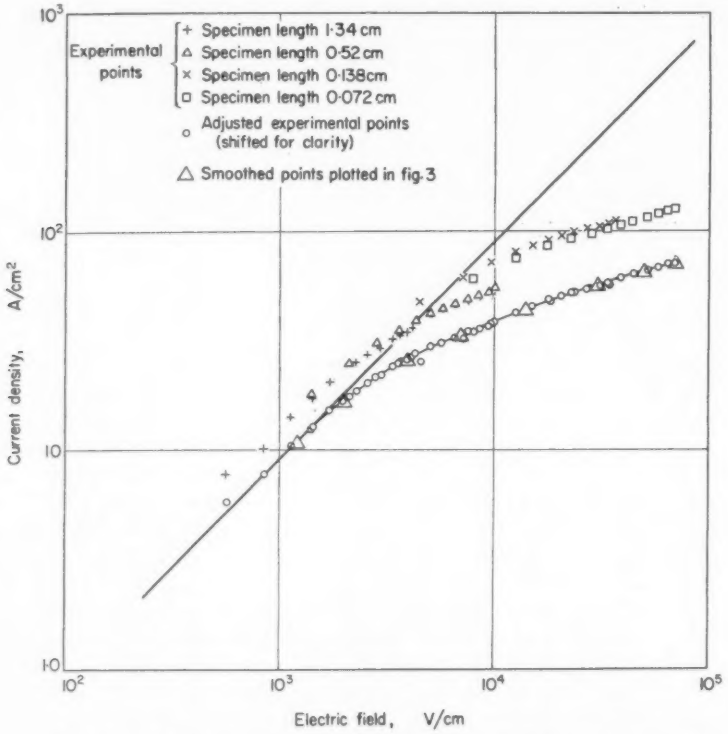

FIG. 1. Variation of current density with electric field in 80-Ω-cm *n*-type silicon.

start of the pulse, but with those of higher resistivity, where substantial oscillation occurred, this procedure was not possible and the existence of injection was difficult to detect. Trouble caused by injection was no worse with the silicon specimens than with the germanium ones with ohmic contacts.

In GUNN's measurements on 2-Ω-cm *n*-type germanium, the limiting field was set by avalanche breakdown, characterized by a very sudden increase in current with time. In none of the present experiments, except perhaps those on *n*-type gradual rises occurred varied for different specimens, and injection from the end contacts seems a more likely explanation. Other limiting factors were sparking through the air between the ends of the specimen, or simply output limitations of the pulse generator.

3. EXPERIMENTAL RESULTS

Although the specimens from each crystal were cut from neighboring portions, the results for different specimens, as for example in Fig. 1, did not always match up well on the current-density/field

curve. No errors in the electrical measurements could be found to account for this, and for the germanium specimens with ohmic contacts the failures to match on the high-field plot agreed with differences of resistivity deduced from low-field measurement. It is assumed therefore that the mismatching is due to resistivity variations, and in Secondly, if there is a variation of resistivity along the length of the specimen, the apparent departures from Ohm's law will be accentuated. Analysis shows that this is very unlikely to result in any error as large as, for example, the difference between the three curves in Fig. 4.

In Figs. 2–5 the smoothed composite curves for

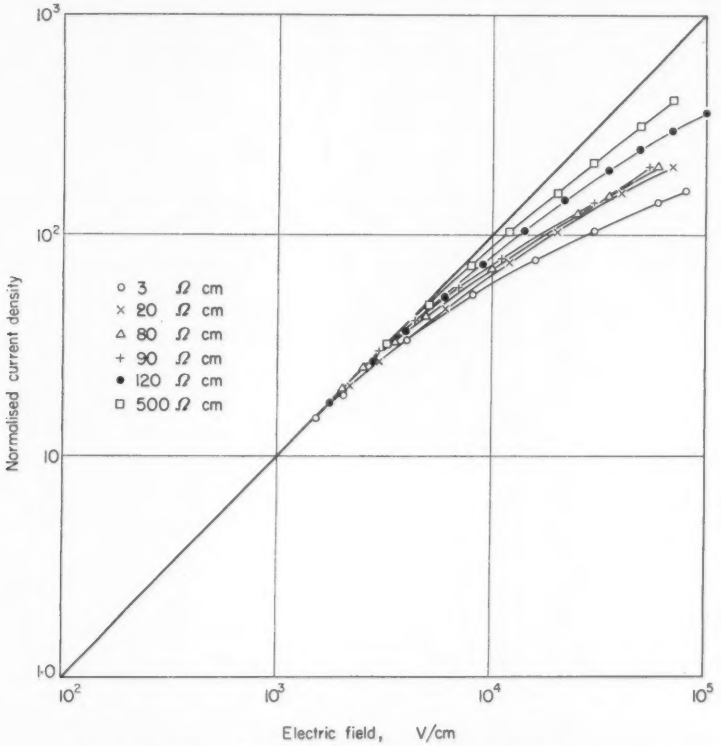

FIG. 2. Variation of current density with electric field in *p*-type silicon.

Fig. 1 are shown the actual experimental points obtained from one crystal and the way in which these points have been combined to give a composite curve. The degree of mismatch shown in Fig. 1 is typical of the *n*-type silicon and *n*-type germanium results, but those for *p*-type silicon and *p*-type germanium showed less variation.

This inhomogeneity of the crystals can result in two sources of error. In so far as the mobility/field relationship is a function of resistivity, the resultant measured relationship will arise from a range of resistivities; however, detailed consideration of the results indicates that this error is negligible. various resistivities of the four materials are shown. For the 34-Ω-cm *n*-type germanium in Fig. 5, the hole contribution to the current was just significant, and a correction was applied to eliminate this.

For *p*-type silicon, the results can be taken as establishing without doubt an increasing departure from linearity with increasing hole concentration. For *n*-type silicon, a similar but much less marked trend is probably significant. However, the possibility that the apparent rise at the highest fields in the 300-Ω-cm specimen was due to injection cannot be ruled out, since, with the shortest specimen (0·6 mm long), the oscillation due to

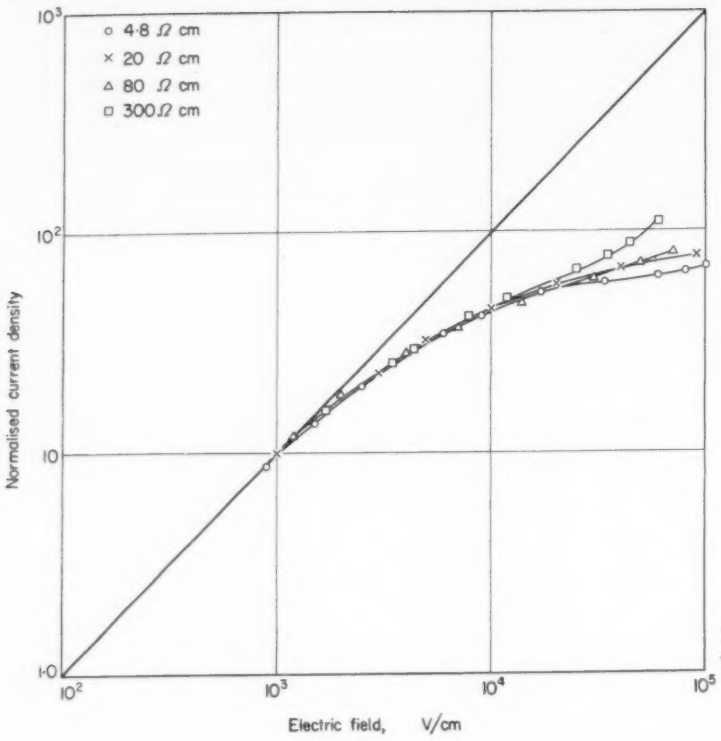

FIG. 3. Variation of current density with electric field in *n*-type silicon.

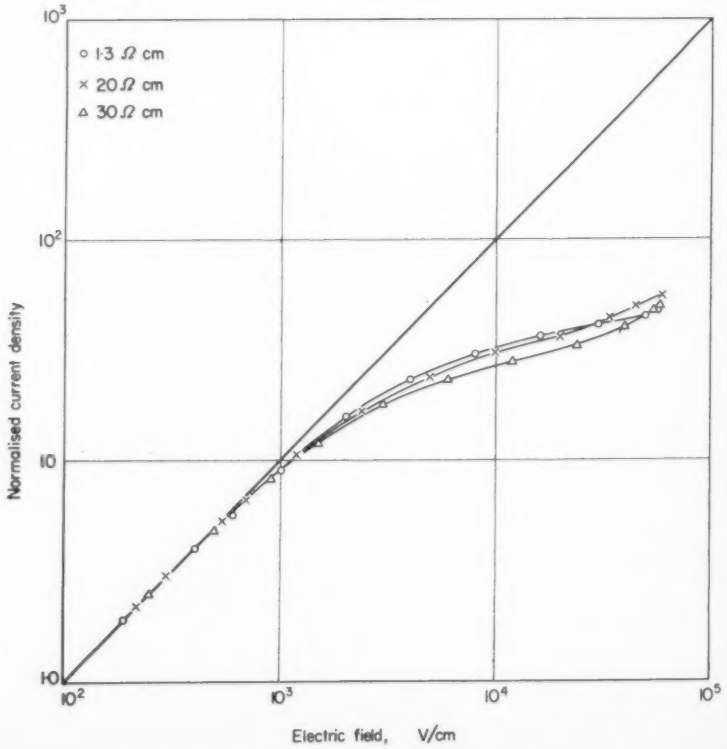

FIG. 4. Variation of current density with electric field in *p*-type germanium.

displacement current was comparable with the d.c. component, and could have masked indications of injection. This last observation could apply equally to the 34-Ω-cm *n*-type germanium. The differences between the three curves for *p*-type germanium can be ascribed to general experimental errors.

To summarize therefore, the resistivity effect is clearly indicated for *p*-type silicon, and a smaller effect is considered probable for *n*-type silicon; no reliable evidence for such an effect has been obtained over the much more restricted resistivity range possible in either type of germanium.

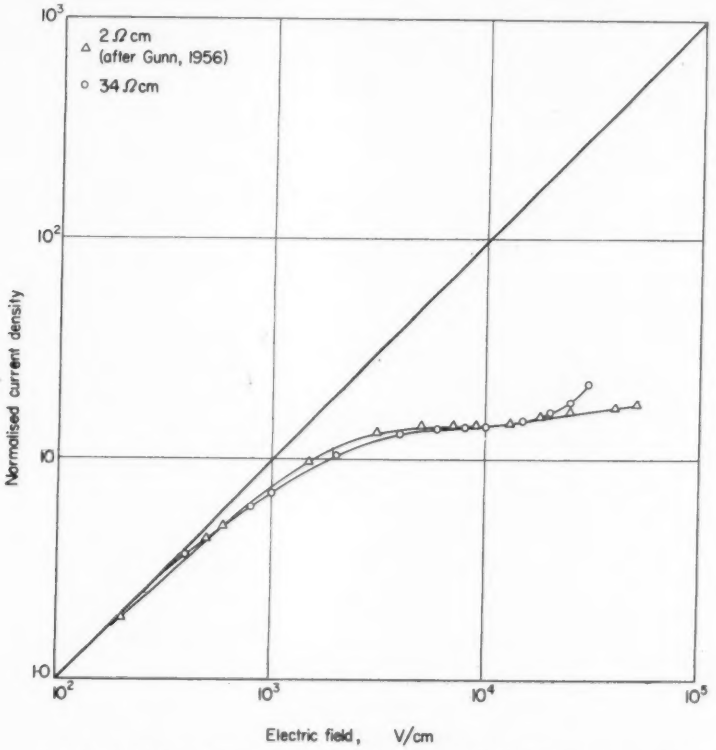

FIG. 5. Variation of current density with electric field in *n*-type germanium.

4. DISCUSSION

The results obtained are in general agreement with those of RYDER[1] and GUNN[2]. These authors have clearly shown that for *n*-type germanium a well-defined region exists in which the drift velocity is independent of the field, and RYDER's paper contains the suggestion that a similar region probably exists for *p*-type germanium and *n*-type silicon. The present work, however, shows that no such region occurs in *p*-type germanium or in *n*- or *p*-type silicon, so that the phenomenon of the saturation of the drift velocity is peculiar to *n*-type germanium.

STRATTON[4] has given an expression for the critical carrier concentration above which carrier–carrier scattering enforces a Maxwellian energy distribution on the carriers. For the field at which the carrier energies are of the order of twice their room-temperature value, his expression gives critical concentrations of $\sim 3\times10^{15}$ cm^{-3} for *p*-type and $\sim 1\times10^{15}$ cm^{-3} for *n*-type silicon. In the present experiments the range of carrier concentration covered was approximately 4×10^{13} to 6×10^{15} cm^{-3} for *p*-type and 3×10^{13} to 2×10^{15} cm^{-3} for *n*-type silicon. Thus the shape of the carrier-energy distribution at high fields would be

expected to vary markedly for the different specimens, and it is suggested that this feature will enter into any explanation of the results, while the completely different shape of the band edges for holes and electrons may account for the different magnitude of the effect for *n*- and *p*-type silicon.

Acknowledgements—The author is greatly indebted to Mr. J. E. PACKMAN who carried out at a good deal of the experimental work; also to Mr. R. F. BATEMAN for assistance and to Mr. G. W. GREEN, Mr. P. T. HOYLAND and Miss J. HUTCHEON for the supply of the crystals. This paper is published by permission of the Controller, H.M. Stationery Office.

REFERENCES

1. RYDER E. J., *Phys. Rev.* **90,** 766 (1953).
2. GUNN J. B., *J. Electronics* **2,** 87 (1956).
3. *Purdue Dept. Physics, 6th Report* PRF 1046 (Oct.–Dec. 1955).
4. STRATTON R., *Proc. Roy. Soc.* A**242,** 355 (1957).

J. Phys. Chem. Solids Pergamon Press 1959. Vol. 12. pp. 181–188. Printed in Great Britain.

ZENER TUNNELING IN SEMICONDUCTORS

E. O. KANE

General Electric Research Laboratory, Schenectady, N.Y.

(*Received* 4 *May* 1959; *revised* 24 *July* 1959)

Abstract—The Zener current in a constant field is calculated both with and without the WANNIER–ADAMS reduction of the interband-coupling terms. The Zener current is only slightly different in the two cases, a fact which has already been noted by WANNIER. The apparent reduction of interband coupling is interpreted as a polarization correction. A detailed calculation of the Zener current is made for a simple two-band model which is applicable to InSb. The evaluation of the tunneling integral follows closely a calculation due to KELDYSH.

VOL. 12 59/60

1. INTRODUCTION

THE possibility that electrons might tunnel through the forbidden band of an insulator in a strong electric field was first suggested by ZENER[1]. Measurements of the current–voltage characteristic of a reverse-biased diode have been interpreted in terms of Zener tunneling.[2] However, other investigations[3] of the so-called "soft-breakdown" characteristic have shown considerable variation from sample to sample in a manner which is hard to reconcile with a Zener tunneling between the valence and conduction bands. More recently, forward current–voltage characteristics in heavily doped junctions have been clearly shown by ESAKI[4] to result from Zener tunneling.

The tunneling problem has been treated theoretically by HOUSTON[5] and MCAFEE *et al.*[6]. WANNIER[7] and ADAMS[8] have shown that the leading terms in the Hamiltonian causing interband transitions can be removed by a perturbation transformation which transforms the original Bloch functions in the field-free crystal to Bloch functions in the presence of the field. At first sight, this transformation appears to affect significantly the calculation of the Zener current. FRANZ[9] and later WANNIER[10] have concluded, however, that this is not the case. Section 2 of the present paper shows in detail that the formula for Zener tunneling is not significantly affected by the WANNIER–ADAMS transformation. The change that does result is partly due to a direct modification of the energy bands by the presence of the electric field and partly due to the introduction of terms which permit transitions with the use of higher or lower bands as virtual intermediate states. The WANNIER–ADAMS transformation is interpreted as taking account of valence-electron polarization, which has very little effect on the Zenner current for small fields.

The most recent calculation of Zener tunneling has been made by KELDYSH[11]. Although KELDYSH was apparently unaware of the WANNIER–ADAMS transformation, his approach is entirely justified, as we show in Section 2. In Section 2 we introduce energy eigenfunctions which provide a simpler and more rigorous treatment than the method used by KELDYSH. However, we arrive at the same integral for the tunneling probability. In Section 3 we follow KELDYSH's method of evaluating the tunneling integral for the case of two simple interacting bands, an approximation which holds well for InSb. Our results agree with KELDYSH's except for a rather large numerical factor. The present calculation is also useful in that it specifies the circumstances for which the band-structure assumptions made by KELDYSH are valid. In Section 4 the results are discussed and numerical examples are given.

2. ZENER CURRENT AND POLARIZATION EFFECTS

The time-independent Schroedinger equation in the presence of a uniform electric field in the

x-direction may be written:

$$\left[E_n(k)-iF\frac{\partial}{\partial k_x}-E\right]a_n(k)-\sum_{n'}FX_{nn'}a_{n'}(k)=0 \tag{1}$$

where F is the force on the electron, $E_n(k)$ is the energy of an electron in the periodic lattice and E is the total energy. We are using ADAM's[12] "crystal momentum" representation where the basis functions are Bloch functions $\psi_n(k, r)$. The position operator x has been decomposed into an intraband operator $i\partial/\partial k_x$ and an "interband" operator $X_{nn'}(k)$. The operator X may also have an intraband component X_{nn} which may be conveniently absorbed in the energy by writing:

$$E_n^{(1)}(k)=E_n(k)-FX_{nn}(k) \tag{2}$$

where the superscript 1 denotes that the energy contains the electric field to first order. The off-diagonal matrix elements $X_{nn'}$ are given by the equation:

$$X_{nn'}=i\int u_{nk}^*\frac{\partial}{\partial k}u_{n'k}\,dr \tag{3}$$

where u_{nk} is the periodic part of ψ_{nk} normalized in the unit cell. The integration in equation (3) extends over the unit cell.

If the interband terms in equation (1) are ignored, the eigenfunctions may be written down immediately:

$$E_n^{(1)}(k)=\kappa^{-1}\exp\left\{\frac{i}{F}\int_0^{k_x}[E-E_n^{(1)}(k')]\,dk'_x\right\}\times$$

$$\times\delta(k_y-k_{y0})\delta(k_z-k_{z0}) \tag{4}$$

The "δ functions" are normalized in the first Brillouin zone. The normalization constant κ is the length of the line (k_x, k_{y0}, k_{z0}) subtended by the first Brillouin zone. This treatment is only rigorously correct when the subtended line is a principal vector of the reciprocal lattice. In the general case, the electron traverses a non-periodic path through k-space and the integration should cover the entire path. A different set of values k_{y0}, k_{z0} would obtain on each line segment of the total path, so the analysis would be appreciably more complicated. When the subtended segment is a principal vector, it is easy to install proper boundary conditions which determine the eigenvalues, E. The proper boundary condition is that the phase factor of equation (4) should be the same for the end points k_1, k_2 of the line of integration, since these points are identical. This leads to the condition:

$$\int_{k_1}^{k_2}[E-E_n^{(1)}(k')]\,dk_x'=2\pi nF \tag{5}$$

$$\Delta E=2\pi F/\kappa \tag{6}$$

where ΔE is the spacing between successive eigenvalues.

In an appendix we discuss the spatial dependence of the eigenfunctions of equation (4) and show that they have the expected character of dying away exponentially in the forbidden region between bands in the manner of a WKB function.

Using the eigenfunctions of equation (4), the interband terms in equation (1) then give the following matrix elements, $M_{nn'}^{(1)}$ connecting states of equal energy in different bands:

$$M_{nn'}^{(1)}=-(F/\kappa)\int X_{nn'}(k)\times$$

$$\times\exp\left\{\frac{i}{F}\int_0^{k_x}[E_n^{(1)}(k')-E_{n'}^{(1)}(k')]\,dk_x'\right\}dk_x \tag{7}$$

The probability per unit time, w, of making a transition from band n to band n' is given by the usual formula:

$$w=\frac{2\pi}{\hbar}|M_{nn'}^{(1)}|^2\rho(E) \tag{8}$$

where $\rho(E)$, the density of states, is obtained immediately from equation (6), since $\rho=(1/\Delta E)$.

$$\rho(E)=(\kappa/2\pi F) \tag{9}$$

The k_{y0} and k_{z0} components of k are constants of the motion which do not change on making a transition from one band to another.

The use of equation (8) is not completely standard, since the density of states does not tend to infinity with infinite volume in the usual manner. For a small field the density of states, as given by equation (9), will be very large but finite. The use of equation (8) is correct only for times $t\ll\tau=h/\Delta E=\hbar\kappa/F$. τ is the time required to traverse the band once when κ is a principal k-vector. For times longer than τ the energy spacing between levels can be resolved and the use of equation (8) is invalid.

In most cases phonons will scatter the electron in a time considerably shorter than τ, so that the energy spacing ΔE would be unresolvable. The use of equation (8) is then permissible. A completely rigorous treatment

of the Zener tunneling problem would require the introduction of phonons from the start.

Another approximation implicitly involved in the use of equation (8) is the assumption that $M^2\rho(E)$ varies slowly from one discrete level to the next, so that the sum over states may be replaced by an integral. If we evaluate $M_{nn'}$ for states differing in energy by an amount $\mathscr{E}$ we obtain:

$$\frac{dM^2\rho(E)}{d\mathscr{E}}\cdot\frac{\Delta E}{M^2\rho(E)}=4\sqrt{(2)}\pi\,\frac{m_r^{\frac{1}{2}}E_G^{\frac{1}{2}}}{\hbar\kappa}$$

where ΔE is given by equation (6). We find that this quantity is generally smaller than 1 for most cases of interest, but not sufficiently smaller that the approximation is highly accurate. (We used parabolic bands to evaluate the above expression.)

We now propose to demonstrate that the expression giving the interband transition probability, w, remains essentially the same even though the interband term in equation (1) is formally transformed to be of higher order in F, in the manner of WANNIER[13] and ADAMS[14].

We make a perturbation transformation on equation (1), eliminating interband terms to first order in F:

$$d_n(k)=e^{iT}a_n(k) \tag{10}$$

$$T=iFX_{nn'}/(E_n^{(1)}-E_{n'}^{(1)}) \tag{11}$$

Equation (1) then becomes, to second order in F:

$$\left[E_n^{(2)}(k)-iF\frac{\partial}{\partial k_x}-E\right]d_n(k)+\sum_{n'\neq n}F^2Q_{nn'}d_{n'}(k)=0 \tag{12}$$

$$E_n^{(2)}(k)=E_n^{(1)}(k)+F^2\sum_{n'\neq n}|X_{nn'}|^2/(E_n^{(1)}-E_{n'}^{(1)}) \tag{13}$$

$$Q_{nn'}=\left[\tfrac{1}{2}\sum_{n''\neq n,n'}X_{nn''}X_{n''n'}\left(\frac{1}{E_n^{(1)}-E_{n''}^{(1)}}+\frac{1}{E_{n'}^{(1)}-E_{n''}^{(1)}}\right)\right]+i\frac{\partial}{\partial k_x}\left(\frac{X_{nn'}}{E_{n'}^{(1)}-E_n^{(1)}}\right) \tag{14}$$

We have used equation (2). Equation (13) gives the correction to the energy bands due to the polarization of the Bloch functions by the applied field.

Equation (12) has the same formal structure as equation (1); hence the previously given calculation of the wave functions and transition probabilities will proceed entirely similarly. The new wave functions are the same as the q_n's given by equation (4), except that $E_n^{(2)}$ replaces $E_n^{(1)}$. The new interband transition matrix elements, $M_{nn'}^{(2)}$, corresponding to the $M_{nn'}^{(1)}$ of equation (7), become:

$$M_{nn'}^{(2)}=(F^2/\kappa)\int Q_{nn'}(k)\times$$

$$\times\exp\left\{\frac{i}{F}\int_0^{k_x}[E_n^{(2)}(k')-E_{n'}^{(2)}(k')]\,dk_x'\right\}dk_x \tag{15}$$

In demonstrating the approximate equivalence of equation (15) to (7), we ignore the bracketed term in equation (14). This term involves at least three distinct bands n, n', n'' and hence is a true higher-order term not included in the earlier treatment. Substituting the unbracketed term for $Q_{nn'}$ yields:

$$M_{nn'}^{(2)}=\frac{iF^2}{\kappa}\int\frac{\partial}{\partial k_x}\left(\frac{X_{nn'}}{E_{n'}^{(1)}-E_n^{(1)}}\right)\times$$

$$\times\exp\left\{\frac{i}{F}\int_0^{k_x}[E_n^{(2)}(k')-E_{n'}^{(2)}(k')]\,dk_x'\right\}dk_x \tag{16}$$

Integrating the right-hand side by parts* gives:

$$M_{nn'}^{(2)}=-\frac{F}{\kappa}\int\left(\frac{E_n^{(2)}-E_{n'}^{(2)}}{E_n^{(1)}-E_{n'}^{(1)}}\right)X_{nn'}\times$$

$$\times\exp\left\{\frac{i}{F}\int_0^{k_x}[E_n^{(2)}-E_{n'}^{(2)}]\,dk_x'\right\}dk_x \tag{17}$$

* G. H. WANNIER has obtained a similar result (private communication).

The contribution from the end points is zero by virtue of the boundary condition of equation (5) together with the periodicity of E_n and $X_{nn'}$ in k-space. (We have proved this rigorously only for the case when the line of integration is a principal lattice vector, but it is undoubtedly true in general.) Equation (17) then differs from equation (7) only to the extent that the second-order energy gaps $E_n^{(2)}-E_{n'}^{(2)}$ differ from the first-order gaps, $E_n^{(1)}-E_{n'}^{(1)}$.

The rather surprising result of the approximate equivalence of equations (7) and (17) has the following origin. For a filled band, the applied field produces two distinct effects, a polarization of the valence electrons similar to an ordinary atomic polarizability, and a Zener tunneling leading to conductivity. Both these effects are contained in the interband term $X_{nn'}$ of equation (1). Since the Bloch functions are not localized in space, and consequently not in energy, this term does not distinguish between the virtual transitions associated with polarization and the energy-conserving transitions associated with Zener tunneling. The energy eigenfunction treatment which we have given does separate these two effects and shows that the matrix elements between states of equal energy are very little affected by the WANNIER–ADAMS transformation.

The WANNIER–ADAMS treatment could be carried out to arbitrary order, removing the interband coupling to any desired order in the field. A succession of integrations by parts would show that the Zener tunneling effect remains substantially unaltered.

3. EVALUATION OF THE TUNNELING PROBABILITY

We follow the procedure of FRANZ[9] and KELDYSH[12] and evaluate the integral of equation (7) by a technique similar to the method of stationary phase. The path of integration in equation (7) can be deformed into the complex plane to pass through the point which makes the maximum contribution to the integral, namely the point $k_x = q$ for which

$$E_n^{(1)}(q) = E_{n'}^{(1)}(q) \tag{18}$$

Equation (18) is satisfied for a branch point in the complex plane where the conduction and valence bands join. KELDYSH has derived the behavior of E and X in the vicinity of this branch point by using some very general properties of the solutions of second-order differential equations. We feel that it is useful to derive his results more explicitly by using a particular model. The model we use is that of two bands "interacting" via the $k \cdot p$ perturbation. InSb is a good example of a material for which this approximation applies.[15]

The two-band Hamiltonian is:

$$H = \begin{pmatrix} E_G+\hbar^2k^2/2m & (\hbar/m)kp \\ (\hbar/m)kp & \hbar^2k^2/2m \end{pmatrix} \tag{19}$$

The band gap is E_G, the zero of energy is the top of the valence band, and the bands "repel" each other via the momentum matrix element p, which may be taken to be real and positive.

The solutions of equation (19) are:

$$E_\pm = \frac{E_G}{2}+\frac{\hbar^2k^2}{2m}\pm\frac{\eta}{2} \tag{20}$$

$$\eta = \sqrt{E_G^2+\frac{4\hbar^2k^2p^2}{m^2}} \tag{21}$$

where + refers to the conduction band and − refers to the valence band. We can calculate the effective masses at the band edge to be:

$$\frac{1}{m_+} = \frac{2p^2}{m^2E_G}\pm\frac{1}{m} \tag{22}$$

(We use the convention that effective masses are positive quantities. The two-band approximation is valid only in cases where equation (22) gives positive masses for both bands.) If we define a reduced mass, m_r, by:

$$\frac{1}{m_r} = \frac{1}{m_+}+\frac{1}{m_-} \tag{23}$$

we can express p in terms of m_r as follows:

$$p = \frac{m}{2}\sqrt{\frac{E_G}{m_r}} \tag{24}$$

Rewriting equation (21) with the use of equation (24), we have:

$$\eta = \sqrt{E_G^2+E_G\hbar^2k^2m_r^{-1}} \tag{25}$$

Equations (20) and (25) show clearly that the

conduction and valence bands are two sheets joined at the branch points, q:

$$q = \pm i\sqrt{\frac{m_r E_G}{\hbar^2} + k_z^2 + k_y^2} \tag{26}$$

(For our purposes we regard only k_x as being a complex variable.) If u refers to the cell-periodic functions for $k = 0$, then the functions U which diagonalize H of equation (19) are given by:

$$U_c = \frac{1}{\sqrt{(2\eta)}}\{(\eta+E_G)^{\frac{1}{2}}u_c + (\eta-E_G)^{\frac{1}{2}}u_v\} \tag{27}$$

$$U_v = \frac{1}{\sqrt{(2\eta)}}\{(\eta-E_G)^{\frac{1}{2}}u_c - (\eta+E_G)^{\frac{1}{2}}u_v\}$$

VOL. 12 59/60

Using these expressions, we can calculate $X_{nn'}$ as given by equation (3):

$$X_{cv} = i\hbar E_G^{\frac{1}{2}}/2m_r^{\frac{1}{2}}\eta^2 \tag{28}$$

$$X_{cc} = X_{vv} = 0 \tag{29}$$

$$E_c - E_v = \eta \tag{30}$$

$$\int_0^{k_x} \eta\, dk_x = \frac{k_x\eta}{2} + \frac{\sqrt{(m_r E_G)}}{\hbar}\left\{E_G + \frac{\hbar^2}{m_r}(k_z^2+k_y^2)\right\}\times \log\left[\frac{\eta+\hbar k_x\sqrt{(E_G/m_r)}}{\{E_G^2+E_G\hbar^2(k_z^2+k_y^2)m_r^{-1}\}^{\frac{1}{2}}}\right] \tag{31}$$

The maximum contribution to the integral of equation (7) comes from the vicinity of the point q for which $\eta = 0$. We deform the contour of integration in the k_x plane to pass by this point, as shown in Fig. 1. The factor X_{cv} has a pole at q. The contribution to the integral from the semicircle, $\int_{sc}$, is:

$$\int_{sc} = \frac{\pi\sqrt{(E_G m_r)}}{4\hbar q\kappa} F \exp\left[\frac{i}{F}\int_0^q \eta\, dk_x\right] \tag{32}$$

The horizontal integral in the neighborhood of q will also contribute to the value of the integral. To calculate this contribution, we make an expansion

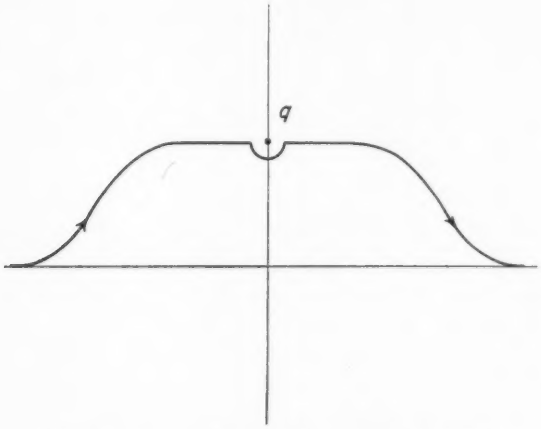

FIG. 1. Contour of integration for equation (33).

of η as a function of k about q:

$$\sigma = k - q \tag{33}$$

$$\eta = (\sqrt{2})\hbar\sqrt{\frac{E_G}{m_r}}\sqrt{(\sigma q)} + \cdots \tag{34}$$

$$\int_0^\sigma \eta\, dk = \frac{2(\sqrt{2})\hbar}{3}\sqrt{\frac{E_G}{m_r}}q^{\frac{1}{2}}\sigma^{\frac{3}{2}} + \cdots \tag{35}$$

We substitute the leading terms of these expansions in equation (7) and extend the limits of integration to $\pm\infty$. These approximations are justified for small F. The integral over the horizontal portion

of the contour in the vicinity of q, $\int_{hor}$ then becomes:

$$\int_{hor} = \frac{\pi\sqrt{(E_G m_r)}F}{12\hbar q\kappa} \exp\left\{\frac{i}{F}\int_0^q \eta\, dk_x\right\} \quad (36)$$

Combining the two contributions to the integral of equation (7) and evaluating equation (31) for $k_x = q$, we find:

$$M_{nn'}^{(1)} = \frac{\pi\sqrt{(m_r E_G)}F}{3\hbar q\kappa} \exp\left\{\frac{-\pi\hbar|q^2|E_G^{\frac{1}{2}}}{4Fm_r^{\frac{1}{2}}}\right\} \quad (37)$$

To compute the rate of Zener tunneling per cm^3, we multiply the transition probability per electron, w, by the number of electrons per cc, $2\kappa(2\pi)^{-3}\, dk_y\, dk_z$ and integrate k_y and k_z over the filled band. (We are including a factor of 2 for spin.) The result is:

$$n = \frac{FE_G m_r}{36\pi\hbar^3}\int \frac{1}{|q|^2}\exp\left\{\frac{-\pi\hbar|q|^2E_G^{\frac{1}{2}}}{2Fm_r^{\frac{1}{2}}}\right\} dk_y dk_z \quad (38)$$

n is the number of electrons per sec per cm^3 leaking from the valence band to the conduction band. Transforming to circular coördinates and replacing q^2 by $E_G m_r/\hbar^2$ in the denominator (an approximation valid for small F), we obtain:

$$n = \frac{F^2 m_r^{\frac{1}{2}}}{18\pi\hbar^2 E_G^{\frac{1}{2}}}\exp\left\{\frac{-\pi m_r^{\frac{1}{2}}E_G^{\frac{3}{2}}}{2\hbar F}\right\} \quad (39)$$

The fact that the quantity κ does not appear in the final result lends credence to the assumption that the calculation for a general field direction proceeds as we have outlined it. Our treatment is rigorous only when κ is a principal vector of the reciprocal lattice, as we have already noted. KELDYSH also justifies his derivation in this way.

4. DISCUSSION

Equation (39) is very similar to equation (19) in KELDYSH's paper.[12] If we compare the two results for InSb, for which the approximations made here should apply, equation (39) gives a value of n which is a factor 72 smaller than KELDYSH's result. Of this factor 72, a factor 9 is due to a numerical error in the evaluation of the contour integral leading to $|M_{nn'}|^2$, a factor 2 is of uncertain origin, and a factor 4 is due to a different method of counting the valence electrons. KELDYSH multiplies his density of states by a factor equal to the number of valence electrons in the unit cell (8 for InSb). Our view is that this factor should be 2, since this is the number of electrons in the light mass band. Only these electrons have an appreciable probability of tunneling into the conduction band.

We find that KELDYSH's constant γ, which he leaves unspecified, should be set equal to zero for the case considered here.*

KELDYSH's result is derived more generally than our own. We find an isotropic mass, m_r, whereas KELDYSH finds an anisotropic mass. Results analogous to equations (32) and (36) can, in fact, be derived quite generally by KELDYSH's method. However, the evaluation of the exponential factor which involves the integral

$$\int_0^q \eta\, dk_x$$

cannot be done in general by using equation (25) (or its generalization to an anisotropic effective mass). Correct evaluation of this integral requires an accurate knowledge of the band structure from $k_x = 0$ to $k_x = q$. KELDYSH's expansion about the branch point, q, will not be sufficiently accurate for this purpose in the general case.

To give some idea of the magnitude of the Zener effect, we evaluate equation (39) for InSb with a field of 5×10^4 V/cm. The parameters we use are $E_G = 0{\cdot}23$ eV, $m_r = 0{\cdot}0065\, m_0$. (The reduced mass is appropriate to an electron and a *light* hole.) The exponential pre-factor has the value:

$$\frac{F^2 m_r^{\frac{1}{2}}}{18\pi\hbar^2 E_G^{\frac{1}{2}}} = 4\times10^{29} \text{ per cc sec}$$

* *Note added in proof:* We have assumed $X_{cc} = X_{vv} = 0$. For a material like InSb which lacks inversion symmetry this is not correct. The wave functions at $k = 0$ may possess dipole moments which lead to a first order stark shift in the energy bands as indicated in equation (2). This term is included in equation (7) and may be shown to lead to KELDYSH's constant, γ. Estimates of γ indicate that it will make only a small correction to equation (39).

and the exponent is

$$\frac{\pi m_r^{\frac{1}{2}} E_G^{\frac{3}{2}}}{2\hbar F} = 10{\cdot}2$$

which yields

$$n = 1{\cdot}4 \times 10^{25} \text{ per cm}^3 \text{ sec.}$$

If the field extends over 10^{-4} cm, the current would then be $j = 220$ A/cm^2. These values are purely for illustrative purposes. In an actual junction the field will not be constant, and equation (39) must be integrated over the junction. If the field is not substantially constant over a region for which the potential varies by one band gap, the derivation leading to equation (39) is not valid.

We can use equation (13) to estimate what error the neglect of polarization corrections to the energy bands has introduced into our calculations. With the help of equation (28) we compute that for $F = 5 \times 10^4$ cm/sec

$$\Delta E_G = 0{\cdot}006 E_G$$

$$\Delta \frac{1}{m_r} = -0{\cdot}06 \frac{1}{m_r}$$

The correction to the effective mass is larger than the band-gap correction, but neither is a big effect for this field. Since the corrections go as F^2, they quite rapidly become important for higher fields.

In our treatment of Zener tunneling we have considered only the conduction band and the light mass valence band. Actually InSb also has a heavy mass valence band degenerate at $k = 0$ with the light mass band. (The most exact description of the bands is even more complicated.[15]) The coupling between the two degenerate bands can be ignored only in the semiclassical limit which corresponds to weak fields. We expect this approximation to break down for fields of the same order as those calculated above.

FRANZ[9] has considered the effect of the coulomb attraction between electron and hole on the Zener current. He finds the effect expressible as a multiplicative factor, f_{eh}, which should multiply the right-hand side of equation (39). FRANZ gives:

$$f_{eh} = \exp\left\{\frac{\sqrt{(2m^*)}e^2}{4\hbar\epsilon\sqrt{(E_G)}}\right\} \tag{40}$$

where ϵ is the dielectric constant (16 for InSb). This factor is almost exactly unity for InSb.

For other III–V materials with minima at $k = 0$, the simple two-band theory is not as accurate as for InSb, because the p-like valence band lowered by spin-orbit interaction has an important influence on the conduction-band mass. It should not be too difficult to insert a more accurate expression for η in equations (32) and (36) to obtain useful numerical results in these cases.

In the case of germanium, the indirect band gap poses additional problems. For low fields, transitions from the valence band to the (111) conduction band minimum will involve phonons to insure k conservation. This point has been discussed by KELDYSH[12]. For high fields and reverse bias, Zener transitions to the $k = 0$ minimum will be most likely, but here, too, the simple two-band theory is invalidated by the spin-orbit split-off band.

REFERENCES

1. ZENER C., *Proc. Roy. Soc.* A**145,** 523 (1934).
2. CHYNOWETH A. G. and MCKAY K. G., *Phys. Rev.* **106,** 418 (1957).
3. PELL E. M., *J. Appl. Phys.* **28,** 459 (1957).
4. ESAKI L., *Phys. Rev.* **109,** 603 (1958).
5. HOUSTON W. V., *Phys. Rev.* **57,** 184 (1940).
6. MCAFEE K. B., RYDER E. J., SHOCKLEY W. and SPARKS M., *Phys. Rev.* **83,** 650 (1951).
7. WANNIER G. H., *Phys. Rev.* **100,** 1227 (1955).
8. ADAMS E. N., *Phys. Rev.* **107,** 698 (1957).
9. FRANZ W., *International Conference on Semiconductors, Garmisch-Partenkirchen* (1956), p. 317. Interscience Publishers, New York (1958).
10. WANNIER G. H., *Résumés of the International Congress on Solid State Physics, Brussels,* p. 89 (1958).
11. KELDYSH L. V., *Sov. Phys. JETP* **6,** 763 (1958).
12. ADAMS E. N., *J. Chem. Phys.* **21,** 2013 (1953).
13. WANNIER G. H., *Phys. Rev.* **100,** 1227 (1955); **101,** 1835 (1956).
14. ADAMS E. N., *Phys. Rev.* **107,** 698 (1957).
15. KANE E. O., *J. Phys. Chem. Solids* **1,** 249 (1957).
16. MORSE P. M. and FESHBACH H., *Methods of Theoretical Physics,* p. 440. McGraw-Hill, New York (1953).

APPENDIX

The meaning of the energy eigenfunctions $q_n(k)$ of equation (4) is more readily appreciated if they are expressed in the familiar r representation:

$$q_n(k) \to Q_n(r) = \kappa^{-\frac{1}{2}} \int e^{ik \cdot r} u_{nk}(r) \times$$

$$\times \exp\left\{\frac{i}{F}\int_0^{k_x} [E - E_n(k')]\, dk_x'\right\} dk_x. \tag{A.1}$$

Equation (A.1) becomes more revealing if it is evaluated approximately by the method of steepest descents.[16] We write the integrand in the form

Integrand $= e^f$

$$f = ik\cdot r+(i/F)\int_0^{k_x}[E-E_n(k')]\,dk_x'+\ln u_{nk}(r) \tag{A.2}$$

The function f is then written as a Taylor series about the point of stationary phase k_{xs}

$$f = f(k_{xs})+\frac{(k-k_{xs})^2}{2}f''(k_{xs})+\cdots \tag{A.3}$$

$$f'(k_{xs}) = 0, \tag{A.4}$$

where equation (A.4) determines the point of stationary phase. The integral then has the value (asymptotic in $1/F$):

$$Q_n(r) = \kappa^{-\frac{1}{2}}[-2\pi/f''(k_{xs})]^{\frac{1}{2}}e^{f(k_{xs})}. \tag{A.5}$$

Equations (A.2) and (A.4) then give the following conditions for k_{xs}, $f''(k_{xs})$

$$E-E_n(k_{xs})+Fx-iF\left(\frac{\partial}{\partial k_x}\ln u_n\right)_{k_{xs}} = 0. \tag{A.6}$$

$$f''(k_{xs}) = -\frac{i}{F}\left(\frac{\partial E}{\partial k_x}\right)_{k_{xs}}+i\left(\frac{\partial^2}{\partial k_x^2}\ln u_n\right)_{k_{xs}} \tag{A.7}$$

The terms involving u_n in equation (A.6) and (A.7) can be ignored in the limit of small F, giving the result:

$$Q_n(r) = \kappa^{-\frac{1}{2}}\left[-2\pi iF\Big/\frac{\partial E_n}{\partial k_x}\right]_{k_{xs}}^{\frac{1}{2}}u_n(k_{xs},r)\exp\left\{\frac{i}{F}\int_0^{k_{xs}}[E-E_n(k_x')+Fx]\,dk_x'+i(k_{y0}y+k_{z0}z)\right\} \tag{A.8}$$

$$E-E_n(k_{xs})+Fx = 0. \tag{A.9}$$

As before, k_{y0} and k_{z0} are constants of the motion.

The integral in the exponent of equation (A.8) can be given a more familiar form by a change of variables $k_x \to x$ where k_x and x are related by an equation of the same form as equation (A.9):

$$E-E_n(k_x)+Fx = 0 \tag{A.10}$$

An integration by parts then yields

$$Q_n(r) = \kappa^{-\frac{1}{2}}\left[2\pi F\Big/\frac{\partial E_n}{\partial k_x}\right]_{k_{xs}}^{\frac{1}{2}}u_n(k_{xs},r)\times$$

$$\times\exp i\left\{\int_{x_0}^{x}k_x\,dx+k_{y0}y+k_{z0}z\right\} \tag{A.11}$$

where x_0 corresponds to $k_x = 0$ in equation (A.10) and we have discarded an unimportant phase factor. The "stationary phase" relationship of equation (A.9) is the "classical" relationship between position and k-vector.

In the limit of low fields the classical requirement of defining position and k-vector at the same time can be satisfied. Equations (A.10) and (A.11) show that the phase of the wave function accumulates along the classical trajectory in the standard manner of a WKB function.

The transformation of variables from k_x to x given by equation (A.10) can also be used to clarify the meaning of equations (7) and (37). Equation (7) may be written:

$$M_{nn'} = -(F/\kappa)X_{nn'}(k)\exp i\left\{\int_{x_0'}^{x'}\bar{k}_x\,dx'-\int_{x_0}^{x}k_x\,dx\right\} \tag{A.12}$$

where x' and x_0' obey a relation analogous to equation (A.10) with $E_{n'}$ replacing E_n. Equation (37) was derived from equation (7) by the method of steepest descents. The point of steepest descent k_σ as given by equation (30):

$$E_c(k_\sigma) = E_v(k_\sigma)$$

is the same as the condition

$$x_\sigma = x'_\sigma \tag{A.13}$$

$$M_{nn'}\sim\exp i\left\{\int_{x_0'}^{x_\sigma}\bar{k}_x\,dx'+\int_{x_\sigma}^{x_0}k_x\,dx\right\} \tag{A.14}$$

Equation (A.14) gives the exponential factor in equation (A.12) evaluated for $x = x'$. The exponent in equation (A.14) is the integral of an imaginary k vector from one band edge to the other where the k vector is determined from equation (A.10) with E_n on one side of the branch point, $E_n = E_{n'}$, and by the analogous equation with $E_{n'}$ on the other. The imaginary k vector leads to attenuation in the manner typical of barrier penetration.

J. Phys. Chem. Solids Pergamon Press 1959. Vol. 12. pp. 189–195. Printed in Great Britain.

THE EPITAXIAL GROWTH OF ICE ON SINGLE-CRYSTALLINE SUBSTRATES

G. W. BRYANT, J. HALLETT, and B. J. MASON

Imperial College, London

(*Received* 18 *February* 1959)

VOL. 12 59/60

Abstract—Epitaxial deposits of ice crystals have been formed on the basal (0001) faces of hexagonal AgI, PbI_2, CuS, CdI_2 and brucite, on the (001) face of freshly-cleaved muscovite, on the (010) face of orthorhombic HgI_2, on the (001) face of orthorhombic iodine, on the (100) face of V_2O_5 and on the rhombohedral faces of calcite. The temperature at which ice crystals first appear on a particular substance is very close to the threshold temperatures at which an aerosol of the same substance nucleates a cloud of supercooled water droplets.

The crystals appear preferentially at cleavage and growth steps on the substrate surface, provided that these exceed $\sim 0{\cdot}1\mu$ in height and preserve their parallel orientation irrespective of the direction of the step.

Thin, hexagonal ice plates, growing on the basal plane of covellite (CuS), show interference colours which give a measure of their thickness. Commonly, the ice crystals increase appreciably in diameter with no discernible change of thickness, suggesting that molecules arriving on the upper surface are not assimilated but migrate over the surface and are built in at the crystal edges. Crystals usually thicken on touching a neighbouring crystal; coloured growth fronts are then seen spreading out across the crystal surface from the point of contact.

Detailed measurements on AgI, PbI_2, CuS and CdI_2 show that, for a given substance, there is a well-defined critical temperature above which ice crystals can appear only if the air exceeds saturation relative to liquid water, but below which ice forms directly from the vapour phase provided that the supersaturation relative to ice exceeds 12 per cent for silver iodide and slightly different values for the other substrates. These critical supersaturations are required for growth at the edges of steps; ice appears on the flat parts of the substrate only at much higher supersaturations ($>$ 100 per cent).

1. INTRODUCTION

INTEREST in the epitaxy of ice on foreign substrates stems mainly from the ability of crystals of certain natural minerals and of some inorganic compounds to nucleate supercooled water and to initiate ice-crystal formation in clouds of supercooled water droplets. The results of very careful tests on the ice-nucleating ability of finely-dispersed aerosols, carried out in both diffusion- and mixing-cloud chambers by MASON and HALLETT[1,2], MASON and MAYBANK[3], and MASON and VAN DEN HEUVEL[4], are summarized in Table 1. In each case the quoted threshold temperature is that at which about one particle in 10^4 produces an ice crystal; for all the substances listed the activity gradually increases as the temperature falls below the threshold value.

It will be seen from Table 1 that, although there is a tendency for the more effective nucleators to possess hexagonal crystalline symmetry and lattice parameters reasonably close to those of ice, there are a number of exceptions; but for all the substances which nucleate at temperatures above −15°C, it is possible to find a low-index face on which the atomic spacings differ from those in either the basal or prism faces of ice by not more than a few per cent. If, in calculating the minimum misfit, one permits the matching of atomic rows in the ice and substrate lattices in ratios of up to 3:1, the values shown in heavy type in Table 1 are the misfits in the two most favoured of the three mutually perpendicular directions, $(1\bar{2}10)$, $(10\bar{1}0)$, (0001), of the ice lattice.

Although, in the literature, epitaxy is usually discussed in terms of the misfit in only the most favourable direction, it seems reasonable to regard the formation of two-/three-dimensional nuclei

Table 1. *Data on substances active as ice nuclei at temperatures above* —16°C

Substance	Crystal symmetry	Lattice constants (Å)			Substrate plane	Misfit between substrate lattice in directions (per cent)*			Threshold temp. (°C)
		a	*b*	*c*		$(1\bar{2}10)$	$(10\bar{1}0)$	(0001)	
Ice	Hex.	4·52		7·36	—	—	—	—	—
					(a) *Natural substances*				
Covellite	Hex.	3·80		16·43	(0001)	$-\ \mathbf{2{\cdot}8}_{(3:2)}$	$-\ \mathbf{2{\cdot}8}_{(1:2)}$	$+11{\cdot}5_{(2:1)}$	−5
Vaterite	Hex.	4·12		8·56	(0001)	$+\ \mathbf{5{\cdot}4}_{(3:2)}$	$+\ \mathbf{5{\cdot}4}_{(1:2)}$	$+16{\cdot}4_{(1:1)}$	−7
β-Tridymite	Hex.	5·03		8·22	(0001)	$-\ \mathbf{3{\cdot}5}_{(2:1)}$	$-\ \mathbf{3{\cdot}5}_{(2:3)}$	$+11{\cdot}7_{(1:1)}$	−7
	Hex.	5·03		8·22	(0001)	$+\mathbf{11{\cdot}3}_{(1:1)}$	$+\mathbf{11{\cdot}3}_{(1:1)}$	$+11{\cdot}7_{(1:1)}$	
Kaolinite	Pseudo-hex. (OH groups)	2·98		7·08	(001)	$-\ \mathbf{1{\cdot}1}_{(2:3)}$	$-\ \mathbf{1{\cdot}1}_{(2:3)}$	$-\ 3{\cdot}8_{(1:1)}$	−9
Hematite	Hex.	5·03		17·35	(0001)	$-\ \mathbf{3{\cdot}5}_{(2:1)}$	$-\ \mathbf{3{\cdot}5}_{(2:3)}$	$+17{\cdot}9_{(2:1)}$	−10
Brucite	Hex.	3·11		4·74	(0001)	$+\ \mathbf{3{\cdot}2}_{(2:3)}$	$+\ \mathbf{3{\cdot}2}_{(2:3)}$	$-\ 3{\cdot}4_{(2:3)}$	−11
Cinnabar	Hex.	4·14		9·49	(0001)	$-\ \mathbf{8{\cdot}4}_{(1:1)}$	$-\ \mathbf{8{\cdot}4}_{(1:1)}$	$-14{\cdot}1_{(3:2)}$	−16
Graphite	Hex.	2·46		6·70	(0001)	$+\ \mathbf{8{\cdot}9}_{(1:2)}$	$+\ \mathbf{8{\cdot}9}_{(1:2)}$	$-\ 9{\cdot}0_{(1:1)}$	−16
					(b) *Inorganic crystals*				
AgI	Hex.	4·58		7·49	(0001)	$+\ \mathbf{1{\cdot}3}_{(1:1)}$	$+\ \mathbf{1{\cdot}3}_{(1:1)}$	$+\ 1{\cdot}8_{(1:1)}$	−4
PbI_2	Hex.	4·54		6·86	(0001)	$+\ \mathbf{0{\cdot}4}_{(1:1)}$	$+\ \mathbf{0{\cdot}4}_{(1:1)}$	$+\ 6{\cdot}8_{(1:1)}$	−6
CuS	Hex.	3·80		16·43	(0001)	$-\ \mathbf{2{\cdot}8}_{(3:2)}$	$-\ \mathbf{2{\cdot}8}_{(1:2)}$	$+11{\cdot}5_{(2:1)}$	−6
HgI_2	Tetrag.	4·36	4·36	12·34	(001)	$-\ \mathbf{3{\cdot}5}_{(1:1)}$	$+\mathbf{11{\cdot}5}_{(1:2)}$	$-16{\cdot}2_{(2:1)}$	−8
	O. Rhombic	4·67	13·76	7·32	(010)	$+\ \mathbf{3{\cdot}3}_{(1:1)}$	$-\ \mathbf{6{\cdot}4}_{(1:1)}$	$-\ 6{\cdot}5_{(2:1)}$	−8
Ag_2S	Monoclinic $\beta = 55°$	4·20	6·93	9·50	(010)	$-\ \mathbf{7{\cdot}1}_{(1:1)}$	$-\ \mathbf{0{\cdot}3}_{(1:1)}$	$-\ 5{\cdot}9_{(1:1)}$	−8
NH_4F	Hex.	4·39		7·02	(0001)	$-\ \mathbf{2{\cdot}9}_{(1:1)}$	$-\ \mathbf{2{\cdot}9}_{(1:1)}$	$-\ 4{\cdot}6_{(1:1)}$	−9
V_2O_5	O. Rhombic	11·48	4·36	3·55	(100)	$-\ \mathbf{3{\cdot}5}_{(1:1)}$	$-\ 2{\cdot}1_{(3:2)}$	$-\ \mathbf{3{\cdot}5}_{(1:2)}$	−10 (plates)
					(001)	$-\ \mathbf{3{\cdot}5}_{(1:1)}$	$-\ \mathbf{2{\cdot}1}_{(3:2)}$	$-\ 3{\cdot}5_{(1:2)}$	−15 (prisms)
Ag_2O	Cubic	4·72			(001)	$+\ \mathbf{4{\cdot}4}_{(1:1)}$	$-\ 9{\cdot}5_{(2:3)}$	$-\ \mathbf{3{\cdot}8}_{(2:3)}$	−11 (prisms)
CdI_2	Hex.	4·24		6·84	(0001)	$-\ \mathbf{6{\cdot}2}_{(1:1)}$	$-\ \mathbf{6{\cdot}2}_{(1:1)}$	$-\ 7{\cdot}1_{(1:1)}$	−12
MnO_2	Tetrag.	4·44	4·44	2·89	(010)	$-\ \mathbf{1{\cdot}8}_{(1:1)}$	$+\mathbf{10{\cdot}8}_{(1:3)}$	$-\ 9{\cdot}5_{(2:3)}$	−12
I_2	O. Rhombic	4·78	7·25	9·77	(001)	$+\ \mathbf{5{\cdot}8}_{(1:1)}$	$-16{\cdot}3_{(3:2)}$	$-\ \mathbf{1{\cdot}5}_{(1:1)}$	−12 (prisms)
						$+\ \mathbf{5{\cdot}8}_{(1:1)}$	$-\ \mathbf{7{\cdot}3}_{(1:1)}$	$-11{\cdot}6_{(3:2)}$	−14 (plates)

* The percentage misfit $\Delta = ((\delta s - \delta i)/\delta i) \times 100$, where δi, δs are the spacings of those atomic rows, in ice and the substrate, which most nearly coincide, with the restriction that δi does not exceed three atomic spacings. If, for example, alternate rows in the substrate are matched to every row in ice, this is shown by the subscript (2:1).

in terms of the misfit in two/three mutually perpendicular directions. The misfit in the third direction is therefore given in lighter type in Table 1. For the rather complex mineral structures, the geometrical similarity between the ice and substrate lattice, as expressed by the misfit in one or more directions combined, is not highly correlated with the nucleating ability as indicated by the threshold temperature. In the case of the simple inorganic structures, however, a reasonable correlation appears to exist between the threshold nucleation temperature (which enters explicitly into the expression for the critical size of the ice nucleus) and the sum of the misfits in the three mutually perpendicular directions. Thus it appears that, as for most other substances, the epitaxial growth of ice on foreign substrates is determined only partly by geometrical factors and overall by the configuration and intensity of the surface force field of the substrate and its interaction with the first layers of the deposit.

In order to study in more detail the orientation of ice crystals on well-defined faces of single-crystalline substrates, their growth has been

directly observed under carefully controlled conditions of temperature and supersaturation of the vapour. Although epitaxial deposits of ice have been observed on AgI, PbI_2 and mica by MONTMORY[5], and JAFFRAY and MONTMORY[6,7], on AgI and PbI_2 by MASON[8] and on AgI, PbI_2, CdI_2 and biorite by KLEBER and WEIS,[9] the conditions under which they appeared were not studied in detail.

In the present experiments, orientation of ice has been observed on the basal (0001) faces of hexagonal AgI, PbI_2, CuS, CdI_2 and brucite, on the (001) face of *freshly-cleaved* muscovite, on the (010) face of orthorhombic HgI_2, on the (001) plane of orthorhombic iodine, on the (100) plane of V_2O_5 and on the surfaces of rhombohedral calcite.

2. EXPERIMENTAL TECHNIQUES

The apparatus, shown in Fig. 1, is a modified version of that used by SHAW and MASON[10] to study the growth of ice crystals on a polycrystalline metal surface. The metal surface supporting the substrate crystal is situated in the centre of a lagged, cylindrical metal chamber, the hollow walls of which may be cooled down to —50°C by circulating petrol chilled with solid carbon dioxide through the annular space. The temperature of the chamber walls is controlled by a heating coil wound on the copper tube carrying the coolant where it leaves the cooling bath. The base of the chamber is coated with ice, so that the air in the experimental space (about 7 cm diameter × 1 cm deep), which is stirred by a small electric fan, is uniformly saturated with respect to ice at a temperature T_1 indicated by a thermocouple attached to the surface of the ice layer. The temperature over the chamber floor does not vary by more than 0·2°C and the thermocouple is placed half-way out along the radius.

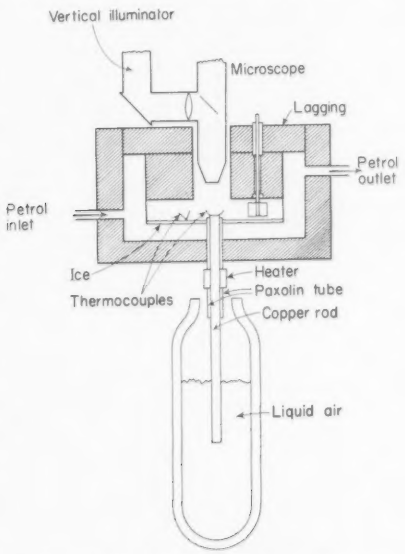

FIG. 1. The experimental apparatus.

The substrate crystal rests on the end surface of a long copper rod which is insulated from the chamber and dips into a Dewar flask containing liquid air. The crystal is thus cooled to a lower temperature, T_2, than that of the surrounding air, and this is controlled by varying the current through the heating coil wound on the copper rod. The temperature T_2 of the thin substrate crystal is recorded by a fine thermocouple immediately below the surface of the copper rod, and the saturation ratio of the air in the neighbourhood of the growing ice crystals is altered by adjusting the temperatures T_1, T_2, and is measured by the ratio of the equilibrium vapour pressures of ice at these two temperatures.

The reliability of the supersaturation measurement was checked by using the apparatus as a dew-point hygrometer; for a fixed value of T_1, the temperature T_2 of the copper surface was adjusted until a deposit of very small water droplets began to form or disappear, and it was confirmed that, at this point, the measured temperatures showed the air to be just saturated relative to liquid water. Moreover, ice crystals grown as hexagonal plates on the substrate began to evaporate at the corners when the indicated temperatures showed the air to be just saturated with respect to a plane surface of ice.

The crystals were viewed through a microscope fitted with a vertical illuminator, an 8-mm objective and × 20 eyepiece being used to give a linear magnification of 350.

3. OBSERVATIONS OF EPITAXIAL GROWTH

(a) *On Silver iodide*

The specimens were prepared by PASHLEY's (see NEWMAN and PASHLEY[11]) technique of evaporating silver on freshly-cleaved mica *in vacuo*,

the (111) faces of silver then being attacked, in darkness, by the vapour from a weak solution of iodine. This produces a very thin layer in which (0001) faces of hexagonal silver iodide and (111) faces of the cubic form are parallel to the surface, both forms giving an identical hexagonal array of iodine ions.

Epitaxial deposits of ice crystals growing on their basal planes were obtained at temperatures below −4°C; at higher temperatures only water droplets appeared. At temperatures between −8 and about −25°C the crystals grew preferentially along the secondary axes to form thin plates (Fig. 2), but at temperatures between −4 and −8°C, and also below −25°C, growth proceeded preferentially in the direction of the *c*-axis, normal to the surface (Fig. 3), in accordance with variation of habit with temperature observed by HALLETT and MASON[12] for freely-growing ice crystals. The crystals showed a strong tendency to form on specific sites (see Fig. 4), which at this stage of development darkened with increasing exposure to light. They appear to be preferred centres for the decomposition of silver iodide to metallic silver and may therefore mark the sites of emergent dislocations.

Prolonged exposure to a strong source of ultra-violet light leads to a rapid decomposition of the silver iodide to metallic silver. After several seconds' exposure to the beam from a 250-W high-pressure mercury-arc lamp, the surface begins to deteriorate and the oriented crystals become more sparse. After further exposure, on a surface which is now dark and discoloured, it becomes very difficult to form an ice deposit; the condensate appears in the form of droplets, 5–10μ in diameter, which may be supercooled down to temperatures as low as −30°C and which then freeze to produce needle-like crystals with random orientation. A more detailed account of measurements on the photolytic decomposition of silver iodide is to appear elsewhere.

In this context it is relevant to refer to the claim by MONTMORY[5] to have observed epitaxy of ice on the (111) face of metallic silver. We are unable to confirm this observation. On clean, fresh surfaces of silver we are able to form only water droplets at temperatures above about −25°C; at lower temperatures the droplets freeze and develop into randomly oriented prisms, as shown in Fig. 5, or needles, as shown in Fig. 6. But, after exposure for a day or two to room air, the silver surface shows a progressive tendency to produce oriented crystals. At first these take the form of widely separated, irregular, plate-like crystals following the freezing of droplets at temperatures below −10°C; with even longer exposures denser deposits of regular hexagonal plates appear direct from the vapour phase. Often two distinct orientations are observed, as in Fig. 7. It was suspected that this activation of the silver surface was due to contamination by traces of iodine vapour and the formation of localized patches of silver iodide, because the activity of the latter is easily destroyed by exposure to ultra-violet light. An electron-diffraction examination of the silver surface confirmed the existence of oriented layers of silver iodide, and a second substance which would appear to be silver sulphide.

(b) *On lead iodide*

Lead iodide crystals, up to 4 mm in diameter, were produced by selection from a commerical preparation, by growth of very thin hexagonal plates from a cooling solution or by selection of crystals from the surface of a solidified melt.

At temperatures above −6°C the initial deposit consisted of liquid water droplets which, at lower temperatures, froze and developed into ice crystals with *a*-axes parallel to those of the lead iodide, their habit varying with temperature as described above for growth on silver iodide.

The crystals grown from solution mostly had flat, featureless faces on which ice crystals rarely appeared except at very high vapour supersaturations exceeding 100 per cent. The tendency was for the ice to appear in irregular aggregates round the edges of these crystals (see Fig. 8), but regular, oriented ice crystals readily appeared along steps which were artificially induced by the overlapping of the thin lead iodide plates. Many of the lead iodide crystals (1 mm in diameter) exhibited trigonal growth spirals whose steps were not usually parallel to the edges of the crystal. Although there was no marked tendency for ice crystals to appear at the edges of the shallow steps (< 500 Å high) in Fig. 9, they did show a marked preference for the edges of steps higher than about 0·1μ at which they assumed the orientation of the crystal edge rather than that of the step.

After melting and evaporation of the ice-crystal deposit, the nucleating activity of the surface was

greatly reduced—a consequence, no doubt, of lead iodide being slightly soluble in water.

(c) *On cadmium iodide*

Crystals of up to 5 mm in diameter were produced from a solution of cadmium iodide saturated at 60°C and slowly cooled to room temperature.

At temperatures above —12°C the condensate was in droplet form; between —12 and —20°C the drops froze without forming regular ice crystals; well-defined crystals appeared only below —20°C.

Whereas cadmium iodide crystals precipitated from a rapidly-cooled solution exhibited shallow, closely-packed, circular growth steps which did not seem to encourage the nucleation of ice crystals, slow cooling produced higher, more widely-spaced steps of hexagonal symmetry at which ice crystals appeared preferentially, as shown in Fig. 10. The distortion of the ice crystals from their hexagonal shape may be explained by asymmetric growth caused by the anisotropic arrival of water molecules.

Melting and evaporation of the ice deposit again destroyed the nucleating properties of the surface and, in this case, left visible damage because of the high solubility of cadmium iodide.

(d) *On cupric sulphide*

The substrate was prepared by cleavage of the mineral covellite parallel to the basal plane.

At temperatures above —6°C water vapour condensed on the covellite surface as droplets, but at lower temperatures ice crystals appeared with their *a*-axis at 30° to those of the cupric sulphide, this relative orientation giving a much closer atomic fit between the deposit and the substrate, as shown in Fig. 11.

In Fig. 12(a) an oriented deposit of thin, hexagonal ice plates, shown in reflected white light, appear on the blue substrate crystal. In the early stages of growth the crystals, being only a few thousand Ångstroms high, show interference colours which give a measure of their thickness. Comparison of Figs. 12(a) and (f) shows that, at first, some crystals (e.g. No. 2 in key) increase noticeably in diameter with no discernible change of thickness. These observations, together with other evidence to be published in detail elsewhere, suggest that molecules arriving on the upper surface of the crystal are not assimilated, but migrate over this surface and are built in at the edges.

Referring to crystals numbered 1–5 in the key, whilst No. 2 remains constant in colour, the others undergo rapid change, showing that thickening is taking place. (One order of colour change is about 0·15μ.) Thickening of a crystal is frequently initiated by contact with another crystal of greater thickness. This is shown in the sequence Fig. 13(a)–(f), where crystals 2, 4, 6 initiate growth layers on crystals 1, 3, 5 as soon as contact occurs.

There is a marked tendency for ice crystals to cluster along cleavage steps on the substrate and to maintain their orientation relative to the substrate lattice irrespective of the direction of the step. A crystal sitting astride a step may be of different thickness on either side, as indicated by the changes of colour in the individual crystals of Fig. 12.

The crystal originating at the large steps in Fig. 12 (crystals No. 7) have grown much more rapidly than those on the flatter areas of the substrate. Here, the crystal thickness having reached several wavelengths, the interference colours have disappeared to be replaced by a uniform pink coloration. Again it is noteworthy that the very shallow steps, only a few hundred Ångstroms high, although able to cause a colour change in an overlying ice crystal, do not act as preferred nucleation sites.

(e) *On iodine*

On the (001) faces of iodine, oriented deposits of ice crystals appeared with both basal and prism faces in contact with the substrate as shown in Fig. 14. The atomic configurations for both orientations are shown in Fig. 15. At temperatures above —7°C the deposit consists entirely of water droplets, among which an occasional ice crystal may appear at temperatures between —7 and —10°C. As the temperature falls below —10°C the number of crystals rapidly increases with no visible liquid deposit. While at higher temperatures the crystals lie preferentially on their prism faces, the other orientation becomes more frequent at lower temperatures and is equally prominent below —20°C. The misfits shown in Table 1 suggest that, of the two orientations, that involving the prism face will be slightly favoured.

VOL. 12 59/60

(f) *On other substances*

Orientation of ice crystals has also been observed on the (0001) face of brucite, the (010) face of mercuric iodide, the rhombohedral faces of calcite and the (001) face of muscovite, which must be freshly cleaved to avoid deterioration of the surface by the rapid adsorption of impurities.

4. THE ROLE OF SUPERSATURATION

In all the preliminary experiments it was evident that the supersaturation of the water vapour, as well as the temperature, influenced the nucleation and growth of the ice deposit. To investigate this in more detail, careful measurements were made, as a function of temperature, of the minimum supersaturations required to produce oriented ice crystals. The supersaturation was calculated from the measured temperatures as described in Section 2. The temperatures were determined to within $\pm 0{\cdot}1$°C, the corresponding error in supersaturation being ± 1 per cent.

The results for silver iodide are shown in Fig. 16. At temperatures above —4°C only water droplets appeared. As the temperature was lowered from —4 to —12°C, increasing numbers of ice crystals formed on selected sites, provided that the air surpassed saturation relative to liquid water. At temperatures below —12°C, however, crystals appeared when the air was subsaturated relative to water but supersaturated with respect to ice by at least 12 per cent. These observations suggest that, at temperatures between —4 and —12°C, the initial deposit may have been liquid water, perhaps in droplets too small to be seen before they froze, while at temperatures below —12°C crystals may appear by sublimation direct from the vapour phase.

A similar behaviour has been observed for an aerosol of silver iodide introduced into a cloud chamber.[4] Similar results were obtained for cupric sulphide and lead iodide with critical supersaturations of 13 and 15 per cent at —13 and —15°C, respectively.

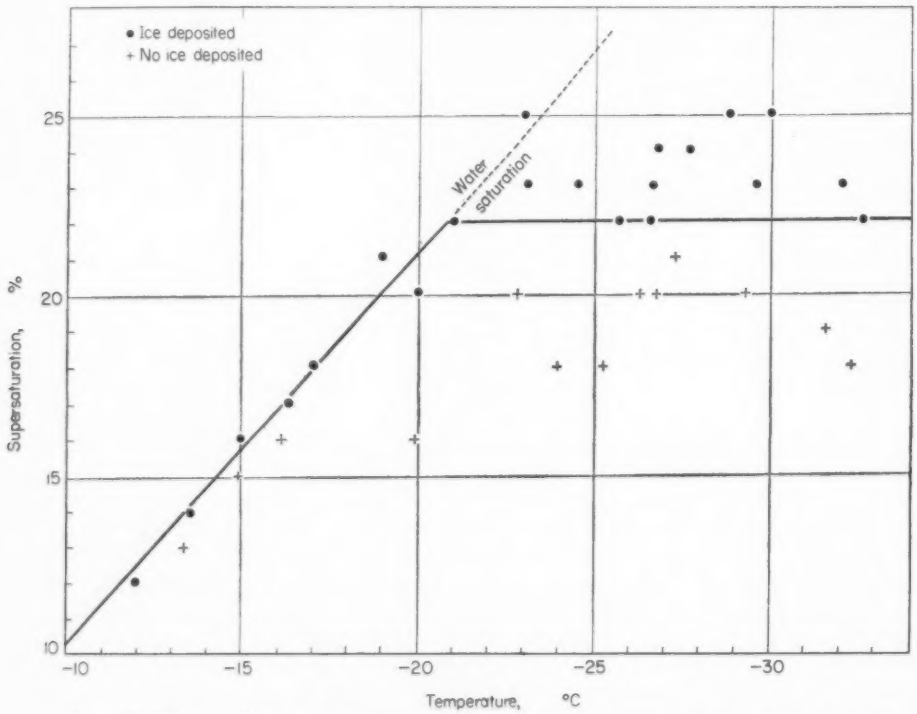

FIG. 17. The conditions of temperature and supersaturation at which oriented ice crystals appeared at steps on the basal plane of a cadmium iodide crystal.

The behaviour of cadmium iodide was notable in that, at temperatures between −12 and −21°C, the initial deposit was in the form of *visible* droplets which subsequently froze into irregular crystals. Only at temperatures below −21°C, with the air supersaturated relative to ice by at least 22 per cent (see Fig. 17), did regular oriented ice crystals appear.

In all cases except silver iodide, on which steps were probably present though not visible, the supersaturations of 10–20 per cent were those required to produce ice crystals at the edges of large visible steps; nucleation on the flat areas of the substrate occurred only at much higher supersaturations which could not be accurately determined but certainly exceeded 100 per cent.

VOL. 12 59/60

5. CONCLUDING REMARKS

Oriented ice crystals deposited from a supersaturated vapour have been observed on the faces of a number of crystals (not necessarily hexagonal) in which the atomic arrangement is similar to that of ice. The nucleating ability of the substrate cannot, however, be completely specified by the degree of misfit, but may be characterized either by the highest temperatures at which it nucleates water droplets or by the minimum supersaturation required for ice crystals to appear direct from the vapour at preferred sites, such as steps. Of course, either the minimum degree of supercooling or the minimum supersaturation, depending upon the operative mechanism, enters explicitly into the expression for the radius of the critical nucleus.

Acknowledgements.—This work was carried out with the aid of grants from The Rockefeller Foundation and the Department of Scientific and Industrial Research, whose generous support is gratefully acknowledged.

The authors also wish to express their gratitude to Dr. M. BLACKMAN and Dr. N. D. LISGARTEN of the Physics Department, Imperial College, for putting their silver-evaporating plant at their disposal.

REFERENCES

1. MASON B. J. and HALLETT J., *Nature, Lond.* **177,** 681 (1956).
2. MASON B. J. and HALLETT J., *Nature, Lond.* **179,** 357 (1957).
3. MASON B. J. and MAYBANK J., *Quart. J. Roy. Met. Soc.* **84,** 235 (1958).
4. MASON B. J. and VAN DEN HEUVEL A., To be published.
5. MONTMORY R., *Bull. Obs. Puy-de-Dôme* **4,** 126 (1956).
6. JAFFRAY J. and MONTMORY R., *C.R. Acad. Sci. (Paris)* **243,** 126, 891 (1956).
7. JAFFRAY J. and MONTMORY R., *C.R. Acad. Sci. (Paris)* **244,** 859 (1957); **245,** 2221 (1957).
8. MASON B. J., *Advances in Phys.* **7,** 221 (1958).
9. KLEBER W. and WEIS J., *Z. Krist.* **110,** 1 (1958).
10. SHAW D. and MASON B. J., *Phil. Mag.* **46,** 249 (1955).
11. NEWMAN R. C. and PASHLEY D. W., *Phil. Mag.* **46,** 927 (1955).
12. HALLETT J. and MASON B. J., *Proc. Roy. Soc.* A**247,** 440 (1958).

J. Phys. Chem. Solids Pergamon Press 1959. Vol. 12. pp. 196–205. Printed in Great Britain.

THE SHIELDING OF A FIXED CHARGE IN A HIGH-DENSITY ELECTRON GAS*

J. S. LANGER and S. H. VOSKO

Carnegie Institute of Technology, Pittsburgh, Pennsylvania

(*Received* 18 *May* 1959)

Abstract—The shielding of a small fixed charge in a high-density electron gas is calculated by means of a technique similar to that used by GELL-MANN and BRUECKNER for calculating the correlation energy. A closed expression for the density of displaced electrons is derived and evaluated numerically for several densities of the electron gas. An asymptotic form is also given.

1. INTRODUCTION

THERE are many problems involving impurities in metals which cannot be understood without including the Coulomb interaction between electrons. FRIEDEL[1,2] and others have introduced various approximate procedures to account for this interaction. For example, FRIEDEL has been quite successful in accounting for the impurity–impurity interactions in alloys and positron lifetimes in metals. The above procedures do not attempt to solve the quantum-mechanical many-body problem, but instead introduce physically reasonable approximations in a self-consistent manner. In this paper we shall derive the shielding of a fixed charge by a systematic application of many-body perturbation theory.

The model with which we shall be concerned is a quantum-mechanical electron gas in its ground state with a uniform positively charged background, so that the whole system is neutral. Into this system we insert a fixed charge. Due to the electric field of this charge, the electrons redistribute themselves so as to shield the charge at large distances. The main physical requirement that must be satisfied is that the charge be completely shielded. For perfect shielding, we require that the potential produced by the fixed charge falls off more rapidly than $1/R$ for large R, where R is the distance from the charge. By application of GAUSS's law we see that this is satisfied when the total displaced electron charge is equal in magnitude to the point charge.

Previous calculations of the potential and charge distribution of the displaced electrons have been in the spirit of the Thomas–Fermi approximation (see, for example, FRIEDEL[1]). Although these calculations satisfy the above requirements, it is not clear to what extent they include the correlations between electrons due to their mutual Coulomb repulsion. Our approach is to apply the many-body perturbation theory recently developed by GELL-MANN and BRUECKNER[3], GOLDSTONE[4] and HUBBARD[5].† In particular we use their techniques to calculate the potential energy of a classical test charge (which can be considered infinitesimally small) as a function of its distance from the fixed charge. Then, by means of Poisson's equation, the displaced charge distribution is calculated.

In Section 2 the formal theory is developed for an arbitrary charge distribution. The calculation to first order in the external charge is carried out in Section 3. Numerical results and a comparison with the Thomas–Fermi type of calculation are given in Section 4. In Section 5 the charge displaced due to interactions with neutral impurities and nuclear magnetic moments is discussed.

* Supported in part by the Office of Naval Research.

† The three papers by HUBBARD given under reference (5) will be referred to as H-I, H-II and H-III, respectively.

VOL. 12 59/60

2. THE EFFECTIVE POTENTIAL FROM A PERTURBATION SERIES

Following H–I, we write the Hamiltonian for the system

$$\mathscr{H} = H_0+H'+H_1+H_2+H_3 \tag{1}$$

where H_0 includes the kinetic energy of the electrons and their potential energy in the external field due to the uniform positive background; H' is the interaction between the electrons; H_1 is the interaction of the electrons with the inserted charge under investigation; H_2 is the interaction of the electrons with the test charge; H_3 is the direct interaction between the inserted charge and the test charge. All terms except H_0 will be treated as perturbations.

In the notation of field theory the perturbation terms may be written:

$$H' = +\tfrac{1}{2}e^2 \int \bar{\psi}(\boldsymbol{x}')\psi(\boldsymbol{x}')v(\boldsymbol{x}-\boldsymbol{x}')\bar{\psi}(\boldsymbol{x})\psi(\boldsymbol{x})\,d\boldsymbol{x}\,d\boldsymbol{x}' - \\ -\tfrac{1}{2}Ne^2v(0) \tag{2}$$

where N is the number of electrons in the system, $\bar{\psi}(\boldsymbol{x})$, $\psi(\boldsymbol{x})$ are the electron field operators, and $v(\boldsymbol{x}-\boldsymbol{x}')$ is the spatial dependence of the interaction. Note that the charge e has been written explicitly.

$$H_1 = -ee_1 \int \bar{\psi}(\boldsymbol{x}')\psi(\boldsymbol{x}')v(\boldsymbol{x}-\boldsymbol{x}')\rho_1(\boldsymbol{x})\,d\boldsymbol{x}\,d\boldsymbol{x}' \tag{3}$$

where e_1 is the total charge inserted. For a point charge ρ_1 is a delta function.

$$H_2 = -ee_2 \int \bar{\psi}(\boldsymbol{x}')\psi(\boldsymbol{x}')v(\boldsymbol{x}-\boldsymbol{x}')\rho_2(\boldsymbol{x})\,d\boldsymbol{x}\,d\boldsymbol{x}' \tag{4}$$

where e_2 is the test charge, and

$$\rho_2(\boldsymbol{x}) = \delta(\boldsymbol{x}-\boldsymbol{R}) \tag{5}$$

with the test charge at $\boldsymbol{R}$. The direct interaction between e_1 and e_2 is

$$H_3 = e_1e_2 \int \rho_1(\boldsymbol{x})v(\boldsymbol{x}-\boldsymbol{x}')\rho_2(\boldsymbol{x}')\,d\boldsymbol{x}\,d\boldsymbol{x}'. \tag{6}$$

The total energy of the system can be written as a sum of four terms

$$E = E_0+e_1e\phi'+e_2e\phi'+e_1e_2\phi_{12}.$$

E_0 is the total energy of electrons in the uniform positive background. It includes the usual correlation energy. $e_1e\phi'(e_1)$ and $e_2e\phi'(e_2)$ are the energy shifts due to the interaction of the electrons with the individual inserted charges by themselves. $e_1e_2\phi_{12}(e_1, e_2, R)$ is the remaining energy. It may be thought of as an effective screened interaction between the inserted charges; that is, it includes the direct interaction between e_1 and e_2 modified by the polarization of the electron distribution.

In the limit of vanishingly small test charge e_2, ϕ_{12} tends to a function which we shall denote by $\phi(e_1, R)$. Formally, ϕ may be obtained from the perturbation series for the total energy by summing those terms which contain H_2 and H_3 only once. Then from Poisson's equation we have:

$$\nabla_R{}^2\phi(e_1, \boldsymbol{R}) = -4\pi\left[\rho_1(\boldsymbol{R}) - \frac{e}{e_1}\Delta n(\boldsymbol{R})\right] \tag{7}$$

where ρ_1 was defined previously and $(-e\Delta n)$ is the charge density due to the displaced electrons. (Note that the charge of an electron is taken to be $-e$.) Equation (7) may then be solved for $\Delta n(R)$.

The total energy shift of the system can be expressed in terms of $S_\alpha(t)$ (see H–I), which is a solution of the integral equation

$$S_\alpha(t) = 1+\frac{1}{i\hbar}\int_{-\infty}^{t} H_\alpha(t')S_\alpha(t')\,dt' \tag{8}$$

where

$$H_\alpha(t) = \exp\left[\frac{it}{\hbar}H_0\right]\{H'+H_1+H_2+H_3\}\times \\ \times \exp\left[\frac{-it}{\hbar}H_0\right]\cdot\exp[-\alpha|t|] \tag{9}$$

where $\alpha \to +0$. The series solution of (8) is:

$$S_\alpha(t) = 1+\sum_{n=1}^{\infty}\frac{1}{n!}\left(\frac{1}{i\hbar}\right)^n\int_{-\infty}^{t}dt_1\int_{-\infty}^{t}dt_2\ldots\times \\ \times\int_{-\infty}^{t}dt_n\times P[H_\alpha(t_1)H_\alpha(t_2)\ldots H_\alpha(t_n)] \tag{10}$$

where P is the chronological ordering operator. This power series has been analyzed in terms of Ferynman graphs by HUBBARD[5]. It should be noted that each graph is representative of all graphs of the same topology, regardless of the time order of the interactions. The energy shift is obtained by including all linked vacuum to vacuum diagrams contributing to $S_\alpha(\infty)$ and inserting a

factor $i\hbar\delta(t_1)$ in the integrand with $\alpha = 0$. In particular to determine $e_1e_2\phi(e_1, R)$ we must add all linked diagrams which include H_2 only once and

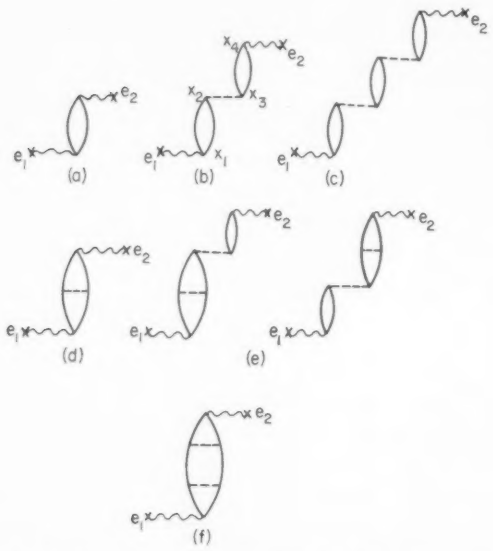

FIG. 1. These graphs correspond to a single interaction (wavy lines) with the perturbing interactions H_1 and H_2.

H_1 *at least* once. Examples of diagrams which contribute to the first power in e_1 are shown in Fig. 1. An example of a diagram which contributes to the

FIG. 2. An example of the inserted charge acting twice.

second power in e_1 is shown in Fig. 2. In particular the part of equation (10) which contributes to $\phi(e_1, R)$ is

$$\sum_{n=2}^{\infty}\frac{1}{n!}\left(\frac{1}{i\hbar}\right)^n\int_{-\infty}^{t}dt_1\int_{-\infty}^{t}dt_2\int_{-\infty}^{t}dt_3\ldots\int_{-\infty}^{t}dt_n\times\sum_{m=2}^{n}\frac{n!}{(n-m)!(m-1)!}\times$$
$$\times P[H_{2\alpha}(t_1)H_{1\alpha}(t_2)\ldots H_{1\alpha}(t_m)H_\alpha'(t_{m+1})H\ldots H_\alpha'(t_n)]. \tag{11}$$

The graphs in Fig. 1 are part of the subset for $m = 2$, while Fig. 2 is one of the graphs for $m = 3$.

3. ELECTRON DISTRIBUTION TO FIRST ORDER IN EXTERNAL CHARGE

We will first consider graphs of the form 1(a), (b), (c) which will be referred to as bubble graphs. GELL-MANN and BRUECKNER[3] have shown that in the limit of very high electron density, it is just this subseries of graphs which gives the leading contribution to the correlation energy. Our calculation is exactly analogous to theirs. For convenience we write H_1 and H_2 in the form

$$H_1 = \frac{-4\pi ee_1}{(2\pi)^3}\int d\boldsymbol{x}'\bar{\psi}(\boldsymbol{x}')\psi(\boldsymbol{x}')\times$$
$$\times\left\{\int d\boldsymbol{x}\rho_1(\boldsymbol{x})\cdot\int\frac{d\boldsymbol{q}}{q^2}e^{i\boldsymbol{q}(\boldsymbol{x}-\boldsymbol{x}')}\right\} = -\frac{4\pi ee_1}{(2\pi)^3}\times$$
$$\times\int d\boldsymbol{x}'\bar{\psi}(\boldsymbol{x}')\psi(\boldsymbol{x}')\left\{\int\frac{d\boldsymbol{q}}{q^2}e^{-i\boldsymbol{q}\cdot\boldsymbol{x}'}\rho_1(\boldsymbol{q})\right\} \tag{12}$$

where

$$\rho_1(\boldsymbol{q}) = \int d\boldsymbol{x}\rho_1(\boldsymbol{x})e^{i\boldsymbol{q}\cdot\boldsymbol{x}} \tag{13}$$

$$H_2 = -\frac{4\pi ee_2}{(2\pi)^3}\int d\boldsymbol{x}'\bar{\psi}(\boldsymbol{x}')\psi(\boldsymbol{x}')\int\frac{d\boldsymbol{q}}{q^2}e^{i\boldsymbol{q}\cdot(\boldsymbol{x}'-\boldsymbol{R})}. \tag{14}$$

Now the energy shift corresponding to Fig. 1(a) is

$$\left(\frac{1}{i\hbar}\right)^2\frac{(-1)^1}{2!}2\int dx_1\int dx_2 i\hbar\delta(t_2)S(x_2,x_1)S(x_1,x_2)\times$$
$$\times\left\{-\frac{4\pi ee_1}{(2\pi)^3}\int\frac{d\boldsymbol{q}_1}{q_1^2}e^{-i\boldsymbol{q}_1\cdot\boldsymbol{x}_1}\rho_1(\boldsymbol{q}_1)\right\}\times$$
$$\times\left\{-\frac{4\pi ee_2}{(2\pi)^3}\int\frac{d\boldsymbol{q}_2}{q_2^2}e^{i\boldsymbol{q}_2\cdot(\boldsymbol{x}_2-\boldsymbol{R})}\right\} \tag{15}$$

where $dx \equiv d\boldsymbol{x}\,dt$ and $S(x_1, x_2)$ is the propagator for an electron as defined in H–I. Noting that $S(x_1, x_2)$ is a function of $|x_1-x_2|$ only, we write

$$\frac{-1}{i\hbar}S(x_2, x_1)S(x_1, x_2) = \frac{1}{(2\pi)^4}\int d\boldsymbol{k}\int d\omega \bar{W}_B(\boldsymbol{k}, \omega)e^{i(\boldsymbol{k}\cdot\boldsymbol{x}_{12}-\omega t_{12})}. \tag{16}$$

Substituting (16) in (15) and carrying out integrations, we get:

$$\frac{1}{(2\pi)^3}\int d\boldsymbol{k}\int d\omega\delta(\omega)\frac{4\pi e_1e_2}{k^2}\frac{4\pi e^2}{k^2}e^{i\boldsymbol{k}\cdot\boldsymbol{R}}\rho_1(\boldsymbol{k})\bar{W}_B(\boldsymbol{k}, \omega) = \frac{1}{(2\pi)^3}\int d\boldsymbol{k}\left(\frac{4\pi e_1e_2}{k^2}\right)\left(\frac{4\pi e^2}{k^2}\right)e^{i\boldsymbol{k}\cdot\boldsymbol{R}}\rho_1(\boldsymbol{k})\bar{W}_B(\boldsymbol{k}, 0). \tag{17}$$

The result (17) is strongly divergent at $k = 0$. However, when all contributions are summed, this divergence disappears, as in GELL-MANN and BRUECKNER[3]. The energy corresponding to Fig. 1(b) can be analyzed in the same way and gives

$$\frac{1}{(2\pi)^3}\int d\boldsymbol{k}\left(\frac{4\pi e_1e_2}{k^2}\right)\left(\frac{4\pi e^2}{k^2}\right)[\bar{W}_B(k, 0)]^2\rho_1(\boldsymbol{k})e^{i\boldsymbol{k}\cdot\boldsymbol{R}}. \tag{18}$$

That is, each bubble contributes a factor $(4\pi e^2/k^2)\bar{W}_B(\boldsymbol{k}, 0)$. Recalling that the contribution of H_3 is

$$\frac{1}{(2\pi)^3}\int d\boldsymbol{k}\left(\frac{4\pi e_1e_2}{k^2}\right)\rho_1(\boldsymbol{k})e^{i\boldsymbol{k}\cdot\boldsymbol{R}}, \tag{19}$$

the series may be summed in an obvious manner, yielding

$$\frac{1}{(2\pi)^3}\int d\boldsymbol{k}\rho_1(k)e^{i\boldsymbol{k}\cdot\boldsymbol{R}}\frac{4\pi e_1e_2}{k^2-4\pi e^2\bar{W}_B(\boldsymbol{k}, 0)}. \tag{20}$$

The evaluation of the function $\bar{W}_B(\boldsymbol{k}, 0)$ is straightforward and yields

$$4\pi e^2\bar{W}_B(\boldsymbol{k}, 0) = -\frac{2}{\pi}\frac{k_F}{a_0}\left[1+\frac{1}{kk_F}\left(k_F^2-\frac{k^2}{4}\right)\ln\left|\frac{k+2k_F}{k-2k_F}\right|\right] \tag{21}$$

where a_0 is the Bohr radius and $(\hbar k_F)$ is the Fermi momentum for the electron gas. One may note that equation (20) is very similar to the Thomas–Fermi potential,[1] which is

$$\frac{1}{(2\pi)^3}\int d\boldsymbol{k}e^{i\boldsymbol{k}\cdot\boldsymbol{R}}\frac{4\pi e_1e_2}{k^2+\frac{4}{\pi}\frac{k_F}{a_0}} \tag{22}$$

for a point charge located at the origin. The screening constant in equations (22) just corresponds to the limit of equation (21) as $\boldsymbol{k}$ goes to zero, as one might expect.

The contributions of Fig. 1(d) can be treated in the same way as Fig. 1(a), except that the closed loop part requires a new function. Define the transform of the closed loop part by

$$\frac{1}{(2\pi)^4}\int d\boldsymbol{k}\int d\omega\bar{W}_{\mathrm{Ex}}(\boldsymbol{k}, \omega)e^{i(\boldsymbol{k}\cdot\boldsymbol{x}_{21}-\omega t_{21})}. \tag{23}$$

This is referred to as the exchange graph. The result of inserting this closed loop in all possible ways, for example as in Fig. 1(e), results in an energy shift

$$\frac{1}{(2\pi)^3}\int d\boldsymbol{k}\int d\omega\delta(\omega)\times \times\frac{4\pi e_1e_2}{k^2-4\pi e^2\{\bar{W}_B+\bar{W}_{\mathrm{Ex}}\}}\rho_1(k)e^{i\boldsymbol{k}\cdot\boldsymbol{R}}. \tag{24}$$

This is identical to the effective potential of HUBBARD, except that we are concerned with the static part (i.e. the delta function of ω). HUBBARD has approximated the sum of all the closed loops of the form 1(a), (d), (f), etc. by the expression

$$\bar{W}_B(\boldsymbol{k}, \omega)+\bar{W}_{\mathrm{Ex}}(\boldsymbol{k}, \omega)+\ldots \approx \frac{\bar{W}_B(\boldsymbol{k}, \omega)}{1+\frac{1}{2}\frac{1}{k^2+k_F^2}\bar{W}_B(\boldsymbol{k}, \omega)} \tag{25}$$

VOL. 12 59/60

which we shall refer to as $\bar{W}_H(\boldsymbol{k}, \omega)$. He has used equation (25) to calculate the correlation energy in H–II. To summarize, we note that $\phi(e_1, \boldsymbol{R})$ is

$$\phi(e_1, \boldsymbol{R}) = \frac{1}{(2\pi)^3}\int d\boldsymbol{k}\rho_1(\boldsymbol{k})e^{i\boldsymbol{k}\cdot\boldsymbol{R}}\frac{4\pi}{k^2-4\pi e^2\bar{W}(\boldsymbol{k}, 0)} \quad (26)$$

where $\bar{W}(k, 0)$ is either $\bar{W}_B(\boldsymbol{k}, 0)$ when only including bubble graphs, and $\bar{W}_H(\boldsymbol{k}, 0)$ when using the HUBBARD approximation for the sum of the various closed loops.

By use of equations (7), (13) and (26) we have:

$$\Delta n(\boldsymbol{R}) = \left(\frac{e_1}{e}\right)\frac{1}{(2\pi)^3}\int d\boldsymbol{k}\rho_1(\boldsymbol{k})\times \times\left[1-\frac{k^2}{k^2-4\pi e^2\bar{W}(\boldsymbol{k}, 0)}\right]e^{i\boldsymbol{k}\cdot\boldsymbol{R}}. \quad (27)$$

If we take e_1 to be a unit positive charge, $\rho_1(\boldsymbol{k})$ becomes unity and Δn becomes

$$\Delta n(\boldsymbol{R}) = \frac{1}{(2\pi)^3}\int d\boldsymbol{k}\left[\frac{-4\pi e^2\bar{W}(\boldsymbol{k}, 0)}{k^2-4\pi e^2\bar{W}(\boldsymbol{k}, 0)}\right]e^{i\boldsymbol{k}\cdot\boldsymbol{R}} = \frac{1}{2\pi^2}\int_0^\infty dk\frac{k\sin kR}{R}\left[\frac{-4\pi e^2\bar{W}(k, 0)}{k^2-4\pi e^2\bar{W}(k, 0)}\right]. \quad (28)$$

For convenience we shall measure k in units of k_F, R in $1/k_F$ and Δn in $(k_F)^3$. Then introducing the density via

$$n_0 = \frac{1}{\frac{4\pi}{3}r_s^3 a_0^3}$$

we can write

$$-4\pi e^2\bar{W}_B(k, 0) = \xi\left[1+\frac{1}{k}\left(1-\frac{k^2}{4}\right)\ln\left|\frac{k+2}{k-2}\right|\right] \quad (29)$$

where $\xi = 0{\cdot}3317 r_s$. The charge distributions for the two cases are

$$\Delta n_B(R) = \frac{1}{2\pi^2}\int_0^\infty dk\frac{k\sin kR}{R}\times \times\left[\frac{\xi\left[1+\frac{1}{k}\left(1-\frac{k^2}{4}\right)\ln\left|\frac{k+2}{k-2}\right|\right]}{k^2+\xi\left[1+\frac{1}{k}\left(1-\frac{k^2}{4}\right)\ln\left|\frac{k+2}{k-2}\right|\right]}\right] \quad (30)$$

and

$$\Delta n_H(R) = \frac{1}{2\pi^2}\int_0^\infty dk\frac{k\sin kR}{R}\times\left[\frac{\xi\left[1+\frac{1}{k}\left(1-\frac{k^2}{4}\right)\ln\left|\frac{k+2}{k-2}\right|\right]}{k^2+\left[1+\frac{1}{1+k^2}\right]\xi\left[1+\frac{1}{k}\left(1-\frac{k^2}{4}\right)\ln\left|\frac{k+2}{k-2}\right|\right]}\right]. \quad (31)$$

The first significant improvement over the Thomas–Fermi calculation is that the electron charge density at $R = 0$ is finite in this calculation, while it goes like $1/R$ as $R \to 0$ in the Thomas–Fermi case. This can be seen immediately by setting $R = 0$ in equation (30) and looking at the contribution from large values of k. For large k

$$\xi\left[1+\frac{1}{k}\left(1-\frac{k^2}{4}\right)\ln\left|\frac{k+2}{k-2}\right|\right] \approx \frac{8}{3}\xi\frac{1}{k^2}\left[1+\frac{4}{5k^2}\ldots\right] \quad (32)$$

while in the Thomas–Fermi calculation this quantity is a constant equal to 2ξ.

Equation (30) cannot be integrated analytically, but the asymptotic form can be obtained by considering the singularity of the integrand at $k = 2$. If we expand the integrand of Fourier transform

about $k = 2$ the first few terms are:

$$g_1(\xi, R)(k-2)\ln|k-2| + g_2(\xi, R)(k-2)^2(\ln|k-2|)^2 \quad (33)$$

which are of the form considered by LIGHTHILL[6]. The result is

$$\Delta n_B \text{ (for large } R) \approx \frac{-2\xi}{\pi(4+\xi)^2}\frac{\cos 2E}{R^3} + \frac{4\xi^2}{\pi(4+\xi)^3}\frac{\sin 2R}{R^4}\{\ln R + \gamma - \tfrac{3}{2}\} \quad (34)$$

where γ is Euler's constant, 0·5772.

A significant difference between the Thomas–Fermi calculation and the results obtained here may be seen by examining equation (34). In the Thomas–Fermi calculation the displaced charge density and the field gradients due to the inserted charge fall off like $\exp[-\sqrt{(2\xi)}R]/R$ for large R. On the other hand we see from equation (34) that the displaced charge density and field gradients really fall off like $1/R^3$ for large R. This difference has important consequences in nuclear magnetic resonance experiments. Previously it was believed that the Thomas–Fermi model was applicable and

Table 1. Δn, *the displaced electron density for* $r_s = 1{\cdot}5$

R $(1/k_F)$	Δn_B $(k_F)^3$	Δn_H $(k_F)^3$	Δn_{T-F} $(k_F)^3$
0	0·07438	0·07857	
0·1	0·06907	0·07325	0·7171
0·4	0·05436	0·05834	0·1328
0·7	0·04131	0·04487	0·05627
1·0	0·03019	0·03320	0·02920
1·3	0·02111	0·02350	0·01665
1·6	0·01404	0·01581	0·01003
1·9	0·008798	0·01002	0·006263
2·2	0·005151	0·005904	0·004010
2·5	0·002794	0·003191	0·002616
2·8	0·001413	0·001560	
3·1	0·0007074	0·0006984	
3·4	0·0004200	0·0003279	
3·7	0·0003488	0·0002246	
4·0	0·0003544	0·0002292	
4·3	0·0003559	0·0002445	
4·6	0·0003201	0·0002265	
4·9	0·0002471	0·0001693	
5·2	0·0001550	0·00008900	
5·5	0·00006654	0·000008925	
5·8	0·0000001087	−0·00005109	
6·1	−0·00003538	−0·00008055	
6·4	−0·00004111	−0·00007962	
6·7	−0·00002571	−0·00005677	
7·0	−0·000001030	−0·00002440	
7·3	0·00002171	0·000005444	
7·6	0·00003476	0·00002428	
7·9	0·00003534	0·00002889	
8·2	0·00002549	0·00002128	
8·5	0·00001023	0·000006839	
8·8	−0·000004815	−0·000008222	
9·1	−0·00001518	−0·00001880	
9·4	−0·00001848	−0·00002207	
9·7	−0·00001486	−0·00007968	
10·0	−0·000006805	−0·000009017	
10·3	0·000002162	0·000001048	

Table 2. Δn, *the displaced electron density for* $r_s = 3{\cdot}0$

R $(1/k_F)$	Δn_B $(k_F)^3$	Δn_H $(k_F)^3$	Δn_{T-F} $(k_F)^3$
0	0·1276	0·1375	
0·1	0·1170	0·1269	1·3755
0·4	0·08847	0·09778	0·2242
0·7	0·06418	0·07233	0·08391
1·0	0·04441	0·05104	0·03847
1·3	0·02904	0·03402	0·01950
1·6	0·01767	0·02108	0·01031
1·9	0·009758	0·01181	0·005688
2·2	0·004651	0·005640	0·003217
2·5	0·001680	0·001925	0·001854
2·8	0·0002138	0·000007876	
3·1	−0·0002945	−0·0007160	
3·4	−0·0002822	−0·0007523	
3·7	−0·00006459	−0·0004840	
4·0	0·0001595	−0·0001654	
4·3	0·0002922	0·00006543	
4·6	0·0003107	0·0001630	
4·9	0·0002395	0·0001439	
5·2	0·0001235	0·00005579	
5·5	0·000008250	−0·00004806	
5·8	−0·00007332	−0·0001259	
6·1	−0·0001070	−0·0001565	
6·4	−0·00009655	−0·0001395	
6·7	−0·00005729	−0·00008974	
7·0	−0·000008618	−0·00002840	
7·3	0·00003210	0·00002434	
7·6	0·00005366	0·00005495	
7·9	0·00005326	0·00005932	
8·2	0·00003585	0·00004239	
8·5	0·00001065	0·00001453	
8·8	−0·00001301	−0·00001311	
9·1	−0·00002826	−0·00003180	
9·4	−0·00003167	−0·00003702	
9·7	−0·00003976	−0·00009148	
10·0	−0·000009703	−0·00001305	
10·3	0·000005129	0·000004431	

that only nearest-neighbor nuclei are appreciably affected by the impurity charge. On the contrary if field gradients are calculated by (34) it is found that fifth and sixth nearest neighbors may be affected. Recently T. J. ROWLAND* has performed experiments where the effect of impurities on the Knight shift in copper is measured. ROWLAND's results are essentially in agreement with equation (34).

Table 3. Δn, *the displaced electron density for* $r_s = 4{\cdot}5$

R $(1/k_F)$	Δn_B $(k_F)^3$	Δn_H $(k_F)^3$	Δn_{T-F} $(k_F)^3$
0	0·1731	0·1887	
0·1	0·1573	0·1729	1·9989
0·4	0·1154	0·1300	0·2976
0·7	0·08089	0·09345	0·1013
1·0	0·05374	0·06368	0·04221
1·3	0·03340	0·04058	0·01934
1·6	0·01899	0·02359	0·009355
1·9	0·009430	0·01191	0·004691
2·2	0·003632	0·004526	0·002413
2·5	0·0005518	0·0004151	0·001264
2·8	−0·0007241	−0·001409	
3·1	−0·0009353	−0·001801	
3·4	−0·0006352	−0·001445	
3·7	−0·0001987	−0·0008323	
4·0	0·0001578	−0·0002683	
4·3	0·0003462	0·0001005	
4·6	0·0003669	0·0002466	
4·9	0·0002698	0·0002171	
5·2	0·0001206	0·00009084	
5·5	−0·00002046	−0·00005328	
5·8	−0·0001135	−0·0001578	
6·1	−0·0001443	−0·0001959	
6·4	−0·0001213	−0·0001700	
6·7	−0·00006599	−0·0001021	
7·0	−0·000003114	−0·00002132	
7·3	0·00004656	0·00004564	
7·6	0·00007029	0·00008170	
7·9	0·00006608	0·00008263	
8·2	0·00004163	0·00005628	
8·5	0·000009221	0·00001715	
8·8	−0·00001971	−0·00001995	
9·1	−0·00003727	−0·00004399	
9·4	−0·00003978	−0·00004954	
9·7	−0·00002863	−0·00003770	
10·0	−0·000009969	−0·00001547	
10·3	0·000008411	0·000007794	

* Private communication.

4. NUMERICAL RESULTS

The evaluation of equations (30) and (31) was carried out numerically. The range of integration was broken up into two regions, 0 to 5 and 5 to ∞.

Table 4. Δn, *the displaced electron density for* $r_s = 6{\cdot}0$

R $(1/k_F)$	Δn_B $(k_F)^3$	Δn_H $(k_F)^3$	Δn_{T-F} $(k_F)^3$
0	0·2141	0·2354	
0·1	0·1931	0·2142	2·2595
0·4	0·1384	0·1580	0·3565
0·7	0·09421	0·1109	0·1120
1·0	0·06050	0·07340	0·04308
1·3	0·03605	0·04505	0·01821
1·6	0·01932	0·02480	0·008132
1·9	0·002588	0·01134	0·003764
2·2	0·002588	0·003221	0·001787
2·5	−0·0003867	−0·0009831	0·000002946
2·8	−0·001394	−0·002559	
3·1	−0·001319	−0·002579	
3·4	−0·0007893	−0·001862	
3·7	−0·0002061	−0·0009710	
4·0	0·0002190	−0·0002354	
4·3	0·0004185	0·0002083	
4·6	0·00004184	0·0003593	
4·9	0·0002896	0·0002956	
5·2	0·0001121	0·0001232	
5·5	−0·00004634	−0·00006016	
5·8	−0·0001437	−0·00001869	
6·1	−0·0001682	−0·0002288	
6·4	−0·0001337	−0·0001933	
6·7	−0·00006674	−0·0001095	
7·0	0·000004876	−0·00001334	
7·3	0·00005883	0·00006381	
7·6	0·00008201	0·0001025	
7·9	0·00007353	0·00009925	
8·2	0·00004347	0·00006461	
8·5	0·000006362	0·00001663	
8·8	−0·00002535	−0·00002723	
9·1	−0·00004358	−0·00005450	
9·4	−0·00004475	−0·00005937	
9·7	−0·00003077	−0·00004370	
10·0	−0·000009048	−0·00001635	
10·3	0·00001137	0·00001128	

For the first region Filon's method was used with a Δk of 0·05. For the second region the integrand was approximated by the first two terms of (32) and treated analytically. The results for various values of r_s are given in the Tables 1–4 and Figs. 3–6 and compared with the Thomas–Fermi calculation.

VOL. 12 59/60

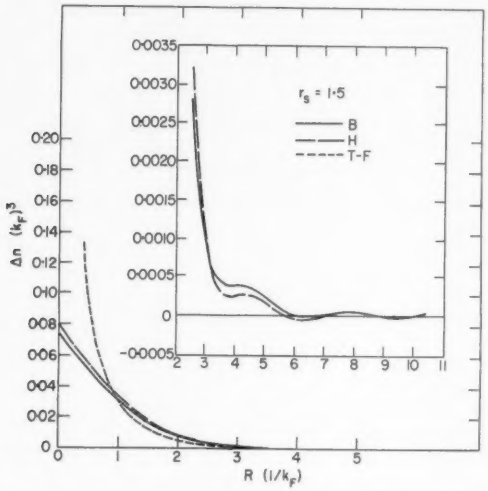

FIG. 3. The displaced electron density for $r_s = 1{\cdot}5$ vs. the distance from the inserted charge.

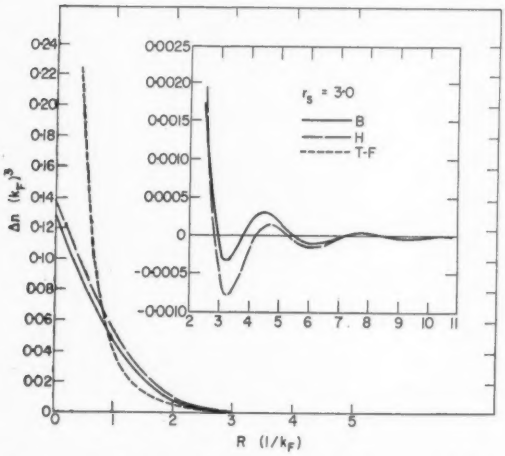

FIG. 4. The displaced electron density for $r_s = 3{\cdot}0$ vs. the distance from the inserted charge.

5. REMARKS ON NEUTRAL IMPURITIES AND NUCLEAR SPINS

The above techniques are also applicable to obtaining the charge displaced due to the electrons interacting with a neutral impurity. A particularly simple example is a short-range interaction between the impurity and the electrons, which can be represented by a square well of depth $(-V_0)$ and width a. The calculation is the same as given

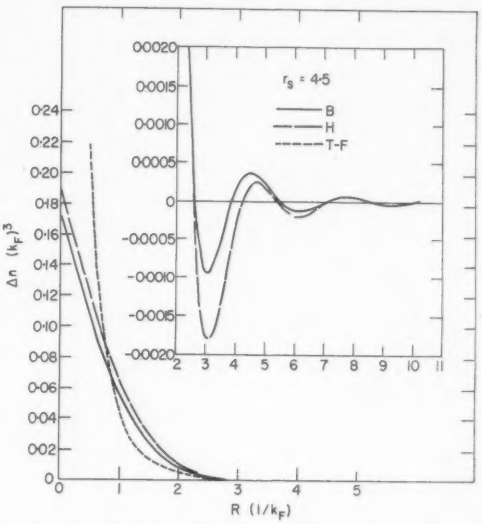

FIG. 5. The displaced electron density for $r_s = 4{\cdot}5$ vs. the distance from the inserted charge.

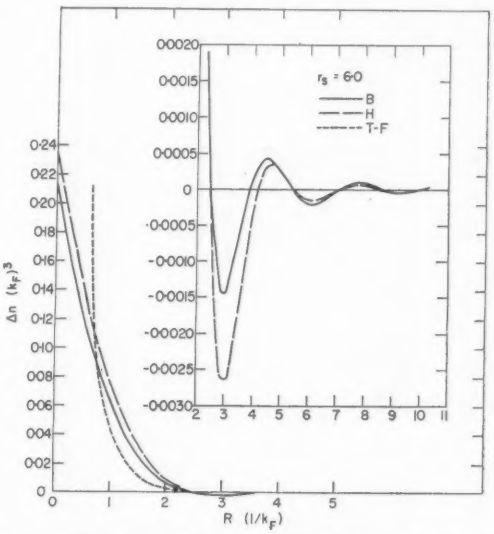

FIG. 6. The displaced electron density for $r_s = 6{\cdot}0$ vs. the distance from the inserted charge.

in Section 3, except that equation (12) is replaced by

$$H_1 = +\frac{1}{(2\pi)^3}\int d\boldsymbol{x}'\,\bar{\psi}(\boldsymbol{x}')\psi(\boldsymbol{x}')\left\{\int d\boldsymbol{q}e^{-i\boldsymbol{q}\cdot\boldsymbol{x}'}f(\boldsymbol{q})\right\} \tag{35}$$

where $f(q)$ is the Fourier transform of the interaction. For the square well

$$f(q) = -\frac{4\pi V_0 a^3}{3}\left[3\frac{\sin qa - qa\cos qa}{(qa)^3}\right]. \quad (36)$$

In terms of $f(q)$ the displaced electron density is given by

$$\Delta n(R) = \frac{1}{(2\pi)^3}\int dk \frac{k^2\left[\frac{-f(k)}{4\pi e^2}\right][-4\pi e^2 \bar{W}(k,0)]e^{ik\cdot R}}{[k^2 - 4\pi e^2 \bar{W}(k,0)]} \quad (37)$$

where $\bar{W}(k,0)$ is the same as in Section 3. In particular if we only include bubble graphs, $\bar{W}(k,0)$ becomes $\bar{W}_B(k,0)$. Substituting for $\bar{W}_B(k,0)$ as given in equation (21) in equation (37) yields:

$$\Delta n(R) = \frac{1}{(2\pi)^3}\int dk \frac{k^2\left[\frac{-f(k)}{4\pi e^2}\right]\left[\xi k_F^2\left\{1+\frac{k_F}{k}\left(1-\frac{k^2}{4k_F^2}\right)\ln\left|\frac{k+2k_F}{k-2k_F}\right|\right\}\right]e^{ik\cdot R}}{\left[k^2+\xi k_F^2\left\{1+\frac{k_F}{k}\left(1-\frac{k^2}{4k_F^2}\right)\ln\left|\frac{k+2k_F}{k-2k_F}\right|\right\}\right]}. \quad (38$$

This, except for multiplicative constants, is the same as equation (34). The result may be written

$$\Delta n(R) \approx 4k_F^5\left[\frac{-f(2k_F)}{4\pi e^2}\right]\frac{16\xi}{\pi(4+\xi)^2}\times\left\{\frac{-(2k_FR)\cos(2k_FR)+\frac{4\xi}{4+\xi}[\ln k_FR+\gamma-\frac{3}{2}]\sin(2k_FR)}{(2k_FR)^4}\right\}. \quad (39)$$

This result may be compared with FRIEDEL's result for the analogous problem (see equation (11), reference 2). With the same validity conditions, namely $(k_Fa) \ll 1$ and no bound states, $f(2k_F)$ is $(4\pi/3)V_0a^3$. In particular if we focus our attention on the cosine term, which dominates for large R, we see that the expressions are the same except that ours has an additional factor $(1+\xi/4)^{-2}$, which arises from the electron–electron interaction. For metals ξ varies from about 0·75 to 1·5. Thus the Coulomb interaction between electrons reduces the long-range oscillation of the electron density by a factor in the range 1·4–1·9.

Another problem that can be handled directly by these methods is the coupling between the magnetic moments of two nuclei via their hyperfine interaction with the conduction-band electrons.[7] This is done by replacing H_1 and H_2 in equations (3) and (4) by the appropriate hyperfine interaction.

It is found that to first order in H_1 and H_2 graphs of the type of Figs. 1(b) and (c) give a vanishing contribution. This is physically due to the fact that a single nuclear spin in the electron gas produces no change in the total charge density, while Figs. 1(b) and (c) describe the screening of a charge accumulation, when such exists. Therefore to leading order in the electron density the Coulomb interaction gives *no* correction over Fig. 1(a), the graph describing the interaction of the nuclear spins in a gas of non-interacting electrons. To higher order there are, of course, corrections from graphs such as Fig. 1(d) and (f) in which the interaction lines with both nuclear moments are connected to the same electron–hole closed loop.

Acknowledgement—We wish to thank Professor WALTER KOHN for suggesting this investigation and for many valuable discussions.

REFERENCES

1. FRIEDEL J., *Advanc. Phys.* **3**, 446 (1954).
2. FRIEDEL J., *Nuovo Cimento*, Suppl. **2**, 287 (1958).

3. GELL-MANN M. and BRUECKNER K., *Phys. Rev.* **106,** 364 (1957).
4. GOLDSTONE J., *Proc. Roy. Soc.* A**239,** 267 (1957).
5. HUBBARD J., *Proc. Roy. Soc.* A**240,** 539 (1957); A**243,** 336 (1957); A**244,** 199 (1958).
6. LIGHTHILL M. J., *An Introduction to Fourier Analysis and Generalized Functions*. Cambridge University Press (1958).
7. RUDERMAN M. A. and KITTEL C., *Phys. Rev.* **96,** 99 (1954).
BLOEMBERGEN N. and ROWLAND T. J., *Phys. Rev.* **97,** 1679 (1955).

VOL.
12
59/60

Charging of nickel films with hydrogen evolved electrolytically in the presence of catalytic poisons

(*Received* 8 *June* 1959; *revised* 8 *July* 1959)

IT has been reported in a previous communication[1] that during electrolysis of aqueous sulphuric acid in the presence of arsenic as catalytic poison, a nickel cathode in the form of a wire absorbed more hydrogen per unit weight of metal, the smaller was the radius, r, of the wire. Up to $r = 75\,\mu$, the curve of limiting concentration of absorbed hydrogen vs. wire radius rose approximately hyperbolically with decrease in r. This suggests that a high degree of saturation with hydrogen occurs in a relatively thin superficial layer and that the thickness of the saturated layer does not depend upon the wire radius.

The aim of our further work has been to determine the thickness of that layer and the limiting concentration of hydrogen in it.

Investigations have been carried out on nickel films, 0·7–88μ thick, electrodeposited on copper wires. Since small differences in the structure of the nickel film led to great fluctuations in the amount of hydrogen absorbed, it was essential to standardize precisely all details of the film-preparation method and of the heat treatment of the specimens before charging them with electrolytically evolved hydrogen. In addition the amount of absorbed hydrogen depended to a very great extent upon the presence of catalytic poisons in the electrolyte. So far, the best results have been obtained by using thiourea.

Fig. 1 presents the changes in the average limiting concentration of hydrogen introduced electrolytically into nickel films in relation to the film thickness. The conditions of electrolytic charging with hydrogen were: 1N-sulphuric acid solution containing 0·2 g thiourea/l., cathodic current density 2×10^{-2} A/cm^2, room temperature. Concentration values were obtained by measuring the volume of hydrogen desorbed from charged specimens at room temperature and atmospheric pressure.

As may be seen, in the range of nickel-film thickness from 0·7 to 30μ, the atomic ratio of hydrogen to nickel is approximately constant and corresponds to about 0·7 atoms of hydrogen per atom of nickel. Since the d-band of nickel is thought to have an average of 0·6 holes per nickel atom,[2] the above ratio seems to confirm the hypothesis of MOTT and JONES[3] concerning the filling of these holes by electrons from the hydrogen. The results of investigations concerning the kinetics of hydrogen desorption and the amount of hydrogen absorbed by nickel films under different experimental conditions showed, in general, a close analogy to the behaviour of the palladium–hydrogen system.[4] However, in the case of palladium the limiting concentration of absorbed hydrogen is much easier to obtain than in that of nickel.

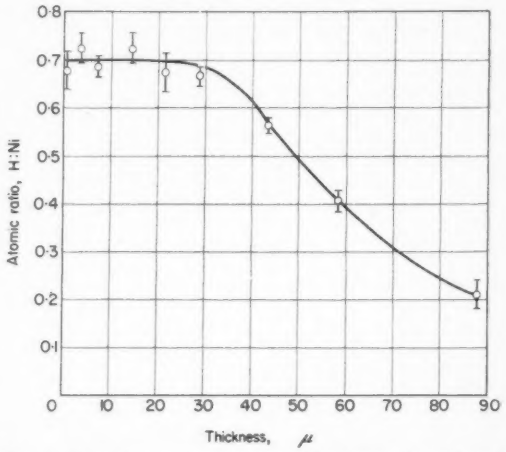

FIG. 1. Limiting concentration of hydrogen introduced electrolytically into nickel films of various thicknesses.

Details concerning the experimental methods and the results obtained will be published shortly in the *Bulletin of the Polish Academy of Sciences.*

Institute of Physical Chemistry of the Polish Academy of Sciences Warsaw, Poland

B. BARANOWSKI
M. SMIALOWSKI

References

1. BARANOWSKI B., SZKLARSKA-SMIALOWSKA Z. and SMIALOWSKI M., *Bull. Acad. Polon. Sci., Ser. Sci. Chim. Geol.* **6**, 179 (1958).

2. SELWOOD P. W., *Magnetochemistry*, 2nd Ed., p. 397. Interscience Publishers, New York (1956).
3. MOTT N. F. and JONES H., *The Properties of Metals and Alloys*, p. 189. Oxford University Press (1936).
4. SMITH D. P., *Hydrogen in Metals*. University of Chicago Press (1948).

VOL. 12 59/60

Effects of plastic deformation at 300°K on the X-ray production of color centers in KCl at 5 and 78°K

(*Received* 3 *August* 1959)

A CENTRAL problem in the field of color centers is the production of ionic vacancies by low-energy radiation[1] (radiation which does not produce knock-on displacement of the ions). SEITZ[2] suggested that this production is related to jogs on dislocation lines; hence there should be a relation between the colorability of a sample and its past mechanical treatment. Indeed, in compressed KCl single crystals, we have noted (as have others) an enhanced formation of *F* centers upon X-raying at room temperature by a factor of at least 430 per cent for a 1-hr exposure to 140 kVp X-rays (650 per cent for KI).

Two methods of introducing vacancy aggregates are: (1) plastic deformation and (2) X-irradiation at room temperature followed by optical bleaching of the *F* centers produced. In a previous study[3] it was observed that *F*-center production by X-rays at 5°K was not enhanced by the presence of vacancy aggregates produced by method (2). In the same crystals, however, X-radiation at room temperature resulted in a large initial production of *F* centers. Thus it was surmised that these vacancy aggregates do not permit the direct production of *F* centers (i.e. isolated negative-ion vacancies) at 5°K by X-rays.

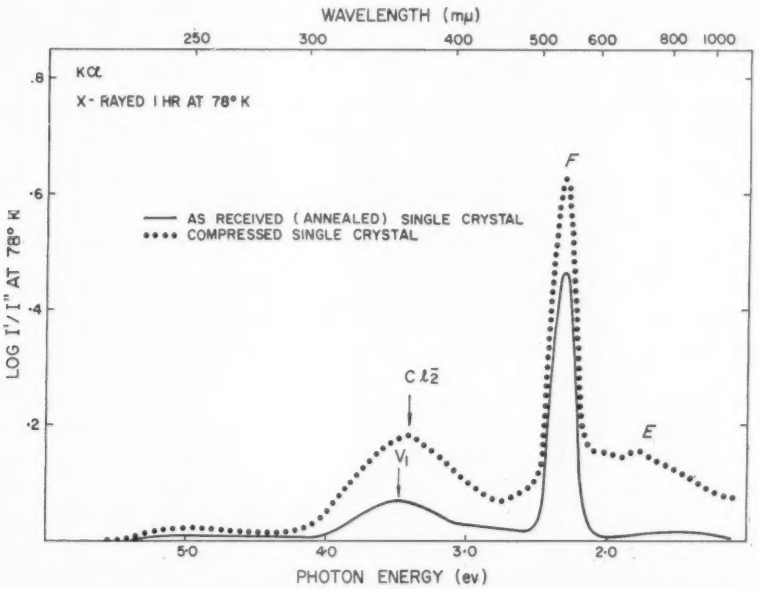

FIG. 1. Absorption spectra of compressed (upper) and annealed KCl single crystals X-rayed (140 kVp, 4 mA) 1 hr at 78°K. Underlying the Cl_2^- absorption is the V_1 which is also produced (as in the lower curve). The *y*-axis is the net induced absorption.

This report, an extension of previous studies,[4] is concerned with X-irradiation at low temperatures of plastically deformed single crystals. The plastic deformation is performed at room temperature, and it is assumed that vacancy aggregates of some kind are formed (method 1).

In contrast to the marked effects at 300°K, at 5 and 78°K we find that the net production of *F*

centers is not appreciably greater than in an undeformed crystal (within about 10 per cent, see Fig. 1). We note that the half-width and peak position of the F band in compressed crystals is no different from their values in annealed crystals indicating that we are producing "true" F centers in both cases.

We have, however, found (Fig. 1) that plastic deformation at 300°K enhances the formation of other color centers which are not found in appreciable quantity in pure, annealed KCl crystals. From a study of their optical and thermal properties, we have identified one of them as the Cl_2^- molecule[5] and the other as an electron center or centers (E) to which it is intimately related. The formation of Cl_2^- seems to require only additional electron traps;[5] if hole traps are also formed by plastic flow, we have not as yet detected them.

Summarizing, plastic flow has a distinct influence on the color centers formed at low temperatures, although this treatment does not enhance F-center production as it does at 300°K. The fact that the shape of the F band is the same in annealed and compressed crystals suggests that the F centers have similar environments in both types of specimens, i.e. the centers are in a "perfect" region of the crystal.[6] (This is not to say that we understand the actual environment of an F center in a good crystal.) Additional electron centers are formed as well as Cl_2^-. This indicates that stable molecular ions are formed only when many electrons are trapped. Our experimental results suggest that the theories[1,2,7] of F-center formation by irradiation must be reviewed.

Acknowledgement—We thank R. JARKA for his taking of the data. Further details of this study will be submitted for publication.

Zenith Radio Corporation HERBERT N. HERSH
Chicago 39, Ill. JORDAN J. MARKHAM

References

1. MARKHAM J. J., *Phys. Rev.* **88,** 500 (1952).
2. SEITZ F., *Phys. Rev.* **80,** 239 (1950).
3. HERSH H. N., *J. Chem. Phys.* **30,** 790 (1959).
4. HERSH H. N., *J. Chem. Phys.* **27,** 1330 (1958); *Bull. Amer. Phys. Soc.* **4,** 47 (1959).
5. DELBECQ C. J., SMALLER B. and YUSTER P. H., *Phys. Rev.* **111,** 1235 (1958).
6. KONITZER J. and MARKHAM J. J., Submitted for publication.
7. VARLEY J. H. O., *J. Nuclear Energy* **1,** 130 (1954).

Optical absorption in germanium*

(*Received* 4 *August* 1959)

THE optical constants of germanium from 1 to 10 eV have recently been measured by PHILIPP and TAFT[1]; their results are shown in Fig. 1.

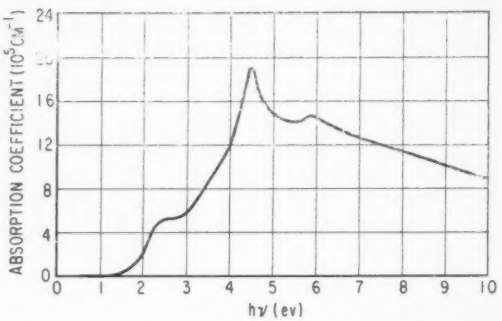

FIG. 1. Spectral dependence of the absorption coefficient of germanium.

Although the optical absorption shows a well-defined structure, no attempt is made to relate this to energy-band models. Such is the object of this note.

Optical absorption in this range is dominated by direct transitions from the valence to the conduction band. ELLIOTT[2] has developed a theory for intensity near absorption edges including exciton absorption. The theory assumes spherical conduction and valence-band edges. It seems likely that the most important modification of his results for anisotropic band edges would be to replace the spherical masses by density-of-states effective masses. In this case he predicts for the optical absorption

$$\kappa \sim \nu\mu^2 x^2 \qquad (1)$$

where ν is the frequency and μ the density-of-states reduced effective mass. Here x is a matrix element which should not vary by more than a factor of 2 throughout the reduced Brillouin zone for direct transitions from the top of the valence band to the bottom of the conduction band. (We have verified this by examining matrix elements between OPW wave functions at Γ, X and L.)

The optical absorption displayed in Fig. 1 shows

* Supported in part by the National Science Foundation.

VOL. 12 59/60

a well-defined edge at 2.1 eV. Inspection of the energy-band models of HERMAN[3] and the present author[4] suggests strongly that this edge is associated with the transition $L_{3'} \rightarrow L_1$. This conjecture can be checked by comparing the strength of this edge with that associated with the direct transition $\Gamma_{25'} \rightarrow \Gamma_{2'}$ studied by DASH and NEWMAN[5]. Here $\nu \cong 0{\cdot}9$ eV and $\mu \cong 0{\cdot}035\,m$. At L the conduction-band masses are known from cyclotron resonance. To estimate the valence-band effective masses at $L_{3'}$, we assume that only perturbations from L_1 need be included; this means that the longitudinal mass is m. The transverse masses may then be determined from the conduction electron effective masses. Thus

$$m\mu_l^{-1} \cong (1{\cdot}5)^{-1} - (1{\cdot}0)^{-1}, \tag{2}$$

$$m\mu_{t\pm}^{-1} \cong (\tfrac{3}{2} \pm \tfrac{1}{2})[(0{\cdot}083)^{-1} - 1] \tag{3}$$

where the $\pm$ signs in (3) refer to the two branches into which the $L_{3'}$ level splits. Remembering that the degeneracy factor at the center of the zone is twice that of the edge (because of spin-orbit splittings of each) but that there are four valleys at the edge, we find from equations (1)–(3), assuming that the matrix elements x are the same, that the absorption edge at L should be about

$$2{\cdot}3 \times 2 \times \frac{(0{\cdot}06)^{4/3} 2^{2/3}}{(0{\cdot}035)^2} \cong 100 \tag{4}$$

times that at Γ. The observed ratio is 50, which we consider to be in reasonable agreement with equation (4) in view of the approximations made.

More convincing evidence that this edge is associated with transitions at L can be obtained from the spin resonance g values of FEHER[6]. According to ROTH[7], g values near L_1 parallel and perpendicular to the (111) principal axis are given by

$$g_\perp \cong 2{\cdot}0 \pm 0{\cdot}2, \tag{5}$$

$$g_\parallel \cong \left(\frac{m}{m_t} - 1\right)\frac{0{\cdot}20}{\Delta E}, \tag{6}$$

where ΔE is the direct energy gap in eV between $L_{3'}$ and L_1. In the two-band approximation $g_\perp$ is 2·0; for magnetic field in a (110) direction (and therefore transverse to two ellipsoids) FEHER finds 1·9, in good agreement with ROTH's prediction. For the magnetic field along a (100) axis, all ellipsoids are equivalent and

$$g_{\text{eff}} = \tfrac{2}{3} g_\perp + \tfrac{1}{3} g_\parallel = 1{\cdot}57, \tag{7}$$

according to FEHER. Using $g_\perp = 1{\cdot}9$ and equation (6), we find $\Delta E \cong 2{\cdot}4$eV, in good agreement with our earlier value of 2·1eV.

The other prominent feature of the absorption is the strong peak near 4·5eV. This requires two singularities in the joint density of states. From considerations of phase space it is tempting to identify this peak with the transition $X_4 \rightarrow X_1$ and guess that transitions from this region produce the change in slope observed at 4·2eV. The two-fold degeneracy required by crystal symmetry at X_1 might then produce the "accidental" pairing of critical points required to explain the peak.

It is interesting to note that our interpretation of the optical data also implies a picture of the quantum efficiency of electron–hole pair production which is quite different from the one proposed by ANTONČÍK[8] (see also TAUC[9]). ANTONČÍK considers only indirect absorption ($\Gamma_{25'} \rightarrow L_1$) for energies up to 4 eV. Above 1 eV the direct transition ($\Gamma_{25'} \rightarrow \Gamma_{2'}$) must dominate up to 2·1eV, where the transition ($L_{3'} \rightarrow L_1$) should dominate. Above 2·1eV additional electron–hole pairs can be produced by (hole, $L_{3'}$) $\rightarrow$ (2 holes, $\Gamma_{25'}$; electron, L_1). Thus a break in the curve of quantum efficiency vs. incident photon energy is expected near 2·1eV, and this is actually observed.[9]

Acknowledgements—I am indebted to Dr. L. ROTH for correspondence concerning g values, and to Professor H. BROOKS for several conversations.

Department of Physics J. C. PHILLIPS*
University of California
Berkeley 4, Calif.

References

1. PHILIPP H. R. and TAFT E. A., *Phys. Rev.* **113,** 1002 (1959).
2. ELLIOTT R. J., *Phys. Rev.* **108,** 1384 (1957).
3. HERMAN F., *Physica s'Grav.* **20,** 801 (1954).
4. PHILLIPS J. C., *Phys. Rev.* **112,** 685 (1958).
5. DASH W. C. and NEWMAN R., *Phys. Rev.* **99,** 1151 (1955).
6. FEHER G., WILSON D. K. and GERE E. A., *Phys. Rev. Letters* **3,** 25 (1959).
7. ROTH L., *Lincoln Laboratory Progress Report,* (unpublished).
8. ANTONČÍK E., *Czech. J. Phys.* **7,** 675 (1957).
9. TAUC J., *J. Phys. Chem. Solids* **8,** 219 (1959).

* National Science Foundation Postdoctoral Fellow.

BOOK REVIEW

The Structure and Properties of Porous Materials. Edited by D. H. EVERETT and F. S. STONE. Butterworths, London, and Academic Press, New York, 1958. 382 pp., 60*s*., $12.00.

THIS book contains the proceedings of an international symposium held at the University of Bristol in March, 1958. There are 18 papers of which approximately half are on fundamentals and half on applications. Among the authors, one finds the names of RIDEAL, BARRER, WYNNE-JONES, KINGTON, DEBOER, EVERETT, FLOOD and KISELEV. The discussions following lectures were tape recorded and are published in full. These discussions comprise almost half of the volume.

There is no doubt that this book is a major publication in its field. Research workers interested in porous materials, especially from a fundamental point of view, will have no choice but to consult it.

T. L. HILL

BOOKS RECEIVED

Powder Metallurgy. Official publication of the Powder Metallurgy Joint Group of the Iron and Steel Institute and the Institute of Metals, London. No. 1/2, 272 pp. (1958); no. 3, 180 pp. (1959).

VOL.
12
959/60

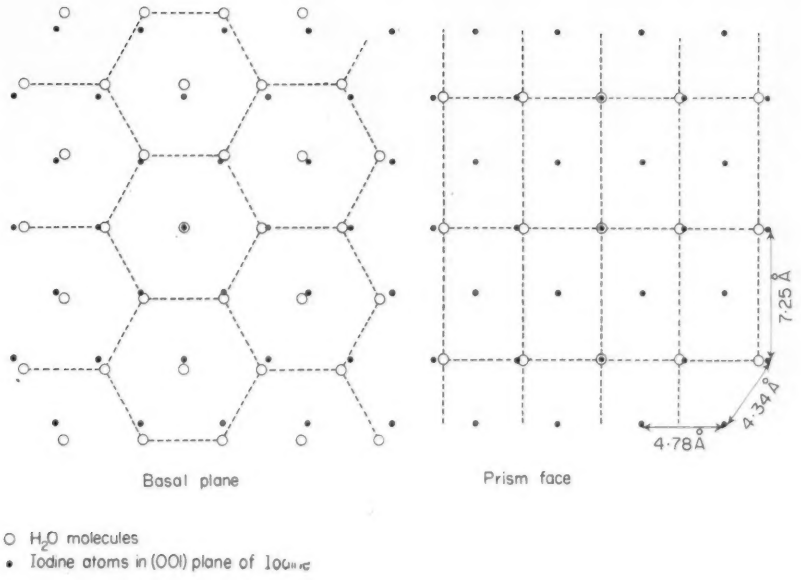

FIG. 15. The atomic configuration on the (001) face of iodine relative to that in the basal and prism planes of ice.

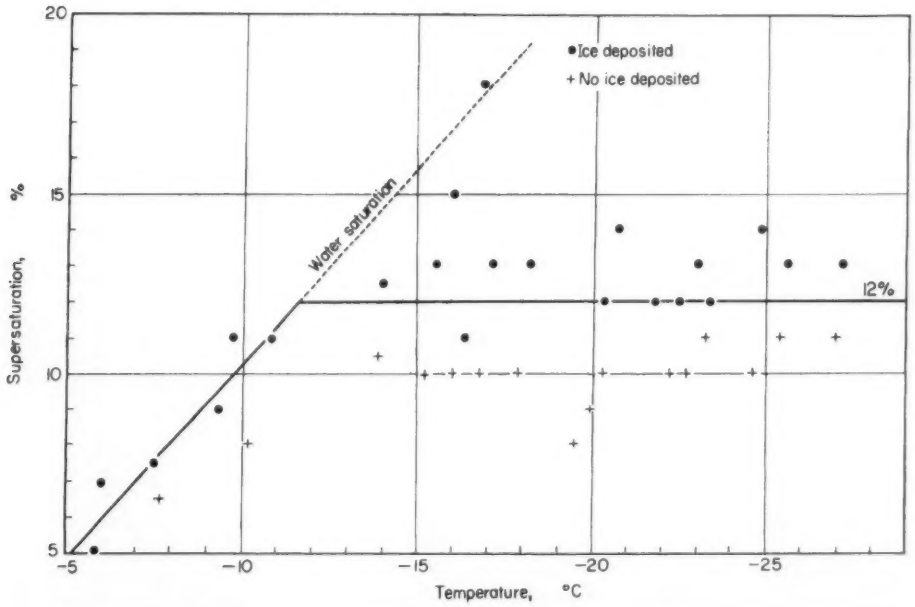

FIG. 16. The conditions of temperature and supersaturation at which oriented ice crystals appeared at special sites on the surface of a silver iodide crystal.

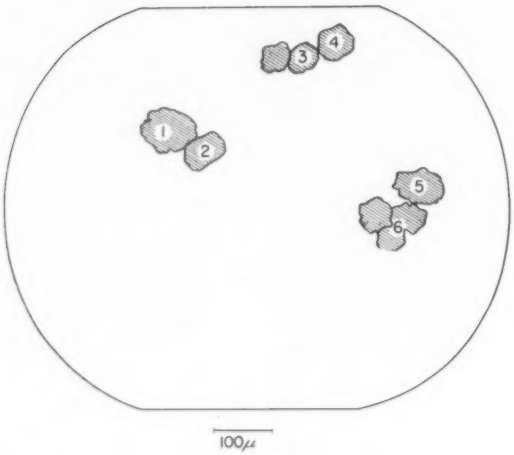

FIG. 13a

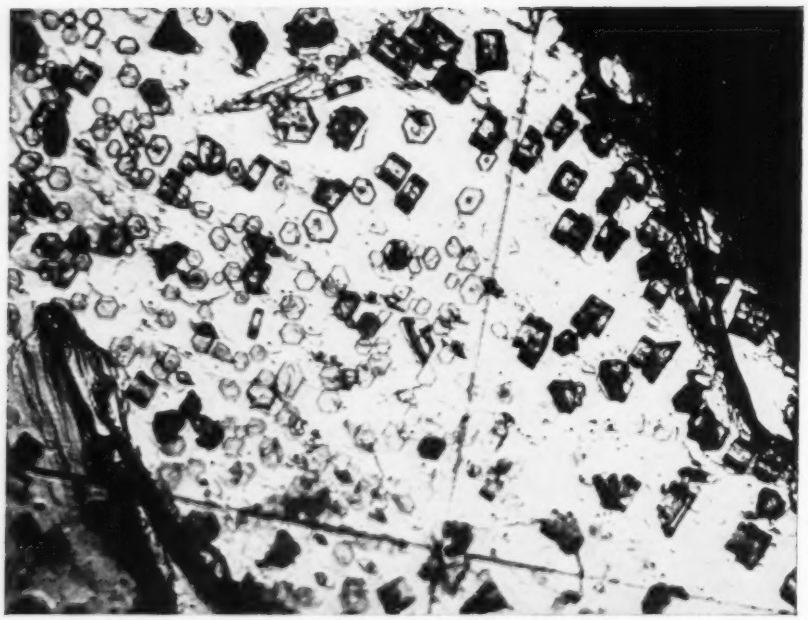

FIG. 14. Oriented ice plates and prisms on the (001) face of an iodine crystal.

VOL.
12
59/60

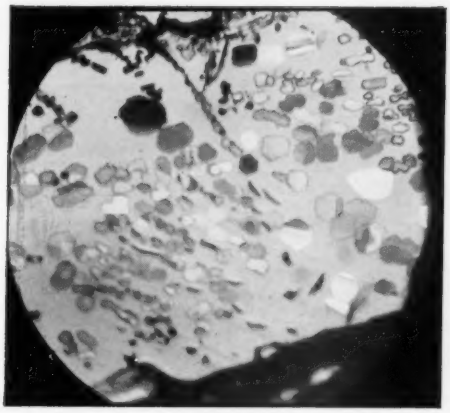

(a)

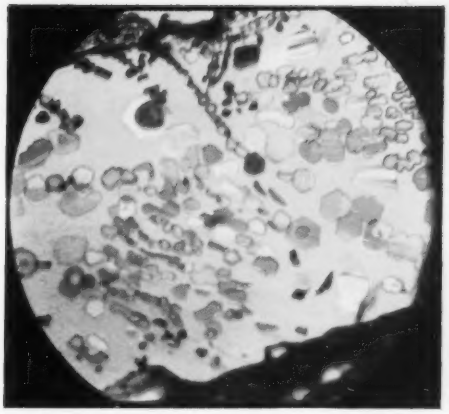

(d)

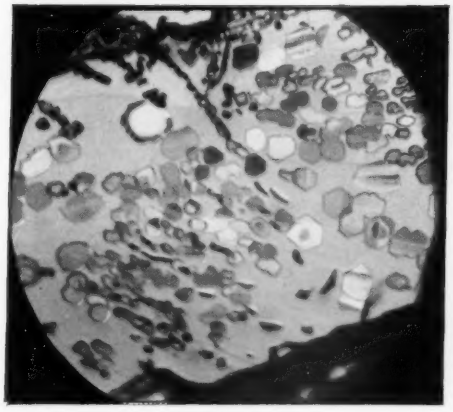

(b)

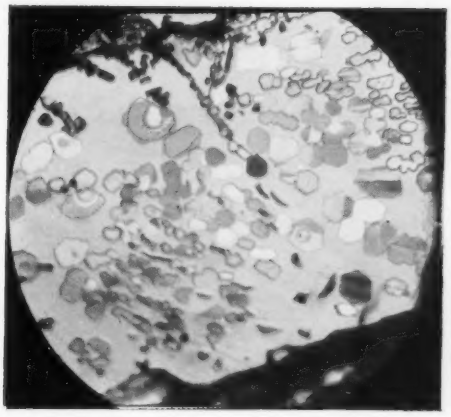

(e)

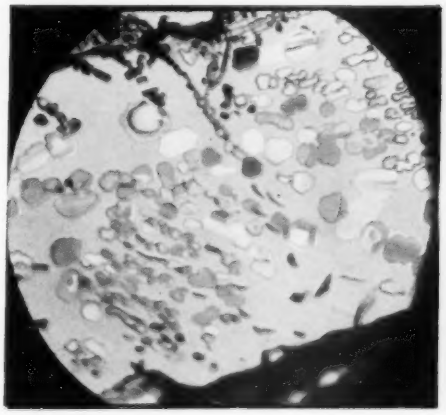

(c)

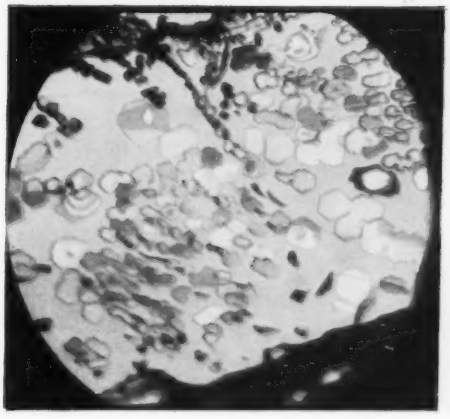

(f)

FIG. 13. A time sequence showing the initiation and spread of growth layers across the surfaces of ice crystals growing on a covellite base. Key in Fig. 13a opposite.

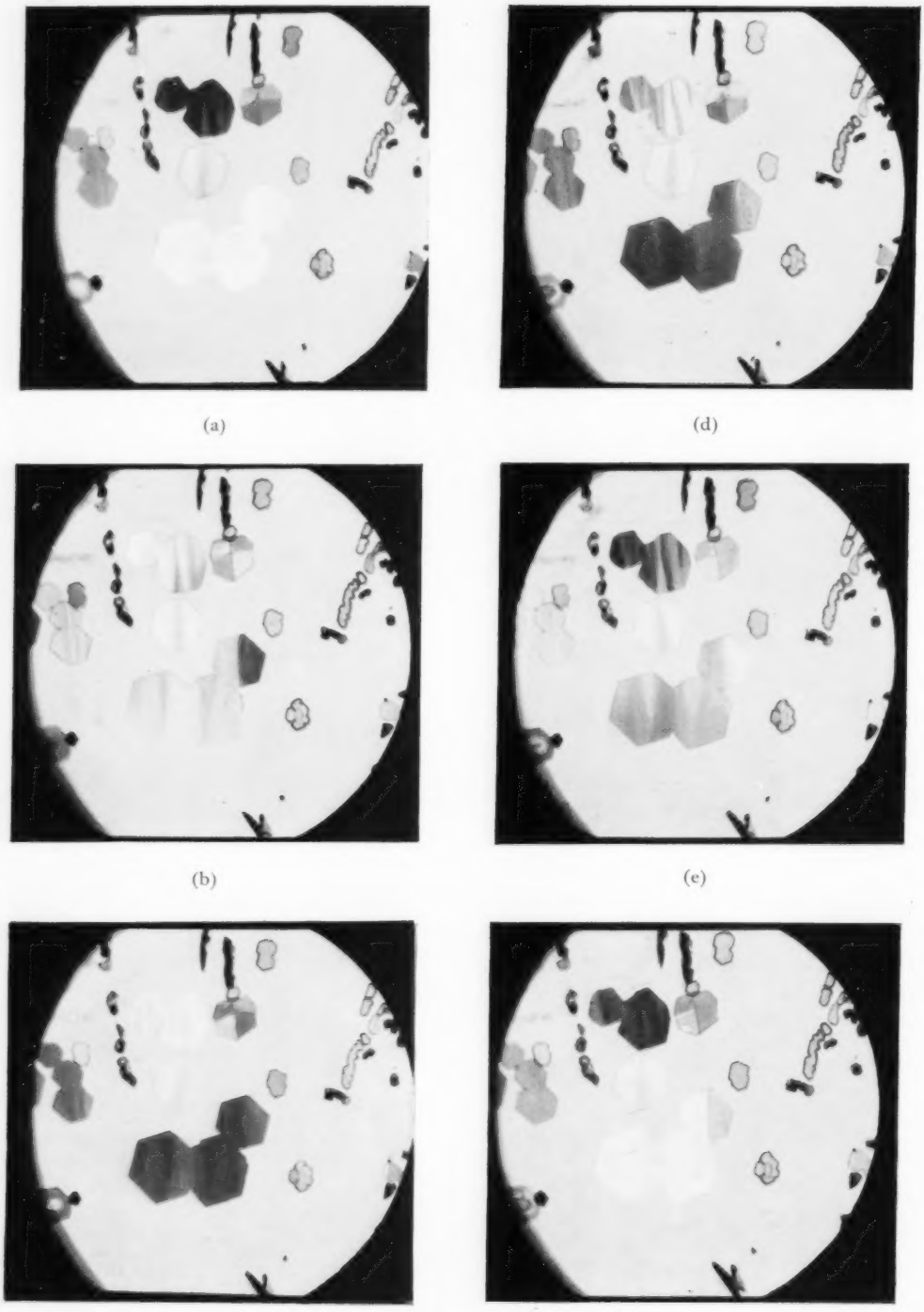

FIG. 12. Epitaxial deposit of ice crystals on the basal plane of a covellite (CuS) crystal. The interference colours provide a measure of the crystal thickness. Further details are given in the text and key in Fig. 12a, opposite.

VOL.
12
59/60

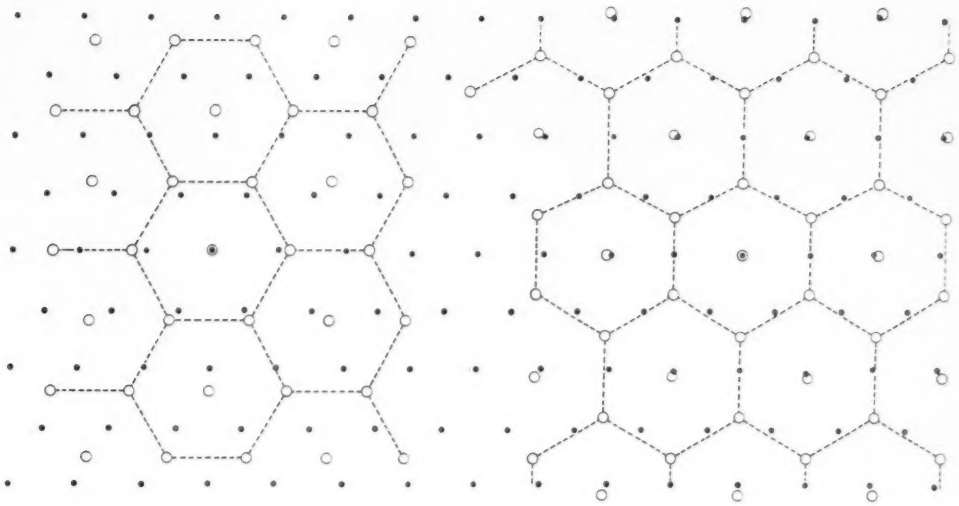

• Cu atoms in the (0001) plane of CuS
○ H_2O molecules in the (0001) plane of ice

FIG. 11. The relative atomic positions in the basal planes of cupric sulphide and ice.

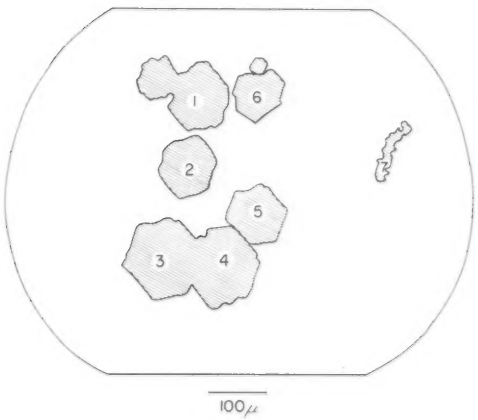

FIG. 12a

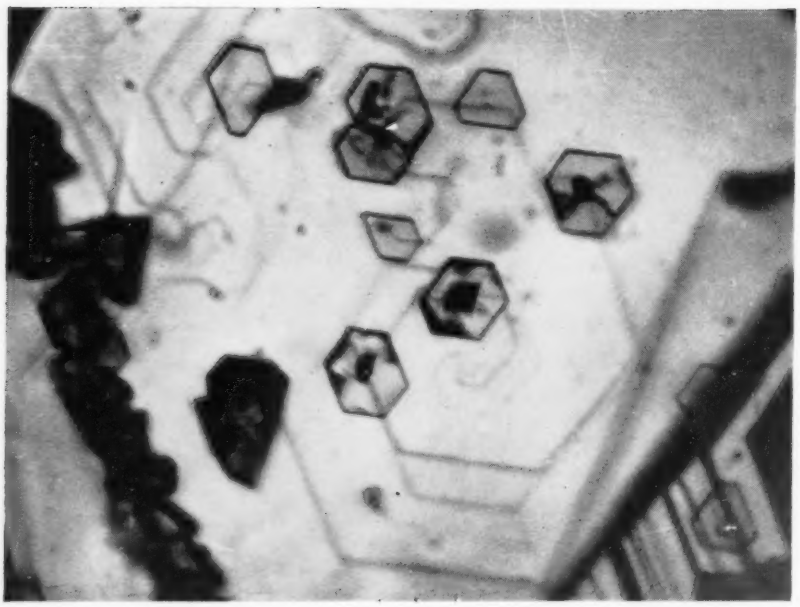

FIG. 10. An epitaxial deposit of ice crystals growing at the steps of a hexagonal growth spiral on cadmium iodide. Again a dense deposit forms along the edge of the crystal.

VO
1
1959/

VOL.
12
59/60

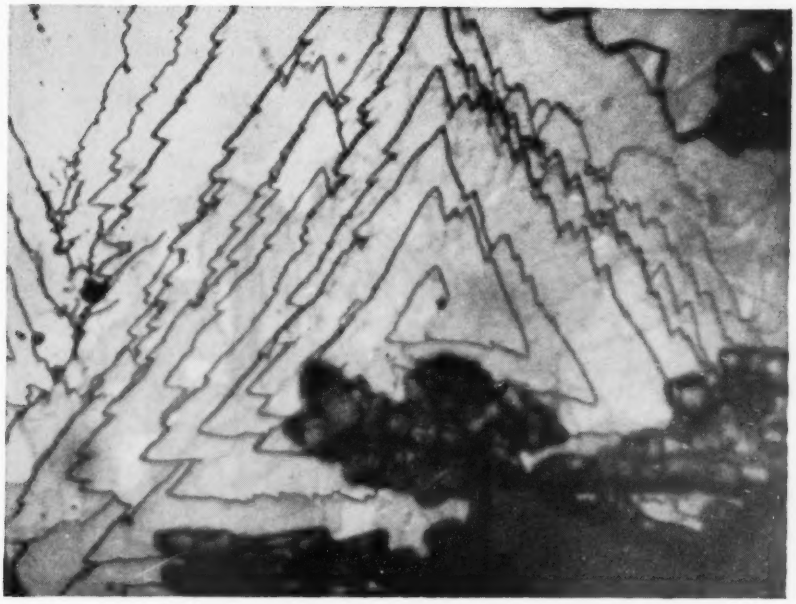

FIG. 8. Ice crystals growing round the edges of lead iodide crystals but not on the surface which is covered by shallow spiral growth steps 500 Å high.

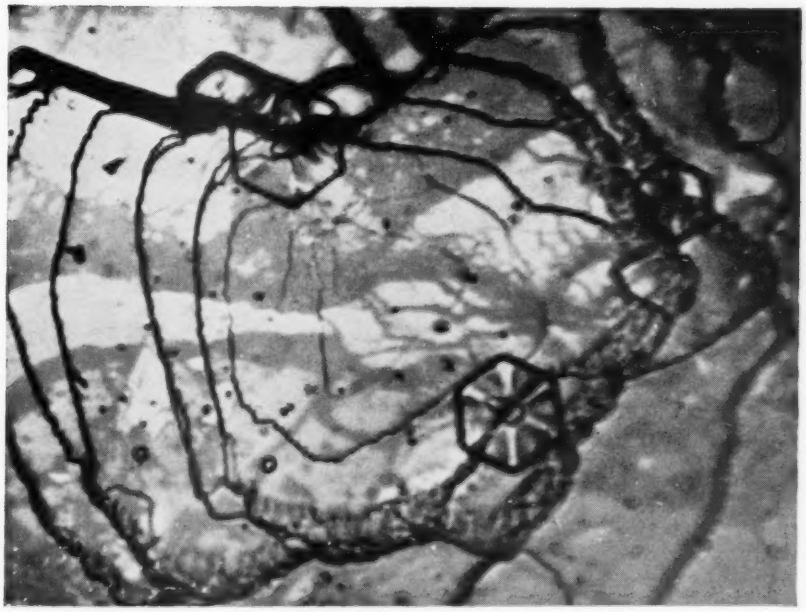

FIG. 9. Oriented ice crystals originating at the edges of deep steps ($> 0{\cdot}1\mu$) on the basal plane of lead iodide. Again there is no preferential growth at the shallow growth steps.

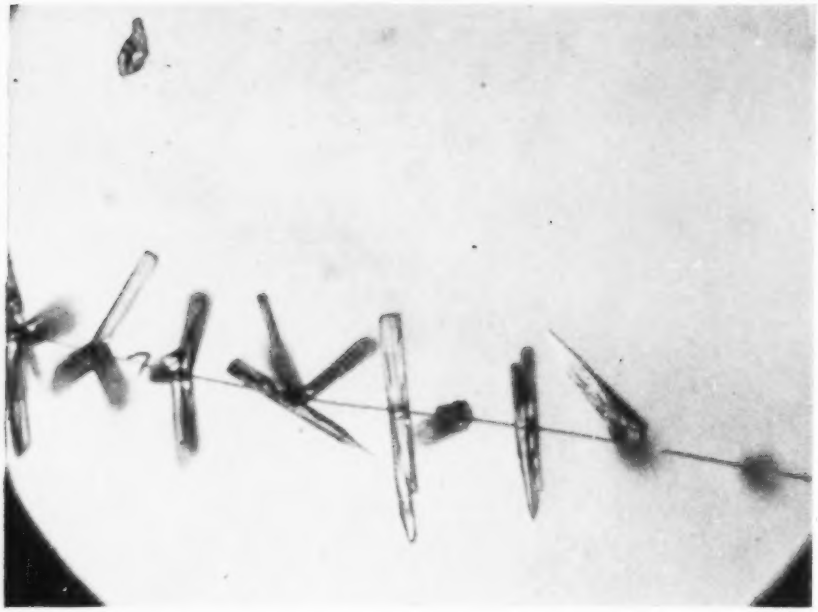

FIG. 6. Randomly oriented ice needles growing along a step on a clean silver surface.

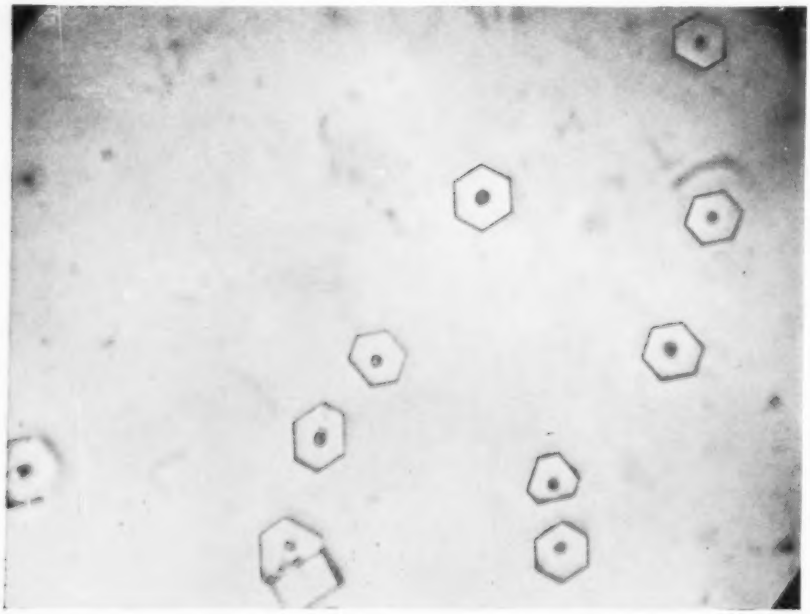

FIG. 7. A sparse deposit of ice crystals, with two different orientations, growing on a contaminated silver surface. Oriented crystals occurred only in patches where silver iodide was produced by adsorption of iodine vapour from the atmosphere.

VOL.
12
959/60

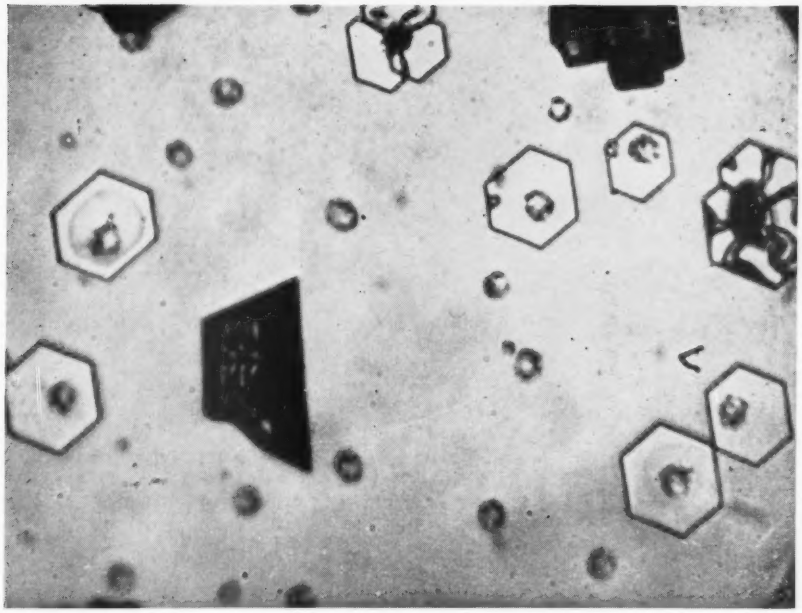

FIG. 4. Hexagonal ice plates forming at special sites on the silver iodide surface. Temperature −15°C.

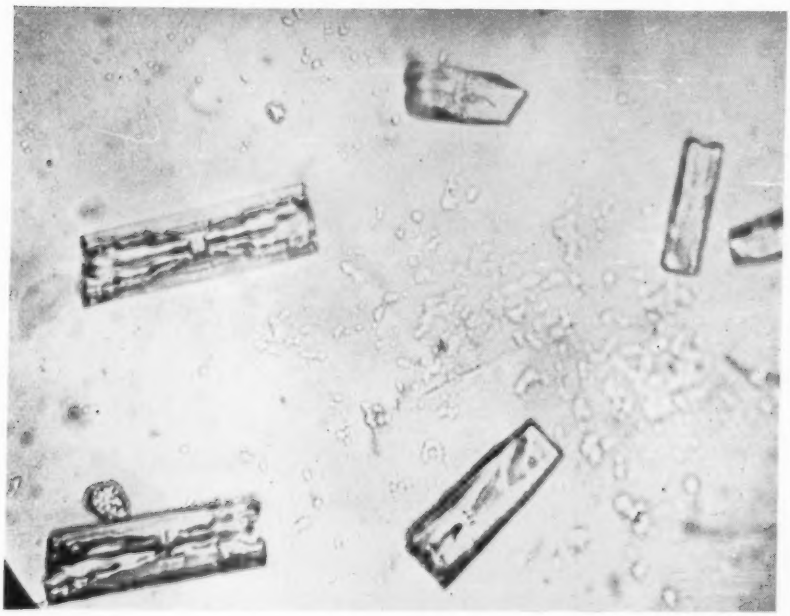

FIG. 5. Randomly oriented ice prisms growing on a clean, fresh silver substrate at −25°C.

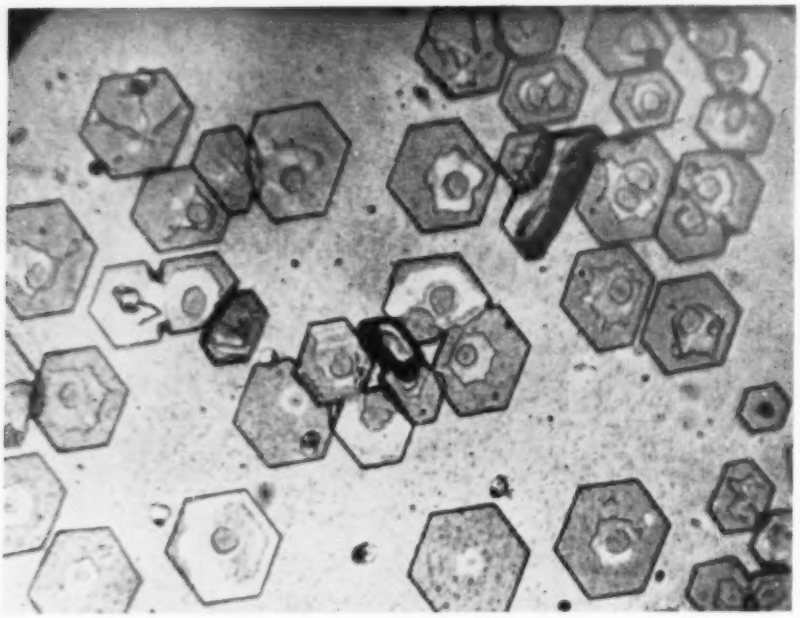

FIG. 2. A deposit of oriented, hexagonal, plate-like ice crystals growing at −15°C on a substrate of silver iodide.

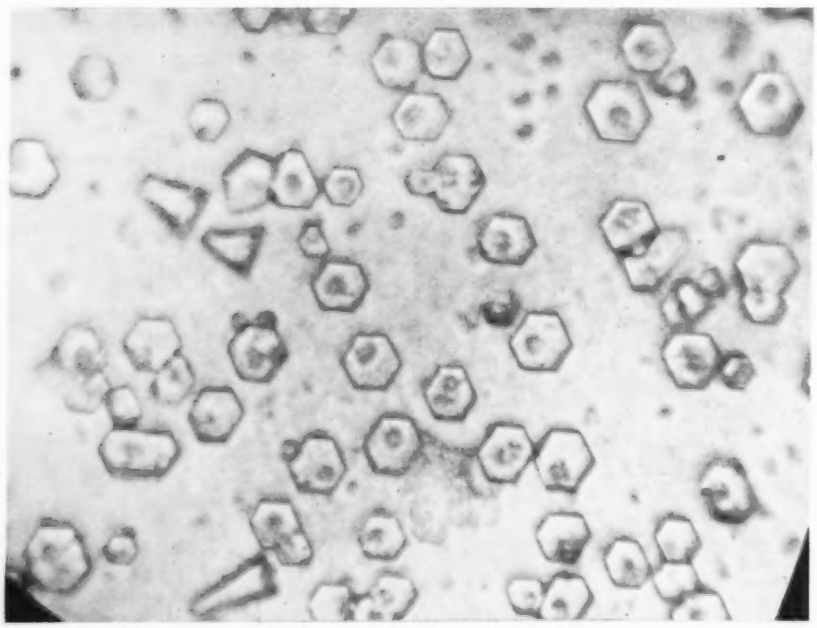

FIG. 3. Oriented ice crystals growing at −30°C on silver iodide; these crystals grew preferentially along the principal axes, normal to the substrate, to form prisms.

[facing p. 190

VO
1
1959/

J. Phys. Chem. Solids Pergamon Press 1960. Vol. 12. pp. 211–215. Printed in Great Britain.

VANADIUM ACTIVATED ZINC AND CADMIUM SULPHIDE AND SELENIDE PHOSPHORS

M. AVINOR* and G. MEIJER

Philips Research Laboratories, N.V. Philips' Gloeilampenfabrieken, Eindhoven, Netherlands

(*Received* 31 *August* 1959)

Abstract—Vanadium activated ZnS, ZnSe, CdS and CdSe powders were prepared. All these powders show a fluorescence at about 2μ. Addition of copper and silver as auxiliary activators enhances the vanadium emission, while the well known silver and copper emissions do not appear.

VOL. 12 59/60

1. INTRODUCTION

VANADIUM is not known to produce visible emission in zinc and cadmium chalcogenides and its addition to such phosphors kills the visible emission. We found that the addition of vanadium helps to incorporate copper and silver in the CdS lattice in a way similar to coactivation by gallium and indium, as judged from the body colour of the phosphors. However, the well known emissions of copper and silver in the red and near infra-red are absent. This prompted an investigation for possible emission farther in the infra-red and indeed such emission was found at about 2μ. In this paper we summarize the emissions observed in vanadium activated ZnS, CdS, ZnSe and CdSe.

2. EXPERIMENTAL

The phosphors were prepared by adding vanadium as a solution of ammonium metavanadate to the pure powder of the base material. Copper and silver were added as solutions of the sulphate and nitrate, respectively. Gold was added as a solution of the chloride. The powders were dried at 120°C overnight. The sulphides were fired in an atmosphere of pure H_2S, at 950°C for 1 hr. The products were then ground and refired in H_2S for another hour at 950°C for CdS and 1100°C for ZnS. The selenides were fired twice in nitrogen at 1000°C for 1 hr. However, the emission from the selenides was very poor and hardly detectable. Therefore, they were refired for 1 hr. at 1000°C in an atmosphere of H_2+H_2Se, prepared by passing hydrogen over hot selenium, and the emission improved considerably.

For measurement, the samples were mounted in a Dewar vessel, in which they could be cooled to liquid nitrogen temperature. A high pressure mercury lamp was used for excitation and a 1·5 cm thick water filter, interposed between the lamp and the phosphor sample, removed all radiation of wavelengths longer than about $1{\cdot}3\mu$. The emission spectra were measured with a Perkin Elmer 12*C* monochromator, equipped with a LiF prism and a thermocouple detector. Corrections have been applied for the dispersion of the prism to obtain equal energy spectra. All the intensities in the figures are presented in the same relative units and give a true relative measure of the emission intensities.

3. RESULTS

ZnS, ZnSe and CdS activated by vanadium only at a concentration of 2×10^{-4} atom/mole show a greenish tint in body colour, which suggests that vanadium probably introduces an absorption band in the near infra-red. Silver and copper were well incorporated into the lattice in the presence of vanadium. Vanadium activated CdS developed an orange body colour with addition of silver, and dark brown with copper. Indeed the body colour of CdS (V,Cu) is quite similar to CdS (Ga,Cu); however, the powder is insulating and non-photoconducting. It is interesting to note that CdS activated by vanadium alone is also insulating and non photoconducting. The usual emissions of copper and

* On leave of absence from the Scientific Department, Ministry of Defence, Israel.

silver in Zn and Cd sulphides are completely quenched by vanadium at the concentrations of 2×10^{-4} atom/mole employed, and only the vanadium emission is observed.

Table 1. *Peak positions in eV*

Activators	Temperature	CdS	ZnS	CdSe	ZnSe
V	300°K	0·59	0·66	0·54	~0·51 0·63
	80°K	0·60	0·68	0·56	~0·51 0·64
V,Ag	300°K	0·55	~0·57 0·63	0·51	~0·46 0·62
	80°K	0·57	0·60 ~0·68	0·53	~0 46 0·57 ~0·65
V,Cu	300°K	0·57	0·59	0·52	~0·63
	80°K	~0·56 0·59	0·62	0·54	~0·50 0·60
V,Au	300°K	0·59			
	80°K	0·55 ~0·60			

The fluorescence spectra are presented in Figs. 1–6, and show the remarkable feature that the peaks always appear at about the same energy. The positions of the various peaks are listed in Table 1.

Except for ZnSe, activation by vanadium alone gives the weakest emission, and the best efficiency seems to be obtained with activation by both copper and vanadium. Fig. 1 shows the emission curves for CdS with different auxiliary activators. The intensities are strongly temperature dependent and the peak shifts to slightly higher energies on cooling. CdS (Cu,V) and CdS (Au,V) show some evidence of structure in the emission band. At low temperature a second band is discernible at 0·56 eV. The spectra for ZnS are given in Fig 2. The emission band of ZnS (Ag,V) at room temperature is broad and of a composite nature. On cooling, one band grows faster than the other and has its peak at 0·60 eV at 80°K. The second band, with a peak at about 0·67 eV at 80°K, shows only a weak temperature dependence.

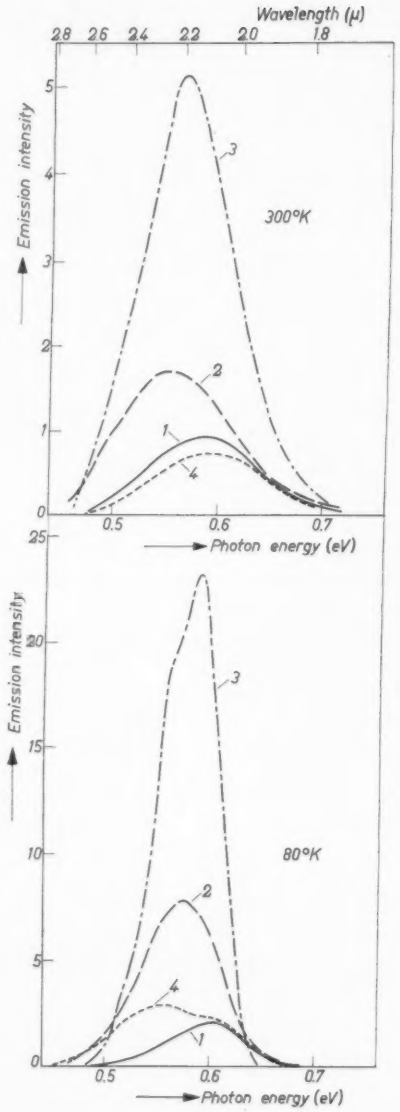

FIG. 1. Fluorescence spectrum. (1) CdS : 2×10^{-4} V; (2) CdS : 2×10^{-4} V, 2×10^{-4} Ag; (3) CdS : 2×10^{-4} V, 2×10^{-4} Cu; (4) CdS : 2×10^{-4} V, 2×10^{-4} Au.

The emissions of CdSe (Fig 3) and ZnSe (Fig. 4) are weaker than those of the sulphides, but are otherwise rather similar. A notable difference is the appearance of an additional weak emission band of ZnSe below 0·5 eV. Also the temperature

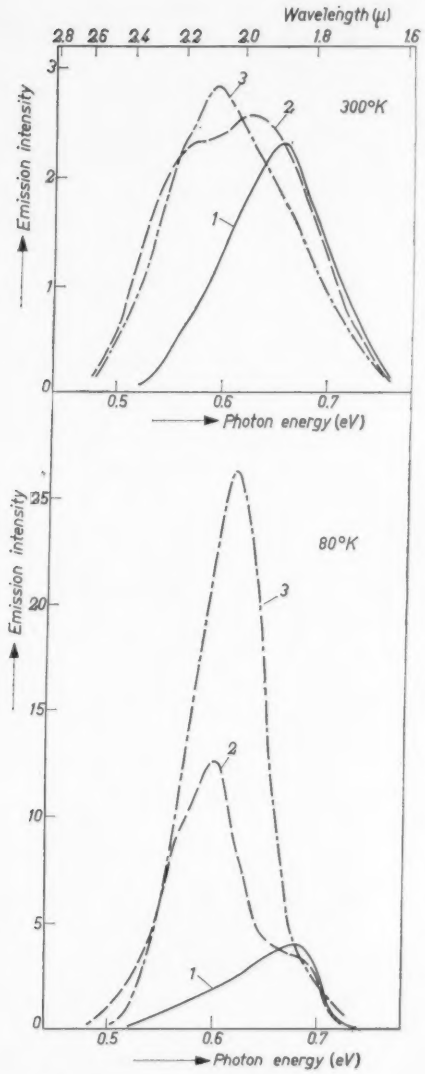

FIG. 2. Fluorescence spectrum. (1) ZnS : 2×10^{-4} V; (2) ZnS: 2×10^{-4} V, 2×10^{-4} Ag; (3) ZnS : 2×10^{-4} V, 2×10^{-4} Cu.

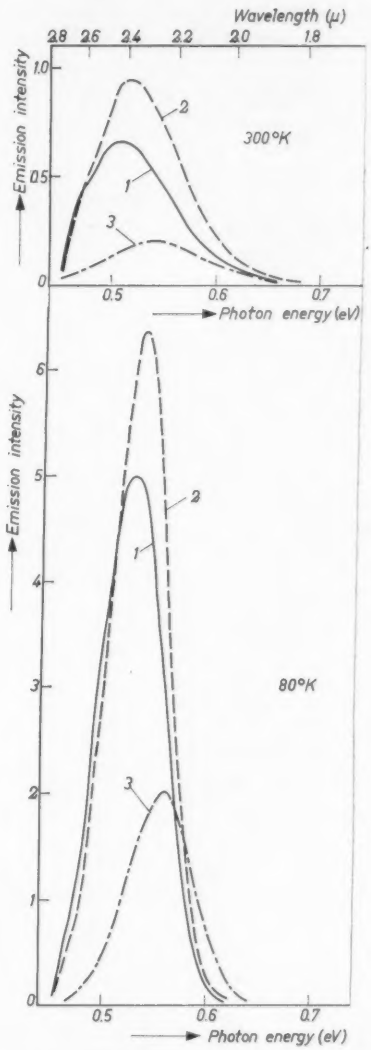

FIG. 3. Fluorescence spectrum. (1) CdSe : 2×10^{-4} V, 2×10^{-4} Ag; (2) CdSe : 2×10^{-4} V, 2×10^{-4} Cu; (3) CdSe : 2×10^{-4} V.

dependence of the emission of ZnSe (Fig 4) differs considerably from the other phosphors.

In order to investigate the effect of atmosphere and temperature on the two distinct bands of ZnS (Ag,V), another ZnS phosphor was prepared with equal amounts of silver and vanadium (2×10^{-4} atom/mole) and fired in H_2S at 950°C. This powder showed an emission band with peaks at 0·67 eV and 0·68 eV at room and liquid nitrogen temperature, respectively (Fig. 5, curve 4). The temperature dependence is only weak and this band seems to correspond to the shoulder of curve 2, Fig. 2. Part of this powder was refired in nitrogen at 1100°C for 1 hr. The fluorescence

became weaker (Fig. 5, curve 4a) but the shape and temperature dependence remained about the same. Another part of the powder was refired in H_2S at 1100°C for 1 hr. The emission and temperature dependence changed (Fig. 5, curve 4b) and became very similar to curve 2, Fig. 2. In order to

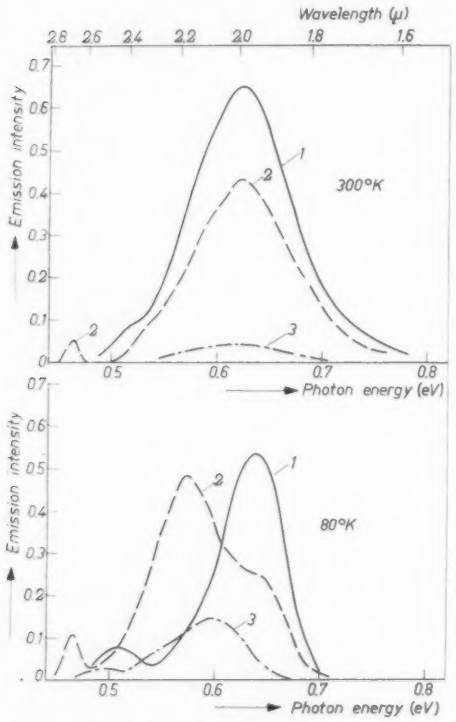

FIG. 4. Fluorescence spectrum (1) ZnSe : 2×10^{-4} V; (2) ZnSe : 2×10^{-4} V, 2×10^{-4} Ag; (3) ZnSe : 2×10^{-4} V, 2×10^{-4} Cu.

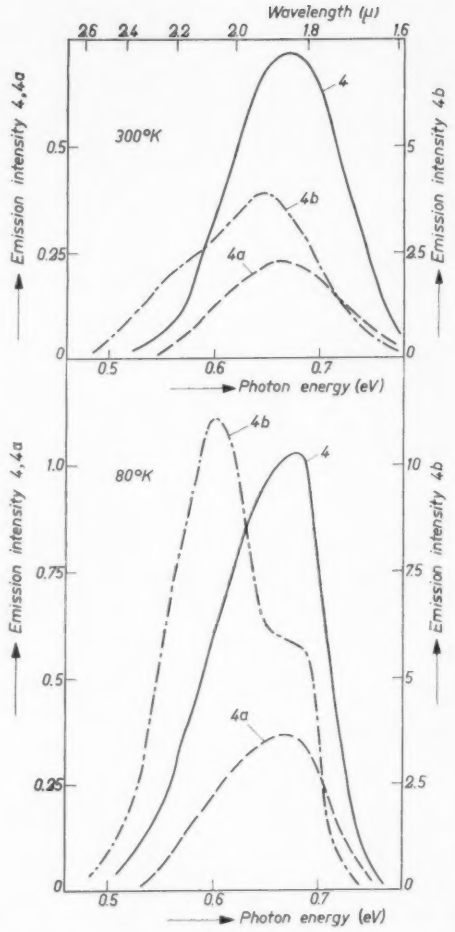

FIG. 5. Fluorescence spectrum of ZnS : 2×10^{-4} V, 2×10^{-4} Ag. (4) Fired in H_2S at 950°C. (4a) Refired in N_2 at 1100°C. (4b) Refired in H_2S at 1100°C.

corroborate the influence of the atmosphere during firing, the ZnS (Ag,V) sample of curve 2, Fig. 2 was refired in nitrogen atmosphere at 1100°C. In Fig. 6 the spectrum of curve 2, Fig. 2 is redrawn together with the spectrum after refiring in nitrogen (Fig. 6, curve 2a). The latter curve is quite similar to curves 4 and 4a of Fig. 5.

The same vanadium emission is also excited by cathode rays. A power efficiency of about 2 per cent was obtained for the best phosphors by using 3 kV cathode rays. In view of the low energy of the emitted quanta and the low energy of the cathode rays the quantum efficiency is comparable to that of other sulphide phosphors.

4. DISCUSSION

There is still no direct evidence for the state of the incorporated vanadium in the ZnS, CdS, ZnSe and CdSe phosphors. However, the fact that vanadium promotes the incorporation of copper and silver into the lattice in a way similar to the trivalent metals suggests that it is incorporated in the trivalent state. This assumption is further supported by the fact that copper and silver raise

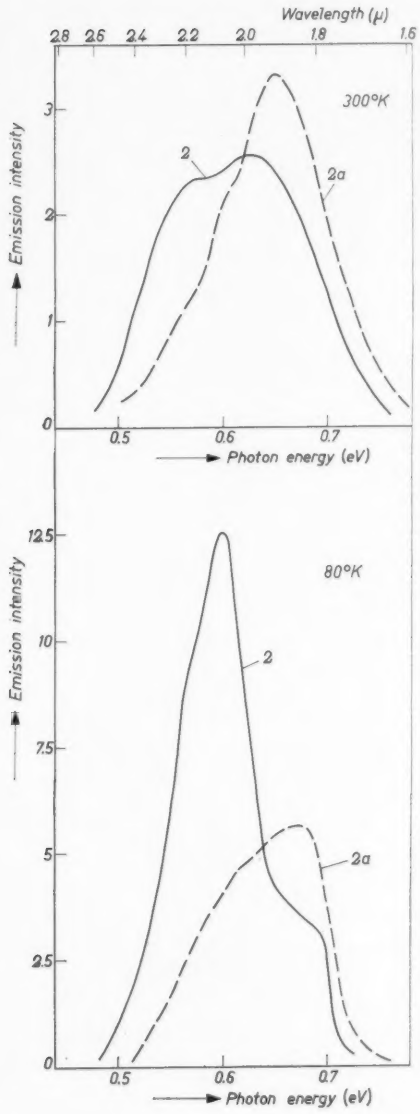

the efficiency of the vanadium emission, presumably by helping to incorporate it in the trivalent state. They are also seen to influence slightly the intensity, position and structure of the emission band. Indeed, copper and silver may be looked upon, in these phosphors, as coactivators of vanadium, because their own emissions do not appear. This behaviour indicates that the division into activator and coactivator is rather arbitrary and should be treated with caution. Because silver and copper also change the absorption spectrum of the phosphors, they might well act as sensitizers of the vanadium emission to excitation in their absorption bands. Indeed, preliminary measurements show excitation bands due to copper and silver in addition to those due to vanadium. Detailed spectra will be published later. The emission itself seems to be a characteristic emission of the vanadium, because changes of host lattice and addition of auxiliary activators have only a small influence. The usual "killing" effect of vanadium in sulphide phosphors is now seen to consist of translating the emission into the infra-red, and not of dissipating the excitation completely into heat.

Acknowledgements—The authors are indebted to Mr. J. W. de JONG for his assistance in the measurements of the spectra, and to Dr. A. BRIL for measuring the power efficiency with cathode rays.

FIG. 6. Fluorescence spectrum of ZnS : 2×10^{-4} V, 2×10^{-4} Ag; (2) Fired in H_2S at 1100°C. (2a) Refired in N_2 at 1100°C.

J. Phys. Chem. Solids Pergamon Press 1960. Vol. 12. pp. 216–232. Printed in Great Britain.

SOME REMARKS ABOUT FREQUENCY SPECTRA OF CRYSTAL LATTICES*

JEAN PERETTI

Physics Department, University of Maryland, College Park, Maryland, U.S.A.

(*Received* 18 *June* 1959)

Abstract—The general construction of the frequency distribution of a crystal lattice when the force constants between atoms are known is treated. The intermediate step is to consider a function $F(z)$, of the complex variable z, which is expressible in terms of the force constants in a compact form. The frequency spectrum $g(x)$ itself is, apart from a multiplicative constant, the imaginary part of $F(z)$.

This general formalism is applied, first, to calculate $g(x)$ for special lattices; secondly, to investigate the singularities of the spectrum; thirdly, to derive a low-temperature expansion of the spectrum; and fourthly, to investigate the analytical nature of one-dimensional frequency spectra.

In the Born–Huang (B–H) model the angular frequency corresponding to any normal mode is the solution of a secular equation:

$$\mathrm{Det}|\omega^2 I - C| = 0 \tag{1}$$

where C is a certain matrix, the elements of which depend on the wave vector $\boldsymbol{\theta}(\theta_1, \theta_2, \theta_3)$ of the normal mode. For example, in a simple cubic lattice with nearest- and next-nearest-neighbor central force interactions only, the matrix is C:

$$C = \begin{vmatrix} A_1 & B_{12} & B_{13} \\ B_{21} & A_2 & B_{23} \\ B_{31} & B_{32} & A_3 \end{vmatrix} \tag{2}$$

with

$$A_i = \frac{2\alpha}{M}(1 - \cos\theta_i) + \frac{4\gamma}{M}(2 - \cos\theta_i \cos\theta_j - \cos\theta_i \cos\theta_k)$$

$$B_{ij} = \frac{4\gamma}{M} \sin\theta_i \sin\theta_j$$

where (i, j, k) is a cyclic permutation of (1, 2, 3). In the most general case, C has the following properties:

(a) C is hermitian;

(b) elements of C are polynomials in $\cos\theta_i$ and $\sin\theta_i$.

If we call the left-hand member of equation (1) $P(\omega^2)$, these two properties of the matrix C lead to the following ones for the polynomial P:

(a) $P(\omega^2)$ has only real roots;

(b) its coefficients are polynomials in $\cos\theta_i$ and $\sin\theta_i$;

(c) as θ_1, θ_2, θ_3 vary from 0 to 2π, the roots of $P(\omega^2)$ are bounded by a certain value $\omega^2_{\max}$.

There exists a matrix Γ, whose eigenvalues are precisely the ω's:

$$\Gamma = \begin{pmatrix} 0 & -i \\ iC & 0 \end{pmatrix}, \tag{3}$$

where 0 and $\pm i$ are scalar matrices of the same dimension as C. We shall call its characteristic polynomial $\Pi(\omega)$; that is,

$$\Pi(\omega) \equiv P(\omega^2) \tag{4}$$

In an infinite crystal, the θ's range uniformly from 0 to 2π (or from 0 to π). To each set correspond m values of ω^2; as $\boldsymbol{\theta}$ varies we get a continuous distribution for the ω's, the density of which we

* This research was partially supported by the United States Air Force through the Air Force Office of Scientific Research and Development Command under Contract No. AF49(638)399.

shall call $g(\omega)$ or Frequency Distribution (F.D.). We shall call $h(u)$ the F.D. of the squares $\omega^2 = u$ of the angular frequencies, so that:

$$\omega > 0 \qquad h(u)\,du = g(\omega)\,d\omega \qquad u = \omega^2 \tag{5}$$

or

$$g(\omega) = 2\omega h(\omega^2) \qquad \omega > 0 \tag{6}$$

The definition of $g(\omega)$ can be extended to negative values of ω by the relation

$$g(-\omega) = g(\omega)$$

It should be noticed that $g(\omega) = 0$ when $|\omega| > \omega_{max}$. By a change in the units measuring frequencies one can have $\omega_{max} = 1$; in all that follows we assume that such a change has been made. We now introduce $F_0(z)$, a function of the complex variable z, which is defined by the equation

$$F_0(z) = \int_{-\infty}^{+\infty} \frac{g(x)}{z-x}\,dx \tag{7}$$

$F_0(z)$ is analytic in the z-plane, except perhaps on the real axis in the interval $(-1, +1)$.

When $|z| > 1$, we can write:

$$F_0(z) = \int_{-\infty}^{+\infty} dx g(x) \sum_{n=0}^{\infty} \frac{x^n}{z^{n+1}} \tag{8}$$

In terms of the moments of $g(\omega)$ defined by*:

$$\mu_n = \int_{-\infty}^{+\infty} g(x) x^n\,dx \tag{9}$$

equation (8) becomes

$$F_0(z) = \sum_{n=0}^{\infty} \frac{\mu_n}{z^{n+1}} \tag{10}$$

On the other hand for a finite lattice μ_n can be considered as the sum of the n-th power of the roots of the secular equation:

$$\mu_n = \lim\left(A \sum_{\theta} \sum_{k=1}^{m} \omega_k^n(\boldsymbol{\theta})\right)$$

where lim means that the crystal goes to an infinite crystal; A is a normalization factor such that $\mu_0 = 1$. MONTROLL[2] has shown that for a given $\boldsymbol{\theta}$,

$$\sum_k \omega_k^n(\boldsymbol{\theta})$$

can be evaluated from the matrix $C(\boldsymbol{\theta})$:

$$\sum_k \omega_k^{2n}(\boldsymbol{\theta}) = \mathrm{Tr.}[C(\boldsymbol{\theta})]^n \qquad \sum_k \omega_k^{2n+1}(\boldsymbol{\theta}) = 0$$

We prefer to relate this sum to the matrix Γ

$$\sum_k \omega_k^n(\boldsymbol{\theta}) = \mathrm{Tr.}[\Gamma(\boldsymbol{\theta})]^n$$

The sum over $\boldsymbol{\theta}$ becomes, in the limit, an integration over $\theta_1, \theta_2, \theta_3$; so finally:

$$\mu_n = \frac{1}{m}\left(\frac{1}{2\pi}\right)^3 \int_0^{2\pi}\int_0^{2\pi}\int_0^{2\pi} \mathrm{Tr.}\Gamma^n(\boldsymbol{\theta})\,d\theta_1\,d\theta_2\,d\theta_3 \tag{11}$$

From equations (10) and (11) it follows that:

$$F_0(z) = \frac{1}{m}\left(\frac{1}{2\pi}\right)^3 \mathrm{Tr} \int_0^{2\pi}\int_0^{2\pi}\int_0^{2\pi} \frac{d\theta_1\,d\theta_2\,d\theta_3}{z-\Gamma(\boldsymbol{\theta})} \tag{12}$$

Let $\Pi'(z)$ represent the derivative of the polynomial $\Pi(z)$ with respect to z; then for a given value of $\boldsymbol{\theta}$ we have:

$$\frac{\Pi'(z)}{\Pi(z)} = \sum_k \frac{1}{z-\omega_k(\boldsymbol{\theta})} = \sum_{n=0}^{\infty} \frac{1}{z^{n+1}}\left[\sum_k \omega_k^n(\boldsymbol{\theta})\right] \tag{13}$$

where we have supposed that $|z| > \omega_{max} = 1$. If we integrate equation (13) over $\theta_1, \theta_2, \theta_3$, we get:

$$\frac{1}{m}\left(\frac{1}{2\pi}\right)^3 \int_0^{2\pi}\int_0^{2\pi}\int_0^{2\pi} \frac{\Pi'(z)}{\Pi(z)}\,d\theta_1\,d\theta_2\,d\theta_3 = \sum_{n=0}^{\infty} \frac{\mu_n}{z^{n+1}} \tag{14}$$

The left-hand side of equation (14) is an analytic function of z in the z-plane, except perhaps on the real axis in the interval $(-1, +1)$, where $\Pi(z)$ can

* The usefulness of moments was first pointed out by MONTROLL[1].

be zero. We shall call this triple integral $F(z)$:

$$F(z) = \frac{1}{m}\left(\frac{1}{2\pi}\right)^3 \int_0^{2\pi}\int_0^{2\pi}\int_0^{2\pi} \frac{\Pi'(z)}{\Pi(z)}\, d\theta_1\, d\theta_2\, d\theta_3 \tag{15}$$

Equation (14) shows that $F(z)$ is equal to $F_0(z)$ defined by equation (7), provided that $|z| > 1$. As these functions are analytic everywhere except on the segment $(-1, +1)$, we can write in their common domain of analyticity:

$$F_0(z) = F(z), \tag{16}$$

or, more explicitly

$$F(z) = \int_{-\infty}^{+\infty} \frac{g(x)}{z-x}\, dx \tag{17}$$

In this equation $F(z)$ is a known function, at least in principle, because in equation (15), the polynomial $\Pi(z)$ and its derivative are easily deduced from the matrix $C(\boldsymbol{\theta})$. For example, for a general simple cubic lattice with nearest-neighbor interactions we have:

$$\Pi(z) \equiv P(z^2) = z^2 - \\ -\tfrac{1}{2}(1+\gamma_1 \cos\theta_1 + \gamma_2 \cos\theta_2 + \gamma_3 \cos\theta_3)$$

where

$$\gamma_1+\gamma_2+\gamma_3 = 1$$

so that

$$F(z) = \left(\frac{1}{2\pi}\right)^3 \int_0^{2\pi}\int_0^{2\pi}\int_0^{2\pi} \frac{4z}{2z^2-1-\gamma_1 \cos\theta_1-\gamma_2 \cos\theta_2-\gamma_3 \cos\theta_3}\, d\theta_1\, d\theta_2\, d\theta_3.$$

We can therefore consider equation (17) as an integral equation for the unknown function $g(x)$.

A general solution of this equation can be obtained with the aid of the theory of Hilbert conjugate functions.

THE METHOD OF HILBERT CONJUGATE FUNCTIONS

A general exposition of the theory of Hilbert conjugate functions is given by TITCHMARSH[11]. In fact we need only a very weak theorem from this theory.

Theorem:

If $\Phi(z)$ is a function of the complex variable z such that:

(a) $\Phi(z)$ is analytic in the half upper plane;
(b) $|z\Phi(z)|$ is bounded when $z \to \infty$;*
(c) $\Phi(z) = u(x, y)+iv(x, y)$, when $y \to 0+$, u and v have limits sufficiently well behaved so that

$$\int_{-\infty}^{+\infty} \frac{u(x, 0)}{z-x}\, dx \text{ and } \int_{-\infty}^{+\infty} \frac{v(x, 0)}{z-x}\, dx$$

exist when $\operatorname{Im} z > 0$, then at $\zeta = \xi+i\eta$, a point in the half upper plane $(\eta > 0)$:

$$u(\xi, \eta) = \frac{1}{\pi}\int_{-\infty}^{+\infty} \frac{x-\xi}{(x-\xi)^2+\eta^2} v(x, 0)\, dx \tag{a}$$

$$v(\xi, \eta) = -\frac{1}{\pi}\int_{-\infty}^{+\infty} \frac{x-\xi}{(x-\xi)^2+\eta^2} u(x, 0)\, dx \tag{b}$$

$$u(\xi, \eta) = \frac{1}{\pi}\int_{-\infty}^{+\infty} \frac{\eta}{(x-\xi)^2+\eta^2} u(x, 0)\, dx \tag{c}$$

$$v(\xi, \eta) = \frac{1}{\pi}\int_{-\infty}^{+\infty} \frac{\eta}{(x-\xi)^2+\eta^2} v(x, 0)\, dx \tag{d}$$

Combining equations (a) and (d), we get:

$$\Phi(\zeta) = u(\xi, \eta)+iv(\xi, \eta) = -\frac{1}{\pi}\int_{-\infty}^{+\infty} \frac{v(x, 0)}{\zeta-x}\, dx \tag{18}$$

which has the same form as equation (17). The function $F(z)$ itself satisfies the conditions (a) and (b): when $z \to \infty$, there exists a positive number A

* This condition can be weakened.

such that $|\Pi'(z)/\Pi(z)| < A/|z|$ for all $\boldsymbol{\theta}$; it follows that

$$|F(z)| < \frac{1}{m}\left(\frac{1}{2\pi}\right)^3 \int_0^{2\pi}\int_0^{2\pi}\int_0^{2\pi} \frac{A}{|z|}\, d\theta_1\, d\theta_2\, d\theta_3 = \frac{1}{m}\frac{A}{|z|}.$$

The function $g(x)$ also satisfies condition (c), as will be seen from subsequent developments. Thus with the identifications

$$F(z) = \Phi(z)$$

$$g(x) = -\frac{1}{\pi} v(x, 0)$$

we obtain finally,

$$g(x) = -\frac{1}{\pi}\,\mathrm{Im}F(x+i0) \tag{19}$$

$F(z)$ being known in principle, equation (19) gives the general solution to the problem of finding the frequency distribution $g(x)$ when the matrix C is given.

Examples

As an example, for a one-dimensional "simple cubic" lattice with nearest-neighbor interactions, we have:

$$F(z) = \frac{1}{2\pi}\int_0^{2\pi} \frac{4z}{2z^2-1-\cos\theta}\, d\theta = \frac{2}{(z^2-1)^{1/2}}$$

in the whole domain of analyticity of $F(z)$. Using equation (19), we find:

(a) $g(x) = 0$ if $x > 1$

(b) $g(x) = \frac{2}{\pi}\frac{1}{\sqrt{(1-x^2)}}$ if $0 < x < 1$,

which is the well-known result.

For the corresponding two-dimensional case, we have:

$$F(z) = \left(\frac{1}{2\pi}\right)^2 \times \int_0^{2\pi}\int_0^{2\pi} \frac{4z}{2z^2-1-\gamma_1\cos\theta_1-\gamma_2\cos\theta_2}\, d\theta_1\, d\theta_2$$

By putting:

$$s = 2z^2-1, \tag{20}$$

we obtain

$$F(z) = \frac{4z}{\pi}\int_0^{\pi} \frac{d\theta}{[(s-\gamma_2\cos\theta)^2-\gamma_1^2]^{1/2}}$$

With

$$\gamma = \gamma_1+\gamma_2 (= 1), \qquad \delta = \gamma_2-\gamma_1 \qquad 0 \leqslant \delta \leqslant \gamma,$$

a straightforward calculation gives:

$$F(z) = \frac{8z}{\pi}\frac{1}{\sqrt{(\gamma^2-\delta^2)}}\, k\boldsymbol{K}(k) \tag{21}$$

where $\boldsymbol{K}$ is the complete Legendre elliptic integral of the first kind:

$$\boldsymbol{K}(k) = \int_0^{\pi/2} \frac{d\phi}{(1-k^2\sin^2\phi)^{1/2}}$$

of the complex modulus

$$k = \left(\frac{\gamma^2-\delta^2}{s^2-\delta^2}\right)^{1/2} \tag{22}$$

To apply equation (19) to the present case, we must know the real and imaginary part of $k\boldsymbol{K}(k)$. When s is real, we have the following three cases:

(a) $0 < s^2 < \delta^2$; k is purely imaginary; we use the relation

$$\boldsymbol{K}(k) = \boldsymbol{K}'[(1-k^2)^{1/2}] = \frac{1}{\sqrt{(1-k^2)}}\boldsymbol{K}\left(\frac{|k|}{\sqrt{(1-k^2)}}\right)$$

which gives

$$F(z) = -\frac{8z}{\pi}\frac{i}{\sqrt{(\delta^2-s^2)}}\boldsymbol{K}\left[\left(\frac{\gamma^2-\delta^2}{\gamma^2-s^2}\right)^{1/2}\right] \tag{21a}$$

Since in this equation the modulus of $\boldsymbol{K}$ is real and < 1, $\boldsymbol{K}$ is real, and:

$$g(z) = \frac{8z}{\pi^2}\frac{1}{\sqrt{(\delta^2-s^2)}}\boldsymbol{K}\left[\left(\frac{\gamma^2-\delta^2}{\gamma^2-s^2}\right)^{1/2}\right]$$

or

$$g(z) = \frac{4z}{\pi^2}\frac{1}{\sqrt{(1-z^2)}}\boldsymbol{K}\left[\frac{(\gamma_1\gamma_2)^{1/2}}{z\sqrt{(1-z^2)}}\right] \tag{23}$$

(*b*) $\delta^2 < s^2 < \gamma^2$; k is real and > 1; we use the relation:

$$K(k) = \frac{1}{k}K\left(\frac{1}{k}\right) - i\frac{1}{k}K\left[\left(1-\frac{1}{k^2}\right)^{1/2}\right],$$

where the real and imaginary part of $K(k)$ are explicitly displayed. It follows that in this case

$$F(z) = \frac{8z}{\pi}\frac{1}{\sqrt{(\gamma^2-\delta^2)}}\left\{K\left(\frac{1}{k}\right) - iK\left[\left(1-\frac{1}{k^2}\right)^{1/2}\right]\right\} \tag{21b}$$

(a) $k \to \infty$:

We use equation (21b) and the expansions

$$K\left(\frac{1}{k}\right) = \frac{\pi}{2}\left[1+2\left(\frac{1}{8k^2}\right)+9\left(\frac{1}{8k^2}\right)^2+\ldots\right]$$

$$K\left[\left(1-\frac{1}{k^2}\right)^{1/2}\right] = \ln(4k)+\tfrac{1}{4}[\ln(4k)-1]\frac{1}{k^2}+\ldots$$

to obtain

$$F(z) = \frac{4z}{\sqrt{(\gamma^2-\delta^2)}}\left[1+2\left(\frac{1}{8k^2}\right)+9\left(\frac{1}{8k^2}\right)^2+\ldots\right] - \frac{i8z}{\pi\sqrt{(\gamma^2-\delta^2)}}\left[\ln 4k+\tfrac{1}{2}(\ln 4k-1)\frac{1}{k^2}+\ldots\right] \tag{26}$$

so that

$$g(z) = \frac{8z}{\pi^2}\frac{1}{\sqrt{(\gamma^2-\delta^2)}}K\left[\left(1-\frac{1}{k^2}\right)^{1/2}\right]$$

or

$$g(z) = \frac{4z}{\pi^2}\frac{1}{(\gamma_1\gamma_2)^{1/2}}K\left[\frac{z\sqrt{(1-z^2)}}{(\gamma_1\gamma_2)^{1/2}}\right] \tag{24}$$

(*c*) $s^2 > \gamma^2$; k is real and < 1. So $F(z)$ is real:

$$F(z) = \frac{8z}{\pi}\frac{1}{\sqrt{(s^2-\delta^2)}}K\left[\left(\frac{\gamma^2-\delta^2}{s^2-\delta^2}\right)^{1/2}\right] \tag{21c}$$

and

$$g(z) = 0 \tag{25}$$

Equations (23), (24) and (25) agree with those derived by MONTROLL[3] by a different method.

One can see that, although $g(z)$ has three different analytical expressions for the three cases (*a*), (*b*) and (*c*), it corresponds to the whole spectrum only *one* function $F(z)$, given by equation (21) and (22). This fact underlines the simplification introduced by considering such a function. The same kind of simplification occurs if we consider the "singularities" of the spectrum.

In the two-dimensional case, $F(z)$ can be singular:

- (*a*) when $k \to \infty$, that is, when $s^2 = \delta^2$;
- (*b*) when $k = 1$, where $K(k)$ is singular, that is, when $s^2 = \gamma^2$.

When k is real, that is, when $s^2 > \delta^2$, $\ln 4k$ is real; when k is imaginary, for $s^2 < \delta^2$, $\ln 4k = (i\pi/2) + \ln 4|k|$, so that in both cases:

$$g(z) \sim \frac{8z}{\pi^2}\frac{1}{\sqrt{(\gamma^2-\delta^2)}}\ln 4\left|\frac{\gamma^2-\delta^2}{s^2-\delta^2}\right|^{1/2}$$

or

$$g(z) \sim \frac{2z}{\pi^2}\frac{1}{(\gamma_1\gamma_2)^{1/2}}\ln 4\left|1-\frac{z^2(1-z^2)}{\gamma_1\gamma_2}\right| \tag{27}$$

this corresponds to a logarithmic singularity in the spectrum, occurring at

$$z^2 = \gamma_1 \text{ and } z^2 = \gamma_2$$

(b) $k \to 1$:

We use equation (21) and the expansion

$$K(k) = \ln\frac{4}{\sqrt{(1-k^2)}} + \frac{1}{4}\left[\ln\frac{4}{\sqrt{(1-k^2)}}-1\right](1-k^2)^2+\ldots$$

to obtain (to first order)

$$F(z) = \frac{4z}{\pi}\frac{1}{\sqrt{(\gamma^2-\delta^2)}}\{\ln 4(s^2-\delta^2) - \ln 4(s^2-\gamma^2)\} \tag{28}$$

In this expression $s^2-\delta^2$ is positive. If $s^2 > \gamma^2$, $F(z)$ is real; when s^2 goes through the value γ^2, $s^2-\gamma^2$ become negative and $i\pi$ is added to the

bracket, so that $g(z)$ has a discontinuity

$$\frac{4z}{\pi}\frac{1}{\sqrt{(\gamma^2-\delta^2)}}:$$

$$\left.\begin{aligned} g(1+0)&=0 \qquad g(1-0)=\frac{2}{\pi}\frac{1}{(\gamma_1\gamma_2)^{1/2}} \\ g(-0)&=0 \qquad g(+0)=0 \end{aligned}\right\} \tag{29}$$

One can see in this example that although $g(\omega)$ has two different kinds of singularities—in case (a) a logarithmic one, in case (b) a discontinuity—the function $F(z)$ itself has only one kind of singularity, a logarithmic one:

$$F(z) \sim A \ln\left(1-\frac{z}{z_0}\right) \tag{30}$$

As will be shown, this is a general property of the function $F(z)$.

In the three-dimensional case, the function $F(z)$ is given by

$$F(z)=\left(\frac{1}{2\pi}\right)^3 \int_0^{2\pi}\int_0^{2\pi}\int_0^{2\pi} \frac{4z\, d\theta_1\, d\theta_2\, d\theta_3}{2z^2-1-\gamma_1\cos\theta_1-\gamma_2\cos\theta_2-\gamma_3\cos\theta_3}. \tag{31}$$

With

$$\gamma=\gamma_1+\gamma_2 \qquad \delta=\gamma_2-\gamma_1,$$

an alternative expression for $F(z)$ is

$$F(z)=\frac{8z}{\pi^2}\int_0^{\pi}\frac{d\theta}{\sqrt{[(u-\gamma_3\cos\theta)^2-\delta^2]}}K\left[\left(\frac{\gamma^2-\partial^2}{(u-\gamma_3\cos\theta)^2-\partial^2}\right)^{1/2}\right]$$

or

$$F(z)=\frac{8z}{\pi}\int_0^{\pi} d\theta K\left[\left(\frac{(u-\gamma_3\cos\theta)^2-\delta^2}{\gamma^2-\delta^2}\right)^{1/2}\right]+i\frac{8z}{\pi}\int_0^{\pi} K\left[\left\{\frac{(u-\gamma_3\cos\theta)^2-\gamma^2}{\gamma^2-\delta^2}\right\}^{1/2}\right] d\theta,$$

which is not expressible in terms of known functions.

We must notice, before leaving these examples, that in each case $g(x)$ satisfies the condition (c) of the general theorem. For the one-dimensional case

$$\int_{-x}^{+x}\frac{g(t)}{\sqrt{(1-t^2)}}\,dt$$

exists for $x=+1$. For the two-dimensional case

$$\int_{-\omega_{\max}}^{+\omega_{\max}} g(x)\,dx$$

does exist for

(a) logarithmic singularities
(b) discontinuity singularities.

GENERAL LINEAR TRANSFORMS

Equation (17) can be considered as a special case of a general linear transform of $g(\omega)$:

$$\hat{g}(y)=\int_a^b K(y|x)g(x)\,dx \quad b\geqslant+1, \quad a\leqslant-1 \tag{32}$$

In principle $\hat{g}(y)$ can always be calculated by the formula:

$$\hat{g}(y)=\frac{1}{m}\mathrm{Tr}\left(\frac{1}{2\pi}\right)^3\int_0^{2\pi}\int_0^{2\pi}\int_0^{2\pi} K(y|\Gamma)\,d\theta_1\,d\theta_2\,d\theta_3 \tag{33}$$

If we know the "inversion formula" for the kernel $K(y|x)$, it is then possible to get the function $g(x)$ itself

$$g(x)=\int_{a'}^{b'} K^{(-1)}(x|y)\hat{g}(y)\,dy$$

This leads naturally to an investigation of the Fourier and Laplace transforms of $g(x)$. The

Fourier transform was used extensively by MONTROLL[1] and $g(x)$ was derived by him for a number of cases. We shall be concerned in the next section only with Laplace transforms.

One can use an alternative formula instead of equation (33). We consider the integral

$$\frac{1}{2i\pi}\oint_C F(z)K(y|z)\,dz$$

where C is a contour encircling the spectrum, and where it is supposed that $K(y|z)$ is an analytic function of z inside and on C; its value follows from equation (17) and the Cauchy integral formula, and is precisely that given by equation (32):

$$\hat{g}(y) = \frac{1}{2i\pi}\oint_C F(z)K(y|z)\,dz \tag{34}$$

Equation (34) means that all linear integral transforms are expressible in terms of the function $F(z)$ itself and underlines anew the importance of this function in the F.D. theory.

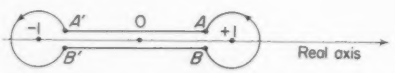

FIG. 1. Contour used in calculating the Fourier Transform of the F.D.

As an example, we can derive the Fourier transform of the 1-D F.D. In this case we have

$$F(z) = \frac{2}{\sqrt{(z^2-1)}}$$

The contour C is the contour $AA'B'B$ shown in Fig. 1. We find that

$$\frac{1}{2i\pi}\oint_C \frac{2\,dz}{\sqrt{(z^2-1)}}\exp(iyz)$$

$$= \frac{2}{2i\pi}\int_{AA'} \frac{2\,dz}{\sqrt{(z^2-1)}}\exp(iyz)$$

$$= \frac{2}{\pi}\int_{-\pi/2}^{+\pi/2} \exp(iy\cos\theta)\,d\theta = 2J_0(y),$$

where J_0 is a Bessel function.

THE LAPLACE TRANSFORM OF THE F.D.—LOW-TEMPERATURE ASYMPTOTIC EXPANSIONS

We define functions $\mathscr{L}(y)$ and $\mathscr{L}_1(y)$ by the equations:

$$\mathscr{L}(y) = \int_0^\infty \exp(-yx)g(x)\,dx \tag{35}$$

$$\mathscr{L}_1(y) = \int_0^\infty \exp(-yu)h(u)\,du \tag{36}$$

The first function is the L-transform of the spectrum itself, while the second, which is the more useful one, is the L-transform of the density $h(u)$ of the squares $u = \omega^2$ of the frequencies.

In the latter case, equation (33) gives:

$$\mathscr{L}_1(y) = \mathrm{Tr}\frac{1}{m}\left(\frac{1}{2\pi}\right)^3 \times$$

$$\times \int_0^{2\pi}\int_0^{2\pi}\int_0^{2\pi} \exp(-yC)\,d\theta_1\,d\theta_2\,d\theta_3 \tag{37}$$

For example, for a 3-D cubic lattice with constants $\gamma_1, \gamma_2, \gamma_3$,:

$$\mathscr{L}_1(y) = \left(\frac{1}{2\pi}\right)^3 \int_0^{2\pi}\int_0^{2\pi}\int_0^{2\pi} \exp\{-y[\tfrac{1}{2}-\tfrac{1}{2}(\gamma_1\cos\theta_1+\gamma_2\cos\theta_2+\gamma_3\cos\theta_3)]\}\,d\theta_1\,d\theta_2\,d\theta_3$$

$$= \exp(-\tfrac{1}{2}y)I_0(\tfrac{1}{2}\gamma_1 y)I_0(\tfrac{1}{2}\gamma_2 y)I_0(\tfrac{1}{2}\gamma_3 y). \tag{38}$$

In general this function is an entire function of y, because it can be expanded as:

$$\mathscr{L}_1(y) = \sum_{n=0}^{\infty} \frac{(-1)^n}{n!} y^n \frac{\mu_{2n}}{2}$$

and

$$\frac{\mu_{2n}}{2} \leqslant 1$$

It has furthermore an asymptotic expansion in $1/y$ for $y \to \infty$. The main interest of this asymptotic expansion is that it enables us to get an asymptotic expansion for $g(\omega)$ near $\omega = 0$. This follows from the theorem:

Theorem A

If $h(u)$ has, near the origin, an asymptotic expansion in u, of the type:

$$h(u) \sim u^{1/2}[A_0 + A_1 u + A_2 u^2 + \ldots] \quad u \text{ real} > 0 \tag{39}$$

then $\mathscr{L}_1(y)$ has an asymptotic expansion of the form:

$$\mathscr{L}_1(y) \sim y^{-1/2}\left[\frac{A_0\Gamma(\frac{3}{2})}{y} + \frac{A_1\Gamma(\frac{5}{2})}{y^2} + \ldots + \frac{A_n\Gamma(n+\frac{3}{2})}{y^{n+1}} + \ldots\right] \tag{40}$$

for $y \to +\infty$.

This theorem is a consequence of Abel's theorems in the theory of Laplace transforms.[4] The reverse theorem (a Tauberian theorem[4]) is not so easy. It says that if $\mathscr{L}_1(y)$ has an asymptotic expansion of the above type, then the primitive function of $h(u)$ has an asymptotic expansion as in equation (39). To obtain $h(u)$ we must suppose that it can be expanded in an asymptotic series. If this is so, the coefficients are given by the above formulae.

For example, for a cubic lattice with $\gamma_1 = \gamma_2 = \gamma_3 = \frac{1}{3}$, we assume for $g(\omega)$ the following expansion:

$$g(\omega) \sim a_1\omega^2 + a_2\omega^4 + a_3\omega^6 + \ldots + a_n\omega^{2n} + \ldots$$

so that

$$h(u) \sim \tfrac{1}{2}u^{1/2}[a_1 + a_2 u + a_3 u^2 + \ldots + a_n u^{n-1} + \ldots]$$

and

$$\mathscr{L}_1(y) \sim \tfrac{1}{2}y^{-1/2}\left[\frac{a_1\Gamma(\frac{3}{2})}{y} + \frac{a_2\Gamma(\frac{5}{2})}{y^2} + \ldots + \frac{a_n\Gamma(n+\frac{1}{2})}{y^n} + \ldots\right] \tag{41}$$

But from equation (38), and from the known asymptotic expansion for the Bessel function $I_0(y)$:

$$I_0(y) \sim \frac{e^y}{(2\pi y)^{1/2}}\left[1 + \sum_{r=1}^{\infty} \frac{[(2r-1)!]^2}{r!8^r y^r}\right]$$

we get for the expansion of $\mathscr{L}_1(y)$:

$$\mathscr{L}_1(y) = \left(2\pi\frac{y}{6}\right)^{-3/2}\left[1 + \sum_{r=1}^{\infty} \frac{[(2r-1)!]^2}{r!8^r(y/6)^r}\right]^3$$

and comparing this result with equation (41) we get the coefficients a_n. The final result is

$$g(\omega) = \frac{4\sqrt{(3)}m^{3/2}}{\pi^2\sqrt{(2)}\alpha^{3/2}}\omega^2 + \frac{9\sqrt{(3)}m^{5/2}}{5\pi^2\sqrt{(2)}\alpha^{5/2}}\omega^4 + \frac{513\sqrt{(3)}m^{7/2}}{140\pi^2\sqrt{(2)}\alpha^{7/2}}\omega^6 + \frac{24{,}543\sqrt{(3)}m^{9/2}}{5040\pi^2\sqrt{(2)}\alpha^{9/2}}\omega^8 + \ldots \tag{42}$$

where m is the atomic mass and α the force constant in the general case.

An asymptotic expansion of $g(\omega)$ in turn enables us to get an asymptotic expansion of the internal energy of the crystal at low temperatures, that is when $T \to 0$. The internal energy U is defined by the equation:

$$U = \int_0^{\infty} g(\omega)\left[\tfrac{1}{2}\hbar\omega + \frac{\hbar\omega}{\exp(\hbar\omega/kT)-1}\right] d\omega$$

$$= U_0 + \int_0^{\infty} \frac{\hbar\omega g(\omega)}{\exp(\hbar\omega/kT)-1}\, d\omega \tag{43}$$

where U_0 is the zero-point energy. To obtain the low-temperature asymptotic expansion for U, we use the following theorem which can be proved in

a number of ways:

Theorem B

If $g(\omega)$ has, near the origin ($\omega > 0$), an asymptotic expansion in ω of the type:

$$g(\omega) \sim a_1\omega^2 + a_2\omega^4 + \ldots + a_n\omega^{2n} + \ldots$$

then U has an asymptotic expansion for $T \to 0$, of the form:

$$U \sim U_0 + 3NkT \sum_{n=1}^{\infty} \left(\frac{2\pi kT}{\hbar}\right)^{2n+1} B_{n+1}a_n \quad (44)$$

where B_n is the n-th Bernouilli number (N is the number of atoms).

It must be recalled that the series in equation (44) is not a convergent series, but it represents the experimental results in the following way. Given a certain low temperature T, it is possible to fit experimental values of $U - U_0$ at this temperature T to any desired accuracy ϵ by taking in equation (44) a certain number, $n(T, \epsilon)$, of terms.

AN EXPRESSION FOR THE INTERNAL ENERGY OF A CRYSTAL

The internal energy U given by the equation (43) looks like a special case of equation (32), in which $K(y|x)$ is replaced by the function

$$\tfrac{1}{2}\hbar x \coth \tfrac{1}{2}\beta\hbar x,$$

which is independent of y. So, in virtue of equation (33) we can write a formal expression for the internal energy

$$U = 3N\frac{1}{m}\left(\frac{1}{2\pi}\right)^3 \mathrm{Tr.} \times$$

$$\times \int_0^{2\pi}\int_0^{2\pi}\int_0^{2\pi} (\tfrac{1}{2}\hbar\Gamma \coth \tfrac{1}{2}\beta\hbar\Gamma)\, d\theta_1\, d\theta_2\, d\theta_3, \quad (45)$$

where the integrand is a function of the matrix Γ. Since the matrix C is simpler than the matrix Γ, it is necessary to have a formula connecting this function of Γ to a function of C. Such a formula was given by DREYFUS[5]. It is

$$\frac{1}{\sqrt{(p)}} \coth \sqrt{(p)} = \int_0^{\infty} \exp(-pt)\theta_3(0, t)\, dt \quad (46)$$

where p is positive, and $\theta_3(0, t)$ is the 3rd θ-function of Jacobi of argument 0, and "parameter" t:

$$\theta_3(0, t) = \sum_{-\infty}^{+\infty} \exp(-\pi^2 n^2 t) \quad (47)$$

With the aid of these formulae and equation (37), U can be written as:

$$U = 3N \int_0^{\infty} \theta_3(0, t)\left\{-\frac{\partial}{\partial t}\mathscr{L}_1\left(\frac{\hbar^2 t}{4}\right)\right\} dt, \quad (48)$$

where $\mathscr{L}_1(y)$ is the Laplace transform of the density of the squares of the frequencies.

For example, for the cubic lattice already investigated, we obtain

$$U = 3NkT \int_0^{\infty} -$$

$$- \frac{d}{dt}\left[\exp(-t)\prod_{i=1}^{3} I_0(\alpha_i t)\right]\theta_3(0, \pi^2\gamma^2 T^2 t)\, dt$$

where

$$\gamma = \frac{2k}{\hbar}\left(\frac{m}{\alpha}\right)^{1/2}$$

m = atomic mass

$\alpha\alpha_i$ = strength constants

$$\sum_{i=1}^{3} \alpha_i = 1.$$

From this formula it is possible to evaluate $U(T)$ numerically and to investigate the deviations from the Debye law (cf. the cited paper).

Another point which follows from equation (45) is that it is not always necessary to evaluate $g(\omega)$ to get information about the thermodynamic quantities such U for a given crystal.

A METHOD FOR EVALUATING THE MOMENTS OF g(x)

As was pointed out by MONTROLL[6], if we know all the moments of $g(x)$, as defined by equation (9), one can obtain the function $g(x)$ itself. This *inversion problem* can be solved in various ways (cf. reference (6)). We shall show first that the

VOL. 12 59/60

"Legendre polynomials method" fits in particularly well with the integral equation (17) given above. Then we shall give a general method for evaluating the moments of $g(x)$.

We denote by $P_n(x)$ the n-th Legendre polynomial with x real and in the interval

$$-1 \leqslant x \leqslant +1,$$

and by $Q_n(z)$ the n-th Legendre function of second kind, where z is complex and not allowed to take real values in the interval $(-1, +1)$ (these functions are defined in WHITTAKER and WATSON[12]). These functions are connected by a formula due to Neumann:

$$Q_n(z) = \frac{1}{2}\int_{-1}^{+1} \frac{P_n(x)}{z-x}\,dx. \tag{49}$$

This formula looks like equation (17):

$$F(z) = \int_{-1}^{+1} \frac{g(x)}{z-x}\,dx.$$

If we assume that $g(x)$ can be expanded in a series of Legendre polynomials:

$$g(x) = \sum_{n=0}^{\infty} a_n P_n(x) \tag{50}$$

then, $F(z)$ is given by the series:

$$F(z) = 2\sum_{n=0}^{\infty} a_n Q_n(z). \tag{51}$$

Therefore, the problem is to expand the known function $F(z)$ in a series of Legendre function of the second kind, i.e. to calculate the coefficients a_n in equation (51).

According to the Neumann expansion, if E is an ellipse with foci at ± 1, z inside E and t on it, we have

$$\frac{1}{z-t} = \sum_{n=0}^{\infty} (2n+1) P_n(z) Q_n(t)$$

and

$$f(z) = \frac{1}{2i\pi}\oint_E \frac{f(t)}{z-t}\,dt = \sum_{n=0}^{\infty} c_n P_n(z)$$

with

$$c_n = \frac{2n+1}{2i\pi}\oint_E f(t) Q_n(t)\,dt \tag{52}$$

provided that $f(z)$ is analytic inside E.

For $f(z) = P_n(z)$ the relations (52) give:

$$\frac{2n+1}{2i\pi}\oint_C P_m(z) Q_n(z)\,dz = \delta_{m,n} \tag{53}$$

where C is a counterclockwise contour encircling the interval $(-1, +1)$. It follows from the "orthogonality" relation (53) that the a_n's are unique:

$$a_n = \frac{2n+1}{2}\,\frac{1}{2i\pi}\oint_C F(z) P_n(z)\,dz. \tag{54}$$

When we choose for C a circle with a radius greater than 1, $F(z)$ can be expressed on C by equation (10):

$$F(z) = \sum_{n=0}^{\infty} \frac{\mu_n}{z^{n+1}}.$$

If we know the coefficients $\gamma_{n,p}$ of the Legendre polynomials,

$$P_n(x) = \sum_{p=0}^{n} \gamma_{n,p} x^p$$

we get from equation (54):

$$a_n = (n+\tfrac{1}{2}) \sum_{p=0}^{n} \gamma_{n,p}\mu_p \tag{11'}$$

a formula which was used extensively by MONTROLL (cf. reference (6)).

In the formula (11') we need the moments μ_p. To calculate these quantities we use equation (10), where $F(z)$ is the function defined by:

$$F(z) = \frac{1}{2m}\left(\frac{1}{2\pi}\right)^3 \int_0^{2\pi}\int_0^{2\pi}\int_0^{2\pi} \frac{\Pi'(z,\theta_1,\theta_2,\theta_3)}{\Pi(z,\theta_1,\theta_2,\theta_3)}\,d\theta_1\,d\theta_2\,d\theta_3. \tag{15}$$

Π is a polynomial of degree $2m$ in z:

$$\Pi(z) \equiv z^{2m} + L_1 z^{2m-2} + L_2 z^{2m-4} + \ldots + L_m \tag{55}$$

where L_k's are polynomials of $\cos\theta_k$ and $\sin\theta_k$.

We shall put $w = z^{-1}$, so that

$$\Pi(z) = z^{2m}[1+f(w)] \quad \Pi'(z) = 2mz^{2m-1}G(w) \tag{56}$$

with

$$\lim_{w \to 0} G(w) = 1$$

$$|f(w)| < Aw^2 \text{ as } w \to 0,$$

where A is independent of $\boldsymbol{\theta}$. $F(z)$ can thus be written as

$$F(z) = \frac{1}{z}\left(\frac{1}{2\pi}\right)^3 \int_0^{2\pi}\int_0^{2\pi}\int_0^{2\pi} \frac{G(w)}{1+f(w)}\, d\boldsymbol{\theta}.$$

When w is sufficiently small $|f(w)| < 1$ so

$$F(z) = w \sum_{n=0}^{\infty} F_n(w) \tag{57}$$

where

$$F_n(w) = (-1)^n\left(\frac{1}{2\pi}\right)^3 \int_0^{2\pi}\int_0^{2\pi}\int_0^{2\pi} G(w) f^n(w)\, d\theta_1\, d\theta_2\, d\theta_3 \tag{58}$$

From equations (55) and (56) we see that the term of lowest degree in $f(w)$ is $L_1 w^2$, so that the degree of the term of lowest degree in $F_n(w)$ is $2n$. If we stop the summation in equation (57) at a certain value of n, we then get exactly the coefficients of $w, w^2 \ldots w^{2n+1}$ in the series (57), that is the value of the moments $\mu_1, \mu_2, \ldots \mu_{2n}$.

An even simpler way of calculating the coefficient of w^{2n+1} in $F(z)$ is to perform the division of the polynomial $G(w)$ by the polynomial $1+f(w)$ in ascending powers of w, using the elementary method of algebra textbooks.

Example. We consider the lattice corresponding to the matrix C given by equation (2) in two dimensions. We put

$$\frac{2\alpha}{M} = a \qquad \frac{4\gamma}{M} = b.$$

The characteristic polynomial $P(z)$ is:

$$P(z) = z^2 - 2Az + \Delta$$

with

$$A = a\left(1 - \frac{c_1+c_2}{2}\right) + b(1-c_1c_2)$$

$$\Delta = (a^2+2ab) - (a^2+ab)(c_1+c_2) + (a^2-2ab-b^2)c_1c_2 + b^2(c_1^2+c_2^2) + abc_1c_2(c_1+c_2) - b^2c_1^2c_2^2$$

where

$$c_1 = \cos\theta_1 \text{ and } c_2 = \cos\theta_2.$$

The expression for $F(z)$ becomes

$$F(z) = w\left(\frac{1}{2\pi}\right)^2 \int_0^{2\pi}\int_0^{2\pi} \frac{1-Aw}{1-2Aw+\Delta w^2}\, d\theta_1 d\theta_2.$$

Dividing $1-Aw$ by $1-2Aw+\Delta w^2$ in ascending powers of w, we obtain:

$$\frac{1-Aw}{1-2Aw+\Delta w^2} = 1+Aw+ (2A^2-\Delta)w^2+(4A^3-3A\Delta)w^3+ \ldots$$

In this expression μ_{2n} is the integral of the coefficient of w^{n+1}, and we see that

$$\mu_0 = 1$$

$$\mu_2 = \left(\frac{1}{2\pi}\right)^2 \int\int A\, d\theta_1 d\theta_2$$

$$\mu_4 = \left(\frac{1}{2\pi}\right)^2 \int\int (2A^2-\Delta)\, d\theta_1 d\theta_2$$

$$\mu_6 = \left(\frac{1}{2\pi}\right)^2 \int\int (4A^3-3A\Delta)\, d\theta_1 d\theta_2 \ldots$$

or, on evaluating the integrals,

$$\mu_0 = 1$$

$$\mu_2 = a+b$$

$$\mu_4 = \tfrac{1}{2}a^2+2ab+\tfrac{7}{4}b^2$$

$$\mu_6 = \tfrac{5}{2}a^3+\tfrac{9}{2}a^2b+\tfrac{15}{4}ab^2+\tfrac{5}{2}b^3.$$

SINGULARITIES OF THE SPECTRUM

The singularities of frequency spectra were investigated in special cases by MONTROLL[7] and SMOLLETT[8], and a general theory of the occurence and the nature of the singularities has been

VOL. 12 59/60

given by VAN HOVE[9] and completed by PHILLIPS[10]. The latter authors were concerned with more general lattices than the Born–Huang lattices in which the ω's are the roots of a certain algebraic polynomial. Our purpose is to show that the use of the function $F(z)$ leads to the correct results for singularities in B–H lattices and that even more information can be obtained in certain cases.

If we return to the definition of $F(z)$, equation (15), we see that singularities of F can occur only on the real axis between -1 and $+1$. Given a set $(\theta_1, \theta_2, \theta_3)$, Π is zero for certain values of z, which we call $z_k (k = 1, 2, \ldots 2m)$, but as the θ_k's vary these z_k change, except when the increment of z_k is of second order with respect to the increment of the θ_k's, that is when

$$\frac{\partial z_k}{\partial \theta_1} = \frac{\partial z_k}{\partial \theta_2} = \frac{\partial z_k}{\partial \theta_3} = 0.$$

At such a point $F(z)$ has a "singularity". As will be shown, these points are not necessarily singularities in the sense of the theory of function, so that it is better to call such points *the critical points*. Combining the preceding condition with $P(z_k^2) = 0$, we get the equations for the location of critical points:

$$P(z) = \frac{\partial P}{\partial \theta_1} = \frac{\partial P}{\partial \theta_2} = \frac{\partial P}{\partial \theta_3} = 0. \qquad (59)$$

The solutions of equation (59) consist of a certain number of sets of the four numbers $(z_c, \theta_{1c}, \theta_{2c}, \theta_{3c})$ from which the sets corresponding to $z = 0$ must be carefully excluded (the origin satisfies equation (59), but is not an ordinary critical point). For example, in the cubic lattice with nearest-neighbor interactions

$$P = z - \tfrac{1}{2}(1 + \gamma_1 \cos\theta_1 + \gamma_2 \cos\theta_2 + \gamma_3 \cos\theta_3)$$

and the system (59) is

$$2z = 1 + \gamma_1 \cos\theta_1 + \gamma_2 \cos\theta_2 + \gamma_3 \cos\theta_3$$
$$\sin\theta_1 = \sin\theta_2 = \sin\theta_3 = 0.$$

The solutions of these equations are

$$\theta_1 = \begin{matrix} 0 \\ \pi \end{matrix} \qquad \theta_2 = \begin{matrix} 0 \\ \pi \end{matrix} \qquad \theta_3 = \begin{matrix} 0 \\ \pi \end{matrix}$$

$$z = \tfrac{1}{2}[1 \pm \gamma_1 \pm \gamma_2 \pm \gamma_3],$$

from which we must exclude $\theta_1 = \theta_2 = \theta_3 = \pi$, $z = 0$.

Now let us suppose that z_c, θ_{1c}, θ_{2c}, θ_{3c} is a critical point; in its neighborhood one can generally write:

$$\Pi(z, \theta_1, \theta_2, \theta_3) = (z - z_c)\left(\frac{\partial \Pi}{\partial z}\right)_c +$$
$$+ \frac{1}{2}\sum_{i,j}\left(\frac{\partial^2 \Pi}{\partial \theta_i \partial \theta_j}\right)_c (\theta_i - \theta_{ic})(\theta_j - \theta_{jc}) +$$
$$+ \frac{1}{2}\left(\frac{\partial^2 \Pi}{\partial z^2}\right)_c (z - z_c)^2 +$$
$$+ \frac{1}{2}\sum_i \left(\frac{\partial^2 \Pi}{\partial z \partial \theta_i}\right)_c (z - z_c)(\theta_i - \theta_{ic})$$

+ higher-order terms.

We assume that Π is irreducible for general θ_k's, so that except for very particular cases, $(\partial\Pi/\partial z)_c \neq 0$. We assume on the other hand that the quadratic form in $(\theta_i - \theta_{ic})$ can be reduced to an elliptic or hyperbolic form. In the neighborhood of z_c, $(z - z_c)^2$ is of second order in comparison with $(z - z_c)$, so we can drop this term. At the same time:

$$\Pi'(z, \theta_1, \theta_2, \theta_3) = \left(\frac{\partial \Pi}{\partial z}\right)_c + (z - z_c)\left(\frac{\partial^2 \Pi}{\partial z^2}\right)_c +$$
$$+ \sum_i \left(\frac{\partial^2 \Pi}{\partial z \partial \theta_i}\right)_c (\theta_i - \theta_{ic}) + \ldots$$

where

$$\left(\frac{\partial \Pi}{\partial z}\right)_c \neq 0.$$

The domain of integration $\mathscr{D}$ in the definition of $F(z)$, equation (15), can be decomposed into several parts. We draw in the vicinity of each critical point in phase space (the coördinates of which are θ_{1c}, θ_{2c}, θ_{3c}) a small domain $\mathscr{D}_c$ containing the point c, so that

$$\mathscr{D} = \sum_c \mathscr{D}_c + \mathscr{D}',$$

where $\mathscr{D}'$ is the remaining part of $\mathscr{D}$. It is evident that for $z \sim z_c$, the integration over $\mathscr{D}'$ gives an analytic function of z, whereas $\mathscr{D}_c$ contributes to a

"critical part", which is

$$\int\int\int_{\mathscr{D}_c} \frac{d\phi_1\, d\phi_2\, d\phi_3}{(z-z_c)+a[\epsilon_1\phi_1+\epsilon_2\phi_2+\epsilon_3\phi_3]}, \qquad (60)$$

where $a>0$, $\epsilon_\alpha = \pm 1$, and $\mathscr{D}_c$ contains the origin $\phi_1=\phi_2=\phi_3=0$. This expression can be deduced rigorously from the beginning by elementary but tedious considerations which we wish to omit here. The number of negative ϵ's is called the *index* of the critical point.

In the following we give the results of the calculation for the 1-, 2- and 3-D lattices. We omit these calculations also because they are very straightforward and uninteresting.

One-dimensional case. $\mathscr{D}_c$ is the segment $(-\epsilon, +\epsilon)$; for a maximum $(i=0)$

$$F(z) = \psi(z) + \frac{\pi}{\sqrt{[a(z-z_c)]}}$$

for a minimum $(i=1)$

$$F(z) = \psi(z) + \frac{\pi}{\sqrt{[a(z_c-z)]}}.$$

Two-dimensional case. $\mathscr{D}_c$ is a circle of radius R; for a maximum $(i=0)$:

$$F(z) = \psi(z) + \frac{\pi}{a}\left[\ln\left(R^2+\frac{z-z_c}{a}\right) - \ln\frac{z-z_c}{a}\right]$$

for a saddle point $(i=1)$

$$F(z) = \psi(z) + \frac{i\pi}{a}[\ln(z-z_c) + \ln\{-iR^2a+\sqrt{(z-z_c)^2-R^4a^2}\}]$$

for a minimum $(i=2)$

$$F(z) = \psi(z) - \frac{\pi}{a}\left[\ln\left(R^2+\frac{z_c-z}{a}\right) - \ln\frac{z_c-z}{a}\right].$$

Three-dimensional case. $\mathscr{D}_c$ is a sphere of radius R for the maximum and minimum; a cylinder of radius R and height T for saddle points;

for a maximum $(i=0)$:

$$F(z) = \psi(z) + \frac{4\pi R}{a} - \frac{2\pi}{a^{3/2}}(z-z_c)^{1/2}$$

for saddle point of the first kind $(i=1)$

$$F(z) = \psi(z) + \frac{\pi}{a}[K+2i\pi a^{-1/2}(z_c-z)^{1/2}]$$

K = a constant

for a saddle point of the second kind $(i=2)$:

$$F(z) = \psi(z) - \frac{\pi}{a}[K+2\pi a^{-1/2}(z-z_c)^{1/2}]$$

for a minimum $(i=3)$

$$F(z) = \psi(z) - \frac{4\pi R}{a} + \frac{2\pi}{a^{3/2}}(z_c-z)^{1/2}.$$

In these expressions $\psi(z)$ is an analytic function of z in the vicinity of z_c. It follows from these formulae that, whatever the index is, the "critical part" of $F(z)$ depends only on the dimensionality of the lattice:

$$\left.\begin{aligned} &\text{in 1D } F(z) \text{ behaves like } (z-z_c)^{-1/2} \\ &\text{in 2D } F(z) \text{ behaves like } \ln(z-z_c) \\ &\text{in 3D } F(z) \text{ behaves like } (z-z_c)^{1/2} \end{aligned}\right\} \qquad (61)$$

Since the numerical coefficient by which these three quantities are multiplied can be real or purely imaginary according to the index, then the behavior of $g(\omega)$, which is the imaginary part of F, depends on the index. In this respect the behavior of g is more complicated than that of $F(z)$. We have already noticed this fact in a simple example.

Using the formula equation (19)

$$g(x) = -\frac{1}{\pi}\operatorname{Im} F(x+i0).$$

and the preceding results for $F(z)$ it is possible to derive exactly the results obtained by VAN HOVE[9] by a quite different method. As a particular example, let us consider a 2-D lattice.

For a maximum we have:

$$g(x) = C + \frac{1}{a}\operatorname{Im}\ln\frac{x-z_c}{a} = \begin{cases} C & x > z_c \\ C+\dfrac{\pi}{a} & x < z_c \end{cases}$$

for a minimum:

$$g(x) = C - \frac{1}{a}\operatorname{Im}\ln\frac{z_c-x}{a} = \begin{cases} C+\dfrac{\pi}{a} & x > z_c \\ C & x < z_c \end{cases}$$

for a saddle point:

$$g(x) = C - \mathrm{Im}\left[\frac{i}{a}\ln(x-z_c)\right]$$

$$= C - \frac{1}{a}\ln|x-z_c| \qquad x \lesssim z_c.$$

The behavior of $F(z)$ near critical points condensed in the formulae (61) shows that this function is a multiform function, the critical points being branch points. This apparently contradicts the definition (15), which for a given z gives a unique value $F(z)$, provided that z is not real between $(-1, +1)$. In fact, the formula (15) gives only one branch of the function: this branch is uniform in the whole z-plane cut by the line $(-1, +1)$; on the other hand if z goes from z_0 in the upper half-plane to z_1 in the lower half-plane, crossing the line $(-1, +1)$ "around" a critical point, the numerical value of the function which is $F(z_0)$ at z_0, becomes $F_{II}(z_1)$ at z_1, different from $F(z_1)$; $F_{II}(z)$ is a second branch of the function. This situation can be illustrated by Fig. 2. The study of

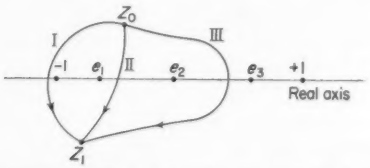

FIG. 2. Diagram illustrating the many-valued nature of the function $F(z)$, e_1, e_2, e_3: critical points. Starting from Z_0, the value of the function F is at Z_1: $F(Z_1)$ along the path I, $F(Z_1)_{II}$ along the path II, $F(Z_1)_{III}$ along the path III.

critical points by a local investigation has given the important result that $F(z)$ is always a multiform function. In view of this we must now study $F(z)$ as a whole. This investigation can be carried out for a 1-D and a 2-D lattice.

ANALYTICAL PROPERTIES OF THE FUNCTION F(z) FOR A ONE-DIMENSIONAL LATTICE

We suppose here that $F(z)$ is the function corresponding to the polynomial P instead of Π:

$$F(z) = \frac{1}{2\pi}\int_0^{2\pi} \frac{\frac{\partial}{\partial z}P(z, \cos\theta, \sin\theta)}{P(z, \cos\theta, \sin\theta)}\, d\theta. \qquad (62)$$

We replace the integration over the segment $(0, 2\pi)$ by an integration over the unit circle (C) in the complex ζ-plane, by the change of variable:

$$\zeta = \exp(i\theta). \qquad (63)$$

If α is the degree of P in $\sin\theta$, $\cos\theta$, the expression

$$Q(z, \zeta) = \zeta^{\alpha} P\left[z, \tfrac{1}{2}(\zeta+\zeta^{-1}), \frac{1}{2i}(\zeta-\zeta^{-1})\right] \qquad (64)$$

is a polynomial in z and ζ, the degree of which is 2α with respect to ζ.

In equation (62) the integrand becomes:

$$\frac{P'}{P} = \frac{\frac{\partial}{\partial z}Q(z, \zeta)}{Q(z, \zeta)}. \qquad (65)$$

The value of the integral (62) depends on the zeroes of $Q(z, \zeta)$ in the ζ-plane, which are inside the circle (C). These zeroes have the following properties:

Given a certain value of z, the algebraic equation:

$$Q(z, \zeta) = 0 \qquad (66)$$

has 2α roots ζ_k $(k = 1, 2 \ldots 2\alpha)$, which are continuous functions of z, except when

$$Q(z, \zeta) = 0 \qquad \frac{\partial}{\partial \zeta}Q(z, \zeta) = 0. \qquad (67)$$

These values of (z, ζ) will be called critical points of Q, when they satisfy equation (67). For a non-critical value of z, one can divide the 2α distinct roots into two classes:

α_1 roots are inside the circle C (inside class)
α_0 roots are outside the circle C (outside class).

We must also classify the critical points. In order that a root ζ_k be of modulus unity, that is $\zeta_k = \exp(i\theta)$, it is necessary that the equation

$$P(z, \cos\theta, \sin\theta) = 0$$

have a solution, that is z must be real and between 0 and 1 (the only roots of P, for a given θ, are real positive and less than (maximum frequency)^2 = 1). The critical point (z, ζ) of Q will be said to be of the *first kind* if $|\zeta| = 1$, which means that z is on the real axis between 0 and 1. The other critical points of Q will be called of the *second kind*. They

correspond to the cases where two "inside" roots of Q are equal.

We wish to investigate the properties of $F(z)$ when z moves along different paths in the z plane. We always start from an "initial value" z. Let us call $\zeta_1, \zeta_2 \ldots$ the "inside" roots of Q corresponding to the initial value z. Then from the residue theorem, we have:

$$F(z) = R(z, \zeta_1)+R(z, \zeta_2)+ \ldots +R(z, \zeta_{\alpha t}) \quad (68)$$

where

$$R(z, \zeta) = \frac{\dfrac{\partial}{\partial z}Q(z, \zeta)}{\dfrac{\partial}{\partial \zeta}Q(z, \zeta)} \quad (69)$$

is a rational function of z and ζ. We shall call the right-hand side of equation (68) $F_0(z)$. From equations (68) and (69) one can see that $F_0(z)$ is an analytic function of z, except at critical points. $F(z)$ and $F_0(z)$ are equal only in a certain domain containing the initial value z, the extent of which is to be discussed below. Outside such a domain $F_0(z)$ must be considered as an analytical continuation of $F(z)$.

The properties of $F_0(z)$ are the following. If z starting from its initial value describes a closed path enclosing no critical point in the z-plane, the ζ_k's describe closed paths and return to their original values; each term in $F_0(z)$ returns to the same value, and hence so does F_0 itself. If z describes in the z-plane a closed path around one critical point of second kind, a certain number of ζ_k are exchanged among themselves, while the others regain their initial values. This exchange leaves the two classes separately invariant; it corresponds only to an exchange among the terms of F_0. So F_0 is invariant by this circuit. Finally, when z describes a closed path around a critical point of the first kind, certain "inside" roots are exchanged with corresponding "outside" roots, and F_0 has a different value when z has returned to its initial value. F_0 is a multi-form function and the critical points of first kind are the only branch points of this function.

To see what are these important critical points of first kind, we put

$$u = \tfrac{1}{2}(\zeta+\zeta^{-1}) \qquad v = \frac{1}{2i}(\zeta-\zeta^{-1})$$

so that

$$\frac{\partial Q}{\partial \zeta} = \frac{1}{\zeta}Q+\zeta^{\alpha}\left[\frac{\partial P}{\partial u}\tfrac{1}{2}(1-\zeta^{-2})+\frac{\partial P}{\partial v}\frac{1}{2i}(1+\zeta^{-2})\right].$$

At a critical point of first kind

$$\frac{\partial P}{\partial u}\tfrac{1}{2}(\zeta-\zeta^{-1})+\frac{\partial P}{\partial v}\frac{1}{2i}(\zeta+\zeta^{-1}) = 0 \qquad \zeta = \exp(i\theta)$$

or

$$P(z, \cos\theta, \sin\theta) = 0 \qquad \frac{\partial P}{\partial \theta} = 0 \quad (70)$$

The critical points of the first kind are precisely the critical points of the spectrum as defined by equation (59). If z describes a certain closed path around a critical point of first kind twice, the ζ_k's in general regain their initial values because, generally, the multiple roots of $Q(z, \zeta) = 0$ are only double roots. Thus, the critical points are of order two, that is, around each critical point $F_0(z)$ is only double-valued. We can summarize the foregoing by saying:

"The function $F_0(z)$ is multiform and admits the critical points of the spectrum as the only branch points which are of order two."

From equations (68) and (69) it is evident that the only possible singularities are the poles of $R(z, \zeta)$ which occur at

$$\frac{\partial}{\partial \zeta}Q(z, \zeta) = 0 \qquad Q(z, \zeta) = 0$$

that is at critical points. In fact, critical points of second kind are not poles, because when z approaches such a point, say z_0, two roots ζ_i and ζ_j (or some other even number) approach the same value ζ_0 (double root), in such a way that:

$$\lim_{z \to z_0} (\zeta_i-\zeta_0)+(\zeta_j-\zeta_0) = 0.$$

It follows that:

$$\lim_{z \to z_0} R(z, \zeta_i)+R(z, \zeta_j) = 0,$$

that is, the two poles of $R(z, \zeta_i)$ and $R(z, \zeta_j)$ cancel. The only remaining poles for $F_0(z)$ are, then, the critical points of the first kind. In general, critical points are only double roots of Q, that is simple roots of $\partial Q/\partial \zeta$, and thus simple poles of R. So, around each critical point of the first kind,

e_j, $F_0(z)$ has the following Laurent-expansion:

$$F_0(z) = \frac{M_{-1}}{(z-e_j)^{1/2}} + \sum_{k=0}^{\infty} M_k (z-e_j)^{k/2}. \quad (71)$$

As F_0 is the analytical continuation of F, we see from this equation that F behaves like $(z-e_j)^{-1/2}$ in the vicinity of the critical points of the spectrum, a result derived in a different way in the preceding pages.

On the other hand if p is the number of critical points, the function $F_0(z)$ has 2^p branches of algebraic kind. By a well-known theorem, $F_0(z)$ itself is an algebraic function, that is, there exists a polynomial $E(x, y)$ in x, and y, such that

$$E[z, F(z)] = 0. \quad (72)$$

If we know this polynomial then the problem of calculating the F.D. is reduced to the evaluation of the roots of a polynomial.

In fact the simplicity of the Riemann surface R of $F_0(z)$ enables us to have a more straightforward method. Let us call $\{v\}$ the set of functions:

$$v_k = (z-e_k)^{-1/2} \qquad k = 1, 2 \ldots p \quad (73)$$

and $\{V\}$ the set

$$V_{\alpha_1 \alpha_2 \ldots \alpha_p} = v_1^{\alpha_1} v_2^{\alpha_2} \ldots v_p^{\alpha_p} \quad (74)$$

where the α's are zero or one. The sets $\{v\}$ and $\{V\}$ have the same Riemann surface as F. Each v_k has two values, which we shall call ${}_{\pm}v_k$; each V has then 2^p values which we denote by

$$V^{\pm, \pm, \ldots \pm}_{\alpha_1, \alpha_2, \ldots \alpha_p} = {}_{\pm}v_1^{\alpha_1} {}_{\pm}v_2^{\alpha_2} {}_{\pm}v_3^{\alpha_3} \ldots {}_{\pm}v_p^{\alpha_p}.$$

To an arbitrary branch of $F_0(z)$ we associate the product $(++++)$. When z describes any closed path this product is replaced by another, and this branch of F_0 is replaced by another branch. We associate, therefore, this product with this branch of $F_0(z)$. If we call $F_{0 \pm\pm \cdots \pm}$ the branch associated with $V^{\pm\pm \cdots \pm}$, the system:

$$F_{0 \pm\pm \ldots \pm} = \sum_{(\alpha)} A_{\alpha_1 \alpha_2 \ldots \alpha_p} V^{\pm\pm \ldots \pm}_{\alpha_1 \alpha_2 \ldots \alpha_p} \quad (75)$$

of 2^p linear equations in the A's defines a system of 2^p functions $A(z)$. These functions are analytic everywhere on R except at the points e_k, where they can have a finite number of poles. It can be proved that they are uniform on the z plane. It follows from the fundamental theorem of meromorphic functions that the A's are rational functions.

In any finite domain of the complex plane (z) their only possible singularities are poles at $\{e^j\}$. But if one A has a simple pole at e_j it would contradict equation (71). So the A are polynomials. The degrees of these polynomials are limited because all the branches of the function $F_0(z)$ are bounded when $z \to \infty$. This can be proved by considering its definition, equation (68). When $z \to \infty$, α_0 roots of Q go to infinity like $z^{1/\alpha}$, the α_i others go to zero; so for the inside roots

$$\frac{\partial}{\partial z} Q(z, \zeta) \sim z^{m-1} \qquad \frac{\partial}{\partial \zeta} Q(z, \zeta) \sim z^m$$

and

$$R(z, \zeta) \sim \frac{1}{z}$$

for the outside roots:

$$\frac{\partial}{\partial z} Q(z, \zeta) \sim z^{m-1} z^{2\alpha/\alpha} \qquad \frac{\partial}{\partial \zeta} Q(z, \zeta) = z^{m-1} z^{2\alpha - 1/\alpha}$$

and

$$R(z, \zeta) = z^{1/\alpha}/z.$$

So all the 2α $R(z, \zeta_k)$ are bounded when $z \to \infty$. So are all the branches of $F_0(z)$. It follows from this that each product $A_{\alpha_1 \alpha_2 \ldots \alpha_p} \times V_{\alpha_1 \alpha_2 \ldots \alpha_p}$ is bounded when $z \to \infty$ so that the degree r of A cannot be more than

$$\frac{1}{2} \sum_{k=1}^{p} \alpha_k:$$

$A_{00 \ldots 0}$; $A_{00 \ldots 010 \ldots 0}$ are constants

$A_{10 \ldots 010 \ldots 0}$; $A_{11100 \ldots 00}$ are linear functions of z, etc.

The function $F(z)$ is therefore determined apart from a certain number of numerical constants (one for each $A_{0,0 \ldots 0,1,0 \ldots 0}$; two for $A_{1,0, \ldots 0,1,0 \ldots 0}$ etc.), the total number of which is:

$$N = 2^{p-2}(p+3). \quad (76)$$

Acknowledgements—The author wishes to express his grateful thanks to Professor E. W. MONTROLL who gave him the opportunity to investigate this problem and to Professor A. A. MARADUDIN for helpful reading of the manuscript and many enlightening discussions on the subject.

REFERENCES

1. MONTROLL E. W., *J. Chem. Phys.* **10,** 218 (1942); **11,** 481 (1943); **12,** 98 (1944).
2. MONTROLL E. W., *loc. cit.*
3. MONTROLL E. W., *Proceedings of the Third Berkeley Symposium* Vol. III, p. 216, Eqs. (3.21) and (3.22).
4. DOETSCH G., *Handbuch der Laplace Transformation* Teil I, Kap. 15 and II, Kap. 3, p. 45 and Teil I, Kap. 16, p. 511.
5. AYANT Y., DREYFUS B. and PERETTI J., *C.R. Acad. Sci. Paris* **244,** 1898 (1957).
6. MONTROLL E. W., *J. Chem. Phys.* **10,** 218 (1942); **11,** 481 (1943).
7. MONTROLL E. W., *J. Chem. Phys.* **15,** 575 (1947).
8. SMOLLETT M., *Proc. Phys. Soc.* A**65,** 109 (1952).
9. VAN HOVE L., *Phys. Rev.* **89,** 1189 (1953).
10. PHILLIPS J. C., *Phys. Rev.* **104,** 1263 (1956).
11. TITCHMARSH E. C., *Introduction to the Theory of Fourier Integrals*, pp. 119–151. Oxford University Press (1948).
12. WHITTAKER E. T. and WATSON G. N., *Modern Analysis*. Cambridge University Press (1940).

VO
1
1959/

J. Phys. Chem. Solids Pergamon Press 1960. Vol. 12. pp. 233–244. Printed in Great Britain.

DAS ULTRAROTE SPEKTRUM DES *U*-ZENTRUMS

G. SCHAEFER*

(*Received* 8 *June* 1959)

II. Physikalisches Institut der Technischen Hochschule, Stuttgart

VOL. 12 59/60

Abstract—For the first time, the infra-red vibration absorption of a point imperfection in alkali halides, the *U*-center, has been measured. The frequency ν corresponding to the absorption maximum depends upon the lattice spacing and, in a first approximation, is given by the equation $h\nu d^2 =$ const. For the examined crystals the wavelength of the absorption maximum lies in the range between 17·75 μ (NaCl) and 27·65 μ (RbI).

The absorption lines show a marked narrowing if the crystal is cooled from room temperature to 57°K. The half width decreases to about one tenth and is then of the order of magnitude 10^{-3} eV.

For KCl and KBr at low temperatures, an oscillator strength of about 0·5 could be determined.

Zusammenfassung — Für ein Störzentrum der Alkalihalogenidkristalle, das *U*-Zentrum, konnte erstmalig eine ultrarote Schwingungsabsorption nachgewiesen werden. Die Lage ihres Maximums hängt von der Gitterkonstanten ab und ist in erster Näherung durch die Gleichung $h\nu d^2 =$ Const. gegeben. Für die untersuchten Kristalle liegt das Maximum im Bereich von 17,75 μ (NaCl) bis 27,65 μ (RbJ).

Die Absorptionskurven zeigen bei der Abkühlung des Kristalls von Zimmertemperatur auf 57°K eine erhebliche Verschärfung. Die Halbwertsbreite nimmt auf etwa 1/10 ab und liegt dann in der Grössenordnung von 10^{-3} eV.

Für KCl und KBr konnte bei tiefen Temperaturen eine Oszillatorenstärke von ungefähr 0,5 ermittelt werden.

1. EINLEITUNG

(*a*) *Allgemeines*

Die optischen Eigenschaften von atomaren Fehlstellen in Alkalihalogenidkristallen sind schon seit langem der Gegenstand von Untersuchungen in der Festkörperphysik. Namentlich die im sichtbaren und ultravioletten Bereich liegenden Banden der Elektronenanregung wurden in einer Reihe von Arbeiten eingehend untersucht, als deren Ergebnis jetzt der Zusammenhang einer Zahl von Störzentren mit den ihnen entsprechenden Absorptionsbanden gesichert scheint. Eine Zusammenfassung wurde von F. Seitz[1] gegeben.

Es erhob sich nun die Frage, wie sich Gitterstörungen auf die im Ultrarot liegenden Eigenschwingungen der Ionenkristalle auswirken. Man darf erwarten, dass die Kenntnis des Schwingungsspektrums das Verständnis der Elektronenbanden erleichtert. Die vorliegende Arbeit soll einen ersten Beitrag zu diesem Thema leisten.

Aus der Vielzahl der bekannten Störzentren der Alkalihalogenide wurden zunächst die im Ultravioletten eingehend untersuchten *U*-Zentren ausgewählt, die experimentell gut zu handhaben sind.[2–5]. Es sind dies in einfacher Beschreibung H^--Ionen, die sich in Anionenlücken befinden (Abb. 1).

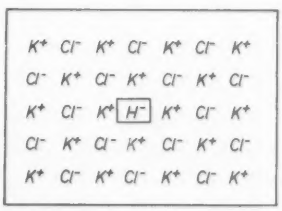

Abb. 1.

(*b*) *Die ultrarote Eigenfrequenz*

Um etwas darüber aussagen zu können, wie sich Störungen eines idealen Gitters auswirken, ist es zweckmässig, zunächst das ungestörte Gitter zu

* Dissertation, Stuttgart 1959.

betrachten. BORN[6] behandelte das Problem in der nach ihm benannten Gittertheorie zunächst am Modellfall der linearen Kette und erweiterte die Rechnung dann auf den dreidimensionalen Fall.

Für die ultrarote Eigenfrequenz eines 2-atomigen Gitters gilt:

$$\omega^2 = \frac{\beta_0}{\mu_0} \tag{1}$$

wobei β_0 die Kraftkonstante des Gitters und μ_0 die reduzierte Masse der Elementarzelle bedeuten. Dieses ideale Gitter sei durch Substitution einer geringen Zahl von Anionen gestört, deren Masse klein ist gegen die der Wirtsgitterionen. Bei den folgenden Untersuchungen wurden für die Substitution H^--Ionen gewählt. Für kleine Störmassen entstehen dann Eigenfrequenzen ω_s. Nach E. FUES, H. STUMPF[16] und E. W. MONTROLL und R. B. POTTS[17] gilt näherungsweise:

$$\frac{\omega_s^2}{\omega_0^2} = \frac{\mu_0 \beta_s}{\mu_s \beta_0} \tag{2}$$

β_s ist die Kraftkonstante in unmittelbarer Nachbarschaft des Störatoms, μ_s ist die effektive Masse der gestörten Elementarzelle. Nimmt man $\beta_s = \beta_0$ an, dann gilt

$$\frac{\omega_s}{\omega_0} = \sqrt{\frac{\mu_0}{\mu_s}} \tag{3}$$

Daraus folgt für die Wellenlänge der Eigenschwingung

$$\lambda_s = \lambda_0 \sqrt{\frac{\mu_s}{\mu_0}}$$

Für KCl hat man folglich unter der Annahme $\beta_s = \beta_0$

$$\lambda_s = 16{,}5\,\mu$$

zu erwarten.

2. VERSUCHSANORDNUNG

Als Versuchssubstanzen wurden Einkristalle verschiedener Alkalihalogenide verwendet, die nach bekannten Verfahren aus p.a.-Material von Merck in Porzellantiegeln an Luft aus der Schmelze gezogen und hydriert wurden.[3,7]

Für die Messungen der Absorption stand ein Perkin–Elmer-Ultrarotspektrometer Modell 21 mit einem CsBr-Prisma im Doppelstrahlbetrieb zur Verfügung. Der Versuchskristall wurde mit einem Glaskühltopf in den Strahlengang gebracht. Das Gefäss konnte evakuiert und der Kristall dann auf tiefe Temperatur gebracht werden. Die Fenster bestanden aus einkristallinen KBr-Scheiben von ca. 8 mm Dicke, deren Oberflächen Spaltflächen waren. Da ihre Eigenabsorption, wie auch die der untersuchten Kristallstücke, vor allem im ferneren Ultrarot merklich zu werden begann, wurden KBr-Scheiben gleicher Dicke und ein dem Versuchskristall gleicher ohne *U*-Zentren in den Vergleichsstrahlengang gebracht, der ausserhalb des Kühltopfes verlief. Dadurch wurden Reflexionsverluste und die Einflüsse der Grundsubstanz eliminiert. In Fällen, wo es nicht gelang, exakt dieselbe Schichtdicke des Vergleichskristalls herzustellen, macht sich dies in einer leichten Neigung der Basislinie für vollständige Durchlässigkeit (gestrichelte Linie in den Abb. 2a–2c) bemerkbar. Das gilt vor allem für Kristalle, deren Eigenabsorption im untersuchten Bereich bereits stark ist. Auch war die Kompensation nicht für alle Temperaturen gleich gut, da der Vergleichskristall auf Zimmertemperatur blieb. während sich die Eigenabsorption des untersuchten Kristalls mit abnehmender Temperatur zu kürzeren Wellen verschob.

Die Registriergeschwindigkeit wurde in der Nähe der Banden so klein wie möglich gewählt. Registriert wurde die Durchlässigkeit linear über einer Wellenlängenskala. Ein automatisches Spaltprogramm variierte die Spaltbreite so, dass die aus dem Monochromator austretende Energie über alle Wellenlängen gleich blieb. Die Kristalldicke wurde möglichst so gewählt, dass die minimale Durchlässigkeit zwischen 30 und 60 Prozent lag; in diesem Bereich waren die Messungen am zuverlässigsten.

Aus apparativen Gründen konnten nur Kristalle untersucht werden, bei denen die Konzentration der *U*-Zentren in der Grössenordnung von 10^{17} cm^{-3} lag. Diese Konzentration wurde durch Messung der ultravioletten Absorptionsbande bestimmt. Aus dem Höchstwert der Absorptionskonstanten und der Halbwertsbreite der *U*-Bande lässt sich nach der von SMAKULA angegebenen Formel die Konzentration der *U*-Zentren berechnen.[8] Eine Zusammenstellung der erforderlichen Zahlenwerte für alle Alkalihalogenidkristalle findet sich in der Abhandlung von F. STÖCKMANN

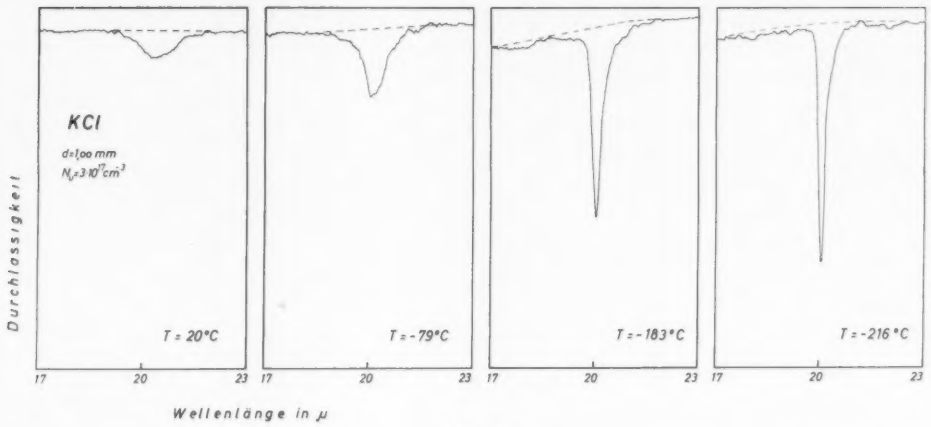

ABB. 2a.

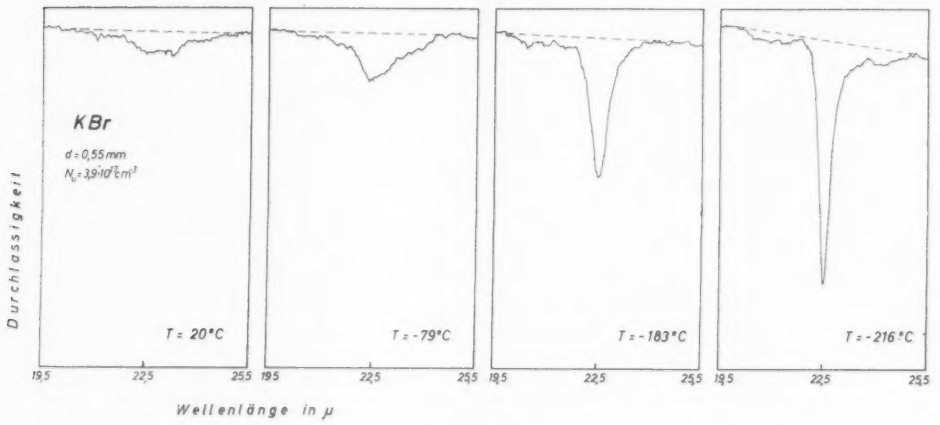

ABB. 2b.

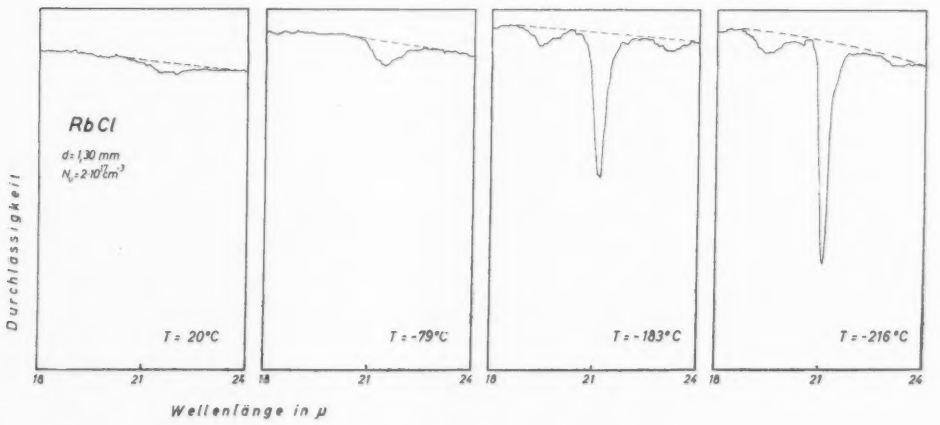

ABB. 2c.

VOL. 12 59/60

im Tabellenwerk von LANDOLT–BÖRNSTEIN[9]. Die Messungen im Ultravioletten wurden mit dem Monochromator M 4 Q II S von Zeiss durchgeführt.

3. EXPERIMENTELLE ERGEBNISSE

(a) Die ultraroten Absorptionsspektren in Abhängigkeit von der Temperatur

Als Beispiel sind in den Abb. 2a–2c typische Originalregistrierkurven gezeigt, wie sie bei den Untersuchungen an KCl, KBr und RbCl für die Temperaturen 20°C, − 79°C, − 183°C und − 216°C erhalten wurden.

Es ist jeweils der Teil des Spektrums zu sehen, in dem eine erkennbare Absorption auftritt. Die Durchlässigkeit ist linear über einer Wellenlängenskala registriert. Die gestrichelte Linie gibt die Durchlässigkeit 100 Prozent an. Die Kristalldicke ist mit *d*, die Konzentration der durch UV-Messungen ermittelten *U*-Zentren mit *Nv* bezeichnet.

Bei Zimmertemperatur ergaben sich sehr breite und flache Banden, von denen nur die im kurzwelligen UR liegenden noch mit Sicherheit festgestellt und ausgemessen werden konnten. Die Abkühlung des Versuchskristalls auf die Temperatur des flüssigen Sauerstoffs bringt eine erhebliche Verschärfung und Erhöhung der Banden mit sich, wie die Abb. 2a, 2b, 2c zeigen.

In der folgenden Tabelle 1 sind die Mittelwerte der bei vielen Messungen gewonnenen experimentellen Daten für die vier verschiedenen Temperaturen zusammengestellt.

Spalte 1 enthält die Gitterkonstanten bei Zimmertemperatur. Die Werte wurden den *Crystal Structures*[10] entnommen. In Spalte 2 wurden diese Werte auf die Temperatur des flüssigen Sauerstoffs reduziert. Die Umrechnung erfolgte mit Hilfe des mittleren thermischen Ausdehnungskoeffizienten, der für die Bereiche −184°C bis −79°C und −79°C bis 0°C in einer Tabelle vorlag[11] und durch Einzelangaben ergänzt wurde. Die Spalten 3a–d enthalten die Lage des Absorptionsmaximums für 20°C, −79°C, −183°C und −216°C jeweils in μ und darunter in eV, während in den Spalten 4a–d die zugehörigen Halbwertsbreiten aufgeführt sind. Der angegebene Fehler ist der aus den Einzelmessungen ermittelte mittlere Fehler. Er ist in den Spalten a wegen der Unsicherheit in der Ablesung des Maximums bei den flachen Kurven grösser als bei *c* und *d*; bei *b* war zwar die Ablesung sicherer, doch lagen hier weniger Messwerte vor.

Tabelle 1.

① Substanz	② Gitterkonstante bei 20°C [Å]	③ Gitterkonstante bei −183,2°C [Å]	④ Lage der ultraroten Absorptionsbande bei ⓐ +20°C	ⓑ −79°C	ⓒ −183°C	ⓓ −216°C	⑤ Halbwertsbreite bei ⓐ +20°C	ⓑ −79°C	ⓒ −183°C	ⓓ −216°C	Masseinheiten
NaCl	5,640	5,600	17,97 ± 0,03 6,89 ± 0,01		17,78 ± 0,02 6,96 ± 0,01	17,76 ± 0,02 6,97 ± 0,01	1,35 ± 0,1 0,52 ± 0,04		0,28 ± 0,02 0,11 ± 0,01	0,17 ± 0,01 0,07 ± 0,005	μ 10^{-2} eV
NaBr	5,973	5,926	20,27 ± 0,05 6,11 ± 0,02		20,16 ± 0,03 6,14 ± 0,01	20,15 ± 0,03 6,14 ± 0,01	2,75 ± 0,2 0,83 ± 0,06		0,75 ± 0,05 0,23 ± 0,02	0,41 ± 0,04 0,12 ± 0,01	μ 10^{-2} eV
KCl	6,293	6,250	20,25 ± 0,03 6,11 ± 0,01	20,17 ± 0,04 6,14 ± 0,01	20,02 ± 0,02 6,18 ± 0,01	20,00 ± 0,02 6,19 ± 0,01	1,25 ± 0,15 0,38 ± 0,04	0,65 ± 0,05 0,20 ± 0,02	0,25 ± 0,01 0,08 ± 0,005	0,15 ± 0,01 0,05 ± 0,005	μ 10^{-2} eV
KBr	6,600	6,553	22,75 ± 0,04 5,44 ± 0,01	22,58 ± 0,06 5,48 ± 0,02	22,49 ± 0,03 5,50 ± 0,01	22,46 ± 0,02 5,51 ± 0,01	2,9 ± 0,15 0,69 ± 0,04	1,25 ± 0,05 0,30 ± 0,01	0,50 ± 0,02 0,12 ± 0,005	0,3 ± 0,02 0,07 ± 0,005	μ 10^{-2} eV
KJ	7,064	7,006	25,75 ± 0,05 4,81 ± 0,01		26,44 ± 0,04 4,68 ± 0,01	26,39 ± 0,04 4,69 ± 0,01	5,6 ± 0,2 1,06 ± 0,04		1,1 ± 0,05 0,20 ± 0,01	0,7 ± 0,05 0,12 ± 0,01	μ 10^{-2} eV
RbCl	6,581	6,537	21,60 ± 0,1 5,73 ± 0,02	21,35 ± 0,05 5,80 ± 0,01	21,12 ± 0,03 5,86 ± 0,01	21,07 ± 0,02 5,88 ± 0,01	4,3 ± 0,15 1,15 ± 0,04	0,85 ± 0,1 0,23 ± 0,03	0,35 ± 0,05 0,10 ± 0,01	0,25 ± 0,05 0,07 ± 0,01	μ 10^{-2} eV
RbBr	6,854	6,807	24,2 ± 0,1 5,11 ± 0,02		23,66 ± 0,05 5,23 ± 0,01	23,53 ± 0,03 5,26 ± 0,01	6,15 ± 0,2 13,2 ± 0,04		0,77 ± 0,03 0,17 ± 0,01		μ 10^{-2} eV
RbJ	7,342	7,283			27,75 ± 0,05 4,46 ± 0,01	27,65 ± 0,05 4,48 ± 0,01			2,5 0,40	1,85 0,30	μ 10^{-2} eV

(b) Lage der Absorptionsmaxima und Gitterkonstante

In Abb. 3 findet man die energetische Lage des Absorptionsmaximums über der Gitterkonstanten in doppelt logarithmischem Massstab für zwei Temperaturen aufgetragen. Hierbei liegen die zu Kristallen mit demselben Kation gehörigen Messwerte auf einer Geraden. Der Zusammenhang zwischen der Quantenenergie des Absorptionsmaximums $h\nu$ und der Gitterkonstanten d lässt sich damit als eine Funktion der Form

$$h\nu d^x = C \qquad (4)$$

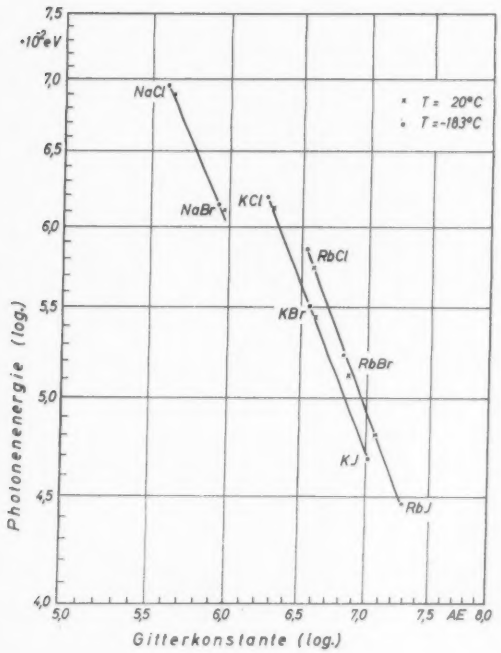

ABB. 3.

darstellen, wobei man folgende Zahlenwerte erhält:

Na-Salze $x = 2{,}22$
$C = 3{,}2$ eV AE^x
K-Salze $x = 2{,}28$
$C = 4{,}0$ eV AE^x
Rb-Salze $x = 2{,}53$
$C = 6{,}8$ eV AE^x
Mittelwert des Exponenten
$\bar{x} = 2{,}3$

Die Frequenz des Absorptionsmaximums hängt also von der Gitterkonstanten ab, und zwar in etwa derselben Weise wie beim *F*-Zentrum, für das MOLLWO[12] empirisch die Beziehung

$$h\nu d^2 = C \qquad (5)$$

gefunden hatte. Auch dort ist der Exponent 2 nur ein Mittelwert, für den man genauer 1,84 schreiben muss[13]. Ausserdem streuen die Punkte, namentlich für die Rb-Salze, wie die zusammenfassende Darstellung von H. PICK[14] (S.7) zeigt.

Bemerkenswert ist, dass (mit Ausnahme von KJ bei 20°C) auch die Temperaturabhängigkeit der Bandenlage durch dieselben Geraden erfasst wird.

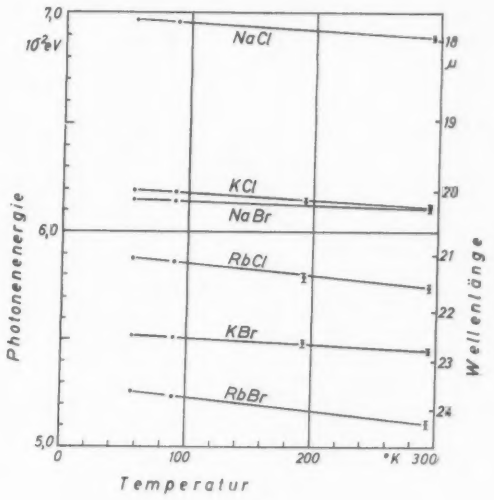

ABB. 4.

Hierin zeigt sich ein sehr wesentlicher Unterschied gegenüber dem Verhalten der elektronischen Absorptionsbande des *U*-Zentrums, bei dem die Verschiebung des Maximums mit der Temperatur wesentlich stärker ist als sich aus der Temperaturabhängigkeit der Gitterkonstanten ergibt. Ausführlicher ist die Verschiebung des Maximums mit abnehmender Temperatur in Tabelle 1 und Abb. 4 aufgeführt. Der Temperaturkoeffizient dieser Verschiebung liegt für alle Substanzen in derselben Grössenordnung und hat für KC1 den Wert

$$\frac{\Delta(h\nu)}{\Delta T} = 3{,}4 \cdot 10^{-6} \text{ eV/Grad.}$$

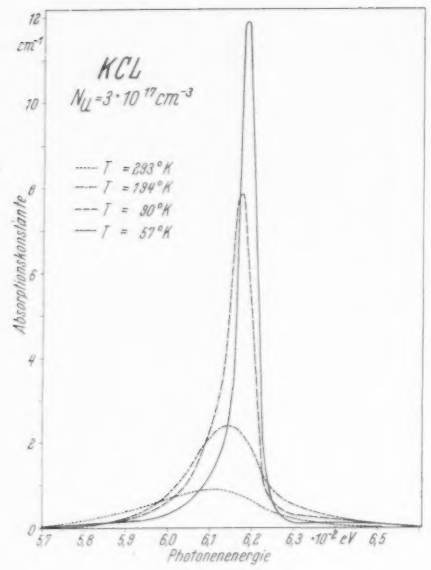

Abb. 5a.

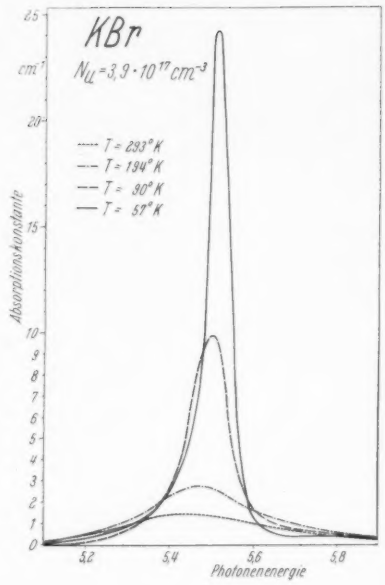

Abb. 5b.

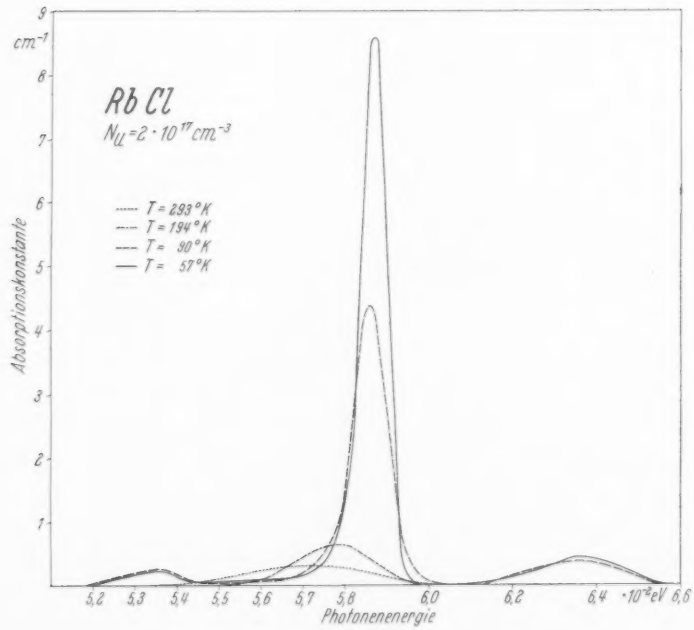

Abb. 5c.

VOL. 12 59/60

(c) Die Halbwertsbreite

Den Abb. 2a–2c konnte schon entnommen werden, dass sich die Halbwertsbreite der Absorptionskurven stark mit der Temperatur ändert. Für eine quantitative Betrachtung deutlicher tritt dieses Ergebnis in den Abb. 5a–5c hervor, in denen die Absorptionskonstante über der Photoenenergie aufgezeichnet ist.

Aus diesen Absorptionskurven (Abb. 5a–5c) entnimmt man die Halbwertsbreiten. Sie sind in den Spalten 4a–d der Tabelle 1 zusammengestellt und in Abb. 6 über der Temperatur aufgetragen.

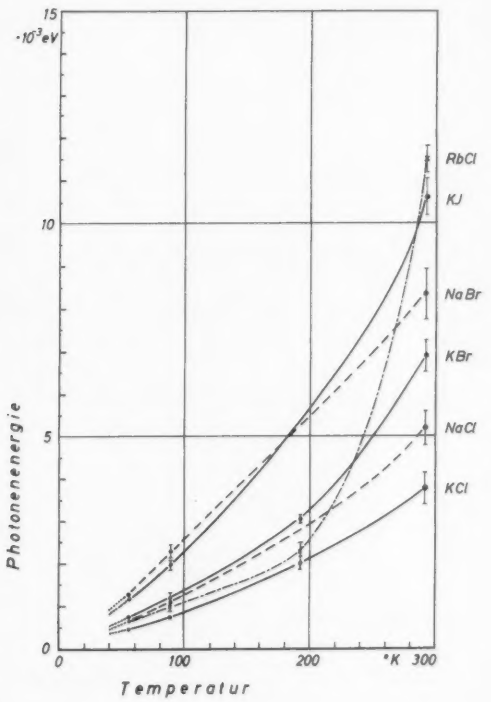

ABB. 6.

Die Messpunkte sind durch die eingezeichneten Kurven verbunden. Ihr Verlauf lässt sich noch nicht genau angeben, da nur wenige Punkte zur Verfügung stehen. Eine genaue Angabe der Änderung der Halbwertsbreite, vor allem im Bereich tiefster Temperaturen, muss einer späteren Untersuchung vorbehalten bleiben. Eine wichtige Feststellung kann jedoch aus den vorliegenden Messungen bereits entnommen werden: Die Halbwertsbreite nimmt in dem betrachteten Temperaturbereich von $+20°C$ bis $-216°C$ auf 10 Prozent ab. Dieses Verhalten unterscheidet sich wesentlich von dem der elektronischen Absorptionsbanden, deren Halbwertsbreite im gleichen Temperaturbereich auf etwa 50 Prozent abnimmt.

(d) Bestimmung der Störstellenkonzentration

Der Betrag sowohl der elektronischen Absorption — im Ultraviolett — als auch der Schwingungsabsorption — im Ultrarot ist ein Mass für die Zahl der Störzentren.

Aus den Ultraviolettspektren (*U*-Banden) lässt sich die Störstellenkonzentration nach einer von SMAKULA[8] angegebenen allgemeinen und von KLEINSCHROD[15] für die *U*-Zentren präzisierten Bestimmungsgleichung der folgenden Form ermitteln:

$$N = \frac{9\epsilon_0 c m}{e^2\hbar} \frac{n}{(n^2+2)^2} \frac{4\hbar\omega_0+H}{4\hbar\omega_0+2H} K_{max}\cdot H \quad (6)$$

Sie ist aus der klassischen Dispersionstheorie entwickelt und benutzt das Maximum der Absorptionskonstanten K_{max} und die Halbwertsbreite H.

Es bedeuten dabei:

N	= Konzentration der Zentren
ϵ_0	= Influenzkonstante = $8{,}86\cdot10^{-12}$ A sec/V m
m	= Masse des H-Atoms = $1{,}6\cdot10^{-27}$kg
e	= Elementarladung = $1{,}6\cdot10^{-19}$ A sec
c	= Lichtgeschwindigkeit im Vakuum = $2{,}996\cdot10^{8}$ m/sec
$\hbar$	= Plancksches Wirkungsquantum = $1{,}04\cdot10^{-34}$ W sec²
n	= Brechungsindex im Bandenmaximum
ω_0	= Kreisfrequenz im Bandenmaximum
K_{max}	= Absorptionskonstante im Bandenmaximum
H	= Halbwertsbreite im Energiemass

Auch das Ultrarot-Spektrum kann in gleicher Weise zur Bestimmung der Konzentration der Störstellen herangezogen werden.

Bei den schmalen Banden, wie sie bei tiefen Temperaturen auftreten, macht sich aber schon der Einfluss der endlichen spektralen Spaltbreite auf die Werte des Maximums der Absorptionskonstanten und der Halbwertsbreite bemerkbar. Es ist deshalb vorzuziehen, an Stelle der Einzelwerte K_{max} und H das Produkt $K_{max}\cdot H$ aus der integralen Absorption A zu entnehmen, die man durch Planimetrieren gewinnt.

Tabelle 2.

Substanz	Vers.-Nr.	N $10^{17}cm^{-3}$	$\alpha = N'/N$ bei*			
			20°C	−79°C	−183°C	−216°C
KCl	*E*3	1,95	0,19	0,32	0,40	0,37
	*E*7	2,80	0,20	0,30	0,50	0,45
	*E*8	1,45	0,15	0,28	0,41	0,41
	*E*9	1,85	0,21	0,30	0,40	0,48
	Mittelwert		0,19	0,30	0,43	0,43
	$\alpha' =$		0,23	0,32	0,43	0,43
KBr	*E*17	3,9	0,25	0,38	0,49	0,85
	*E*18	3,1	—	0,27	0,50	0,63
	Mittelwert		0,25	0,32	0,49	0,74
	$\alpha' =$		0,33	0,34	0,50	0,74

* N' aus der integralen Absorption nach Gl. (6) (7) berechnet.

Für den Fall einer Lorentzkurve gilt für die integrale Absorption

$$A = \frac{\pi}{2} K_{max} \cdot H. \qquad (7)$$

So kommt man zu N', der Konzentration der an der Ultrarotabsorption beteiligten Störstellen.

Auch diese Bestimmung enthält einen Unsicherheitsfaktor, der vor allem bei hohen Temperaturen beträchtlich werden kann: Das ist die Festlegung der Linie voller Durchlässigkeit, also der Basislinie.

Das Verhältnis $\alpha = N'/N$ ist in Tabelle 2 für KCl und KBr eingetragen.

Die Mittelwerte zeigen einen deutlichen Temperaturgang. Als wichtigstes Ergebnis ist festzuhalten: Das Ultrarotspektrum führt zu einem rund halb so grossen Wert für die an dieser Absorption beteiligten Störstellen wie das Ultraviolettspektrum.

(e) Nebenbanden

Neben den in Tabelle 1 aufgeführten Hauptbanden findet man bei einigen Kristallen auch noch kleinere Nebenbanden. In Abb. 2c sind solche bei den beiden tiefen Temperaturen beim RbCl zu sehen. Sie sind meist bei Zimmertemperatur nicht zu bemerken und treten hier nur bei sehr grosser Konzentration bzw. Schichtdicke als kleine Höcker an der Hauptbande hervor. Erst bei tiefer Temperatur sind sie deutlich getrennt zu erkennen. Tabelle 3 gibt für einige Kristalle eine Zusammenstellung der bei −183°C gemessenen Nebenmaxima.

Die Versuche, die Existenz dieser Nebenmaxima zu deuten, blieben bisher ohne Erfolg (siehe hierzu auch Teil 5). Im folgenden sind die experimentellen Befunde kurz zusammengestellt:

(1) Nebenmaxima wurden bei KCl, KBr, RbCl und RbBr gefunden, bei Na-Salzen nicht. Sie sind bei den Rb-Salzen wesentlich stärker als bei den K-Salzen. Ihre Grösse nimmt also mit der Masse des Kations zu. Über die Jodide erlaubten die Registrierkurven keine Aussage.

(2) Die Nebenmaxima liegen etwa symmetrisch zur Hauptbande; ihren Abstand gibt Tabelle 3.

(3) Die Absorptionskonstanten der Nebenmaxima können bei tiefen Temperaturen bis 1/10 der Hauptmaxima erreichen.

4. DISKUSSION DER MESSERGEBNISSE

(a) Die Eigenfrequenz

Die in der Einleitung gebrachte Abschätzung der ultraroten Eigenfrequenz der *U*-Zentren lieferte die richtige Grössenordnung. Eine genauere Theorie wird die Annahme, dass die Kraftkonstante des ungestörten Gitters erhalten bleibt, fallen lassen und wohl auch nicht-harmonische Anteile einbeziehen müssen. Das Ziel wird die Ermittlung des Potentialverlaufs am Ort des H^--Ions sein. Die vorliegende empirische Beziehung $h\nu d^2 = \text{const}$ für sich allein erlaubt wohl

Tabelle 3.

Substanz	Hauptmax.	1. Nebenmax.	2. Nebenmax.	Abstand v. Hauptmax des 1. Nebenmax.	des 2. Nebenmax.	Einheiten
KCl	20,02 6,18	17,80 6,95	22,65 5,46	2,22 0,77	2,63 0,72	μ 10^{-2}eV
KBr	22,49 5,50	20,05 6,17	24,95 4,96	2,44 0,67	2,46 0,54	μ 10^{-2}eV
RbCl	21,12 5,86	19,50 6,35	23,20 5,33	1,62 0,49	2,08 0,53	μ 10^{-2}eV
RbBr	23,66 5,23	21,90 5,65	25,50 4,85	1,76 0,42	1,84 0,38	μ 10^{-2}eV

VOL. 12 59/60

kaum einen verbindlichen Schluss auf die Gestalt des Potentialtopfes.

(*b*) *Die Halbwertsbreite*

Die Halbwertsbreite lässt sich bei Resonanzabsorption durch eine Dämpfungskonstante beschreiben, deren reziproker Wert die Verweilzeit des Oszillators in angeregtem Zustand ergibt. Die Ursache der Dämpfung der *Grundgitterschwingung* sieht man meistens in anharmonischen Gliedern des Gitterpotentials. Die anharmonischen Terme verursachen eine Kopplung der Oszillatoren, was zu einer Energieübertragung führt. Dieser Ansatz ist sinngemäss auf die *Störschwingungen* zu übertragen.

Für das Verständnis der *Temperaturabhängigkeit* liegen bisher weder theoretische Ansätze vor, noch scheinen die verfügbaren experimentellen Daten ausreichend. Doch verspricht die genauere Untersuchung der Temperaturabhängigkeit der Halbwertsbreite, die ja sehr viel stärker ist als das von den Elektronenspektren der *U*-Zentren bekannt ist, wichtige Aufschlüsse zu liefern.

(*c*) *Die Oszillatorenstärke*

Das Verhältnis der Zahl der an einem Absorptionsvorgang beteiligten Zentren N^*zu der Zahl der tatsächlich vorhandenen N, nennt man Oszillatorenstärke

$$f = \frac{N^*}{N}.$$

Setzt man voraus, dass die aus den Ultraviolettspektren (*U*-Banden) gemessenen Konzentrationen $N_v = N$ sind, dann sollten die α-Werte der Tabelle 2 direkt die Oszillatorenstärken sein. Man steht dann vor zwei Problemen :

1. der Temperaturabhängigkeit von α und
2. dem absoluten Wert von rund 0,5.

Zu 1. Es wurde versucht, die Temperaturabhängigkeit von α mit einer thermischen Anregung zu erklären. In der Tat entsprechen die Energien der Ultrarotschwingungen wenigen hundert Grad Celsius und bei Zimmertemperatur ist bereits ein Teil der *U*-Zentren angeregt. Man berechnet für KCl und KBr unter Voraussetzung einer Bose-Verteilung für die angegebenen Temperaturen folgende Besetzungszahlen des angeregten Niveaus :

Substanz	20°C	−79°C	−133°C	−183°C
KCl	9,5	2,5	0,6	0,034%
KBr	12,7	3,85	1,0	0,08 %

Daraus folgen die Übergangswahrscheinlichkeiten w als Produkt der Zahl der im Grundzustand besetzten und im Anregungszustand freien Plätze zu:

Substance	20°C	−79°C	−133°C
KCl	82	95	99%
KBr	76	92,5	98%

Mit Hilfe der Gleichung

$$(N')_{\text{korr.}} = N' \cdot w \qquad (8)$$

wurden die α-Werte der Tabelle 2 korrigiert und als α' eingetragen. Auch nach dieser Korrektur verbleibt ein Temperaturgang von α'. Wir sind geneigt, ihn mindestens zum Teil auf Fehler in der Bestimmung der experimentellen Werte der integralen Absorption zurückzuführen. Vor allem bei den höheren Temperaturen ist mit Korrekturen von 20–30 Prozent zu rechnen, die dadurch entstehen, dass man die Integration der Lorentzkurve nur bis zu endlichen Grenzen ausführt.

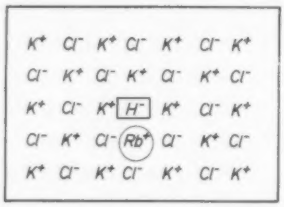

Abb. 7.

Beschränkt man sich auf die zuverlässigeren Werte bei tiefen Temperaturen, dann beträgt die Oszillatorenstärke etwa 0,5. Dieser Wert lässt die Frage entstehen, ob das gesamte Absorptionsspektrum der Ultrarotschwingungen des Störzentrums erfasst worden ist. Man kann sicher sein, dass auf der kurzwelligen Seite keine nennenswerte Absorption existiert. Es war hier, auch mit grösseren Schichtdicken, nach Oberschwingungen gesucht worden, die als Folge einer Anharmonizität auftreten könnten. Da auf der langwelligen Seite sehr bald die ultrarote Eigenabsorption folgt, ist es kaum möglich, dort unterlagerte Störstellenabsorptionen ausfindig zu machen.

5. MISCHKRISTALLE

Das Auftreten der in Teil 3(e) beschriebenen Nebenmaxima warf die Frage auf, ob diese nicht durch Verunreinigungen hervorgerufen sein könnten, die evtl. schon im Ausgangsmaterial vorhanden waren. Es wurden deshalb Mischkristalle hergestellt und mit *U*-Zentren versehen. Wenn die gestellte Frage auch nicht beantwortet werden konnte, so ergaben sich doch interessante Resultate :

KCl–KBr-Mischkristalle, bei denen die Konzentration beider Komponenten in derselben Grössenordnung lag, zeigten eine sehr breite und flache Absorptionsbande, die auch bei 90°K nicht aufgelöst wurde.

Ein wesentlich anderer Befund ergab sich bei der Untersuchung des Mischkristalls KCl +2 Molprozent RbCl. Hier sind nicht mehr nur K^+-Ionen die nächsten Nachbarn des H^--Ions, sondern ein kleiner Teil derselben ist durch Rb^+

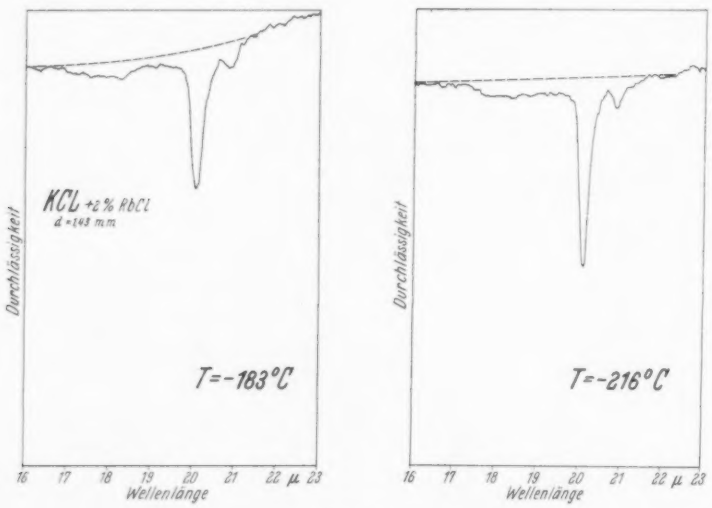

Abb. 8.

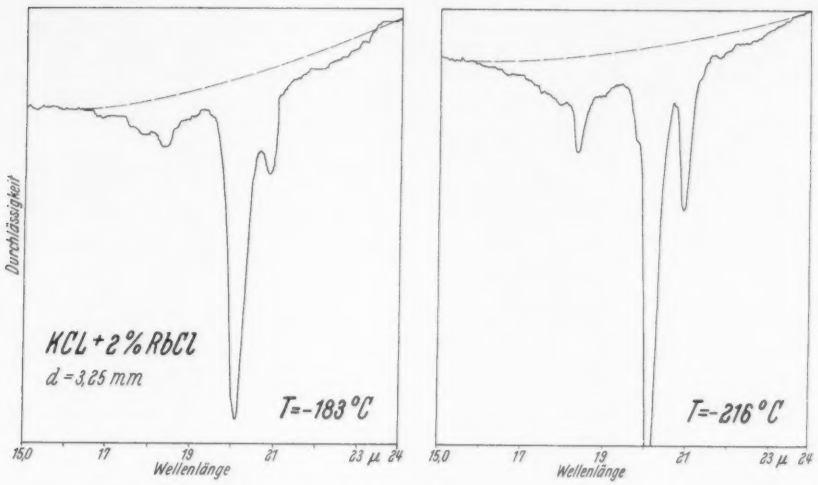

ABB. 9.

ersetzt (Abb. 7). Neben der KCl-Bande taucht auf der langwelligen Seite noch eine kleine Nebenbande auf (Abb. 8 und 9), die sich besonders bei −216°C sehr gut trennen lässt. Sie hat ihr Maximum bei 20,83μ.

Eine weitere Absorptionsbande findet sich im kurzwelligen Gebiet, deren Absorptionskonstante ungefähr halb so gross war wie die der langwelligeren. Sie hat ihr Maximum bei 18,3 μ.

Für das Verhältnis der Absorptionskonstanten des Hauptmaximums K_1 zu der des langwelligen Nebenmaximums K_2 ergab sich als Mittelwert über mehrere Messungen $K_1 : K_2 = 8{,}4$. Diesem Befund steht das Verhältnis beider Komponenten des Mischkristalls 50 : 1 gegenüber.

Zur Erklärung kann man nach der Wahrscheinlichkeit fragen, mit der ein oder mehrere Rb^+-Ionen in der Umgebung eines H^--Ions angetroffen werden.

Die Rechnung ergibt für die Wahrscheinlichkeit b_k, dass man k Rb^+-Ionen als nächste Nachbarn des H^- antrifft, die folgenden Werte :

für kein Rb^+-Ion	$b_0 = 88{,}65\%$,
für ein Rb^+-Ion	$b_1 = 10{,}74\%$,
für zwei Rb^+-Ionen	$b_2 = 0{,}59\%$,
für drei Rb^+-Ionen	$b_3 = 0{,}02\%$,
	100,00%.

Man findet das Verhältnis von $b_0 : b_1 = 8{,}2$ in sehr guter Übereinstimmung mit dem empirisch gefundenen Wert von $K_1 : K_2 = 8{,}4$. Daraus kann man schliessen, dass diese Nebenbande dann entsteht, wenn *ein* Rb^+-Ion nächster Nachbar eines H^--Ions ist.

Man entnimmt der Rechnung auch, dass das kurzwellige Nebenmaximum keinesfalls einer zweifachen Besetzung mit Rb^+-Ionen zuzuschreiben ist, denn das Verhältnis des Hauptmaximums zum Nebenmaximum müsste $b_0 : b_2 = 150$ sein, oder des langwelligen zum kurzwelligen Nebenmaximums $b_1 : b_2 = 18$, während das Experiment hierfür nur etwa 2 ergibt. Die Ursache der kurzwelligen Nebenbande bleibt also ungeklärt.

Herrn Professor Dr. H. Pick danke ich herzlich für die Anregung zu dieser Arbeit und die Förderung, die er mir bei ihrer Durchführung durch wertvolle Hinweise und Diskussionen zuteil werden liess. Herrn Professor Dr. Goubeau bin ich dafür dankbar, dass ich in seinem Institut die Ultrarot-Aufnahmen machen konnte. Meinen Kollegen, insbesondere Herrn Dr. Lüty und Herrn Dipl.-Phys. Gebhardt, danke ich für viele anregende Hinweise, sowie der Deutschen Forschungsgemeinschaft für ihre Unterstützung durch Überlassung von Geldmitteln und Apparaten.

LITERATUR

1. SEITZ F., *Rev. Mod. Phys.* **26**, 7 (1954).
2. HILSCH R. und POHL R.W., *Nachr. Akad. Wiss. Göttingen* **139** (1936).

3. HILSCH R., *Ann. Phys.* **29**, 407 (1937).
4. POHL R. W., *Z. Phys.* **39**, 36 (1938).
5. THOMAS H., *Ann. Phys.* **38**, 601 (1940).
6. BORN M. *Dynamik der Kristallgitter* in *Fortschr. Mathem. Wiss.* **4** (1915), Teubner, Berlin.
7. RÖGENER H., *Ann. Phys.* **29**, 386 (1937).
8. SMAKULA A., *Z. Phys.* **59**, 603 (1930).
9. STÖCKMANN F. und LANDOLT–BÖRNSTEIN, Teil 4, *Kristalle* Nr. 15114. Springer, Berlin (1955).
10. WYKOFF R. W. G., *Crystal Structures* Vol. 2, Chap. 3, p. 14c. Interscience Publishers, New York.
11. D'ANS J. und LAX E., *Taschenbuch f. Physiker*, 2. Aufl. S.749. Springer, Berlin (1949).
12. MOLLWO E., *Nachr. Akad. Wiss. Göttingen* **97**, (1931).
13. IVEY H. F., *Phys. Rev.* **72**, 341 (1947).
14. PICK H. *Nuovo Cimento*, **7** (Ser. 10), Suppl. 2, 504 (1958).
15. KLEINSCHROD F. G., *Ann. Phys.* **27**, 97 (1936).
16. FUES E. und STUMPF H., *Z. Naturf.* **9a**, 897 (1954).
17. MONTROLL E. W. und POTTS R. B., *Phys. Rev.* **100**, 525 (1955).

VO
1
1959/

J. Phys. Chem. Solids Pergamon Press 1960. Vol. 12. pp. 245–259. Printed in Great Britain.

LOW-TEMPERATURE HALL COEFFICIENT AND CONDUCTIVITY IN HEAVILY DOPED SILICON*†

G. A. SWARTZ‡

University of Pennsylvania, Philadelphia, Pa.

(*Received* 19 *March* 1958; *revised* 11 *March* 1959 *and* 6 *July* 1959)

VOL. 12 59/60

Abstract—The Hall coefficient and conductivity of fifteen heavily doped silicon samples have been measured. The Hall-coefficient measurements were generally made in the temperature region 15–300°K, while the conductivity measurements were taken in the region 3–30°K. The general behavior of the Hall coefficient and conductivity is similar to that in germanium and other semiconductors exhibiting impurity conduction. Two types of impurity conduction were observed: one believed to be non-band conduction and the other, band conduction. Investigation of the temperature region where the transition between normal band conduction and impurity conduction takes place shows a minimum in the impurity conduction resistivity vs. reciprocal temperature curve. Comparison of various samples shows that for a given impurity concentration, the lower impurity conductivity is found in the samples containing majority impurity atoms with the larger ionization energy. A possible model for impurity conduction is discussed.

1. INTRODUCTION

PREVIOUS measurements on the temperature-dependence of the Hall coefficient and resistivity in silicon from 20°K to room temperature have been made by MORIN and MAITA[1] and CARLSON[2], who found that relatively impure samples exhibited anomalous conduction. Measurements on these samples showed that the log of the resistivity (ρ) and the log of the Hall coefficient (R) when plotted against $1/T$ were straight lines, as in purer samples, down to about 25°K, below which temperature the slopes of the curves decreased sharply. The Hall-coefficient measurements usually stopped at this point, but the resistivity measurements, which were continued to lower temperatures, showed the log ρ vs. $1/T$ plot below 25°K to be a straight line with a finite positive slope much less than the slope above 25°K.

The investigation of the low-temperature Hall coefficient and resistivity properties of germanium is of prime importance to the study of silicon because of the similar structure of the two materials. This investigation was started by HUNG and GLIESSMAN[3] and continued by FRITZSCHE and LARK-HOROVITZ[4]. The log ρ vs. $1/T$ plot was similar to that obtained in silicon, except that the change in slope occurred at about 7°K, The log R vs. $1/T$ curve showed a pronounced peak at the same temperature. It should be noted that, on the low-temperature side, either the Hall mobility became so small that a measurement of R was no longer possible, or R flattened out and started to increase slightly. In no case did R change sign. The impurity content needed for anomalous conduction was a factor of 100 smaller than in silicon.

A qualitative explanation of this anomalous behavior in germanium was first proposed by HUNG[5].§ He suggested that two conduction processes were taking place in parallel: normal conduction (electrons or holes moving in the conduction or valence band formed by the germanium lattice) and "impurity band" conduction (electrons or holes moving in a band formed by

* Research supported by the Office of Naval Research.

† Based on a dissertation presented to the University of Pennsylvania in partial fulfilment of the requirements for the degree of Doctor of Philosophy.

‡ Philco Research Fellow 1956–1957. Present address: RCA Laboratories, Princeton, New Jersey.

§ A similar explanation was given by BUSCH and LABHART[6] for anomalous conduction in silicon carbide.

the overlap of the impurity atoms' electron wave functions). At high temperatures the former type of conduction is dominant and at low temperatures the latter. The transition occurs in germanium at about 7°K, the exact temperature depending on the impurity content. Hereafter, "impurity band" conduction will be referred to as impurity conduction, since the correct explanation of it may not involve the formation of a band.

An extension of the impurity-conduction measurements in silicon will enable a comparison to be made with germanium, which is similar to silicon in structure but different in important respects such as dielectric constant and impurity activation energy. In addition, the wide range of impurity activation energies, and, consequently, impurity electron wave functions in silicon should aid in an evaluation of this property with respect to impurity conduction.

2. APPARATUS

A conventional Pyrex glass double dewar system for retention of liquid helium was used (Fig. 1). The sample, together with a carbon resistance and platinum resistance thermometer, were mounted on a rectangular piece of Bakelite and placed inside a cylindrical copper can, $1\frac{1}{2}$ in. long, 1 in. in dia., and with $\frac{1}{8}$-in. thick walls. The can was supported at the bottom of a Monel plunger. A heater, wrapped on a spiral form, was placed $\frac{1}{2}$ in. below the bottom of the copper can.

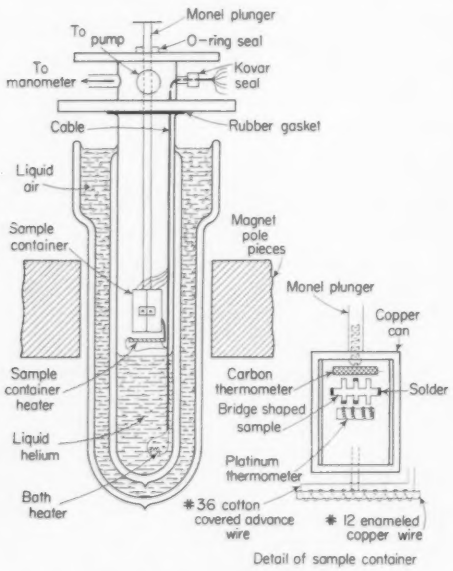

FIG. 1. Cryogenic apparatus.

To attain temperatures below 4·2°K, the entire can was immersed in the liquid helium and the helium vapor pressure was lowered by means of a fore-pump.

Temperature control between 4·2 and 60°K was attained by placing the sample container above the helium bath and matching the heat input to the heat output. The heat output was absorbed by the flow of cold helium gas, which could be regulated by the bath heater. The heat input came from outside radiation and from the heater under the sample container. In the range of temperatures from 4·2°K to several degrees higher, the container heater was unnecessary, and additional helium had to be boiled off to take up all the heat coming from radiative sources. At higher temperatures, the bath heater was turned off and the power supplied to the container heater was used to control the temperature.

To measure the temperature above 20°K a platinum resistance thermometer was used; between 20 and 4·2°K a carbon resistance thermometer was used, while below 4·2°K the helium vapor pressure indicated the temperature of the bath in which the apparatus was immersed.

A Leeds and Northrup type-K2 potentiometer, combined with a Leeds and Northrup galvanometer with a sensitivity of 4×10^{-10} A/mm. was used as the primary voltage-measuring instrument. Resistance up to 5×10^{9} Ω could be measured with this arrangement. The voltage probes from the thermometers led to a potentiometer and a Brown recorder which gave a continuous temperature reading. A small voltage pulse was thrown on to the recorder when a sample measurement was made so that the resistance of the thermometer was known at the exact time of measurement. A magnetic field of 3400 G was used to measure the Hall coefficient.

An aluminum oxide abrasive cutting device served to cut bridge-shaped samples from silicon wafers. Rhodium was electroplated on to each end of the main bar and the ends of the six arms. These ends were dipped into molten solder and allowed to cool. When the solder was placed all around the arm end in this manner, the difference in the coefficient of expansion between the silicon and solder did not cause the solder to fall off at liquid-helium temperatures.

3. EXPERIMENTAL RESULTS

The temperature-dependence of the Hall coefficient and of the resistivity were measured in fifteen highly doped silicon samples that included six p-type samples and nine n-type samples. The samples are listed in Table 1, together with their origin, room-temperature resistivity and the type of impurity. Two of the boron-doped samples, 1–BA and 2–BA, were from a single melt and four arsenic-doped samples, 1–AA, 2–AA, 3–AA and 4–AA were also taken from a single melt. All the others were from separate melts.

The Hall coefficient and resistivity were

Table 1. *List of samples investigated, with their room-temperature resistivity source and impurity*

	Samples	Room-temp. (297°K) resistivity (Ω cm)	Source	Impurity
p-type	1–BA	0·0775	B.T.L. Allentown	Boron
	2–BA	0·0851	,, ,,	,,
	1–BB	0·123	B.T.L. Murray Hill	,,
	1–BS	0·127	Signal Corps Labs.	,,
	1–GF	0·0813	Federal Telecommunications Lab.	Gallium
n-type	1–AM	0·258	Minneapolis Honeywell	Alluminum
	1–SP	0·0666	Philco	Antimony
	1–SA	0·0293	B.T.L. Allentown	,,
	1–SF	0·017	Federal Telecomm. Lab.	,,
	1–PA	0·0646	B.T.L. Allentown	Phosporus
	1–AC	0·143	,, ,,	Arsenic
	4–AA	0·0283	,, ,,	,,
	1–AA	0·0253	,, ,,	,,
	3–AA	0·0191	,, ,,	,,
	2–AA	0·0137	,, ,,	,,

VOL. 12 59/60

measured at room temperature, liquid-air or liquid-nitrogen temperature, and at intervals from 60°K down to a temperature at which either the electrical apparatus was too insensitive to measure the very high resistivities and small Hall voltages, or to the lowest temperature attainable in the helium bath. The former limitation was the usual one.

Fields no higher than 3V/cm were used to avoid intermediate field effects such as are found in germanium.[7]

The curves of $\ln R$ and $\ln\rho$ vs. $1/T$ for fourteen of the samples are shown in Figs. 2–9. Sample 1–AC is not included because it did not exhibit impurity conduction. For brevity, in most samples the sections of the $\ln\rho$ vs. 1/T curves exhibiting normal conduction have been omitted.

In the temperature range just below the onset of impurity conduction, the resistivity is, except for sample 2–AA, proportional to $\exp(\epsilon_i/kT)$. There is a lack of data on sample 1–AM below 20°K and therefore the value of ϵ_i associated with this sample is only approximate. Table 2 lists the value of ϵ_i for each sample and the temperature range in which ϵ_i was measured. In some of the more highly doped samples, such as 1–AA, 3–AA, 2–AA and 1–SF, the resistivity assumes an entirely different temperature-dependence at the lowest temperatures. In the case of sample 2–AA this latter temperature-dependence is dominant immediately below the onset of impurity conduction. It would be difficult to determine from the data the exact nature of this new temperature-dependence.

Table 2. *Impurity conduction activation energy of samples*

Sample	ϵ_i (eV)	Temp. range in which ϵ_i was measured (°K)
1–BA	0·0065	5·5–11
2–BA	0·007	6·3–17
1–BB	0·006	6·0–13
1–BS	0·0067	5·5–13
1–GF	0·0139	11 –22
1–AM	0·0085	19 –25
1–SP	0·0054	7·5–14
1–SA	0·0064	5·5–11
1–SF	0·004	10 –28
1–PA	0·0056	6·0–13
4–AA	0·0095	10 –16
1–AA	0·0102	10 –14
3–AA	0·0079	10 –17

An attempt was made to measure the magnetoresistance of several of the samples. With a field of 3400 G the magnetoresistance in the normal conduction region was found to be of the order of 1 or

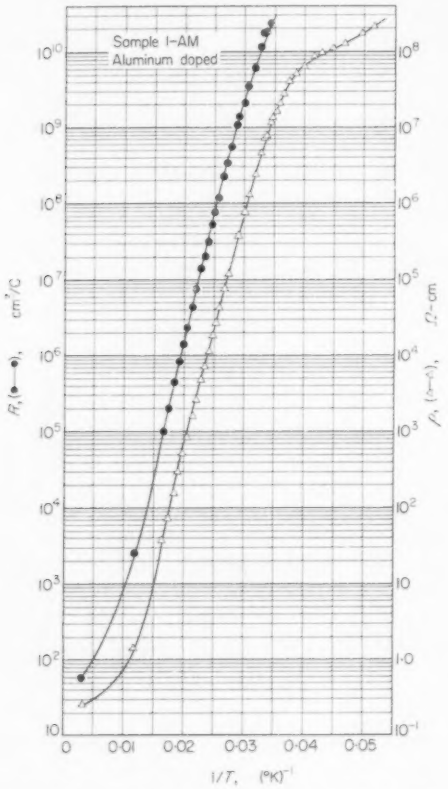

FIG. 2. Hall coefficient and resistivity of aluminum-doped sample.

2 per cent, dropping to immeasurably small values in the impurity conduction region.

4. CALCULATED RESULTS

(*a*) *The number and ionization energy of the major impurities*

Certain information about the silicon may be calculated from the experimental results obtained in the higher temperature range of normal conduction and the semiconductor model with parabolic valence and conduction bands, a set of donor levels at an energy E_D below the bottom of the conduction band and a set of acceptor levels at an energy E_A above the valence band. For this calculation, it is arbitrarily assumed that the number of donor levels N_D is greater than the number of acceptor levels N_A. (For the remainder of the paper the conduction band applies to either band. N_D is the density of major impurities unless otherwise specified.) The equations are equally valid for $N_A > N_D$ except that holes are considered instead of electrons. Another assumption is that the energy difference between donor levels and acceptor levels is very large compared to kT, so that all the N_A acceptor levels will be filled with electrons. The charge-carrier concentration n in the conduction band is related to the other parameters by:

$$\frac{n(n+N_A)}{(N_D-N_A)} = \frac{N_C}{g}\exp(-E_D/kT) \qquad (1)$$

Here g is the degeneracy of the donor levels and N_C, the "effective density of states" in the conduction band, is given by:[8]

$$N_C = f2\left(\frac{2\pi m_e^* kT}{h^2}\right)^{3/2} \qquad (2)$$

where f is the number of equivalent minima in the conduction band and m_e^* is the effective density-of-states mass calculated from cyclotron-resonance data.[9]

At temperatures such that $kT \geqslant E_D$, $n \cong N_D - N_A$. When $kT \ll E_D$ the slope of the log $nT^{-3/2}$ vs. $1/T$ plot yields a value for E_D.

In all cases except one the values of E_D were smaller than previously published values for purer silicon.[10] This effect is already well known. For example, in infra-red photoabsorption experiments on p-type silicon, NEWMAN[11] found that the energy spectrum of the excited states of the acceptor atoms broadened and merged with the valence band as the impurity concentration increased. Similar behaviour would be excepted in n-type silicon. The net effect would be to decrease E_D and to add a tail to the bottom of the conduction band. This tail would change the temperature-dependence and absolute value of N_C. If the temperatures were sufficiently high, however, most of the charge carriers would be moving in the parabolic portion of the band and N_C would approach its theoretical value. The tail of the conduction

VOL.
12
59/60

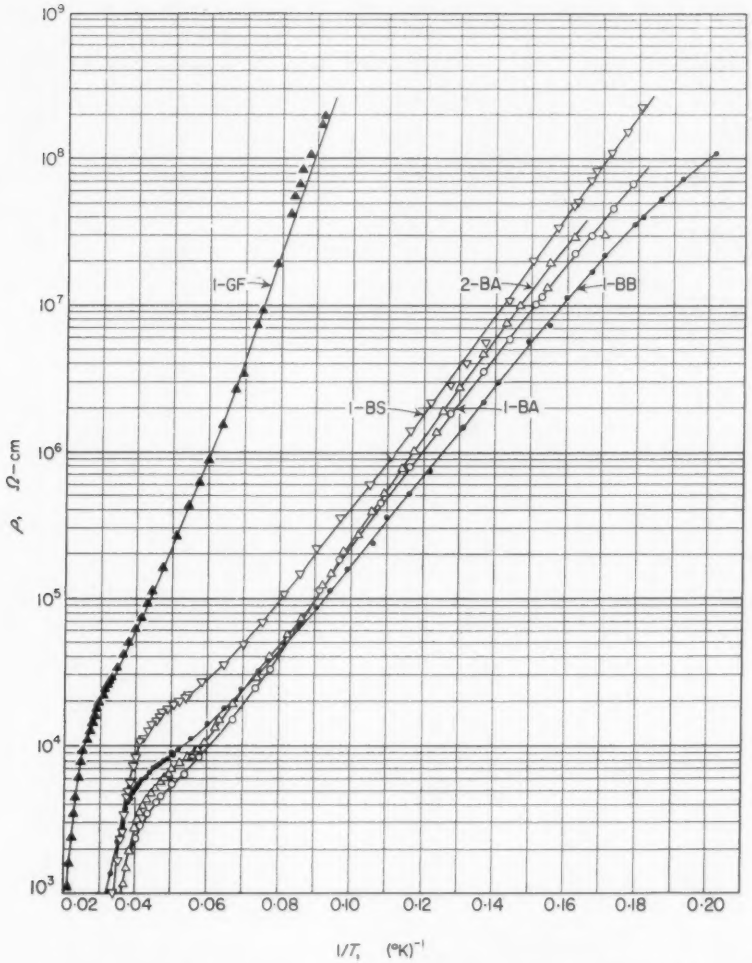

FIG. 3. Resistivity of four boron-doped samples (1 and 2–BA, 1–BS and 1–BB) and one gallium-doped sample (1–GF).

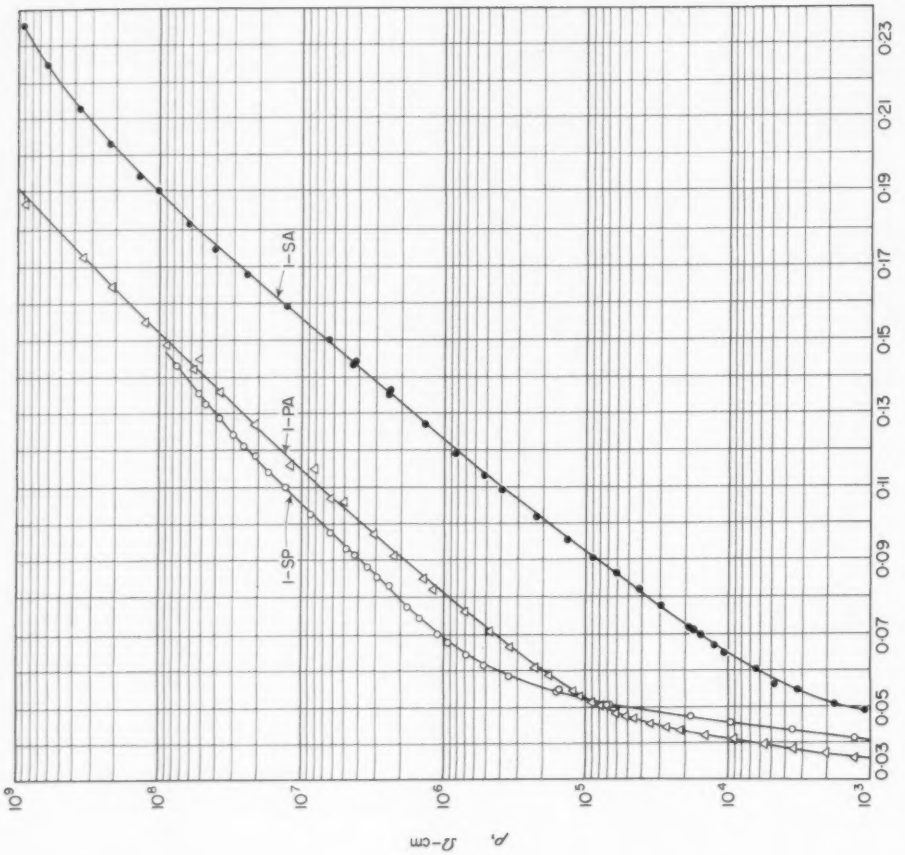

FIG. 5. Resistivity of two antimony-doped samples (1–SP and 1–SA) and one phosphorus-doped sample (1–PA).

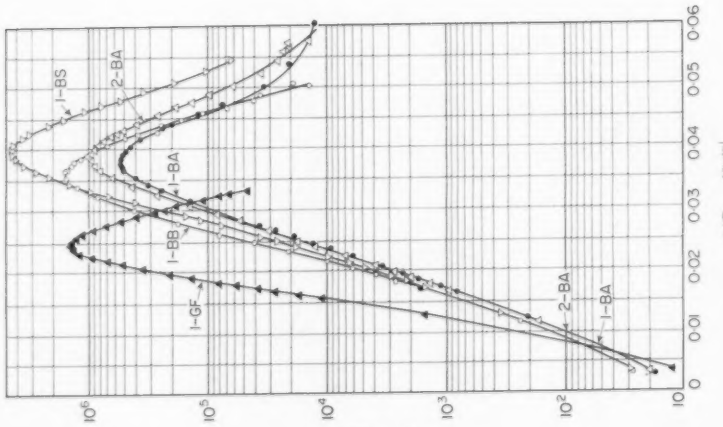

FIG. 4. Hall coefficient of four boron-doped samples (1 and 2–BA, 1–BS and 1–BB) and one gallium-doped sample (1–BF),

band and the expected broadening of the density-of-states curve for the ground-state impurity levels would make E_D also temperature-dependent. Thus,

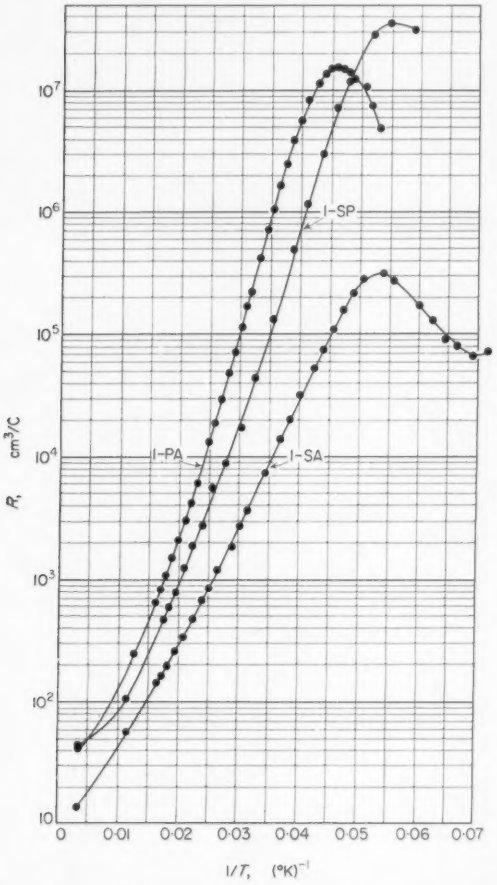

FIG. 6. Hall coefficient of two antimony-doped samples (1–SP and 1–SA) and one phosphorus-doped sample (1–PA).

the usefulness of equation (1) is in doubt. It certainly is not reliable enough to be used to calculate N_A. However, values of N_D can be calculated from equation (1). The impurity concentrations of these samples are so large that it should be reasonable to expect N_A (the minority impurity concentration) to be at most only a few percent of N_D (the majority impurity concentration). The high temperature limit becomes $n \simeq N_D$. Since this limit is being approached at room temperature, moderate errors in N_C or E_D should result in only small errors in N_D.

Two methods of calculating N_D were used. The first applied equation (1) only at room temperature, using the theoretical value for N_C, the value of E_D obtained from 30–60°K section of the $\ln(n/T^{3/2})$ vs. $1/T$ curve, and neglecting N_A. The second method utilized the Hall-coefficient measurements made at room temperature and liquid-air temperature. Knowing T and n at two points, using the theoretical value of N_C and neglecting N_A, we obtained two simultaneous equations with N_D and E_D as the two unknowns. In the above calculation the following values were assumed: $f = 6$, $g = 2$, $m_e^* = 0{\cdot}33m_e$ for electron conduction; $f = 1$, $g = 2$, $m_e^* = 0{\cdot}59\ m_e$ for hole conduction; and a ratio of Hall to drift mobility equal to $3\pi/8$ for both types of conduction. This last value is at variance, particularly for holes, with measurements on pure silicon made by MORIN and MAITA[1]. In view of the lack of drift-mobility data for impure silicon, a nominal value of $3\pi/8$ was used.

In two samples, 1–AM and 1–GF, n was so small at liquid-air temperature that N_A was probably greater than n and should not be neglected. Thus, the values of N_D obtained by the second method for these two samples were not reliable. In the case of sample 1–SF, normal conduction did not extend down to liquid-air temperature and the value of N_D was estimated from the room temperature Hall coefficient and resistivity measurements.

As previously mentioned, equation (1) is a better description of the actual situation the higher the temperatures. Therefore, except for the samples 1–AM and 1–GF, the second method is considered better. Table 3 lists values of N_D and E_D obtained by both methods.

(b) Impurity conductivity

One of the important features of the $\ln\rho$ vs.$1/T$ curves is the slight concavity occurring just below the temperature at which impurity conduction becomes dominant. The effect can be observed in about half the samples measured. Samples 2–BA, 1–BB, 1–GF and 1–AA are good examples. It would be of interest to determine the temperature-dependence of the impurity conductivity at temperatures just above the concave section. This determination involves separating the total

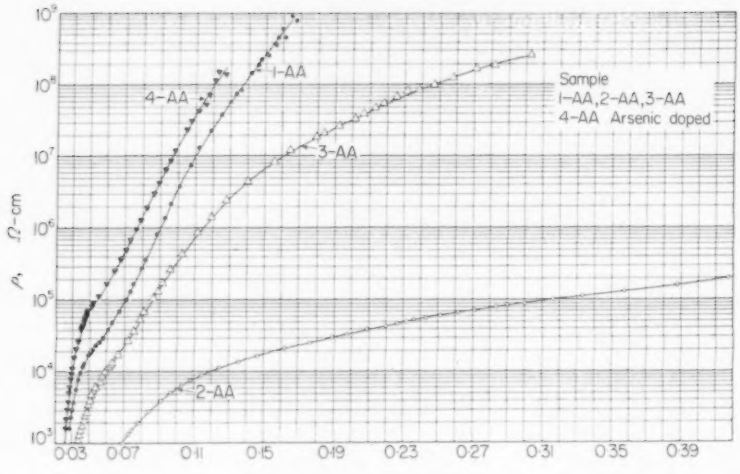

FIG. 7. Resistivity of four arsenic-doped samples from a single melt.

Table 3. Concentration and ionization energy of impurities and spacing between impurity atoms

Sample	First method using room temp. and slope of $\ln(n/T^{3/2})$ vs. $1/T$ line		Second method using room-temp. and liquid-air measurements only		Major impurity spacing r_D* $r_D=\left(\frac{2}{\frac{3}{4\pi}N_D}\right)^{\frac{1}{3}}$ (Å)
	E_D (eV)	Major impurity conc. N_D (No. /cm³)	E_D (eV)	Major impurity conc. N_D (No. /cm³)	
1–BA	0·0261	$6{\cdot}58 \times 10^{17}$	0·036	$7{\cdot}5 \times 10^{17}$	60
2–BA	0·0265	$5{\cdot}6 \times 10^{17}$	0·036	$6{\cdot}3 \times 10^{17}$	63
1–BB	0·0374	$3{\cdot}78 \times 10^{17}$	0·0381	$3{\cdot}82 \times 10^{17}$	75
1–BS	0·031	$3{\cdot}26 \times 10^{17}$	0·0386	$3{\cdot}66 \times 10^{17}$	76
1–GF	0·053	$1{\cdot}48 \times 10^{18}$	0·072	$2{\cdot}5 \times 10^{18}$	48
1–AM	0·059	$1{\cdot}72 \times 10^{17}$	0·072	$2{\cdot}26 \times 10^{18}$	98
1–SP	0·0292	$1{\cdot}71 \times 10^{17}$	0·0304	$1{\cdot}74 \times 10^{17}$	98
1–SA	0·0171	$5{\cdot}92 \times 10^{17}$	0·0305	$6{\cdot}2 \times 10^{17}$	64
1–PA	0–0318	$1{\cdot}82 \times 10^{17}$	0·0406	$1{\cdot}86 \times 10^{17}$	95
4–AA	0–039	$5{\cdot}68 \times 10^{17}$	0·0412	$5{\cdot}75 \times 10^{17}$	65
1–AA	0·0256	$8{\cdot}65 \times 10^{17}$	0·0382	$9{\cdot}13 \times 10^{17}$	56
3–AA	0·0214	$1{\cdot}62 \times 10^{18}$	0·0154	$1{\cdot}56 \times 10^{18}$	47
2–AA	0·0123	$3{\cdot}05 \times 10^{18}$	0·0106	$2{\cdot}96 \times 10^{18}$	38
1–AC	0·044	$6{\cdot}35 \times 10^{16}$	0·049	$6{\cdot}37 \times 10^{16}$	136
1–SF	—	—	—	3×10^{18}†	38

* The values of N_D used to calculate r_D came from the second method except for samples 1–AM and 1–GF where the first method yields the better value of N_D.

† Estimated from room temperature Hall coefficient and resistivity measurements.

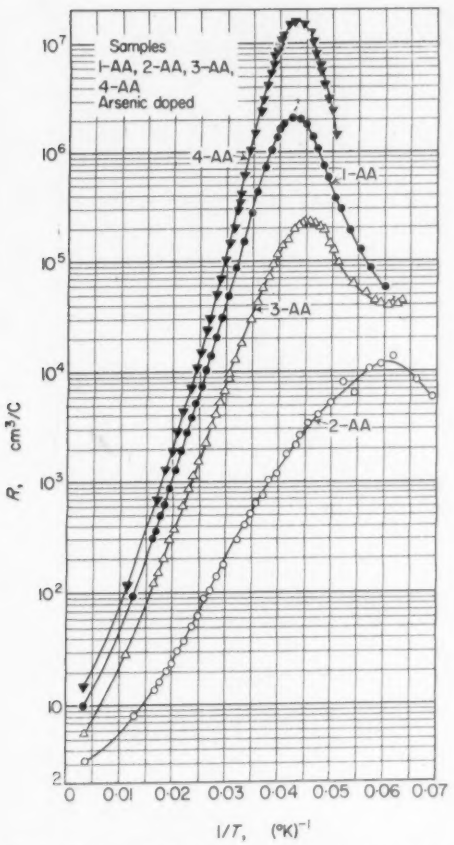

FIG. 8. Hall coefficient of four arsenic-doped samples from a single melt.

conductivity into its two component parts, the impurity conductivity and conduction-band conductivity.

By making three assumptions: (1) the two-carrier model is assumed in which there are n_c carriers in the conduction band with mobility u_c and n_i "impurity carriers", all of which are assumed to have the same mobility u_i, (2) the modes of conduction are non-interacting and (3) the ratio of Hall to drift mobility for impurity conduction is $3\pi/8$, the following equations can be used:

$$R = \frac{3\pi}{8}\frac{1}{e}\frac{n_c u_c^2 + n_i u_i^2}{(n_c u_c - n_i u_i)^2} \tag{3}$$

$$\sigma = n_c \epsilon u_c + n_i \epsilon u_i \tag{4}$$

The peak of the Hall coefficient and the knee in the resistivity curve occur at about the same temperature. These two features are the result of the transition from one type of conduction to the other. Thus, in this temperature region, $n_c u_c$ has the same order of magnitude as $n_i u_i$; n_c is known to be less than 10^{13} at these temperatures, and all current theories of impurity conduction suggest that n_i is of the order of 10^{14} or greater. It follows that u_i is less than 10 per cent of u_c and that $n_i u_i^2$ is less than 10 per cent of $n_c u_c^2$. We shall therefore calculate σ_c to within 10 per cent or better from the two equations. Equations (3) and (4) can then be rewritten:

$$R = \frac{3\pi e}{8}\frac{n_c u_c^2}{\sigma^2} \tag{5}$$

$$\sigma_i = \sigma - n_c \epsilon u_c \tag{6}$$

In assumption (3) it is only necessary that the ratio of Hall to drift mobility for impurity conduction shall have a value about unity in order to arrive at equations (5) and (6).

The linear plot of $\ln(n/T^{3/2})$ vs. $1/T$ obtained from the higher-temperature Hall data was extrapolated to the lower temperatures at which the transition to impurity conduction occurred. This extrapolation yieded the value of n_c at lower temperatures. Knowing n_c, equations (5) and (6) can then be solved for u_c and σ_i at each temperature.

Fig. 10 shows $\ln\rho_i$ vs. 1/T for samples 1, 3 and 4–AA. The impurity resistivity exhibits a minimum in the transition region. This occurred in all ten samples in which the subtraction process was possible. The probable error of the measurements in this temperature range is about 1 per cent, and the error in σ_c is less than 10 per cent. Since the values of ρ_i on the negative slope of the $\ln\rho_i$ vs. $1/T$ curve vary from 50 to 10 per cent of the total ρ, it seems quite probable that this minimum is a real effect. The arrow on the curve denotes the temperature at which the conduction-band conductivity becomes negligible.

(c) *Conduction-band mobility*

In the transition region u_c is calculated from the two simultaneous equations (5) and (6), discussed in the previous section. Figs. 11–13 show Hall mobility (u_{Hc}) as a function of the temperature for all the samples except 1–SF. The vertical arrow on most of the curves separates the high-temperature one-carrier region from the low-temperature

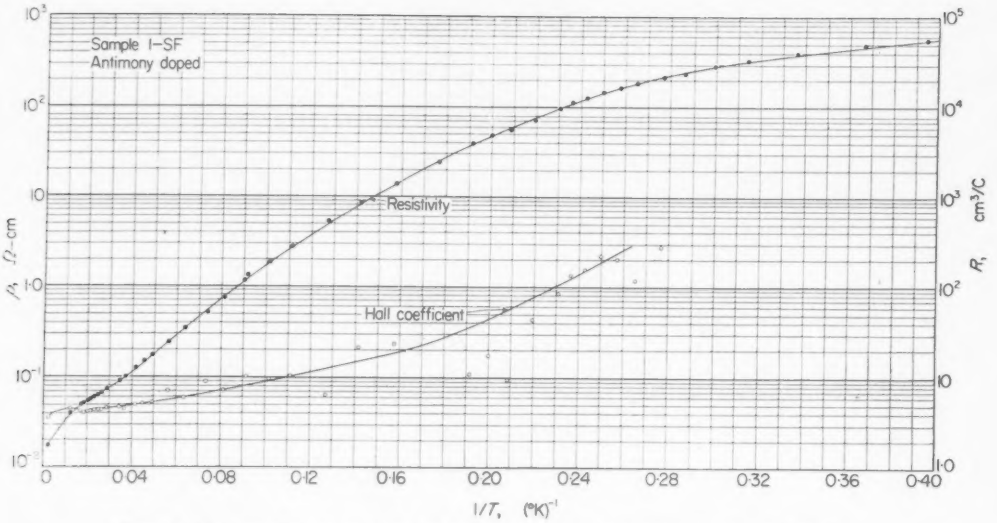

FIG. 9. Hall coefficient and resistivity of very heavily antimony-doped silicon.

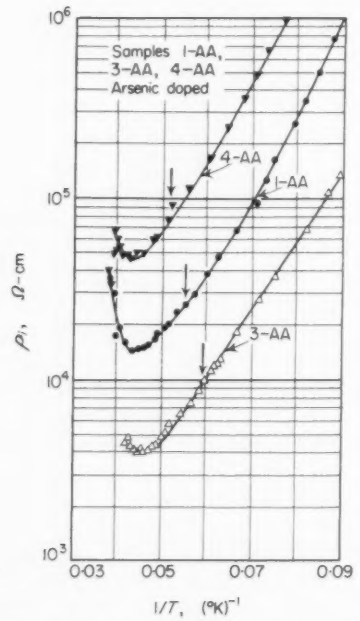

FIG. 10. Impurity resistivity of three arsenic-doped samples at temperatures in which the transition between normal conduction and impurity conduction takes place. At temperatures to the left of the arrow the normal conductivity was subtracted from the total measured conductivity, as described in the text.

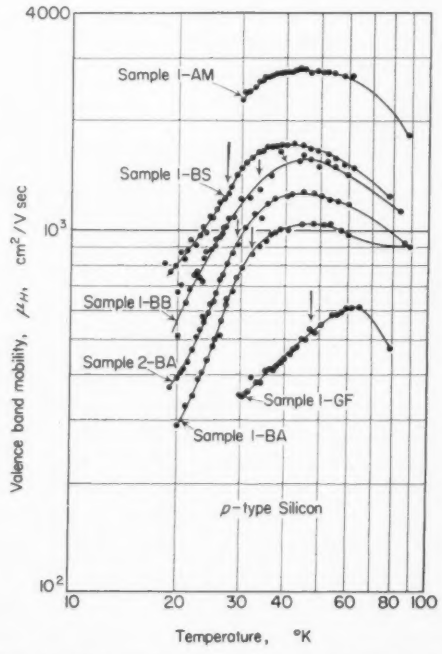

FIG. 11. Valence-band mobility as a function of temperature for six p-type samples. The transition temperature region occurs to the left of the vertical arrow.

transition region. Absence of the arrow indicates that one carrier predominates over the entire curve.

The general picture of the conduction-band mobility is as follows: at 80°K there is a slow increase of mobility with decreasing temperature, and between 60 and 30°K the mobility decreases as T^s, where s varies from 1 to 5/2, depending on the sample; s appears to increase with major impurity concentration. It is believed that there are two scattering mechanisms: scattering by neutral impurities above 30°K and scattering by ionized impurities below 30°K.

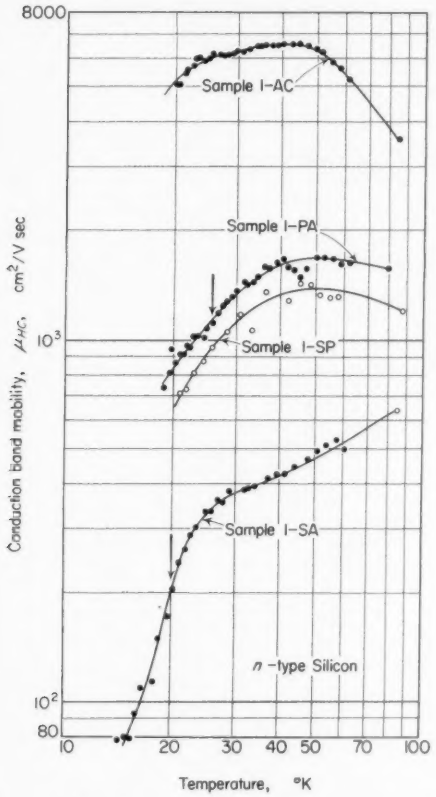

FIG. 12. Conduction-band mobility as a function of temperature for four n-type samples. Transition temperature region is left of vertical arrow.

5. THEORY AND DISCUSSION

(a) *Band formation*

The impurity conduction in the samples with major impurity concentrations of 10^{17}/cm³ to 10^{18}/cms is characterized by an exponential dependency on the temperature with activation energies ranging from 0·0054 to 0·0139 eV. In the case of samples 1, 2, 3–AA and 1–SF, which have larger major impurity concentrations (10^{18}/cm³), another type of impurity conduction appears at the lowest temperatures. This is strongly temperature-dependent but does not seem to have an exponential character.

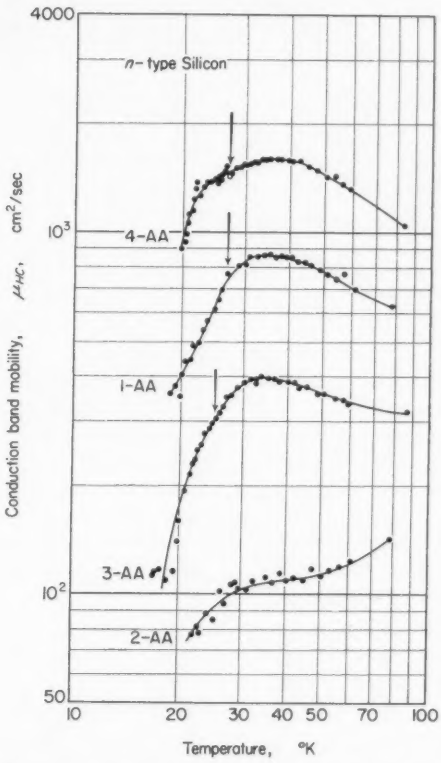

FIG. 13. Conduction-band mobility as a function of temperature for four arsenic-doped samples. Transition temperature region is left of vertical arrow.

The most probable distance between randomly located impurities is

$$r_D = \left(\frac{1}{2\pi N_D}\right)^{1/3}$$

and ranges between 120 and 55 Å for those samples having impurity concentrations between

10^{17}/cm^3 and 10^{18}/cm^3. It would be more profitable to have these distances in terms of the effective Bohr radius a^*_h. This quantity is obtained by considering a hydrogenic atom imbedded in a material with a dielectric constant κ and the electron having an effective mass m^*. Thus, the effective Bohr radius is given by:

$$a^*_h = \frac{\kappa}{m^*/m} a_h \tag{7}$$

where a_h is the Bohr radius of the hydrogen atom. Considering the n-type only, $\kappa = 12$, $m^*/m = 0{\cdot}38$ and $a^*_h = 18{\cdot}5$ Å, so that the distance between impurities for exponentially temperature-dependent impurity conductivity is between 6·5 and 3·0 a^*_h. The second type of impurity conduction occurs at impurity spacings less than 3·0 a^*_h.

In the second type of conduction, it seems possible that the impurity-atom wave functions overlap sufficiently to enable the electron to move freely from one impurity atom to another, and the impurity levels broaden into a band wide enough to permit conduction. This band may form thread-like through the material and give impurity carriers with large effective masses and low mobilities. Samples 1,3 and 2–AA show the development of this banding quite well. When the impurities are less than 10^{18} cm^3, the overlap of the wave functions is so small that it is difficult to believe that this mechanism can give rise to appreciable conduction, and the first type of conduction must be due to some other process.

Some work has been done to calculate the density-of-states curve for an impurity band made up of a random array of impurities for the one-dimensional[12,13] and three-dimensional[14] cases. The mobility of a charge carrier in such a band has not been calculated, and comparison with experiment is not possible at this time.

(*b*) *Mott model*

A most interesting explanation of exponentially temperature-dependent impurity conduction with relatively low impurity concentration has been proposed by MOTT[15] and put into analytical form by PRICE[7]. MOTT's theory is concerned with a semiconductor having an impurity concentration low enough to preclude band formation, so that at 0°K, the conductivity is zero. A semiconductor contains a density of compensating minority impurities which become charged by attracting electrons or holes from the neutral major impurities. This process produces a charged pair with the charged major impurity called a defect. Electrons or holes can move from other major impurities into the defect, with the subsequent movement of the defect in the opposite direction, and thus conduction can take place. If there are d major impurities (trap sites) in the immediate vicinity of each charged minority impurity, a defect in one of the major impurities will be attracted to the minority impurity and will require an activation energy if it is to move to a free site away from the minority impurity, where it can take part in the conduction process. Consider an n-type sample in which r_D and r_A are the spacings between major impurities and minor impurities respectively. By assuming that $r_D \ll r_A$, PRICE has calculated the activation energy.[7] This activation energy is the difference in potential energy of a defect in a trap site nearest a minority impurity ($e^2/\kappa r_D$) and the potential energy of a defect half-way between minority impurities ($e^2/\kappa r_{A/2}$):

$$\epsilon_i = \frac{e^2}{\kappa}\left(\frac{1}{r_D} - \frac{2}{r_A}\right) \tag{8}$$

The number of free defects n_i can be shown by a statistical argument to be:

$$\frac{n_i^2}{(N_D - dN_A - n_i)(N_A - n_i)} = \frac{1}{d}\exp(-\epsilon_i/kT) \tag{9}$$

When $kT \gg \epsilon_i$, $n_i \cong N_A$. When $kT \ll \epsilon_i$:

$$n_i = \left(\frac{(N_D - dN_A)N_A}{d}\right)^{1/2} \exp(-\epsilon_i/2kT) \tag{10}$$

Assuming the mobility is not exponentially dependent on temperature, the measured activation energy of the $ln\rho_i$ vs. $1/T$ plot should be $\epsilon_i/2$. Comparison with experiment is difficult because N_A is not known, although it may be safely assumed to be not less than 10^{14}/cm^3 or greater than 5×10^{16}/cm^3. Within this minority impurity range the calculated activation energy is generally less than the measured energy. Hall-coefficient and conductivity measurements in germanium made by KOENIG and GUNTHER-MOHR have been used to verify MOTT's theory qualitatively.[7]

VOL. 12 59/60

(c) Sample comparison

The impurity conduction process obviously takes place by some movement of the charge carrier from one impurity atom to the next. Therefore, the impurity resistivity should decrease when the impurities are in closer proximity. One can see this immediately in Fig. 7, which shows the AA melt.

The other point to be considered in this respect is the electron wave function of the impurity atom. The larger the wave function, the easier it will be for the electron to move from one impurity to the next for a given concentration. Thus, one might expect that an impurity with more tightly bound electrons and consequently radially smaller wave functions than another will exhibit a higher resistivity for a given concentration, and conversely, if both impurities have the same resistivity, the impurity with the smaller electronic wave functions will have the higher concentration. The impurity resistivity ρ_i is proportional to $A \exp(-\epsilon_i/kT)$. In order to compare the coefficient A in two samples, the quantity ϵ_i/kT must be the same for both (see Table 4).

Two samples that can be compared in the impurity-band region are antimony-doped 1–SF and arsenic-doped 2–AA. In this case the resistivities are much less temperature-dependent and can be compared at the same temperature. The temperature actually used was 4·23°K.

Despite the somewhat qualitative nature of the comparison, the effect is so large that Table 4 clearly illustrates the dependence of the impurity resistivity on the ionization energy of the impurity atom.

An examination of the data indicates that there may be some relationship between the impurity-atom ionization energy and the impurity-conduction activation energy. In order to verify this relationship satisfactorily, two samples with different major impurities but equal concentrations of major and minor impurities should be compared. This latter condition is necessary because of MOTT's theory and FRITZSCHE's recent experiment on germanium,[16] which suggest a variation of the activation energy with either of these quantities. In our experiments, the majority impurity concentration is known, whereas the minority concentration is not. Table 5 compares the samples in pairs, each set of two having about equal majority impurity concentrations. In both cases, the impurity with the larger ionization energy has the larger activation energy ϵ_i In the third set, comparing 1–AM and 1–BS, one might expect, according to MOTT's theory, that sample 1–BS, with the higher major impurity concentration and

Table 4. Sample comparisons showing the dependence of impurity resistivity on ionization energy

Sample	Impurity	Ionization energy (eV)	ϵ_i/T_i (eV/°K)	T_i* (°K)	Major impurity Conc. (No./cm^3)	ρ_i at T_i (Ω cm)
4–AA	Arsenic	0·049	$6{\cdot}7 \times 10^{-3}$	14·3	$5{\cdot}75 \times 10^{17}$	$4{\cdot}5 \times 10^{5}$
1–SA	Antimony	0·039	$6{\cdot}7 \times 10^{-3}$	9·6	$6{\cdot}2 \times 10^{17}$	$2{\cdot}4 \times 10^{5}$
1–GF	Gallium	0·065	$7{\cdot}0 \times 10^{-3}$	20	$1{\cdot}48 \times 10^{18}$	$2{\cdot}4 \times 10^{5}$
2–BA	Boron	0·044	$7{\cdot}0 \times 10^{-3}$	10	$5{\cdot}6 \times 10^{17}$	$2{\cdot}4 \times 10^{5}$
1–AM	Aluminum	0·057	$4{\cdot}3 \times 10^{-3}$	25	$1{\cdot}72 \times 10^{17}$	2×10^{8}
1–SP	Antimony	0·039	$4{\cdot}3 \times 10^{-3}$	12·7	$1{\cdot}74 \times 10^{17}$	2×10^{6}
2–AA	Arsenic	0·049	—	4·23	3×10^{18}	$5{\cdot}2 \times 10^{4}$
1–SF	Antimony	0·039	—	4·23	$\sim 3 \times 10^{18}$	$1{\cdot}1 \times 10^{2}$

* The temperatures at which the resistivities of the two samples are compared are chosen such that ϵ_i/kT_i (sample 1) $= \epsilon_i/kT_i$ (sample 2).

consequently closer spacing, might have the larger activation energy, but again it is 1–AM, the sample with the larger ionization energy, that has the larger activation energy. This general trend is followed in all the samples.

One comparison set, by itself, cannot be used to establish the relationship because of ignorance of the minority concentration. However, the three sets together present strong, although certainly not conclusive, evidence that the relationship exists. It is to be noted that MOTT's theory does not predict a dependence of the activation energy ϵ_i on the ionization energy E_D (or E_A). More such sample comparisons are needed in which the minority concentrations are very small in each sample or are equal in both samples.

Table 5. Comparisons showing possible dependence of impurity activation energy on ionization energy

Sample	Impurity	Impurity ionization energy (eV)	Impurity conduction activation energy ϵ_i (eV)	Density of major impurities N_D (No./cm^3)
4–AA	Arsenic	0·049	0·0095	$5{\cdot}75 \times 10^{17}$
1–SA	Antimony	0·039	0·0064	$6{\cdot}2 \times 10^{17}$
1–AM	Aluminum	0·057	0·0085	$1{\cdot}72 \times 10^{17}$
1–SP	Antimony	0·039	0·0054	$1{\cdot}74 \times 10^{17}$
1–AM	Aluminum	0·057	0·0085	$1{\cdot}72 \times 10^{17}$
1–BS	Boron	0·045	0·0067	$3{\cdot}66 \times 10^{17}$

6. CONCLUSIONS

Impurity conduction, which has been found in fourteen out of fifteen samples measured, is of two types: non-band conduction characterized by an exponentially temperature-dependent resistivity, and impurity-band conduction characterized by a moderately temperature-dependent resistivity. The latter type of conductivity requires impurity concentrations of 10^{18}/cm^3 or greater, while the former type occurs with lower concentrations.

Comparisons of samples shows that impurities with more tightly bound electrons and radially smaller wave functions will exhibit a higher impurity resistivity for equal impurity concentrations. Further comparison indicates that impurity-conduction activation energy may increase with carrier ionization energy. The evidence is not conclusive because of the lack of information about the minority impurity concentration.

A two-carrier model of conduction is utilized in ten samples to determine the impurity resistivity from the data in the transition temperature region. In all of these samples, a minimum in the impurity resistivity curve was found.

The conduction-band mobility appears to be governed by two kinds of scattering mechanisms; neutral impurity scattering between 30 and 80°K and probably ionized impurity scattering below 30°K.

Some of the present theories on impurity conduction have been considered, but they do not seem to be advanced enough to compare with experiments. A sound theory of ionized impurity scattering is necessary to be able to determine from the data the minority impurity concentration, a vital quantity to any theory of impurity conduction.

Acknowledgements—The author wishes to express his appreciation to Dr. KENNETH ATKINS, for his considerable help in designing the cryogenic apparatus and for valuable advice throughout the course of the experiment, and to Dr. WALTER KOHN for the invaluable help given during numerous discussions of the experimental results. He is grateful to Dr. P. H. MILLER for his advice in the initial stages of the work; to M. HINES, Bell Telephone Laboratories, Allentown; A. NUSSBAUM, Minneapolis Honeywell; C. SUTCLIFFE, Philco; W. KECK, Signal Corps Laboratories; and A. GOBAT, Federal Telecommunications Laboratories for supplying the silicon samples reported on in this paper.

REFERENCES

1. MORIN F. J. and MAITA J. P., *Phys. Rev.* **96**, 28 (1954).
2. CARLSON R. D., *Phys. Rev.* **100**, 1075 (1956).
3. HUNG C. S. and GLIESSMAN J. R., *Phys. Rev.* **79**, 726 (1950); **96**, 1226 (1954).
4. FRITZSCHE H. and LARK-HOROVITZ K., *Physica, s' Grav.* **20**, 834 (1954).
   FRITZSCHE H., *Phys. Rev.* **99**, 406 (1955).
5. HUNG C. S., *Phys. Rev.* **79**, 727 (1950).
6. BUSCH G. and LABHART H., *Helv. Phys. Acta* **19**, 463 (1946).
7. KOENIG S. H. and GUNTHER-MOHR G. R., *J. Phys. Chem. Solids* **2**, 268 (1957).
8. BROOKS H., *Advances in Electronics and Electron Physics* **7**, 87 (1956).
9. LAX B. and MAVROIDES J. G., *Phys. Rev.* **100**, 1650 (1955).
10. BURTON J. A., *Physica, s' Grav.* **20**, 845 (1954).
11. NEWMAN R., *Phys. Rev.* **103**, 103 (1956).
12. JAMES H. M. and GINZBARG J., *J. Phys. Chem.* **57**, 840 (1957).
13. LAX M. and PHILLIPS J. C., *Bull. Amer. Phys. Soc.* **2**, No. 6 (1957).
14. AIGRAIN P., *Physica, s' Grav.* **20**, 978 (1954).
15. MOTT N. F. *Canad. J. Phys.* **34**, 1356 (1956); *Nuovo Cimento*, Suppl. **7**, 312 (1958).
    KLINGER M. I. and ZOZULIA I. I., *Soviet Phys., Tech. Phys.* **2**, 2123 (1957).
16. FRITZSCHE H. and LARK-HOROVITZ K. *Phys. Rev.* **113**, 999 (1959).

VOL. 12 59/60

J. Phys. Chem. Solids Pergamon Press 1960. Vol. 12. pp. 260–264. Printed in Great Britain.

VACANCY RELAXATION IN CUBIC CRYSTALS

L. A. GIRIFALCO and V. G. WEIZER

Lewis Research Center, National Aeronautics and Space Administration, Cleveland, Ohio

(*Received* 22 *June* 1959)

Abstract—The configuration of the atoms surrounding a vacancy in four face-centered cubic and three body-centered cubic metals has been computed, using a pairwise, central-force model in which the energy of interaction between two atoms was taken to have the form of a Morse function. Only radial relaxations were considered. The first and second nearest-neighbor relaxations for the face-centered systems were found to be: Pb (1·42, —0·43), Ni (2·14, —0·39), Cu (2·24, —0·40) and Ca (2·73, —0·41, expressed in percentages of normal distances. For the body-centered systems the relaxations out to the fourth nearest neighbors to the vacancy were: Fe (6·07, —2·12, —0·25, —), Ba (7·85, —2·70, 0·70, —0·33) and Na (10·80, —3·14, 3·43, —0·20). The positive signs indicate relaxation toward the vacancy and the negative signs indicate relaxation away from the vacancy. The energies of relaxation (eV) are: Pb (0·162), Ni (0·626), Cu (0·560), Ca (0·400), Fe (1·410), Ba (0·950) and Na (0·172).

An estimate of the ease of motion of the atoms surrounding a vacancy in sodium was made, and it was concluded that NACHTRIEB's relaxion concept is probably valid in sodium.

1. INTRODUCTION

THEORETICAL studies of the geometrical configuration of the atoms surrounding vacancies in cubic crystals have recently been performed by several investigators. On the basis of a pairwise, central-force model for argon, KANZAKI[1] has computed the displacement of six sets of nearest neighbors from their normal lattice sites, using an inverse-power 6–10 potential for the interaction of two atoms. Detailed calculations for vacancy relaxation in a rare-gas-type crystal have also been performed by HALL[2], using an inverse-power 6–12 potential. In an attempt to obtain results that could be applied to metals, GIRIFALCO and STREETMAN[3] computed the lattice distortion around a vacancy in a body-centered crystal whose atoms interact according to an inverse-power 5–7 potential. The 5–7 potential energy function has been shown by FÜRTH to describe adequately the macroscopic properties of molybdenum, chromium and tungsten.[4] HUNTINGTON and SEITZ[5] and TEWORDT[6] have used a non-pairwise approach in their calculations for copper.

The purpose of the present paper is to compute the configuration of the atoms around a vacancy in cubic metals in such a way as to retain the simplicity of the pairwise interatomic potential approach, while minimizing the shortcomings encountered in the previous attempts. These shortcomings are that:

(1) The results of KANZAKI[1] and of HALL[2] are applicable only to inert-gas crystals and should not be extrapolated to metals.

(2) The inverse-power 5–7 potential is inconsistent with the Born stability criteria for body-centered cubic crystals.[7]

Recently it has been shown that pairwise Morse potentials can be constructed that adequately reproduce the energy of cohesion, lattice parameter, compressibility and equation of state of metals.[8] Furthermore, the Born stability criteria are satisfied for both face-centered and body-centered crystals whose atoms interact according to a Morse potential, and, although the pairwise calculations lead to the Cauchy relations which are not satisfied in metals, the magnitude of the agreement between the experimental and theoretical elastic constants is satisfactory. Thus, calculations based on Morse potentials should give results for metals that are more reliable than those previously obtained by using other types of pairwise force laws.

VOL. 12 59/60

2. THE MORSE POTENTIAL FUNCTION

The interaction energy, ϕ_{ij}, of a pair of isolated particles i and j, interacting by means of a Morse potential, is:

$$\phi_{ij} = D[\exp\{-2\alpha(r_{ij}-r_0)\}-2\exp\{-\alpha(r_{ij}-r_0)\}] \tag{1}$$

where D is the dissociation energy of the pair, r_0 is the equilibrium separation, r_{ij} is the actual separation and α is a constant.

The equation for the energy of interaction of one atom i with every other atom j in the crystal is:

$$\phi_i' = D[\sum_j \exp\{-2\alpha(r_j-r_0)\} - 2\sum_j \exp\{-\alpha(r_j-r_0)\}] \tag{2}$$

It is convenient at this point to define the following terms:

$$\beta = \exp(\alpha r_0)$$

$$r_j = (m_j^2+n_j^2+l_j^2)^{1/2}a$$

where l, m, n are position indices of the atoms in the crystal, and a is the half-cell lattice spacing.

$$\phi_i' = D\{\beta^2\sum_j \exp(-2\alpha a[(m_j^2+n_j^2+l_j^2)]^{1/2}) - 2\beta\sum_j \exp(-\alpha a[(m_j^2+n_j^2+l_j^2)]^{1/2})\} \tag{3}$$

For the perfect crystal ϕ_i' is independent of i and is

$$\phi_i' = 2\Phi/N \tag{4}$$

where Φ/N is the energy of cohesion per atom.

Equation (3) holds for the case in which the origin of the coördinate system is a normal lattice site. To perform calculations about points other than normal lattice sites, it is necessary to translate the origin of the system. Thus, equations (1) and (3) are:

$$\phi_{ij} = D\{\beta^2\exp(-2\alpha a[(m_j-\delta_1)^2+(n_j-\delta_2)^2 + (l_j-\delta_3)^2]^{1/2} - 2\beta\exp(-\alpha a[(m_j-\delta_1)^2+(n_j-\delta_2)^2+(l_j-\delta_3)^2]^{1/2})\} \tag{5}$$

$$\phi_i' = D\{\beta^2\sum_j \exp(-2\alpha a[(m_j-\delta_1)^2+(n_j-\delta_2)^2 + (l_j-\delta_3)^2]^{1/2}) - 2\beta\sum_j \exp(-\alpha a[(m_j-\delta_1)^2+(n_j-\delta_2)^2+(l_j-\delta_3)^2]^{1/2})\} \tag{6}$$

where δ_1, δ_2 and δ_3 are the position indices of the translated origin.

3. METHOD OF CALCULATION

To obtain the equilibrium configuration of the atoms about a vacancy after relaxation, a process of successive approximations is employed in which it is assumed that the atomic relaxation is radial. In this process, the energy of the first nearest neighbors to the vacancy is found as a function of the radial displacement of the whole set toward or away from the vacant site. Meanwhile, the other sets of neighbors are held in their normal lattice sites. The point of minimum energy is assumed to be the equilibrium position of the first nearest neighbors to the first approximation. Next, while the first nearest neighbors are held in their relaxed positions, a point of minimum energy is found for the second nearest neighbors in a similar manner. This procedure is repeated for successive sets of nearest neighbors until a set of atoms is found which has an energy minimum a negligible distance from its normal position. This completes the first approximation.

Because of the motion of the second and successive sets of neighbors, the equilibrium position of the relaxed first set of neighbors has been disturbed. A second approximation to the position of the first nearest neighbors is found by repeating the calculation using the first approximation of the relaxed positions as the normal positions in the second approximation. This is repeated for all sets of neighbors until the relaxed positions of the atoms do not change appreciably upon further approximation. The relaxing atoms have now taken the positions of lowest energy, and it is assumed that this is the final configuration of atoms about a vacancy after relaxation.

The energy of relaxation is the energy change that takes place during relaxation, that is, the energy of the crystal before relaxation less the energy of the crystal after relaxation.

All calculations were performed over a cubic lattice having twenty atoms on a side. A crystal of this size acts as an infinite lattice for calculations done near the center of the lattice. A coördinate system is constructed with axes parallel to the cubic axes of the lattice and with the origin at the vacant site, which is located in the center of the lattice. Then, in order to perform summations about

any point in the system, the origin is translated to a point $\delta_1,\delta_2, \delta_3$.

The energy of an atom i in the lattice consists of the following terms:

(1) The energy of interaction of atom i with every other atom in the lattice which has not relaxed. This is found by means of equation (6), where l, m and n are limited to the position indices of every atom in the lattice that has not yet been relaxed, and δ_1, δ_2 and δ_3 are the position indices of atom i in the original coördinate system.

(2) The energy of interaction of atom i with all sets of relaxed neighbors other than the set to which the atom i belongs. Equation (6) is used here also, with the values of l, m and n limited to the position indices of the atoms concerned.

(3) One half of the energy of interaction of atom i with the other atoms in the same set of neighbors as the atom i. Equation (6) is again used here, with l, m and n limited to the position indices of the atoms concerned. The factor one-half must be included because the interactions between the atoms of the relaxing set are counted twice, and thus must be divided by two.

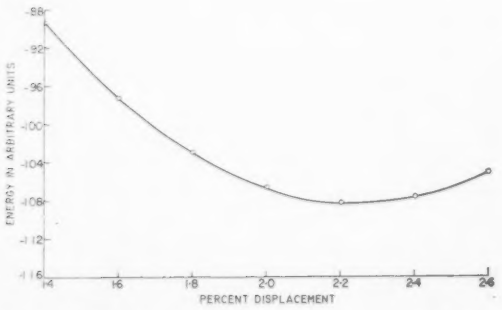

FIG. 1. A plot of energy against displacement for a first nearest-neighbor approximation in copper.

Since each of the atoms belonging to a certain set of neighbors has an equivalent environment, the energy of a set of neighbors may be found by calculating the energy of one atom in the set and multiplying it by the number of atoms in the set.

The equilibrium position and energy of an atom are found by plotting the energy of this atom against displacement as the atom is moved in increments radially toward or away from the vacancy, and selecting the displacement of minimum energy as the equilibrium displacement. An example of such a plot is given in Fig. 1.

In this manner the equilibrium configuration and energy is found for each set of relaxing neighbors in turn. This process is repeated, as outlined previously, until a steady-state condition is reached.

4. ENERGY OF RELAXATION

The energy of relaxation is the energy of the crystal before relaxation less the energy of the crystal after relaxation. If E^U is the energy of interaction between the relaxing atoms in their normal lattice positions and the rest of the lattice, E^R is the energy of interaction between the relaxing atoms at their relaxed positions and the rest of the lattice and E^L is the energy of interaction among all the atoms in the crystal which do not change position during relaxation, then the energy of relaxation, E, is:

$$E = E^U+E^L-E^R-E^L = E^U-E^R$$

For face-centered cubic lattices:

$$E^U = 12\epsilon_1^U+6\epsilon_2^U-\phi^U$$

$$E^R = 12\epsilon_1^R+6\epsilon_2^R-\phi^R$$

For body-centered cubic lattices:

$$E^U = 8\epsilon_1^U+6\epsilon_2^U+12\epsilon_3^U+24\epsilon_4^U-\phi^U$$

$$E^R = 8\epsilon_1^R+6\epsilon_2^R+12\epsilon_3^R+24\epsilon_4^R-\phi^R$$

where

ϵ_n^U is the energy of an nth neighbor in its normal position,

ϵ_n^R is the energy of an nth neighbor in its relaxed position.

ϕ^U and ϕ^R are interaction energies between sets of neighbors in the unrelaxed and relaxed positions, respectively, which have been counted twice and, therefore, must be subtracted.

For face-centered lattices:

$$\phi^U = \phi(1,2)$$

$$\phi^R = \phi(1',2')$$

For body-centered lattices:

$$\phi^U = \phi(1,2)+\phi(1,3)+\phi(1,4)+\phi(2,3)+\phi(2,4)+\phi(3,4)$$

$$\phi^R = \phi(1',2')+\phi(1',3')+\phi(1',4')+\phi(2',3') + \\ + \phi(2',4')+\phi(3',4')$$

The terms $\phi(m,n)$ and $\phi(m',n')$ are the sums of the interaction energies between all the atoms in neighbor set m and all the atoms in neighbor set n, all in their unrelaxed and relaxed positions, respectively.

5. RESULTS AND DISCUSSIONS

The results of the configuration calculations are given in Table 1 for both body-centered and face-centered metals. The summation in equation (6) and other numerical calculations were performed on a high-speed digital computer. A list of the constants used in the calculations is compiled in Table 2.

Table 1. Relaxed configuration of atoms about a vacancy in percent of normal distance from the vacancy. Negative values refer to motion away from the vacancy

	1st	2nd	3rd	4th	
Pb	1·42	−0·43	—	—	F.c.c.
Ni	2·14	−0·39	—	—	
Cu	2·24	−0·40	—	—	
Ca	2·73	−0·41	—	—	
Fe	6·07	−2·12	−0·25	—	B.c.c.
Ba	7·85	−2·70	0·70	−0·33	
Na	10·80	−3·14	3·43	−0·20	

Table 2. List of constants used in the Morse potential function
(See Ref. 8)

	β	α(Å^{-1})	D(eV)	r_0(Å)
Pb	83·02	1·1836	0·2348	3·733
Ni	51·78	1·4199	0·4205	2·780
Cu	49·11	1·3588	0·3429	2·866
Ca	39·63	0·80535	0·1623	4·569
Fe	51·97	1·3885	0·4174	2·845
Ba	34·12	0·65698	0·1416	5·373
Na	23·28	0·58993	0·06334	5·336

It will be noted that the magnitude of relaxation in the Morse crystal is not very large, the nearest-neighbor relaxation averaging about 2 per cent for the face-centered and about 8 per cent for the body-centered metals. Also, it was only necessary to calculate out to the second nearest neighbors in the face-centered case, though the fourth nearest neighbors had to be considered in the cases of body centered barium and sodium.

The highly relaxed configurations in the body-centered metals relative to the face-centered metals is a result of the combined effect of the open body-centered structure and the long-range repulsions exhibited by the Morse function in body-centered crystals.

The energies of relaxation are tabulated in Table 3. These energies, being a fraction of an electron volt, are small compared to the energies of vaporization.

Table 3. The energy of relaxation, E, (eV)

	E(eV)
Pb ..	0·162
Ni ..	0·626
Cu ..	0·560
Ca ..	0·400
Fe ..	0·410
Ba ..	0·950
Na ..	0·172

Another notable point is that the relaxation process in the Morse lattice is a complicated one, involving the inward (toward the vacancy) relaxation of some sets of neighbors and the outward relaxation of some other sets. This is in essential agreement with the results obtained from previous pairwise model calculations, but it is in disagreement with the work of TEWORDT in that his calculations show an inward motion of the second nearest neighbors in the case of copper. This discrepancy arises from the use of the pairwise Morse potential, in which the effects of the electron gas are neglected.

It should be noted that the Morse functions used in these calculations were derived from macroscopic data and reflect the electron distribution of

the perfect crystal. It is not known how the redistribution of the conduction electrons on forming a vacancy affects the constants in the Morse function.

The large relaxations in the case of sodium require comment. It has been suggested on the basis of diffusion experiments that the atoms surrounding vacancies in sodium are highly relaxed and have a density and energy content characteristic of the liquid phase.[9] The atom movement within this relaxed structure, called a "relaxion", is assumed to be similar to that occurring in a liquid. The theoretical calculations show that the vacancy relaxation is most extensive in sodium. In order to decide whether or not the relaxion exists in sodium, some measure of the ease of motion of the atoms in the relaxed structure is needed. In the present investigation, the activation energy for the rotation of the cube formed by the eight nearest neighbors to the vacancy was taken to be a measure of the internal mobility of the atoms surrounding the vacancy. In calculating this activation energy, the saddle point configuration was assumed to be one in which the nearest-neighbor cube was rotated by 45° about a cubic axis. The volume of the cube was assumed to be the same in the saddle point and in the initial relaxed position. Using the Morse potential for sodium, the energy barrier for this model was found to be 0·70 eV. This number is certainly an overestimate, since further relaxation in the activated position was ignored. Furthermore, some other rotation model, such as rotation about a body diagonal, or rotation of a ring of four atoms might have a lower activation energy than 0·35 eV. It can be concluded, therefore, that the atoms around a vacancy in sodium have an appreciable mobility and the present work supports NACHTRIEB's suggestion that a relaxion exists in this system. It seems unlikely, however, that the relaxion would exist in the face-centered metals or in those body-centered metals for which the nearest-neighbor relaxations are much less than that for sodium.

6. SUMMARY AND CONCLUSIONS

The configuration of atoms about a vacancy and the energy of relaxation for several body-centered and face-centered cubic metals were computed from Morse potentials and found to be in essential agreement with previous calculations. Although relaxation effects were found to be small, they were larger in the case of the body-centered metals than in the case of the face-centered metals.

Finally, an estimate was made of the ease of motion of the atoms surrounding a vacancy in sodium. The results show that NACHTRIEB's relaxion concept is probably valid in the case of sodium but not valid in those solids for which the relaxations are small.

REFERENCES

1. KANZAKI H., *J. Phys. Chem. Solids* **2**, 24 (1957).
2. HALL G. L., *J. Phys. Chem. Solids* **3**, 210 (1957).
3. GIRIFALCO L. A. and STREETMAN J. R., *J. Phys. Chem. Solids* **4**, 182 (1958).
4. FÜRTH R., *Proc. Roy. Soc.* **A183**, 87 (1944).
5. HUNTINGTON H. B. and SEITZ F., *Phys. Rev.* **61**, 315 (1942).
6. TEWORDT L., *Phys. Rev.* **109**, 61 (1958).
7. BORN M. and MISRA R. D., *Proc. Camb. Phil. Soc.* **36**, 173 (1940).
8. GIRIFALCO L. A. and WEIZER V. G., *NASA Rep.* No. 5 (1958) and *Phys. Rev.* **114**, 687 (1959).
9. NACHTRIEB N. H., *WADC Tech. Rep.* 55–68 (1954).

J. Phys. Chem. Solids Pergamon Press 1960. Vol. 12. pp. 265–275. Printed in Great Britain.

THEORY OF THE ENERGY LEVELS OF DONOR-ACCEPTOR PAIRS

F. E. WILLIAMS

General Electric Research Laboratory, Schenectady, New York

(*Received* 3 *July* 1959)

VOL. 12 59/60

Abstract—The electronic energy levels of the donor–acceptor pair are investigated theoretically in the effective mass approximation in a way similar to the Heitler–London treatment of the hydrogen molecule. The cores are approximated by point charges; the medium, by a continuous dielectric; and the two-particle wave function, by a single product of the separated donor and acceptor wave functions. No exchange integral arises, and the total ionization energy decreases with increasing degree of association. The analysis is generalized to pairs whose electron and hole masses are unequal and to pairs in polar media. The optical transition energies involved in the creation and evolved in the annihilation of the bound exciton are calculated. The effect of state of ionization on the electron and hole levels is determined. In highly-associated pairs the ionization of the electron or hole greatly reduces the ionization energy of the remaining particle. The analysis is applied to zinc sulfide containing Group IIIB donors and Group IB acceptors, and supports the identification of the long-wavelength luminescent emission as the transition between the ground states of donor and acceptor in quite highly-associated pairs. Other possible applications are suggested.

1. INTRODUCTION

THE existence of associated donor–acceptor pairs has been discussed by REISS[1] for germanium and by PRENER and WILLIAMS[2] for zinc sulfide. The latter have estimated the energy-level structure of the nearest-neighbor pair by considering the electron and hole individually bound in the dipole field and neglecting electron-hole interactions. More recently, HOOGENSTRAATEN[3] has considered the energy levels of donor-acceptor pairs as perturbed coulomb states and included the van der Waals interaction between donor and acceptor but neglected the effect of the overlap of the separated donor and acceptor wave functions. We have reexamined the problem and now report an analysis which takes account of the overlap of the electron and hole wave functions and also, for compound semiconductors, of the polar character of the media. The analysis is adapted from the analysis of HEITLER and LONDON[4] on the hydrogen molecule. The separated donor and acceptor are taken as point positive and negative charges to which are bound coulombically an electron and a positive hole, respectively. The donor–acceptor pairs in non-polar semiconductors are first treated, and then the analysis is generalized to polar semiconductors.

The interparticle distances of a donor–acceptor pair are illustrated in Fig. 1. The interimpurity

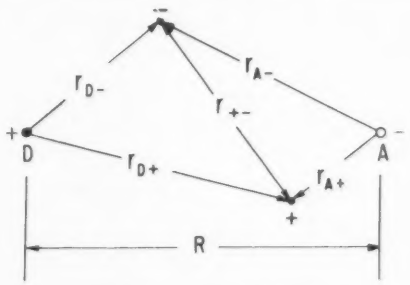

FIG. 1. Interparticle distances of donor–acceptor pair.

distance between the donor D and acceptor A is R and the coördinates of the electron and positive hole with respect to these nuclei and to each other are indicated by r with pairs of the subscripts $-$, $+$, D and A. The interimpurity distance R is taken

as fixed, whereas the coördinates of the electron and the hole are in general described by a two-particle wave function $\Psi(-,+)$. The system can be described as an exciton bound in the field of a finite dipole, and the energy levels to be considered are excited crystal states. The qualitative energy-level structure of an associated donor–acceptor pair is illustrated in Fig 2.

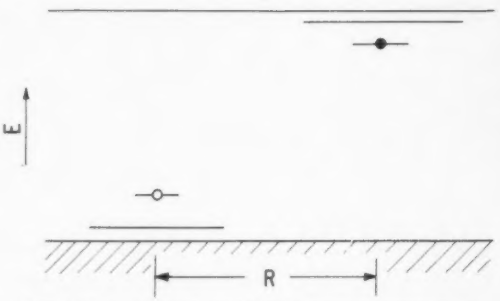

FIG. 2. Band theory model of donor–acceptor pair.

2. DONOR–ACCEPTOR PAIRS IN NONPOLAR SEMICONDUCTORS†

In a nonpolar medium only electronic polarization occurs, and the interaction of charged particles is in accordance with a dielectric constant K. The Hamiltonian operator for the donor-acceptor pair is:

$$H = -\frac{\hbar^2}{2}\left(\frac{1}{m_-}\Delta_- + \frac{1}{m_+}\Delta_+\right) + \frac{e^2}{K}\left(-\frac{1}{r_{A+}} - \frac{1}{r_{D-}} + \frac{1}{r_{A-}} + \frac{1}{r_{D+}} - \frac{1}{r_{+-}} - \frac{1}{R}\right) \quad (1)$$

where m_- and m_+ are the effective masses of the electron and hole, respectively. The two-particle wave function is taken, in this analysis as well as in the analysis for polar semiconductors, as a single product function of the separated donor and acceptor one-particle wave functions.

$$\Psi(-,+) = \psi_D(-)\psi_A(+) \quad (2)$$

The permuted product $\psi_D(+)\psi_A(-)$ is clearly not part of the bound exciton state, since the electron and hole are distinguishable particles, and this product refers therefore to a configuration of quite different energy. Incidentally, the permuted product does not refer to the ground state of the crystal, since in the ground state the electron and hole have annihilated each other.

The total energy of the donor–acceptor pair is, of course:

$$E = \frac{\int\int \Psi^*(-,+) H \Psi(-,+)\, dv_-\, dv_+}{\int\int \Psi^*(-,+)\Psi(-,+)\, dv_-\, dv_+} \quad (3)$$

The substitution of equations (1) and (2) into (3) yields the following if $\psi_D(-)$ and $\psi_A(+)$ are normalized:

$$E = \int\int \psi_D^*(-)\psi_A^*(+)\left[-\frac{\hbar^2}{2}\left(\frac{1}{m_-}\Delta_- + \frac{1}{m_+}\Delta_+\right) + \frac{e^2}{K}\left(-\frac{1}{r_{A+}} - \frac{1}{r_{D-}} + \frac{1}{r_{A-}} + \frac{1}{r_{D+}} - \frac{1}{r_{+-}} - \frac{1}{R}\right)\right]\psi_D(-)\psi_A(+)\, dv_-\, dv_+ \quad (4)$$

The kinetic-energy terms and the first two potential-energy terms can be identified with the energies of the separated donor and acceptor, E_D and E_A, respectively. The total energy E is therefore:

$$E = E_D + E_A + \frac{e^2}{K}\int\int \psi_D^*(-)\psi_A^*(+)\left[\frac{1}{r_{A-}} + \frac{1}{r_{D+}} - \frac{1}{r_{+-}} - \frac{1}{R}\right]\psi_D(-)\psi_A(+)\, dv_-\, dv_+ = E_D + E_A + J \quad (5)$$

where the integral J can be described as coulombic and can be subdivided as follows:

$$J = J_{A-} + J_{D+} + J_{+-} - \frac{e^2}{KR} \quad (6)$$

Because of the unpermuted form of equation (2), no exchange integral appears in equation (5). The donor-acceptor pair also differs from the hydrogen molecule in that the electronic particles attract each other coulombically, do not avoid each other because of the Pauli principle and are repelled

† Part of the material of this section has been reviewed in a survey paper on large-band-gap semiconductors by PRENER J. S. and WILLIAMS F. E., *J. Phys. Chem. Solids* **8**, 461 (1959).

VOL. 12 59/60

coulombically by each other's charged cores. Both systems, however, involve the perturbation of two neutral atoms: two hydrogen atoms in one case; the neutral donor and the neutral acceptor in the other. The perturbation is weaker for the donor and acceptor because of the absence of exchange.

For a donor and an acceptor whose electron and positive hole, respectively, have equal effective masses, the one-particle wave functions and energies for 1*s*-type states are in the effective mass approximation[5]:

$$\psi = \pi^{-1/2}a^{-3/2}e^{-r/a} \tag{7}$$

and

$$E_D = E_A = -\frac{\hbar^2}{2ma^2} \tag{8}$$

where:

$$a = \frac{K\hbar^2}{me^2} \tag{9}$$

The coulombic integral J for a donor–acceptor pair satisfying the above conditions is equal in magnitude, but opposite in sign, to the corresponding integral for a hydrogen molecule with electrons of mass m in a nonpolar medium with dielectric constant K. This integral is therefore readily obtained from the original work of HEITLER and LONDON[4].

$$J = -\frac{e^2}{KR}e^{-2R/a}\left[1+\frac{5}{8}\frac{R}{a}-\frac{3}{4}\frac{R^2}{a^2}-\frac{1}{6}\frac{R^3}{a^3}\right] \tag{10}$$

The components of J indicated in equation (6) are also readily obtained from the corresponding integrals for the hydrogen molecule.[4]

$$J_{A-} = J_{D+} = \frac{e^2}{KR}\left[1-\left(1+\frac{R}{a}\right)e^{-2R/a}\right] \tag{11}$$

$$J_{+-} = -\frac{e^2}{KR}\left[1-\left(1+\frac{11}{8}\frac{R}{a}+\frac{3}{4}\frac{R^2}{a^2}+\frac{1}{6}\frac{R^3}{a^3}\right)e^{-2R/a}\right] \tag{12}$$

For a donor and an acceptor whose electron and positive hole, respectively, have unequal effective masses, the one-particle wave functions and energies will be characterized by different parameters a_D and a_A, respectively. Again, for 1*s*-type states the components of the coulomb integral J are obtained by integration in elliptical coördinates.[6] The equations for J_{A-} and J_{D+} are the same as equation (11) except that a_D and a_A, respectively, replace a. The equation for J_{+-} is, however, the following:

$$J_{+-} = -\frac{e^2}{KR}\left\{1-\left[\frac{a_A^{-6}\left(1+\frac{R}{a_D}\right)-a_A^{-4}a_D^{-2}\left(3+\frac{R}{a_D}\right)}{(a_A^{-2}-a_D^{-2})^3}\right]e^{-2R/a_D}-\left[\frac{a_D^{-6}\left(1+\frac{R}{a_A}\right)-a_D^{-4}a_A^{-2}\left(3+\frac{R}{a_A}\right)}{(a_D^{-2}-a_A^{-2})^3}\right]e^{-2R/a_A}\right\} \tag{13}$$

From these equations, the total energy E can be obtained by substitution in equations (6) and (5). In addition, the cohesive energy E_F of the donor-acceptor pair is:

$$E_F = E-E_D-E_A = J \tag{14}$$

For nonpolar media E_F, obtained from equation (14), is positive except for $a \gtrsim R$, where the HEITLER–LONDON calculation, which is a first-order perturbation calculation, becomes inaccurate. This analysis neglects, therefore, the correlational energy of the electron and hole. In the limit of no overlap of the donor and acceptor wave functions, the correlational energy becomes the van der Waals interaction, which is attractive and has been estimated by HOOGENSTRAATEN[3]. Therefore, the cohesive energy E_F for the donor-acceptor pair is small and negative for large interimpurity distances $a \ll R$ where overlap is negligible. At somewhat smaller interimpurity distances $a < R$, E_F is positive as a consequence of the overlap of the electron and hole charge densities with each other and with each other's charged cores. The donor and acceptor are, however, metastable at their characteristic pair distance, R, while in these excited crystal states. We are particularly interested in pairs with appreciable overlap of the electron and hole wave functions, since this overlap is also involved in the transition probabilities for the optical creation and annihilation of the electron and hole.

We are primarily concerned with the energy changes accompanying changes in the state of ionization or of excitation of the donor–acceptor pair. The total ionization energy E_I involved in ionizing both the electron and the hole into their respective conduction bands is:

$$E_I = E_D + E_A + J + \frac{e^2}{KR} \tag{15}$$

The last term arises because the core interaction remains following ionization. The donor and acceptor states of Fig. 2 are perturbed towards their respective conduction band edges as a consequence of the association into pairs. The dependences of E_F or J, e^2/KR and E_I on R are shown in Fig. 3 for a typical material.

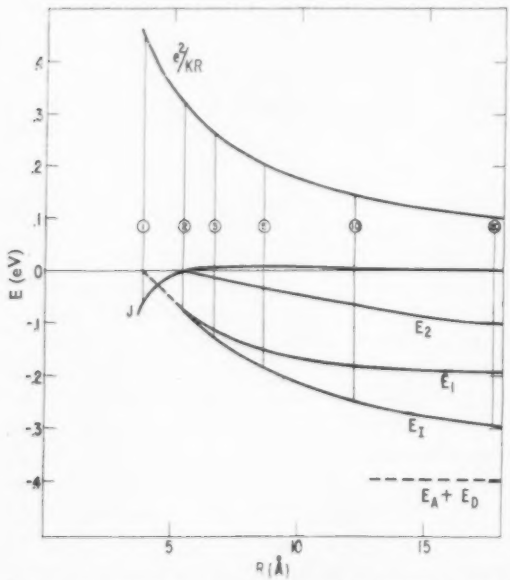

Fig. 3. Core repulsion e^2/KR, coulombic integral J, total ionization energy E_I and ionization energies for first (E_1) and second (E_2) particles ionized for representative donor and acceptor pairs in the zincblende lattice. Both donor and acceptor are at sites of the same sign. The medium is assumed to be nonpolar with $K = 8{\cdot}3$ and $R_1 = 3{\cdot}84$Å.

The annihilation energy, E_a, evolved in the radiative recombination of electron and hole in the donor–acceptor pair is:

$$E_a = E_G + E_I \tag{16}$$

where E_G, the band gap, corresponds to the energy evolved in the recombination of an electron and a hole from their conduction band edges. The sign of E_I in equation (16) arises from the ionization energies being taken as negative. The energy E_a corresponds to the optical transition energy between the bound exciton state, illustrated in Fig. 2, and the ground state of the crystal, maintaining, of course, the equilibrium nuclear coördinates of the bound exciton state during the transition. If the energies E_D and E_A of the separated donor and acceptor, respectively, and the interimpurity distance R are independent of state of ionization, that is, independent of whether the electron and hole states, respectively, are occupied or not, the creation energy E_c of the bound exciton by optical absorption in the associated pair in a nonpolar medium will be equal to the annihilation energy E_a.

For an individual electron or hole transition, the state of ionization of the pair must be specified before the transition energy can be determined. In other words, the transition energies between electron states will be different depending on the occupancy of the hole states; the transition energies between hole states, on occupancy of electron states. The limitations of the one-particle band model, illustrated in Fig. 2, are thus apparent. For example, if we are concerned with individually ionizing the electron and hole from the donor–acceptor pair, we must specify the order of the ionizations in order to arrive at the separate ionization energies for the electron and for the hole.

For pairs in continuous nonpolar media the total ionization energy E_I is equal to the sum of the ionization energies for the first and second particle ionized, E_1 and E_2, since there is no atomic relaxation between the two ionizations. If $R \gg a$, E_2 can be estimated from first-order perturbation theory. In this approximation E_2 is equal to the ionization energy, E_D or E_A, of the isolated donor or acceptor reduced by the coulombic interaction with the other charged core, J_{A-} or J_{D+}, respectively. In contrast to the two-particle system of Fig. 1, in which the particles are shielded from each other's charged cores, the one-particle system is strongly perturbed for the associated pairs of interest. The exact solution to the one-particle system is, of course, the solution of the following:

$$\left[-\frac{\hbar^2}{2m}\Delta + \frac{e^2}{K}\left(\pm\frac{1}{r_A} \mp \frac{1}{r_D} - \frac{1}{R}\right)\right]\psi = E\psi \tag{17}$$

where the upper signs apply for an electron; the lower, for a positive hole; and:

$$E_2 = E + \frac{e^2}{KR} \tag{18}$$

WALLIS *et al.*[7] have obtained numerical solutions to equation (17) for an electron in a medium of unit dielectric constant. For a medium of dielectric constant K, one scales the real inter-impurity distance R by K^{-1} to enter their tables and scales the tabulated ionization energies by K^{-2} to obtain E_2. The dependences of E_1 and E_2 on R are shown in Fig. 3. It is evident that the levels of the first particle to be ionized from the donor–acceptor pair are perturbed appreciably less toward their conduction band edge than are the levels of the second particle perturbed towards the other conduction band edge as a consequence of association.

VOL. 12 59/60

3. DONOR–ACCEPTOR PAIRS IN POLAR SEMICONDUCTORS

In a polar medium both electronic and ionic polarization must be considered, and the interaction of charged particles is in accordance with the static dielectric constant, K_s, if both polarizations occur, but is in accordance with the optical dielectric constant, K_0, if only electronic polarization occurs. The interparticle interactions illustrated in Fig. 1 will therefore be different depending on whether we are concerned with the optical creation or the optical annihilation of the bound exciton. In the creation process the only ionic polarization arises from the fixed charges of the donor and acceptor cores, whereas in the annihilation process the ionic polarization arising from the charge distributions of the electron and hole must also be included. Before taking these effects into account for associated donor–acceptor pairs, the earlier work[8–11] on isolated donors and acceptors in polar media will be reviewed.

MOTT and GURNEY[8] noted that the field acting on an electron trapped by a fixed positive charge e in a polar medium consists of an electronic part e/K_0r^2 due to the fixed charge and an ionic part which remains constant when the electron moves. This low frequency part of the polarization is produced by the fixed positive charge and by the fraction of the electronic charge that is normally within the radius r. The contribution to the field arising from ionic polarization is, therefore:

$$-\frac{e}{r^2}\left[1-4\pi\int_0^r r'^2\psi^*\psi\,dr'\right]\left(\frac{1}{K_0}-\frac{1}{K_s}\right) \tag{19}$$

for a spherically symmetrical electron density $\psi^*\psi$. Contributions to the field arising from differences in electronic polarization of the impurity core and the lattice atoms and arising from the discontinuous nature of the medium are neglected. The total field which binds the electron is therefore:

$$F(r) = \frac{e}{K_s r^2} + \frac{4\pi e}{r^2}\left(\frac{1}{K_0}-\frac{1}{K_s}\right)\int_0^r r'^2\psi^*\psi\,dr' \tag{20}$$

SIMPSON[9] substituted equation (20) in the Schrödinger equation and obtained self-consistent solutions for an electron bound to a halogen vacancy and for an electron bound to an interstitial positive ion in alkali halides. For $1s$ wave functions of the form of equation (7), the potential due to the charged core, polarization by the core and ionic polarizations by the charge distribution is:

$$V(r) = \frac{e}{K_s r} + e\left(\frac{1}{K_0}-\frac{1}{K_s}\right)\left[\frac{1}{r}-\left(\frac{1}{a}+\frac{1}{r}\right)e^{-2r/a}\right] \tag{21}$$

The radius of the Bohr orbit is found to be given by equation (9) with K replaced by K_e:

$$\frac{1}{K_e} = \frac{5}{16}\frac{1}{K_0} + \frac{11}{16}\frac{1}{K_s} \tag{22}$$

LEHOVEC[10] and CURIE[11] extended the analysis to isolated donor and acceptor impurities in polar semiconductors. The transition energy for the optical ionization of the bound electron is obtained by substituting the potential given by equation (21) and the $1s$ wave function given by equation (7) into (3). The energy of the state for optical ionization, which corresponds to annihilating an electron in the donor, is:

$$E_D^a = -\frac{me^4}{2K_e\hbar^2}\left[\frac{1}{K_0}+\frac{1}{16K_s}\right] \approx -\frac{me^4}{2K_eK_0\hbar^2} \tag{23}$$

The preceding analysis and equation (23) apply only if the time constant τ for the orbital electron motion, given by h/E, is small compared to the time constant τ_r for the polar lattice modes. The period for longitudinal lattice polarization waves is:

$$\tau_r = \left(\frac{K_0}{K_s}\right)^{1/2} \frac{\lambda_r}{c} \tag{24}$$

where λ_r is the wavelength of the residual rays.[12] For $\tau > \tau_r$, the optical ionization energy E_D^s involves K_s^{-2}, rather than $K_e^{-1}K_0^{-1}$, in equation (23), because the ionic polarization follows the orbital electron motion. The energy of the state following optical deionization, which corresponds to creating an electron in the donor, is:

$$E_D^c = -\frac{me^4}{2K_s^2\hbar^2} \tag{25}$$

for all values of τ, since for $\tau < \tau_r$ the ionic polarization by the electron distribution has not occurred during optical deionization and for $\tau > \tau_r$ the ionic polarization follows the orbital electron motion. In both cases the field with which the electron interacts depends only on the polarization by the charged core and not on the polarization by the electron itself, since the latter is spherically symmetrical. For $\tau < \tau_r$ the magnitude of the field at the electron is $e/K_s r^2$ and this leads to equation (25), whereas the field at the core is $e/K_0 r^2$. When the system subsequently relaxes with respect to the lattice modes, both become $e/K_s r^2$. Incidentally, the condition $\tau < \tau_r$ applies to the perturbed coulomb states of the two-particle systems of interest, whereas the condition $\tau > \tau_r$ applies to the dipole states of the one-particle systems of interest.

We return now to the donor–acceptor pair and consider first the creation of a bound exciton by an optical transition from the ground state of the crystal. The fixed charges of the donor and acceptor cores will have already produced electronic and ionic polarization of the medium. The electron and hole distributions, however, do not in the creation process lead to ionic polarization. The Hamiltonian which replaces equation (1) for the creation process in a polar medium is, therefore

$$H_c = -\frac{\hbar^2}{2}\left(\frac{1}{m_-}\Delta_- + \frac{1}{m_+}\Delta_+\right) + \\ + \frac{e^2}{K_s}\left(-\frac{1}{r_{A+}} - \frac{1}{r_{D-}} + \frac{1}{r_{A-}} + \frac{1}{r_{D+}} - \frac{1}{R}\right) - \frac{e^2}{K_0 r_{+-}} \tag{26}$$

The substitution of equations (2), (7) and (26) into equation (3) yields the coulomb integral J, from which the creation energy E_c can be obtained with the aid of equations (15) and (16):

$$E_c = E_G + E_D^c + E_A^c + J_{A-}^s + J_{D+}^s + J_{+-}^0 \tag{27}$$

where E_D^c is given by equation (25) and E_A^c is the acceptor counterpart of equation (25), and the components of the coulomb integral J are given by equations (11) and (12) or (13), except that the supercript indicates whether K_s or K_0 substitutes for K. From equation (27) it can be shown that in the limit of no overlap of the donor and acceptor wave functions, the transition energy E_c is increased by $e^2/R(2/K_s - 1/K_0)$ as a consequence of association.

We now consider the optical annihilation of the bound exciton. In addition to the ionic polarization by the fixed charges of the donor and acceptor cores, the ionic polarization by the electron and hole charge distributions must be included in the Hamiltonian H_a. We assume that the ionic polarization in the donor–acceptor pair is the sum of the ionic polarizations in the separated donor and acceptor. In this analysis the one-particle wave functions are taken to be given by equation (7). The total potential for each particle involves two terms of the form of equations (21) with r replaced by r_D and r_A and e replaced by $+e$ and $-e$, plus a term for the contribution to the potential by the other particle. The term for the electron–hole interaction involves K_0, because ionic polarization does not follow the instantaneous field of the electron or hole and the contributions to the potential by the ionic polarization arising from the fields of the stationary distribution have already been included in the two terms of the form of equation (21). On substituting in equation (3) to obtain the total energy, the kinetic-energy term and potential-energy term for each particle interacting with its own core yield E_D^a and E_A^a of the form of equation (23). The interaction J_{A-} is strongly modified by

the ionic polarization produced by the hole distribution and is:

$$J^{0'}_{A-} = \int_0^\infty \psi^*_D(-)eV(r_{A-})\psi_D(-)\,dv_- \qquad (28)$$

where $V(r_{A-})$ is given by equation (21) with r_{A-} and a_A replacing r and a. A similar expression with $\psi_D(-)$, r_{A-} and a_A replaced by $\psi_A(+)$, r_{D+} and a_D holds for $J^{0'}_{D+}$. The substitution of $\psi_D(-)$ and $\psi_A(+)$ according to equation (7) and integration yields:

$$J^{0'}_{A-} = J^{0'}_{D+} = \frac{e^2}{K_0 R}\left[1-\left(1+\frac{R}{a}\right)e^{-2R/a}\right] - \frac{e^2}{24a}\left(\frac{1}{K_0}-\frac{1}{K_s}\right)\left[4\left(\frac{R}{a}\right)^2+18\frac{R}{a}+9\right]e^{-2R/a} \qquad (29)$$

The choice of superscript for this interaction is based on the fact that if $R > a$, equation (29) is approximately equal to equation (11) with K replaced by K_0. For wave functions similar to equation (7) except that $a_A \neq a_D$, J_{A-} is as follows, substituting α for R/a_A and β for R/a_D:

$$J^{0'}_{A-} = \frac{e^2}{K_0 R}[1-(1+\beta)e^{-2\beta}] - \frac{e^2}{R}\left(\frac{1}{K_0}-\frac{1}{K_s}\right)\beta^3[\alpha^2-\beta^2]^{-3}\{[2\alpha^4-3\alpha^2\beta^2-3\alpha^2\beta+\beta^3+\beta^4]e^{-2\beta}+[\alpha^3\beta+3\alpha^2\beta-\alpha\beta^3-\beta^3]e^{-2\alpha}\} \qquad (30)$$

which is to be compared with equation (11) with a_D substituted for a for nonpolar semiconductors. An expression similar to equation (30), but with a_A and a_D permuted, gives $J^{0'}_{D+}$. The electron–hole interaction is found to be given by equation (12) or (13), depending on whether or not a_D and a_A are equal; with K replaced by K_0, therefore, this interaction is designated J^0_{+-}. Incidentally, the analysis of HAKEN[12] for free excitons also involves the optical dielectric constant for the electron–hole interaction if the electron–hole orbit lies within approximately 1 and 10 interatomic distances, as is the case for the donor–acceptor pairs of interest. The annihilation energy is:

$$E_a = E_G+E^a_D+E^a_A+J^{0'}_{A-}+J^{0'}_{D+}+J^0_{+-} \qquad (31)$$

which is based, of course, on equations (15) and (16), as well as on the preceding analysis. In the limit of no overlap, the transition energy E_a is increased by e^2/K_0R as a consequence of association.

The transition energies involved in creating or annihilating one particle in the pair and the other particle in its conduction band can be obtained from the deionization and ionization energies for the system of one particle bound in the field of the finite dipole. For polar media, the deionization energy can be obtained from the solution of equation (17) with K_s replacing K. The transition energy for creation, E'_c is the following for similar arguments to those used for equations (16):

$$E'_c = E_G+E_2 \qquad (32)$$

To obtain the ionization energy for a particle in a dipole field in a polar medium, it would appear necessary to modify equation (17) to take account, self-consistently, of ionic polarization by the particle distribution itself altering the potential. However, for highly associated pairs the ionization energy is sufficiently small so that the period for orbital electron or hole motion becomes large compared to the period for longitudinal lattice polarization waves τ_r, given by equation (24). The ionic polarization can, therefore, follow the orbital motion, and equation (17) is again directly applicable with K replaced by K_s. For these pairs the annihilation energy E'_a will equal the creation energy E'_c. For pairs characterized by $R \gg a$, perturbation theory is applicable, and the ionization energy of the isolated donor or acceptor is reduced by the appropriate coulombic interaction with the other charged core.

4. APPLICATIONS OF THE THEORY

Zinc sulfide containing Group IB or VB acceptors and Group IIIB of VIIB donors exhibits several luminescent emission bands. PRENER and WILLIAMS[2] have attributed an emission band

whose spectrum depends only on the identity of the acceptor to transitions between excited states of the donor and the ground state of the acceptor in an associated, but non-nearest-neighbour, donor–acceptor pair. This concept has been extended to include pairs with sufficiently great interimpurity spacings such that only radiative transitions between excited donor states and the ground state of the acceptor can occur with appreciable probability.[13] The ground state of the donor for these pairs will function as an electron trap.

More recently, a longer-wavelength luminescent emission band of zinc sulfide containing copper or silver acceptors and gallium or indium donors has been extensively investigated. APPLE and WILLIAMS[14] found the spectrum of this band to depend on the identities of both donor and acceptor, and attributed the emission to transitions between the ground state of the donor and the ground state of the acceptor in more highly associated pairs. The dependences of the intensities of the two emission bands on temperature and on donor and acceptor concentrations are in accord with these identifications of the transitions.

Although the theory can be applied to transitions involving excited donor states, we will be concerned in the present application of the theory to zinc sulfide with excitation and emission involving the ground states of donor and acceptor. These processes correspond, respectively, to the creation and annihilation of an exciton bound to the dipole field of the donor–acceptor pair. The static and optical dielectric constants of zinc sulfide K_s and K_0 are, respectively, 8·3 and 5·07. CURIE[15] has provided some theoretical justification for the use of the free election mass in the effective mass treatment of deep donors and acceptors and has attained approximate agreement with the experimental depths of electron traps in zinc sulfide using this mass, therefore, we shall use the free electron mass in applying the theory of donor–acceptor pairs to zinc sulfide.

*Table 1. Optical creation**

Pair	R(Å)	$J^s_{A-} = J^s_{D+}$	J^0_{+-}	$E_C - E_G$ (eV)	$E'_C - E_G$ (eV)
1	3·84	+0·305	−0·366	−0·150	-3×10^{-5}
2	5·43	+0·260	−0·333	−0·207	−0·004
3	6·65	+0·229	−0·316	−0·252	−0·013
5	8·59	+0·190	−0·279	−0·293	−0·033
10	12·14	+0·141	−0·221	−0·333	−0·067
20	17·60	+0·099	−0·160	−0·356	−0·102
∞	∞	0	0	−0·394	−0·197

* Interimpurity distance R, coulombic integrals J, optical creation energy E_C for an electron and hole at representative donor–acceptor pairs in the zinc blende lattice, and optical creation energy E'_C for one particle in the pair and the other particle in its conduction band. Both donor and acceptor are at sites of the same sign. Medium is polar with $K_0 = 5{\cdot}07$ and $K_s = 8{\cdot}30$.

More recently, a longer-wavelength luminescent emission band of zinc sulfide containing copper or silver acceptors and gallium or indium donors has been extensively investigated. APPLE and WILLIAMS[14] found the spectrum of this band to depend on the identities of both donor and acceptor, and attributed the emission to transitions between the ground state of the donor and the ground state of the acceptor in more highly associated pairs. The dependences of the intensities of the two emission bands on temperature and on donor and acceptor concentrations are in accord with these identifications of the transitions.

Although the theory can be applied to transitions involving excited donor states, we will be concerned in the present application of the theory to zinc sulfide with excitation and emission involving the ground states of donor and acceptor. These processes correspond, respectively, to the creation and annihilation of an exciton bound to the dipole field of the donor–acceptor pair. The static and optical dielectric constants of zinc sulfide K_s and K_0 are, respectively, 8·3 and 5·07. CURIE[15] has provided some theoretical justification for the use of the free election mass in the effective mass treatment of deep donors and acceptors and has attained approximate agreement with the experimental

The optical deionization energies of the separated donor or acceptor are given by equation (25). The radii a_D and a_A before lattice relaxation are $K_s a_0$ or 4·39Å. The optical creation energies, E_c, of the electron and hole in the pairs are given by equation (27), and the difference between this quantity and the energy to create a free electron and free hole is given in Table 1 for representative pairs in cubic zinc sulfide. These pairs involve donors and acceptors at sites of the same sign, and therefore include pairs of Group IB acceptors and Group IIIB donors or pairs of Group VB acceptors and Group VIIB donors. The energy E'_c involved in creating one particle in the pair and the other in its conduction band is calculated from

VOL. 12 59/60

equations (32) and (18) and the solution to (17), and this quantity is given in Table 1. Incidentally, the dipole states for the highly-associated pairs up to the fifth are characterized by the period of orbital motion being greater than the period of the lattice waves given by equation (24). For the coulomb states of all pairs and for the dipole states of the less-associated pairs, the period of orbital motion is less than that of the lattice waves. The interimpurity distances and the coulomb integrals are also shown in Table 1.

The optical ionization energies of the separated donor and acceptor are given by equations of the form of equation (23). The radii a_D and a_A after lattice relaxation are $K_e a_0$ or 3·66Å. The optical annihilation energies, E_a, of the electron and hole in the pairs are given by equation (31), and the difference between this quantity and the energy evolved in the recombination of a free hole and a free electron is given in Table 2 for the same pairs as those discussed previously. The energy for optically ionizing the second particle E_2 from the highly-associated pairs up to the fifth is equal to $E_c' - E_G$ of Table 1, which is, of course, also equal to $E_a' - E_G$. The energy for optically ionizing the first particle E_1 is approximately $E_a - E_G$ minus $E_c' - E_G$ for these pairs.

The excitation spectra observed with zinc sulfide containing Group IB acceptors and Group IIIB donors are in approximate agreement with the optical creation energies of Table 1. The excitation spectra for the longer-wavelength emission lie several tenths of an electron volt from the absorption edge and shift to smaller transition energies with increasing pair concentration.* At the lower concentration where association is smaller, the excitation is believed to involve the creation of a bound hole and a conduction electron; whereas at the higher concentration where association is greater, the excitation is believed to involve the creation of a bound electron and a bound hole.

The luminescent emission observed with these phosphors and attributed to transitions between the ground state of the donor and the ground state of the acceptor in quite highly-associated pairs[14] is in less satisfactory quantitative agreement with the optical annihilation energies of Table 2. The optical ionization energies of the donors and acceptors in zinc sulfide are found experimentally to be several times as great as those given by equation (23). In other words, the Stokes shift between the absorption and emission spectra of donor–acceptor pairs is greater than the continuous-dielectric model predicts. The present analysis indicates that the magnitude of the experimental Stokes shift is not a consequence of association but must arise from local atomic polarization, which is to a good approximation characteristic of separated donors and acceptors. We therefore modify the analysis for optical annihilation empirically by substituting experimental values of E_D^c and E_A^c in equation (31) and evaluating the coulomb integrals with values of a_D and a_A which are consistent with E_D^c and E_A^c. For zinc sulfide containing Group IIIB donors and Group IB acceptors, E_D^c and E_A^c

*Table 2. Optical Annihilation**

Pair	R(Å)	$J_{A-}' = J_{D+}^{0\prime}$	J_{+-}^{0}	$E_a - E_G$(eV)
1	3·84	+0·504	−0·426	−0·193
2	5·43	+0·429	−0·382	−0·299
3	6·65	+0·379	−0·349	−0·366
5	8·59	+0·314	−0·299	−0·446
10	12·14	+0·232	−0·228	−0·539
20	17·60	+0·161	−0·161	−0·613
∞	∞	0	0	−0·776

* Coulombic integrals J and optical annihilation energy E_a for an electron and hole at representative pairs as described in the footnote to Table 1.

* Unpublished data of Dr. F. J. STUDER of this laboratory.

are approximately 0·5 and 1·0 eV, and a_D and a_A are 2·76 and 1·95Å. The optical annihilation energies for pairs of these donors and acceptors are given in Table 3.

Incidentally, the present analysis also shows that the long-wavelength emission bands studied by APPLE and WILLIAMS[14] cannot be attributed to transitions between conduction band and acceptor states which are perturbed by an associated donor, since this transition energy E'_a increases as a consequence of association. The same consideration rules out the transition between unperturbed valence-band and perturbed donor states. The present analysis therefore supports the identification of the long-wavelength emission as the transition between the ground states of donor and acceptor in quite highly-associated pairs.

The analysis of Section 3 for polar semiconductors is applicable to alkali halides. However, the limitations of the continuous-dielectric approximation are even more pronounced for alkali halides than for zinc sulfide. A divalent cation substituted at an alkali site and an associated alkali vacancy constitute a donor–acceptor pair. The excitation and luminescent emission of magnesium-activated potassium chloride observed by MAKISHIMA[19] can be explained on the basis of the optical creation and annihilation of an electron and a hole in the ground states of the donor and acceptor of such an associated pair.

The energy-level structure of donor–acceptor pairs appears significant to semiconductivity, the applicability of the present analysis can be determined.

*Table 3. Optical Annihilation**

Pair	R(Å)	$J^{0'}_{A-}$	$J^{0'}_{D+}$	J^{0}_{+-}	$E_a - E_G$(eV)
1	3·84	+0·606	+0·646	−0·568	−0·740
2	5·43	+0·483	+0·497	−0·468	−0·959
3	6·65	+0·411	+0·417	−0·404	−1·063
5	8·59	+0·327	+0·328	−0·325	−1·166
10	12·14	+0·234	+0·234	−0·234	−1·266
20	17·60	+0·162	+0·162	−0·162	−1·338
∞	∞	0	0	0	−1·500

* Coulombic integrals J and optical annihilation energy E_a for an electron and hole at representative pairs whose isolated donor and acceptor have optical ionization energies of 0·5 and 1·0 eV, respectively. Other characteristics are as described in the footnote to Table 1.

In the case of polar semiconductors with sufficiently small E_A, E_D and τ_r given by equation (24), the ionic polarization will follow the orbital motions of the electron and hole, and the optical creation and annihilation energies will be equal. This may account for the absence of a Stokes shift reported by GARLICK *et al.*[16] for cadmium telluride.

The analysis of Section 2 for nonpolar semiconductors is applicable to elementary semiconductors. Modification of the theory must be made to take account of the interstitial character of the donor in the associated pairs originally reported for germanium.[1] The atomic character of the complexes involving transition metals[17] or oxygen[18] in germanium and silicon must be determined before photoconductivity, luminescent and possibly catalytic phenomena in highly-doped and compensated crystals.

5. CONCLUSIONS

From the present analysis it is evident that donor and acceptor states are perturbed towards their respective band edges as a consequence of association into pairs. The optical ionization energy for the first particle ionized from the pair is only slightly reduced, whereas the optical ionization energy for the second particle is greatly reduced by association. This effect predicts the mobilization of charge carriers of both signs on optical absorption by either particle in highly-associated

pairs. In polar media the optical creation and annihilation energies for an exciton bound at a donor–acceptor pair differ because of the ionic polarization by the electron and hole distributions. The theory is in qualitative accord with experiment for zinc sulfide containing Group IIIB donors and Group IB acceptors and supports the identification of the long-wavelength emission as the transition between the ground states of donor and acceptor in quite highly-associated pairs. The continuous-dielectric theory does not appear to be adequate to account for the depths of the ground donor and acceptor states when these states are occupied by their respective particles and equilibrium has been established with the polar medium. In general the present analysis has the same limitations as those of the effective mass treatment of one-center systems.[5]

An improved theory of the energy-level structure of the two-center systems in zinc sulfide depends on a treatment of the one-center systems which takes account of the atomic structure of the dielectric, including the effect of state of ionization on the equilibrium nearest-neighbor coördinates.

In the present analysis the problem of the transition probabilities for the optical creation and annihilation of electron–hole pairs and for the optical ionization and deionization of the individual particles at donor-acceptor pairs has not been considered quantitatively. Preliminary analysis reveals that a simple extension of the Hietler–London method is inadequate and that the fact that the hydrogen-atom-like wave functions are envelope functions modulating the unperturbed crystal states must be included in the calculation of transition probabilities.

Acknowledgements—The author is indebted to Drs. J. S. PRENER, S. ROBERTS and B. SEGALL for many helpful discussions. Several encouraging discussions with Professor J. BARDEEN are acknowledged. The author is also indebted to Dr. R. HERMAN for a helpful discussion and for a copy of ref. 7 in advance of publication. Finally, the mathematical and computational assistance of Miss E. KREIGER and Mr. D. STORY is gratefully acknowledged.

REFERENCES

1. REISS H., *J. Chem. Phys.* **25**, 400 (1956).
   REISS H., FULLER C. S. and MORIN F. J., *Bell Syst. Tech. J.* **35**, 535 (1956).
2. PRENER J. S. and WILLIAMS F. E., *Phys. Rev.* **101**, 1427 (1956); *J. Electrochem Soc.* **103**, 342 (1956); *J. Phys. Radium* **17**, 667 (1957).
3. HOOGENSTRAATEN W., *Philips Res. Rep.* **13**, 682 (1958).
4. HEITLER W. and LONDON F., *Z. Phys.* **44**, 455 (1927). See also PAULING L. and WILSON E. B., *Introduction to Quantum Mechanics*, pp. 340–345. McGraw-Hill, New York (1935).
5. BETHE H. A., *Radiation Lab. Rep.* **43**, 12 (1942). KOHN W., *Solid State Physics* Vol. 5, p. 257, Academic Press, New York, (1957).
6. MARGENAU, H. and MURPHY G. M., *The Mathematics of Physics and Chemistry*, pp. 407–412. Van Nostrand, New York (1943).
7. WALLIS R. F., HERMAN R. and MILNES H. W., *Bull. Amer. Phys. Soc.* **3**, 53 (1958).
8. MOTT N. F. and GURNEY R. W., *Electronic Processes in Ionic Crystals*, p. 85. Oxford University Press, (1940).
9. SIMPSON J., *Proc. Roy. Soc.* A**197**, 269 (1949); A**231**, 308 (1955).
10. LEHOVEC K., *Phys. Rev.* **92**, 253 (1953).
11. CURIE D., *C. R. Acad. Sci. Paris* **238**, 579 (1954).
12. HAKEN H., *Z. Phys.* **147**, 323 (1957).
13. WILLIAMS F. E., *J. Opt. Soc. Amer.* **47**, 869 (1957).
14. APPLE E. F. and WILLIAMS F. E., *J. Electrochem. Soc.* **106**, 224 (1959).
15. CURIE D., *J. Phys. Radium* **19**, 694 (1958).
16. GARLICK G. F. J., HOUGH J. M. and FATEHALLY R. A., *Proc. Phys. Soc. Lond.* **72**, 925 (1958).
17. LUDWIG G. W., CARLSON R. O. and WOODBURY H. *Bull. Amer. Phys. Soc.* **4**, 144 (1959).
18. FULLER C. S. and DOLEIDEN F. H., *J. Appl. Phys.* **29**, 1264 (1958).
19. MAKISHIMA S. Private communication.

VOL. 12 59/60

J. Phys. Chem. Solids Pergamon Press 1960. Vol. 12. pp. 276–284. Printed in Great Britain.

ON SOME OBSERVABLE PROPERTIES OF LONGITUDINAL EXCITONS

J. J. HOPFIELD and D. G. THOMAS

Bell Telephone Laboratories, Murray Hill, New Jersey

(*Received* 6 *July* 1959)

Abstract—The continuum theory of the dielectric properties of direct excitons is briefly developed for uniaxial crystals (optically isotropic crystals are a special case). The finite energy difference between longitudinal and transverse excitons can quench the linear Zeeman effect in certain geometries in both isotropic and uniaxial crystals. In uniaxial crystals it should be possible to observe "longitudinal" excitons in optical absorption. These "longitudinal" excitons are expected to have energies and oscillator strengths which depend strongly on the direction of propagation of the exciton. "Longitudinal" excitons are not observable along the principal axes of a crystal. Optical absorption measurements carried out on hexagonal ZnO have demonstrated the existence of these excitons. Even for the rather complicated case of ZnO, in which two interacting longitudinal excitons are observed, the simple continuum theory is shown to agree quantitatively with experiment.

1. INTRODUCTION

It has long been recognized that in ionic cubic crystals there is a finite difference between the energy of a longitudinal optical phonon and the energy of a transverse optical phonon at $\mathbf{k} = 0$. (Throughout the paper, "at $\mathbf{k} = 0$" is to be understood to describe the limiting process in which first the crystal size becomes infinite and then $\mathbf{k}$ is allowed to approach zero.) This energy difference arises from the long-range coulomb interaction of the polarization field. For the same reason, an energy difference is to be expected between optically active longitudinal and transverse excitons at $\mathbf{k} = 0$ in cubic crystals. The energy difference between longitudinal and transverse excitons in molecular crystals has been shown from a theoretical point of view by Fox and Yatsiv[1] and for excitons in cubic crystals by Pekar[2] and Heller and Marcus[3].

Infinitesimally close to $\mathbf{k} = 0$, the excitons (or phonons) can be classified as purely longitudinal or purely transverse for any direction of $\mathbf{k}$ in cubic crystals. Light, being a purely transverse wave, interacts only with the transverse excitons (or phonons) in cubic crystals. The longitudinal excitons are therefore optically unobservable in cubic crystals. We shall show that longitudinal excitons and the nonanalytic nature of $E(\mathbf{k})$ for excitons at $\mathbf{k} = 0$ are easily observed in hexagonal crystals.

In Section 2, a continuum theory of the dielectric properties of excitons in a uniaxial crystal is developed. The theory is based upon replacing the crystal dielectric oscillators and their local field effects by a continuum of virtual oscillators. These virtual oscillators *without* local field effects have dielectric properties equivalent to the actual crystal oscillators *with* local field effects. The energies of optically active longitudinal and transverse excitons can then be obtained from the solution of a simple eigenvalue problem.

A measurement of the optical absorption due to excitons in ZnO is described in Section 3. Two "longitudinal" excitons are observed. The energies and strengths of these lines can be calculated from measurements made on transverse excitons in ZnO and the theory of Section 2. The measured energies and strengths are both in agreement with the simple theory of Section 2.

In Section 4, it is shown that there exist some observable effects of the energy difference between longitudinal and transverse excitons even in cubic crystals, where longitudinal excitons are not directly observable. In cubic crystals the energy difference between longitudinal and transverse excitons lifts a degeneracy which would otherwise

VOL. 12 59/60

be present, and can thereby produce a quenching of the linear Zeeman effect in excitons.

2. THEORY

It is most convenient to separate the radiation field from electrostatic interactions in a solid by use of the coulomb gauge. The coulomb interactions between charged particles in the crystal are then the instantaneous coulomb interactions; the radiation field then contains only transverse waves. In this form, the exciton is a particle which represents the quantization of a classical polarization field.[4] The dipole distribution associated with a hydrogenic exciton cannot be calculated unless detailed wave functions of electrons and holes are known. In the absence of such knowledge, two simple approximations could be used; the continuum approximation (the dipole moment is assumed to be spread uniformly) and the point dipole approximation. The dipole moment distribution which is assumed to be a point dipole (in the point dipole approximation) or to be spread uniformly over an entire unit cell (in the continuum approximation) is the dipole moment distribution

$$\mathbf{P}(\mathbf{r}) = \int_{\text{cell}} \mathbf{r}'\delta(\mathbf{r}'-\mathbf{r})u_1^*(\mathbf{r}')u_2(\mathbf{r}')\,d^3\mathbf{r}'.$$

In this expression, for simple bands having $\mathbf{k}=0$ minima, u_2 is the periodic part of the Bloch function of the conduction band at $\mathbf{k}=0$, and u_1 is the periodic part of the valence-band Bloch function at $\mathbf{k}=0$. The spatial extent of the exciton does not matter.

Neither of these approximations represents the actual state of affairs in a real crystal. To avoid this difficulty, we develop the continuum theory of virtual oscillators. It is well known that for long wavelengths, there exists a continuum virtual oscillator without local field effects which is equivalent to point dipole oscillators with local field effects.[5] We will make use of these equivalent continuum oscillators. The equivalent continuum model avoids the problem of relating actual observed excitons to the microscopic theory of the dielectric, and permits the calculation of relationships between observed parameters independent of the microscopic model.

It is sufficient to treat the unquantized form of dielectric theory, with excitons replaced by polarization oscillators. In a uniaxial crystal there are two kinds of polarization oscillators. One kind is constrained to have its polarization in the x,y plane (normal to the c-axis). The second set is constrained to have its polarization vector in the z-direction (along the c-axis). The first kind of polarization oscillator represents excitons belonging to the representation (x,y) in hexagonal crystals. These will be denoted by a subscript $\perp$. The second kind of polarization oscillator represents excitons belonging to the representation (z) in hexagonal crystals. These will be denoted by a subscript $\parallel$. From this point of view, a cubic crystal is a special case of an hexagonal crystal in which, for each set of polarization oscillators of the first kind, there is a set of polarization oscillators of the second kind having the same strength and the same natural frequency. The constitutive equation can most simply be written by separating the longitudinal and the transverse parts of the electric field. The transverse part is to be thought of as representing the radiation field only, while the longitudinal part belongs to the bulk properties of the crystal in the coulomb gauge.* The constitutive relations then are

$$\frac{1}{(\omega_{\perp,i})^2}\frac{\partial^2\mathbf{P}_{\perp,i}}{\partial t^2} + \mathbf{P}_{i,\perp} = \beta_{\perp,i}\mathbf{e}\times[(\mathbf{E}_{\text{transverse}} + \mathbf{E}_{\text{longitudinal}})\times\mathbf{e}] = \beta_\perp\mathbf{E}_\perp \tag{1}$$

$$\frac{1}{\omega_{\parallel,i}^2}\frac{\partial^2\mathbf{P}_{\parallel,i}}{\partial t^2} + \mathbf{P}_{i,\parallel} = \beta_{\parallel,i}\mathbf{e}\,[(\mathbf{E}_{\text{transverse}} + \mathbf{E}_{\text{longitudinal}})\cdot\mathbf{e}] = \beta_\parallel\mathbf{E}_\parallel \tag{2}$$

* This separation appears highly artificial in classical theory. The origin of the separation is the use of the coulomb gauge. The use of this gauge is arbitrary, but *extremely* convenient, because the quantum-mechanical solid is held together by coulomb forces. In the classical dielectric theory, however, one does not ask what holds the dielectric together on a microscopic level, and gauge becomes unimportant. In making the transition from the quantum-mechanical system to the classical continuum, one loses the apparent reason for preserving the coulomb gauge. It is preserved in order to include the static coulomb interaction in the crystal Hamiltonian. In the classical case, the sense of the physics is better preserved if the separation is made, in that the energy levels thus derived will then correspond to the dispersion frequencies of oscillators observed by means of a transverse electromagnetic wave.

In these equations, $\mathbf{e}$ is a unit vector in the direction of the hexagonal c-axis, here taken to be the z-direction. In general, there will be many different oscillators i, each having its own characteristic frequency. The numbers β_i are the zero-frequency polarizabilities of the oscillators i. It should be noted that in the equivalent continuum model, local field effects are taken into account in the frequencies and polarizabilities of the oscillators. The total polarization field $\mathbf{P}$ is given by the sum of the individual contributions $\mathbf{P}_{\perp,i}$ and $\mathbf{P}_{\parallel,i}$.

The electric field can be separated into the longitudinal and transverse components in a plane wave representation. Let $\mathbf{k}$ be the propagation vector of a plane wave. The transverse component of the electromagnetic field is due to the incident radiation. The longitudinal component of the electric field is caused by the charge density of the longitudinal component of the polarization field, and is given (for propagation vector $\mathbf{k}$) by

$$\mathbf{E}_{\text{longitudinal}} = -4\pi \frac{\mathbf{k}}{|\mathbf{k}|^2}\left\{\mathbf{k}\cdot\left[\sum_i \mathbf{P}_{i,\perp} + \sum_i \mathbf{P}_{i,\parallel}\right]\right\}. \tag{3}$$

Equation (3) is equivalent to the condition of no "free charge."[5] The exciton energies are determined by the disperson relation which can be obtained by combining equations (1), (2) and (3), at the same time setting $\mathbf{E}_{\text{transverse}}$ equal to zero (i.e. no interaction with radiation is considered in finding the exciton energies).

In order to gain a qualitative appreciation of the dispersion relation, we treat the special case in which one $\omega_{\perp,t}$ has a frequency sufficiently removed from all other resonant frequencies that all other oscillators will contribute a constant amount to a background dielectric constant ϵ. For convenience, this background term will be taken to be isotropic. In a cubic crystal, there would necessarily be an oscillator $\omega_{\parallel,t}$ having the same frequency as $\omega_{\perp,t}$. The idealized uniaxial crystal treated here deviates as far as possible from a cubic crystal, and has no $\parallel$ oscillator corresponding to $\omega_{\perp,t}$.

Equations (1) and (3) then become:

$$\frac{1}{\omega_\perp^2}\frac{\partial^2 \mathbf{P}_\perp}{\partial t^2} + \mathbf{P}_\perp = \beta_\perp \mathbf{e}\times[\mathbf{E}_{\text{longitudinal}}\times\mathbf{e}]$$

$$\mathbf{E}_{\text{longitudinal}} = -\frac{4\pi\mathbf{k}}{\epsilon|\mathbf{k}|^2}(\mathbf{k}\cdot\mathbf{P}_\perp).$$

The contribution of all other oscillators far removed in frequency enters through ϵ. The dispersion relation is then simply:

$$\mathbf{P}_\perp\frac{\omega^2(\mathbf{k})}{\omega^2} = \mathbf{P}_\perp + \frac{4\pi}{\epsilon}\beta_\perp\{\mathbf{e}\times(\mathbf{k}\times\mathbf{e})\}(\mathbf{k}\cdot\mathbf{P}_\perp). \tag{4}$$

There are two solutions to equation (4):

$$\mathbf{P}_\perp\cdot\mathbf{k} = 0 : \omega^2(\mathbf{k}) = \omega_\perp \quad \text{(transverse mode)}$$

$$\mathbf{P}_\perp\cdot(\mathbf{k}\times\mathbf{e}) = 0 : \omega^2(\mathbf{k}) = \omega_\perp^2\left[1 + \frac{4\pi\beta_\perp}{\epsilon}\frac{|\mathbf{k}\times\mathbf{e}|^2}{|\mathbf{k}|^2}\right] \quad \text{(mixed mode).} \tag{5}$$

The transverse mode has its polarization vector in the x–y plane and normal to $\mathbf{k}$. The mixed mode has its polarization vector in the projection of $\mathbf{k}$ on the x–y plane. The transverse mode is purely transverse; the mixed mode is in general mixed, going from pure longitudinal for $\mathbf{k}$ perpendicular to the c-axis to pure transverse for $\mathbf{k}$ parallel to the c-axis. The energy surface for the two modes is sketched in Fig. 1 for the plane in $\mathbf{k}$ space defined

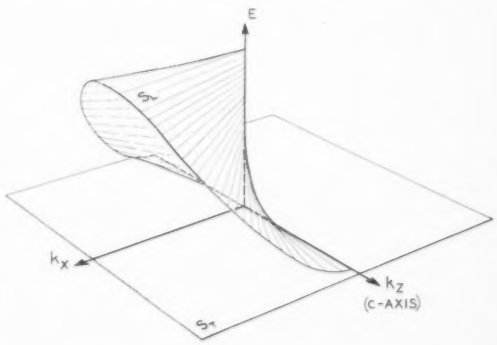

FIG. 1. $E(\mathbf{k})$ for an isolated $\perp$ exciton near $\mathbf{k} = 0$ in the plane $k_y = 0$. The energy surface S_T belongs to the pure transverse exciton. The energy surface S_L belongs to the exciton which is purely longitudinal for $\mathbf{k}$ parallel to the c-axis, and purely transverse for $\mathbf{k}$ perpendicular to the c-axis.

by $k_y = 0$. For **k** perpendicular to the c-axis, the modes are related by

$$\omega_l = \left(\frac{\epsilon + 4\pi\beta_\perp}{\epsilon}\right)^{1/2} \omega_t$$

the usual LYDDANE–SACKS–TELLER[6] relation for cubic crystals.

In order to observe the mixed modes in hexagonal crystals, it is necessary to use light whose propagation vector in the crystal makes an angle $\phi \neq 90°$ or $0°$ with the c-axis. For light polarized in the plane containing both **k** and the c-axis, only the mixed mode would be observed. For light polarized perpendicular to the c-axis, only the transverse mode would be observed. For these two experiments, respectively one would obtain the results in Table 1.

Table 1

Frequency of observed line	Oscillator strength of absorption line (in proper units)
$\omega_\perp \sqrt{1 + \frac{4\pi\beta_\perp}{\epsilon} \sin^2\phi}$	$4\pi\beta_\perp \cos^2\phi$
$\omega_\perp$	$4\pi\beta_\perp$

In cubic crystals, due to the presence of a $\parallel$ oscillator, all excitons would be purely transverse or purely longitudinal.

Optical phonons

The effects which have been described so far exist for both excitons and optical phonons in hexagonal crystals. In the case of optical phonons, the effects should be particularly small. For the optical phonons, $\omega_\perp$ and $\omega_\parallel$ are usually quite close. The effect of the polarization field interaction is to try to make all polarization normal modes either purely transverse or purely longitudinal. The strength of this electrostatic interaction is given by

$$\omega_\perp \left[1 - \sqrt{\left(\frac{\epsilon_0}{\epsilon_\infty}\right)}\right].$$

For most hexagonal ionic crystals the strength of this electrostatic interaction is experimentally about $\omega_\perp/4$. On the other hand, the crystal field splitting $|\omega_\perp - \omega_\parallel|$ in typical materials is roughly $\omega_\perp/100$. (The experimental numbers used here are those appropriate to hexagonal SiC.[7]) Because the electrostatic energy is so much larger than the crystal field splitting, all modes will be very nearly pure longitudinal and pure transverse. In restrahl measurements, the longitudinal phonons will be only very weakly active for nonprincipal directions of **k**. In practice, these lines might be observed for certain polarizations of the incident light in nonprincipal directions. In crystals which deviate further from optical isotropy, the effects would be correspondingly larger.

Excitons

In general, it would be rather difficult to investigate by optical means the "longitudinal" (mixed) phonons in hexagonal crystals due to the dominance of the electrostatic interaction over the crystal field splittings. For excitons in hexagonal crystals, the electrostatic interaction is no longer dominant ($4\pi\beta$ is very small for excitons of large radius). The absorption which one hopes to observe due to mixed excitons is qualitatively different from that which might have been off-hand expected. A few degrees from a principal direction, one expects to see new absorption lines which differ in energy from *all* ordinary (transverse) exciton lines seen in *any* principal direction. These absorption lines interact with *all* the light in a properly chosen geometry (as would not be the case for a slightly misaligned plane of polarization), and can easily be strong enough to lead to complete absorption in crystals a few microns thick for angles of deviation as small as 5° from principal directions. These absorption lines are due to "longitudinal" excitons (i.e. mixed excitons having chiefly a longitudinal component).

In ZnO, a situation rather similar to that described in the text occurs for the excitons. There are two modes (excitons) $P_{\perp 1}$ and $P_{\perp 2}$ which have been identified by appropriate reflection measurements.[8] The lines are well enough separated from all other reflection lines that ϵ is approximately constant and isotropic. The parameters $\omega_{1\perp}$, $\omega_{2\perp}$, $\beta_{1\perp}$, $\beta_{2\perp}$ and ϵ have been determined by an analysis of the reflectivity measured with **E** and **k** perpendicular to the c-axis. The values of

VOL. 12 59/60

the parameters are $\omega_{1\perp} = 3{\cdot}376_8$eV, $\omega_{2\perp} = \omega_{1\perp} + 0{\cdot}006_2$, $\beta_{1\perp} = 0{\cdot}0074 \pm 15$ per cent.

$\beta_{2\perp} = 0{\cdot}024 \pm 15$ per cent and $\epsilon = 5{\cdot}0 \pm 10$ per cent at 4·2°K. The energies $\omega_{1\perp}$ and $\omega_{2\perp}$ are slightly temperature-dependent, but their difference (which is the energy of importance for the calculations) is not.

Two longitudinal excitons, corresponding to the two oscillators $\omega_{1\perp}$ and $\omega_{2\perp}$ are expected. The experiment is designed to observe these "longitudinal" excitons by virtue of their small transverse part (which does not exist for cubic crystals). The frequencies and strengths of the expected mixed excitons can be found by solving equations (1) and (3) for the case in which only two oscillators are present. The solution of the eigenvalue problem defined by (1) and (3) for the transverse mode energies is trivial. There are two "longitudinal" (mixed) solutions. One eigenstate has almost equal amounts of the two polarization fields $\omega_{\perp 1}$ and $\omega_{\perp 2}$ oscillating 180° out of phase, with a resultant small energy shift and small strength. The higher-frequency eigenstate has almost equal amounts of the two polarization fields oscillating in phase, with a resultant large energy shift and large strength. Qualitatively, the lower-energy longitudinal line has a large effective ϵ due to the upper line, so its shift is small. The higher-energy longitudinal line has a small effective ϵ due to the lower line, so its shift is large.

The two modes $\omega_{1\perp}$ and $\omega_{2\perp}$ are the lowest-lying excitons of appreciable strength. An exciton of approximately the same strength lies approximately 0·040 eV above these two excitons, out of the current range of interest. All excited states of these two low-lying excitons also lie more than 0·040 eV above these two strong lines. In addition, there exists a very weak (exciton) mode $P_{\parallel}$ having almost the same frequency as $P_{\perp 1}$. The optical activity of this weak line is associated with the small spin-orbit coupling which splits the excitons $P_{\perp 1}$ and $P_{\perp 2}$. All other excitons falling in the region of experimental interest are known from group theory (confirmed by experiment) to be optically inactive.[9]

3. EXPERIMENT

An experiment was performed on ZnO to check the theory and to determine whether some absorption lines which had already been observed in ZnO were due to "longitudinal" excitons. The absorption constant of ZnO was measured as a function of the angle of incidence. The geometry used is shown in Fig. 2. A continuum source of illumination was used, and the transmitted light analyzed

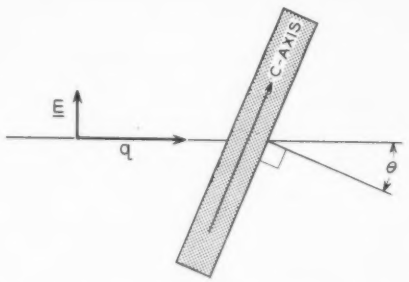

FIG. 2. The experimental geometry of **k**, **E** and *c*-axis. All vectors drawn lie in the plane of the drawing.

by a Bausch and Lomb spectrograph. A focused beam of 3° full angle was used because of the small size of the ZnO crystals. Densitometer traces of the spectrograph photographs were analyzed to determine the absorption constant. Polarized light was used (as is indicated in the figure) in order to calibrate the transmission measurements. Small deviations of the plane of polarization from the nominal plane of polarization are unimportant. Such an error would result in the presence of a small amount of light polarized perpendicular to the *c*-axis. For this component, the absorption constant is so great (about 10^5 cm^{-1}) in the spectral region of interest that essentially none of this unwanted component can get through the 10μ thick crystal.

The qualitative results of the absorption experiment at 4·2°K are shown in Fig. 3. The energies $\omega_{\perp 1}$ and $\omega_{\perp 2}$ are indicated by arrows. Line A is due to the previously mentioned weak exciton $\omega_{\parallel}$. (This exciton is "weak" compared with $\omega_{\perp 1}$, which, as a transverse exciton, has a peak absorption coefficient of about 10^6 cm^{-1}.) The sloping background is due to the tail of a very strong exciton absorption line lying to higher energy. Lines B and C are the lines of interest. Within the accuracy of experimental measurement, these lines lie at the same energy for $\theta = 0°$, 2°, 4° and 6°. Lines B and C have roughly the same strength at 2° as at 0°, but increase in strength rapidly as θ

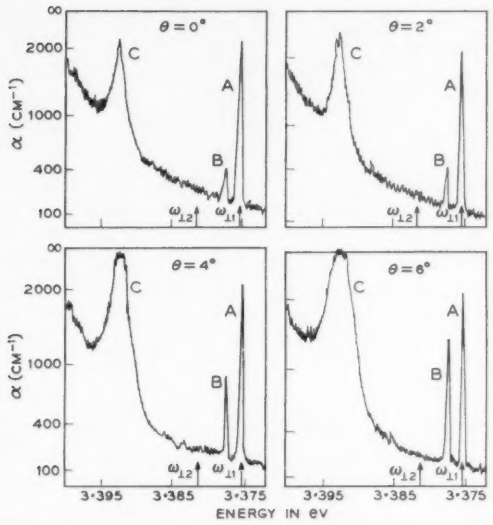

FIG. 3. The absorption spectrum of ZnO as a function of θ at 4°K. Note that the absorption constant scale is non-linear.

becomes larger than 4°. Line A, on the other hand, remains constant in strength. The rapidly increasing strengths of lines B and C is characteristic of excitons which are nearly completely longitudinal; the constant strength of line A indicates that this exciton is (as was assumed) chiefly transverse.

The same absorption experiment was also carried out at 77°K to obtain more quantitative information about the line strength as a function of angle. At 77°K the exciton lines are broadened and peak absorption coefficients are therefore smaller. Unfortunately, due to the increased background absorption, it was possible to measure only the behaviour of line B. The results of this experiment are given in Fig. 4, which shows the peak absorption coefficient (after the subtraction of the background absorption) as a function of angle for line B at 77°K. The line width for line B was also measured at 77°K to provide a means of evaluating the oscillator strength. This width was independent of angle over the range of angles measured. The experimental points fall within experimental accuracy on a straight line.

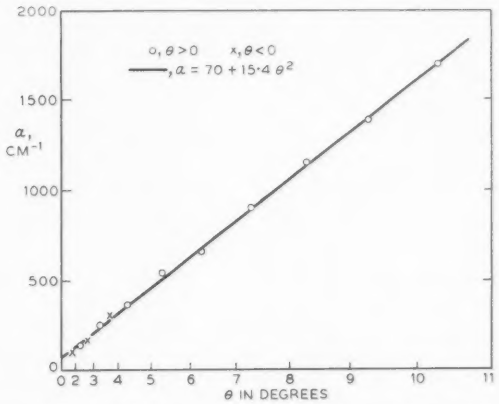

Fig. 4. The peak absorption coefficient of peak B at 77°K. as a function of θ. The angular scale is linear in θ^2. The circles are experimental points for $\theta > 0$ and the crosses for $\theta < 0°$.

From the theory of Section 2, the parameters ϵ, $\beta_{\perp 1}$, $\beta_{\perp 2}$, $\omega_{\perp 1}$ and $\omega_{\perp 2}$ given at the end of Section 2, and the measured width of line B at 77°K, the complete behaviour of lines B and C can be computed. A comparison of theory (for small angles) and experiment is given below. The energy $\omega_{\perp 1}$ is taken as a reference zero.

A refractive correction is included in the calculations to relate the exterior angle θ to the interior angle ϕ. The "Theory" column of Table 2 is computed from the reflection measurements alone; there are no free parameters to adjust.

Table 2

	Theory	Experiment
Energy of line B	0·0010	0·0016 eV
Energy of line C	0·0158	0·0168 eV
$\left(\frac{\text{Strength of line B}}{\text{Strength of line C}}\right)$ at 4·2°K	0·035	0·05 + 100% −50%
Peak absorption coefficient of line B at 77°K	$\alpha_{peak} = 10\theta^2$	$\alpha_{peak} = 70 + 15{\cdot}4\theta^2$

Most of the experimental data agree with the theory within the error introduced into the theoretical calculation by the uncertainty of the parameters used. It should be noted that the ratio of strengths and the slope of the peak absorption are sensitive functions of $\omega_{2\perp} - \omega_{1\perp}$, changing about 30 per cent for a change of 0·001 eV in $\omega_{2\perp} - \omega_{1\perp}$. One point, however, is in definite disagreement with theory. The theory states unambiguously that the longitudinal lines should be unobservable for $\theta = 0°$, whereas Figs. 3 and 4 indicate* that the lines are small but present. We believe that their presence is due not to experimental error (the 0° residual absorption is an order of magnitude too large to be due to the 3° convergent beam), but is instead due to the failure of the infinite-wavelength theory used. Ordinarily, in treating optical processes in crystals, the effect of the finite wave vector of the light in the crystal is neglected. The error thus introduced is of the order $(ka)^2$, where k is the wave vector of the light in the crystal and a is a typical lattice dimension. In the case at hand, $(ka)^2 \approx 10^{-4}$. From the known strengths of the lines $\omega_{\perp 1}$ and $\omega_{\perp 2}$ and the width of peak B, one could then expect a residual "error" for α_{max} of the order of 100 cm^{-1}. This is of the same order of magnitude as the observed residual absorption. The effect can be regarded as due to the small but finite photon momentum or, equivalently, to the fact that optical transitions are not precisely vertical. Such effects are not unkown in cubic crystals, and must be invoked, for example, to explain the existence of the "$n = 1$" line in the exciton absorption spectrum of Cu_2O.[10]

The observed widths of the two longitudinal exciton lines differ considerably, as can be seen in Fig. 3. The decreased lifetime of the higher-energy longitudinal exciton may simply be due to the fact that the higher-energy exciton of small $\mathbf{k}$ may be scattered by impurities or phonons into states of the lower-energy exciton of higher $\mathbf{k}$. No corresponding states exist for scattering of the lower-energy longitudinal exciton. A second possibility is that the scattering is related to the size of the oscillating dipole, and that the large dipole matrix elements of the higher exciton lead to strong interactions and rapid scattering.

A few qualitative points should be emphasized concerning the "longitudinal" effects in hexagonal crystals. First, as is well known in the case of cubic crystals, group theory can be misleading with reference to exciton lines. The usual analysis of the group theory of exciton lines applies at $\mathbf{k} = 0$. To apply this result to excitons of small but finite $\mathbf{k}$ is not strictly permissible, because of the non-analytic nature of the exciton energy surface. In cubic crystals the errors which are made by extending the results of group theory at $\mathbf{k} = 0$ to finite $\mathbf{k}$ are not important in determining selection rules, since the chief error is the energy difference between the longitudinal (unobservable) exciton and the transverse excitons. *In hexagonal crystals*, on the other hand, because the "longitudinal" (mixed) modes are optically observable, *it is necessary to understand the nature of the singularity in* $E(\mathbf{k})$ in order to understand quantitatively the positions and oscillator strengths of observed exciton absorption lines. Second, it is essential to use single crystals in investigating the exciton states in hexagonal crystals. In the case of ZnO, for instance, the use of polycrystalline films would have produced a confusing jumble of experimental results due to the varying energy position of the "longitudinal" exciton line. Finally, the finite angular aperture of an optical system can contribute strongly to observed effects. For the small-aperture Bausch and Lomb spectrometer used in this study, the correction due to the finite aperture was about 15 per cent of the observed residual absorption at 0°.

4. OTHER EFFECTS IN CUBIC CRYSTALS

The linear Zeeman effect in certain crystal geometries can be quenched by the energy difference between the longitudinal and transverse excitons. As an example of this, we consider the case of the Cu_2O yellow exciton series which has been studied extensively by Gross and co-workers.[10] In Cu_2O the direct transition is forbidden, and excitons are observed in p-like orbital states. (The $n = 1$ line, though present, is very weak.) The electron spin effectively does not enter the problem.

Let the magnetic field be along the z-direction, let y be the direction of the incident light and let z be the direction of polarization of the incident light.

* The mixed mode at 0° angle of incidence was below noise level for the experiment at 77°K. Quantitative measurements could be made at 77°K only for external angles of incidence greater than 1·5°.

At first sight, one would have expected a linear Zeeman effect to be observed in this geometry. However, because of the direction of propagation of the incident light, the energy difference between the longitudinal and transverse excitons is important. The Hamiltonian matrix for the linear Zeeman effect in this geometry is:

$$H = \begin{array}{c} \\ \mathbf{P}_x \\ \mathbf{P}_y \\ \mathbf{P}_z \end{array} \begin{array}{c} \begin{array}{ccc} \mathbf{P}_x & \mathbf{P}_y & \mathbf{P}_z \end{array} \\ \begin{pmatrix} E+\delta & i\mu H & 0 \\ -i\mu H & E & 0 \\ 0 & 0 & E \end{pmatrix} \end{array}$$

where

$$\delta = E\left[\sqrt{\left(1+\frac{4\pi\beta}{\epsilon}\right)}-1\right].$$

E is the energy of the exciton and β and ϵ are as defined earlier in the text. The existence of the term δ will quench the linear Zeeman effect if $\delta \gtrsim \mu H$. For the case of Cu_2O, in the largest fields used by GROSS, the effect would be quenched if

$$\frac{4\pi\beta}{\epsilon} \gtrsim 10^{-4}$$

if the electron and hole masses differ by a factor of 2. For comparison, in ZnO $4\pi\beta/\epsilon \approx 4\times 10^{-3}$. The Cu_2O excitons are "forbidden," so $4\pi\beta/\epsilon$ would be less by a factor of

$$\left(\frac{\text{exciton radius}}{\text{lattice constant}}\right)^2$$

than for ZnO. On the other hand, the excitons are more tightly bound in Cu_2O, which would tend to make $4\pi\beta/\epsilon$ larger. Unfortunately, $4\pi\beta/\epsilon$ is not known from experiments in Cu_2O.

GROSS has observed the absence of a linear Zeeman effect in Cu_2O, and has attributed this absence to the equality of the electron and hole masses ($\mu = 0$). It would appear that quenching due to longitudinal excitons can equally well be the cause of the absence of the linear Zeeman effect in the low-lying exciton lines of Cu_2O.*

The quenching hypothesis can be rather easily checked. If the light is instead sent *along* the magnetic field, the Hamiltonian becomes:

$$H = \begin{array}{c} \\ \mathbf{P}_x \\ \mathbf{P}_y \\ \mathbf{P}_z \end{array} \begin{array}{c} \begin{array}{ccc} \mathbf{P}_x & \mathbf{P}_y & \mathbf{P}_z \end{array} \\ \begin{pmatrix} E & i\mu H & 0 \\ -i\mu H & E & 0 \\ 0 & 0 & E+\delta \end{pmatrix} \end{array}$$

and a linear Zeeman effect will be obtained if μ is not zero.

This quenching is to be predicted for all direct exciton Zeeman effects in which the Zeeman splitting is expected to arise from the splitting of an exciton which belongs to a three-dimensional irreducible representation. The stronger the exciton line, the more important this quenching becomes. Conversely, the longitudinal—transverse energy difference goes to zero faster than the exciton binding energy for highly excited exciton states, and so rapidly becomes unimportant for excited states. There is no effect for continuum states.

Linear Zeeman effects in excitons can sometimes arise from a near degeneracy of exciton levels of different symmetry which are mixed by a magnetic field (such a case has been observed by THOMAS in ZnO). Accidental degeneracies can easily arise in hydrogenic excitons, for spin–spin interactions between electrons and holes are very short-range forces. If the continuum approximation is not valid, it is possible for the long-range coulomb effects to shift the transverse exciton states as well as the longitudinal states. This shift could remove the accidental degeneracy which is responsible for the linear Zeeman effect in the case of near degeneracy that might otherwise have been expected, and lead to a quenching of this Zeeman effect also.

All the effects treated so far have referred to direct excitons. The effect of the long-range electrostatic interaction on indirect excitons is a much more difficult problem, for deviations from the continuum approximations must necessarily occur for excitons of large $\mathbf{k}$. (Such deviations are necessary to preserve the periodicity of the exciton in the Brillouin zone.) The effects will probably be far less interesting. It is clear, however, that the long-range electrostatic interaction should give rise to finite energy corrections and configuration mixings which do not appear explicitly in the effective mass

* *Note added in proof:* One of us (D.G.T.) has since made measurements which indicate that $4\pi\beta/\epsilon$ is too small to quench the Zeeman effect in Cu_2O.

VOL. 12 959/60

approximation. Suppose, for example, the holes were extremely heavy compared to the electrons. The usual effective mass problem would yield an exciton binding energy which would be the same as the binding energy of a donor. The electrostatic effects, however, could produce an energy shift from this calculated energy which could be as large as 20 per cent of the exciton binding energy for some states. This effect is not due to polaron effects, but is caused by the same electrostatic interactions which lead to the finite energy difference between longitudinal and transverse excitons near $\mathbf{k} = 0$.

REFERENCES

1. Fox D and Yatsiv S., *Phys. Rev.* **108**, 938 (1957).
2. Pekar S. I., *Zh. eksp. teor. fiz.* **8**, 360 (1958).
3. Heller W. R. and Marcus A., *Phys. Rev.* **84**, 809 (1951).
4. Hopfield J. J., *Phys. Rev.* **112**, 1555 (1958).
5. Born M. and Huang K., *Dynamical Theory of Crystal Lattices*, Section 7. Oxford University Press (1954).
6. Lyddane R. H., Sachs R. G. and Teller E., *Phys. Rev.* **59**, 673 (1941).
7. Spitzer W. G., Kleinman D. and Walsh D., *Phys. Rev.* **113**, 127 (1959).
8. Thomas D. G., *Bull. Amer. Phys. Soc.* **4**, 154 (1959).
9. Hopfield J. J., *Bull. Amer. Phys. Soc.* **4**, 154 (1959).
10. Gross E. F. and Zakharchenya B. P., *J. Tech. Phys. (U.S.S.R.)* **2**, 1808 (1957).
    Gross E. F., Zakharchenya B. P. and Pavenskii P. P., *Zh. tekh. fiz.* **2**, 2018 (1957).
    Gross E. F. and Zakharchenya B. P., *J. Phys. Radium* **18**, 68 (1957).

J. Phys. Chem. Solids Pergamon Press 1960. Vol. 12. pp. 285–294. Printed in Great Britain.

THE EFFECT OF STRAIN ON THE SEEBECK COEFFICIENT OF *n*-TYPE GERMANIUM*

J. R. DRABBLE and R. D. GROVES

(*Received* 15 *July* 1959)

Abstract—The effect of uniaxial strain on the Seebeck coefficient of *n*-type germanium has been studied in the temperature range where phonon-drag effects are important. The changes in the Seebeck coefficient were found to be closely correlated with the changes in the resistivity under the same conditions. The theory of the effect is discussed, and it is shown that the measurement of both these changes leads in a fairly direct way to an estimate of the anisotropy of the phonon-drag part of the Peltier tensor for a single valley. Results are presented and analysed for a number of specimens.

VOL. 12 59/60

1. INTRODUCTION

HERRING and VOGT[1] put forward a theory which was able to give a successful description of the conductivity and galvanomagnetic effects in *n*-type germanium. The basis of this theory was the introduction of an energy-dependent relaxation time tensor for the group of electrons within a valley. The physical effects discussed could be recast in a form involving moments of varying order of the components of the relaxation time tensor over the electron distribution. In the simple case of non-degenerate statistics these moments reduce to Maxwellian averages. The ratio of these moments for the different components of the relaxation-time tensor, coupled with a knowledge of the band structure provides information on the scattering processes to which the electrons are subjected.

Recently, HERRING *et al.*[2] have extended the theory to include thermoelectric and thermomagnetic effects with special reference to the region of temperature where phonon-drag effects are important. For a description of these effects, an energy-dependent phonon drag Peltier tensor has to be introduced into the Herring-Vogt model. The energy-dependence of the components of this tensor and the ratios of the various moments have been determined by the above authors from thermomagnetic data. These quantities provide information on the electron-phonon interaction and indirectly on phonon-phonon interactions.

The present paper discusses an alternative method of studying the anisotropy of the phonon-drag Peltier tensor for a single valley in *n*-type germanium. This is done by studying the effect of strain on the Seebeck coefficient together with simultaneous measurements of piezoresistance. Although this method does not give directly the energy-dependence of the components, as does the thermomagnetic approach, it appears in principle to be able to determine the anisotropy to a considerable degree of accuracy.

The main concerns of this paper are three in number. First, the theory is discussed, in Section 2, for many-valley semiconductors of overall cubic symmetry with special reference to *n*-type germanium. In Section 3, the experimental technique is discussed, and finally, in Section 4, results which have been obtained so far are analysed in terms of the theory to indicate the possibilities and limitations of the method.

2. THEORY OF THE EFFECT OF STRAIN ON THE PELTIER COEFFICIENT OF A MANY-VALLEY SEMICONDUCTOR

(*a*) *General theory for many-valley semiconductors of cubic symmetry*

The theory of the effect of strain on the Peltier coefficient of a many-valley semiconductor is closely related to the theory of elastoresistance for such materials. HERRING and VOGT[1] have

* Communication from the Staff of the Research Laboratories of the General Electric Company Limited, Wembley, England.

discussed the elastoresistance of many-valley semiconductors which possess overall cubic symmetry. Their discussion applies in particular to *n*-type germanium and silicon. KEYES[3] has extended the discussion to many-valley semiconductors possessing an axis of symmetry.

There seems little doubt that the large elastoresistance effects which have been observed in *n*-type germanium and silicon are dominated by the strain-induced transfer of electrons between different valleys. This comes about because, in general, an anisotropic strain produces shifts in the minimum energies of the valleys which are different for different valleys. The detailed work of MORIN *et al.*[4] on the elastoresistance of *n*-type germanium and silicon, when compared with the theoretical predictions of HERRING and VOGT, shows that the electron transfer effect can account for practically all of the observed elastoresistance in the impurity saturation range of temperature. Contributions associated with inter-valley scattering become increasingly important with increasing temperature, though these still appear to be small at 200°K.

In view of the above considerations, it is of interest to consider the effect of the strain induced electron transfer on the Peltier coefficient of a many-valley semiconductor. For the purposes of direct comparison and because the results refer to the measurements discussed later, the theory will be given for the same conditions as those assumed by HERRING and VOGT in their discussion of the elastoresistance. The relevant features are the overall cubic symmetry, the use of non-degenerate statistics and the assumption that the total number of carriers is unaffected by the strain. The notation and general approach of HERRING and VOGT will be adhered to as closely as possible throughout.

For the purposes of comparison, it is useful to summarise the relevant features of the theory of elastoresistance. The components of the fourth-order elastoresistance tensor $\mathbf{m}$ are defined for a cubic semiconductor by the relation:

$$m_{\alpha\beta\gamma\delta} = -\frac{1}{\sigma_0}\frac{\partial\sigma_{\alpha\beta}}{\partial u_{\gamma\delta}} \tag{1}$$

where $u_{\gamma\delta}$ is the strain tensor and $\sigma_{\alpha\beta}$ is the conductivity tensor, which in the absence of strain has the form of $\sigma_0\delta_{\alpha\beta}$. The components $\sigma_{\alpha\beta}$ are given by:

$$\sigma_{\alpha\beta} = \sum_i \sigma^{(i)}_{\alpha\beta} \tag{2}$$

where $\sigma^{(i)}_{\alpha\beta}$ is the conductivity tensor of the i'th valley referred to a common set of axes for all valleys. Neglecting all effects of strain other than those associated with the changes in energies of the valleys, the combination of equations (1) and (2) leads to:

$$m_{\alpha\beta\gamma\delta} = -\frac{1}{\sigma_0}\sum_{i,j}\frac{\partial\sigma^{(i)}_{\alpha\beta}}{\partial\epsilon^{(j)}}\frac{\partial\epsilon^{(j)}}{\partial u_{\gamma\delta}} \tag{3}$$

where $\epsilon^{(j)}$ is the minimum energy of valley j. The quantities $\partial\epsilon^{(j)}/\partial u_{\gamma\delta}$ are the deformation potential constants, which can all be expressed in terms of the corresponding constants for a single valley.

Expressing the dependence of $\sigma^{(i)}_{\alpha\beta}$ on the difference between the position of the Fermi level ϵ_F and $\epsilon^{(i)}$ and using the property that the variation of the Fermi level with strain in the impurity saturation range is the average of all those of the $\epsilon^{(j)}$ (total density of carriers is constant with strain), the electron transfer effect leads to:

$$-\frac{1}{\sigma_0}\frac{\partial\sigma^{(i)}_{\alpha\beta}}{\partial\epsilon^{(j)}} = \pm\frac{1}{kT}\frac{\mu^{(i)}_{\alpha\beta}}{\mu_0}\left[\frac{\delta_{ij}}{N_v} - \frac{1}{N_v{}^2}\right] \tag{4}$$

where the upper and lower signs apply for electrons and holes respectively, N_v is the total number of valleys, $\mu^{(i)}_{\alpha\beta}$ is the mobility tensor for the i'th valley and μ_0 is the overall zero strain mobility.

If the axes on which the valleys lie are specified, the expression (4) can be substituted into (3) and the summations can be carried out. This has been done by HERRING and VOGT for valleys on (111), (100) and (110) axes. The resultant expressions for the elastoresistance components are all inversely proportional to the temperature T and involve the deformation-potential constants for a single valley, the components of the mobility tensor for a single valley and the overall mobility tensor.

For a parallel treatment of the effect of strain on the Peltier coefficient, a second-order tensor $\boldsymbol{\nu}$ is considered. This is defined by

$$\boldsymbol{\nu} = \boldsymbol{\Pi}\,.\,\boldsymbol{\sigma} \tag{5}$$

where $\boldsymbol{\Pi}$ is the Peltier tensor of the crystal. A

VOL. 12 59/60

fourth-order tensor $\mathbf{p}$ is defined by a relation analogous to equation (1):

$$p_{\alpha\beta\gamma\delta} = -\frac{1}{\nu_0}\frac{\partial \nu_{\alpha\beta}}{\partial u_{\gamma\delta}} \tag{6}$$

where in the absence of strain $\nu_{\alpha\beta}$ has the form $\nu_0\delta_{\alpha\beta}$ with $\nu_0 = \Pi_0\sigma_0$. The components $\nu_{\alpha\beta}$ have the property analogous to (2) viz.

$$\nu_{\alpha\beta} = \sum_i \nu_{\alpha\beta}^{(i)} = \sum_i \sum_\lambda \Pi_{\alpha\lambda}^{(i)}\sigma_{\lambda\beta}^{(i)} \tag{7}$$

Combining equations (7) and (6) and using the same assumption as those used in deriving equation (3) leads to the analogous equation

$$p_{\alpha\beta\gamma\delta} = -\frac{1}{\Pi_0\sigma_0}\times$$

$$\times \sum_{i,j}\left\{\sum_\lambda\left[\Pi_{\alpha\lambda}^{(i)}\frac{\partial\sigma_{\lambda\beta}^{(i)}}{\partial\epsilon^{(j)}} + \sigma_{\lambda\beta}^{(i)}\frac{\partial\Pi_{\alpha\lambda}^{(i)}}{\partial\epsilon^{(j)}}\right]\right\}\frac{\partial\epsilon^{(j)}}{\partial u_{\gamma\delta}} \tag{8}$$

From equation (4), the first term inside the parentheses is

$$-\frac{1}{\Pi_0\sigma_0}\sum_\lambda \Pi_{\alpha\lambda}^{(i)}\frac{\partial\sigma_{\lambda\beta}^{(i)}}{\partial\epsilon^{(j)}}$$

$$= \pm\frac{1}{kT}\frac{(\mathbf{\Pi}^{(i)}\cdot\boldsymbol{\mu}^{(i)})_{\alpha\beta}}{\Pi_0\mu_0}\left[\frac{\delta_{ij}}{N_v} - \frac{1}{N_v^2}\right] \tag{9}$$

which is of the same form as equation (4) except that the components of the mobility tensor are replaced everywhere by the components of the product of the Peltier and mobility tensors. These two sets of components, however, transform in identical ways from one valley to another. Thus, the first part of equation (8) can be obtained in particular cases by taking the expression for the corresponding elastoresistance component and replacing the components of the mobility tensor in this by the corresponding components of the product of the Peltier and mobility tensors. For example, HERRING and VOGT[1] give the elastoresistance components for valleys on (111) axes as:

$$m_{11} = 0,\ m_{12} = 0 \text{ and } m_{44}$$

$$= \pm\frac{1}{9}\frac{\Xi_u}{kT}\left(\frac{\mu_\parallel^{(i)} - \mu_\perp^{(i)}}{\mu_0}\right) \tag{10}$$

where Ξ_u is the deformation-potential constant associated with a uniaxial shear compounded out of a stretch along the symmetry axis of a valley and a contraction in the two normal directions. The contributions of the first part of equation (8) to the corresponding components of $\mathbf{p}$ are:

$$0,\ 0 \text{ and } \pm\frac{1}{9}\frac{\Xi_u}{kT}\frac{(\Pi_\parallel^{(i)}\mu_\parallel^{(i)} - \Pi_\perp^{(i)}\mu_\perp^{(i)})}{\Pi_0\mu_0} \tag{11}$$

Similar rules apply to the other cases discussed by HERRING and VOGT[1].

The second part of equation (8) can be obtained easily. The dependence of $\Pi_{\alpha\lambda}^{(i)}$ on the valley energies arises through the presence of a term

$$\mp(\epsilon^{(i)} - \epsilon_F)/e.$$

Differentiating this with respect to the strain components and using the conditions on the variation of the Fermi level leads to:

$$\frac{\partial\Pi_{\alpha\lambda}^{(i)}}{\partial\epsilon^{(j)}} = \mp\frac{1}{e}\left[\delta_{ij} - \frac{1}{N_v}\right] \tag{12}$$

The second part of equation (8) is therefore:

$$\pm\frac{1}{\Pi_0\sigma_0}\sum_{i,j}\sum_\lambda \frac{\sigma_{\lambda\beta}^{(i)}}{e}\left[\delta_{ij} - \frac{1}{N_v}\right]\frac{\partial\epsilon^{(j)}}{\partial u_{\gamma\delta}} \tag{13}$$

By rearranging the summations and introducing the mobility tensor, this can be put in the form:

$$\frac{kT}{e\Pi_0}\sum_\lambda\left[\sum_{i,j}\pm\frac{\mu_{\lambda\beta}^{(i)}}{kT\mu_0}\left(\frac{\delta_{ij}}{N_v} - \frac{1}{N_v^2}\right)\frac{\partial\epsilon^{(j)}}{\partial u_{\gamma\delta}}\right] \tag{14}$$

The part in square brackets in equation (14) is the elastoresistance component, $m_{\lambda\beta\gamma\delta}$. Thus the contribution of the second part of equation (8) to $p_{\alpha\beta\gamma\delta}$ is

$$\frac{kT}{e\Pi_0}\sum_\lambda m_{\lambda\beta\gamma\delta} \tag{15}$$

and can therefore be obtained immediately from the expressions given by HERRING and VOGT[1].

All the components of $\mathbf{p}$ can thus be obtained. Finally, returning to the original definition of $\mathbf{p}$ in equation (6), this can be put in the alternative form

$$p_{\alpha\beta\gamma\delta} = -\frac{1}{\Pi_0\sigma_0}\sum_\lambda\left\{\Pi_{\alpha\lambda}\frac{\partial\sigma_{\lambda\beta}}{\partial u_{\gamma\delta}} + \sigma_{\lambda\beta}\frac{\partial\Pi_{\alpha\lambda}}{\partial u_{\gamma\delta}}\right\} \tag{16}$$

and in view of the scalar form of $\mathbf{\Pi}$ and $\boldsymbol{\sigma}$, this is:

$$p_{\alpha\beta\gamma\delta} = -\frac{1}{\sigma_0}\frac{\partial \sigma_{\alpha\beta}}{\partial u_{\gamma\delta}} - \frac{1}{\Pi_0}\frac{\partial \Pi_{\alpha\beta}}{\partial u_{\gamma\delta}} \qquad (17)$$
$$= m_{\alpha\beta\gamma\delta} + r_{\alpha\beta\gamma\delta}$$

where

$$r_{\alpha\beta\gamma\delta} = -\frac{1}{\Pi_0}\frac{\partial \Pi_{\alpha\beta}}{\partial u_{\gamma\delta}} \qquad (18)$$

may be called the elasto-Peltier tensor for the crystal. The components of $\mathbf{r}$ can thus be obtained for the cases of valleys on (100), (111) and (110) axes by using the expressions for the elastoresistance components given by HERRING and VOGT.

(b) Theory for n-type germanium

The measurements discussed in the subsequent section have been performed on *n*-type germanium, and so it is useful to discuss this case more fully to see the sort of information which can be obtained from measurements of the elasto-Peltier effect.

In *n*-type germanium, the valleys are on (111) axes, and the rules given in the preceding section lead to the expressions for the components of the elasto-Peltier tensor

$$r_{11} = 0,\ r_{12} = 0$$

$$r_{44} = +\frac{1}{9}\frac{\Xi u}{kT}\left[\frac{\Pi_{\parallel}^{(i)}\mu_{\parallel}^{(i)} - \Pi_{\perp}^{(i)}\mu_{\perp}^{(i)}}{\Pi_0\mu_0}\right] + \frac{kT}{e\Pi_0} m_{44} - m_{44} \qquad (19)$$

with m_{44} given by equation (10). Eliminating the deformation potential constant between equations (10) and (19) and using the further relations:

$$\mu_0 = (2\mu_{\perp}^{(i)} + \mu_{\parallel}^{(i)})/3$$

$$\Pi_0\mu_0 = (2\Pi_{\perp}^{(i)}\mu_{\perp}^{(i)} + \Pi_{\parallel}^{(i)}\mu_{\parallel}^{(i)})/3 \qquad (20)$$

leads to

$$r_{44} = m_{44}\left\{\frac{-3K(L-1)}{(K-1)(2K+L)} + \frac{kT}{e\Pi_0}\right\} \qquad (21)$$

where the dimensionless parameters K and L are defined by

$$K = \mu_{\perp}^{(i)}/\mu_{\parallel}^{(i)},\ L = \Pi_{\parallel}^{(i)}/\Pi_{\perp}^{(i)} \qquad (22)$$

Thus, the ratio of the elasto-Peltier effect to the elastoconductance effect, measured under identical conditions, together with a measurement of the zero-strain Peltier coefficient gives directly the function $3K(L-1)/(K-1)(2K+L)$. This will be the case for all measurements in which the (44) components are involved, independently of the orientation, provided that the (11) and (12) components are truly zero. For the case of longitudinal and transverse measurements on a $\langle 100\rangle$ orientated specimen, both effects should vanish.

In terms of the transport theory of HERRING and VOGT[1] the mobilities within a valley parallel and perpendicular to the symmetry axis of a valley are given by:

$$\mu_{\parallel}^{(i)} = e\langle l_{\parallel}\Delta\epsilon\rangle/\langle\Delta\epsilon\rangle\ \mu_{\perp}^{(i)} = e\langle l_{\perp}\Delta\epsilon\rangle/\langle\Delta e\rangle \qquad (23)$$

where $l_{\perp} = \tau_{\perp}/m_{\perp}$, $l_{\parallel} = \tau_{\parallel}/m_{\parallel}$ are functions of energy through the energy-dependence of the relaxation times $\tau_{\perp}$ and $\tau_{\parallel}$, $\Delta\epsilon$ is the energy of electrons measured relative to the band edge in an energy shell and the angular brackets denote Maxwellian averages over the states of a valley. Thus K is given by:

$$K = \langle l_{\perp}\Delta\epsilon\rangle/\langle l_{\parallel}\Delta\epsilon\rangle \qquad (24)$$

For pure accoustic lattice scattering, both relaxation times have the same energy-dependence and we can write

$$l_{\perp}(\Delta\epsilon) = W l_{\parallel}(\Delta\epsilon) \qquad (25)$$

where the anisotropy parameter W is independent of energy. In this case

$$K = W \qquad (26)$$

If W is assumed to be independent of energy, its value can be obtained in principle from magnetoresistance measurements. This has been done by GOLDBERG[5] using low-field magnetoconductance measurements on specimens of different impurity concentrations. An alternative method is to measure the high-field longitudinal magnetoresistance on $\langle 100\rangle$ or $\langle 111\rangle$ orientated specimens. When W is not independent of energy, as seems to be the case when ionized-impurity scattering is appreciable, this second method is preferable, since the averages involved are one order less in the relaxation times as compared with the averages occurring in the first method.

To see the significance of the parameter L in a similar form involving Maxwellian averages, let $\nu_\parallel(\Delta\epsilon)$ and $\nu_\perp(\Delta\epsilon)$ be the components of the (partial) Peltier tensor for the electrons in an energy shell $\Delta\epsilon$. Then:

$$\Pi_\parallel^{(i)}\mu_\parallel^{(i)} = e\langle \nu_\parallel l_\parallel \Delta\epsilon\rangle / \langle \Delta\epsilon\rangle \tag{27}$$

and

$$L = K\langle \nu_\parallel l_\parallel \Delta\epsilon\rangle / \langle \nu_\perp l_\perp \Delta\epsilon\rangle \tag{28}$$

Each of the components ν consists of an electronic part ν_e and a phonon-drag part ν_p. The electronic part is the energy transported per electron relative to the Fermi level and is given by:

$$\nu_e = \nu_{e,\parallel} = \nu_{e,\perp} = -(\Delta\epsilon+\epsilon_c-\epsilon_F)/e \tag{29}$$

where ϵ_c is the band-edge energy and ϵ_F is the Fermi level.

Using equations (27) and (23), the electronic part thus gives contributions to $\Pi_\parallel$ and $\Pi^\perp$ of the form:

$$\Pi_{e,\parallel}^{(i)} = \langle \nu_e l_\parallel \Delta\epsilon\rangle / \langle l_\parallel \Delta\epsilon\rangle$$
$$\Pi_{e,\perp}^{(i)} = \langle \nu_e l_\perp \Delta\epsilon\rangle / \langle l_\perp \Delta\epsilon\rangle \tag{30}$$

If $\tau_\parallel$ and $\tau_\perp$ depend on energy in the same way, then clearly:

$$\Pi_{e,\perp}^{(i)} = \Pi_{e,\parallel}^{(i)} \tag{31}$$

Departures from this relation caused by moderate amounts of impurity scattering are almost certainly insignificant for fairly pure material, since by far the largest contribution comes from the part $(\epsilon_c-\epsilon_F)$ of equation (29) and this is always isotropic. Thus, under the conditions of interest, equation (31) will be obeyed to a high degree of accuracy.

It follows then that the departure of L from a value of unity is determined by the anisotropy of the phonon-drag contributions $\Pi_{p,\parallel}^{(i)}$, $\Pi^{(i)}{}_\perp$ and, of course, the magnitudes of these relative to Π_e. Equation (21) can be put in the alternative form:

$$r_{44} = m_{44}\left\{\frac{-3K(M-1)}{(K-1)(2K+M)}\frac{\Pi_p}{\Pi_0}+\frac{kT}{e\Pi_0}\right\} \tag{32}$$

where Π_p is the phonon-drag contribution to the total Peltier coefficient Π_0 and

$$M = \Pi_{p,\parallel}^{(i)}/\Pi_{p,\perp}^{(i)}$$
$$= K\langle \nu_{p,\parallel} l_\parallel \Delta\epsilon\rangle / \langle \nu_{p,\perp} l_\perp \Delta\epsilon\rangle \tag{33}$$

Since M is expected to be of the same order as K (HERRING *et al.*[2]), the ratio of the two terms in equation (32) will be governed largely by the ratio of Π_p to kT/e. This ratio increases rapidly with decreasing temperature and dominates the elasto-Peltier effect in the liquid nitrogen range, where our measurements have been made. Thus, in this range the ratio of the elasto-Peltier effect to the elastoresistance effect combined with values of Π_p/Π_0 yields the function $3K(M-1)/(K-1)(2K+M)$.

(c) *Method of extrapolation of experimental data*

The discussion of the theory of the relation between the elasto-Peltier effect and the elastoconductivity that has been given in the preceding sections clearly refers to the limiting relation as strain tends to zero. In practice, to get accurate measurements it is necessary to work with finite, strains, and the problem arises how to extrapolate the results to zero strain.

If the assumption is retained that for finite strain the scattering processes are unaffected to first order in the strain, this problem can easily be solved. The solution may be most simply illustrated by reference to a specific case, viz., the longitudinal effects in the $\langle 111\rangle$ direction.

For this case, from symmetry considerations, a strain parallel to $\langle 111\rangle$ will give rise to a situation in which there are, say, n_1 carriers in the valleys on the $\langle 111\rangle$ axis and n_2 electrons in each of the other valleys. These numbers are related by

$$n_1+3n_2 = 4n_0 \tag{34}$$

where n_0 is the zero strain population for each valley, this being the condition that the total number of carriers is unaltered by the strain. The conductivity parallel to $\langle 111\rangle$, assuming that the mobilities are independent of strain, is:

$$\sigma = \sum_i n^{(i)} e\mu^{(i)}$$

where $\mu^{(i)}$ is the component of the mobility tensor for valley i parallel to $\langle 111\rangle$. Carrying out the summation for the particular case considered

$$\sigma = \sum_i [n_2 e\mu^{(i)}]+(n_1-n_2)e\mu_\parallel$$
$$= 4n_2 e\mu_0+(n_1-n_2)e\mu_\parallel$$

In the absence of strain $n_1 = n_2 = n_0$ and the zero strain conductivity is σ_0. Eliminating n_2 by means of equation (34) gives

$$\Delta\sigma/\sigma_0 = \frac{2}{9}\frac{(n_0-n_1)}{n_0}\left\{\frac{\mu_\perp-\mu_\parallel}{\mu_0}\right\} \qquad (35)$$

— a form analogous to equation (10), where the quantity n_1 is a function of the strain.

Carrying through a similar argument for the product of the Peltier coefficient and the conductivity gives:

$$\boldsymbol{\Pi}\,.\,\boldsymbol{\sigma} = \sum_i \boldsymbol{\Pi}^{(i)}\,.\,\boldsymbol{\sigma}^{(i)} \qquad (36)$$

The Peltier tensor $\boldsymbol{\Pi}^{(i)}$ for valley i involves the density of carriers through a term $kT \ln (n^{(i)})/e$. Using this expression, carrying out the summation and eliminating n_2 by means of equation (34) leads to an expression for $\Pi\sigma - \Pi_0\sigma_0$ involving n_1, the mobilities $\mu_\perp$ and $\mu_\parallel$ and the components of the Peltier tensor for a valley, $\Pi_\parallel$ and $\Pi_\perp$. Finally, eliminating n_1 between this expression and equation (35) leads to the relation

$$-\left(\frac{\Delta\Pi}{\Pi_0}\right)\Big/\left(\frac{\Delta\rho}{\rho_0}\right) = \frac{-3K(L-1)}{(K-1)(2K+L)} + \frac{kT}{e\Pi_0} + \left(\frac{\Delta\sigma}{\sigma_0}\right)\frac{kT}{e\Pi_0}\frac{(2K+1)^2}{2(K-1)^2} + \text{higher terms in } (\Delta\sigma)/\sigma_0 \qquad (37)$$

with

$$\Delta\rho/\rho_0 = -(\Delta\sigma)/(\sigma_0+\Delta\sigma) \qquad (38)$$

For vanishingly small changes equation (37) goes over to equation (21) as required. Equation (37) is, however, the one to be used for practical measurements. The last term in this equation is very small under the conditions used in our experiments, although its effect can just be seen on the ⟨111⟩ measurements. The argument can be carried through in a similar way for ⟨110⟩ orientation. The first part is then the same, but the last term involves a different function of K to that occurring in equation (37). This gives a somewhat larger contribution to the ratio of $\Delta\Pi/\Pi_0/\Delta\rho/\rho_0$ for ⟨110⟩ specimens as compared with ⟨111⟩ specimens, and this again agrees with our observations. Both contributions of this type are small, however.

3. EXPERIMENTAL

The analysis of the preceding section leads to the following conclusions. If $\Delta Q/Q_0$ ($\equiv\Delta\Pi/\Pi_0$) is the fractional change in the Seebeck coefficient for a given stress and a given temperature and $\Delta\rho/\rho_0$ is the fractional change in the resistivity measured under identical conditions of stress and temperature, then the quotient $\Delta Q/Q_0 \div \Delta\rho/\rho_0$ should depend only on the temperature and should be independent of the stress, at least over a certain range. Thus, an accurate calibration of the stress was not required, the only requirements being that for a given situation the same stress should give the same changes consistently.

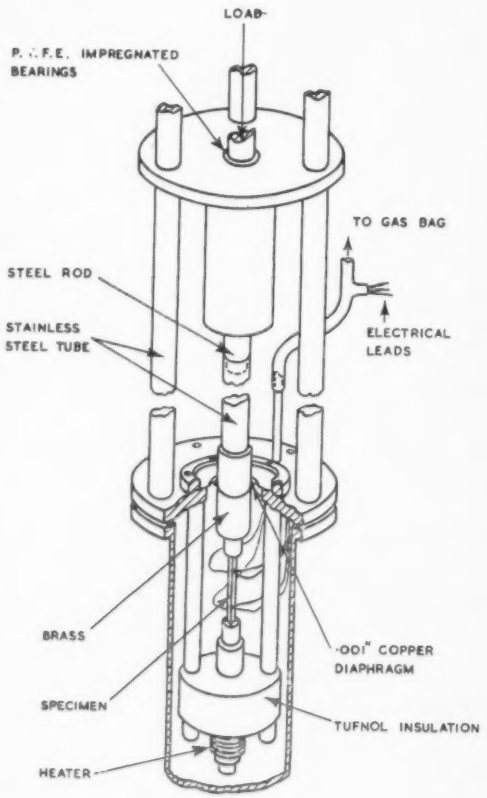

FIG. 1.

The main features of the apparatus are illustrated in Fig. 1. Stainless-steel tubes were used to insulate thermally the upper part of the system from the

VOL. 12 59/60

lower. One end of the specimen was connected thermally to the cooling bath via a short length of brass rod passing through a thin metal diaphragm so that stress could be transmitted to the specimen. The other end was connected thermally to a small heating coil. Short-term fluctuations in the Seebeck voltage across the measuring probes were found to be troublesome in the early stages. These were associated with convection currents in the helium gas inside the specimen chamber and were eventually eliminated by packing cotton wool around the specimen. In the final form of the apparatus it was possible to achieve conditions in which the Seebeck voltage across the measuring probes showed only long-term drifts with time of the order of 1 or 2 μV/min.

The probes consisted of 0·002 in. gold wire containing 1 per cent antimony. Two of these were welded at a known distance apart on one face of the specimen. Two copper/Eureka thermocouples were attached to an adjacent face at approximately the same distance apart by first forming antimony-doped solder dots and subsequently attaching the thermocouples to these by means of a 50 per cent indium–tin low-melting point solder. Both thermocouples and probes were attached after the specimen had been mounted in the apparatus. This mounting was done by using indium as a solder to form the contacts between the ends of the specimen and the brass rods, the ends of the specimen having previously been plated with rhodium. This method of mounting was the only one out of a number of attempts which gave trouble-free contacts at low temperatures (see later).

In a given experiment, the heater voltage was adjusted to give a temperature difference between the thermocouples of the order of 1°. When the Seebeck voltage V_s across the probes had reached a steady value, stress was applied and the change ΔV_s in the Seebeck voltage was measured. The changes were measured to within 1 μV and were found to be reversible with stress and repeatable on successive applications of the stress to this accuracy. The magnitude of the changes varied from 30 μV to over 300 μV, depending on the stress, mean temperature, temperature gradient and orientation of the specimen. Thus the ratio $\Delta V_s/V_{s0}$ could be measured very accurately, certainly to better than 1 per cent for the larger stresses. The stresses used ranged from 5×10^7 to 5×10^8 dynes/cm^2, assuming that no appreciable frictional forces were present.

The ratio $\Delta V_s/V_{s0}$ was, of course, equal to the fractional change in the Seebeck coefficient $\Delta Q/Q_0$ only if the temperature difference between the probes did not alter with the stress. When this temperature difference was of the order of 1°, it was not possible to say with sufficient accuracy whether the stress had any effect on the temperature gradient. Although no appreciable effect on the individual thermocouple voltages could be observed, changes in these voltages of the order of 0·1 μV might well have escaped detection. Since the sensitivity of the thermocouples in the liquid-nitrogen range was of the order of 18 μV/°K, it would have been possible for the temperature gradient to have changed by 1 part in 90 with stress without any noticeable change in the thermocouple voltages. Such changes would have induced the corresponding fraction of the zero-strain Seebeck voltage, which was of the order of 2000 μV under the conditions of our experiments. Thus ΔV_s could have contained a contribution from this effect > 20 μV as well as a contribution arising from a change in the Seebeck coefficient with stress. The presence of such a contribution would have given very appreciable errors in equating $\Delta V_s/V_{s0}$ to $\Delta Q/Q_0$. It is believed that effects of this kind were present in some of our earlier measurements, since the results on these were not always consistent from one run to another. Errors due to this cause were eventually reduced by measurements based on the following reasoning.

In the short time required to make the measurements, any changes in the temperature gradient with stress could only have arisen as a result of a direct change with stress of some part of the thermal resistance between the heater and the sink. The fractional effect of such changes on the temperature gradient would have been largely independent of the value of the gradient. This fractional effect could therefore be measured to a much higher degree of precision by increasing the gradient. Thus, when the gradient was increased by a factor of ten, the absence of any detectable effect of stress on the thermocouple voltages allowed us to say that the fractional change was less than one part in 900. Under the normal conditions, therefore, with 1° difference between the probes, the

contribution to ΔV_s from this effect would have been $< 2\ \mu$V.

Whenever the presence of stress-sensitive thermal resistance was detected by this method, it could invariably be reduced to below detection limit by reforming the end contacts. The changes in the temperature gradient when present were invariably such as to increase the gradient for the compressive stresses used in our experiments. This would be expected, since any stress-sensitive thermal resistance would be reduced by compressive stress and thus increase the heat flow.

4. RESULTS

Analysis will be restricted to the results on three specimens, designated *D*, *E* and *F*, for which it can be assumed that any changes in temperature gradient with stress gave a contribution to ΔV_s of less than 2 μV. The relevant properties and results for these specimens are summarized in Table 1.

The orientations were determined to within 10′ by the use of an X-ray goniometer. The carrier concentrations were obtained from low-field Hall-effect measurements on adjacent specimens from the same single-crystal ingot.

Table 1. *Results for n-type germanium specimens*

Specimen	Orientation	Extrinsic carrier concentration (cm^{-3})	Mean temperature (°K)	$\Delta Q/Q_0 \div \Delta\rho/\rho_0$
D	(100)	$\sim 3\times10^{14}$	81·5	$\Delta Q \sim 0$, $\Delta\rho \sim 0$
E	(111)	$8{\cdot}5\times10^{13}$	81·7 95·2	$0{\cdot}409 \pm 0{\cdot}002$ $0{\cdot}330 \pm 0{\cdot}003$
F	(110)	$8{\cdot}5\times10^{13}$	81·8 94·6	$0{\cdot}394 \pm 0{\cdot}002$ $0{\cdot}323 \pm 0{\cdot}004$

Since also for such stresses the magnitude of V_s increased, it follows that $\Delta V_s/V_{s0}$ always represented an upper limit to $\Delta Q/Q_0$. For those measurements where no stress-sensitive thermal resistances were detected by the above method $\Delta V_s/V_{s0}$ should be within 2 per cent of $\Delta Q/Q_0$.

The measurement of $\Delta\rho/\rho_0$ under the same conditions was carried out by first backing off the Seeback voltage across the probes and then measuring the resistivity voltage V_ρ by a mechanical-chopper technique to eliminate residual thermoelectric voltages. The chopper reversed the current through the specimen some 25 times/sec and simultaneously reversed the leads to the potentiometer. Use of a high resistance in series with the specimen prevented any measurable change of current flow with stress. Dimensional changes could be neglected for the stresses used, and so $\Delta V_\rho/V_{\rho 0}$ could be assumed to be equal to $\Delta\rho/\rho_0$. This ratio could be measured to well within 1 per cent.

Using liquid nitrogen for the cooling bath and the largest possible stresses ($\sim 5\times10^8$ dynes/cm^2), the change in the Seebeck voltage of specimen *D* was too small to measure accurately, but was of the order of 1 μV in 3200. The corresponding changes in the resistivity were less than one part in 5×10^4. Comparing these results with those obtained on other orientations, for which under corresponding conditions the changes in the Seebeck voltage were $> 200\ \mu$V, it is possible to say that r_{11} is less than 0·5 per cent of r_{44}. Equation (19) would predict that r_{11} is zero, so that the results on this specimen may be regarded as providing very good confirmation of the theory based on the electron-transfer effect.

According to the theory, as shown by equation (32), the figures in the last column should have the same value for specimens *E* and *F* at a given temperature and should decrease rapidly with increasing temperature as the phonon-drag component of the Peltier coefficient decreases. The

limits given in Table 1 enclose the values obtained over a range of stresses. The observed differences between E and F at 81·7°K seems to be outside the range of experimental error. This difference persists at higher temperatures if due allowance is made for the fact that E was measured at an appreciably higher temperature than F.

No satisfactory explanation of this difference can be given at present, although a number of possibilities exist. Slight differences in composition between the two specimens would not be expected to affect the ratio appreciably. A useful check in this context would have been to calibrate the stress accurately and to measure the low-stress piezoresistance of the two specimens. These would be in the ratio 4:3 if the two specimens were identical in composition. This check could not be done in our measurements owing to the presence of unknown frictional forces in the bearing which supported the central rod transmitting the stress.

VOL. 12 59/60

A second possible explanation is that there was a residual stress-sensitive thermal resistance present in the measurements on specimen E, which was too small to be detected by the method of increasing the temperature gradient. This, however, would account for only about half the discrepancy. There are a number of other possibilities which can only be resolved by further study.

Pending a satisfactory explanation, for the present purposes it will be assumed, in line with the discussion of the preceding section, that the smaller ratio in Table 1, i.e. the results for specimen F, is the most correct at a given temperature. Comparison of equation (37) with equation (32) shows that the negative of these ratios can be equated to r_{44}/m_{44}. Thus, the numerical value of the function of K, M, Π_p and Π_0 on the right-hand side of equation (32) can be obtained at 81·7 and 94·6°K.

To proceed further, some knowledge of Π_p and Π_0 at the two temperatures is required. Although attempts were made by us to measure the zero-strain Seebeck coefficient $Q_0(\equiv\Pi_0/T)$ during the stress experiments, the results obtained were variable and must be considered unreliable. This was almost certainly associated with poor thermal contact between the thermocouples and the germanium surface. The errors arising from this source were much less severe at higher temperatures, and our measurements of Q_0 in the region of 0°C were in good agreement with the values estimated from the data of HERRING *et al.*[2]. Since these authors used a method which allowed good thermal contact to be made between the germanium and the thermometers, we prefer to rely on their data for estimating Q_p and Q_0 at low temperatures.

A small correction to the values of Q_p given by HERRING *et al.*[2] is necessary to allow for the different cross-sectional area of our specimens. The value of Q_0 is then obtained by adding Q_p to the electronic part Q_e, where Q_e is given by:

$$Q_e(\mu\text{V/°K}) = -198{\cdot}6[\log_{10}(8{\cdot}3\times10^{-4}R_0)+ +1{\cdot}5\log_{10}T-0{\cdot}43]-172 \qquad (39)$$

where R_0 is the low-field Hall coefficient. This equation is strictly accurate only for accoustic scattering, but is rather insensitive to small amount of impurity scattering. Since our measurements of R_0 and ρ_0 on a specimen adjacent to E and F in the parent ingot showed that the amount of impurity scattering was small at liquid-nitrogen temperature, no correction has been made and Q_e was assumed to be given by:

$$Q_e = -444-297{\cdot}7\log_{10}T \qquad (40)$$

The values derived by the above process are shown in Table 2, together with the values of the function $3K(M-1)/(K-1)(2K+M)$ obtained by using the values of Π_p/Π_0 in equation (32) with the experimental values of r_{44}/m_{44}.

The values of K of our specimens have not been measured directly. As discussed in a previous

Table 2

Temperature °K	$Q_p(\mu\text{V/}^0)$	$Q_0(\mu\text{V/}^0)$	$3K(M-1)/(K-1)(2K+M)$
81·7	−1000	−2010	0·706
94·6	− 686	−1720	0·684

section, the most reliable determination of K is obtained from high-field magneto-resistance data. Measurements of this type have been made by HERRING *et al.*[2] on a number of specimens of n-type germanium of varying impurity concentration. For specimens with impurity concentrations of the order of $10^{13}/cm^3$, the parameter ω_1 ($\equiv 1/K$) which gives the anisotropy of the first moments of the components of the relaxation-time tensor was found to be equal to 0·0610 ($K=16{\cdot}4$) independently of temperature in the range 77–94°K. For higher impurity concentrations ω_1 increases and becomes temperature-dependent, decreasing with increasing temperature as the proportion of ionized-impurity scattering decreases. For their specimen 601 (impurity concentration $\sim 3\times 10^{14}$), HERRING *et al.* found a value of ω_1 of 0·069 ($K=14{\cdot}5$) at 94°K. Comparison of these figures with the data on the variation with impurity concentration and temperature of the third moments ω_3 obtained by GOLDBERG[5] from low-field magnetoconductance data would lead to a value of K for our specimens of about 15·5 at 94°K, decreasing to 15·0 or so at 82°K.

The ratio of M/K obtained from the last column in Table 2 is almost independent of K in this region. Thus, as K varies from 14 to 17, the ratio M/K varies from 0·651 to 0·645 at 81·7°K and from 0·628 to 0·621 at 94·6°K. Thus, our measurements give M/K to a fairly high accuracy, even if K is known only approximately. Use of the K values estimated in the preceding paragraph would lead to a value of $M=9{\cdot}7$ at both temperatures. This is in good agreement with the value of M deduced by HERRING *et al.*[2] from an analysis of thermomagnetic data. These authors found a value of $M=9{\cdot}6$ which was practically independent of temperature in the range 60–100°K. However, in the absence of definite values of K for our specimens, such agreement cannot be emphasized too much.

Acknowledgements—The authors express their thanks to Dr. C. HERRING for sending them, prior to publication, a copy of the work analysing the thermomagnetic data.[2]

REFERENCES

1. HERRING C. and VOGT E., *Phys. Rev.* **101**, 944 (1956).
2. HERRING C., GEBALLE T. H. and KUNZLER J. E., *Phys. Rev.* **111**, 36 (1958); *Bell Syst. Tech. J.* **38**, 657 (1959).
3. KEYES R. W., *J. Electronics* **2**, 279 (1956).
4. MORIN F. J., GEBALLE T. H. and HERRING C., *Phys. Rev.* **105**, 525 (1957).

J. Phys. Chem. Solids Pergamon Press 1960. Vol. 12. pp. 295–297. Printed in Great Britain.

NMR AND IR STUDY OF $(NH_4)_2SO_4$ AND $(NH_4)_2BeF_4$

R. BLINC and I. LEVSTEK

Institute J. Stefan, Ljubljana, Yugoslavia

(*Received* 24 *July* 1959)

Abstract—The NMR and IR spectra of $(NH_4)_2SO_4$ and $(NH_4)_2BeF_4$ have been investigated both in the non-ferroelectric and in the ferroelectric phases. From the measured second moments it was found that at room temperature the reorientations of the NH_4^+ ions do not remain correlated with any specific axis of rotation. In $(NH_4)_2SO_4$ a line-width transition was found below −110°C. Below the transition two components were resolved, which are interpreted as being due to "frozen-in" and rotating ammonium ions, respectively. Above −180°C, no line-width transition was found in $(NH_4)_2BeF_4$. This shows that the hydrogen bonds N–H ··· F are weak.

In the IR spectra of both compounds bands involving the torsional modes of NH_4^+ ions were found. Thus the possibility of free rotation at room temperature must be excluded. The splitting of the $\nu_4(NH_4)$, $\nu_3/SO_4/$ and $\nu_3/BeF_4/$ bands below the Curie points indicates the deformation of these ions in the ferroelectric phase.

VOL. 12 59/60

It is well known that ammonium sulphate and ammonium fluoberyllate undergo phase transitions at −50 and −97°C, respectively. Recently it has been shown[1,2] that these crystals become ferroelectric below the transition point. However, X-ray and neutron-diffraction studies have not yet been completed,[3] and so the mechanism of the transitions is not clear. Therefore it seemed worthwhile to investigate the proton magnetic resonance and infrared spectra which might prove helpful in understanding the nature of the transitions in these crystals.

The derivatives of the proton absorption lines are reproduced in Fig. 1. The line widths, defined as the separation in gauss of the maximum and minimum of the derivatives, are plotted in Fig. 2 as a function of temperature. A similar plot of the second moments, obtained by numerical integration from the derivatives, is given in Fig. 3.

Two important facts from the above data should be stressed. First of all, the structure changes occurring in the vicinity of the ferroelectric transition point are accompanied only by very small changes in the proton magnetic absorption. Further, ammonium sulphate and ammonium fluoberyllate, which have very similar absorption lines at room temperature, show an entirely different behaviour at low temperatures. This may be related to the fact that the ferroelectric phases of $(NH_4)_2SO_4$ and $(NH_4)_2BeF_4$ are not isomorphous.[3]

In $(NH_4)_2BeF_4$ the absorption line changes but little in the whole region between +150 and −180° The second moment at −180°C is not larger than 8 G^2, which demonstrates the complete disappearance of the intra-NH_4^+ magnetic interactions due to random reorientations of the NH_4^+ ions. The frequency of the effective reorientation motion must therefore be more than 10^5 c/s at −180°C. The potential barrier hindering the movement of the ammonium ions is evidently very low, and the hydrogen bonds occurring between the ammonium ions and the fluorine atoms appear to be weak.

On the other hand in $(NH_4)_2SO_4$ a sharp line-width transition occurs below −110°C. However, in contrast to NH_4Cl, in this case the derivative of the absorption line splits into two well-resolved components. Apparently such a behaviour has not previously been reported in any pure ammonium salt.

There are many possible interpretations of the origin of the two components at low temperatures. The most probable interpretation is that the broad band arises from "frozen-in" ammonium ion protons, and the narrow band from rapidly reorientating ammonium ions. The observed value of the second moment below the transition is

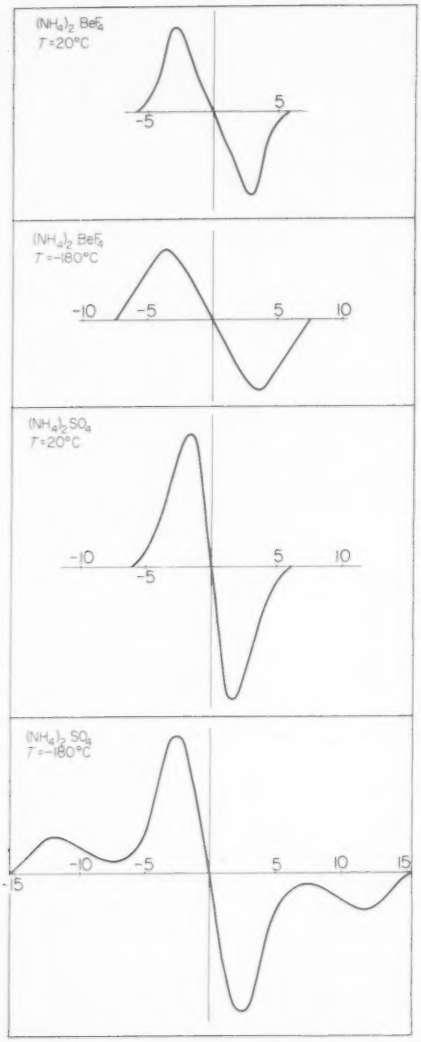

FIG. 1. Derivatives of the proton magnetic resonance absorption lines for $(NH_4)_2SO_4$ and $(NH_4)_2BeF_4$ powders.

consistent with this interpretation, since it is approximately equal to:

$$\Delta H_2^2[NH_4)_2SO_4] = \tfrac{1}{2}\Delta H_2^2[(NH_4)_{\text{frozen-in}}] + \\ + \tfrac{1}{2}\Delta H_2^2[(NH_4)_{\text{rot}}]$$

The ratio of the first moment of the two components is approximately 1:1. This supports further the proposed interpretation. In any case these data should be supplemented by a single-crystal study before definite conclusions are drawn about the low-temperature structure. However, from the second-moment data for powdered $(NH_4)_2SO_4$ we may conclude definitely that the

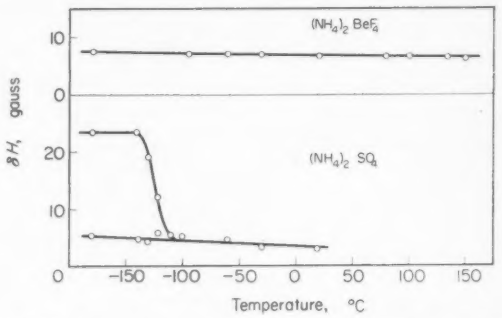

FIG. 2. Line widths of the proton magnetic resonance absorption plotted against temperature.

reorientations of the NH_4^+ ions do not remain correlated with any specific axis of rotation for times longer than 10^{-5} sec at temperatures above the line-width transition. The observed line-broadening results from inter-NH_4^+ interactions.

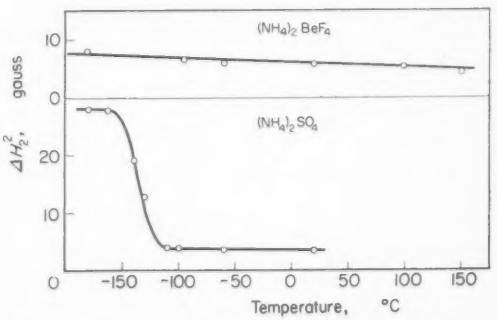

FIG. 3. Second moments of the proton magnetic resonance absorption plotted against temperature.

The IR spectra of $(NH_4)_2SO_4$ and $(NH_4)_2BeF_4$ are surprisingly complex. Assuming tetrahedral symmetry for the NH_4^+ ion in $(NH_4)_2SO_4$, only two triply degenerate vibratons (ν_3 and ν_4) from the four NH_4 fundamentals should be IR active. These bands are found at 3100 and 1410 cm^{-1}, respectively. Following PLUMB and HORNIG[4], we would further expect to find the first overtone of the bending mode ($2\nu_4$) and two combination bands

($\nu_4+\nu_6$, $\nu_2+\nu_6$) involving the torsional mode (ν_6). A band found at 2880 cm^{-1} corresponds to the former mode.

The combination bands should occur at 1770 and 2100 cm^{-1}, respectively. However, instead of the expected two we find in $(NH_4)_2SO_4$ at room temperature three bands located at 1750, 2050 and 2350 cm^{-1}. On cooling to 90°K these bands shift to 1820, 2150 and 2340 cm^{-1}, respectively. In agreement with the data of POHLMAN[5], the ν_4 band splits below the Curie point into three components (at 1405, 1425 and 1465 cm^{-1}), indicating a deformation of the NH_4^+ ion.

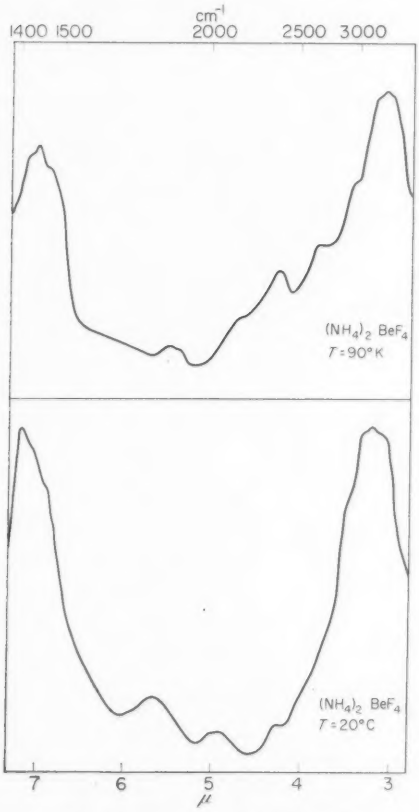

FIG. 4. IR spectra of $(NH_4)_2BeF_4$.

The splitting of the $\nu_3/SO_4/$ band at 1105 cm^{-1} below the transition point demonstrates that the SO_4^{--} ion is deformed too.

The results for $(NH_4)_2BeF_4$ differ to some extent from those for $(NH_4)_2SO_4$ (cf. Fig. 4). The $\nu_3/BeF_4/$band appears at 785 cm^{-1}. The ν_3 and ν_4 ammonium bands are located at 3120 and 1410 cm^{-1}. The first overtone of the bending mode $2\nu_4$ is found at 2870 cm^{-1} at room temperature and shifts to 2900 cm^{-1} at 90°K. At this temperature the ν_4 band is split as a result of deformation of the NH_4^+ ion and has components at 1410, 1430 and 1455 cm^{-1}. The combination bands involving the torsional mode appear at room temperature at nearly the same position as in $(NG_4)_2SO_4$, occurring at 1770, 2040 and 2350 cm^{-1}. At low temperatures, however, differences appear: four bands are found at 1820, 2100 (shoulder), 2340 and 2600 cm^{-1}. The deuterated crystals exhibit at room temperature analogous bands at 1190, 1265 and 1350 cm^{-1}.

Since no Raman data are available, no definite assignments of these bands can be made. However, the occurrence of bands involving the torsional mode proves the existence of hindered rotational motions of the ammonium ions as revealed by the NMR data. The possibility of free rotation at room temperature may be definitely excluded. But in contrast to NH_4Cl it seems very probable that the bands mentioned are combinations not only with one, but with two low-frequency modes, which should occur at 360 and 600 cm^{-1}, respectively. Since these modes should be very sensitive to changes in lattice dimensions and electrostatic environment, the shifts of the combination bands on passing through the Curie point can be understood. The splitting of the $\nu_4(NH_4)$, $\nu_3/SO_4/$ and $\nu_3/BeF_4/$ bands, respectively, indicates the deformation of these groups in the ferroelectric phase and demonstrates the importance of the N–H · · · O and N–H · · · F hydrogen bonds in the transition.

Acknowledgements—The authors are very indebted to Professor D. HADŽI and Professor I. KUŠČER, who read the manuscript critically, and to Mr. M. SCHARA for the preparation of the materials.

REFERENCES

1. MATTHIAS B. T. and REMEIKA J. P., *Phys. Rev.* **103**, 262 (1956).
2. PEPINSKY R. and JONA F., *Phys. Rev.* **105**, 344 (1957)
3. OKAYA I., VEDAM K. and PEPINSKY R., *Acta Cryst., Camb.* **11**, 307 (1958).
4. PLUMB R. C. and HORNIG D. F. *J. Chem. Phys.* **21**, 366 (1952).
5. POHLMAN R., *Z. Phys.* **79**, 394 (1932).

J. Phys. Chem. Solids Pergamon Press 1960. Vol. 12. pp. 298–313. Printed in Great Britain.

DIE EINMÜNDUNG IN DIE FERROMAGNETISCHE SÄTTIGUNG—I

ALLGEMEINE THEORIE DES EINFLUSSES INNERER SPANNUNGEN AUF DAS EINMÜNDUNGSGESETZ, MIT ANWENDUNGEN AUF ZWISCHENGITTERATOME UND ABGESCHRECKTE METALLE

A. SEEGER und H. KRONMÜLLER

Max-Planck-Institut für Metallforschung, Stuttgart, und Institut für theoretische und angewandte Physik der Technischen Hochschule Stuttgart

(*Received* 29 *April* 1959)

VO
1
1959/

Zusammenfassung—Die differentielle Suszeptibilität von Ferromagnetica wird im sog. Einmündungsbereich berechnet, wobei die inneren Spannungen entweder in der Form der Versetzungsdichte oder der Inkompatibilitätsverteilung als gegeben angesehen werden. Die Kenntnis der Verteilung der inneren Spannungen selbst ist nicht erforderlich. Es tritt eine von der magnetischen Erregung H abhängige charakteristische Länge auf, die typisch von der Grössenordnung einiger 100 Å ist. Innere Spannungsfelder, die über Entfernungen dieser Grössenordnung variieren, haben einen empfindlichen Einfluss auf die Suszeptibilität und können durch Einmündungsmessungen experimentell untersucht werden. In der vorliegenden Arbeit werden Versetzungsringe, wie sie in abgeschreckten Metallen auftreten, und Zwischengitteratome behandelt. Die Anwendung auf verformte Metalle wird in Teil II gegeben werden.

Abstract—The differential susceptibility of ferromagnetic materials is calculated in the region of the approach to saturation. The internal stresses are assumed to be known through the dislocation density or the distribution of incompatibilities. An explicit knowledge of the stress field is not required, however. The theory contains a characteristic length that depends on the magnetic field H and that in typical cases is of the order of magnitude of 100 Å. Internal stress fields that vary over such distances affect the susceptibility rather strongly and may be studied by measurements of the approach to saturation. The present paper treats dislocation rings of the type found in quenched metals, and interstitial atoms. The application to deformed metals will be given in part II.

1. EINLEITUNG

Es ist seit langem bekannt, dass die Magnetisierungskurve ferromagnetischer Metalle durch innere Spannungen stark beeinflusst wird. Eine moderne quantitative Theorie dieses Einflusses hat davon auszugehen, dass die Quellen der inneren Spannungen sich—zumindest formal—als Versetzungen beschreiben lassen[1]. In vielen Fällen, z. B. bei den durch Verformung oder Abschrecken von hohen Temperaturen in das Material eingeführten inneren Spannungen, entspricht deren Zurückführung auf Versetzungen der physikalischen Wirklichkeit.

Versetzungen beeinflussen die Magnetisierungsvorgänge vor allem durch ihre Wechselwirkung mit Blochwänden, die sehr kompliziert ist und an Hand von speziellen Vorstellungen von verschiedenen Autoren diskutiert worden ist. Besonders einfache Verhältnisse bekommt man jedoch in jenem Bereich der Magnetisierungskurve, in dem Blochwandverschiebungen keine Rolle mehr spielen, sondern die Vergrösserung der Magnetisierung im wesentlichen von Drehprozessen bewirkt wird, also im Bereich der *Einmündung in die Sättigung*. In der vorliegenden Arbeit werden wir das Problem, den Einfluss einer beliebigen Versetzungsverteilung auf die Einmündung in die ferromagnetische Sättigung zu berechnen, unter voller Berücksichtigung eventuell auftretender innerer

VOL. 12 59/60

magnetischer Streufelder allgemein lösen und das Ergebnis auf die in abgeschreckten Metallen vorhandenen Versetzungsanordnungen anwenden.

Schon 1940 hat W. F. BROWN[2,3] die Versetzungstheorie auf die Analyse der Einmündung in die Sättigung in plastisch verformten Drähten angewendet. In jüngster Zeit konnte gezeigt werden, dass bei Berücksichtigung der inneren Streufelder die Einmündung in die ferromagnetische Sättigung von plastisch verformten Nickeleinkristallen als magnetostriktive Wirkung der durch die Verformung eingeführten Versetzungen quantitativ verstanden werden kann[4]. Die ausführliche theoretische Behandlung dieser Fragen wird als Teil II der vorliegenden Arbeit gegeben werden. Wir benötigen hier lediglich das Ergebnis, dass die magnetostriktive Wechselwirkung zwischen dem Spannungsfeld der Versetzungen und der Magnetisierung zur Deutung der Experimente ausreicht, es also nicht erforderlich ist, eine spezifische Wirkung des Versetzungskerns, wie sie gelegentlich als Analogie zu der entmagnetisierenden Wirkung von Hohlräumen[5] diskutiert worden ist, zu betrachten.

Wir werden zunächst in Anlehnung an BROWN in Abschnitt 2 eine allgemeine Behandlung des Einmündungsgesetzes geben. In der sogenannten Brownschen Näherung bekommt man für die Abweichung der Magnetisierungsrichtung von der Richtung des äusseren Feldes lineare partielle Differentialgleichungen mit konstanten Koeffizienten, die sich allgemein mit Hilfe einer Fourierdarstellung lösen lassen. In der Lösung treten die Fouriertransformierten der im Kristall vorhandenen inneren Spannungen auf. In Abschnitt 3 werden wir diese in Beziehung setzen zu den Fouriertransformierten der Versetzungsdichte bzw. der Inkompatibilitätsverteilung, die sich für die meisten praktisch interessierenden Probleme verhältnismässig leicht berechnen lässt. Auf diese Weise wird die Berechnung der differentiellen Suszeptibilität im Einmündungsgebiet auf Quadraturen zurückgeführt. Im Abschnitt 4 wird der Einfluss von Zwischengitteratomen (repräsentiert durch Dilatationszentren) berechnet. Man findet, dass sie erst bei sehr hohen Feldstärken eine Rolle spielen, was für die Interpretation der Messungen mit kleiner Feldstärke an verformten Kristallen wichtig ist. Abschnitt 5 schätzt die Wirkung von kreisförmigen Versetzungsringen ab (wie sie beim Abschrecken mancher Metalle gebildet werden). Es zeigt sich, dass man unter normalen Bedingungen gut messbare Effekte bekommen sollte, deren experimentelle Untersuchung eingeleitet ist.

2. DAS EINMÜNDUNGSGESETZ BEI BERÜCKSICHTIGUNG DER MAGNETOSTRIKTIVEN ANISOTROPIE UND DES STREUFELDES

(*a*) *Der Energieausdruck*

Das übliche Verfahren[6] zur Bestimmung der Magnetisierung ist es, das Minimum der Summe aller von der Magnetisierung abhängenden Beiträge zur freien Energie (pro Volumeneinheit) zu ermitteln. Wir beschränken uns dabei auf kubische Kristalle und berücksichtigen die folgenden Beiträge :

(1) Die Kristallenergie

$$F_K = K_4(\gamma_1'^2\gamma_2'^2+\gamma_1'^2\gamma_3'^2+\gamma_2'^2\gamma_3'^2)+K_6\gamma_1'^2\gamma_2'^2\gamma_3'^2. \tag{2.1}$$

γ_1', γ_2', γ_3' sind die Richtungskosinusse des Magnetisierungsvektors $\mathfrak{J}$ gegen die kubischen Achsen ; K_4 und K_6 sind die Konstanten der magnetischen Anisotropie.

(2) Die magnetoelastische Kopplungsenergie, deren spannungswirksames Glied (bei Vernachlässigung der Volumenmagnetostriktion sowie von höheren Potenzen der Spannungen)

$$F_\sigma = -(3/2)\lambda_{100}(\sigma'_{xx}\gamma_1'^2+\sigma'^2_{yy}\gamma_2'^2+\sigma'^2_{zz}\gamma_3'^2)- \\ -(3/2)\lambda_{111}(2\gamma_1'\gamma_2'\sigma'_{xy}+2\gamma_1'\gamma_3'\sigma'_{xz}+2\gamma_2'\gamma_3'\sigma'_{yz}) \tag{2.2}$$

lautet. σ'_{ik} sind die Komponenten des Spannungstensors, bezogen auf kubische Achsen, λ_{100} und λ_{111} die magnetostriktiven Konstanten für Zug in $\langle 100\rangle$-bzw. $\langle 111\rangle$-Richtung.

(3) Die Austauschenergie, die nach LANDAU und LIFSHITZ[7] sowie HERRING und KITTEL[8] die Form

$$F_c = \frac{C}{2}[(\nabla\gamma_1)^2+(\nabla\gamma_2)^2+(\nabla\gamma_3)^2] \tag{2.3}$$

besitzt, wobei die γ_i die Richtungskosinusse von $\mathfrak{J}$ gegenüber einem beliebigen kartesischen Koordinatensystem sind. Die Bestimmung der Konstanten C aus experimentellen Daten wird von STONER[9] und KITTEL und GALT[10] behandelt. Für kubisch-flächenzentrierte Metalle wird häufig

als Näherung

$$C = \frac{k\Theta_c}{a_0} \tag{2.4}$$

gesetzt, wo k die Boltzmannsche Konstante, Θ_c die Curie-Temperatur und a_0 die Kantenlänge des Elementarwürfels ist. Nach einem Gedanken von LIFSHITZ[11] kann man C mit Hilfe der Spinwellentheorie aus den Messungen zum Blochschen $T^{3/2}$-Gesetz (Temperaturvariation der Sättigungsmagnetisierung bei tiefen Temperaturen) ableiten; nach den Messungen von FALLOTT[12] gilt[13] für Nickel $C = 1{,}6\cdot10^{-6}$ erg/cm, während Gl. (2·4) für dieses Metall $C = 2{,}4\cdot10^{-6}$ erg/cm liefert.

(4) Die magnetische Streufeld-Energie

$$F_s = \text{grad } U \cdot \mathfrak{J}, \tag{2.5}$$

wobei das magnetische Potential U mit der Magnetisierung gemäss

$$\Delta U = 4\pi \,\text{div}\,\mathfrak{J} \tag{2.6}$$

zusammenhängt.

(5) Die potentielle Energie der Magnetisierung $\mathfrak{J}$ im wirksamen Feld $\mathfrak{H}$ (angelegtes Feld minus $\mathfrak{J}$ mal Entmagnetisierungsfaktor N_E)

$$F_H = -\mathfrak{H} \cdot \mathfrak{J}. \tag{2.7}$$

(b) Berechnung der Magnetisierung

Das Variationsproblem

$$\delta(F_K+F_\sigma+F_c+F_s+F_H) = 0$$

führt, wenn $\mathfrak{H}$ in y-Richtung liegt und die sog. Brownsche Näherung $\gamma_1 \ll 1, \gamma_3 \ll 1, \gamma_2 \approx 1$ verwendet wird, auf die folgenden beiden inhomogenen partiellen Differentialgleichungen

$$\Delta\gamma_1 - \kappa^2\gamma_1 - \frac{\partial u}{\partial x} = -\frac{1}{C}\frac{\partial}{\partial\gamma_1}(F_\sigma+F_K)\Big|_{\substack{\gamma_1=\gamma_3=0\\ \gamma_2=1}} \tag{2.8a}$$

$$\Delta\gamma_3 - \kappa^2\gamma_3 - \frac{\partial u}{\partial z} = \frac{1}{C}\frac{\partial}{\partial\gamma_3}(F_\sigma+F_K)\Big|_{\substack{\gamma_1=\gamma_3=0\\ \gamma_2=1}} \tag{2.8b}$$

mit $\kappa^2 = \dfrac{HI_s}{C}$ (I_s = Betrag der spontanen Magnetisierung) (2.8c)

$$u = \frac{U - N_E I_s y}{C} I_s \tag{2.8d}$$

$$\Delta u = h^2\left(\frac{\partial\gamma_1}{\partial x} + \frac{\partial\gamma_3}{\partial z}\right) \tag{2.8e}$$

$$h^2 = \frac{4\pi I_s^2}{C}. \tag{2.8f}$$

Wie angedeutet, ist auf der rechten Seite der Gl. (2.8a) und (2·8b) nach Ausführung der Differentiation $\gamma_1 = \gamma_3 = 0$, $\gamma_2 = 1$ zu setzen.* Wird diese Vereinfachung vorgenommen, so kann man die Lösungen der Gl. (2.8a) u. (2.8b) mit Hilfe von Fouriertransformationen in der Form (der Index i soll die Werte 1, 3 bzw. x, z annehmen)

$$\tilde\gamma_i = -\frac{\tilde g_i}{k^2+\kappa^2} + h^2\frac{k_i}{k^2+\kappa^2}\cdot\frac{\tilde g_z k_z + \tilde g_x k_x}{k^4+(\kappa^2+h^2)k^2-h^2k_y^2} \tag{2.9}$$

schreiben, wobei

$$\gamma_i(\mathfrak{r}) = (2\pi)^{-3/2}\int\int\int \tilde\gamma_i(\mathfrak{k})\exp(i\mathfrak{k}\mathfrak{r})\,d\tau_\mathfrak{k} \tag{2.10a}$$

$$\tilde\gamma_i(\mathfrak{k}) = (2\pi)^{-3/2}\int\int\int \gamma_i(\mathfrak{r})\exp(-i\mathfrak{k}\mathfrak{r})\,d\tau_\mathfrak{r} \tag{2.10b}$$

$$g_i(\mathfrak{r}) = (2\pi)^{-3/2}\int\int\int \tilde g_i(\mathfrak{k})\exp(i\mathfrak{k}\mathfrak{r})\,d\tau_\mathfrak{k} \tag{2.11a}$$

$$\tilde g_i(\mathfrak{k}) = (2\pi)^{-3/2}\int\int\int g_i(\mathfrak{r})\exp(-i\mathfrak{k}\mathfrak{r})\,d\tau_\mathfrak{r} \tag{2.11b}$$

mit

$$g_i(\mathfrak{r}) = -\frac{1}{C}\frac{\partial}{\partial\gamma_i}(F_K+F_\sigma)\Big|_{\substack{\gamma_i=0\\ \gamma_2=1}} \tag{2.12}$$

gilt.

* Sind die inneren Spannungen klein, so wird die Magnetisierung im Einmündungsgebiet im wesentlichen durch F_K bestimmt. Will man diesen Term, den wir im folgenden vernachlässigen, mit in Rechnung stellen, so hat man F_K auf die linken Seiten von Gl. (8a, b) zu schreiben. Berücksichtigt man nur das Glied mit K_4, so erhält man weiterhin lineare Differentialgleichungen mit konstanten Koeffizienten, die sich mit der hier verwendeten Fouriermethode ohne grundsätzliche Schwierigkeiten lösen lassen. Wir vernachlässigen im Folgenden jedoch den Beitrag von F_K, da er bei $H = 2\,000$ Oe im Falle von Nickel den Wert von κ^2 nur um etwa 1 Prozent (bei Raumtemperatur) bzw. 5 Prozent (bei −100°C) ändern würde.

Die Magnetisierung parallel zum Feld $\mathfrak{H}$ ist gegeben durch

$$I_y = I_s\bar{\gamma}_2 = I_s\sqrt{[1-\overline{\gamma_1^2(\mathfrak{r})}-\overline{\gamma_3^2(\mathfrak{r})}]}$$
$$\approx I_s[1-\tfrac{1}{2}(\overline{\gamma_1^2(\mathfrak{r})}+\overline{\gamma_3^2(\mathfrak{r})})], \qquad (2.13)$$

wo die Querstriche die Mittelwerte über das betrachtete Volumen V andeuten. Zur Berechnung dieser Mittelwerte benützt man zweckmässig die Parsevalsche Gleichung[14] in der Form

$$\overline{\gamma_i^2(\mathfrak{r})} = \frac{1}{V}\int\int\int |\tilde{\gamma}_i^2(\mathfrak{k})|^2\, d\mathfrak{k}. \qquad (2.14)$$

Dabei gilt

$$|\tilde{\gamma}_1|^2+|\tilde{\gamma}_3|^2 = \frac{|\tilde{g}_x|^2+|\tilde{g}_z|^2}{(k^2+\kappa^2)^2} - \left\{2h^2 - \frac{h^4(k_x^2+k_z^2)}{k^4+k^2(\kappa^2+h^2)-h^2k_y^2}\right\}\times$$
$$\times\left\{\frac{|\tilde{g}_x|^2k_x^2+|\tilde{g}_z|^2k_z^2+2k_xk_z(\mathfrak{Re}\tilde{g}_x\cdot\mathfrak{Re}\tilde{g}_z+\mathfrak{Im}\tilde{g}_x\cdot\mathfrak{Im}\tilde{g}_z)}{(k^2+\kappa^2)^2(k^4+k^2(\kappa^2+h^2)-h^2k_y^2)}\right\}. \qquad (2.15)$$

($\mathfrak{Re}$ = Realteil, $\mathfrak{Im}$ = Imaginärteil.) Das erste Glied in Gl. (2.15) entspricht dem meist allein berücksichtigten rein magnetostriktiven Anteil, während das zweite Glied dem durch die magnetoelastische Kopplung hervorgerufenen Streufeld Rechnung trägt. Das Streufeld bewirkt eine Verringerung der Auslenkung von $\mathfrak{J}$ aus der Feldrichtung, so dass die Berücksichtigung des Streufeldes die Zulässigkeit der Brownschen Näherung verbessert. Für eine gegebene Verteilung innerer Spannungen ist damit die Berechnung der Magnetisierung im Einmündungsgebiet auf Quadraturen zurückgeführt.

Bevor wir uns in Abschnitt 3 der Ermittlung von $\tilde{g}_i$ für eine gegebene Versetzungsverteilung zuwenden, besprechen wir noch kurz den Zusammenhang zwischen den verschiedenen hier zu benutzenden Koordinatensystemen.

(c) Koordinatensysteme bei kubischen Kristallen

Der Übersichtlichkeit wegen stellen wir die drei verschieden orientierten kartesischen Koordinatensysteme zusammen, die in der vorliegenden Arbeit verwendet werden.

(1) Im x, y, z-System ist die y-Achse parallel zur Feldrichtung, also bei stabförmigen Proben parallel zur Probenachse. Die Richtungskosinusse der Magnetisierung in diesem System werden mit γ_i bezeichnet. Dieses System wird eingeführt, um die Brownsche Näherung $|\gamma_1|\ll 1, |\gamma_3|\ll 1, |\gamma_2|\approx 1$ verwenden zu können.

(2) Die Achsen des x', y', z'-Systens fallen mit den kubischen Achsen des Kristalls zusammen. Die Richtungskosinusse der Magnetisierung seien γ'_i. In diesem System gelten die Gl. (2.1) und (2.2) für die Kristallenergie und die magnetoelastische Kopplungsenergie. Die Richtungskosinusse des x, y, z-Systems gegenüber dem x', y', z'-System seien β_{ik}, so dass gilt

$$\gamma'_i = \sum_k \beta_{ik}\gamma_k. \qquad (2.16)$$

(3) Bei geradlinigen Versetzungen wählen wir die Achsen des x'', y'', z''-Koordinatensystems so, dass die x''-Richtung parallel zum Burgersvektor $\mathfrak{b}$ der Versetzung ist und die y''-Achse auf der Gleitebene senkrecht steht. Hat man gekrümmte, aber in einer Ebene verlaufende Versetzungslinien, so wählen wir die z''-Achse senkrecht zu dieser Ebene und x''-Achse parallel zur Projektion von $\mathfrak{b}$ auf diese Ebene. Die Richtungskosinusse der Achsen des x'', y'', z''-Systems gegenüber denjenigen des x, y, z-Systems seien β''_{ik}, so dass in den zugehörigen $\mathfrak{k}$-Räumen

$$k_i = \beta''_{ik}k''_k \qquad (2.17)$$

gilt. Ferner benötigen wir noch die Richtungskosinusse β'_{ik} des x'', y'', z''-Systems gegenüber dem x', y', z'-System. Als Beispiel sei die Transformation eines Tensors 2. Stufe

$$\epsilon''_{ik} = \sum_l\sum_m \beta'_{il}\beta'_{km}\epsilon'_{lm} \qquad (2.18)$$

angegeben. Im x'', y'', z''-System werden wir gelegentlich Zylinderkoordinaten einführen,

z. B. gemäss

$$\mathfrak{k}'' = \begin{pmatrix} k_\rho'' \cos\phi \\ k_\rho'' \sin\phi \\ k_z'' \end{pmatrix} \tag{2.19}$$

(d) Die magnetoelastische Kopplungsenergie

Die magnetoelastische Kopplungsenergie Gl. (2.2) lässt sich als doppelt-skalares Produkt zweier symmetrischer Tensoren schreiben, nämlich des Spannungstensors σ'_{ik} und des Tensors der sog. Extradehnung

$$(\epsilon'_{ik}) = 3\begin{pmatrix} \lambda_{100}\gamma'^2_1 & \lambda_{111}\gamma'_1\gamma'_2 & \lambda_{111}\gamma'_1\gamma'_3 \\ \lambda_{111}\gamma'_1\gamma'_2 & \lambda_{100}\gamma'^2_2 & \lambda_{111}\gamma'_2\gamma'_3 \\ \lambda_{111}\gamma'_1\gamma'_3 & \lambda_{111}\gamma'_2\gamma'_3 & \lambda_{100}\gamma'^2_3 \end{pmatrix}, \tag{2.20}$$

in der Form

$$F_\sigma = -\frac{1}{2}\sum_{i,k} \epsilon'_{ik}\sigma'_{ik}. \tag{2.21}$$

Der Spannungstensor nimmt im allgemeinen im Koordinatensystem (3) eine besonders einfache Form σ'_{ik} an. Man erhält dann

$$F_\sigma = -\frac{1}{2}\sum_{i,k} \epsilon''_{ik}\sigma''_{ik}, \tag{2.22}$$

wobei sich ϵ'_{ik} gemäss Gl. (2.18) transformiert.

Da F_K in der hier verwendeten Näherung nicht in Erscheinung tritt, gilt

$$g_i = -\frac{1}{2C}\frac{\partial}{\partial\gamma_i}\sum_{k,l}\epsilon''_{kl}\sigma''_{kl} \equiv \frac{1}{2C}\sum_{k,l} c^i_{kl}\sigma''_{kl}, \tag{2.23}$$

wobei natürlich γ_i gemäss Gl. (2.16) in ϵ'_{kl} einzuführen ist. Die in Gl. (2.23) auftretenden Ableitungen kürzen wir mit

$$c^i_{kl} = \frac{\partial\epsilon''_{kl}}{\partial\gamma_i} \tag{2.24}$$

ab. Diese Ausdrücke müssen für die jeweils vorliegenden geometrischen Verhältnisse mit Hilfe der vorstehenden Transformationsformeln berechnet werden.

Setzt man

$$\epsilon'_{ik} = C_{ik}\gamma'_i\gamma'_k, \tag{2.25}$$

wo

$$C_{ik} = \begin{cases} 3\lambda_{100}, \text{ wenn } i = k \\ 3\lambda_{111}, \text{ wenn } i \neq k, \end{cases} \tag{2.25a, b}$$

und geht zu den Richtungskosinussen im Koordinatensystem (1) über, so bekommt man gemäss Gl. (2.24)

$$c^\nu_{ij} = \frac{\partial}{\partial\gamma_\nu}\left\{\sum_{k,l}\left[\beta'_{ik}\beta'_{jl}C_{kl}\times\right.\right.$$

$$\left.\left.\times\sum_{m=1}^{3}\beta_{mk}\gamma_m\sum_{n=1}^{3}\beta_{nl}\gamma_l\right]\right\} \quad \nu = 1,3. \tag{2.26}$$

Anwendung der Brownschen Näherung nach dem Differenzieren gibt schliesslich

$$c^\nu_{ij} = \sum_{k,l}\beta'_{ik}\beta'_{jl}C_{kl}(\beta_{2k}\beta_{\nu l}+\beta_{\nu k}\beta_{2l}). \tag{2.27}$$

(e) Mittelbildungen

Bei der Anwendung auf plastisch verformte Einkristalle, bei denen ein ausgezeichnetes Gleitsystem vorhanden ist (Teil II dieser Arbeit), braucht man keinerlei weitere Mittelbildungen durchzuführen.

Bei kubisch-symmetrischer Verteilung der inneren Spannungen in einem Kristall muss man durch Mittelbildung die Gleichwertigkeit der kubischen Achsen berücksichtigen.

Bei der Anwendung auf Vielkristalle mit statistischer Verteilung der Kornorientierungen kommen alle Orientierungen zwischen Feldrichtung und Versetzungslinien gleich häufig vor. Führt man die entsprechende Mittelbildung durch, so ist die Mittelung über die verschiedenen kristallographischen Orientierungen der Versetzungen innerhalb eines Kornes inbegriffen. Wir führen die Mittelbildung bei Vielkristallen für die in Abschnitt 4 und 5 zu behandelnden Probleme durch.

Man hat hierbei die Mittelwerte von $c^\nu_{ik}\cdot c^\nu_{mn}$ für $\nu = 1,3$ zu bestimmen und dabei die Richtungsmittel der Ausdrücke $\beta^2_{ik}\,\beta^2_{lm}$ auszurechnen. Wie üblich führt man Eulersche Winkel ϕ, ψ, θ ein und erhält dann

$$\overline{\beta^2_{ik}\beta^2_{lm}} = \frac{1}{8\pi^2}\int\int\int \beta^2_{ik}\beta^2_{lm}\sin\theta\, d\phi\, d\psi\, d\theta. \tag{2.28}$$

Das Ergebnis der Mittelung ist ($i \neq k \neq l \neq i$)

$$\overline{\beta^2_{ii}\beta^2_{kk}} = \overline{\beta^2_{ii}\beta^2_{kl}} = \overline{\beta^2_{ik}\beta^2_{kl}} = \overline{\beta^2_{ik}\beta^2_{ki}} = \overline{\beta^2_{ik}\beta^2_{li}} = \frac{2}{15}$$

$$\overline{\beta^2_{ii}\beta^2_{ki}} = \overline{\beta^2_{ik}\beta^2_{lk}} = \frac{1}{15}. \tag{2.29}$$

VOL. 12 59/60

Man findet für $\nu = 1,3$

$$c^{\nu}_{ik} \cdot c^{\nu}_{mn} = \frac{6}{5} \sum_{\kappa,\lambda} \beta'_{ik} \beta'_{k\lambda} \beta'_{m\kappa} \beta'_{n\lambda} \Lambda_{\kappa\lambda}, \quad (2.30)$$

wo

$$\Lambda_{\kappa\lambda} = \begin{cases} \lambda^2_{100} \text{ für } \kappa = \lambda \\ 2\lambda^2_{111} \text{ für } \kappa \neq \lambda. \end{cases} \quad (2.30a)$$

Für den späteren Gebrauch führen wir die Abkürzungen

$$\overline{c_{ik}c_{mn}} = \overline{c^1_{ik}c^1_{mn}} + \overline{c^3_{ik}c^3_{mn}} \quad (2.31)$$

ein.

Beim Beispiel der Ziffer 4 ist $\beta'_{ik} = \delta_{ik}$. Dann gilt

$$\overline{c^2_{ii}} = \frac{6}{5}\lambda^2_{100}\,; \quad \overline{c^2_{ik}} = \frac{24}{5}\lambda^2_{111};$$

$$\overline{c_{ik} \cdot c_{mn}} = 0 (i \neq m, k \neq n). \quad (2.32)$$

Beim Beispiel der Ziff. 5 ist

$$\beta'_{ik} = \begin{bmatrix} -\frac{\sqrt{(6)}}{3} & 0 & \frac{\sqrt{(3)}}{3} \\ \frac{\sqrt{(6)}}{6} & -\frac{\sqrt{(2)}}{2} & \frac{\sqrt{(3)}}{3} \\ \frac{\sqrt{(6)}}{6} & \frac{\sqrt{(2)}}{2} & \frac{\sqrt{(3)}}{3} \end{bmatrix} \quad (2.33)$$

In diesem Fall lauten die dort benötigten Mittelwerte

$$\begin{aligned} \overline{c^2_{11}} &= \frac{4}{3}\lambda^2_{100} + \frac{32}{15}\lambda^2_{111}; \\ \overline{c^2_{22}} &= \overline{c^2_{33}} = \overline{c^2_{23}} = \frac{14}{15}\lambda^2_{100} + \frac{44}{15}\lambda^2_{111} \\ \overline{c^2_{12}} &= \overline{c^2_{13}} = \frac{8}{15}\lambda^2_{100} + \frac{56}{15}\lambda^2_{111} \\ \overline{c_{11}c_{22}} &= \overline{c_{11}c_{33}} = \frac{8}{15}\lambda^2_{100} - \frac{16}{15}\lambda^2_{111} \\ \overline{c_{22}c_{33}} &= \frac{14}{15}\lambda^2_{100} - \frac{28}{15}\lambda^2_{111}. \end{aligned} \quad (2.34)$$

3. DER ZUSAMMENHANG ZWISCHEN DEN INNEREN SPANNUNGEN UND DER VERSETZUNGSVERTEILUNG

(a) *Allgemeines*[1]

Die Versetzungsanordnung wird durch den Tensor $\boldsymbol{\alpha}$ der Versetzungsdichte beschrieben, der durch

$$d\mathfrak{b} = d\mathfrak{f} \cdot \boldsymbol{\alpha} \quad (3.1)$$

definiert ist. Dabei ist $d\mathfrak{b}$ der resultierende Burgers-Vektor der durch das Flächenelement $d\mathfrak{f}$ hindurchtretenden Versetzungslinien. Wie das Beispiel einer aus Versetzungen aufgebauten Korngrenze zeigt, rufen nicht alle Versetzungsverteilungen $\boldsymbol{\alpha}(\mathfrak{r})$ innere Spannungen hervor. Spannungswirksam sind vielmehr nur jene, die einen Beitrag zum Inkompatibilitätstensor

$$\boldsymbol{\eta} = \mathrm{Sym}\{\boldsymbol{\alpha} \times \nabla\} \quad (3.2)$$

liefern, wo Sym $\{\boldsymbol{\alpha} \times \nabla\}$ den symmetrischen Anteil des in geschweiften Klammern stehenden Tensors bedeutet.

Den Spannungstensor $\boldsymbol{\sigma}$ erhält man aus dem Spannungsfunktionstensor $\boldsymbol{\chi}$ gemäss

$$\boldsymbol{\sigma} = \mathrm{Ink}\,\boldsymbol{\chi} \equiv \nabla \times \boldsymbol{\chi} \times \nabla, \quad (3.3)$$

wobei

$$\chi_{mn} = -\mathbf{X}_{mnpq}(\nabla) \int\int\int \eta_{pq}(\mathfrak{r}')U(\mathfrak{r}-\mathfrak{r}')\,d\tau_{\mathfrak{r}'} \quad (3.4)$$

gilt. $\mathbf{X}(\nabla)$ ist ein tensorieller Differentialoperator 2. Ordnung, der dieselbe Symmetrie wie der Hookesche Tensor C_{ijkl} besitzt. Die Funktion $U(\mathfrak{r})$ genügt der Differentialgleichung ($\delta(\mathfrak{r})$ = dreidimensionale δ-Funktion)

$$f(\nabla)U(\mathfrak{r}) + \delta(\mathfrak{r}) = 0 \quad (3.5)$$

mit

$$f(\nabla) = \det(C_{ijkl}\nabla_i\nabla_k). \quad (3.5a)$$

(b) *Berechnung der Fourier-Transformierten* $\tilde{\boldsymbol{\sigma}}$

Die nach Abschnitt 2 zur Berechnung der Magnetisierung benötigte Fourier-Transformierte $\tilde{\boldsymbol{\sigma}}(\mathfrak{k})$ des Spannungstensors $\boldsymbol{\sigma}(\mathfrak{r})$ kann direkt aus dem Inkompatibilitätstensor $\boldsymbol{\eta}(\mathfrak{r})$ bzw. dessen Fourier-Transformierten $\tilde{\boldsymbol{\eta}}(\mathfrak{k})$ erhalten werden. Es handelt sich dabei um eine Erweiterung eines in der Theorie der Kleinwinkelstreuung von Versetzungen — mit der in mathematischer Hinsicht das vorliegende Problem vieles gemeinsam hat — verwendeten Verfahrens.[15]

Aus Gl. (3.5) folgt, dass die Fourier-Transformierte $\tilde{U}(\mathfrak{k})$ der Gleichung

$$\tilde{U}(\mathfrak{k}) = -\frac{1}{f(-i\mathfrak{k})} \tag{3.6}$$

genügt. Nach dem Faltungssatz[16] ergibt sich also

$$\int\int\int \eta(\mathfrak{r}')U(\mathfrak{r}-\mathfrak{r}')\,d\tau_{\mathfrak{r}'}$$

$$= -\int\int\int \frac{\tilde{\eta}(\mathfrak{k})}{f(-i\mathfrak{k})}\exp(i\mathfrak{k}\mathfrak{r})\,d\tau_{\mathfrak{k}}. \tag{3.7}$$

Geht man mit Gl. (3.7) in Gl. (3.3) und Gl. (3.4) und benützt noch den total antisymmetrischen Tensor 3. Stufe ϵ_{ikl}, so bekommt man schliesslich

$$\tilde{\sigma}_{kl}(\mathfrak{k}) = \epsilon_{ikm}\cdot\epsilon_{jln}X_{mnpq}(i\mathfrak{k})\frac{k_ik_j\tilde{\eta}_{pq}(\mathfrak{k})}{f(-i\mathfrak{k})}. \tag{3.8}$$

Für kubische Symmetrie ist der Tensor $\mathbf{X}(\nabla)$ bei Kröner[17] (siehe auch[15]) angegeben. Hat man isotrope Verhältnisse, so reduziert sich Gl. (3.8) auf

$$\tilde{\sigma}_{kl} = \frac{2G}{k^2}\left\{\tilde{\eta}_{kl}+\frac{1}{1-\nu}\tilde{\eta}_I\left(\frac{k_kk_l}{k^2}-\delta_{kl}\right)\right\} \tag{3.9}$$

(G = Schubmodul, ν = Poissonsche Konstante, $\tilde{\eta}_I$ = erster Skalar (Spur) von $\tilde{\boldsymbol{\eta}}$). Gl. (3.9) kann auch auf direktem Wege aus den Beltramischen Gleichungen (vergl. auch Ref. 15) abgeleitet werden.

Vielfach ist $\boldsymbol{\eta}(\mathfrak{r})$ nur auf Linien oder Flächen von Null verschieden, so dass die Berechnung von $\eta(\mathfrak{k})$ im allgemeinen ohne Schwierigkeiten möglich ist. Da in Gl. (2.23) σ''_{kl} linear auftritt, ist es n Hand der nachstehenden Formeln ohne weiteres möglich, die in Gl. (2.9) eingehenden Fourier-Transformierten $\tilde{g}_i$ in $\tilde{\eta}_{ik}$ auszudrücken. Die Berechnung von I_y ist damit auf die Berechnung des Integrals Gl. (2.14) zurückgeführt.

In dem speziellen Fall, dass $\boldsymbol{\alpha}$ nur längs einer Linie von Null verschieden ist, gilt folgendes über die Versetzungslinien zu erstreckende Integral:

$$\tilde{\boldsymbol{\eta}} = i(2\pi)^{-3/2}\int\exp(-i\mathfrak{k}\mathfrak{r})\,\mathrm{Sym}\{_d\mathbf{I}\cdot\mathfrak{b}\times\mathfrak{k}\}. \tag{3.10}$$

4. ZWISCHENGITTERATOME

(a) *Der Inkompatibilitätstensor eines Dilatationszentrums*

Im Rahmen der linearen Elastizitätstheorie werden Zwischengitteratome, welche das Kristallgitter in symmetrischer Weise verzerren, im allgemeinen als Dilatationszentren beschrieben. Den Inkompatibilitätstensor eines Dilatationszentrums kann man auf folgende Weise finden (E. Kröner, private Mitteilung):

Die inkompatible Dehnung eines Dilatationszentrums ist gegeben durch

$$\epsilon_{ik} = \delta_{ik}\delta(\mathfrak{r})\Delta V, \tag{4.1}$$

wo $\delta(\mathfrak{r})$ die 3-dimensionale δ-Funktion und ΔV die Volumvergrösserung (ohne Berücksichtigung eventueller Bildkraftwirkungen) ist. Bezeichnet $\mathbf{I}$ den Einheitstensor 2. Stufe, so gilt wegen

$$\boldsymbol{\eta} = \nabla\times\boldsymbol{\epsilon}\times\nabla \tag{4.2}$$

für das Dilatationszentrum

$$\boldsymbol{\eta} = \Delta V\nabla\times\mathbf{I}\times\nabla\delta(\mathfrak{r}). \tag{4.3}$$

Wünscht man die endliche Ausdehnung des Dilatationszentrums zu berücksichtigen, so kann man statt Gl. (4.1)

$$\epsilon_{ik} = \delta_{ik}\frac{\Delta V}{r_0^3\pi^{3/2}}\exp(-r^2/r_0^2) \tag{4.4}$$

verwenden, wo r_0 ein effektiver Radius des Zentrums ist. Führt man Fourier-Transformierte ein, so bekommt man

$$\tilde{\boldsymbol{\eta}} = -\frac{\Delta V}{(2\pi)^{3/2}}(\mathfrak{k}\mathfrak{k}-\mathbf{I}\mathfrak{k}\cdot\mathfrak{k})\exp(-k^2r_0^2/4), \tag{4.5}$$

woraus nach Gl. (3.9)

$$\tilde{\boldsymbol{\sigma}} = \frac{2G}{k^2}\frac{1+\nu}{1-\nu}(\mathfrak{k}\mathfrak{k}-\mathfrak{k}^2\mathbf{I})\exp(-k^2r_0^2/4) \tag{4.6}$$

folgt.

(b) *Berechnung der Suszeptibilität*

Wie wir sehen werden, benötigt man zum experimentellen Nachweis der Zwischengitteratome magnetische Feldstärken, die erheblich über $4\pi J_s$ liegen, so dass man in Gl. (2.15) $h = 0$ setzen kann. Man erhält dann (da gemischte Produkte bei der $\mathfrak{k}$-Integration Null ergeben)

$$\overline{|\tilde{\gamma}_1|^2+|\gamma_3|^2} = \frac{G^2(\Delta V)^2}{(2\pi)^3 C^2 V}\left(\frac{1+\nu}{1-\nu}\right)^2 \iiint \frac{\sum_{i,j}[(k_i k_j - k^2\delta_{ij})^2][(c_{ij}^1)^2+(c_{ij}^3)^2]\epsilon_{ij}\cdot\exp(-k^2 r_0^2/2)}{k^4(k^2+\kappa^2)^2}\, d\tau_t \qquad (4.7)$$

mit $\epsilon_{ij}=1$ für $i=j$ und $\epsilon_{ij}=2$ für $i\neq j$.

In Polarkoordinierten lassen sich die Integrationen der Gl. (4.7) elementar ausführen und ergeben

$$\overline{|\tilde{\gamma}_1|^2+|\tilde{\gamma}_3|^2} = \frac{1}{15\pi^2}\frac{G^2(\Delta V)^2}{C^2 V}\left(\frac{1+\nu}{1-\nu}\right)^2 \sum_{i,j=1}^{3}[(c_{ij}^1)^2+(c_{ij}^3)^2]\epsilon'_{ij}\int_0^\infty \frac{k^2\exp(-k^2 r_0^2/2)}{(k^2+\kappa^2)^2}\, dk, \qquad (4.8)$$

wobei $\epsilon'_{ij}=2$ für $i=j$ und $\epsilon'_{ij}=1$ für $i\neq j$. Gl. (4.8) gilt für beliebige Orientierung der kubischen Achsen gegenüber der Magnetisierungsrichtung.

Das Integral in Gl. (4.8) lässt sich mit Hilfe von

$$\int_0^\infty \frac{k^2\exp(-k^2 r_0^2/2)}{(k^2+\kappa^2)^2}\, dk = \frac{d^2}{d\kappa^2\, d(r_0^2/2)}\int_0^\infty \frac{\exp(-k^2 r_0^2/2)}{k^2+\kappa^2}\, dk = \frac{d^2}{d\kappa^2 d^2(r_0^2/2)}\left\{\frac{\pi}{2\kappa}[1-\Phi(\kappa r_0/2)]\exp(\kappa^2 r_0^2/2)\right\}, \qquad (4.9)$$

wo

$$\Phi(x) = \frac{1}{\sqrt{(\pi)}}\int_0^x \exp(-t^2)\, dt, \qquad (4.10)$$

auswerten. Da $\kappa r_0 \ll 1$, genügt für unsere Zwecke die Näherung

$$\int_0^\infty \frac{k^2\exp(-k^2 r_0^2/2)}{(k^2+\kappa^2)^2}\, dk = \frac{\pi}{4\pi}\left(1-\frac{\kappa r_0}{\sqrt{(2\pi)}}+\frac{3\kappa^2 r_0^2}{2}-+\ldots\right). \qquad (4.11)$$

Die differentielle Suszeptibilität ergibt sich aus

$$\chi = \frac{dIy}{dH} = -\frac{I_s^2}{2C}\frac{d}{d\kappa^2}\overline{[\tilde{\gamma}_1^2+\tilde{\gamma}_3^2]} \qquad (4.12)$$

für einen Vielkristall (Mittelung gemäss Ziff. 2e) zu

$$\chi = \frac{3}{100}\frac{I_s^{1/2}}{(CH)^{3/2}}\left(1-\frac{3(\kappa r_0)^2}{2}\right)(\lambda_{100}^2+4\lambda_{111}^2)NG^2(\Delta V)^2\left(\frac{1+\nu}{1-\nu}\right)^2. \qquad (4.13)$$

5. ANWENDUNG AUF ABGESCHRECKTE METALLE

(a) *Allgemeines*

Die beim Abschrecken eines kubisch-flächenzentrierten Metalls von hohen Temperaturen eingefrorenen Leerstellen können sich, wie eine Reihe neuerer Untersuchungen[18–22] gezeigt hat, entweder zu Versetzungsringen oder zu Stapelfehlertetraedern, deren Kanten aus Versetzungen gebildet werden, zusammenlagern. Bei Nickel[21] beobachtet man Versetzungsringe von der Art der R-Versetzungen, während man bei kobaltreichen NiCo-Legierungen wegen der kleinen Stapelfehlerenergie Tetraeder zu erwarten hat. In den bisher untersuchten Fällen hatten diese Gebilde Durchmesser in der Grössenordnung 100 Å–500 Å. Diese Grössenordnung ist im Zusammenhang mit Messungen des ferromagnetischen Einmündungsgesetzes von besonderem Interesse.

Sieht man von der Wirkung der Streufelder ab (setzt also $h=0$), so enthalten die Gleichungen

von Abschnitt 2 als einzige Grösse von der Dimension einer Länge die sog. Austauschlänge κ^{-1}, die bei Nickel bei $H = 1000$ Oe den Wert $\kappa^{-1} = 180$ Å hat. Man erwartet maximale Effekte, wenn der Radius ρ_0 der Versetzungsringe die Bedingung $\rho_0\kappa \approx 1$ erfüllt.

Die Durchrechnung eines Beispiels bestätigt diese Erwartung und zeigt darüber hinaus, dass sich der Einfluss der Versetzungsringe in abgeschreckten Metallen auf das Einmündungsverhalten gut experimentell nachweisen lassen sollte.

(b) Berechnung von $\tilde{\eta}''$ für einen kreisförmigen Versetzungsring.

Wir betrachten kreisförmige Versetzungsringe mit Radius ρ_0, die in der (111)-Ebene eines kubisch-flächenzentrierten Kristalls liegen sollen. Die Komponente von $\mathfrak{b}$ senkrecht zur Ringebene sei b_z, diejenige in der Ring-Ebene b_ρ. Dann folgt, wenn wir von Gl. (2.19) Gebrauch machen, aus Gl. (3.10)

$$\tilde{\eta}''_{11} = i\rho_0(2\pi)^{-3/2} \int_{\psi=0}^{2\pi} \exp[-ik''_\rho\rho_0 \cos(\psi-\phi)]b_z k''_\rho \sin\phi \sin\psi \, d\psi,$$

$$\tilde{\eta}''_{12} = -\frac{i}{2}\rho_0(2\pi)^{-3/2} \int_{\psi=0}^{2\pi} \exp[-ik''_\rho\rho_0 \cos(\psi-\phi)][(b_z k''_\rho \cos\phi - b_\rho k''_z)\sin\psi - b_z k''_\rho \sin\phi \cos\psi] \, d\psi,$$

$$\tilde{\eta}''_{13} = -\frac{i}{2}\rho_0(2\pi)^{-3/2} \int_{\psi=0}^{2\pi} \exp[-ik''_\rho\rho_0 \cos(\psi-\phi)]b_\rho k''_\rho \sin\phi \sin\psi \, d\psi, \tag{5.1}$$

$$\tilde{\eta}''_{22} = i\rho_0(2\pi)^{-3/2} \int_{\psi=0}^{2\pi} \exp[-ik''_\rho\rho_0 \cos(\psi-\phi)](b_z k''_\rho \cos\phi - b_\rho k''_z)\cos\psi \, d\psi,$$

$$\tilde{\eta}''_{23} = \frac{i}{2}\rho_0(2\pi)^{-3/2} \int_{\psi=0}^{2\pi} \exp[-ik''_\rho\rho_0 \cos(\psi-\phi)]b_\rho k''_\rho \sin\phi \cos\psi \, d\psi,$$

$$\tilde{\eta}''_{33} = 0.$$

Zur Auswertung der vorstehenden Integrale macht man von der Entwicklung

$$\exp(-ik''_\rho\rho_0 \cos\Phi) = J_0(k''_\rho\rho_0) + 2\sum_{m=1}^{\infty} (-i)^m \cos m\Phi J_m(k''_\rho\rho_0) \tag{5.2}$$

Gebrauch. Man erhält damit

$$(\tilde{\eta}'') = \pi\rho_0 J_1(k''_\rho\rho_0)(2\pi)^{-3/2} \begin{pmatrix} 2b_z k''_\rho \sin^2\phi & b_\rho k''_z \sin\phi - b_z k''_\rho \sin 2\phi & -b_\rho k''_\rho \sin^2\phi \\ b_\rho k''_z \sin\phi - b_z k''_\rho \sin^2\phi & 2(b_z k''_\rho \cos^2\phi - b_\rho k''_z \cos\phi) & b_\rho k''_\rho \sin\phi \cos\phi) \\ -b_\rho k''_\rho \sin^2\phi & b_\rho k''_\rho \sin\phi \cos\phi & 0 \end{pmatrix} \tag{5.3}$$

mit der Spur

$$\tilde{\eta}''_I = 2\pi\rho_0 J_1(k''_\rho\rho_0)(2\pi)^{-3/2}(b_z k''_\rho - b_\rho k''_z \cos\phi). \tag{5.4}$$

Für die Fourier-Transformierten der Komponenten des Spannungstensors $\tilde{\boldsymbol{\sigma}}'$ gilt mit

$$A = \frac{4\pi G\rho_0 b_z}{(2\pi)^{3/2}}; \qquad A_1 = Ak''_\rho J_1(k''_\rho\rho_0)k^{-4}$$

$$\tilde{\sigma}''_{11} = A_1\left\{k^2\sin^2\phi - \frac{1}{1-\nu}(k''^2_y+k''^2_z)\left(1-\frac{b_\rho k''_z}{b_z k''_\rho}\cos\phi\right)\right\},$$

$$\tilde{\sigma}''_{22} = A_1\left\{k^2\left(\cos^2\phi - \frac{b_\rho k''_z}{b_z k''_\rho}\cos\phi\right) - \frac{1}{1-\nu}(k''^2_z+k''^2_x)\left(1-\frac{b_\rho k''_z}{b_z k''_\rho}\cos\phi\right)\right\}, \tag{5.5}$$

$$\tilde{\sigma}''_{33} = -A_1\frac{1}{1-\nu}(k''^2_x+k''^2_y)\left(1-\frac{b_\rho k''_z}{b_z k''_\rho}\cos\phi\right),$$

$$\tilde{\sigma}''_{23} = A_1\left\{k^2\frac{b_\rho}{2b_z}\sin\phi\cos\phi + \frac{1}{1-\nu}k''_y k''_z\left(1-\frac{b_\rho k''_z}{b_z k''_\rho}\cos\phi\right)\right\},$$

$$\tilde{\sigma}''_{31} = A_1\left\{-k^2\frac{b_\rho}{2b_z}\sin^2\phi + \frac{1}{1-\nu}k''_x k''_z\left(1-\frac{b_\rho k''_z}{b_z k''_\rho}\cos\phi\right)\right\},$$

$$\tilde{\sigma}''_{12} = A_1\left\{-\frac{k^2}{2}\left(\sin 2\phi - \frac{b_\rho k''_z}{b_z k''_\rho}\sin\phi\right) + \frac{1}{1-\nu}k''_x k''_y\left(1-\frac{b_\rho k''_z}{b_z k''_\rho}\cos\phi\right)\right\}.$$

(*c*) *Das Einmündungsgesetz*

Von nun an vernachlässigen wir das Streufeld ($h = 0$). Man bekommt dann mit Hilfe von Gl. (2.15) und Gl. (2.23) als Mittelwert über den ganzen Kristall (Volumen V)

$$\overline{|\tilde{\gamma}_1|^2+|\tilde{\gamma}_3|^2} = \frac{1}{4C^2V}\sum_{k,l,m,n}(c^1_{kl}\cdot c^1_{mn}+c^3_{kl}\cdot c^3_{mn})\iiint\frac{\tilde{\sigma}''_{kl}\cdot\tilde{\sigma}''_{mn}}{(k^2+\kappa^2)^2}d\tau_{\mathfrak{k}}. \tag{5.6}$$

Beschränken wir uns zur Abschätzung der Grössenordnung auf den Fall $b_\rho = 0$ und benützen für die Vielkristallmittelung (Abschnitt 2e) die Verabredung, dass $\overline{c_{kl}\ c_{mn}}$ für $\overline{c^1_{kl}\ c^1_{mn}+c^2_{kl}\ c^3_{mn}}$ stehen soll, so bekommt man, wenn man die ϕ-Integration sogleich ausführt,

$$\overline{|\tilde{\gamma}_1|^2+|\tilde{\gamma}_3|^2} = \frac{\pi A^2}{2C^2V}\int_{k''_\rho=0}^{\infty}\int_{k''_z=0}^{\infty}\frac{k''^3_\rho J^2_1(k''_\rho\rho_0)}{k^8(k^2+\kappa^2)^2}\{a_0k^4+a_1k^2k''^2_z+a_2k''^4_z\}\,dk''_z\,dk''_\rho, \tag{5.7}$$

wo

$$a_0 = (\overline{c^2_{11}}+\overline{c^2_{22}})\left(\frac{1}{2}-\frac{3}{2}\frac{1}{1-\nu}+\frac{3}{4}\frac{1}{(1-\nu)^2}\right)+\overline{c^2_{33}}\frac{2}{(1-\nu)^2}+4\overline{c^2_{12}}\left(\frac{1}{4}+\frac{1}{(1-\nu)^2}\right)+$$
$$+(\overline{c_{11}c_{22}}+\overline{c_{22}c_{33}})\left(\frac{1}{1-\nu}+\frac{2}{(1-\nu)^2}\right)+\frac{1}{2}\overline{c_{11}c_{22}}\left(\frac{1}{1-\nu}+\frac{1}{(1-\nu)^2}\right),$$

$$a_1 = \frac{1}{2}(\overline{c^2_{11}}+\overline{c^2_{22}})\left(-\frac{1}{1-\nu}+\frac{1}{(1-\nu)^2}\right)-\overline{c^2_{33}}\frac{4}{(1-\nu)^2}+$$
$$+(-\overline{c^2_{12}}+\overline{c^2_{13}}+\overline{c^2_{23}})\frac{8}{(1-\nu)^2}+(\overline{c_{11}c_{33}}+\overline{c_{22}c_{33}})\frac{2}{1-\nu}+3\overline{c_{11}c_{22}}\left(-\frac{1}{1-\nu}+\frac{1}{(1-\nu)^2}\right),$$

$$a_2 = \left[\frac{3}{4}(\overline{c^2_{11}}+\overline{c^2_{22}})+2\overline{c^2_{33}}+\{\overline{c^2_{12}}-(\overline{c^2_{13}}+\overline{c^2_{23}})\}4-2(\overline{c_{11}c_{33}}+\overline{c_{22}c_{33}})+\frac{1}{2}\overline{c_{11}c_{22}}\right]\frac{1}{(1-\nu)^2}. \tag{5.8}$$

Entnimmt man die $\overline{c_{lk}\ c_{lm}}$ aus Gl. (2.34) und setzt $\nu = 1/3$, so bekommt man

$$\begin{aligned} a_0 &= \ \ 19{,}9\,\lambda_{100}^2 + 30{,}6\,\lambda_{111}^2, \\ a_1 &= \ \ 14{,}25\,\lambda_{100}^2 + 18{,}3\,\lambda_{111}^2, \\ a_2 &= -\ 6{,}38\,\lambda_{100}^2 + 7{,}35\,\lambda_{111}^2. \end{aligned} \tag{5.9}$$

Bei Raumtemperatur gilt in Nickel: $\lambda_{100} = 54\cdot10^{-6}$ $\lambda_{111} = 20\cdot10^{-6}$, so dass man für dieses Metall $a_0 = 70\cdot10^{-9}$, $a_1 = 48{,}8\cdot10^{-9}$, $a_2 = 15{,}7\cdot10^{-9}$ hat.

Werden in der k_z'', k_ρ'' -Ebene Polarkoordinaten k, θ gemäss

$$\begin{aligned} k_z'' &= k\cos\theta \\ k_\rho'' &= k\sin\theta \end{aligned} \tag{5.10}$$

eingeführt, so treten Integrale der Form

$$B_n^m(k\rho_0) = \int_0^{\pi/2} J_n^2(k\rho_0\sin\theta)\sin^{2n+1}\theta\cos^{2m}\theta\,d\theta \tag{5.11}$$

auf. Benutzt man die Neumannsche Formel

$$J_\nu(z)\cdot J_\mu(z) = \frac{2}{\pi}\int_0^{\pi/2} J_{\nu+\mu}(2z\cos\psi)\times \\ \times\cos[(\mu-\nu)\psi]\,d\psi\ \ \Re\mathrm{e}(\nu+\mu) > -1 \tag{5.12}$$

und führt dann die Integration über θ mit Hilfe von Sonines erstem Integral

$$\int_0^{\pi/2} J_\lambda(z\sin\theta)\sin^{\lambda+1}\theta\cos^{2\rho+1}\theta\,d\theta \\ = 2^\rho\Gamma(\rho+1)z^{-(\rho+1)}J_{\rho+\mu+1}(z) \tag{5.13}$$

aus, so erhält man

$$B_1^m(k\rho_0) \\ = \frac{2}{\pi}2^{m-1/2}\Gamma(m+\tfrac{1}{2})\int_0^{\pi/2}\frac{J_{m+5/2}(2k\rho_0\cos\psi)\,d\psi}{(2k\rho_0\cos\psi)^{m+1/2}}. \tag{5.14}$$

Setzt man Gl. (5.14) in*

$$\rho_0^3 D^\nu(\kappa\rho_0) \equiv \int_0^\infty \frac{B_1^m(k\rho_0)}{(k^2+\kappa^2)^2}\,dk \tag{5.15}$$

ein, wobei $\nu = m + 5/2$ ist, und wendet die Rekursionsformel

$$z^{2-\nu}J_\nu(z) = 2(\nu-1)z^{1-\nu}J_{\nu-1}(z) - z^{2-\nu}J_{\nu-2}(z) \tag{5.16}$$

sowie die Beziehung[23]

$$\int_0^\infty \frac{x^{-\mu}J(xy)}{x^2+\kappa^2}\,dx = \frac{\pi}{2}\kappa^{-\mu-1}(I_\mu(xy) - \boldsymbol{L}_\mu(xy)) \tag{5.17}$$

an, so erhält man

$$\rho_0^3 D^\nu(\kappa\rho_0) = 2^{\nu-3}\Gamma(\nu-2)\frac{d}{d\kappa^2}\left\{\frac{1}{\kappa}\int_0^{\pi/2}(2\rho_0\kappa\cos\psi)^{2-\nu}\left[I_\nu(2\kappa\rho_0\cos\psi) - \boldsymbol{L}_\nu(2\kappa\rho_0\cos\psi) + \frac{(\rho_0\kappa\cos\psi)^{\nu-1}}{\Gamma(\nu+\frac{1}{2})\Gamma(\frac{1}{2})}\right]d\psi\right\}. \tag{5.18}$$

In Gl. (5.17) bedeuten $I\mu(z)$ und $\boldsymbol{L}\mu(z)$ die modifizierten Besselschen und Struveschen Funktionen, die durch Potenzreihen

$$\begin{aligned} \left(\frac{z}{2}\right)^{-\mu} I_\mu(z) &= \sum_{n=0}^\infty \frac{\left(\frac{z}{2}\right)^{2n}}{n!\,\Gamma(\mu+n+1)} \\ \left(\frac{z}{2}\right)^{-\mu} \boldsymbol{L}_\mu(z) &= \sum_{n=0}^\infty \frac{\left(\frac{z}{2}\right)^{2n+1}}{\Gamma(n+\frac{3}{2})\Gamma(\mu+n+\frac{3}{2})} \end{aligned} \tag{5.19}$$

definiert sind.

* $\rho_0^3 D^\nu(\kappa\rho_0)$ ist gleich dem in Gl. (5.7) auftretenden Doppelintegral, wenn dort $a_m = 1$, $a_n = 0$ $(n \neq m)$ gesetzt wird.

Mit Hilfe dieser Potenzreihenentwicklungen erhält man folgenden, bei der Berechnung der Suszeptibilität benötigten Zusammenhang:

$$-E^{\nu}(\kappa\rho_0) \equiv (\kappa\rho_0)^5 \frac{d}{d(\kappa\rho_0)^2} D^{\nu}(\kappa\rho_0)$$

$$= \frac{\sqrt{(\pi)}}{4}\Gamma(\nu-2)\sum_{n=0}^{\infty}\left[\frac{2^{\nu-1/2}(\kappa\rho_0)^{2n+2}(n^2-\frac{1}{4})}{(n!)^2(n+1)(2n+3)\ldots(2n+2\nu)} - \right.$$

$$\left. -(\kappa\rho_0)^{2n+3}\frac{n(n+1)}{[(n+\frac{1}{2})!]^2(n+\frac{3}{2})(n+2)(n+3)\ldots(n+\nu+\frac{1}{2})}\right]. \qquad (5.20)$$

Die Funktionen $E^{\nu}(\kappa\rho_0)$ sind in Fig. 1 aufgetragen ($\nu = 5/2, 7/2, 9/2$). Dabei wurde für $\nu = 5/2$ die im Anhang behandelte asymptotische Entwicklung für grosse Werte von $\kappa\rho_0$ benützt.

Legt man N Versetzungsringe pro Volumeinheit zugrunde, so gilt für die differentielle Suszeptibilität (vergl. Gl. (4.12)).

$$H^3\chi = \frac{\pi A^2 N}{4I_s}\kappa\sum_{m=0}^{2} a_m E^{m+5/2}(\kappa\rho_0) \qquad (5.21)$$

$$= \frac{N\rho_0^2 b_z}{2I_s} G^2 b_z \kappa \sum_{m=0}^{2} a_m E^{m+5/2}(\kappa\rho_0).$$

Unter den beim Nickel vorliegenden numerischen Verhältnissen ist in Gl. (15.21) $E^{5/2}$ das massgebende Glied. Aus Gl. (A.8) folgt, dass dann für $\kappa\rho_0 \to \infty$

$$\chi H^3 = \frac{\pi A^2 N a_0}{8 I_s \rho_0}\ln\frac{2\kappa\rho_0}{2{,}193} \qquad (5.22)$$

gilt.

6. DISKUSSION

In der vorliegenden Arbeit wird folgendes Problem behandelt: Gegeben die Verteilung der Quellen innerer Spannungen (als Versetzungsdichte oder als Inkompatibilitätsverteilung) in einem ferromagnetischen Ein- oder Vielkristall, gesucht die differentielle magnetische Suszeptibilität χ als Funktion der magnetischen Erregung H im sog. Einmündungsgebiet, d.h. in jenem Bereich der Magnetisierungskurve, in dem keine Wandverschiebungen mehr, sondern nur noch Drehprozesse ablaufen. Dieses Problem wird vollständig gelöst, d.h. auf die numerisch immer mögliche Auswertung eines Volumintegrals zurückgeführt, und zwar im Gültigkeitsbereich der Brownschen Näherung. Diese verlangt, dass die lokale Magnetisierungsrichtung so wenig von der Richtung des wirkenden Feldes abweicht, dass man die vierten Potenzen dieser Abweichung

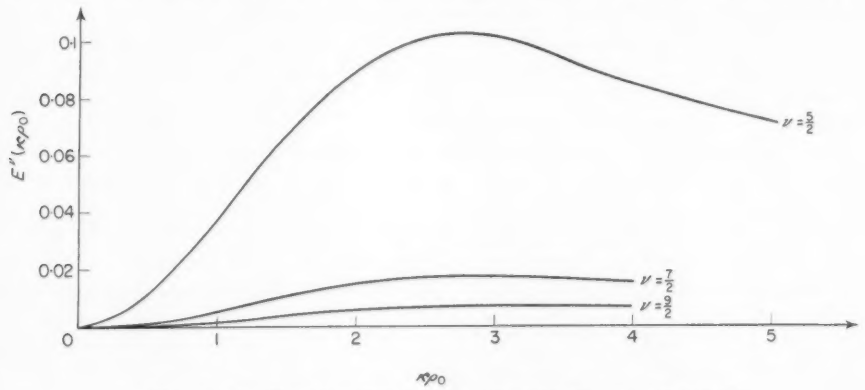

FIG. 1. Die Funktion $E^{\nu}(\kappa\rho_0)$ nach Gl. 5.20 für $\nu = 5/2, 7/2, 9/2$.

VOL. 12 59/60

neben den Quadraten vernachlässigen kann. Bei genügend grossen Feldern ist diese Bedingung immer erfüllt. Arbeitet man bei mittleren Feldern, wo die Erregung H vergleichbar mit oder kleiner als $4\pi I_s$ ist, so muss man zwar nicht für grössenordnungsmässige Abschätzungen, wohl aber für quantitative Untersuchungen die infolge der räumlichen Variation der Magnetisierung auftretenden inneren Streufelder berücksichtigen. Dies ist im allgemeinen Teil der vorliegenden Arbeit geschehen. Die Berücksichtigung der Streufelder verbessert gerade bei mittleren Feldern, wo die Verhältnisse etwas kritisch sind, die Brauchbarkeit der Brownschen Näherung erheblich, so dass man diese wohl in allen praktisch interessierenden Fällen anwenden darf.

Die grössten Winkel zwischen Magnetisierungsrichtung und Erregungsrichtung treten in der unmittelbaren Umgebung von Versetzungslinien auf. An Hand eines Beispiels werden die dort vorliegenden Verhältnisse in Teil II dieser Arbeit diskutiert werden. In Teil II wird auch der quantitative Vergleich zwischen der Theorie und Experimenten an plastisch gedehnten Nickel- und Nickel-Kobalt-Einkristallen[4] durchgeführt werden. Dabei wird sich zeigen, dass die Übereinstimmung zwischen Experiment und Theorie sehr gut ist.

Die gute Übereinstimmung zwischen Experiment und Theorie und die in der vorliegenden Arbeit gegebene, bequem anwendbare Formulierung der Theorie gestattet es, die Untersuchung der Einmündung in die Sättigung zur Erforschung der Versetzungsdichte und Versetzungs-Anordnung in ferromagnetischen Stoffen zu verwenden. Dieses Verfahren ist entweder zuverlässiger zu interpretieren oder einfacher anzuwenden als die meisten anderen Methoden. Einer seiner Vorzüge (den es mit der Messung der thermischen Gitterleitfähigkeit von Isolatoren und Legierungen teilt), ist der, dass es einen durch die Versuchsführung beeinflussbaren Längenmassstab

$$\kappa^{-1} = \sqrt{\left(\frac{C}{HI_s}\right)}$$

besitzt.

Die Suszeptibilität wird besonders stark beeinflusst durch innere Spannungen, die in Entfernungen von der Grössenordnung κ^{-1} stark variieren. (Für $H = 2\,000$ Oe ist bei Nickel $\kappa^{-1} = 130$ Å.) Dies sind vor allem die von Versetzungen, insbesondere in aufgestauten Versetzungsgruppen, herrührenden Spannungen, die sich auf diese Weise bequem von den von atomaren Fehlstellen (Zwischengitteratomen, Verunreinigungen) stammenden Einflüssen trennen lassen.

Um die vorstehende Behauptung zu erläutern, haben wir in Abschn. 4 den Einfluss von Dilatationszentren (als Modelle für Zwischengitteratome) auf χ berechnet. Setzt man in die Schlussformel für Vielkristalle Gl. (4.13) Zahlenwerte ein [Ni: $G = 7{,}5\cdot10^3$ (kp/mm^2), $\Delta V = 3\Omega/2$ (Ω = Atomvolumen), $N = 0{,}9\cdot10^{19}$ entsprechend einer Konzentration $c = 10^{-4}$ der Zwischengitteratome], so erhält man für $H = 2\,000$ Oe

$$\chi H^3 = 117 \text{ Oe}^2\text{G}. \qquad (6.1)$$

Da bei dieser Feldstärke ausgeglühte Nickeleinkristalle bei Raumtemperatur $\chi H^3 \sim 10^6 \text{Oe}^2\text{G}$ ergeben, kann man unter diesen Bedingungen den Einfluss von Zwischengitteratomen vollkommen vernachlässigen.

Bei extrem hohen Werten von H hat man in günstigen Fällen gewisse Aussichten, den Einfluss von Zwischengitteratomen auf χ nachweisen zu können, da deren Beitrag zu χ wie $H^{-3/2}$ variiert, während der Versetzungsanteil und der Anteil der Kristallenergie etwa wie H^{-3} abnehmen. Allerdings variiert der von HOLSTEIN u. PRIMAKOFF[24] behandelte "paramagnetische" Anteil χ_0 der Suszeptibilität wie $H^{-1/2}$; da χ_0 jedoch proportional zu T ist, kann dieser Anteil durch Messung bei tiefen Temperaturen verkleinert werden. Treten Zwischengitteratome zu Gruppen von z Atomen zusammen, so wächst deren Effekt etwa proportional zu z. Vielleicht lässt sich auf diese Weise die Ansicht einiger Autoren, dass bei der Erholung strahlungsgeschädigter kubisch-flächenzentrierter Metalle sich ein grosser Teil der Zwischengitteratome zu Paaren und grösseren Gruppen zusammenlagert, experimentell nachprüfen. Allerdings wären solche Messungen keineswegs einfach durchzuführen. Einfacher und an unserem Institut bereits in die Wege geleitet sind Messungen, die das Koagulieren von Leerstellen, die beim Abschrecken eingefroren wurden, zu Versetzungsringen verfolgen (vergl. Abschn. 5a). Einzelne Leerstellen und auch kleine sphärische Hohlräume geben praktisch keinen magnetostriktiven Beitrag zu χ, da die auftretenden Spannungen sehr klein sind. (Dagegen wirken hinreichend

grosse Hohlräume durch ihre Streufelder[5], jedoch um mindestens eine Grössenordnung schwächer als die entsprechenden Versetzungsringe). Scheiden sich die Leerstellen plattenförmig aus, so rufen sie das einem Versetzungsring entsprechende Spannungsfeld und damit verhältnismässig starke magnetostriktive Wirkungen hervor, deren Einfluss auf die magnetische Suszeptibilität für ein einfaches Beispiel in Abschn. 5 berechnet wurde.

Nach Gl. (5.21) ergibt sich für Nickel

$$\chi H^3 = 4{,}66 \cdot 10^5 N \rho_0^2 \kappa \sum_{m=0}^{2} a_m E^{m+5/2}(\kappa\rho_0). \tag{6.2}$$

Zwischen der Zahl der Leerstellen pro Volumeinheit N_L und der Dichte N der Ringe mit Radius ρ_0, besteht der Zusammenhang

$$N\rho_0^2 = \frac{N_L \Omega}{\pi b_z} = 1{,}71 \cdot 10^{-16} N_L \text{ cm}^2. \tag{6.3}$$

Für $N_L = 0{,}9 \cdot 10^{19} \text{cm}^{-3}$, $H = 2000$ Oe und $\rho_0 = 340$ Å ergibt sich

$$\chi H^3 = 4{,}5 \cdot 10^6 \text{ Oe}^2 G. \tag{6.4}$$

Die Vernachlässigung von b_ρ/b_z sowie des inneren Streufeldes (siehe Abschn. 5c) hat keinen Einfluss auf die Grössenordnung von Gl. 6.4. Dies bedeutet, dass χH^3 gut messbar ist und dass sich somit Einmündungsmessungen dazu eignen, die Koagulation eingefrorener Leerstellen zu Versetzungsringen (oder Tetraedern) zu verfolgen.

Für $\rho_0\kappa \ll 1$ wirken die Versetzungsringe ähnlich wie Dilatationszentren. In diesem Grenzfall gibt Gl. (5.21)

$$\chi H^3 = \frac{G N \rho_0^4 b_z^2 \pi \kappa^3}{120}\left(a_0 + \frac{a_1}{7} + \frac{a_2}{21}\right), \tag{6.5}$$

also $\chi \sim H^{-3/2}$ wie in Abschn. 4. Setzt man zum quantitativen Vergleich mit Abschn. 4

$$\rho_0 b_z \pi = \Delta V, \tag{6.6}$$

so ergibt sich das Verhältnis der Suszeptibilität nach Gl. (6.5) zu derjenigen nach Gl. (4.13) mit den Konstanten für Nickel (Raumtemperatur) 1,20. Die Abweichung vom Wert 1 liegt natürlich daran, dass die Mittelbildung in den beiden Fällen verschieden durchgeführt wurde.

Die Verfasser danken der Deutschen Forschungsgemeinschaft für die Unterstützung dieser Arbeit und Professor J. KELLER für interessante Diskussionen im Anfangsstadium der Untersuchung.

ANHANG

Für $\rho_0^3 D^\nu(\kappa\rho_0)$ (vergl. Gl. 5.15) geben wir hier im Spezialfall $\nu = 5/2$ ($m = 0$) eine Darstellung, die zur numerischen Auswertung bei grossen Werten von $\kappa\rho_0$ geeignet ist.

Nach BAILEY[25] gilt:

$$B_1^0(\kappa\rho_0) = \int_0^{\pi/2} J_1^2(k\rho_0 \sin\theta)\sin^3\theta\, d\theta$$

$$= \frac{2}{k\rho_0}\sum_{n=0}^{\infty}\frac{(n+1)(n+2)}{(2n+1)(2n+5)} J_{2n+3}(2k\rho_0). \tag{A.1}$$

Setzt man Gl. (A.1) in (5.15) ein, wendet die Rekursionsformel für Besselfunktionen an und integriert mit Hilfe von ERDÉLYI[26], so bekommt man den formalen Ausdruck:

$$D^{5/2}(y) = -\frac{d}{dy^2}\left[32\sum_{n=0}^{\infty} A_n \frac{1}{2(2n+3)}\frac{1}{y}\left\{\frac{1}{\sin(2n+2)\pi}(\boldsymbol{I}_{2n+2}(y) - J_{2n+2}(y)) + \right.\right.$$

$$\left.\left. + \frac{1}{\sin(2n+4)\pi}(\boldsymbol{I}_{2n+4}(y) - J_{2n+4}(y))\right\}\right]. \tag{A.2}$$

Dabei bedeutet:

$$A_n = \frac{1}{4} - \frac{1}{4}\frac{1}{(2n+1)(2n+5)}$$

$$y = 2\kappa\rho_0$$

$\boldsymbol{I}(y)$ bedeutet die Weber-Angersche Funktion.

Ferner gelten folgende Gleichungen (vergl. WATSON[27]):

$$\frac{\pi}{\sin m\pi}(\boldsymbol{I}_m(y)-J_m(y)) = \int_0^\infty \exp(-mt-y\,\mathfrak{Sin}\,t)\,dt$$

$$= \tfrac{1}{2}(-)^{m+1}(S_m(y)+\pi\boldsymbol{E}_m(y)+\pi N_m(y)) \qquad \text{(A.3)}$$

$$\equiv \tfrac{1}{2}(-)^{m+1}F_m(y).$$

Mit Hilfe von (A.3) kann (A.2) teilweise summiert werden, denn A_n ist für grosse $n\sim\frac{1}{4}$; bei $n=2$ beträgt die Abweichung 1/180. Dann kann die Summe in folgendes Integral übergeführt werden:

$$D^{5/2}(y) = -4\frac{d}{dy^2}\left[\frac{1}{y^2}\int_0^y\int_0^\infty \exp(-2t-y'\,\mathfrak{Sin}\,t)\,dt\,dy'\right]+\frac{d}{dy^2}R(y)$$

$$= \lim_{A\to\infty}\left\{-4\frac{d}{dy^2}\left[\frac{1}{y^2}\int_0^A\int_0^\infty \exp(-2t-y'\,\mathfrak{Sin}\,t)\,dt\,dy' - \frac{1}{2y^2}\int_A^y F_2(y')\,dy'\right]\right\}+\frac{d}{dy^2}R(y). \qquad \text{(A.4)}$$

Hierbei bedeutet:

$$R(y) = -\frac{4}{y^2}\sum_{n=0}^{\infty}\frac{1}{(2n+1)(2n+5)}\left(F_{2n+3}(y)-\frac{1}{n+\frac{3}{2}}\right). \qquad \text{(A.5)}$$

Die Funktionen $F_m(y)$ besitzen nach WATSON[27] die folgenden asymptotischen Entwicklungen:

$$F_m(y) = \sum_{n=0}^{(m-1)/2}\left[\frac{(\frac{1}{2}m+n-\frac{1}{2})!}{(\frac{1}{2}m-n-\frac{1}{2})!(\frac{1}{2}y)^{2n+1}}\right]-\frac{2}{y}\left(\frac{m}{y}-\frac{m(2^2-m^2)}{y^3}+\frac{m(2^2-m^2)(4^2-m^2)}{y^5}-+\ldots\right)$$

$$\text{für } m = 2\nu+1 \qquad \text{(A.6a)}$$

und

$$F_m(y) = \sum_{n=0}^{m/2}\left[\frac{(\frac{1}{2}m+n-1)!}{(\frac{1}{2}m-n)!(\frac{1}{2}y)^{2n}}\right]-\frac{2}{y}\left(1-\frac{1^2-m^2}{y^2}+\frac{(1^2-m^2)(3^2-m^2)}{y^4}-+\ldots\right)$$

$$\text{für } m = 2\nu. \qquad \text{(A.6b)}$$

Mittels (A.6b) sowie der Integraldarstellung:

$$\ln A = \int_0^\infty \frac{\exp(-x)-\exp(-xA)}{x}\,dx \qquad \text{erhält man aus (A.4):}$$

$$D^{5/2}(y) = \frac{d}{dy^2}R(y)+4\left\{\frac{\ln y}{y^4}-\frac{1}{y^4}\left(\psi\left(\frac{3}{2}\right)+\frac{1}{2}\right)+\frac{2}{y^5}-\frac{3}{y^6}+\frac{45}{4y^8}-+\ldots\right\}. \qquad \text{(A.7)}$$

Aus (A.7) errechnet sich die differenzielle Suszeptibilität :

$$\chi H^3 = \frac{\pi A^2 N \kappa}{4 I_s} a_0 E^{5/2}(\kappa\rho_0), \qquad \text{(A.8)}$$

wobei $(\Psi(\frac{3}{2}) = 0{,}0365)$

$$E^{5/2}(\kappa\rho_0) = -4\rho_0^5\kappa^5 \frac{d}{dy^2}\{D^{5/2}(y)\}$$

$$= \frac{1}{2y}\left\{2\cdot \ln y - 2\left(\psi\left(\frac{3}{2}\right)+\frac{3}{4}\right) + \frac{7{,}5}{y} - \frac{9}{y^2} + \frac{45}{y^4} - \frac{1050}{y^6} + \frac{6255\cdot 15}{4y^8} - \frac{458\,000}{y^{10}} + - \ldots\right\} +$$

$$+ \sum_{n=0}^{\infty} \frac{y}{16\cdot(2n+1)(2n+5)}\left\{\left(\frac{1}{2} - \frac{16}{y^2}\right)F_{2n+3}(v) + \frac{5}{y}(F_{2n+2}(y) - F_{2n+4}(y)) - \right.$$

$$\left. - \frac{1}{2}F_{2n+1}(y) - \frac{1}{2}F_{2n+5}(y) - \frac{32}{y^2}\frac{1}{n+\frac{3}{2}}\right\}. \qquad \text{(A.9)}$$

LITERATUR

1. Kröner E., *Kontinuumstheorie der Versetzungen und Eigenspannungen*. Springer, Berlin (1958).
2. Brown W. F., *Phys. Rev.* **58**, 736 (1940).
3. Brown W. F., *Phys. Rev.* **60**, 132 (1941).
4. Kronmüller H., *Z. Phys.* **154**, 574 (1959).
5. Néel L., *J. Phys. Radium* **9**, 185, 193 (1949).
6. Becker R. und Döring, W., *Ferromagnetismus* Springer, Berlin (1939).
7. Landau L. und Lifshitz E., *Phys. Z. Sowjet.* **8** 153 (1955).
8. Herring C. und Kittel C., *Phys. Rev.* **81**, 869 (1951).
9. Stoner E. C., *Rep. Progr. Phys.* **13**, 83 (1950).
10. Kittel C. und Galt J. K., *Solid State Phys.* **3**, 437 (1956).
11. Lifshitz E., *J. Phys. USSR* **8**, 337 (1944).
12. Fallot M., *Ann. Phys., Paris* **6**, 305 (1936).
13. Herring C., *Phys. Rev.* **85**, 1003 (1952).
14. Schmeidler H., *Integralgleichungen*. Akademische Verlagsgesellschaft, Leipzig (1950) S.17.
15. Seeger A. und Kröner E., *Z. Naturforsch.* **14a**, 75 (1959).
16. Schmeidler H., *Integralgleichungen*, S. 75. Akademische Verlagsgesellschaft, Leipzig (1950).
17. Kröner E., *Z. Phys.* **141**, 393 (1955).
18. Hirsch P. B., Silcox J., Smallman R. E. und Westmacott K. H., *Phil. Mag.* **3**, 897 (1958).
19. Hirsch P. B. und Silcox J., *Growth and Perfection of Crystals*, hrsg. von Doremus R. H., Roberts B. W. und Turnbull D., S.262. Wiley, New York (1958).
20. Hirsch P. B. und Silcox J., *Phil. Mag.* **4**, 72 (1959).
21. Smallman R. E., Westmacott K. H. und Coiley J. H., *J. Inst. Met.* **5**, 127 (1959).
22. Smallman R. E., Westmacott K. H., *J. App. Phys.* **30**, 603 (1959).
23. Erdélyi A., *Tables of Integral Transforms Bd.* 2, S.23, Gl.14. McGraw-Hill, New York (1954).
24. Holstein T. und Primakoff H., *Phys. Rev.* **58**, 1098 (1940).
25. Bailey W., *Quart. J. Math.* Oxford Ser. 9, 141–147 (1938).
26. Erdélyi A., *Tables of Integral Transforms Bd.* 2, S.340, Gl. 2. McCraw-Hill, New York (1954).
27. Watson G. N., *A Treatise on the Theory of Bessel Functions*, S.286, Gl. 14; S.315, Gl. 2. Cambridge University Press (1952).

VOL. 12 59/60

J. Phys. Chem. Solids Pergamon Press 1960. Vol. 12. pp. 314–325. Printed in Great Britain.

ZUR HALBEMPIRISCHEN BESTIMMUNG DER BORN–MAYER-KONSTANTEN VON KUBISCH-FLÄCHENZENTRIERTEN METALLEN, INSBESONDERE VON KUPFER

E. MANN und A. SEEGER

Max-Planck-Institut für Metallforschung, Stuttgart, und Institut für theoretische und angewandte Physik der Technischen Hochschule Stuttgart.

(*Received* 29 *April* 1959)

Zusammenfassung — Die nicht-elektrostatische Wechselwirkung zwischen den abgeschlossenen Schalen der Ionenrümpfe in den Edelmetallen wird meist durch Zentralkräfte zwischen nächstbenachbarten Atomen beschrieben, wobei für die Wechselwirkungsenergie zweier Ionen im Abstand r (Gleichgewichtsabstand r^0) ein Born–Mayer-Potential der Form $\phi(r) = A \exp[-B(r/r_0-1)]$ angenommen wird. Die Parameter A und B in diesem Gesetz werden in der vorliegenden Arbeit halbempirisch bestimmt, und zwar mit den folgenden verschiedenen Methoden: (*a*) Aus den gewöhnlichen (linearen) Schermoduln (wie bei HUNTINGTON und SEITZ); (*b*) aus der Druckabhängigkeit der Schermoduln; (*c*) aus dem Kompressionsmodul mit Hilfe eines theoretischen Ausdrucks für die Energie des Grundzustandes, der die Kohäsionsenergie des Kupfers auf wenige Prozent genau wiedergibt; (*d*) aus der (nicht-linearen) Volumen–Druck-Beziehung, wie sie neuerdings durch Stosswellenversuche bestimmt worden ist.

Die auf die verschiedenen Weisen erhaltenen Werte-Paare A, B fallen sehr verschieden aus, doch besteht ein näherungsweiser Zusammenhang zwischen A und B (s. Abb. 3). Die Anwendung der Ergebnisse auf Zwischengitteratome wird in einer weiteren Arbeit gegeben werden.

Abstract—The non-electrostatic interaction between the closed shells of the ion cores in the noble metals is usually described by a Born–Mayer energy per ion-pair of the form $\phi(r) = A \exp[-B(r/r_0-1)]$, where r denotes the separation between the neighbouring atoms and r_0 the equilibrium separation. In the present paper the parameters A and B in the Born–Mayer relation are determined semi-empirically by the following methods: (*a*) From the ordinary (linear) elastic shear constants (following HUNTINGTON and SEITZ); (*b*) from the pressure dependence of the shear moduli; (*c*) from the bulk modulus, utilizing a theoretical expression for the energy of the ground state, which accounts, within a few per cent, for the energy of cohesion of copper; (*d*) from the (non-linear) volume-pressure relation as recently determined in shock wave experiments.

Different methods give widely different pairs A, B. There exists, however, an approximate relationship between A and B (see Fig. 3). The application of the results to interstitial atoms will be given in a later paper.

1. EINLEITUNG

BEI der Berechnung der Bildungs- und Wanderungsenergien von Zwischengitteratomen in Kupfer (und sicherlich auch in den übrigen Edelmetallen Silber und Gold) spielt derjenige Anteil die grösste Rolle, der von der (nicht-elektrostatischen) Wechselwirkung zwischen den Ionenrümpfen herrührt. Es handelt sich dabei um die gegenseitige Abstossung der abgeschlossenen Schalen benachbarter Ionen, die besonders bei den Edelmetallen wegen deren relativ grossen Ionenradien stark in Erscheinung tritt. Eine Berechnung dieser Wechselwirkungsenergie ist bisher nicht in befriedigender Weise gelungen, weshalb man meist für die Wechselwirkung Zentralkräfte zwischen den nächstbenachbarten

Atomen annimmt, die sich aus einem sog. Born–Mayer-Potential ableiten:

$$\phi(r) = A \exp[-B(r/r_0-1)]. \quad (1)$$

Hier bedeutet $\phi(r)$ die potentielle Energie zweier Ionen im Abstand r (Gleichgewichtsabstand r_0) infolge der oben erwähnten Abstossung, deren starker Veränderlichkeit mit dem Abstand durch die Exponentialform Rechnung getragen wird.

Die beiden Konstanten A und B in dem einfachen Ansatz Gl. (1) sucht man gewöhnlich auf halb-empirische Weise zu bestimmen. Da die Ionenabstossungs- oder Born–Mayer-Energie auch einen Anteil an der gesamten Bindungsenergie des idealen Kristalls darstellt und die elastischen Eigenschaften des Kristalls, die sich aus der Bindungsenergie ableiten lassen, wesentlich durch die Born–Mayer-Energie beeinflusst werden, können die Born–Mayer-Konstanten durch Kombination elastischer Daten mit den theoretischen Ausdrücken für die übrigen Anteile in der Bindungsenergie näherungsweise bestimmt werden. In dieser Weise haben HUNTINGTON und SEITZ[1] und HUNTINGTON[2] aus den drei elastischen Konstanten eines kubischen Kristalls und unter Berücksichtigung gewisser Anteile der Elektronenenergie die Born–Mayer-Konstanten für Kupfer erstmalig berechnet. Als Mittelwerte einzelner, stark streuender Bestimmungen bzw. als mögliche Grenzwerte erhielten sie:

HUNTINGTON u. SEITZ:

$$A = 0{,}032 \text{ eV}, \; B = 17{,}0$$

HUNTINGTON: (2)

$$(a)\; A = 0{,}053 \text{ eV}, \; B = 13{,}9$$
$$(b)\; A = 0{,}038 \text{ eV}, \; B = 17{,}2.$$

In der vorliegenden Arbeit werden wir ausser den "gewöhnlichen" elastischen Konstanten auch noch die in neuerer Zeit gemessenen Werte für deren Druckabhängigkeit bei der Bestimmung der Born–Mayer-Konstanten mit heranziehen, wie es seit Abschluss unserer Rechnungen auch DANIELS u. SMITH[3] getan haben. Von den anderen Anteilen in der Bindungsenergie werden wir — im Gegensatz zu manchen früheren Autoren — sämtliche Beiträge berücksichtigen, und zwar in der Art und Weise, wie sie sich nach dem Verfahren von WIGNER u. SEITZ für die Berechnung der Bindungsenergie ergeben; insbesondere werden wir in der Fermi-Energie eine effektive Masse $m^* = 1{,}45m$ verwenden und für die Grundzustandsenergie nicht die Berechnungen von FUCHS[4], sondern die neueren und zuverlässiger erscheinenden von KAMBE[5] zugrunde legen, wodurch sich übrigens auch eine Kohäsionsenergie ergibt, die bis auf weniger als 5 Prozent mit der gemessenen übereinstimmt.

2. DIE BINDUNGSENERGIE NACH DER WIGNER–SEITZ-METHODE

Zur Berechnung der Konstanten im Born–Mayer-Gesetz Gl. (1) benötigen wir, wie schon erwähnt, einen theoretischen Ausdruck für die gesamte Bindungsenergie des idealen Kristalls. Für die einwertigen Metalle wurde ein solcher von WIGNER und SEITZ abgeleitet, der trotz seiner einfachen Voraussetzungen schon vielfach zu guten Resultaten geführt hat und den wir im folgenden auch verwenden und anschliessend kurz beschreiben wollen; bezüglich einer näheren Diskussion sei z. B. auf die zusammenfassenden Darstellungen von Brooks[6] und SEITZ[7] verwiesen.

Bei der WIGNER–SEITZ-Methode wird der ideale Kristall bekanntlich in gleichgrosse polyedrische Zellen eingeteilt, in deren Zentrum je ein Ion sitzt; für die Rechnung werden der Einfachheit halber diese Zellen häufig durch Kugeln von gleichem Volumen mit Radius r_s ersetzt, so dass gilt $\Omega = 4\pi r_s^3/3$ (Ω = Atomvolumen). Im Durchschnitt befindet sich bei den einwertigen Metallen neben dem einfach positiv geladenen Ion je ein (Valenz-) Elektron in einer Zelle, so dass die Zellen im Zeitmittel nach aussen hin als neutral betrachtet werden können.

Nach der Methode von WIGNER u. SEITZ ergibt sich als gesamte Energie pro Atom

$$\epsilon = \epsilon_0 + \epsilon_F + \epsilon_C + \epsilon_A + \epsilon_K + \epsilon_{\text{Ion}}. \quad (3)$$

Dies ist das Negative der Energie pro Atom, die erforderlich ist, um den Kristall in einzelne positive Ionen und freie Elektronen auseinanderzunehmen, stellt also die Summe aus der Kohäsionsenergie ϵ_{Koh} und der Ionisierungsenergie ϵ_I des freien Atoms dar.

In Gl. (3) bedeutet ϵ_0 die (kinetische + potentielle) Energie eines Elektrons im Grundzustand im Potential des Ions einer Grundzelle. Man erhält sie durch Lösen der Schrödinger-Gleichung in einer Zelle mit der Nebenbedingung, dass die

Wellenfunktion am Zellenrand eine verschwindende Normalableitung besitzt. Auf diese Weise hat FUCHS[4] für Kupfer Wellenfunktionen erhalten, die fast im gesamten Bereich der Grundzelle, mit Ausnahme des kernnahen Gebiets, nahezu konstant sind, was bedeutet, dass in dieser Näherung auch die Dichte der Leitungselektronen konstant ist.

ϵ_F ist die Fermi-Energie pro Atom, das ist die zusätzliche kinetische Energie der (Valenz-) Elektronen, die durch das Pauli-Prinzip erzwungen wird. Die Valenzelektronen werden dabei als quasifreies Elektronengas betrachtet, wobei der Einfluss des periodischen Gitterpotentials durch eine effektive Masse m^* berücksichtigt wird.

ϵ_C ist die gesamte elektrostatische Energie pro Atom zwischen den Ionen und Elektronen abzüglich der schon in ϵ_0 enthaltenen potentiellen Energie eines Elektrons im Felde des Ions in derselben Grundzelle. Berechnet man die elektrostatische Energie so, als ob die Elektronenladung gleichmässig-kontinuierlich über das Ionengitter verteilt wäre, so stellt, nach der Konzeption neutraler Zellen, ϵ_C praktisch die Selbstenergie der Elektronenladung in einer Zelle dar. Diese Energieerhöhung, die man sich von der gleichzeitigen Anwesenheit mehrerer Elektronen in einer Grundzelle herrührend denken kann, wird grösstenteils wieder kompensiert durch die Austauschenergie ϵ_A und die Korrelationsenergie ϵ_K infolge der Wechselwirkung (Abstossung) von Elektronen mit parallelem Spin bzw. antiparallelem Spin.

ϵ_{Ion} bedeutet die schon erwähnte nicht-elektrostatische Wechselwirkungsenergie zwischen den Ionenrümpfen (im folgenden auch Born–Mayer-Energie genannt), die bei den Edelmetallen eine Rolle spielt, nicht aber bei den Alkalimetallen mit wesentlich kleineren Ionenradien.

Von den verschiedenen Energiebeiträgen in Gl. (3) hängen ϵ_0, ϵ_F, ϵ_A und ϵ_K praktisch nur vom Volumen der Grundzelle ab, nicht aber von deren Gestalt ; bei volumentreuen Verzerrungen des Gitters ändern sich nur ϵ_C (infolge der elektrostatischen Wechselwirkung verschiedener Zellen) und ϵ_{Ion}.

Für ein gleichförmig komprimiertes Gitter lässt sich die Energie darstellen als

$$\epsilon = \epsilon_0 + \epsilon_F + \epsilon_{\text{Ion}} + \epsilon_{\text{Korr}}, \qquad (4)$$

wo $\epsilon_{\text{Korr}} = \epsilon_C + \epsilon_A + \epsilon_K$, wie schon angedeutet, nur eine Korrektur bedeutet. In der Näherung freier Elektronen ergibt sich dafür der Ausdruck (r_s = Radius der Wigner–Seitz-Kugel)

$$\epsilon_{\text{Korr}} = 0{,}142\frac{e^2}{r_s} - 0{,}288\frac{e^2}{r_s + 5{,}1\,a_H}$$

$$= 0{,}284\frac{1}{r_s} - 0{,}576\frac{1}{r_s+5{,}1}\,[\text{Ry}]. \qquad (5)$$

Die zweite Zeile in Gl. (5) entsteht durch Verwendung von Atomeinheiten, wobei Längen in a_H-Einheiten (a_H=Bohrscher Wasserstoffradius= $0{,}5292\cdot10^{-8}$cm) und Energien in Rydberg-Einheiten (1 Ry = 13,54 eV) zu messen sind.

Die Fermi-Energie ϵ_F ist gegeben durch

$$\epsilon_F = \frac{3}{5}\zeta = \frac{3}{5}\frac{\hbar^2}{2m^*}(3\pi^2)^{2/3}\Omega^{-2/3}$$

$$= 2{,}210\frac{m}{m^*}\frac{1}{r_s^2}\,[\text{Ry}]. \qquad (6)$$

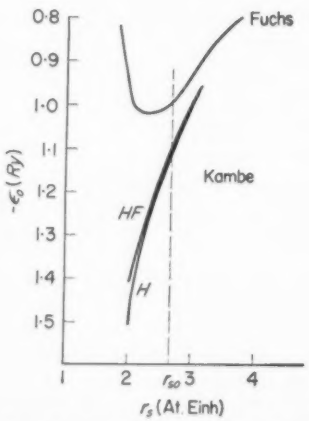

ABB. 1. Grundzustandsenergie ϵ_0 für Kupfer in Abhängigkeit vom Zellenradius r_s nach FUCHS und KAMBE. (H = Wasserstoffpotential, HF = Hartree–Fock-Potential, r_{s0} = Gleichgewichtsradius.)

Die Grundzustandsenergie ϵ_0 in Abhängigkeit vom Zellenradius r_s wurde für Kupfer erstmalig von FUCHS[4] durch Integration der Schrödinger-Gleichung in einer Grundzelle und unter Zugrundelegung des Hartree–Fock-Potentials für Kupfer berechnet. In neuerer Zeit hat KAMBE[5] nach einem Verfahren, bei dem man den Potentialverlauf nicht in der ganzen Zelle, sondern nur

in Nähe des Zellenrandes zu kennen braucht, die Grundzustandsenergie der Edelmetalle neu berechnet. KAMBE hat die Lösung einmal für den Fall des reinen Wasserstoff-Potentials und zum andern für den Fall des Hartree–Fock-Potentials am Rand der Zelle angegeben. Die Ergebnisse von FUCHS und KAMBE sind in ABB. 1 dargestellt.

Für die Funktion $\epsilon_0(r_s)$ läst sich, wie BARDEEN[8] gezeigt hat, eine Differentialgleichung aufstellen. Allein mit Hilfe der Schrödinger-Gleichung und der Bedingung, dass die Normalableitung der Wellenfunktion am Zellenrand verschwindet, ergibt sich

$$\frac{d\epsilon_0(r_s)}{dr_s} = \frac{3}{r_s}\left[V(r_s) - \epsilon_0(r_s)\right]\gamma(r_s). \qquad (7)$$

Hierbei ist, mit

$$\Omega = 4\pi r_s^3/3 \text{ und } \int_0^{r_s} \psi_0^2(r)\, d\tau = 1,$$

$$\gamma(r_s) = \Omega\psi_0^2(r_s) = \frac{\psi_0^2(r_s)}{r_s} = \frac{\psi_0^2(r_s)}{\frac{1}{\Omega}\int_0^{r_s}\psi_0^2(r)\, d\tau}, \qquad (8)$$

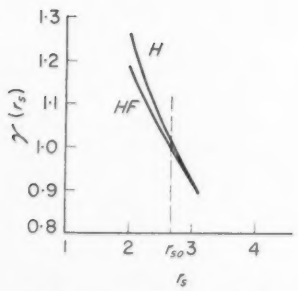

ABB. 2. Verlauf der Funktion $\gamma(r_s)$ für Kupfer (nach KAMBE). (Bezeichnungen wie in ABB. 1.)

also gleich dem Verhältnis des Quadrats der Wellenfunktion für $r = r_s$ zum Mittelwert des Quadrats der Wellenfunktion in der ganzen Zelle. Da die Grundzustandsfunktion ψ_0 im grössten Teil des Zellvolumens nahezu konstant ist, hat $\gamma(r_s)$ etwa den Wert 1. KAMBE hat für Kupfer auch den Verlauf dieser Funktion berechnet (ABB. 2). Für beide Potentiale ist $\gamma(r_s)$ für den Gleichgewichtswert von r_s, r_{s0}, ziemlich genau gleich 1 und kann in dessen Umgebung durch folgende lineare Funktion approximiert werden:

$$\gamma(r_s) = 1-\mu(r_s-r_{s0}),\ \mu \approx \frac{1}{4}\ (r \text{ in Atomeinheiten}). \qquad (9)$$

Die Integration der Gleichung (7) ist zwar prinzipiell möglich, doch lässt sich die resultierende Quadratur wegen der Funktion $\gamma(r_s)$ im allgemeinen nicht geschlossen ausführen. Setzt man aber willkürlich $\gamma(r_s) \equiv 1$, so ergibt sich unter der Annahme des reinen Wasserstoffpotentials am Zellenrand, $V(r_s) = -e^2/r_s$, nach einfacher Integration in Atomeinheiten

$$\epsilon_0(r_s) = \frac{C}{r_s^3} - \frac{3}{r_s}\ [\text{Ry}], \qquad (10)$$

wodurch die von KAMBE berechnete Kurve relativ gut wiedergegeben werden kann. Zur Berechnung der höheren Ableitungen von ϵ_0, die wir später brauchen werden, werden wir jedoch auf die exaktere Gleichung (7) zurückgreifen.

3. BESTIMMUNG DER BORN-MAYER-KONSTANTEN AUS DEN SCHERMODULN UND DEREN DRUCKABHÄNGIGKEIT

(a) Bestimmung aus den beiden Schermoduln mit Hilfe des theoretischen Ausdrucks für die elektrostatische Scherenergie

Bei einer homogenen Scherung des Gitters, die nicht mit einer Volumänderung verbunden ist, ändern sich in der gesamten Gitterenergie Gl. (3) nur die elektrostatische Energie ϵ_C und die Born–Mayer-Energie ϵ_{Ion}; aus diesen beiden Anteilen setzt sich also die Scherenergie zusammen. Die Änderung der elektrostatischen Energie ϵ_C lässt sich näherungsweise berechnen, so dass aus dieser und der gemessenen Scherenergie (bzw. den Scherkonstanten) die Born–Mayer-Energie und die darin enthaltenen Born–Mayer-Konstanten bestimmt werden können.

Die drei elastischen Konstanten c_{11}, c_{12}, c_{44} eines kubischen Mediums lassen sich zusammenfassen zu dem Kompressionsmodul $K \equiv \frac{1}{3}(c_{11}+2c_{12})$ und den beiden Schermoduln $C \equiv c_{44}$ und $C' \equiv \frac{1}{2}(c_{11}-c_{12})$.

Zu diesen Schermoduln gehören zwei homogene Scherungen, denen folgende Verschiebungen (Komponenten u_x, u_y, u_z) und Energiedichten w (pro Volumeneinheit) entsprechen:

$$\begin{aligned} u_x &= \gamma z \\ u_y &= 0 \quad , \quad w = \tfrac{1}{2} C\gamma^2, \\ u_z &= 0 \end{aligned} \tag{11a}$$

$$\begin{aligned} u_x &= \tfrac{1}{2}\gamma(x+y) \\ u_y &= -\tfrac{1}{2}\gamma(x+y) \quad , \quad w = \tfrac{1}{2} C'\gamma^2. \\ u_z &= 0 \end{aligned} \tag{11b}$$

Die Grösse γ (nicht zu verwechseln mit $\gamma(r_s)$) bedeutet hier jeweils die Winkeländerung in *linearer* Näherung, jedoch lassen beide Scherungen das Volumen *exakt* konstant.

Entsprechend der Zusammensetzung der Scherenergie (pro Volumeneinheit) aus den Änderungen der Energiebeiträge ϵ_C und ϵ_{Ion} (pro Atom),

$$w = \frac{\Delta\epsilon_C + \Delta\epsilon_{\text{Ion}}}{\Omega}, \tag{12}$$

setzen sich auch die Scherkonstanten aus zwei Anteilen zusammen, die wir mit v (Valenzelektronen) und i (Ionenwechselwirkung) kennzeichnen wollen:

$$C = C^v + C^i, \; C' = C'^v + C'^i. \tag{13}$$

Die Anteile C^v wurden unter der Annahme, dass das Gitter aus positiven Punktladungen und einer überlagerten, gleichmässig verteilten negativen Ladung besteht, für Kupfer erstmals von FUCHS[4] nach dem Ewald-Verfahren berechnet und können in etwas einfacherer Weise in der Darstellung von LEIBFRIED[9] nach dem Madelung-Verfahren ermittelt werden. Ist im wirklichen Kristall die negative Ladungsdichte ausserhalb der Ionenrümpfe nicht, wie im Idealfall, $-e/\Omega$, so ist e/Ω durch $e\psi_0^2(r_s)$ oder, nach der Beziehung (8), e durch $e\gamma(r_s)$ zu ersetzen. Damit ergibt sich für die elektrostatischen Anteile an den Scherkonstanten (a= Gitterkonstante)

$$\begin{aligned} C^v &= \frac{1}{\Omega} 0{,}9479 \frac{e^2}{2a}\gamma^2(r_s) \\ C'^v &= \frac{1}{\Omega} 0{,}1058 \frac{e^2}{2a}\gamma^2(r_s). \end{aligned} \tag{14}$$

Bei der Herleitung der Ausdrücke (14) wurde, entsprechend dem zugrundegelegten Modell, vorausgesetzt, dass die negative Ladungsdichte bei der Scherung konstant bleibt. Allgemein wird jedoch angenommen,[2] dass bei der Scherung die Elektronen sich neu verteilen und dadurch eine Erniedrigung — möglicherweise bis auf die Hälfte — der elektrostatischen Scherenergie resultiert. Wir tragen diesem Umstand Rechnung durch Einfügen eines Faktors q ($0<q<1$) in die rechten Seiten der Gleichungen (14). In Atomeinheiten lauten diese dann

$$\begin{aligned} C^v &= 0{,}9479 \frac{1}{a\Omega}\gamma^2(r_s)\cdot q \\ C'^v &= 0{,}1058 \frac{1}{a\Omega}\gamma^2(r_s)\cdot q. \end{aligned} \tag{15}$$

Zur Berechnung des Ionenanteils an der Scherenergie betrachtet man die Abstandsänderungen der 12 nächsten Nachbarn eines Atoms im kubisch-flächenzentrierten Gitter gemäss den Verschiebungen Gl. (11) und berechnet mittels des Born–Mayer-Gesetzes Gl. (1) die Energieänderung $\Delta\epsilon_{\text{Ion}}$ pro Atom. Daraus ergeben sich nach den Beziehungen (11), (12), (13) die Ionenanteile an den Scherkonstanten zu

$$C^i = \left.\frac{d^2 w^i}{d\gamma^2}\right|_{\gamma=0} = \frac{1}{\Omega}\left.\frac{d^2\Delta\epsilon_{\text{Ion}}}{d\gamma^2}\right|_{\gamma=0}. \tag{16}$$

Geht man nicht vom Gitter im Gleichgewichtszustand aus (Gitterkonstante a_0, Abstand nächster Nachbarn $r_0 = a_0/\sqrt{2}$), sondern allgemeiner vom homogen komprimierten Gitter (Gitterkonstante a, Abstand nächster Nachbarn $r_a = a/\sqrt{2}$), so erhält man

$$\begin{aligned} C^i &= \frac{1}{a}\left(\phi''(r_a) + 3\frac{\phi'(r_a)}{r_a}\right) \\ C'^i &= \frac{1}{2a}\left(\phi''(r_a) + 7\frac{\phi'(r_a)}{r_a}\right). \end{aligned} \tag{17}$$

Zur Berechnung der Born–Mayer-Konstanten kombinieren wir die Gln. (13), (15) und (17), wobei wir den unkomprimierten Kristall voraussetzen, also $r_a = r_0$ setzen. Die experimentellen elastischen Konstanten entnehmen wir OVERTON

u. GAFFNEY[10]; bei 0°K ist (in Einheiten 10^{11} dyn/cm²) $C = 8{,}18$ und $C' = 2{,}56$. Demgegenüber betragen die vollen elektrostatischen Beiträge nach Gl. (15) ($a = 3{,}61 \cdot 10^{-8}$ cm, $\Omega = a^3/4$, $\gamma(r_{s0}) = 1$, $q = 1$) $C^v = 2{,}57$ und $C'^v = 0{,}28$. Aus den beiden Gleichungen für $\phi''(r_0) = AB^2/r_0^2$ und $\phi'(r_0)/r_0 = -AB/r_0^2$ lassen sich nun die Born–Mayer-Konstanten A, B berechnen. Die Ergebnisse mit den elastischen Konstanten bei 0°K und 300°K und jeweils verschiedenen Werten

Tabelle 1. *Die Born–Mayer-Konstanten A, B berechnet aus den experimentellen Scherkonstanten unter verschiedenen Annahmen für die elektrostatischen Anteile*

q	0°K		300°K	
	A[eV]	B	A[eV]	B
1	0,0159	24,3	0,0114	26,9
0,5	0,0458	16,45	0,0408	16,6
0	0,0815	13,74	0,0765	13,6

des Faktors q sind in Tabelle 1 aufgeführt. Mamerkennt hier, wie sehr die Konstanten A, B von den Annahmen über die elektrostatische Scherenergie abhängen und wie wünschenswert es wäre, darüber genauer Bescheid zu wissen.

(b) Bestimmung aus der Druckabhängigkeit der Schermoduln und der elektrostatischen Scherenergie

Die Zerlegung der Scherkonstanten nach Gl. (13) und die Ausdrücke Gl. (15) u. Gl. (17) für die beiden Anteile gelten auch, wenn man die Scherung nicht vom normalen, unkomprimierten, sondern vom homogen komprimierten Zustand des Kristalls aus vornimmt. Allerdings sind die Scherkonstanten und die beiden Anteile dann vom hydrostatischen Druck p abhängig. Wir bekommen also zwei neue Gleichungen für die Born–Mayer-Konstanten A, B, wenn wir die Beziehungen (13) mit den Ausdrücken (15) und (17) nach dem Druck p bzw. der Gitterkonstanten a differenzieren. Der Zusammenhang zwischen den Ableitungen nach p und a ist $\partial C/\partial a = -(3K/a)\partial C/\partial p$. Berücksichtigt man noch die Gleichung (9) für $\gamma(r_s)$ und bezieht die Gleichungen auf den Gleichgewichtsabstand, so ergibt sich schliesslich

$$\begin{aligned} r_0\phi'''(r_0)+2\phi''(r_0) - 6\frac{\phi'(r_0)}{r_0} &= \\ = -3a_0K\frac{\partial C}{\partial p}+q\frac{4\cdot 0{,}9479}{\Omega}\left(1+\frac{1}{2}\mu r_{s0}\right) & \\ r_0\phi'''(r_0)+6\phi''(r_0)-14\frac{\phi'(r_0)}{r_0} &= \\ = -6a_0K\frac{\partial C'}{\partial p}+q\frac{8\cdot 0{,}1058}{\Omega}\left(1+\frac{1}{2}\mu r_{s0}\right), & \end{aligned} \tag{18}$$

woraus mit $r_0\phi'''(r_0) = \sim AB^3/r_0^2$ und ϕ'' und ϕ' wie oben die Konstanten A, B bestimmt werden können.

Die experimentellen Werte $\partial C/\partial p$ und $\partial C'/\partial p$ wurden für Kupfer von LAZARUS[11] und DANIELS u. SMITH[3] gemessen. Unter Verwendung der Werte von LAZARUS ergeben sich jedoch aus Gl. (18) Konstanten A, B, die nicht beide positiv sind, was im Widerspruch zu den Voraussetzungen steht. Auch sind die verschiedenen Bestimmungen von LAZARUS untereinander nicht konsistent, und der von BIRCH[12] ermittelte Wert für die Druckabhängigkeit des Schubmoduls in polykristallinem Kupfer, $\partial G/\partial p$, liegt nicht, wie man erwarten sollte, zwischen $\partial C/\partial p$ und $\partial C'/\partial p$; vor allem der Wert $\partial C/\partial p$ erscheint viel zu klein. Sehr zuverlässig scheinen jedoch die Werte von DANIELS u. SMITH zu sein:

$$\partial C/\partial p = 2{,}35 \text{ und } \partial C'/\partial p = 0{,}580.$$

Mit diesen Werten und dem isothermen Kompressionsmodul für 300°K[10], $K = 13{,}32 \cdot 10^{11}$ dyn/cm², ferner $\mu = 1/4$ und $r_{s0} \approx 8/3$, bestimmt man aus Gl. (18) für verschiedene Werte von q die in Tabelle 2 angegebenen Wertepaare von A und B.

Tabelle 2. *Die Born–Mayer-Konstanten A, B, ermittelt aus der Druckabhängigkeit der Scherkonstanten und der elektrostatischen Scherenergie.*

q	A[eV]	B
1	0,0745	12,55
0,5	0,0910	12,10
0	0,1081	11,75

Ein Vergleich mit Tab. 1 zeigt, dass die nach der zweiten Methode bestimmten Werte A, B zwar in einem anderen Bereich, aber wesentlich dichter beieinander liegen, die elektrostatischen Anteile hier also von wesentlich geringerem Einfluss sind.

4. BESTIMMUNG DER BORN-MAYER-KONSTANTEN AUS DEM KOMPRESSIONSMODUL UND DESSEN DRUCKABHÄNGIGKEIT.

(a) Bestimmung aus dem Kompressionsmodul mit Hilfe des theoretischen Ausdrucks für die Grundzustandsenergie

Wie in Abschnitt 2 erläutert, lässt sich die Energie eines homogen komprimierten Kristalls darstellen durch den Ausdruck Gl. (4), wobei die Born–Mayer-Energie pro Atom ϵ_{Ion} im kubisch-flächenzentrierten Gitter gegeben ist durch $\epsilon_{\text{Ion}} = 6\phi(r_a)$. Durch einen äusseren hydrostatischen Druck p ändert sich die Energie pro Atom um $d\epsilon = -pd\Omega$. Mit $\Omega = a^3/4$ lässt sich also schreiben

$$p = -\frac{d\epsilon}{d\Omega} = -\frac{4}{3a^2}\frac{d\epsilon}{da}. \tag{19}$$

Der Kompressionsmodul K, definiert durch $K = -Vdp/dV$, ergibt sich daraus zu

$$K = \Omega\frac{d^2\epsilon}{d\Omega^2} = \frac{4}{9a}\frac{d^2\epsilon}{da^2} - \frac{8}{9a^2}\frac{d\epsilon}{da}. \tag{20}$$

Im Gleichgewichtszustand ($p = 0$) ist

$$\left.\frac{d\epsilon}{da}\right|_{a=a_0} = 0 \text{ und } K_0 = \left.\frac{4}{9a_0}\frac{d^2\epsilon}{da^2}\right|_{a=a_0}. \tag{21}$$

Die beiden Gleichungen (21) ergeben zusammen mit dem Energieausdruck (4) zwei Bestimmungsgleichungen für die Born–Mayer-Konstanten A, B. Fassen wir noch in ϵ die Beiträge der Valenzelektronen zu $\epsilon_v = \epsilon_0 + \epsilon_F + \epsilon_{\text{Korr}}$ zusammen, so dass gilt $\epsilon = \epsilon_v(r_s) + 6\phi(r)$, so ergibt sich aus den Beziehungen (21) für die Konstanten A, B:

$$\begin{aligned} A\,B &\equiv -r_0\phi'(r_0) = \tfrac{1}{6}\,r_{s0}\,\epsilon_v'(r_{s0}) \\ A\,B^2 &\equiv r_0^2\phi''(r_0) = \tfrac{2}{9}\,a_0^3K_0 - \tfrac{1}{6}\,r_{s0}^2\,\epsilon_v''(r_{s0}). \end{aligned} \tag{22}$$

Für die in ϵ_v noch enthaltene Funktion der Grundzustandsenergie $\epsilon_0(r_s)$ wollen wir von den zwei existierenden theoretischen Berechnungen von FUCHS[4] und KAMBE[5] die neuere und genauer erscheinende von KAMBE verwenden. Zur Berechnung der Ableitungen ϵ_0' und ϵ_0'' können wir direkt die Bardeen'sche Differentialgleichung (7) benützen, die entsprechend ihrer Herleitung durch die Funktion $\epsilon_0(r_s)$ exakt erfüllt werden muss; für die Kurve von KAMBE ist dies auch tatsächlich der Fall, nicht jedoch für die von FUCHS berechnete Kurve. Von den zwei von KAMBE angenommenen Potentialfunktionen $V(r)$ beschränken wir uns auf die sicherlich genauere, nämlich Hartree–Fock-Potential in der Nähe des Zellenrandes, wofür KAMBE einen analytischen Ausdruck angegeben hat. Unter Berücksichtigung von Gl. (9) kann dann Gl. (7) nochmals nach r_s differenziert werden. Auf diese Weise ergibt sich zusammen mit dem Wert von ϵ_0 für den Gleichgewichtswert $r_{s0} \approx 8/3$ (in Atomeinheiten):

$$\epsilon_0 = -1{,}096, \quad \epsilon_0' = 0{,}372, \quad \epsilon_0'' = -0{,}286. \tag{23}$$

Die übrigen Anteile in ϵ_v lassen sich nach den Gln. (5) u. (6) berechnen, wobei wir für die effektive Masse in der Fermi-Energie wie SEEGER u. BROSS[13] für Kupfer $m^*/m = 1{,}45$ annehmen. Damit erhalten wir für die Energie $\epsilon_v = \epsilon_0 + \epsilon_F + \epsilon_{\text{Korr}}$ und ihre Ableitungen (in Atomeinheiten):

$$\begin{aligned} \epsilon_v(r_{s0}) &= -1{,}096 + 0{,}214 + 0{,}032 = -0{,}850 \\ \epsilon_v'(r_{s0}) &= 0{,}372 - 0{,}161 - 0{,}030 = 0{,}181 \\ \epsilon_v''(r_{s0}) &= -0{,}286 + 0{,}181 + 0{,}027 = -0{,}078. \end{aligned} \tag{24}$$

Man erkennt hier übrigens, dass ϵ_0'' keinesfalls gegenüber ϵ_F'' vernachlässigt werden kann, wie HUNTINGTON[2] und BRENIG[14] in ähnlichen Rechnungen angenommen haben.

Mit den Werten (24) und dem isothermen Kompressionsmodul bei 300°K erhält man aus den Gln. (22) für die Born–Mayer-Konstanten

$$A = 0{,}0747 \text{ eV}, \quad B = 14{,}60. \tag{25}$$

Aus Gl. (22) entnimmt man auch, dass der Beitrag der Valenzelektronen zum Kompressionsmodul negativ ist und nur etwa 10 Prozent beträgt.

Die im Vorstehenden verwendete Grundzustandsenergie von KAMBE verdient auch insofern besonderes Vertrauen, als sie auf eine fast exakte

Kohäsionsenergie führt. Mit den Beziehungen $\epsilon = \epsilon_v + 6A$ und $-\epsilon = \epsilon_{Koh} + \epsilon_I$ (ϵ_I = Ionisierungsenergie des freien Atoms = 7,70 eV für Kupfer) ergibt sich unter Verwendung der Zahlenwerte (24) und (25) für die Kohäsionsenergie $\epsilon_{Koh} = 3{,}36$ eV/Atom = 77,4 kcal/Mol,† während der experimentelle Wert 81,2 kcal/Mol beträgt. Mit dem Wert für ϵ_0 von FUCHS erhält man dagegen eine Kohäsionsenergie von ungefähr 47 kcal/Mol, also nur etwa 60 Prozent des experimentellen Wertes.

(b) Bestimmung aus der Druck–Volumen-Relation

Als weitere experimentelle Aussage über das Born–Mayer-Gesetz steht die gemessene Variation des Volumens mit dem Druck zur Verfügung. So hat BRIDGMAN[15] an Kupfer nach einer statischen Methode die Volumänderung bei Drucken von 0 bis 30 000 atm gemessen, während WALSH *et al.*[16] mittels Stosswellen die Volumfunktion $V(p)$ für Drucke von etwa 200 000 bis 500 000 atm bestimmt haben.

Um zu einem einfachen analytischen Ausdruck für die gemessene p–V-Kurve zu gelangen, kann man versuchsweise annehmen, dass der Kompressionsmodul K nur linear vom Druck p abhängt:

$$K(p) = K_0 + \alpha p. \tag{26}$$

Mit diesem Ansatz ergibt sich aus der Definitionsgleichung für den Kompressionsmodul, $K(p) = -V(p)dp/dV$, durch Integration folgendes, Druck und Volumen verknüpfendes Gesetz:

$$\frac{V}{V_0} = \left(\frac{1}{1+\frac{\alpha}{K_0}p}\right)^{1/\alpha} \text{ bzw. } p = \frac{K_0}{\alpha}\left(\frac{1}{\left(\frac{V}{V_0}\right)^{\alpha}} - 1\right). \tag{27}$$

Es stellt sich nun heraus, dass die von WALSH *et al.* abgeleiteten Isothermen erstaunlich gut durch ein Gesetz der Art Gl. (27) mit dem einen freien Parameter α wiedergegeben werden könenn. Für beide Isothermen (0°K und 300°K) ergibt sich mit den entsprechenden Kompressionsmoduln K_0 nach OVERTON u. GAFFNEY[10] im gemessenen Bereich die beste Annäherung durch einen Wert von etwa

$$\alpha \equiv \frac{\partial K}{\partial p} = 4{,}85, \tag{28}$$

während zur vollständigen Übereinstimmung in einzelnen Punkten zwischen 200 000 atm und 500 000 atm Werte zwischen 4,7 und 5,2 erforderlich sind. Auch die Isotherme von BRIDGMAN (27°C) verlangt einen ähnlichen Wert, wenn man den aus dieser Kurve zu entnehmenden Kompressionsmodul zugrundelegt.

Andere vorliegende Messungen von $\partial K/\partial p$ an Kupfer (meist bei niedereren Drucken) sind‡:

DANIELS u. SMITH[3] (1958):	$\partial K/\partial p = 5{,}59$
LAZARUS[11] (1949):	$\partial K/\partial p = 4{,}0$
BRIDGMAN (1935) [nach LAZARUS[11]]:	$\partial K/\partial p = 5{,}0.$

Hier wurden die ersten beiden Werte nicht direkt gemessen, sondern aus den Druckabhängigkeiten verschiedener elastischer Konstanten zusammengesetzt. Da es schwer fällt, zwischen den einzelnen Werten eine Wahl zu treffen, werden wir den Wert (28) verwenden, der entsprechend seiner Ableitung auch bei sehr grossen Kompressionen noch Gültigkeit besitzt.

Als neue empirische Daten verwenden wir nun erstens den Wert von $\partial K/\partial p = \alpha$ für $p = 0$ und zweitens die Tatsache, dass $\partial K/\partial p = \alpha$ konstant, d.h. unabhängig von p gewählt werden kann, um die Messwerte sehr gut wiederzugeben, also $\partial^2 K/\partial p^2 = 0$. Um diese beiden Informationen unterzubringen, muss man nach Gl. (20) bis zur 4. Ableitung der Energie ϵ gehen. Wir führen noch anstelle von r_s als neue Variable das relative Volumen $x = V/V_0 = \Omega/\Omega_0$ ein und schreiben die Energie Gl. (4) in der Form

$$\epsilon(x) = \epsilon_a(x) + F \cdot x^{-2/3} + 6A \exp\left[-B(x^{1/3}-1)\right] \tag{29}$$

mit $\epsilon_a = \epsilon_0 + \epsilon_{Korr}$ und $F = 3/5\ \zeta_0 = 2{,}90$ eV (mit $m^*/m = 1{,}45$). Bildet man die ersten 4

† Nach D. PINES [*Solid State Phys.* **1**, 367 (1955)] ist der Ausdruck von WIGNER für die Korrelationsenergie in Gl. (5) mit einem Fehler behaftet und sollte lauten $-0{,}88/(r_s+7{,}79)$. Mit dieser Korrektur ergibt sich eine theoretische Kohäsionsenergie von 80,5 kcal/Mol, also fast vollkommene Übereinstimmung mit dem Experiment.

‡ In der Darstellung der $V(p)$-Kurve durch $\Delta V/V_0 = -ap + bp^2$ ist $\partial K/\partial p = 2b/a^2 - 1$.

Ableitungen von $\epsilon(x)$ an der Stelle $p = 0$ bzw. $x = 1$ und drückt diese mittels der Beziehung $d\epsilon/dx = -\Omega_0 p$ durch die experimentellen Grössen aus, am einfachsten mit Hilfe der empirischen Funktion (27), so erhält man:

$$\begin{aligned}
\frac{d\epsilon}{dx} &\equiv 0 && = \frac{d\epsilon_a}{dx} - \frac{2}{3}F - 2AB \\
\frac{d^2\epsilon}{dx^2} &\equiv \Omega_0 K_0 && = \frac{d^2\epsilon_a}{dx^2} + \frac{10}{9}F + \\
& && \quad + \frac{2}{3}AB(B+2) \\
\frac{d^3\epsilon}{dx^3} &\equiv -\Omega_0 K_0(1+\alpha) && = \frac{d^3\epsilon_a}{dx^3} - \frac{80}{27}F - \\
& && \quad - \frac{2}{9}AB(B^2+6B+10) \\
\frac{d^4\epsilon}{dx^4} &\equiv \Omega_0 K_0(1+\alpha)(2+\alpha) && = \frac{d^4\epsilon_a}{dx^4} + \frac{880}{81}F + \\
& && \quad + \frac{2}{27}AB(B^3+12B^2+52B+80)
\end{aligned} \tag{30}$$

Die beiden ersten Gleichungen sind identisch mit den Gln. (22) im vorigen Abschnitt; die beiden letzten Gleichungen sind neu hinzugekommen.

Zur Bestimmung der Born–Mayer-Konstanten A, B aus dem Gleichungssystem (30) kann man z.B. je zwei Gleichungen kombinieren und daraus A, B berechnen, falls die Ableitungen von $\epsilon_a = \epsilon_0 + \epsilon_{\text{Korr}}$ bekannt sind. Theoretisch lassen sich diese berechnen durch nochmalige Differentiation des Ausdrucks für die Korrekturenergie ϵ_{Korr} Gl. (5) und der Differentialgleichung (7) für die Grundzustandsenergie ϵ_0 unter Berücksichtigung der Angaben von Kambe für das Hartree–Fock-Potential $V(r)$ und die Funktion $\gamma(r_s)$. Die Resultate für den Gleichgewichtsabstand ($x = 1$) sind (die Beiträge von ϵ_{Korr} sind jeweils kleiner als 10 Prozent):

$$\begin{aligned}
\epsilon_a'(x) &= 4{,}10 \text{ eV} & \epsilon_a'''(x) &= 11{,}84 \text{ eV} \\
\epsilon_a''(x) &= -5{,}50 \text{ eV} & \epsilon_a''''(x) &= -32{,}9 \text{ eV}.
\end{aligned}$$

Mit diesen Werten und $\alpha = 4{,}85$ ergibt sich aus der 3. und 4. Gleichung von (30):

$$A = 0{,}078 \text{ eV}, \qquad B = 13{,}2. \tag{31}$$

Aus der 2. und 3. Gleichung ermittelt man

$$A = 0{,}129 \text{ eV}, \qquad B = 10{,}9. \tag{32}$$

Man erkennt also, dass nicht alle 4 Gleichungen durch ein Wertepaar A, B gleichzeitig erfüllt werden können. Die Anteile der Valenzelektronen in den Gln. (30) sind übrigens zum Teil recht gering; sie betragen in der 2., 3., 4. Gl. jeweils 23, 6, 0,4 Prozent.

Ohne auf theoretische Werte für ϵ_a einzugehen, kann man auch versuchen, für $\epsilon_a(x)$ einen zweiparametrigen Ansatz zu machen und dann aus dem System (30) A und B eindeutig zu bestimmen. Jedoch scheint dies nur dann gerechtfertigt, wenn der Ansatz theoretisch begründet ist oder die Ergebnisse nur wenig von der Form des Ansatzes abhängen. Mit einem durch den Ausdruck (10) nahegelegten Ansatz

$$\epsilon_a(x) = Cx^{-1} - Dx^{-1/3} \tag{33}$$

erhält man $A = 0{,}0127$ eV, $B = 20{,}0$, (33a)

während sich mit einem Ansatz der Form

$$\epsilon_a(x) = kx^n + \text{Const.} \tag{34}$$

$$A = 0{,}0436 \text{ eV}, \quad B = 15{,}3 \tag{34a}$$

ergibt. Die Ergebnisse differieren also sehr stark, wobei die Werte (34a) besser in das allgemeine Bild passen als das Wertepaar (33a).

5. DISKUSSION

Die nach den verschiedenen genannten Methoden ermittelten Born–Mayer-Konstanten A, B sind in der graphischen Darstellung ABB. 3 nochmals zusammengestellt. Mit aufgenommen sind auch die unter Gl. (2) aufgeführten Werte von HUNTINGTON u. SEITZ (*HS*) und HUNTINGTON (H_a u. H_b). Die den Rechnungen zugrundegelegte Temperatur ist jeweils 300°K.

Die Übersicht zeigt, dass die Streuung der Werte ziemlich gross ist. Selbst bei den beiden Methoden der Bestimmung aus den Scherkonstanten und deren Druckabhängigkeit, wo die etwas unsichere Grundzustandsenergie nicht eingeht, liegen die Ergebnisse weit auseinander, so dass man auch über die Grösse des Reduktionsfaktors q auf diesem Wege keine Aussage machen kann. Aus der ABB. 3 lässt sich entnehmen, dass die Werte von A und B in bestimmter Weise

einander zugeordnet sind, aber es ist schwierig, einem bestimmten Wert von B den Vorzug zu geben. Aus den grossen Differenzen muss man im übrigen schliessen, dass, abgesehen von experimentellen Unsicherheiten, das zugrundegelegte

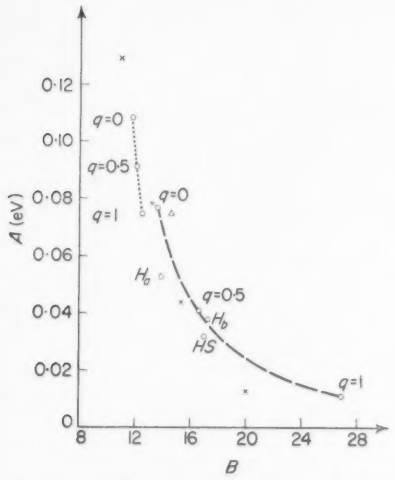

ABB. 3. Graphische Darstellung der nach den verschiedenen Methoden ermittelten Born–Mayer-Konstanten A und B. (– – – nach Methode 3a, · · · · nach Methode 3b; q = Bruchteil der berücksichtigten elektrostatischen Scherenergie; △ nach Methode 4a, × nach Methode 4b unter verschiedenen Voraussetzungen; HS nach HUNTINGTON und SEITZ[1], H_a u. H_b nach HUNTINGTON[2].)

Energiemodell einschliesslich der Annahmen über die Ionenwechselwirkungsenergie zu einfach ist, um eine vollständige Übereinstimmung der Ergebnisse der verschiedenen Methoden geben zu können.

Die Anwendung dieser Erkenntnisse auf die Berechnung der Bildungsenergie von Zwischengitteratomen in Kupfer wird in einer gesonderten Arbeit behandelt werden.

Die Verfasser danken der DEUTSCHEN FORSCHUNGSGEMEINSCHAFT für die Unterstützung der Arbeit.

ANHANG A

Ein erweiterter Ansatz für die Elektronen-Energie.

Auf Empfehlung des Referenten haben wir zusätzlich untersucht, wie sich die nach den Methoden 4a und 4b bestimmten Born–Mayer-Konstanten ändern, wenn man (1) eine Abhängigkeit der effektiven Masse der Leitungselektronen von der Gitterkonstanten annimmt, (2) in der kinetischen Energie der Elektronen noch ein k^4-Glied berücksichtigt. Die Änderungen können im einzelnen beträchtlich sein, doch bleibt der im Vorstehenden gefundene Zusammenhang zwischen A und B erhalten.

(1) Bisher hatten wir in der Fermi-Energie Gl. (4)

$$\epsilon_F = 2{,}21 \frac{m}{m^*} \frac{1}{r_s^2} \tag{A1}$$

die effektive Masse m^* als konstant betrachtet ($m^*/m = \alpha$). Nunmehr nehmen wir an, dass sie sich bei Dilatation des Gitters mit der Gitterkonstanten a ändere:

$$\frac{m}{m^*} = \frac{1}{\alpha}\left(1-\gamma\frac{\Delta a}{a}\right). \tag{A2}$$

Diese Abhängigkeit ist von HUNTER und NABARRO[17] theoretisch untersucht worden. Dort ergibt sich für den k-abhängigen Anteil der Elektronenenergie bei reiner Dilatation

$$E(k,\Delta) = \frac{\hbar^2}{2m_1} k^2 \left(1+\frac{m_1}{m_2}\Delta\right), \tag{A3}$$

wo $\Delta = \Delta V/V = 3\Delta a/a$ die Volumdilatation bedeutet. Die effektiven Massen m_1 und m_2 wurden von HUNTER und NABARRO für Kupfer zu $m/m_1 = 1{,}887$ und $m/m_2 = -0{,}228$ abgeschätzt. Durch Vergleich mit (A2) ergibt sich daraus $\gamma = 0{,}36$. Setzt man m_1, das unserem m^* entspricht, wie auch sonst in der vorliegenden Arbeit gleich 1,45 m, so erhält man $\gamma = 1{,}0$. Mit diesen beiden Werten von γ wurden die Bestimmungen der Born–Mayer-Konstanten A, B nach den Methoden in Abschnitt 4, mit Ausnahme der Methoden Gl. (33) und Gl. (34), wiederholt. Die Ergebnisse sind in Fig. 4 aufgetragen. Trotz grosser Änderungen im einzelnen bleibt der Zusammenhang zwischen A und B im wesentlichen unverändert.

(2) Der übliche Ansatz für die Elektronenenergie

$$E(k) = \frac{\hbar^2}{2m^*} k^2 \tag{A4}$$

gilt nur in der Näherung quasifreier Elektronen. In der nächsten Näherung tritt unter der Voraussetzung, dass E nur von $k = |\mathbf{k}|$ abhängt, noch ein Glied $\sim k^4$ hinzu. Wir schreiben die Energie dann in der Form

$$E(k) = \frac{\hbar^2}{2m^+}(k^2+Ck^4). \tag{A5}$$

Die Zustandsdichte $n(E)$, bezogen auf das Einheitsvolumen, ist

$$n(E) = \frac{1}{(2\pi)^3} \int\limits_{E=\text{const.}} \frac{dS_{\mathbf{k}}}{|\text{grad}_{\mathbf{k}} E|} = \frac{1}{2\pi^2} \frac{k^2}{dE/dk}. \tag{A6}$$

Die Zahl der Elektronen pro Volumeinheit wird damit

$$n_0 = \int_0^{E_F} 2n(E)\,dE = \int_0^{k_F} \frac{1}{\pi^2} k^2\,dk = \frac{k_F^3}{3\pi^2},$$

also

$$k_F = (3\pi^2 n_0)^{1/3}. \tag{A7}$$

Dabei bedeutet $E_F = E(k_F)$ die Energie an der Fermioberfläche. Für einwertige Metalle ist $n_0 = 1/\Omega$ (Ω = Atomvolumen). Die mittlere Energie pro Elektron ergibt sich zu

$$\epsilon_F = \int_0^{E_F} 2n(E)E\,dE \Big/ \int_0^{E_F} 2n(E)\,dE$$

$$= \frac{3}{5}\frac{\hbar^2}{2m^+} k_F^2 + \frac{3}{7}\frac{\hbar^2}{2m^+} C k_F^4 \tag{A8}$$

oder, in Atomeinheiten,

$$\epsilon_F = 2{,}21\,\frac{m}{m^+}\frac{1}{r_s^2} + 5{,}81\,\frac{m}{m^+} C\,\frac{1}{r_s^4} \tag{A8a}$$

(r_s = Radius der Wigner–Seitz-Kugel).

Zur Bestimmung der beiden Konstanten m^+ und C kann man, wie KRONMÜLLER[18], die aus der spezifischen Elektronenwärme und aus optischen Messungen ermittelten effektiven Massen heranziehen. Die kalorische und die optische effektiven Massen sind definiert durch

$$m^*_{\text{al}} = 2\pi^2\hbar^2 n(E_F)/k_F \tag{A9}$$

und

$$\frac{n_0}{m^*_{0\,\text{pt}}} = \frac{1}{12\hbar^2\pi^3}\int_0^{k_F} \Delta_{\mathbf{k}} E\,d\tau_{\mathbf{k}}. \tag{A10}$$

Legt man den gewöhnlichen Energieausdruck (A4) zugrunde, so sind die beiden effektiven Massen, per definitionem, identisch. Dasselbe ergibt sich aber auch mit dem erweiterten Energieansatz (A5). Erst wenn man statt des bezüglich des Wellenvektors $\mathbf{k}$ isotropen Ansatzes einen anisotropen Ansatz macht, ergibt sich nach KRONMÜLLER[18] für die beiden effektiven Massen etwas Verschiedenes.

Aus (A 9) oder (A 10) erhält man mit (A 5) die Beziehung

$$\frac{m^+}{m^*} = 1 + 2Ck_F^2. \tag{A11}$$

Wir haben zur Zeit keine Möglichkeit, m^+ und C einzeln zu bestimmen. Es besteht aber Grund zur Annahme (diese wird durch die oben erwähnten anisotropen Rechnungen gestützt), dass m^+/m nahe bei 1 liegt. Wir setzen $m^+ = m$ und wählen als Mittelwert aus den kalorischen und optischen Messungen $m^*/m = 1{,}45$. Damit ergibt sich für Kupfer $Ck_F^2 = -0{,}155$.

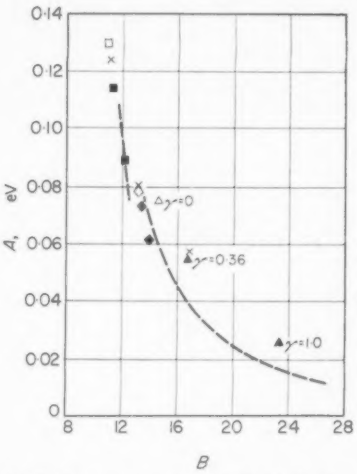

ABB. 4. Einfluss der Veränderlichkeit der effektiven Masse und eines erweiterten Ansatzes für die Elektronenenergie auf die Born–Mayer-Konstanten von Kupfer. (△ nach Methode 4a bzw. aus der 1. und 2. Gl. der Gln. (30), □ aus 2. u. 3. Gl., ◇ aus 3. u. 4. Gl., γ = Mass für die Veränderlichkeit der effektiven Masse; × berechnet auf obige 3 Arten mit Hilfe des erweiterten Ansatzes in Anhang A(2).

Mit dem erweiterten Energieausdruck (A8) wurde die Berechnung der Born–Mayer-Konstanten ebenfalls wiederholt. Die neuen Werte, die in ABB. 4 eingetragen sind, fügen sich wiederum gut in das Gesamtbild ein.

ANHANG B

Die Born–Mayer-Konstanten für Silber und Gold.

Auf dieselbe Weise wie für Kupfer haben wir auch die Born–Mayer-Konstanten für Silber und Gold berechnet. Für die Funktionen $\epsilon_0(r_s)$ und $\gamma(r_s)$ haben wir wiederum die theoretischen Werte von KAMBE[5] verwendet; die elastischen Konstanten und deren Druckabhängigkeiten sind DANIELS und SMITH[3] entnommen. Während die letztgenannten Autoren für die Druckabhängigkeit des Kompressionsmoduls für Silber und Gold $\partial K/\partial p = 6{,}18$ bzw. 6,43 angeben, haben wir aus den Druck-Volumen-Relationen von WALSH *et al.*[16] $\partial K/\partial p \approx 5{,}7$ bzw. 6,0 ermittelt. Unseren Rechnungen sind die letzteren Werte zugrundegelegt. Als effektive Massen m^*/m haben wir (vgl. SEEGER u. BROSS[13]) für Silber 1,0 und für Gold 1,2 verwendet.

Die nach den verschiedenen Methoden berechneten Werte A, B sind in ABB. 5 eingetragen. Qualitativ ist der Verlauf derselbe wie bei Kupfer, jedoch weisen die einzelnen Werte eine grössere Streuung auf. In besonderem

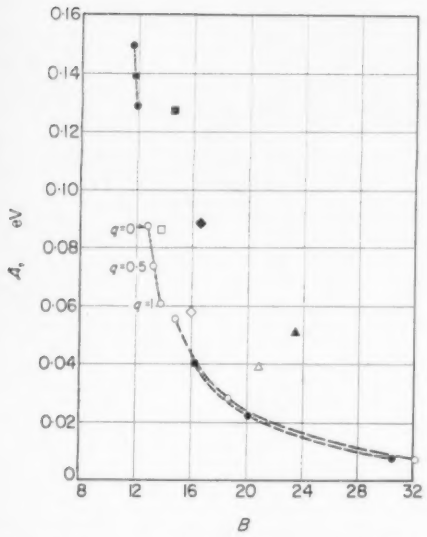

ABB. 5. Die Born–Mayer-Konstanten von Silber und Gold. (Leere Symbole = Ag, volle Symbole = Au; – – –, · · · · q wie in Fig. 3; △, □, ◇ wie in ABB. 4.)

Masse gilt dies für Gold. Zum Teil mag das an der mangelhaften Kenntnis der Grundzustandsenergie ϵ_0 liegen (die Werte von KAMBE führen z.B. auf eine um 20 Prozent bzw. 40 Prozent zu kleine Kohäsionsenergie für Silber bzw. Gold); zum grösseren Teil aber dürfte dafür verantwortlich sein (wie schon DANIELS und SMITH[3] bemerkt haben), dass der zentralkraftartige Ansatz für die Born–Mayer-Energie bei den hier vorliegenden grossen Ionenrümpfen nicht mehr gültig ist.

LITERATUR

1. HUNTINGTON H. B. u. SEITZ F. *Phys. Rev.* **61**, 315 (1942).
2. HUNTINGTON H. B. *Phys. Rev.* **91**, 1092 (1953).
3. DANIELS W. B. u. SMITH C. S. *Phys. Rev.* **111**, 713 (1958).
4. FUCHS K. *Proc. Roy. Soc.* A**151**, 585 (1935); A**153**, 622 (1936).
5. KAMBE K. *Phys. Rev.* **99**, 419 (1955).
6. BROOKS H. *Nuovo Cimento* **7**, Suppl. X, 165 (1958).
7. SEITZ F. *Modern Theory of Solids*, New York u. London, 1940.
8. BARDEEN J. *J. Chem. Phys.* **6**, 372 (1938).
9. LEIBFRIED G. *Handbuch der Physik* Bd. **7**, Teil 1 S.104. Springer, Berlin (1955).
10. OVERTON W. u. GAFFNEY J. *Phys. Rev.* **98**, 969 (1955).
11. LAZARUS D. *Phys. Rev.* **76**, 545 (1949)
12. BIRCH F. *J. Appl. Phys.* **8**, 129 (1937).
13. SEEGER A. u. BROSS H. *Z. Phys.* **145**, 161 (1956).
14. BRENIG W. *Z. Phys.* **142**, 163 (1955).
15. BRIDGMAN P. W. *Proc. Amer. Acad. Arts Sci.* **77**, 187 (1949).
16. WALSH J. M. u. CHRISTIAN R. H. *Phys. Rev.* **97**, 1544 (1955);
    WALSH J. M., RICE M. H., MCQUEEN R. G. u. YARGER F. L. *Phys. Rev.* **108**, 196 (1957).
17. HUNTER S. C. u. NABARRO F. R. N. *Proc. Roy. Soc.* A**220**, 542 (1953).
18. KRONMÜLLER H. Diplomarbeit, Techn. Hochschule Stuttgart (1956).

VOL. 12 59/60

J. Phys. Chem. Solids Pergamon Press 1960. Vol. 12. pp. 326–340. Printed in Great Britain.

BILDUNGSENERGIEN UND GITTERVERZERRUNGEN VON ZWISCHENGITTERATOMEN UND LEERSTELLEN IN KUBISCH-FLÄCHENZENTRIERTEN KRISTALLEN, INSBESONDERE IN KUPFER

A. SEEGER und E. MANN

Max-Planck-Institut für Metallforschung, Stuttgart, und Institut für theoretische und angewandte Physik der Technischen Hochschule Stuttgart

(*Received* 3 *August* 1959)

VO
1
1959/

Zusammenfassung — In der vorliegenden Arbeit wird die Bildungsenergie und die Volumexpansion von Zwischengitteratomen und Leerstellen in kubisch-flächenzentrierten Metallen, insbesondere in Kupfer, berechnet. In Anlehnung an frühere Arbeiten wird dabei ein semi-empirisches Modell mit Born-Mayer-Kräften zwischen benachbarten Ionenrümpfen verwendet. Die wichtigste Neuerung ist die konsequente Benützung der Bornschen Gittertheorie, deren Kopplungsparameter im Falle von Kupfer gemessen sind. Von diesen Kopplungsparametern wird der mit dem Ionenabstand rasch variierende Anteil der Born-Mayer-Wechselwirkung abgezogen. Der verbleibende, den Valenzelektronen zuzuschreibende Rest variiert viel langsamer mit dem interatomaren Abstand. Auf diese Weise wird eine Darstellung der interatomaren Kräfte erreicht, die bei den grossen Verzerrungen in der Umgebung der Zwischengitteratome anwendbar bleibt und gleichzeitig alle Stabilitätsforderungen befriedigt. Darüber hinaus gestattet die Verwendung der Gittertheorie einen willkürfreien Übergang zwischen den atomistisch und den kontinuumsmechanisch zu behandelnden Bereichen. Die wichtigsten Ergebnisse der Arbeit für Kupfer sind die folgenden: Bildungsenergie eines Zwischengitteratoms $E_Z = 3$ eV, einer Leerstelle $E_L = 1$ eV; Volumexpansion durch ein Frenkel-Paar $\Delta V = 1{,}3$ Atomvolumina.

Abstract—In the present paper the energies of formation and the volume expansion due to interstitials and vacancies in f.c.c. metals, in particular copper, are calculated. Following earlier papers, a semi-empirical model using Born-Mayer forces between neighbouring ions is employed. The most important new feature is the purposeful use that is made of Born's theory of crystal lattices. In the case of copper the coupling parameters appearing in this theory are known from experiment. The contribution to these coupling parameters from the Born–Mayer interaction (which varies rapidly with interatomic distance) is subtracted out. The remainder is due to the action of the valence electrons and varies much less with the separation of the atoms. Thus we were able to obtain a representation of the interatomic forces that should remain valid even for the large distorsions occurring in the environment of an interstitial atom. This representation has the additional advantage of satisfying all stability requirements. Furthermore, the employment of the theory of crystal lattices enables us to perform the transition between the continuum region and the atomic region of the strain field practically without introducing arbitrary elements. The main results for copper are as follows: Energy of formation of an interstitial $E_Z = 3$ eV, of a vacancy $E_L = 1$ eV; volume expansion by a Frenkel pair $\Delta V = 1.3$ atomic volumes.

1. EINLEITUNG UND ÜBERBLICK

Die vorliegende Arbeit befasst sich mit der Berechnung der Bildungsenergie von Zwischengitteratomen und Leerstellen in kubisch-flächenzentrierten Metallen, insbesondere in Kupfer, sowie mit der Bestimmung der von diesen Fehlstellen hervorgerufenen Verzerrungen des Kristallgitters. Die klassischen Arbeiten zu diesem Thema sind

diejenigen von HUNTINGTON und SEITZ[1–4] (siehe auch das Referat von BROOKS[5]). Das wichtigste Ergebnis dieser Untersuchungen, dass nämlich bei den Edelmetallen zur Schaffung eines Zwischengitteratoms eine wesentlich grössere Energie benötigt wird als zur Bildung einer Gitterlücke, trifft auch nach heutiger Anschauung zu. Dieser Unterschied zwischen Leerstellen und Zwischengitteratomen rührt davon her, dass die Atome der Edelmetalle grosse und wenig kompressible Ionenrümpfe besitzen, die beim Einzwängen eines Edelmetallatoms auf einen Zwischengitterplatz starke Verzerrungen des Kristallgitters erzwingen, während die entsprechenden Effekte bei der Bildung einer Gitterlücke verhältnismässig klein sind.

Leider gibt es bis heute kein praktisch brauchbares Verfahren, die Wechselwirkung zwischen den benachbarten Ionenrümpfen mit der erforderlichen Genauigkeit quantenmechanisch zu berechnen. Man verwendet statt dessen halbempirische Verfahren, bei denen die Ionenabstossung durch sog. Born–Mayer-Potentiale beschrieben wird. Zuverlässige Zahlenangaben über Zwischengitteratome kann man nur dann erwarten, wenn das zur theoretischen Behandlung der Fehlstelle verwendete Kristallmodell nicht im Widerspruch mit der Bestimmungsweise der Konstanten dieser Potentiale steht. Wir hielten diese Fragen für wichtig genug, um ihnen eine eigene Arbeit[6]* zu widmen, von deren Ergebnissen wir in der vorliegenden Mitteilung Gebrauch machen werden.

Die genauere Berechnung der Bildungsenergie und der Gitterverzerrungen (insbesondere des Einflusses auf das Kristallvolumen und auf die Gitterkonstante) von Zwischengitteratomen in Kupfer beansprucht in jüngster Zeit erhebliches Interesse im Hinblick auf die Deutung der Experimente zur Strahlungs-schädigung[7–9] von Metallen und deren Erholung. Zu deren quantitativer Auswertung ist die Kenntnis der Bildungsenergie, der Volumaufweitung oder des zusätzlichen elektrischen Widerstands von Leerstellen und Zwischengitteratomen erforderlich. Wie zuerst JONGENBURGER[10] betont hat, müssen die starken Verzerrungen in der Umgebung von Zwischengitteratomen bei der Berechnung des elektrischen Widerstands mit in Betracht gezogen werden. Alle derartigen Rechnungen waren jedoch bisher dadurch in ihrer Genauigkeit beschränkt, dass die von HUNTINGTON[4] ermittelten Gitterverzerrungen zugrunde gelegt wurden, die nach den Ergebnissen der vorliegenden Arbeit wesentlich zu gross sind.

Nach Abschluss der hier mitzuteilenden Rechnungen wurde uns eine Arbeit von TEWORDT[11] zugänglich,† die im wesentlichen denselben Fragenkomplex untersucht. Das von TEWORDT verwendete Kristallmodell ist in mancherlei Hinsicht von dem unseren verschieden; wir werden darauf im Laufe der Arbeit näher eingehen.

Die speziellen Erörterungen dieser Arbeit führen wir für Zwischengitteratome durch, obwohl dieselben Methoden mutatis mutandis (manchmal mit erheblichen Vereinfachungen) auch für Leerstellen gelten. Die numerischen Ergebnisse für Leerstellen in Kupfer sind in Abschn. 7b) aufgeführt.

Bei der Behandlung der Zwischengitteratome beschränken wir uns auf die sog. symmetrische Konfiguration, d. h. auf Zwischengitteratome in der Mitte des kubischen Elementarwürfels. Zu dieser Einschränkung waren wir genötigt, um die Zahl der unabhängigen Parameter des Problems klein halten und dennoch eine ausreichende numerische Genauigkeit erreichen zu können. Mit Hilfe einer elektronischen Rechenmaschine werden zur Zeit die Rechnungen auf niedersymmetrische, mit mehr Parametern behaftete Probleme ausgedehnt.

Die Grundzüge des verwendeten Verfahrens werden in Abschn. 2 geschildert. Die wichtigste und weittragendste Neuerung gegenüber ähnlichen Rechnungen anderer Autoren ist die konsequente Verwendung der Bornschen Gittertheorie, die u. a. erlaubt, die Wechselwirkungen eines Atoms mit seinen nächsten, übernächsten und drittnächsten Nachbarn zu berücksichtigen, die Stabilitätsfragen leicht zu übersehen und das schwierige Problem des Anschlusses der atomistischen Rechnungen an den Gültigkeitsbereich der Elastizitätstheorie auf einfache und übersichtliche Weise zu lösen. Eine ausführliche Diskussion der damit verbundenen Vorteile findet sich in Abschn. 5 und Abschn. 8.

* im folgenden mit Teil I bezeichnet.

† Für die Übersendung seiner Arbeit vor der Veröffentlichung sei Herrn Dr. L. TEWORDT herzlich gedankt.

VOL. 12 59/60

2. DAS ALLGEMEINE VERFAHREN ZUR BERECHNUNG DER BILDUNGSENERGIE UND DER GITTERVERZERRUNGEN

Ein in jeder Hinsicht befriedigendes, unmittelbar an die Schrödingergleichung anknüpfendes Verfahren zur Behandlung der durch Gitterfehler in den Edelmetallen verursachten Wirkungen existiert bis heute nicht. Wir werden uns an die früher schon vorgeschlagenen Methoden anlehnen, jedoch an einigen Stellen Abänderungen oder Erweiterungen vornehmen.

Die durch punktförmige Fehlstellen im Kristallgitter hervorgerufenen Verzerrungen nehmen mit zunehmender Entfernung von den Zentren rasch ab und können dann näherungsweise durch die elastische Lösung in einem das Gitter ersetzenden elastischen Kontinuum beschrieben werden. Wir dürfen daher den gesamten Kristall mit Ausnahme kleiner, die Fehlstellen umschliessender Bereiche als elastisches Kontinuum behandeln, während diese Bereiche selbst diskret, atomistisch zu betrachten sind. Je grösser man diese Bereiche wählt, desto genauer wird auch das Verfahren werden, doch bestehen wegen des rasch zunehmenden numerischen Aufwands praktische Grenzen. Zur Vereinfachung nehmen wir den elastischen Bereich als isotrop an, was zwar nicht für die Verschiebungen der einzelnen Atome, wohl aber für die Berechnung der Energie und der Volumänderung eine ausreichende Näherung darstellen dürfte.

Entsprechend dieser Betrachtungsweise werden wir auch die zusätzliche Energie eines Kristalls mit Fehlstellen aufteilen in einen elastischen Anteil und einen nichtelastischen, atomistischen Anteil. Der Übergang zwischen den beiden Gebieten bereitet zunächst gewisse Schwierigkeiten, die jedoch, wie in Abschn. 5 gezeigt werden wird, weitgehend behoben werden konnten.

Der Grundgedanke bei der Berechnung der Bildungsenergie einer Fehlstelle ist nun folgender: Für das elastische Gebiet setzt man die aus der elastischen Behandlung folgenden Verschiebungen an, die nur von einem einzigen Parameter abhängen (der Stärke des elastischen Dilatationszentrums), wohingegen man für sämtliche Atome des diskreten Bereichs beliebige, nur durch Symmetrieforderungen beschränkte, Verschiebungen zulässt, zu deren Beschreibung entsprechend mehr Parameter erforderlich sind. Sodann berechnet man die mit diesen Verschiebungen sich ergebende Energieänderung und variiert die Parameter so, dass die Energie einen Minimalwert annimmt. Diese Energie stellt dann die Bildungsenergie dar, und die dazugehörigen Verschiebungen bilden die Gleichgewichtsverschiebungen.

Die Energie der inneren, diskreten Bereiche setzt sich — entsprechend den allgemeinen Ausführungen in Teil I — grundsätzlich aus zwei Anteilen zusammen: der Abstossungsenergie der Ionenrümpfe (Born–Mayer-Energie) und der Energie der Valenzelektronen. Der erste Anteil lässt sich, wenn man, wie allgemein üblich, nur Zentralkräfte zwischen den nächstbenachbarten Atomen annimmt, in Funktion der Atomlagen relativ einfach berechnen. Anders steht es mit der Energie der Valenzelektronen; handliche theoretische Ausdrücke hierfür bestehen nur für langsam variierende Verzerrungen des Gitters (vgl. Teil I), nicht aber für beliebige Verschiebungen der Atome.

Die formale Lösung eines Teilproblems, nämlich die Berechnung der Energieänderung bei kleinen, sonst aber beliebigen relativen Atomverschiebungen gegenüber dem Gleichgewichtszustand des idealen Gitters, ermöglicht jedoch die sog. Bornsche Gittertheorie.* Hierbei wird die gesamte Energie, also die Summe aus den beiden oben genannten Anteilen, nach den Relativverschiebungen sämtlicher Atome entwickelt und die entsprechende Reihe im allgemeinen nach den quadratischen Gliedern abgebrochen. Die Entwicklungskoeffizienten werden geeigneten Experimenten entnommen; für Kupfer sind sie von JACOBSEN[13] aus der diffusen Streuung von Röntgenstrahlen bestimmt worden. Zieht man von der so berechneten Energie den als bekannt vorausgesetzten Anteil der Ionenabstossung, d. h. die Born–Mayer-Energie, ab, so bekommt man den Energieanteil der Valenzelektronen.

Diese Berechnungsweise versagt bei den starken Störungen, wie sie mit der Entfernung eines Ions bei der Bildung einer Leerstelle oder mit dem Einbau eines Zwischengitteratoms verbunden sind. Die dadurch bedingten Änderungen in der Energie der Valenzelektronen behandeln wir mit dem in Abschn. 6 näher zu diskutierenden Verfahren von FRIEDEL[14] und FUMI[15].

* Siehe z. B. G. LEIBFRIED[12].

VO
1
1959/

VOL. 12 59/60

Mit Hilfe der genannten Methoden werden wir die Bildungsenergie eines Zwischengitteratoms (Anti-Schottky-Defekt) berechnen. (Für eine Leerstelle gilt dann das Entsprechende.) Hierzu denken wir uns das Zwischengitteratom auf folgendem Wege entstanden:

(I) Verschiebung aller Atome des ursprünglich vorhandenen idealen Gitters in die Endlagen, die sie nach dem Einbau des Zwischengitteratoms einnehmen werden.

(II) Wegnahme eines Atoms von der Kristalloberfläche und Einführung in den beim Vorgang (I) geschaffenen freien Raum.

Das Wesentliche ist, dass die Verzerrung des Gitters zuerst, also im idealen Gitter (ohne Zwischengitteratom), vorgenommen und entsprechend auch die gesamte Energieänderung berechnet wird.

Von der Energieänderung beim ersten Schritt, E_I, kann der Beitrag des elastischen Gebiets aufgrund der elastizitätstheoretischen Behandlung sofort angegeben werden. Im atomistisch zu behandelnden Bereich sind die Verschiebungen zum Teil so gross, dass die oben erwähnte quadratische Näherung der Bornschen Gittertheorie nicht ausreicht und die damit berechnete Energie noch korrigiert werden muss. Da aber die Born–Mayer-Energie eine sehr viel rascher variierende Funktion des relativen Ionenabstandes ist als die Energie der Valenzelektronen und bei starker Annäherung der Ionen bei weitem überwiegt, dürfte es ausreichen, nur die Born–Mayer-Energie in der Korrektur zu berücksichtigen. Die korrigierte Gitterenergie kann dann zusammengesetzt werden aus der in quadratischer Näherung berechneten Gitterenergie und der exakten Born–Mayer-Energie abzüglich deren quadratischer Näherung.

Beim zweiten Schritt, dem Einbau des an der Kristalloberfläche entnommenen Ions, ändert sich die Born–Mayer-Energie infolge der Lösung der Bindungen an der Oberfläche und der Schaffung neuer Bindungen auf dem Zwischengitterplatz. Gleichzeitig ändert sich die Energie der Valenzelektronen, und zwar erstens wegen der Erhöhung der Fermi-Energie infolge der Verringerung des Kristallvolumens, und zweitens bei der Einführung des Zwischengitterions infolge der Abschirmung dessen Ladung durch die Valenzelektronen. Den letztgenannten Beitrag werden wir, wie schon oben erwähnt, in Abschn. 6 näher besprechen.

3. ERGEBNISSE DER ELASTIZITÄTSTHEORETISCHEN BEHANDLUNG PUNKTFÖRMIGER GITTERFEHLSTELLEN

Die durch die Elastizitätstheorie beschreibbaren Wirkungen von Fehlstellen in Kristallen sind vor allem von ESHELBY untersucht und zusammenfassend dargestellt worden.[16] Wir bringen hier nur die für das folgende benötigten Ergebnisse.

Eine punktförmige elastische Singularität, durch welche eine atomare Fehlstelle im kontinuumsmässigen Bild ersetzt werden kann, erzeugt in einem isotropen, unendlich ausgedehnten Medium eine radiale Verschiebung vom Betrag

$$u^{\infty}(r) = C/r^2, \tag{1}$$

wobei C ein Mass für die Stärke der Singularität ist. Bei Anwesenheit mehrerer Singularitäten überlagern sich einfach die Verschiebungen der Form Gl. (1). Ist das Medium endlich, so ergeben sich zusätzliche Verschiebungen, die durch die Spannungsfreiheit der Oberfläche bedingt sind.

Die Volumänderungen pro Fehlstelle im unendlichen (Gl.2a) bzw. endlichen (Gl.2b) Medium sind, unabhängig von der Art der Verteilung der Fehlstellen und der Form der Oberfläche,

$$\Delta V^{\infty} = 4\pi C \tag{2a}$$

$$\Delta V^{\infty} = 4\pi\gamma C \tag{2b}$$

mit

$$\gamma = \frac{3K+4\mu}{3K} = \frac{3(\lambda+2\mu)}{3\lambda+2\mu} = 3\frac{1-\nu}{1+\nu}. \tag{3}$$

(K = Kompressionsmodul, λ, μ = Lamésche elastische Konstanten, ν = Poissonsche Konstante).

Die Integration der zur Verschiebung Gl. (1) gehörigen Energiedichte kann wegen des singulären Verhaltens für $r \to 0$ nicht über den ganzen Raum erstreckt werden, was natürlich damit zusammenhängt, dass das Gesetz Gl. (1) für kleine r keine gute Annäherung an die Verhältnisse im wirklichen Kristall gibt. Wir werden vielmehr die elastische Näherung und damit die Integration erst bei einem gewissen Radius, dem „Abschneideradius" r_A, beginnen lassen. Damit ergibt sich für die elastische Energie einer einzelnen Singularität in einem Medium, dessen Abmessungen gross gegen r_A sind,

$$W = \frac{8\pi\mu C^2}{r_A^3}. \tag{4}$$

Beim Vorhandensein mehrerer Singularitäten ergibt sich im unendlichen Medium pro Singularität derselbe

Wert Gl. (4), da hier keine elastische Wechselwirkung zwischen den Singularitäten besteht. Eine solche tritt aber im endlichen Medium auf, und man erhält dann für den Fall, dass die Fehlstellen (Singularitäten) statistisch-gleichmässig im Kristall verteilt sind, als elastische Energie pro Fehlstelle

$$W' = \frac{8\pi\mu C^2}{r_A^3} - \frac{8\pi^2\gamma(\gamma-1)KC^2}{\Omega} \cdot c, \qquad (5)$$

wo c die Atom-Konzentration der Fehlstellen und Ω das Atomvolumen bedeuten. Das zweite Glied in Gl. (5) stellt die Wechselwirkungsenergie dar und hat für Kupfer etwa den Wert $-4\ c$[eV], ist also für übliche Konzentrationen (bis 10^{-3}) gegenüber der gesamten Bildungsenergie einer Fehlstelle zu vernachlässigen.

Das konzentrationsabhängige Glied in Gl. (5) mag bei grossen c allenfalls eine Rolle spielen für die Bestimmung von C aus den Minimalbedingungen; doch wollen wir darauf nicht weiter eingehen. Entsprechend der damit verbundenen Beschränkung auf niedrige Konzentrationen werden wir durchweg das für unendlich ausgedehnte Medien geltende Gesetz Gl. (1) verwenden.

Zum Schluss sei noch erwähnt, dass sich in einem kubisch-anisotropen Medium dieselbe gesamte Volumänderung ΔV von Gl. (2) ergibt. — Die in der isotropen Rechnung benutzten elastischen Konstanten können nach LEIBFRIED[17] aus den kubischen Konstanten des Kristalls abgeleitet werden. Mit den effektiven isotropen Konstanten

$$\begin{aligned} 5c_{11}^0 &= 3c_{11}+2c_{12}+4c_{44} \\ 5c_{12}^0 &= c_{11}+4c_{12}-2c_{44} \\ 5c_{44}^0 &= c_{11}-c_{12}+3c_{44} \end{aligned} \qquad (6)$$

wird

$$\mu = c_{44}^0, \qquad \gamma = \frac{c_{11}^0}{K}. \qquad (7)$$

Mit den elastischen Konstanten von OVERTON und GAFFNEY[18] bei 300°K ergeben sich dann für Kupfer die Werte

$$\mu = 5{,}46 \cdot 10^{11}\ \text{dyn/cm}^2, \qquad \gamma = 1{,}55. \qquad (8)$$

4. DIE BORN-MAYER-ENERGIE

Die Ionenabstossungs- oder Born–Mayer-Energie zweier nächstbenachbarter Ionen im Abstand r mit dem Gleichgewichtsabstand r_0 ($= a/\sqrt{2}$ im kubisch-flächenzentrierten Gitter) wird gewöhnlich dargestellt durch

$$\phi(r) = A \exp\left(-B\left(\frac{r}{r_0}-1\right)\right) \text{ pro Paar.} \qquad (9)$$

Wir betrachten nun ein Zwischengitteratom im Zentrum einer Elementarzelle (ABB. 1) und berechnen die Born–Mayer-Energie des verzerrten Gitters in dessen Umgebung. Um die nachfolgenden Rechnungen ohne Verwendung elektronischer Rechenanlagen bewältigen zu können, nehmen wir an, dass die Grenze zwischen dem diskreten und dem elastischen Bereich als Kugelfläche mit Radius r'_A zwischen den Atomen der 3. und 4. Kugelschale verlaufe, wobei eine „Schale" durch die Atome mit gleichem Abstand vom Zentrum gebildet wird.

Aus Symmetriegründen ist es klar, dass die Atome der 1. und 2. Schale sich radial verschieben werden. Von den Atomen der 3. Schale nehmen wir wie HUNTINGTON[3] Verschiebungen in $\langle 110\rangle$-Richtungen an, was bei einer Betrachtung der Nachbarverhältnisse naheliegend erscheint. Von der 4. Schale an setzen wir, entsprechend dem elastischen Verschiebungsgesetz Gl. (1), rein radiale Verschiebungen voraus. Die Verschiebungen werden im einzelnen folgendermassen (mit insgesamt vier zu variierenden Parametern) gekennzeichnet:

1. Schale: Versch. radial um $\epsilon \cdot a/2$
2. Schale: Versch. radial um $\beta \cdot \sqrt{3}a/2$
3. Schale: Versch. in $\langle 110\rangle_n$ $\delta \cdot \sqrt{2}a/2$
4. Schale: Versch. radial um $\lambda \cdot 3a/2 \equiv \lambda r_4$
5., 6., Schalen: Versch. radial um C/r^2,

wobei C sich aus der Verschiebung der Atome der 4. Schale (der 1. im elastischen Gebiet) bestimmt:

$$\frac{C}{r_4^2} = \lambda r_4, \text{ daraus } C = \lambda r_4^3 = \lambda\left(3\frac{a}{2}\right)^3. \qquad (10)$$

Es ist bequem, die Verschiebungen der Atome der 5., 6., ... Schalen auch in der Form „Konstante mal Abstand vom Zentrum" anzugeben:

5. Schale: Versch. radial um $\lambda_5 r_5$, $\lambda_5 = (r_4/r_5)^3\lambda = 0{,}740\lambda$
6. Schale: Versch. radial um $\lambda_6 r_6$, $\lambda_6 = (r_4/r_6)^3\lambda = 0{,}576\lambda$

Aus den angegebenen Verschiebungen berechnet man die Abstände zu den 12 nächsten Nachbarn eines jeden Gitteratoms der ersten 3 Schalen und daraus nach Gl. (9) die Born–Mayer-Energie dieses Bereichs. Wie wir in Abschn. 5 im einzelnen rechtfertigen werden, zählen wir dabei die über die Grenze r'_A hinausreichenden „Bindungen"

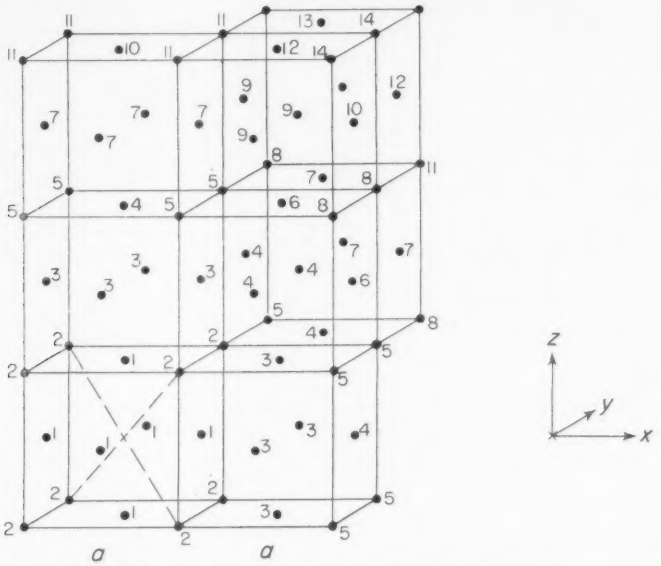

ABB. 1. Die Umgebung eines Zwischengitterplatzes (×) im kubisch-flächenzentrierten Gitter. (Die an die Atome angeschriebenen Zahlen bezeichnen die Nummer der betreffenden Kugelschale um ×.)

Lage und Zahl der Nachbaratome (Koordinatenursprung in ×):

Nr.	Lage	(Abstand)²	Zahl	Nr.	Lage	(Abstand)²	Zahl
1	$a/2$ (1,0,0)	$(a/2)^2 \cdot 1$	6	9	$a/2$ (4,2,1)	$(a/2)^2 \cdot 21$	48
2	(1,1,1)	3	8	10	(4,3,0)	25	24
3	(2,1,0)	5	24		(5,0,0)	25	6
4	(3,0,0)	9	6	11	(3,3,3)	27	8
	(2,2,1)	9	24		(5,1,1)	27	24
5	(3,1,1)	11	24	12	(4,3,2)	29	48
6	(3,2,0)	13	24		(5,2,0)	29	24
7	(4,1,0)	17	24	13	(4,4,1)	33	24
	(3,2,2)	17	24		(5,2,2)	33	24
8	(3,3,1)	19	24	14	(5,3,1)	35	48

ganz mit. Die gesamte Born–Mayer-Energie des aufgeweiteten Gitters (ohne Zwischengitteratom) stellt sich nun dar als

$$U^{\mathrm{I}} = 12\phi\left(\frac{a}{2}\sqrt{(2)}(1+\epsilon)\right)$$

$$+24\phi\left(\frac{a}{2}[2(1+\beta)^2+(\epsilon-\beta)^2]^{1/2}\right)$$

$$+24\phi\left(\frac{a}{2}[(1+\delta)^2+(1+\delta-\epsilon)^2]^{1/2}\right)$$

$$+48\phi\left(\frac{a}{2}[(1+\delta-\beta)^2+(1+\beta)^2+(\delta-\beta)^2]^{1/2}\right)$$

$$+24\phi\left(\frac{a}{2}[2(1+2\lambda-\beta)^2+(\lambda-\beta)^2]^{1/2}\right)$$

$$+24\phi\left(\frac{a}{2}\sqrt{(2)}(1+\delta)\right)+12\phi\left(\frac{a}{2}\sqrt{(2)}\right)$$

$$+24\phi\left(\frac{a}{2}[(1+\delta)^2+(1+3\lambda-\delta)^2]^{1/2}\right)$$

$$+48\phi\left(\frac{a}{2}[(1+2\lambda-\delta)^2+(1+\lambda)^2+(2\lambda-\delta)^2]^{1/2}\right)$$

$$+48\phi\left(\frac{a}{2}[(1+3\lambda_5-\delta)^2+(1+\lambda_5)^2+(\lambda_5-\delta)^2]^{1/2}\right)$$

$$+24\phi\left(\frac{a}{2}[(1+3\lambda_6-\delta)^2+(1+2\lambda_6-\delta)^2]^{1/2}\right). \tag{11}$$

Das konstante Glied in Gl. (11) rührt davon her, dass bei den angenommenen Verschiebungen einige Atome ihren gegenseitigen Abstand nicht ändern.

Bei der Einführung des Zwischengitteratoms werden zusätzliche Bindungen geschaffen. Wir berücksichtigen hier auch noch die Bindungen zu den zweitnächsten Nachbarn, da diese nur wenig mehr vom Zwischengitteratom entfernt sind, als dem normalen Atomabstand entspricht. Damit ergibt sich für die zusätzliche Born–Mayer-Energie (ohne die von der Kristalloberfläche herrührenden Terme)

$$U^{II}=6\phi\left(\frac{a}{2}(1-\epsilon)\right)+8\phi\left(\frac{a}{2}\sqrt{(3)}(1+\beta)\right). \tag{12}$$

5. DIE GITTERENERGIE

Nach der Bornschen Gittertheorie kann die Energieänderung eines Gitters bei kleinen Verschiebungen* der Atome aus den Gleichgewichtslagen dargestellt werden durch

$$\Phi=\frac{1}{2}\sum_{\substack{\mathfrak{m},\mathfrak{n}\\ i,k}}\Phi_{ik}^{\mathfrak{m}\mathfrak{n}}s_i^{\mathfrak{m}}s_k^{\mathfrak{n}}. \tag{13}$$

Hier bedeutet $s_k^{\mathfrak{n}}$ die k-te Komponente des Verschiebungsvektors $\mathfrak{s}^{\mathfrak{n}}$ des durch den ganzzahligen Vektor $\mathfrak{n}$ gekennzeichneten Gitterpunktes. Die Entwicklungskoeffizienten $\Phi_{ik}^{\mathfrak{m}\mathfrak{n}}$, Kopplungsparameter genannt, hängen nur von der Differenz $\mathfrak{h}=\mathfrak{m}-\mathfrak{n}$ ab, so dass auch geschrieben werden kann

$$\Phi=\frac{1}{2}\sum_{\substack{\mathfrak{n},\mathfrak{h}\\ i,k}}\Phi_{ik}^{\mathfrak{h}}s_i^{\mathfrak{n}+\mathfrak{h}}s_k^{\mathfrak{n}}. \tag{13a}$$

* Vorausgesetzt sind eigentlich nur kleine *relative* Verschiebungen; es ist jedoch bequemer, die Gitterenergie in der Form (13) mit absoluten Verschiebungen zu schreiben.

Die Kopplungsparameter sind ein Mass für die direkte Kopplung zwischen den Atomen $\mathfrak{m}$ und $\mathfrak{n}$. In Metallen reicht diese Kopplung (über das Elektronengas) nur bis zu den Atomen in der nächsten Nachbarschaft. Wir führen die Summation in Gl. (13a) deshalb ausser über alle $\mathfrak{n}$ nur über die $\mathfrak{h}$ bis zu den 3. Nachbarn durch. Infolge der Symmetrie des Gitters reduziert sich die Zahl der voneinander verschiedenen Kopplungsparameter bis auf einige wenige. Bezüglich der Form der Kopplungsmatrizen $\Phi_{ik}^{\mathfrak{h}}$ für das kubisch-flächenzentrierte Gitter sei auf die Darstellungen von LEIBFRIED[12] und BRENIG[19] hingewiesen. In unserem Falle gibt es neun voneinander verschiedene, nicht verschwindende Kopplungsparameter, die für Kupfer von JACOBSEN[13] experimentell bestimmt worden sind.

Als Vorarbeit zur Berechnung der Energie des aufgeweiteten Gitters betrachten wir die Wahl der Grenzfläche zwischen dem elastischen und dem atomistischen Bereich etwas näher. Wir haben bis jetzt diese Grenze als Kugel vom Radius $r_A=r_A'$ irgendwo zwischen der 3. und der 4. Schale angenommen.

Die Unbestimmtheit in der genauen Wahl von r_A' bringt für die Energieberechnung folgende zwei Unsicherheiten mit sich:

(1) Da die elastische Energie nach Gl. (4) proportional r_A^{-3} ist, wäre sie bei der obigen Annahme für den Abschneideradius,

$$\frac{a}{2}\sqrt{(5)}<r_A'<\frac{a}{2}3,$$

bis auf einen Faktor 2,4 unbestimmt. Dies hätte einen starken Einfluss auf die resultierenden Verschiebungen zur Folge.

(2) Das „Abschneiden" der Born–Mayer-Energie wie auch der Gitterenergie ist ebenfalls einer gewissen Willkür unterworfen mit nicht unbeträchtlichem Einfluss auf das Endergebnis.

Diese Schwierigkeiten können grösstenteils überwunden werden durch folgendes Vorgehen: Wie seither nehmen wir an, dass die Verschiebung der Atome von der 4. Schale an nach dem elastischen Gesetz C/r^2 erfolge, aber für die Energieberechnung schieben wir die Grenze weiter nach

VOL. 12 59/60

aussen bis zu einer Kugel mit Radius r_A''. Die Verschiebungen in dem Gebiet zwischen den Radien r_A' und r_A'' sind wohl hinreichend gering, um die Energie in diesem, jetzt diskret zu betrachtenden Gebiet ganz nach der (quadratischen) Gittertheorie berechnen zu können. Die Summe aus dieser Energie und der nach Gl. (4) mit $r_A = r_A''$ berechneten elastischen Energie, beide proportional C^2, ist offenkundig von derselben Grössenordnung wie die mit $r_A = r_A'$ berechnete elastische Energie und deshalb gross gegen die mit $r_A = r_A''$ berechnete. Daher spielen die mit der letzteren verbundenen Unsicherheiten keine Rolle mehr. Das Entsprechende gilt auch für das Abschneiden der Gitterenergie.

Die neue Grenze r_A'' legen wir zwischen die 6. und 7. Schale, so dass sämtliche in unserer Arbeit berücksichtigten Born–Mayer-Bindungen ganz innerhalb dieser Grenze liegen. Es ist naheliegend, den Abschneideradius r_A'' so zu wählen, dass er dem Volumen der 116 Atome der ersten 6 Schalen entspricht:

$$\frac{4\pi}{3} r_A''^3 = 116 \frac{a^3}{4}, \quad r_A'' = 3{,}81 \frac{a}{2}. \tag{14}$$

Die zugehörige elastische Energie ist dann nach den Gln. (4), (8) und (10)

$$W = 658\,\lambda^2\ [\mathrm{eV}]. \tag{15}$$

Die Energie des diskreten Bereichs (bis zur Grenze r_A'') im aufgeweiteten Gitter (ohne Zwischengitteratom) setzen wir nun, entsprechend den Darlegungen in Abschn. 2, zusammen aus der quadratischen Gitterenergie Φ des gesamten Bereichs und der durch die starken Verschiebungen bedingten Korrekturenergie Φ_K, die sich aus der Born–Mayer-Energie U^{I} durch Abzug der quadratischen Näherung ergibt. Bezeichnen wir die konstanten, linearen und quadratischen Glieder mit entsprechenden Indizes, so ist

$$\Phi_K = U^{\mathrm{I}} - (U_0^{\mathrm{I}} + U_1^{\mathrm{I}} + U_2^{\mathrm{I}}). \tag{16}$$

Für die spätere Diskussion ist das lineare Glied U_1^{I} von besonderem Interesse; in unserem Falle ist

$$U_1^{\mathrm{I}} = -24AB \cdot 10{,}90\lambda. \tag{17}$$

Die Gitterenergie Φ wird nach Gl. (13a) berechnet, wobei wir $\mathfrak{n}$ über sämtliche Atome der ersten 6 Schalen und $\mathfrak{h}$ neben $\mathfrak{h} = (0,0,0)$ über alle Nachbarn 1., 2. und 3. Ordnung jedes Atoms $\mathfrak{n}$ laufen lassen. Auf diese Weise kommen in der Summe noch Atome bis zur 14. Schale vor.

Die gesamte Energieänderung bei Aufweitung des Gitters ohne Zwischengitteratom ist also

$$\begin{aligned} E_{\mathrm{I}} &= \Phi + \Phi_K + W \\ &= U^{\mathrm{I}} - (U_0^{\mathrm{I}} + U_1^{\mathrm{I}}) + (\Phi - U_2^{\mathrm{I}} + W), \end{aligned} \tag{18}$$

wobei die letzte Klammer nur Glieder enthält, die in den Verschiebungsparametern quadratisch sind.

6. DIE ELEKTRONENENERGIE NACH FRIEDEL UND FUMI

Bei dem Verfahren von FRIEDEL[14] und FUMI[15] zur Berücksichtigung der Elektronenumlagerung in der unmittelbaren Umgebung des Zwischengitteratoms geht man so vor, dass man zunächst das Metallion, also den Atomrumpf ohne die zugehörigen Valenzelektronen, von der Kristalloberfläche auf den Zwischengitterplatz bringt und anschliessend daran das Elektronengas auf das verkleinerte Kristallvolumen komprimiert. Die neu eingeführte positive Ladung des Ions muss durch Umlagerungen der Valenzelektronen abgeschirmt werden; da es sich um eine anziehende Wechselwirkung handelt, wird dabei Energie gewonnen. Beschreibt man das Elektronengas als quasifrei mit der effektiven Masse m^*, so ergibt sich diese Energieänderung zu

$$E_{\mathrm{el}} = -\frac{\hbar^2}{m^*} \int_0^{k_F} Z(k) k\, dk \tag{19}$$

mit

$$Z(k) = \frac{2}{\pi} \sum_{l=0}^{\infty} (2l+1)\eta_l(k). \tag{20}$$

Hier bedeuten k die Wellenzahl, k_F deren Wert an der Fermi-Oberfläche und η_l die durch das Störpotential hervorgerufenen Phasenverschiebungen der Wellenfunktionen. Die sog. Friedelsche Bedingung lautet

$$Z(k_F) = Z, \tag{21}$$

wobei Z die (in Vielfachen der positiven Elementarladung gerechnete) eingeführte Ladung angibt.

In der Bornschen Näherung, gültig für schwache Störungen, ergibt sich die Elektronenenergie E_{el},

unabhängig vom genauen Verlauf des Störpotentials, zu[15]

$$E_{el} = -\frac{2}{3}\frac{\hbar^2 k_F^2}{2m^*}Z = -\frac{2}{3}\zeta Z, \qquad (22)$$

wo ζ die sog. Fermi-Energie darstellt.

Bei der ursprünglichen Anwendung der vorstehenden Überlegungen auf Leerstellen in einwertigen Metallen[15] waren die Verschiebungen der Nachbaratome der Leerstelle so gering, dass deren Einfluss auf die Elektronenenergie vernachlässigt werden konnte. Beim vorliegenden Problem sind aber diese Verschiebungen verhältnismässig gross, so dass man deren Einfluss jetzt nicht mehr ohne weiteres vernachlässigen kann. Unsere Rechnung ist jedoch so angelegt, dass dieser schwer abzuschätzende Beitrag möglichst klein gehalten wird. Wir haben ja im Schritt I das Gitter schon im „richtigen" Masse aufgeweitet, so dass der Einbau des Zwischengitteratoms ohne gleichzeitige Verschiebung der Nachbaratome erfolgt. Allerdings ist natürlich im Schritt I die Elektronenverteilung geändert worden. Da wir jedoch ohnehin vom genauen Verlauf der Wellenfunktionen abgesehen haben, ist es konsequent anzunehmen, dass die zusätzliche Ladung Z (im Falle von Kupfer $Z = 1$) in ein quasifreies Elektronengas, also in eine räumlich konstante positive Ladungsverteilung, eingebaut wird.

Die einfachste Annahme für den Verlauf des Störpotentials V, das sich aus dem Feld der zusätzlichen Ladung Z und dem Feld der abschirmenden Elektronen zusammensetzt, ist ein kugelförmiges Kastenpotential, d. h. ein Potentialverlauf der Form

$$\begin{aligned} V(r) &= -D \qquad (r < a) \\ &= 0 \qquad\quad (r > a). \end{aligned} \qquad (23)$$

$D > 0$ bedeutet ein anziehendes Potential. Die Grössen D und a sind nicht beide frei wählbar, sondern über die Friedelsche Bedingung Gl. (21) miteinander verknüpft.

E_{el} wurde für den Potentialverlauf G1. (23) unter der Annahme berechnet, dass a gleich dem Radius r_s der Wigner–Seitz-Kugel ist. (Wie wir in Abschn. 7 näher besprechen werden, ist a in Wirklichkeit etwas grösser anzunehmen.) Die $\eta_l(k)$ lassen sich an Hand der von MOTT und MASSEY[20] für ein Kastenpotential angegebenen Formeln berechnen. Der Zahlenwert von $k_0 = (2m^* D/\hbar^2)^{1/2}$, der die Friedelsche Bedingung mit $Z = 1$ befriedigt, und die zugehörigen Werte der Phasenkonstanten an der Fermioberfläche $k = k_F$ sind in Tab. 1 aufgeführt. Aus den mit diesem k_0 berechneten Phasenkonstanten $\eta_l(k)$ (vgl. ABB. 2) ergibt sich nach Gl. (19).

$$E_{el} = -0{,}7966\,\zeta, \qquad (24)$$

während die Bornsche Näherung nach Gl. (22) $E_{el} = -0{,}6667\,\zeta$ liefert.

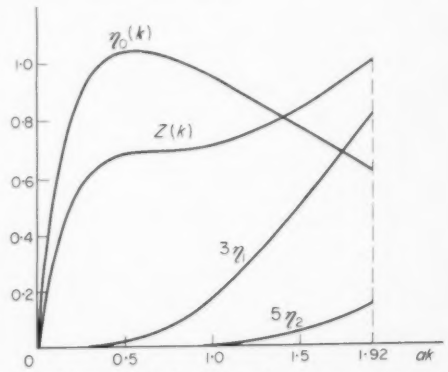

ABB. 2. Abhängigkeit der Phasenkonstanten $\eta_l(k)$ und der Funktion $Z(k)$ von der Wellenzahl k für ein anziehendes kugelförmiges Kastenpotential mit $ak_0 = 1{,}476$.

Tabelle 1. *Die Potentialstärke* k_0 *und die Phasenkonstanten* $\eta_l(k_F)$ *für ein kugelförmiges Kastenpotential mit* $a = r_s$ *und* $Z = 1$

ak_F	ak_0	η_0	η_1	η_2	η_3	η_4	$\frac{2}{\pi}\sum_{l=0}^{\infty}(2l+1)\eta_l(k_F)$
1,9200	1,4758	0,6140	0,2686	0,0278	0,0016	0,0001	1,0000

Der Verlauf von $\eta_0(k)$ (ABB. 2) zeigt, dass man sich mit dem gewählten Potential nicht mehr sehr weit vom Auftreten eines gebundenen Zustandes entfernt befindet. (Gebundene Zustände würden auftreten für $a k_0 \geq \pi/2$.) Die Vergrösserung von a (bei festem Z) wirkt dem Auftreten eines gebundenen Zustands entgegen, so dass man in dieser Hinsicht wohl keine Komplikationen zu befürchten hat.

VOL. 12 59/60

7. ERGEBNISSE

(a) *Für ein Zwischengitteratom*

Zur Berechnung der gesamten Energieänderung $E = E_{\mathrm{I}} + E_{\mathrm{II}}$ benötigen wir noch den Anteil, der mit der Loslösung eines Atoms von der Oberfläche verbunden ist. Im kubisch-flächenzentrierten Gitter werden bei diesem Vorgang durchschnittlich 6 Born–Mayer-Bindungen gelöst, verbunden mit der Energieänderung

$$\Delta U = -6A. \tag{25}$$

Ferner wird durch die Verringerung des Kristallvolumens um 1 Atomvolumen die Fermi-Energie der Elektronen um

$$\Delta E_F = \frac{2}{5}\zeta \tag{26}$$

erhöht.[15] Die Aufweitung des Gitters brauchen wir hier nicht zu berücksichtigen, da wir die Atomumlagerung im schon aufgeweiteten Gitter vornehmen.

Die gesamte Energieänderung bei Bildung eines Zwischengitteratoms ist damit

$$E = U^{\mathrm{I}} + U^{\mathrm{II}} - U_1^{\mathrm{I}} + (\Phi - U_2^{\mathrm{I}} + W) + \\ + (\Delta U - U_0^{\mathrm{I}}) + (E_{\mathrm{el}} + \Delta E_F). \tag{27}$$

Die beiden letzten Klammern in diesem Energieausdruck sind in unserem Modell als konstant, d.h. von den Verschiebungen unabhängig, zu betrachten. Die Minimumsbedingung für die Energie E ergibt 4 transzendente Gleichungen für die 4 eingeführten Verschiebungsparameter, die auf graphisch-numerische Weise gelöst wurden. Die Ergebnisse für verschiedene Born–Mayer-Potentiale sind in Tabelle 2 aufgeführt. Dazu ist folgendes zu bemerken :

(1) Die Bestimmung der Born–Mayer-Potentiale wurde in Teil I ausführlich besprochen. Leider ergab sich dabei kein bevorzugtes Wertepaar A, B, sondern lediglich ein näherungsweiser Zusammenhang zwischen A und B. Als repräsentative Beispiele haben wir die numerischen Rechnungen der vorliegenden Arbeit durchgeführt für

$$\begin{aligned} &\text{(a)} \quad A = 0{,}0127 \text{ eV} \quad B = 20 \\ &\text{(b)} \quad A = 0{,}0240 \text{ eV} \quad B = 20 \\ &\text{(c)} \quad A = 0{,}053 \text{ eV} \quad B = 13{,}9. \end{aligned} \tag{28a}$$

Da sich die Potentiale (a) und (b) nur in A unterscheiden, kann hier der Einfluss der Grösse von A studiert werden ; die beiden Werte für A sind gewissermassen als Schranken zu betrachten. Die Verwendung des Potentials (c), das von HUNTINGTON[3] angegeben wurde und der erwähnten Beziehung zwischen A und B genügt, erlaubt uns einen besseren Verglcich mit den ebenfalls in Tab. 2 aufgeführten Ergebnissen von HUNTINGTON[4] und TEWORDT[11], die u. a. dieses Potential verwendet haben. Tewordt verwandte ausserdem das Potential von HUNTINGTON u. SEITZ[1] :

$$\text{(d)} \quad A = 0{,}032 \text{ eV} \quad B = 17{,}0. \tag{28b}$$

(2) Der Zahlenwert der Elektronenenergie E_{el} ist etwas unsicher, da man den genauen Wert des Abschirmradius a nicht kennt. HUNTINGTON[2] (vgl. auch H. BROOKS[5]) hat gezeigt, dass sich im Falle einer Leerstelle die lokale Störung des Elektronengases bis zu einem Radius von etwa $2\,r_s$ erstreckt. Ähnliches dürfte auch für ein Zwischengitteratom gelten. Da nun mit zunehmendem Radius a die Bornsche Näherung immer besser gilt, wollen wir als Grenzfälle für die Elektronenenergie E_{el} die beiden Werte Gl. (24) (für ein Kastenpotential mit $a = r_s$) und Gl. (22) (für ein beliebiges Potential mit $a \gg r_s$) verwenden. Die Summe $E_{\mathrm{el}} + \Delta E_F$ in den beiden Fällen wird :

$$\begin{aligned} &a = r_s : \\ &E_{\mathrm{el}} + \Delta E_F = -0{,}797\,\zeta + 0{,}4\,\zeta = -0{,}397\,\zeta \\ &a \gg r_s : \\ &E_{\mathrm{el}} + \Delta E_F = -\frac{2}{3}\zeta + \frac{2}{5}\zeta = -\frac{4}{15}\zeta = -0{,}267\,\zeta. \end{aligned} \tag{29}$$

Setzt man für die effektive Masse $m^*/m = 1{,}45$ (in Übereinstimmung mit SEEGER und BROSS[21]), so hat die Fermi-Energie ζ den Betrag $\zeta = 4{,}84$ eV.

(b) *Für eine Leerstelle*

Die im Vorstehenden entwickelten und auf ein Zwischengitteratom angewandten Methoden können ohne grosse Mühe auf eine Leerstelle übertragen werden. Vieles wird sogar erheblich einfacher, da eine Leerstelle wesentlich geringere Verschiebungen hervorruft. An die Stelle einer Aufweitung des Gitters tritt hier eine Kontraktion. Als unabhängig betrachten wir die Verschiebungen der 1. und 2. Nachbarn (beide in radialer Richtung) ; von den 3. Nachbarn an gelte das elastische Verschiebungsgesetz. Der Abschneideradius r_A für die elastische Energie W wird so gewählt, dass er dem Volumen der 19 Atome der ersten beiden Schalen entspricht.

Die Verschiebungen sind wohl genügend gering, um die Energie des atomistisch zu behandelnden Bereichs ganz nach der Gittertheorie, also ohne zusätzliche Korrektur, berechnen zu können. Die Summation über $\mathfrak{n}$ in Gl. (12a) wird über die 1. und 2. Nachbarn durchgeführt ; die Kopplungen reichen dann noch bis zu Atomen der 9. Schale.

Bei der Herausnahme des „Leerstellenatoms" aus dem kontrahierten Gitter und dem Anbau an die Kristalloberfläche ändert sich die Born–Mayer-Energie insgesamt um

$$U = -12A \exp(-B\epsilon)+6A, \qquad (30)$$

wenn ϵr_0 die Verschiebung der 1. Nachbarn darstellt. Die Berechnung der Elektronenenergie E_{el} für eine Leerstelle erfolgt entsprechend wie beim Zwischengitteratom und wurde unter der Annahme eines kugelförmigen Kastenpotentials mit $a = r_s$ und $Z = -1$ von FUMI[15] und SEEGER und BROSS[21] durchgeführt. Die Rechnungen der letztgenannten Autoren für $a > r_s$ lassen vermuten, dass für $a \sim 2r_s$ bereits der Wert der Bornschen Näherung erreicht wird. Mit den beiden Grenzwerten ergibt sich dann als gesamte Änderung der Elektronenenergie

$$a = r_s : E_{el}+\Delta E_F = 0{,}567\,\zeta - 0{,}4\,\zeta = 0{,}167\,\zeta$$

$$a \gg r_s : E_{el}+\Delta E_F = \frac{2}{3}\zeta - \frac{2}{5}\zeta = 0{,}267\,\zeta. \qquad (31)$$

Die Bildungsenergie einer Leerstelle stellt sich nun dar als

$$E = \Phi + W + U + E_{el} + \Delta E_F. \qquad (32)$$

Entwickelt man noch U in eine Potenzreihe und vernachlässigt die höheren als quadratischen Glieder in ϵ, so führt die Gleichgewichtsbedingung auf ein lineares Gleichungssystem für die 3 eingeführten Verschiebungsparameter. Die Ergebnisse unserer Rechnungen, zusammen mit denen von TEWORDT, sind in Tabelle 2 aufgeführt.

8. DISKUSSION

(a) *Diskussion des Verfahrens*

Das in der vorliegenden Arbeit verwendete Verfahren benützt verschiedene Modellvorstellungen. Dies bedingt natürlich gewisse Unsicherheiten. Deren Einfluss sowie mögliche Verbesserungen sollen im folgenden diskutiert werden. Ferner werden wir einen Vergleich mit den Verfahren anderer Autoren vornehmen, insbesondere mit der bis jetzt ausführlichsten Arbeit von TEWORDT[11].

Die Voraussetzung der elastischen Isotropie kann natürlich den wirklichen Verhältnissen nicht gerecht werden. Vielmehr sind in den kubischen Kristallen stark anisotrope Verzerrungen zu erwarten, und zwar auch noch in grossen Entfernungen von den Fehlstellen, in denen die Elastizitätstheorie gut anwendbar ist. Dies ergibt sich auch aus den Untersuchungen von KANZAKI[22] und HALL[23], die auf der Grundlage der Bornschen Gittertheorie die durch punktförmige Fehlstellen hervorgerufenen Verschiebungen der Gitteratome in kubisch-flächenzentrierten Kristallen berechnet haben. Wenngleich auch die zugrundegelegten Modelle (zum Teil einfaches Federmodell) auf Kupfer nicht anwendbar sind, so dürfte doch das allgemeine Bild auch hier zutreffen. Den Einfluss der Anistropie auf die gesamte Volumänderung und die Bildungsenergie halten wir jedoch für gering. — TEWORDT hat zu der isotropen Lösung C/r^2 zwar noch eine nicht-radialsymmetrische Verschiebung hinzugenommen, die aber mit $1/r^6$ abnimmt und deshalb sehr bald gegenüber C/r^2 zu vernachlässigen ist.

Unser Verfahren unterscheidet sich von anderen vor allem dadurch, wie der diskrete Bereich behandelt wurde. Neu ist die Anwendung der Bornschen Gittertheorie. Wir konnten in unserem Falle hiervon Gebrauch machen, da für Kupfer die Kopplungsparameter seit den Messungen von JACOBSEN[13] zur Verfügung stehen. Die Vorteile liegen erstens in einer genaueren Energieberechnung, da die Wechselwirkungen eines Atoms

VOL. 12, 59/60

Tabelle 2. Numerische Ergebnisse für Zwischengitteratome und Gitterlücken in Kupfer für verschiedene Born–Mayer-Potentiale [definiert durch Gln. (9) u. (28)]. Zum Vergleich sind die Ergebnisse anderer Autoren (HUNTINGTON[4] [*H*], TEWORDT[11] [*T*]) *mit aufgeführt. Die Verschiebungen sind angegeben in Einheiten* $a_0/2$ (a_0 = *Gitterkonstante*), *die Volumänderungen in Einheiten* Ω ($= a_0^3/4$ = *Atomvolumen*), *die Energien in* [*eV*].

Born–Mayer-Potential		Zwischengitteratom						Gitterlücke					
		a	b	c	H c	T c	T d	a	b	c	T c	T d
Verschiebungen	1. Nachb. (ϵ)	0,195	0,240	0,217	0,21	0,246	0,257	($\epsilon\sqrt{2}$) −0,009	−0,018	−0,029	−0,033	−0,027
	2. „ ($\beta\sqrt{3}$)	0,014	0,017	0,013		−0,022	−0,014	0,001	0,002	0,003	−0,002	−0,002
	3. „ ($\delta\sqrt{2}$)	0,039	0,060	0,046	0,073	0,071	0,078	−0,001$_5$	−0,003	−0,005	−0,009	−0,008
	4. „ ($\lambda \cdot 3$)	0,014	0,020	0,016								
Volumänderung	$\Delta V^{\infty} = 4\pi C$	0,78	1,15	0,90	2,01	1,11	1,34	−0,06	−0,12	−0,19	−0,34	−0,29
	$\Delta V = 4\pi\gamma C$	1,21	1,78	1,39	3,11	1,72	2,07	−0,09	−0,19	−0,29	−0,53	−0,45
Born–Mayer-Energie $U^{\mathrm{I}} + U^{\mathrm{II}} - U_1^{\mathrm{I}} - U_0^{\mathrm{I}} + \Delta U$		2,50	3,84	4,07		2,3	2,1	U −0,10	−0,23	−0,52		
Gitterenergie + elast. Energie $\Phi - U_2^{\mathrm{I}} + W$		1,52	0,87	0,51				$\Phi + W$ 0,01	0,05	0,11		
Elektronenenergie $E_{\mathrm{el}} + \Delta E_F$												
	$a = r_s$	−1,92	−1,92	−1,92				0,81	0,81	0,81		
	$a \gg r_s$	−1,29	−1,29	−1,29		0,2	0,5	1,29	1,29	1,29	0,9	1,0
Bildungsenergie E												
	$a = r_s$	2,10	2,79	2,66				0,72	0,63	0,40		
	$a \gg r_s$	2,73	3,42	3,29		2,5	2,6	1,20	1,11	0,88	0,9	1,0

nicht nur mit seinen nächsten, sondern auch mit den zweit- und drittnächsten Nachbarn berücksichtigt werden. Zweitens lässt sich, wie in Abschn. 5 gezeigt wurde, mit Hilfe der Gittertheorie der Übergang vom diskreten zum kontinuierlichen Bereich einigermassen glatt vollziehen, und drittens sind, wie weiter unten ausgeführt werden wird, vom Standpunkt der Gittertheorie aus die Stabilitätsverhältnisse leichter zu übersehen.

Unter sonst gleichen Verhältnissen wird jedes Verfahren umso genauer, je grösser man den Bereich mit den unabhängig betrachteten Atomen wählt. Während wir uns auf 4 Parameter beschränken mussten, war TEWORDT[11] durch die Verwendung einer elektronischen Rechenmaschine in der Lage, insgesamt 13 Verschiebungsparameter einzuführen. Freilich genügt es dann nicht, wie TEWORDT im diskreten Bereich nur die Born–Mayer-Energie zu betrachten; vielmehr spielt auch die (in der Gitterenergie mitenthaltene) elektrostatische Energie eine nicht zu vernachlässigende Rolle.

Ein wesentlicher Unterschied zu TEWORDT besteht hinsichtlich der Stabilität des Gitters. Von jeder zur Berechnung der Bildungsenergie von Gitterfehlern entwickelten Methode muss man wohl verlangen, dass sie bei Anwendung auf das ideale Gitter (ohne Fehlstellen) dessen Stabilität gewährleistet. Setzt man, wie dies bei TEWORDT der Fall ist, für die Energie im kontinuierlichen Bereich die elastische Energie und im diskreten Bereich allein die Born–Mayer-Energie an, so ändert sich bei einer Aufweitung des Gitters vom Gleichgewichtszustand aus die erstgenannte Energie quadratisch, die letztgenannte linear mit den Verschiebungen. Demzufolge wäre also das ideale Gitter nicht im Gleichgewicht, es würde sich von selbst aufweiten. Um Stabilität zu erreichen, muss der lineare Anteil der Born–Mayer-Energie abgezogen werden; bei uns ist dies das Glied U_1^{I}, dargestellt in Gl. (17). Geht man, wie wir das getan haben, von der Gittertheorie aus, so tritt ein solches lineares Glied überhaupt nicht erst auf; die Stabilität des idealen Gitters ist von vornherein gesichert. (Die in Abschn. 5 beschriebene, zu der quadratischen Gitterenergie Φ hinzutretende Korrekturenergie Φ_K enthält nur höhere als quadratische Glieder.) HUNTINGTON[4] hat das Stabilitätsglied ebenfalls berücksichtigt.

Ziemlich verschieden von TEWORDT ist auch unsere Berechnungsweise der Elektronenenergie. TEWORDT verwandte sowohl für die Änderung der Fermi-Energie nach Gl. (26), $\Delta E_F = 2/5\,\zeta\,Z$, als auch in der Friedelschen Bedingung Gl. (21) zur Berechnung der Abschirmenergie anstatt der wahren Ladung Z ($= +1$ für das Zwischengitteratom, -1 für die Leerstelle) eine effektive Ladung $Z' = Z - \Delta V^{\infty}/\Omega$, die dem Einfluss der Volumänderung Rechnung tragen soll. Zweifellos wäre im Rahmen des zugrundegelegten Fumischen Elektronengasmodells nichts hiergegen einzuwenden, doch bereitet die Übertragung auf Kristalle grundsätzliche Schwierigkeiten. Die mit Z' proportionale Energie hängt vom Volumen, also den Verschiebungen, ab und muss deshalb in die Energiebilanz mit einbezogen werden. Da aber die Volumänderung linear in den Verschiebungen ist, bedeuteten diese linearen Glieder für das ideale Gitter ($Z = 0$) eine zusätzliche Instabilität.

Bei dem von uns eingeschlagenen Weg treten diese Schwierigkeiten nicht auf. Wir haben die zur Aufweitung des idealen Gitters benötigte Energie vorwegberechnet, und zwar im Prinzip exakt. Bei der Einführung der Ladung Z in das nunmehr starr gedachte Gitter muss zweifellos die gesamte Ladung Z durch Umlagerungen der Elektronen abgeschirmt werden. Da aber die von der vorangegangenen Gitteraufweitung herrührende Elektronenverteilung von derjenigen des idealen Gitters verschieden ist, mag es durchaus sein, dass die Friedel–Fumische Methode nicht die richtige Energieänderung liefert. Die Elektronenenergie E_{el} könnte also noch von den Gitterverzerrungen abhängen, wenngleich auch nur in schwachem Masse und nicht in der von TEWORDT angenommenen Form. Eine Klärung dieser Fragen kann nur eine eingehende quantenmechanische Untersuchung bringen. Im Gegensatz dazu ist die Änderung der Fermi-Energie, ΔE_F, bei unserem Modell in Strenge von den Verschiebungen unabhängig. Im übrigen werden sich diese Unsicherheiten wohl am ehesten bei Zwischengitteratomen auswirken, weniger bei Leerstellen, die nur geringfügige Verzerrungen verursachen (vgl. Tab. 2).

(b) *Diskussion der Ergebnisse und Vergleich mit dem Experiment*

Die Ergebnisse unserer Rechnungen für verschiedene Born–Mayer-Potentiale und mit den

beiden Annahmen über den Abschirmradius a sind in Tabelle 2 aufgeführt. Während man die Bildungsenergien E_Z der Zwischengitteratome in den Edelmetallen bis jetzt noch nicht direkt messen kann, können die Bildungsenergien E_L der Leerstellen aus Abschreckexperimenten ermittelt werden. Im Falle von Kupfer haben die Messungen von AIROLDI *et al.*[24] $E_L = (1{,}0 \pm 0{,}1)$ eV ergeben. Nimmt man den experimentellen Wert für die Aktivierungsenergie der Selbstdiffusion (bei Cu 2,07 eV) zu Hilfe, so kann man auch aus Messungen der Wanderungsaktivierungsenergie W_L von Leerstellen einen Wert für E_L ableiten. Wie eine ausführliche Diskussion der verschiedenen experimentellen Ergebnisse zeigt[9], beträgt der so ermittelte Wert für E_L etwa 1,1 eV. Er stimmt also innerhalb der Fehlergrenzen mit dem durch die erwähnten Abschreckversuche ermittelten Zahlenwert überein. AIROLDI *et al.*[24] finden aus dem Anlassverhalten der abgeschreckten Proben eine Aktivierungsenergie von 1,3 eV, die sie mit W_L identifizieren. Dies würde aber bedeuten, dass E_L wesentlich kleiner als 1 eV sein müsste, was wir auf Grund der vorliegenden Experimente für unzutreffend halten. Das Auftreten einer scheinbaren Aktivierungsenergie von 1,3 eV kommt nach unserer Ansicht zustande durch die Überlagerung von W_L mit einer wesentlich grösseren Aktivierungsenergie, die wohl mit Leerstellengruppen zusammenhängt. An unserem Institut konnte das fast gleichzeitige Auftreten zweier solcher Aktivierungsenergien bei Untersuchungen an kaltverformtem Gold nachgewiesen werden, wo neben der Aktivierungsenergie für Leerstellenwanderung $W_L = 0{,}82$ eV noch eine zweite Aktivierungsenergie von etwa 1,5 eV beobachtet wird.

Ein Blick auf Tab. 2 zeigt, dass alle mit $a = r_s$ berechneten Werte unterhalb des experimentellen Wertes von E_L liegen. Annähernde Übereinstimmung erreicht man nur unter der Annahme $a > r_s$. Nach der in Abschn. 7 erwähnten Untersuchung von HUNTINGTON[2] ist tatsächlich ein Abschirmradius $a \approx 2 r_s$ wahrscheinlich, und durch Extrapolation der von SEEGER und BROSS[20] für $a \gtrsim r_s$ berechneten Elektronenenergien ergibt sich, dass der zu $a = 2r_s$ gehörige Wert nicht mehr allzusehr von dem für $a \gg r_s$ (d. h. in Bornscher Naherung) sich ergebenden Wert verschieden sein wird. Deshalb sind die für $a \gg r_s$ angegebenen Werte der Bildungsenergie eher wahrscheinlich, und da diese obere Schranken darstellen, ergibt sich nach Tab. 2 nur für die Born–Mayer-Potentiale mit grösserem Exponenten B Übereinstimmung mit dem experimentellen Wert. Wertet man dies als Entscheidung zugunsten der „härteren" Potentiale ($B \sim 20$), so muss man hieraus folgern, dass die Volumänderung bei Leerstellen nur 10–20 Prozent des Atomvolumens beträgt, also wesentlich weniger als bei TEWORDT. Auffallend ist auch, dass bei TEWORDT die zweitnächsten Nachbaratome einer Leerstelle sich nach innen verschieben, während bei uns, übereinstimmend mit den Ergebnissen von KANZAKI[22] und HALL[23] bei flächenzentrierten Kristallen mit einfacheren Kraftgesetzen, diese Verschiebungen nach aussen gerichtet sind.

Während die Konstante A (bei gleichem B) auf die Bildungsenergie der Leerstellen nur einen geringen Einfluss hatte, wirkt sich die Unsicherheit in der Wahl von A beim Zwischengitteratom stärker aus. Als Bildungsenergie bekommen wir etwa 3 eV, die Volumänderung beträgt ungefähr 1,5 Ω. Dass TEWORDT bei gleichem Potential (c) eine wesentlich geringere Bildungsenergie erhielt, hängt unserer Auffassung nach mit der oben erwähnten Instabilität seines Kristallmodells zusammen. Verglichen mit den experimentellen Werten ergibt sich die Bildungsenergie für Leerstellen bei TEWORDT als zu klein. Seine angegebenen Werte berücksichtigen nur die Elektronenenergie; hiervon muss aber noch ein Betrag $> 6A$ ($\sim 0{,}3$ eV) abgezogen werden, der von der Umlagerung des Leerstellenatoms und der Relaxation des Gitters herrührt.

Wie Tabelle 2 zeigt, kompensieren sich einige der mit der Wahl des Born–Mayer-Potentials verknüpften Unsicherheiten etwas, wenn man nicht isolierte Leerstellen und Zwischengitteratome, sondern Frenkelpaare betrachtet. Für diese ergibt sich eine Bildungsenergie $E_F \approx 4$ eV und eine Volumexpansion $\Delta V \approx 1{,}3$ Ω. Frenkel-Paare spielen bei der Strahlungsschädigung von Metallen, insbesondere durch Bestrahlung mit energiereichen Elektronen und Deuteronen, eine wichtige Rolle. Es liegen hierzu Messungen der bei der Erholung freiwerdenden Energie und der Volumexpansion vor, die man — allerdings etwas indirekt — mit den Ergebnissen der vorliegenden Arbeit vergleichen kann. Dieser Vergleich ist an anderer Stelle[9] ausgeführt worden und hat innerhalb

VOL. 12 59/60

einer Fehlergrenze von etwa 20 Prozent Übereinstimmung von Theorie und Experiment ergeben. Wir sind deshalb der Ansicht, dass die vorliegende Behandlung von Zwischengitteratomen und Leerstellen befriedigende Ergebnisse liefert, obschon — wie erwähnt — eine bessere und vollständigere quantenmechanische Theorie sehr wünschenswert wäre. Zum Abschluss erwähnen wir noch, dass sich durch die Kombination der Resultate dieser Arbeit mit Messungen des elektrischen Widerstands strahlungsgeschädigter Metalle als elektrischer Widerstand von Frenkelpaaren in Kupfer $\Delta\rho = 2{,}9\ \mu\Omega$ cm/Prozent Frenkelpaare ergibt.[9]

Die Verfasser danken der Deutschen Forschungsgemeinschaft für die Förderung dieser Arbeit.

LITERATUR

1. HUNTINGTON H. B. und SEITZ F., *Phys. Rev.* **61**, 315 (1942).
2. HUNTINGTON H. B., *Phys. Rev.* **61**, 325 (1942).
3. HUNTINGTON H. B., *Phys. Rev.* **91**, 1092 (1953).
4. HUNTINGTON H. B., *Acta Met.* **2**, 554 (1954).
5. BROOKS H., *Impurities and Imperfections*, S.1. American Society for Metals, Cleveland, Ohio, (1955).
6. MANN E. und SEEGER A., *J. Phys. Chem. Solids*, **12**, 314 (1959).
7. SIMMONS R. O. und BALLUFFI R. W., *Phys. Rev.*, **109**, 1142 (1958).
8. VOOK R. W. und WERT Ch., *Phys. Rev.* **109**, 1529 (1958).
9. SEEGER A. K., *The Theory of Radiation Damage and Radiation Hardening of Metals. Progress in Nuclear Energy, Metallurgy and Fuels* Bd. 3 im Druck. Siehe auch: *Proc. 2nd Int. Conf. Peaceful Uses Atomic Energy, Geneva, 1958*, Vol. 6, p. 250. United Nations, New York (1958).
10. JONGENBURGER P., *Nature, Lond.* **175**, 546 (1955).
11. TEWORDT L., *Phys. Rev.* **109**, 61 (1958).
12. LEIBFRIED G., *Handbuch der Physik* Bd. 7/1, S.104. Springer, Berlin (1955).
13. JACOBSEN E. H., *Phys. Rev.* **97**, 654 (1955).
14. FRIEDEL J., *Phil. Mag.* **43**, 153 (1952).
15. FUMI F. G., *Phil. Mag.* **46**, 1007 (1955).
16. ESHELBY J. D., *Solid State Physics* (Hrsg. F. SEITZ und D. TURNBULL) Bd. 3, S.79. Academic Press, New York (1956).
17. LEIBFRIED G., *Z. Phys.* **135**, 23 (1953).
18. OVERTON W. und GAFFNEY J., *Phys. Rev.* **98**, 969 (1955).
19. BRENIG W., *Z. Phys.* **142**, 163 (1955).
20. MOTT N. F. und MASSEY H. S. W., *The Theory of Atomic Collisions*, 2nd ed., Chap. 2. Oxford University Press (1950).
21. SEEGER A. und BROSS H., *Z. Phys.* **145**, 161 (1956).
22. KANZAKI H., *J. Phys. Chem. Solids* **2**, 24 (1957).
23. HALL G. L., *J. Phys. Chem. Solids* **3**, 210 (1957).
24. AIROLDI G., BACCHELLA G. L. und GERMAGNOLI E., *Phys. Rev. Letters* **2**, 145 (1959).

VO
1
1959/

J. Phys. Chem. Solids Pergamon Press 1960. Vol. 12. pp. 341–343. Printed in Great Britain.

BRILLOUINSTREUUNG AN KÜNSTLICHEN QUARZGLÄSERN

W. GEIGER und M. KULP

Recheninstitut der Technischen Hochschule, Stuttgart, Germany

(*Received* 2 *July* 1959)

VOL. 12 59/60

Zusammenfassung — Eine lichtstarke Anordnung zur Messung der Brillouinaufspaltung an künstlichen Quarzen wird beschrieben. Bei den gewählten Belichtungszeiten wurde keine Brillouinstreuung gefunden. Es wird gezeigt, dass die Brillouinkomponenten nach der Theorie schon bei einer um zwei Grössenordnungen kleineren Belichtungszeit hätten erscheinen müssen. Das Ergebnis wird mit früheren Arbeiten auf diesem Gebiet verglichen.

Abstract—An experimental arrangement providing for strong light intensity to measure Brillouin splitting of artificial quartz is described. Within the exposure times employed, no Brillouin scattering was found. It is shown that according to theory the Brillouin components should have appeared at exposure times two orders of magnitude less than those employed. This result is compared with earlier papers on the subject.

1. APPARATUR UND ERGEBNISSE

Die Streuversuche wurden mit 3 Sorten blasenfreier Quarzgläser der Heräus-Quarzschmelze durchgeführt: Herasil (optische Qualität I), Homosil und homogenisiertem Ultrasil. Von diesen hat Ultrasil die beste Homogenität und die kleinste Absorption. Die 3 Materialien standen in Stabform mit den Abmessungen $14 \times 14 \times 200$ mm^3 zur Verfügung.

Als Streuwinkel wurde $\theta = 90°$ gewählt, weil sich hierbei falsches, von Reflexionen stammendes, Streulicht am ehesten vermeiden lässt. (Abb. 1). Der Blendenkörper wurde so angefertigt, dass die Lichtstrahlung der Lampe (s. u.) möglichst gut ausgenützt werden konnte: Quadratische Blenden aus 0,1 mm starkem Messingblech, mit einem quadratischen Loch in der Mitte, wurden mit solchen Abständen hintereinandergesetzt, dass der Streuwinkelbereich $\Delta\theta \leqq \pm 11°$ wird. Der stabförmige Streukörper wird durch die Mittellöcher eingeschoben. Eingestrahlt wird parallel zu den Blenden, beobachtet wird das aus einer Stirnfläche des Streukörpers austretende Streulicht.

Als Lichtquelle wurde die Resonanzstrahlung 2537 Å einer Niederdruck-Quecksilberdampflampe benützt. Die von Professor Schulz, Karlsruhe, konstruierte und von der Firma Osram angefertigte Lampe* ist ein U-förmiges Quarzrohr,

* Es sei hierfür auch an dieser Stelle unser besonderer Dank gesagt.

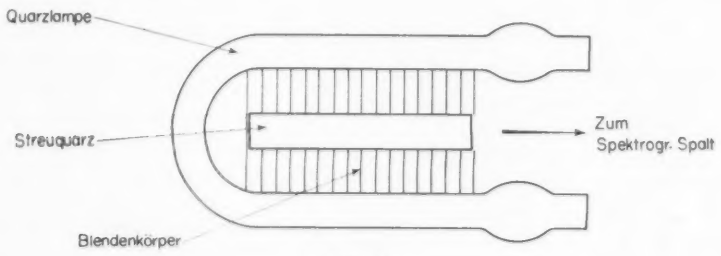

Abb. 1.

zwischen dessen Schenkel der Blendenkörper mit Streustab so eingesetzt werden kann, dass eine Einstrahlung von 2 Seiten möglich ist. Die mit Wechselstrom betriebene Lampe (Brennspannung etwa 75 V, Dauerstrom 18–20 A) besitzt Glühelektroden aus Wolfram und wird nicht gekühlt. Die Füllung besteht aus Neon (10 Torr), Argon (10^{-2} Torr) und Quecksilber. Flüssiges Quecksilber befindet sich in einem Ansatz der Lampe, durch dessen Temperatur der Quecksilberdampfdruck geregelt werden kann. Bei der benutzten Temperatur von 70°C des Ansatzes, entsprechend einem Hg-Dampfdruck von etwa $5 \cdot 10^{-2}$ Torr, ist die Resonanzlinie sehr intensiv und scharf. Mit sehr viel geringerer Intensität erscheint ein Kontinuum in der Umgebung der Resonanzlinie, dessen Intensität mit wachsendem Abstand von $\lambda 2537$ abnimmt.

Zur Aufnahme des Streulichts wurde ein Quarz-Prismenspektrograph in Autokollimation verwendet. Die lineare Dispersion bei 2537 Å beträgt 1,35 Å/mm, das Öffnungsverhältnis ist 1:35. Wegen des kleinen Querschnitts des aus der Stirnfläche des Streustabs austretenden Streulichtbündels konnte bei Verwendung eines Kondensors grosser Brennweite die Lichtstärke des Spektrographen voll ausgenützt werden. Das Spektrum wurde auf Ilford HPS-Platten aufgenommen.

Zur Steigerung der Lichtausbeute der Anordnung wurde ein zylinderförmiger Reflektor aus Aluminiumblech koaxial um Stab und Lampe gelegt, wodurch Primär-und Streuintensität um den Faktor 2 gesteigert werden konnten. Weiter wurden die hinteren Endflächen der Stäbe im Hochvakuum mit Aluminium verspiegelt. Mit $\theta = 90°$ nach hinten (dem Spektrograph abgewandt) gestreutes Licht wird dort senkrecht reflektiert und erhöht die Streuintensität um einen weiteren Faktor 2.

Bei Belichtungszeiten bis zu 25 Std. wurden keine Brillouinkomponenten gefunden, auch nicht andeutungsweise als Trabanten in den Linienflanken des primären falschen Streulichtes. Länger zu belichten hatte keinen Sinn, weil dann die Exposition für das falsche, frequenzunverschobene Streulicht (hauptsächlich von den restlichen Inhomogenitäten des Streukörpers herrührend) so stark wurde, dass das Begleitkontinuum der Primärlinie 2537 Å auf der Platte erschien, wodurch die bei längerer Belichtung eventuell noch auftretenden Brillouinkomponenten überdeckt worden wären.

2. THEORETISCHE ABSCHÄTZUNG DER STREUINTENSITÄT

LEONTOWITSCH und MANDELSTAM[1] spezialisierten die allgemeinen Brillouinschen Überlegungen für verschiedene Kristallklassen. Danach ergibt sich bei einem Streuwinkel $\theta = 90°$ für den isotropen festen Körper

$$\frac{I}{I_0} = \frac{\pi^2 kT}{\lambda^4} \cdot \frac{n^8}{2} \cdot \left[\frac{p_{12}^2 + p_{44}^2}{C_{11}} + \frac{p_{44}^2}{C_{44}} \right] \cdot \frac{V}{R^2} \qquad (1)$$

I Streuintensität im Abstand R vom Streuvolumen V (für beide Brillouinkomponenten zusammen)
I_0 Primärintensität
p_{1k} optisch–elastische Konstanten
C_{1k} elastische Konstanten

Diese Formel für die Intensität ergibt sich auch bei Annahme einer rein statistischen Verteilung von Dichteschwankungen im Sinne von EINSTEIN–SMOLUCHOWSKI (allerdings dann ohne Frequenzänderung).

Unter Benutzung von Messungen der p_{1k} und C_{1k} für geschmolzenen Quarz* von VEDAM[2] hat KRISHNAN[3] den Wert $S = (I/I_0) \cdot R^2/V$ (RAYLEIGH's ratio) berechnet. Bei $T = 300°\text{K}$ und $\lambda = 4358$ Å wird $S = 1{,}63 \cdot 10^{-7}\ \text{cm}^{-1}$. In unserem Falle war $T' \approx 520°\text{K}$, $\lambda' = 2537$ Å, sodass sich ergibt

$$S' = \left(\frac{\lambda}{\lambda'}\right)^4 \frac{T'}{T} \cdot S = 2{,}5 \cdot 10^{-6}\ \text{cm}^{-1} \qquad (2)$$

Bei dieser Umrechnung war angenommen, dass die Änderung der p_{1k} und C_{1k} bei Übergang zu höherer Temperatur unwesentlich ist. Da die C_{1k} in Wirklichkeit dabei abnehmen, ist der Zahlenwert in Gl. (2) etwas zu klein, sodass die folgende Abschätzung nach der sicheren Seite geht.

Stellt man mit dem Primärlicht durch genügend kurze Belichtungszeit eine schwache, aber noch deutlich erkennbare Linie auf der photographischen Platte des Spektrographen her, so lässt sich mit dem Zahlenwert von S' aus Gl. (2) und bei Berücksichtigung der Geometrie der Anordnung

* Bei den die Brillouinstreuung verursachenden Debyewellen langer Wellenlänge ist es unwesentlich, ob das Material kristallin oder nichtkristallin ist.

berechnen, wie lange man belichten muss, um mit dem Brillouinstreulicht Linien derselben Schwärzung zu erhalten, d.h. die Brillouinstreuung gerade noch einwandfrei nachzuweisen. Die Rechnung ergibt mit der experimentell bestimmten relativen Intensität des Primärlichtes als mindestens notwendige Belichtungszeit 4 Min. für Ultrasil, 18 Min. für Homosil und Herasil (der letztere, höhere Wert wegen der stärkeren Absorption dieser Materialien). Nach dieser Abschätzung wäre im Fall des Ultrasil, welches die besten optischen Eigenschaften hat, bei einer Exposition von 7 Std. die Mindestbelichtungszeit schon 100fach überschritten. Tatsächlich konnte auch nach noch längerer Belichtung der Effekt nicht festgestellt werden.

Das Ausbleiben der Brillouinkomponenten lässt vermuten, dass die Debyesche Theorie der Wärmebewegung im unteren Ausläufer des elastischen Spektrums zu unvollständig ist, um die Lichtstreuung quantitativ beschreiben zu können. Es sei angemerkt, dass die Vorstellung der Wärmebewegung nach RAMAN[4] sogar ein vollständiges Fehlen frequenzverschobenen Streulichtes beim Festkörper verständlich macht. Allerdings sind die Vorstellungen von RAMAN umstritten.

3. FRÜHERE MESSUNGEN

Die Brillouinstreuung an festen Körpern untersuchten GROSS[5], RAMAN und VENKATESWARAN[6], KRISHNAN[7], SIRKAR und KASTHA[8].

GROSS, der ein Stufengitter verwandte, bekam im Spektrum eine unübersichtliche Vielfalt von Linien, so dass eine eindeutige Zuordnung nicht möglich war.

RAMAN und VENKATESWARAN verwendeten eine Lummer–Gehrcke-Platte. Sie glaubten mit grösserer Bestimmtheit als GROSS in den aufgenommenen Spektren die Brillouinkomponenten bestimmen zu können ; doch zeigt zumindest die in ihrer Veröffentlichung wiedergegebene Aufnahme ebenfalls eine verwirrende Linienzahl ohne eine ausgeprägte Marke, von der aus die Identifizierung der Linien erfolgen könnte.

KRISHNAN verwendete einen Quarzprismenspektrographen und als Primärlicht die Quecksilberresonanzlinie 2537 A, die bei seiner Lampe eine beträchtliche Verbreiterung zeigt. Um falsches Streulicht nicht in den Spektrographen eindringen zu lassen, setzte er vor den Spalt ein Hg-Dampffilter, welches je nach Grösse und Dampfdruck ein mehr oder weniger breites zentrales Stück aus der verbreiterten Resonanzlinie herausfiltert. Wir haben dieses Verfahren zur Unterdrückung des falschen Streulichtes ebenfalls versucht, es jedoch als ungeeignet abgelehnt, da es bei zu grosser Breite der Absorptionslinie die Brillouinkomponenten ebenfalls absorbiert und bei genügend schmaler Absorptionslinie die stehengebliebenen Flanken der als falsches Streulicht in den Strahlengang gelangten Resonanzlinie als Brillouinkomponenten vortäuscht.

SIRKAR und KASTHA erhielten bei Verwendung eines Konkavgitters eine Aufspaltung der eingestrahlten Linien in Dubletts bei völligem Fehlen eines Streulichtanteils ungeänderter Frequenz. Überraschend und in Widerspruch mit der Theorie ist die hier sehr hohe Intensität des Brillouinstreulichts im Vergleich zum Primärlicht.

Ein einwandfreier Nachweis der Brillouinstreuung in festen Körpern scheint uns daher mit den bisherigen Versuchen nicht erbracht.

Dank der Freundlichkeit von Herrn Professor H. O. KNESER konnten diese untersuchungen im I. Phys. Institut der T.H. Stuttgart durchgeführt werden. Der Spektrographwurde uns vom Bonner Physikalischen Institut, Herrn Professor PAUL, zur Verfügung gestellt und auf Kosten der Deutschen Forschungsgemeinschaft in Stand gesetzt, wofür bestens gedankt sei.

LITERATUR

1. LEONTOWITSCH M. und MANDELSTAM S. *Phys. Z. Sowjet.* **1**, 317 (1932).
2. VEDAM K. *Phys. Rev.* **77**, 472 (1950).
3. KRISHNAN R. S. *Proc. Ind. Acad. Sci.* **37**, 377 (1953).
4. RAMAN C. V. *Proc. Ind. Acad. Sci.* **44**, 99 (1956); **44**, 153 (1956); **44**, 361 (1956).
5. GROSS E. *Z. Phys.* **63**, 685 (1930).
6. RAMAN C. V. und VENKATESWARAN C. S. *Nature, Lond.* **142**, 250 (1938).
7. KRISHNAN R. S. *Nature, Lond.* **159**, 740 (1947); **165**, 406 (1950); **165**, 933 (1950); *Proc. Ind. Acad. Sci.* **37**, 377 (1953).
8. SIRKAR S. C. und KASTHA G. S. *Nature, Lond.* **166**, 1073 (1950).

VOL. 12 59/60

J. Phys. Chem. Solids Pergamon Press 1960. Vol. 12. pp. 344–348. Printed in Great Britain.

ULTRAVIOLET ABSORPTION IN THALLOUS HALIDES*

S. TUTIHASI†

Institute of Optics, University of Rochester, Rochester, New York

(*Received* 3 *August* 1959)

Abstract—The ultraviolet absorption in TlCl and TlBr has been measured on thin films and fused samples as a function of temperature. The effect of excessive chlorine or thallium on the optical absorption of TlCl has been studied. The experiments of VYSOCHANSKII are discussed in the light of our observations.

The first absorption band in TlCl, which peaks at 3·44 eV at −185°C, is absent in films condensed on a cold substrate of KCl and appears after annealing. It seems that the crystal structure of evaporated films of TlCl changes from the NaCl-type to the CsCl-type.

1. INTRODUCTION

IN alkali halides, where the nature of the bond is predominantly ionic, the first absorption bands due to exciton creation are, generally, relatively discrete and presumably well-separated from the onset of continuous absorption associated with band-to-band transition.[1,2,3] In crystals with higher di-electric constants, however, exciton transitions generally are less well resolved from the continuous absorption. This has been found in such materials as germanium[4] and the silver halides.[5] A precise understanding of the relationship of such discrete transitions to the apparently underlying continuous absorption has not been achieved.

In this paper, we report on recent observations of the ultraviolet absorption in thallous halides. The absorption spectra of the thallous halides resemble those of the silver halides. There have been reports[6] on this subject and this paper is hoped to supplement those already published.

2. EXPERIMENTAL

The optical absorption of thallous chloride or bromide was measured on thin film samples, which were evaporated on a quartz, KCl, KBr or NaCl substrate in vacuum, and on fused samples. In the case of evaporated thin films, both the evaporation and the measurements were carried out in the same cryostat so that the films were maintained *in vacuo*, except in the case where chlorine gas was introduced into the cryostat to determine its effect on the absorption.

The optical absorption was measured in terms of the quantity $-\log_{10}(I/I_0)$, where I_0 is the intensity of the incident beam and I is the intensity of the light transmitted by the sample. The data are corrected for the reflection loss which is calculated using the refractive indices for the sodium D line for thallous halides and substrate materials.

The thickness of the evaporated films of TlCl was determined from the position of interference maxima in the transmission spectra of each film. From those data the absolute absorption coefficient was calculated for TlCl.

3. RESULT

In Fig. 1 are given the optical absorption curves of a thin evaporated TlCl film near the absorption edge. The first absorption band, which was first reported by NIKITINE and REISS[7], peaks at 3·44 eV at −185°C and broadens and shifts toward higher energy with increasing temperature. This is peculiar since the exciton absorption bands in alkali halides generally shift toward lower energy with increasing temperature except in a very few cases. The same kind of temperature shift of absorption peaks has been observed in TlBr, Fig. 2, and in CsI.[1] It is interesting to note that these

* Research supported in part by the U.S. Air Force through the Air Force Office of Scientific Research of the Air Research and Development Command.

† Present address: Sylvania Electric Products, 60 Boston Street, Salem, Massachusetts.

materials, in which the opposite shift of exciton bands with temperatures has been observed, all possess the CsCl crystal structure.

The first band in TlCl has a half-width of 0·04 eV at −185°C. Applying the generalized SMAKULA equation,[8] we find the oscillator strength for this

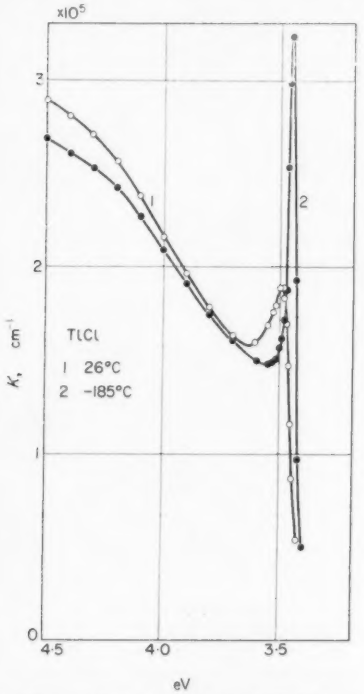

FIG. 1. The optical absorption of TlCl near the edge. The film was evaporated on a single crystal of KCl at room temperature. Curve 1 was measured at room temperature and curve 2 at liquid nitrogen temperature.

transition to be ~0·01, if we neglect any local field correction. If the LORENTZ field correction were applicable, we would obtain a smaller value of the order ~0·002. These numbers are small compared with the value ~0·07 found for the *A*-band in KCl–Tl phosphors.[9]

It is instructive to make a closer study of the temperature dependence of the absorption edge of TlCl (Fig. 3). As has been discussed previously,[6] above about 150°K the apparent absorption edge in macroscopic crystals shifts toward lower energy with increasing temperature. The absorption coefficient above 150°K satisfies

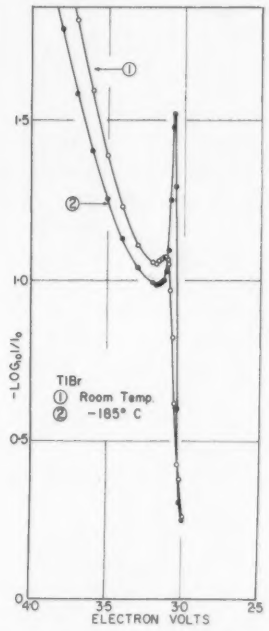

FIG. 2. The optical absorption of TlBr near the edge. The film was evaporated on a quartz substrate at room temperature. Curve 1 was measured at room temperature and curve 2 at liquid nitrogen temperature.

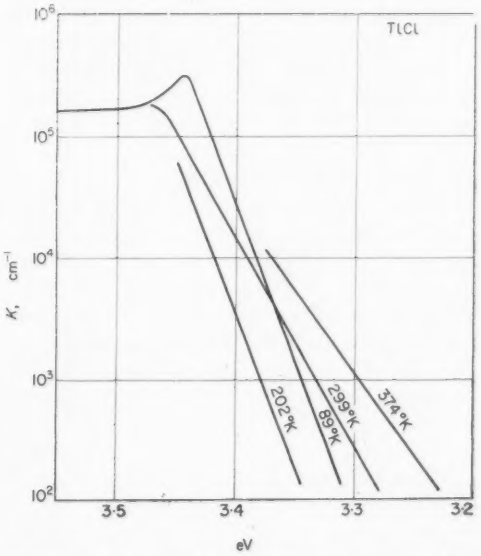

FIG. 3. The absorption edge of TlCl between 89°K and 374°K.

URBACH's[10] exponential rule,

$$K = K_0 \exp\left(-\sigma \frac{h\nu_0 - h\nu}{kT}\right) \qquad (1)$$

with the parameter $\sigma = 1{\cdot}1$. However at lower temperatures, as the apparent edge shifts toward higher energy from its minimum value, the exciton peak shifts toward lower energy becoming more prominent. At liquid nitrogen temperature the absorption edge of TlCl still satisfies an exponential law but with a considerably different value of the coefficient, $\sigma = 0{\cdot}5$. This may indicate that a different absorption process is becoming predominant, perhaps the tail of a discrete exciton line as contrasted with the tail of band-to-band transitions. On the other hand, the quantity kT in equation (1) should probably be interpreted as proportional to the lattice disorder, and at low temperatures one would expect the zero-point oscillation to dominate. Thus the apparent reduction in σ may reflect an absence of a decrease in lattice disorder with decreasing temperature, for reasons both of zero-point vibrations and of permanent disorder in these imperfect films.

The investigation of the temperature dependence of the absorption edge of TlCl reveals further interesting facts. When a film of TlCl is evaporated onto a substrate of KCl crystal, which is kept at −190°C, we find the first exciton band missing completely. The missing exciton band begins to show up upon warming, becoming noticeable at −140°C, Fig. 4. In Fig. 4, optical absorption curves of a thin TlCl film are given at various temperatures. The film of TlCl was evaporated onto a KCl single crystal which was kept at liquid nitrogen temperature. Curve 1 was measured immediately after the evaporation at −190°C. Curves 2, 3 and 4 were measured at −180°C, −160°C and −140°C, respectively. After annealing at room temperature for approximately one hour, the film was cooled to liquid nitrogen temperature. Curve 5 was then measured at −190°C, and is found to be essentially identical to the results observed at −185°C on films evaporated onto the same substrate at room temperature.

SCHULZ[11] has found that very thin films of TlCl crystallize in the NaCl-type crystal structure when grown from the vapor phase on substrates such as KCl or KBr. Combined with SCHULZ's findings, our results can be interpreted as follows. When evaporated onto a cold KCl crystal, TlCl crystallizes in the high temperature modification, the NaCl-type crystal structure, and

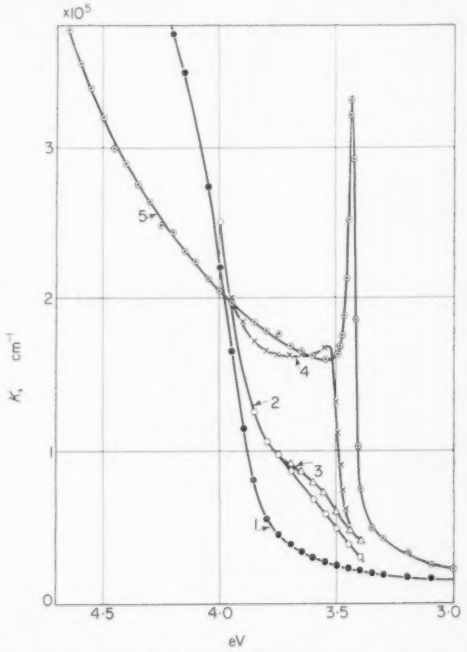

FIG. 4. The optical absorption of TlCl. The film of TlCl was evaporated on a KCl substrate, which was kept at −190°C. The optical absorption was measured immediately after the evaporation (curve 1). Then the film was allowed to warm up. The optical absorption was measured at −180°C (curve 2), at −160°C (curve 3) and at −140°C (curve 4). After the film was annealed for approximately one hr. at room temperature, it was cooled to −190°C again and the absorption was measured (curve 5).

remains frozen. When allowed to warm up, as the temperature of the substrate increases, TlCl transforms into the CsCl type structure, which is stable at low temperatures. The first exciton band, which appears only in annealed films, is evidently characteristic of the CsCl-type modification of the TlCl crystal.

Finally, we would like to make some comments on VYSOCHANSKII's experiments.[12] He has studied the excitation spectrum of luminescence in TlCl at liquid nitrogen temperature and found two maxima, which peak at 3·52 eV and 3·26 eV.

VOL. 12 59/60

He attributes these peaks in excitation to absorption centers associated with a non-stoichiometric excess of thallium in the crystal. The principal support for this conclusion is the circumstance that the peaks disappear after the material has been exposed to chlorine. Our optical absorption measurements on thin films of TlCl before (curve 1) and after (curve 2) the films are exposed to

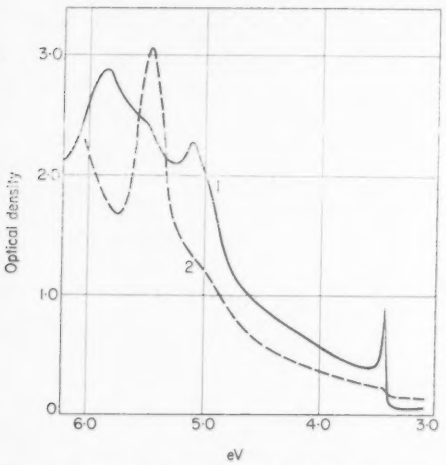

FIG. 5. The optical absorption of thin film of TlCl before and after it has been exposed to chlorine. The film was evaporated on a KCl substrate at room temperature. The optical absorption was measured at liquid nitrogen temperature (curve 1). After the measurement the film was warmed to room temperature and Cl_2 gas of 1–10 mm mercury was introduced into the cryostat. After the film was exposed to Cl_2 gas for approximately 10 minutes, Cl_2 gas was pumped out. The optical absorption of the film was then remeasured at liquid nitrogen temperature (curve 2). Because of the possible change in the thickness of the film after chlorination, no attempt was made to calculate the absolute absorption coefficient for Fig. 5. Absolute absorption coefficient may be obtained, however, by comparing Fig. 5 with Fig. 1.

chlorine gas at a pressure of 1–10 mm of mercury are shown in Fig. 5. The gross dissimilarities between the two curves suggest that a new chemical compound is prepared by the chlorination procedure. This conclusion is supported by chemical analysis of powdered TlCl exposed to chlorine, which demonstrates that the new material is Tl_2Cl_3. Thus the chlorination experiment with TlCl has no pertinence for VYSOCHANSKII's hypothesis that the two peaks in the excitation spectrum at 3·52 eV and 3·26 eV are due to excess thallium centers.

Thin films of TlCl with excess of metallic thallium were made in our laboratories by evaporating TlCl salt and metallic thallium simultaneously on a substrate of either quartz or KCl. With low concentration of thallium, the optical absorption spectra of these films were similar to those of undoped TlCl films. When the concentration of thallium was high, we found the first and second bands of curve 1 in Fig 5 slightly shifted toward higher energies and lowered in magnitude as compared with undoped TlCl. No new band was, however, found at 3·52 eV or 3·26 eV.

The excitation spectrum of luminescence of an alkali halide crystal is known to bear a mirror impression of the absorption spectrum of the crystal.[3, 13] It is likely that the photo-luminescence of TlCl near its absorption edge is caused by the absorption in the bulk material, and the deep drop in the excitation spectrum at 3·44 eV is merely due to high absorption at the exciton peak, as seems to be the case in KI. Such surface effects are commonly observed in luminescence and photoconductivity experiments. All of these observations argue against VYSOCHANSKII's hypothesis regarding the role of excess Tl.

Acknowledgements—It is a pleasure to express my gratitude to Professor D. L. DEXTER for his advice and encouragement throughout this work. I thank Dr. D. B. DUTTON and Dr. R. S. KNOX for their helpful comments and suggestions, and Dr. Y. TOYOZAWA for his valuable discussions.

APPENDIX

Subsequent to the preparation of this manuscript, a paper by ZINNGREBE[14] came to our attention. The observations described here may be compared with those of ZINNGREBE in the following respects: (*a*) the results for temperature dependence of the first absorption band and the apparent absorption edge observed on films evaporated at room temperature are in good agreement with those of ZINNGREBE; (*b*) the change in the absorption spectrum in the vicinity of the first absorption peak, which was observed with increasing temperature in films of TlCl evaporated on a KCl crystal at −190°C, is in qualitative agreement with his results; (*c*) ZINNGREBE has attributed the change to an annealing effect on an amorphous state of the material, whereas we attribute the change, based upon SCHULZ's work,[11] to a crystal structure change from the NaCl-type to the CsCl-type. Recently an effect of the same nature was observed by EBY of our laboratories on thin films of CsCl evaporated on a LiF substrate at room temperature.[15] EBY's observations indicate that fresh films of CsCl condensed

on a LiF substrate crystallize in the NaCl-type crystal structure and transform to the CsCl-type structure with time at room temperature.

REFERENCES

1. MARTIENSSEN W. *J. Phys. Chem. Solids* **2**, 257(1957).
2. TAFT E. A. and PHILIPP H. R. *J. Phys. Chem. Solids* **3**, 1 (1957).
3. TEEGARDEN K. J. *Phys. Rev.* **108**, 660 (1957).
4. MACFARLANE G. G., MCLEAN T. P., QUARRINGTON J. E. and ROBERTS V. *Phys. Rev.* **108**, 1377 (1957). ZWERDLING S. LAX B., ROTH L. M. and BUTTON K. J. *Phys. Rev.* **114**, 80 (1959).
5. OKAMOTO Y. *Nachr. Akad. Wiss. Göttingen* **14**, 275 (1956). TUTIHASI S. *Phys. Rev.* **105**, 882 (1957).
6. MARTIENSSEN W. *J. Phys. Chem. Solids* **8**, 294 (1959). DEXTER D. L. *J. Phys. Chem. Solids* **8**, 473 (1959).
7. NIKITINE S. and REISS R. *C.R. Acad. Sci., Paris* **242**, 1003 (1956).
8. DEXTER D. L. *Phys. Rev.* **101**, 48 (1956).
9. KNOX R. S. and DEXTER D. L. *Phys. Rev.* **104**, 1245 (1956).
10. URBACH F. *Phys. Rev.* **92**, 1324 (1953); MOSER F. and URBACH F. *Phys. Rev.* **102**, 1519 (1956).
11. SCHULZ L. G. *Acta Cryst., Camb.* **4**, 487 (1951).
12. VYSOCHANSKII A. S. *Bull. Akad. Nauk SSSR* **112**, 228 (1957).
13. TEEGARDEN K. *Phys. Rev.* **105**, 1222 (1957).
14. ZINNGREBE H. *Z. Phys.* **154**, 495 (1959).
15. EBY J. E. to be published.

VO
1
1959/

VOL. 12 59/60

The density and lattice parameters of ruby

(*Received* 16 *September* 1959)

CHROMIUM, which is responsible for the red colour of ruby, and which is known to replace aluminium in the corundum (α–Al_2O_3) lattice, produces an increase both in density and in lattice parameters. At low concentrations chromium ions may be considered as point defects, and an experimental study of density and lattice parameters is of interest from the standpoint of the theory of point defects in solids. Earlier work on the subject was rarely concerned with samples in the low concentration range and often lacked precision.

The present measurements were made on 20 artificial crystals of commercial corundum and ruby. The chromium concentration was determined by chemical analysis on the samples used for the measurements, and lay between 0 and 2 molecular percent Cr_2O_3.

Lattice parameters were determined by the back-reflection X-ray powder technique, using aluminium or zinc as an internal standard. Some measurements were made on film in a 57-mm-dia. Seemann–Bohlin camera and others on a Geiger-counter diffractometer. Altogether 17 lattice spacings were measured, from which the parameters a and c of the hexagonal lattice cell were calculated by the method of least squares. The results exhibit a linear dependence on the chromium concentration, and are expressed by the following formulae, valid at 25°C:

$$\left.\begin{aligned} a &= 4{\cdot}7591\ (1+0{\cdot}0527\ C_m)\ \text{Å} \\ &\pm 0{\cdot}0004\ \ \pm 0{\cdot}0016 \\ c &= 12{\cdot}9894\ (1+0{\cdot}0452\ C_m)\ \text{Å} \\ &\pm 0{\cdot}0030\ \ \pm 0{\cdot}0030 \end{aligned}\right\} \quad (1)$$

where C_m is the molecular concentration of Cr_2O_3, varying between 0 and 2 per cent.

The density ρ was measured by hydrostatic weighings in distilled water, bromoform (density at 20°C = 2·892 g/cm³) and an aqueous solution containing 0·5 g/l. of "Nonic 218" as wetting agent. The densities and expansion coefficients of the last two liquids had been previously measured. The temperature of the bath was accurately controlled during weighing. The average of several series of measurements also gives a linear function of C_m; at 25°C:

$$\rho = 3{\cdot}9860\ (1+0{\cdot}341\ C_m)\ \text{g/cm}^3 \\ \pm 0{\cdot}0004\ \ \pm 0{\cdot}003. \quad (2)$$

The X-ray density ρ_r, calculated from equation (1), is

$$\rho_r = 3{\cdot}9864\ (1+0{\cdot}340\ C_m)\ \text{g/cm}^3 \\ \pm 0{\cdot}0020\ \ \pm 0{\cdot}006 \quad (3)$$

in excellent agreement with the measured density. The agreement between the values for the density of corundum supports an observation by SCOTT[1] that this crystal, when grown by the flame-fusion method, has stoichiometric composition. The agreement between the density variations as a function of chromium concentration confirms the substitutional character of chromium.

Our densities are in good agreement with the results of SLAVNOVA and SONIN[2], whose measurements were also made on industrial rubies. We also found reasonable agreement with the lattice-parameter measurements of SHAL'NIKOVA and YAKOVLEV[3], but we disagree with the results of THILO *et al.*[4], who found the lattice parameters unchanged up to 8 molecular per cent Cr_2O_3. THILO *et al.*, as well as SHAL'NIKOVA and YAKOVLEV studied only two or three samples in the low concentration range considered here.

A theoretical interpretation of the results can be based on the continuum theory of lattice defects, as presented by ESHELBY[5]. Detailed calculations have been published recently by one of us,[6] on the assumption that, in an isotropic model, ruby can be described as a corundum continuum, in which spherical holes, corresponding to Al_2O_3 molecules or groups of molecules, are filled by an equal number of Cr_2O_3 molecules, represented by spheres. The relative volume change per unit molecular concentration is

$$\frac{1}{C_m}\frac{\Delta V}{V_0} = \frac{V'-V}{V}\cdot\frac{B'}{B}\cdot\frac{3B+4G}{3B'+4G}. \quad (4)$$

Here B is the bulk modulus of corundum, B' that of Cr_2O_3 and G the shear modulus of corundum;

V is the average volume occupied by one Al_2O_3 molecule in corundum, and V' the corresponding volume in Cr_2O_3. If $B = B'$, this would lead to $\Delta V/C_m V_0 = 0{\cdot}133$, the observed value being 0·151. Considering the crudeness of the model, the agreement is good. A more detailed comparison between theory and experiment is not possible, because the bulk modulus of Cr_2O_3, to our knowledge, has not been measured.

Details of this work will be published in *Helvetica Physica Acta*.

Laboratoire Suisse de Recherches Horlogères
Neuchâtel, Switzerland

J.-P. JAN
S. STEINEMANN
P. DINICHERT

References

1. SCOTT E. J., *J. Chem. Phys.* **23,** 2459 (1955).
2. SLAVNOVA E. N. and SONIN I. N., *Trudy Inst. Kristallogr. Akad. Nauk S.S.S.R.* **8,** 35 (1953).
3. SHAL'NIKOVA N. A. and YAKOVLEV I. A., *Kristallografiya* **1,** 531 (1956).
4. THILO E., JANDER J. and SEEMANN H., *Z. anorg. Chem.* **279,** 2 (1955).
5. ESHELBY J. D., *Solid State Physics* Vol. 3, p. 79. Academic Press, New York (1956).
6. DINICHERT P., *Helv. Phys. Acta* **30,** 463 (1957); *Bull. Soc. Suisse Chron.* **4,** 94 (1957).

Mobility in high-resistivity germanium at high d.c. electric fields

(*Received* 10 *July* 1959; *revised* 3 *September* 1959)

ALTHOUGH there are considerable data on high-field mobility in germanium in the resistivity range 1–10 Ω cm, there are very few data on higher-resistivity material, particularly for fields above 10^4 V/cm. This has already been pointed out by SEEGER[1]. The reasons for this are the difficulty in achieving non-injecting contacts to such material at high fields and in eliminating surface breakdown above 10^4 V/cm. To avoid these difficulties, SEEGER measured the mobility of several *n*- and *p*-type high-resistivity germanium samples, using 34·67-kMc/s microwaves. We have measured the mobility of similar samples up to $\sim 3 \times 10^4$ V/cm, using 3-μ sec d.c. pulses. Such high fields were made possible by using a geometry in which short, very thin filaments were cut on the faces of germanium wafers; a cross-section is shown in Fig. 1. Contacts were made to the end of the filament and to the rim of the wafer. By arranging the polarity so that the outer contact was in the injecting direction, injection could be avoided up to quite high fields. Surface breakdown was successfully eliminated by immersing the filaments in silicone oil. Lattice heating at high

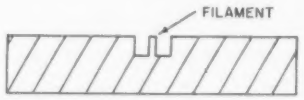

FIG. 1. Cross-section of the samples.

field intensity should not significantly affect the data because of the relative insensitivity of the mobility of hot carriers to lattice temperature. This point was checked by taking measurements at pulse-repetition frequencies between 1 and 20 pulses/sec. This variation in pulse-repetition frequency led to no measurable change in the data, although it should have caused a change in lattice temperature. One may also show the insensitivity of the mobility of hot carriers to lattice temperature by comparing the mobility (or conductivity) as a function of electric field intensity for 300 and 78°K. Whereas the ratio of conductivities of the samples at the two temperatures varies between 6·4 and 14·5 for low electric field intensity, this ratio falls to $\sim 1{\cdot}3$ at 20,000 V/cm. Therefore, the small rise in lattice temperature caused by high voltage pulses should not measurably affect the data.

The data, plotted together with those of SEEGER, are given in Figs. 2 and 3. It is seen that while the results are in fair agreement with those for SEEGER's *p*-type sample at 78°K and his low-resistivity *n*-type sample at 300°K, the fit is poor for the high-resistivity *n*-type sample at 78 and 300°K and for the *p*-type sample at 300°K. SEEGER found a large dependence upon carrier concentration of the slopes of the μ vs. E curves, with the purer samples having smaller negative slopes. No such dependence is found in the d.c. pulse data. The μ vs. E curves for all *n*-type samples measured (in the range 4·6 to 24 Ω cm) were found to be identical. There is a region of -1 slope around 10^4 V/cm for all these samples, in agreement with GUNN's data on 2-Ω cm *n*-type

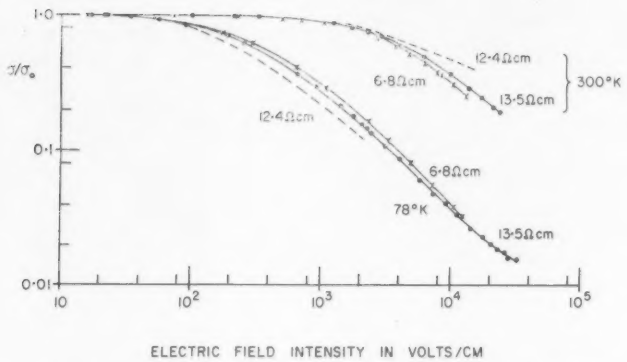

FIG. 2. High d.c. pulse electric field dependence of the mobility of *n*-type germanium plotted with SEEGER's microwave data (dashed curves) on similar samples.

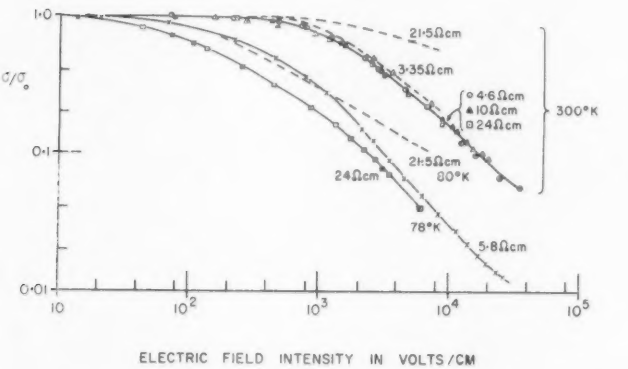

FIG. 3. High d.c. pulse electric field dependence of the mobility of *p*-type germanium plotted with SEEGER's microwave data (dashed curves) on similar samples.

germanium.[2] The —1 slope was also found in the *n*- and *p*-type samples at 78°K. A region of —0·8 slope was found in the curves for the *p*-type samples at 78°K in the field range 10^3 to $\sim 3\times10^3$ V/cm, in agreement with MENDELSON and BRAY[3]. The *p*-type samples at 300°K gave curves having slopes between —0·7 and —0·8 at 10^4 V/cm.

One obvious source of the discrepancy between microwave data and d.c. pulse data lies in frequency effects, since $w\tau$ should not be negligible compared to unity for these samples. If this were the source, the disagreement between microwave and d.c. data should be greater at 78 than at 300°K, since τ is greater for these samples at the lower temperature. It is seen, however, that the disagreement is not greater at 78°K.

Some of the poor fit could be attributed to the relatively poor accuracy in electric-field determination due to small microwave power absorbed in high-resistivity material, as was pointed out by SEEGER. If this were a cause, the fit should be worse for purer samples and for higher fields, as is seen to be the case.

Acknowledgements—I should like to thank Dr. E. M. CONWELL of this laboratory for her continued interest in this work and for discussions on the interpretation of the data, and Dr. A. MANY of the Hebrew University for suggesting the use of samples with one massive end.

Thanks are also due to Mr. A. WILLIS for technical assistance and to Dr. K. ARNOLD and Miss M. TILTON for furnishing the crystals.

Sylvania Research Laboratories J. ZUCKER
Sylvania Electric Products, Inc.
Bayside, N.Y.

References

1. SEEGER K. H., *Phys. Rev.* **114,** 476 (1959).
2. GUNN J. B., *J. Electronics* **2,** 87 (1956).
3. MENDELSON K. S. and BRAY R., *Proc. Phys. Soc. Lond.* B**70,** 899 (1957); *Bull. Amer. Phys. Soc.* **2,** 153 (1957).

VO
1
1959/

L. H. VAN VLACK: **Elements of Materials Science.** Addison-Wesley Publishing Company, Reading, Mass. 1959. 528 pp. $8.50.

ENGINEERING educators are showing an increasing interest in substituting the scientific approach for the descriptive empirical approach in courses on engineering materials. In addition, courses that include ceramics, polymeric and natural materials, as well as metals, are being substituted for service and higher level courses on metals alone. In many instances a principal problem is the current lack of a comprehensive textbook on the subject. Professor VAN VLACK's book is the first elementary text designed to fill this need.

VOL. 12 59/60

After a short introductory chapter, some 300 pages (in 9 chapters) are devoted to a discussion of the structure and properties of materials. Chapters II and III consider the interaction between atoms and molecules and their arrangement in real materials. Chapter IV is devoted to metals and their properties, Chapter V to ceramics and their properties, Chapter VI to organic materials and their properties, Chapters VII and VIII are devoted to multiphase systems, Chapter IX to the modification of properties through changes in microstructure and Chapter X to the effect of macrostructure from the properties of materials. The remainder of the book, some 200 pages, is devoted to a description of the behavior of materials in service, under conditions involving mechanical stresses, thermal reactions, corrosion, electromagnetic fields and radiation. A number of problems follow each chapter, and the answer to every second problem is included in an appendix. The book is beautifully illustrated and printed.

This text is designed for freshmen and sophomore engineering students with a background in physics and chemistry. As such it either ignores or underplays most of the important scientific principles involved in our present understanding of the behavior of engineering materials. It is, therefore, largely descriptive, and uses the language and results of the scientific approach without developing a real understanding. It is the reviewers opinion that the real value of the modern approach to engineering materials in engineering education will be gained when the subject is presented at a rather more sophisticated level to students who have had their proper background in physical chemistry, physics and mathematics.

R. S. DAVIS

U. FANO and G. RACAH: **Irreducible Tensorial Sets.** *Pure and Applied Physics*, Vol. 4. Academic Press, New York, 1958. $6.80.

THE authors, in this book, present a unified account of the methods that underly the quantum theory of angular momentum. In a field where so much work has been done by authors with many points of view and a variety of notations, a coherent presentation in book form is always welcome. This is especially true when one of the authors has pioneered most of the more recent developments in the field.

The book deals with those properties of tensorial sets (for example eigenstates of a given angular momentum, angular momentum operators, etc.) which arise from their transformation properties under three dimensional rotations. The point of view is algebraic and little use is made of group theoretical language. The presentation, is, however, such that it closely parallels a group theoretical development of the same subject.

The organization is in three sections. Part I develops the general algebra of tensorial sets. Part II discusses the application of these to a variety of quantum mechanical problems. The third section of the book contains eleven appendices which discuss in detail points incidental to the developments in Part I. This arrangement allows Part I to be a concise, readable and coherent presentation of the general theory.

In Part I, after a brief description of tensorial sets in general, attention is focused on irreducible tensorial sets. The members of an irreducible set when put in standard form transform into each other as the magnetic substates of a given angular momentum. The conventions of putting irreducible tensorial sets in standard form are discussed. The remainder of Part I discusses products of sets and the reduction of these products to standard form. For the product of two irreducible sets, there is nothing more than the familiar coupling of

angular momentum through the Clebsch–Gordan or Wigner coefficients. The possibility of more than one coupling scheme, which first arises from the coupling of three tensorial sets, is then discussed. With this comes a treatment of the "Racah" coefficients and similar coefficients arising from the transformations between coupling schemes of more than three angular momenta.

The appendices incidental to Part I derive expressions for matrices representing the transformation properties of the irreducible tensorial sets, as well as some of the properties of these matrices. In addition, there are appendices discussing the calculation of the Wigner coefficients, "Racah" coefficients, some of the group theoretical properties of three dimensional rotations, and recoupling diagrams.

The first application discussed in Part II of this book is the coupling and recoupling of eigenstates of various angular momentum operators, leading, in the case of identical particles, to a rather brief discussion of the coefficients of fractional parentage. After pointing out the existence of irreducible sets of operators in quantum mechanical problems, the authors discuss the Wigner–Eckart Theorem, products of irreducible sets of operators, and the interaction of coupled systems with each other and with external fields. The last two sections of this part of the book deal with the expansion of a arbitrary operator into a sum of operators with proper irreducible transformation properties, and the application of these ideas to the distribution of radiation from atomic and nuclear systems, and to angular correlations.

G. F. KOSTER

VO
1
1959/

ERRATUM

E. HIRAHARA and M. MURAKAMI, Magnetic and electrical anisotropies of iron sulfide single crystals, *J. Phys. Chem. Solids* **7**, 283 (1958).

Instead of ln σ, e.s.u. the ordinates of Figs. 2 and 4 should read ln σ, $\Omega^{-1}\text{cm}^{-1}$.

VOL.
12
59/60